THE MECHANISM OF PROTON IRRADIATION-INDUCED CREEP IN ULTRA-FINE GRAIN GRAPHITE

by

Anne Allene Campbell

A dissertation submitted in partial fulfillment
of the requirements for the degree of
Doctor of Philosophy
(Nuclear Engineering and Radiological Sciences)
in the University of Michigan
2014

Doctoral Committee:

Professor Gary S. Was, Chairman
Professor John W. Halloran
John D. Hunn, Oak Ridge National Laboratory
Professor Lumin Wang

This thesis is dedicated to my family

Be it through blood relation, marriage, or friends that I regard as family

None of this would have been possible without your support

ACKNOWLEDGEMENTS

First, I would like to thank my advisor, Professor Gary S. Was, for his guidance and support through my tenure in graduate school, and for his guidance and assistance in completing this work. I would also like the thank the other members of my dissertation committee, Professor John Halloran, Professor Lumin Wang, and Dr. John Hunn, for their insight throughout the graduate process.

Secondly, I would like to thank my colleagues for their unrivaled support and encouragement, thought-provoking discussions, and assistance in the laboratory. To those who were here before me, Gaurav Gupta, Micah Hackett, Deepak Kumar, Pantip Ampornrat, and Elaine West, your guidance has been greatly appreciated. To those who started with me, Janelle Wharry and Kelly Wichman, your continuing support will never be forgotten. To those who have come more recently, Cheng Xu, Mike McMurtrey, Gokce Gulsoy, Kale Stephenson Tyler Moss, Shyamsundar Dwaraknath, Stephen Raiman, Elizabeth Beckett, Anthony Monterrosa, and Justin Hesterberg, I wish all of you the best for all your future endeavors. Special thanks go to Zhijie (George) Jiao, Rongsheng Zhou, Vani Shankar, and Cheng Xu, for their help in the early stages of getting my experimental system operational.

I would like to thank Ovidiu Toader and Fabian Naab for all their assistance during my numerous protons irradiation at the Michigan Ion Beam Laboratory, and Alexander Flick for all the times he has given me assistance with electrical problems. I would like the thank John Mansfield, Kai Sun, Haiping Sun, and Ying Qi, at the Electron Microbeam Analysis Laboratory for their assistance with XRD, TEM, and nanoindentation measurements. Additionally I would like to thank Professor Michael Atzmon for his time, guidance, and insightful discussions about the Williamson-Hall analysis of XRD spectra.

Lastly, but most importantly, I need to extend my most heartfelt gratitude to my parents (Bill and Mary Ann Davis), my brother (Will Davis), my extended family, my

husband's family, my friends that are as close to me as family, and most importantly my husband (Kent Campbell) for their belief in my dreams, and the continuous support and encouragement in all the endeavors I have set out to accomplish.

This work was supported by the U.S. Department of Energy under NERI Contract #FC07-06ID14732 and Idaho National Laboratory under Contract #DE-AC07-05ID14517

TABLE OF CONTENTS

LIST OF FIGURES

LIST OF TABLES

LIST OF APPENDICES

LIST OF ABBREVIATIONS

AOI	Area of Interest
BAF	Bacon Anisotropy Factor
CGDB	Climb and Glide from Dislocation Bias
DVRT	Differential Variable Reluctance Transducer
EDM	Electrical Discharge Machining
FFT	Fast Fourier Transform
GAAP	Graphite Anisotropy Analysis Program
LSE	Laser Speckle Extensometer
PAG	Preferential Absorption Glide
PBN	Pyrolytic Coated Boron Nitride
PG	Pyrolytic Graphite
PKA	Primary Knock-on Atoms
R	Orientation Parameter
ROI	Regions of Interest
SAED	Selected Area Electron Diffraction
SIPA	Stress-Induced Preferential Absorption
SIPN	Stress-Induced Preferential Nucleation of Loops
SKA	Secondary Knock-on Atom
SRIM	Stopping and Range of Ions in Matter
TEM	Transmission Electron Microscopy
XRD	X-Ray diffraction

ABSTRACT

THE MECHANISM OF PROTON IRRADIATION-INDUCED CREEP IN ULTRA-FINE GRAIN GRAPHITE

by

Anne Allene Campbell

Chair: Gary S. Was

The objective of this work was to determine the mechanism of proton irradiation-induced creep of ultra-fine grain graphite. Graphite is currently used as a structural material in nuclear reactors in the United Kingdom and is planned for future use in the Very High Temperature Reactor. Temperature and dose gradients within these structural components result in build-up of stresses that would surpass the fracture stress, but irradiation-induced creep allows for relaxation of some of these stresses. Thus it is critical to understand the mechanism that controls irradiation-induced creep in graphite to be able to predict the integrity of these current and future structural components.

This work used POCO Graphite Inc. grade ZXF-5Q, which is an ultra-fine grain graphite. The proton irradiation-induced creep experiments were performed with a range of experimental conditions to investigate the effects of applied tensile stress, dose rate, irradiation temperature, and total accumulated dose. These experiments showed a linear dependence of creep rate on applied stress and dose rate, an Arrhenius dependence of creep compliance on temperature, and no effect of accumulated dose out to 1dpa.

Using the experimental dependencies, it was found via process of elimination that the most probable mechanism controlling irradiation-induced creep Stress-Induced Preferential Absorption (SIPA) of defects at dislocations. This mechanism was further supported with the investigation of the post-irradiation Young's modulus. The Young's modulus was not affected by total dose thus agreeing with a steady-state creep regime, higher applied stress reduced Young's modulus thus agreeing with either traditional SIPA or anisotropic diffusion SIPA; and finally, Young's modulus increased with increasing temperature thus agreeing with the calculated interstitial concentrations being higher for the higher temperature experiments.

Microstructural analysis investigated the effect of experimental conditions on the lattice spacing, uniformity of lattice spacing, and crystallite sizes. The results of these measurements agreed with the dependencies expected for the newly-proposed mechanism of radiation damage in graphite, which occurs when vacancy lines and loops disassociate into two dislocations, instead of the traditional theory that dimensional changes were due to the formation and growth of interstitial loops.

CHAPTER 1

INTRODUCTION

The Very High Temperature Reactor (VHTR) will revolutionize the way nuclear energy is utilized in the United States of America and throughout the world. The reactor will provide not just electricity, but will also be used to provide process heat and hydrogen production for industrial applications [1]. The current reactor and site design will co-locate the plant with an industrial complex that will utilize the electricity and the process heat. The process heat will be utilized to provide steam for ammonia and fertilizer plants, petrochemical plants, and oil refineries. The electricity, hydrogen, and process steam will be used in the conversion of coal and natural gas to liquid fuels, and to enhance recovery of Bitumen from oil sands[1]. The other benefit of this reactor is the high operating temperature, which will produce electricity with a higher efficiency, and therefore lower cost.

The high operating temperatures of the VHTR result in numerous advantages, but also in some design challenges. The current design will operate with gas outlet temperatures ranging from 750°C to 1000°C, but these conditions will require the implementation of high temperature materials. The high temperature materials are required for the fuel to withstand temperatures as high as 1600°C, core structural materials must be stable at temperatures up to 1300°C, and metal components will have to withstand temperatures up to 1000°C. These requirements are met with the use of graphite as the core structural material, ceramic coated fuel, and high temperature alloys where metal is required instead of a ceramic.

The graphite core structural materials will be used for a range of applications. Primarily the structural materials will support the fuel or act as inner and outer core reflectors. All of the graphite components in the reactor will be subjected to temperature and irradiation dose gradients. It has been shown that these temperature and dose gradients cause stress build-up within the components that would exceed the fracture

stress of the graphite, but irradiation creep allows for relaxation of some of these stresses and keeps the components whole [2].

When any material is exposed to temperatures above 40% of the melting temperature, under an applied stress, the material will undergo a time-dependent permanent plastic deformation called thermal creep. When exposed to irradiation, it can undergo creep at temperatures much lower than those for thermal creep; this process is called irradiation-induced creep. This thesis will focus on the irradiation-induced creep behavior of graphite for its use as structural components within the VHTR.

The mechanism of irradiation-induced creep of graphite must be known to be able to reliably predict components behavior. Space limitations of the reactor-based irradiation creep experiments make temperature control, dimensional change measurements, and stress application very difficult to control. The temperature of the samples has never been directly measured, instead a thermocouple measures the temperature of a near-by component and then computer models are used to estimate the sample temperature. The change in dimension of the sample is generally determined by measuring the size of the sample before and after irradiation. Another problem arising from reactor-based creep experiments is that the experiments are performed on only nuclear applicable grades of graphite, which have numerous features within microstructure [3] that may have different effects on creep behavior. Knowing the precise sample temperature, the continuous dimensional change, and the applied stress are necessary to determine the mechanism of irradiation creep.

This thesis will present work that uses protons instead of neutrons as the irradiation particle to cause irradiation-induced creep. One advantage is that the experiments with protons can achieve a factor of ten higher irradiation damage rates, which reduces irradiation time from a number of months to a few days. Another advantage is that irradiation with protons results in minimal sample activation so post-irradiation analysis can be performed days after completion of the experiment in a laboratory, rather than having to wait for many months for the sample activation to decrease to safe handling levels or performing analysis in special radiation-safe facilities. The third advantage is that there is more available space with accelerator facilities so the sample temperature and dimensional changes can be measured and recorded continuously

throughout the experiment without the measurement methods being limited by size. The primary drawback is that the proton experiments must be kept under vacuum which limits how the temperature and dimensional changes can be measured. These confines required that methods of non-contact temperature and dimensional change measurements be utilized for these experiments.

The objective of this research is to determine the mechanism of irradiation-induced creep in ultra-fine grain POCO graphite. The second chapter of this thesis will cover the background literature on graphite, including microstructure, irradiation effects, and the irradiation-induced creep behavior. The third chapter of this thesis will give a detailed discussion of the experimental procedures used for this research. The fourth chapter will present the experimental results from the irradiation-induced creep experiments, and the post-experiment analysis performed on the samples. The fifth chapter will determine the mechanism of irradiation-induced creep in graphite and compare the experimental results with the proposed mechanism. The last chapter will present the conclusions of this thesis.

CHAPTER 2
BACKGROUND

This chapter will provide a review of the published research that is of importance for studying irradiation creep of graphite. Carbon, denoted as C, is the sixth element in the periodic table. Carbon consists of two naturally occurring isotopes, C-12 and C-13, with atomic weights of 12.0amu and 13.003amu, and abundances of 98.93% and 1.07% respectively [4]. The electron structure of carbon is $1s^2 2s^2 2p^2$ resulting in a valence of 4. The two naturally occurring structures of pure carbon are diamond and graphite. The primary carbon form being studied is graphite, which is a naturally occurring structure for carbon, but the graphite for this research is synthetic.

2.1 Structure

This section presents the primary structures of graphite: the hexagonal, rhombohedral, and turbostratic structures. Early graphite grades used in the nuclear industry were from naturally-occurring graphite. These early grades had a high concentration of impurities which increase the neutron absorption cross section. The only way to reduce the impurities is to use artificially created grades of graphite.

The valence state of a carbon atom is 4, which results in very different carbon atom bonding possibilities. In diamond, carbon atoms are in a tetragonal covalently-bonded structure, while graphite has carbon atoms in trigonal covalently-bonded basal planes with van der Waal bonding between planes. Even within graphite there are three crystal structures that arise: hexagonal, rhombohedral, and turbostratic. In all three structures, the carbon atoms are arranged in a hexagonal pattern to form the basal planes with interatomic spacing of 1.42Å [5]. The primary difference between the three structures arises from the stacking nature of the basal planes.

2.1.1 Hexagonal

The primary structure for graphite is the hexagonal structure, shown in Figure 2.1. In this structure, the basal planes are stacked in an ABAB sequence. In each hexagonal ring of carbon atoms, three locations have atoms located on the same site in each basal plane, shown on the left side of Figure 2.1. In Figure 2.1, the carbon hexagonal ring is emphasized on the A planes, and a trace of the ring is shown on the B plane. The blue atoms represent the sites that are occupied by atoms on each basal plane, the pink atoms represent the sites where atoms are only present in the A planes, and the orange atoms represent the sites where atoms are only present in the B planes.

The unit cell of the hexagonal crystal structure is highlighted on the right side of Figure 2.1. The unit cell has 12 shared corner atoms (green), two shared face atoms (yellow), and one internal atom (purple) resulting in 4 total atoms in each cell. The dimensions of the unit cell are a=2.4612Å, c=6.7079Å [6].

2.1.2 Rhombohedral

The rhombohedral structure, Figure 2.2, is similar to hexagonal, except that the basal planes are stacked in the ABCABC sequence. In Figure 2.2, the carbon hexagonal ring is emphasized on the A planes, and a trace of the ring is shown on the B and C planes. The blue atoms represent the sites that are occupied on the A and B planes, the pink atoms represent the sites that are occupied on the A and C planes, and the orange atoms represent the sites that are occupied on the B and C planes.

The unit cell of the rhombohedral crystal structure is highlighted on the right side of Figure 2.2. The unit cell has 12 shared corner atoms (green), two shared face atoms (yellow), and three internal atoms (purple) resulting in 6 total atoms in each cell. The dimensions of the unit cell are a=2.4612Å, c=10.0619Å [6].

2.1.3 Turbostratic

The third structure for graphite is turbostratic. Turbostratic still has carbon atoms arranged in the hexagonal basal plane structure, but unlike hexagonal and rhombohedral, there is no defined stacking pattern between basal planes. Instead of ABAB or ABCABC

stacking the basal planes are randomly translated and rotated from one plane to the next. This type of stacking results in basal plane spacing greater than the 3.35395Å that occurs in the two crystalline microstructures.

2.2 Microstructure Defects

This section will present the microstructure defects that occur in graphite. First single defects will be presented with the preferred locations and resulting changes in the microstructure. Then the larger defect structures that can occur will be presented.

2.2.1 Small Defects

Vacancies and interstitials are the primary singular defects in graphite. The review paper by Thrower and Mayer [7], provided a thorough discussion of experiments that resulted in the thermodynamic properties of defect production. These values included the entropy of formation (Sf), entropy of migration (Sm), energy of formation (Ef), energy of migration parallel to and through the basal planes (Ema and Eca respectively), and jump frequency (ν), for both interstitials and vacancies; these are listed in Table 2.1. The displacement energy to form Frenkel defects is dependent on orientation relative to the basal planes, but the average value was determined to be 33eV [8].

Interstitials can occupy many different locations in the hexagonal structure. Five primary locations are discussed by Kelly [9]. A schematic of these five positions is presented in Figure 2.3 as green atoms labeled A-E. The bonds between the interstitials and neighboring atoms are shown as dashed lines. The interstitial location A is a carbon interstitial bonded to two carbon atoms (orange atoms in schematic) on non-coincident sites on the adjacent basal planes. The interstitial location B is an interstitial bonded between two carbon atoms (light blue atoms in schematic) that are on coincident sites on the adjacent basal planes. The interstitial location C is a carbon interstitial bonded to three carbon atoms (purple atoms in schematic) on the basal plane above and one carbon atom below. The interstitial location D is only bound to two or three carbon atoms (yellow atoms in schematic) on a single basal plane. The interstitial location E is not

bound to any carbon atoms. Two newer positions are presented by Telling and Heggie [10] and are also shown in Figure 2.3. The spiro (S) positions differ from A and C, in that the interstitial is bound to two atoms on each surrounding basal plane (brown atoms in schematic). The ylid (Y) position is the saddle point for the migration of an interstitial through progressive S-type configuration (dark blue atoms in schematic). The spiro (S) position differs from A and C above, in that the interstitial is bound to two atoms on each surrounding basal plane (brown atoms in schematic). The ylid (Y) position is the saddle point for the migration of an interstitial from the S to S'through progressive S-type configuration (dark blue atoms in schematic). The spiro and ylid cross-link the planes and can be possible dislocation pinning points [10]. The problem with these interstitial configurations is that some of the atoms in the basal planes are bound with 4 neighbor atoms (diamond bonding) which should require a large amount of energy to occur. Some of these configurations may occur, but it is more likely that the interstitials occur in sites between basal planes, directly below one atom and above a hexagon center, forming no bonds with the surrounding atoms and are in their ground state [7].

Di-interstitials (C_2) are also present in graphite. The formation of a C_2 cluster releases 7eV, with a bond length of 1.24Å, and the migration energy is 0.05eV [9]. The C_2 cluster has one possible orientation, one atom is located below the center of the hexagon ring on the upper basal plane and the other is located above the center of the hexagon ring on the lower basal plane. The cluster is not parallel to the basal planes, instead the atoms are slightly shifted towards the respective ring centers, so the mid-point of the bond is located an equal distance from the two surrounding planes. A linear C_3 can be formed by a single carbon atom approaching a C_2, with atomic spacing of 1.28Å [9]. A linear C_4 is possible but not likely, it is more probable that it will break into two C_2 or form a tetragonally bonded cluster [9].

A single vacancy has one effect on the surrounding structure. When a vacancy occurs, the surrounding unbound atoms are 2.46Å apart, and then the structure undergoes reconstruction, where two of the unbound atoms bind forming a pentagonal ring with a bond length of 2.1Å and the third unbound atom raises off the basal plane by ~0.5Å [10]. A di-vacancy stabilizes by forming two pentagonal rings and one octagonal ring where the distance of the unbounded atoms decreases from 2.46Å to 1.7Å [10]. A schematic of

the unreconstructed (A) and reconstructed (A') vacancy arrangement, and the di-vacancy (B) arrangements, are shown in Figure 2.4.

Besides defined interstitials and vacancies, two other single defects that occur are the intimate Frenkel-pair and the Stone-Wales defect. A schematic representation of the intimate Frenkel-pair is presented in Figure 2.5. The intimate Frenkel-pair occurs when the displaced carbon interstitial (green atom) is still covalently bonded with one of the original nearest neighbor atoms and forms two covalent bonds with two carbon atoms in the basal plane below (orange atoms) and the vacancy is indicated with the dashed circle. The intimate Frenkel-pair was proposed by Ewels et al. [11] and was observed by Urita et al. [12]. The Stone-Wales defect occurs when two carbon atoms rotate 90 degrees around the center of their bond, forming two pentagonal carbon rings and two heptagonal rings. A schematic representation of the Stone-Wales defect is presented in Figure 2.6, where the original atom locations and bonds are indicated with the dashed lines. This defect was proposed by Dienes [13] as a mechanism for self-diffusion in graphite with a formation energy of 3.9eV per atom, and received its name from work presented by Stone and Wales [14].

2.2.2 Large Defects

Dislocations in graphite have two orientations, non-basal and basal. The non-basal, partial prismatic edge dislocation loops are edge dislocation types with $\vec{\boldsymbol{b}} = \frac{c}{2}[0001]$, and are due to the insertion or removal of a circular or hexagonal area of a basal plane, while the insertion or removal of two planes changes to a perfect prismatic dislocation [9, 10]. These loops are hexagonal when the temperature is below 1173K because growth is dominated by interstitial addition to the lowest energy growth zone, and for temperature above 1473K the loops are circular because the shape is dominated by the need to minimize the dislocation line energy [10]. The basal plane dislocations occur in pairs with each being a partial dislocation, the total dislocation is $\frac{a}{3}\langle 11\bar{2}0\rangle$ [9]. The glide plane in graphite is the basal plane, so the Burger's vector must be perpendicular to the c-direction for the dislocation to be glissile. The non-glissile basal

dislocations require the breaking of multiple c-c bonds to move. Two non-glissile ring dislocations will decrease the energy by dissociating into two single-layer rings, which results in the center of the loop being unfaulted from the surrounding material. Figure 2.7, from [15], shows a schematic of this dissociation process (a) and a micrograph of graphite with this dissociation visible (b).

Vacancies form into two large features, disc type and line-like. A through description of the disc and line vacancy formations is presented by Telling and Heggie [10], and is briefly presented here. The disc types are very similar to interstitial clusters. It has been observed that a single layer cavity will transform into a partial prismatic dislocation with $\vec{\boldsymbol{b}} = \frac{1}{2}c\langle 0001\rangle + \frac{1}{3}a\langle \bar{1}2\bar{1}0\rangle$ for a critical cavity diameter of 225Å, while a two layer cavity will transform to a perfect prismatic dislocation with $\vec{\boldsymbol{b}} = c[0001]$ for a critical radius of 425Å. The line-like dislocations are different from the discs because of the tendency of the lines to reconstruct within the basal plane. There are two line dislocations types, boat edge and zig-zag. Schematics of the two types are presented in Figure 2.8. The boat edge is more energetically favorable because the bond reconstruction length is shorter than zig-zag. Also shown in Figure 2.8 are the different ends that occur when the vacancy lines collapse. For a collapsed line, with an even number of vacancies, the ends consist of a closed seven atom ring and a closed five atom ring, while a collapsed line, with an odd number of vacancies, the ends consist of an open eight atom ring and a closed six atom ring.

2.3 Manufacture

This section presents the manufacture process for graphite. The microstructure is very dependent on the manufacture process, but primarily depends on the supply materials. Graphite is produced from either coke sources or a pyrolytic method. The coke source process will be discussed here because it is the manufacture method for the graphite samples being used in the nuclear industry.

The coke source comes from either naturally occurring pitch sources or from by-products from the petroleum industry. The coke is calcined in the range of 900°C-

1300°C, which removes any volatile contents. Next the coke is crushed, milled, and sized into different fractions. The shape and properties of the crushed coke is dependent on the source. The desired coke sizes are mixed and blended with a coal tar pitch, heated to ensure homogeneity and then formed into the desired shape by extrusion or molding. Isostatic forming is used to achieve an isotropic final material. The shaped material is baked to coke the pitch binder from 700°C-900°C for 30-70 days, which volatizes ~1/3 of the pitch binder. After baking, the material is impregnated with coal tar pitch to replace some of the lost pitch binder. The impregnation pitch has a lower melting temperature so that it can flow into the pores. Rebaking occurs to pyrolise the impregnated carbon. The density and strength increase for up to six cycles of impregnation, but 2-3 are usually sufficient. The final step is graphitization from 2600°C-3000°C for 15 days [9].

During the graphitization step the differences of thermal expansion coefficients in the c-direction (high) and a-direction (low) result in large internal stresses. During cooling, while still above 2000°C, creep reduces some of the stress due to these CTE differences. Below 2000°C creep cannot accommodate these stresses and cracks form to relieve the stress. Mrozowski was the first person to observe and analyze these cracks, hence they are referred to as Mrozowski cracks. Morozowski found that at 3000°C there was an 8% thermal expansion in the c-axis from room temperature, but creep only relieves ~3% above 2200°C, so a minimum 5% porosity occurs in polycrystalline graphite [9].

2.4 Thermal Creep Behavior

This section will present the thermal creep behavior of graphite. The high temperature creep behavior of graphite has been studied but most of the work fit the experimental data with empirical fits. Understanding thermal creep behavior will assist in understanding the irradiation creep behavior.

Initial studies of thermal creep were performed on natural graphite crystals and a Union Carbide graphte [9]. These studies found that even though the total strain varied between samples, the time dependent strain is well represented by:

$$\varepsilon = \varepsilon_0 + \beta t^m + kt\,. \tag{2.1}$$

For low stresses the time exponential, *m*, is best fit for a value of 0.121 meaning low stress thermal creep is near logarithmic. For higher stresses the time exponential is best fit for a value of 0.33 meaning that for higher applied stress the creep is Andrade. The Union Carbide graphite did not have the different time exponentials; instead it has a logarithmic dependence of all stresses.

Reactor graphite, petroleum and pitch graphites, cellulose carbon, carbon black, and natural graphite were studied for 1000°C-2000°C [9]. It was found that for all the materials studied, the relationship holds for all as long as the correct moduli are used. The strain equation from Davidson & Lotsy, described in [9], gives an equation for the strain as a function of time:

$$\varepsilon = \sigma\left[\frac{1}{E_T} + \frac{C}{E_0}\exp\left(\frac{-E_1}{kT}\right)\log_{10}\frac{t}{1} + Dt\exp\left(\frac{-E_2}{kT}\right)\right], \tag{2.2}$$

where time (*t*) is measured in minutes, temperature (*T*) is in Kelvin, strain is measured beginning after time of 1minute, E_0 and E_T are Young's modulus at room temperature and at experiment temperature in Kelvin, *C*-universal constant ~13, *D*=constant, and E_1 and E_2 are activation energies. Kelly [9] also reported work from Malstrom, who reported the first creep experiments from 2400°C-3000°C. The equation for strain as a function of time is:

$$\varepsilon = \frac{\sigma}{E_T} + f_1(\sigma) * \ln t * \exp\left(\frac{-E_3}{kT}\right) + f_2(\sigma) * t * \exp\left(\frac{-E_4}{kT}\right), \tag{2.3}$$

where f_1 and f_2 are functions of σ, E_3=3-4.5eV, E_4=4-8eV. Malstrom also found that load removal results in recovery of <1/2 transient strain. Work from Martens, presented by Kelly [9], studied creep in commercial polycrystalline graphite for temperatures greater than 1500°C. This work found that Equation (2.3) best fit the experimental data. It was found that there is a square dependence on stress and the creep rate increases continually with temperature. Preheating the sample to a temperature above the creep temperature reduces the creep rate. Also seen is that approximately one third of the creep strain at 2600°C is recoverable with stress removal, increasing the recovery temperature increases

the recovery rate, and the recovery rate is logarithmic. This recoverable creep means there must be two distinct processes [9].

Wagner studied creep in both tension and compression from 2000°C-3000°C [16, 17]. Only the secondary creep regime was fit for time, temperature, and stress resulting in strain as a function of time given by:

$$\frac{d\varepsilon}{dt} = K\left(\frac{\sigma}{\sigma_f}\right)^{3.8} \exp\left(\frac{-E_4}{kT}\right), \tag{2.4}$$

where K is 40 for compression K is 4 for tension, σ_f is failure stress, E_4 is 2eV compression and E_4 is 2.5eV tension.

Work from Zukas and Green [18], presents the most comprehensive set of thermal creep experiments on polycrystalline graphite. This work led to Green et.al. [19] presenting a mechanism that describes thermal creep of polycrystalline graphite. The creep experiments studied the tensile and compressive creep as a function of temperature, and stress relative to an angle, ϕ, off the preferred c-axis orientation direction. They found that strain rate in compression has little dependence on ϕ (only a factor of 4 from minimum to maximum), the maximum creep rate occurs at ϕ of 45°, and the compression strain to failure was around 3% and is also independent of ϕ. While the strain rate in tension has a strong dependence on ϕ where strain rate at ϕ of zero is five orders of magnitude larger than the strain rate for ϕ of 90°, as is the strain to failure, but for ϕ of 90 the strain to failure is around 3% as seen for compression. It was found that the strain rate has a stress to the eighth power dependence. The tension activation energy was determined to be 277kcal/mol and has no ϕ dependence. The tensile creep samples show a large number of cracks parallel to the basal planes that increase as strain increases. This cracking has an effect on the apparent creep rate, ductility, and ϕ. When strain measurements were made between cracks the strains were close to zero, but when measurements were made over several cracks the strain was of the same order of magnitude as the macroscopic strain. The possible mechanisms are discussed with these initial results. For creep to be a shear process, the rate of slip and thus creep rate, should be a function of shear stress. Hexagonal crystals have only one slip plane, but six equally spaced directions, so the maximum shear stress occurs when the basal plane is inclined 45° to the stress direction. However if creep is cleavage based then the maximum creep

rate should occur when the cleavage plane (basal), is perpendicular ϕ of zero. For compression, the maximum creep rate occurred when ϕ was 45° indicating that compression undergoes a slip mechanism. Since the activation energies of compression and tension and the stress dependence are almost equal it stands that the same mechanism for compression should apply for tension, but tension has a crack growth feature that dominate the slip process.

From the data and trends presented in [18], Green et al. [19] present a theory for the creep mechanism for tensile stress. The basis of the mechanism is that cracks of width 2*w* nucleate dislocations with Burger's vector perpendicular to the crack plane, with an edge character. The dislocations move away from the crack tip by climb and vacancies flow from the dislocation to crack tip (or interstitials to the dislocation from the crack) under tensile stress. It is assumed that a crack width is between 1-10x10^{-4}cm such that dislocation description rather than macroscopic plasticity is suitable at the crack tip. It is also assumed that *w* doesn't change, but the crack faces separate as vacancies are absorbed by the crack and further dislocations are emitted from the tip. These assumptions give strain and initial strain according to:

$$\varepsilon = \frac{\pi N \sigma w \left(b^2 - w^2\right)^{1/2}}{\mu\left[1 - \frac{2}{\pi}\sin^{-1}\left(\frac{w}{b}\right)\right]}, \tag{2.5}$$

$$\varepsilon_0 = \frac{N\bar{\sigma}}{2\mu} w^2 \pi^2 \tag{2.6}$$

where *N* is the crack/area, 2*w* is crack width, *b* is the position of the dislocation that is furthest from the crack, μ shear modulus for a hexagonal material, N_c carbon atomic density, *D* separation of crack surfaces. It was found that $\varepsilon - \varepsilon_0 < 3\varepsilon_0$ the resulting strain equation is:

$$\varepsilon - \varepsilon_0 = \frac{2\pi^2 w N \sigma}{3}\left[\frac{D}{N_c \mu k T}\right]^{1/2} t^{1/2}, \tag{2.7}$$

but for $\varepsilon - \varepsilon_0 >> 3\varepsilon_0$ the resulting strain equation is:

$$\varepsilon - \varepsilon_0 = \frac{4N\sigma D}{N_c kT} t \,. \tag{2.8}$$

For creep recovery, the initial strain is recovered instantly, and the time dependence of the recovery term relied on the rate of climb of dislocations back into the cracks. It was noticed that the stress dependence was not linear but was closer to a power of 3-4. The authors proposed that, as the load is applied, the number density of cracks increased due to the opening of small cracks in the stress field of larger cracks. The Griffith equation was used to estimate:

$$w \cong \frac{2\gamma\mu}{\pi\sigma^2}, \tag{2.9}$$

where γ is the surface energy of cracks in basal planes of graphite. Using $Nw^2 \sim 1$ for infinite crack or $Nw^3 \sim 1$ for finite cracks gives:

$$\varepsilon - \varepsilon_0 = \frac{\pi^3}{6}\frac{\sigma^3}{\gamma\mu^2}\left[\frac{\mu D}{N_c kT}\right]^{1/2} t^{1/2} = \varepsilon_0 \frac{2\pi}{3}\frac{\sigma^2}{\gamma\mu}\left[\frac{\mu D}{N_c kT}\right]^{1/2} t^{1/2}, \tag{2.10}$$

which gives reasonable stress dependence, and agreement of the total strain as long as the elastic strain constants of the material are corrected for thermal expansion [19].

There has been limited thermal creep studied on single crystal graphite, but some work was performed on highly oriented pyrolytic graphite (HOPG) at temperatures above 2500°C and with stress parallel to the basal planes [9]. The first stage of thermal creep showed removal of the growth cones up to 10%, but further elongation produced a smooth surface that gradually developed irregular undulation that was visible in the direction of applied stress.

Jenkins [20] presents a theoretical model of high temperature deformation of HOPG. Due to the low interaction between the planes, he assumes that each plane deforms as a separate unit. Dewrinkling of the basal planes resulted in basal shear. If the basal dislocations intersect and pass through the c-axis screw dislocation then the screw is broken into short lengths. This mechanism dies as the growth cones disappear.

2.5 Irradiation Effects

This section will present and discuss the changes that occur in graphite when exposed to irradiation without any applied external stress. This section, combined with the thermal creep section will be helpful for later interpretation of the irradiation creep behavior.

The overall behavior of graphite is fairly consistent for the grades being studied for nuclear reactors. The currently proposed and accepted behavior process is that the graphite undergoes volumetric shrinkage, which is due to the basal plane contraction and expansion of c-direction into the porosity of the Mrozowski cracks, but as the cracks get filled in, the volumetric contraction slows down until shrinkage is no longer possible and swelling takes over. The point where the volumetric change changes from shrinkage to swelling is called the turn-around point. The amount of shrinkage that can occur and the dose at which turn-around occur are very dependent on the irradiation temperature. At higher temperatures, thermal expansion of the crystals has already filled a portion of the porosity thus the pore volume that can accommodate c-direction swelling is less, resulting in less expansion before the pores are filled. Thus as the temperature of irradiation is increased the total shrinkage at turn-around decreases as does the dose at which turn-around occurs. When graphite is discussed for use in reactors, the lifetime is given, where the lifetime is the amount of dose that causes the graphite to undergo shrinkage and swell back to initial volume. The end of life has the same dependence on temperature, where a higher temperature results in a shorter lifetime.

The current accepted mechanism of irradiation effects in graphite is that displaced atoms from irradiation move to the interstitial locations, leaving vacancies in the basal planes, and as the interstitials become more mobile they form clusters and eventually new planes while vacancy lines collapse to cause basal contraction [21, 22]. These displaced atoms cause the increase in graphite strength and Young's modulus, which is attributed to the increase of pinning of basal dislocation by these defects.

The first research into the effects of irradiation on graphite was in support of the Magnox gas reactor fleet. The earliest work studied Pile Grade A (PGA) graphite, which was the main material first used for core components in the Magnox reactors. The initial work on PGA was presented by Bridge et al. [23] who studied the effect of irradiation on

PGA and HOPG graphite at 225°C, 250°C, 300°C, 350°C, 450°C, 650°C. They found at low doses that the Young's modulus changes were independent of direction, but at higher doses the direction and temperature had very strong effects on the change. It was observed that below 250°C PGA expanded in the c-direction and at temperatures of 300°C and above the c-direction contracted, while the a-direction contracted at all temperatures. The other observation was that the c-direction in HOPG expanded at all temperatures, while the a-direction contracted at all temperatures except 650°C, where it appeared not to change.

Work from Henson et al. [24] looked at effects over a larger temperature range for PGA graphite. For irradiation temperature of 400°C-440C and 550°C-600°C, it was observed that PGA contraction parallel to the extrusion direction was large while perpendicular to the extrusion direction it showed initial contraction and the then elongation. Also observed at these temperatures was volume contraction, turn-around, and swelling, with the dose to turn-around and volume contraction was larger for the 400°C-440°C range. At 900°C there was initial expansion observed in both direction, which quickly reverted to contraction. At 1250°C-1350°C contraction was seen in both directions. In these experiments, the dimensional changes up to 400°C were attributed to interstitial clusters, interstitial loops, vacant lattice sites, and vacancy lines. Electron microscopy has given direct observation of interstitial loop nucleation and growth. Others have postulate that vacancies occur in collapsed lines, which account for contraction in the basal planes. Vacancy loops have been observed in graphite at 900°C, 1200°C, and 1350°C.

Burchell and Eatherly [21] irradiatied GraphNOL at 600°C and 875°C. At 600°C the maximum volume contraction was 7.5% at 21dpa with the end of life occurring at 33dpa. At 875°C the maximum volume contraction was 5% at 15dpa and the end of life occurred at 22dpa. These were compared to the POCO AXF grade that had a lifetime of 29dpa at 600°C and 17dpa at 875°C, and H-451 that had lifetimes of 28dpa and 15dpa at 600°C and 875°C respectively. The GraphNOL data clearly shows that the maximum strength and Young's modulus occur when the graphite is at turn-around, and has the highest density and lowest volume. The initial increase is attributed to dislocation pinning and closure of fine pores due to c-axis expansion, while the reduction after turn-

around is due to the generation of new pores which lead to eventual disintegration of the material at very high doses. The coefficient of thermal expansion initially increases with dose reaching a maximum around 8dpa at 600°C and 3dpa at 875°C, returns to the initial value after 12dpa and 7dps respectively, and continues to decrease. The initial increase is due to the porosity closure and the decrease is due to the production of new pores. The plots in Figure 2.9 show the (a) volume change, (b) Young's modulus change, and (c) CTE change as a function of dose for the two irradiation temperatures. The dependence of total shrinkage and turn-around dose are easily observed in these plots.

For some other nuclear graphite grades, the dose to turn-around and lifetime have been investigated. H-451 reaches turn-around at 900°C at 7.48dpa with 6% shrinkage and end of life occurs at 11.5dpa, while at 1350°C turn-around is at 4.76dpa with 7.75% shrinkage and end of life occurs at 9.86dpa [25]. For IG-110, which is a newer isotropic nuclear grade, turn-around occurs at 15dpa with 7% shrinkage at 600°C and end of life occurs at 30dpa [26]. It was seen that the Young's modulus maximum occurred at 20dpa and was approximately 2.5 times larger than the initial value.

A methodology to numerically model the dimensional changes in graphite is presented by Brocklehurst and Kelly [27]. Since a polycrystalline material can be described as an aggregate of crystals which have identical properties and property changes after irradiation dose at a temperature, the macroscopic properties can be related to the microscopic properties through the use of various structure factors. For dimensional change rate g_x in direction x it is proposed that:

$$g_x = A_x\left[\frac{1}{X_c}\frac{dX_c}{d\gamma} - \frac{1}{X_a}\frac{dX_a}{d\gamma}\right] + \frac{1}{X_a}\frac{dX_a}{d\gamma} + f_x, \tag{2.11}$$

where A_x is a structure factor, *1/Xc*dXc/dy* is rate of change of crystallite dimension for unit dose in c-axis, *1/Xa*dXa/dy* is rate of change of crystallite dimension for unit dose in basal planes, and f_x describes expansion due to generation of new pores by large crystal strains. The shape change of crystallites, X_T is defined as:

$$X_T = \left[\frac{\Delta X_c}{X_c} - \frac{\Delta X_a}{X_a}\right], \tag{2.12}$$

where $\Delta X_c/X_c$ is the crystallite dimensional change in the c-direction and $\Delta X_a/X_a$ is the crystallite dimensional change in the a-direction. This results in g_x of:

$$g_x = A_x \frac{dX_T}{d\gamma} + \frac{1}{X_a}\frac{dX_a}{d\gamma} + f_x \tag{2.13}$$

or for “not too large strains” gives the integral form:

$$G_x = \int_0^{\gamma} A_x \frac{dX_T}{d\gamma} d\gamma + \frac{\Delta X_a}{X_a} + F_x . \tag{2.14}$$

The earliest analysis of thermal annealing of radiation damage (unknown irradiation temperature), from Bacon and Warren [28], found that the thermal annealing could return the material to the pre-irradiation lattice parameters and crystallite dimensions. This suggested that the crystallites were not broken up by irradiation and instead the basal planes, instead of changing size, were forced apart and were able to buckle and bend, effectively breaking up the crystallite size but being fully recoverable.

Heggie et al. [29] have recently proposed a new mechanism of irradiation damage and dimensional changes in graphite called Buckle, Ruck and Tuck. The crystal dimensional change behavior is different for temperatures below and above 250°C, which leads to two different mechanisms. Below 250°C the shape of crystal dimensional change versus dose is sigmoidal and saturates, this behavior is described by the Buckle process. Above 250°C the shape of crystal dimensional change versus dose is linear or parabolic and does not saturate, this behavior is described by the Ruck and Tuck process.

Buckling occurs when longer sheets are pinned in two places to a shorter plane, causing the longer plane to buckle. It is unsure if an isolated dislocation can cause buckling, but a dislocation localized by pinning points or when dislocations interact with others of opposite sign will cause buckling. Figure 2.10, shows a superlattice model of buckling in graphite, where the basal edge dipoles are held in place by interlayer pinning points [29].

Above 250°C, the dislocation mobility is higher and mutual interaction becomes more likely. Interaction of dislocations with opposite signs on different glide planes can occur multiple times resulting in a “Pile up”. An example of four perfect basal dislocation pile up is shown in Figure 2.11a. The pile up results in an accumulation of matter at the crossing and annihilation locations of the four dislocations, but in layered materials the matter still belongs to the layer so a folding of the layer occurs, which Heggie et al. call a “Ruck and Tuck”. This defect has two descriptions in dislocation

theory, either pile up of climb dipoles, Figure 2.11a with $\vec{b} = \frac{1}{3}\langle 11\bar{2}0\rangle, \vec{l} = \langle 1\bar{1}00\rangle$, or an unfaulted climb dipole, Figure 2.11b with $\vec{b} = c\langle 0001\rangle, \vec{l} = \langle 1\,\bar{1}00\rangle$. The prismatic climb dipole is similar in nature to the loops of the currently accepted model, but in the standard model climb via point defect migration is necessary but in the Ruck and Tuck model it can happen with only basal glide. Pile up of climb is usually resisted by the Peach Köhler force, but in graphite this force is minimal due to elastic anisotropy and the ease of accommodating material through expansion in the c-direction. Figure 2.12a-c shows the process by which the passing of a single basal dislocation can extend the prismatic dipole since the passing dislocation deposits a segment of an extra half plane in the Ruck and Tuck defect. The authors note that the mechanism needs more experimental evidence from high resolution TEM and diffraction techniques to examine the dislocation and defects [29]. However, at irradiation temperatures above 800ºC, over 60-80% of the damage is not annealed, which indicates that the mechanism above this temperature is not Ruck and Tuck and is most likely from the standard damage model [29].

Recent *in-situ* TEM analysis [30] has shown results that are in disagreement with the historical view of radiation damage in graphite. They observed that interstitial loops are not the cause of the radiation-induced changes and instead vacancy loops form and dissociate into two dislocations that increase in length by positive climb. An example of this process is shown in Figure 2.13, where the vacancy loop forms (a), then dissociates into two dislocations (b), the resulting dislocations climb in a positive direction (c), and a region with multiple dislocations (d).

2.6 Irradiation Creep Behavior

This final section presents the current historical research on the irradiation creep behavior of graphite. First a summary of the irradiation creep experiments and the results will be discussed for graphite. Then the historically proposed mechanisms steady-state creep for graphite will be presented. Lastly, the mechanisms of irradiation-induced creep for metals will be presented as they will be utilized in the analysis of the experimental results from this work.

2.6.1 Experimental Results from Neutron Irradiation-Induced Creep

Some of the first irradiation creep work on graphite was presented by Perks and Simmons [31]. These experiments were on PGA graphite. The experiments were only performed out to low doses, but they are the one of the first to propose that creep is either due to stress preferred annealing of the radiation induced defects or the motion of basal plane dislocations.

Jenkins and Stephen [32] irradiated graphite that had been machined into springs. They measured a transient creep strain of 0.31 initial elastic strain, it is negligible beyond $6x10^{19}n/cm^2$ (E>0.18MeV), and it is recoverable upon irradiating without stress, but steady state creep is not recoverable. The transient strain was 3 times lower than other measurements, but the authors attribute this to the fact that strain measurements in these experiments were taken during irradiation, while the others measured strain outside of the reactor. The steady state creep rate at 300°C was determined to be 0.26(initial elastic strain)/($10^{20}n/cm^2$) (E>0.18MeV). The creep constant was observed to increase by a factor of 1.6 from 100°C-300°C. This was compared with data from Kennedy who saw a factor of 3 increase of steady state creep constant when temperature was lowered from 350°C to 150°C but this work was done on different samples and had to be corrected for flux gradients. Jenkins and Stephen state that the transient creep is caused by movement of the basal plane dislocations, which may be due to the removal of pinning points but it is more likely due to intergranular stresses due to anisotropic growth. Since transient is recoverable it stores elastic energy but does not add to ductility.

Gray et al. [33] studied tensile and compression samples of PGA and an unknown isotropic graphite in the temperature range of 250°C-500°C. Creep strain was calculated from the difference of stressed and unstressed sample. The creep rates in both compression and tension were temperature independent in the work. They were the first to observe that compressive stress increases the change of the CTE, while tensile stress decreases the change of the CTE. From this they propose that creep strain affects the closure of small pores and the non-linearity of the bulk behavior is expected at large strains and thus presents a possible difference in creep coefficients for tensile and compressive states.

Brocklehurst and Brown [34] studied tensile and compressive experiments on near-isotropic graphite from 350°C-450°C. The fit of the dimensional change of the reference sample showed a small amount of swelling before the onset of contraction (around $7x10^{20}n/cm^2$). Creep coefficient in tension was $0.25x10^{-6}(psi*10^{20}n/cm^2)^{-1}$, while the coefficient for compression was $0.19x10^{-6}(psi*10^{20}n/cm^2)^{-1}$. The creep strains in tension and compression for the isotropic graphite are similar up to 1% strain and exhibits no temperature effect from 300°C-600°C. Their work saw the same dependence of the change of CTE on the stress type as [33]. They also observed that there was no noticeable effect of stress state on the change of Young's modulus. When these results are compared with creep of anisotropic graphite the correlation of creep and elastic deformation suggest creep is controlled by crystal shear.

Work by Gray [35], studied compression on grades AGOT, H-337, and POCO AXF-8QBG1, at 550°C and 800°C with 1000psi, 2000psi, and 3000psi stresses. As presented earlier the AXF-8QBG1 unstressed sample swells at 800°C until ~$8x10^{21}n/cm^2$ (E>0.18MeV) and returns to initial volume around $11x10^{21}n/cm^2$. H-337 shows slight swelling at 800°C but the swelling of H-337 is 4 times smaller than AXF-8QBG1. Creep at 550°C was approximately linear with fluence for all three grades, but at 800°C creep was linear with fluence for AGOT, but the other two have initial linearity with fluence and decrease at higher dose. Also noted was the creep occurred near constant volume at 550°C, but occurred with decreasing volume at 800°C.

Two sets of experiments were performed at JAERI on newer nuclear graphite grades, SMI-24 [36], and IG-110 [37]. On the SMI-24 the experiments were in tension with 3.3MPa, 4.5MPa, and 6.4MPa and creep coefficient values of $3.19x10^{-29}(MPa/m^2)^{-1}$ and $2.77x10^{-29}(MPa/m^2)^{-1}$, it was noted that the flux for the second value was slightly higher. The IG-110 experiments were in tension with 9.05MPa, 10.9MPa, and 13.5MPa from 756°C-985°C. The values of the creep coefficient and kE_0 fall within the ranges presented for other graphites.

Kelly [38] presents a methodology to adjust creep strain for strains greater than 0.5% due to the continuous change of the crystallite dimensions X_T as defined in Equation (2.12) and thermal expansion coefficients where α_x α_a α_c are the thermal expansion coefficients in the measurement direction (x), and in the basal plane (a) and in

the c- direction (*c*). This also accounts for the fact that an applied stress effects the change of thermal expansion coefficients as a function of dose resulting in:

$$\varepsilon^1 = \varepsilon_m - \int_0^{\gamma} \left(\frac{\alpha_x^1 - \alpha_x}{\alpha_c - \alpha_a} \right) \left\langle \frac{dX_t}{d\gamma} \right\rangle d\gamma \,. \tag{2.15}$$

Kelly and Burchell [39] support this model with analysis of compressive creep data for H-451 at 900°C with 13.8 and 20.7MPa compressive stress. Creep strain shows a decreasing creep rate with increasing dose. Applying correction resulted in constant creep rate with dose. It seems that the apparent reduction in creep rate is an artifact due to the effect of creep strain on the dimensional change rate of the stressed specimen compared to the unstressed control.

Davies and Bradford [40] present a new modification to the equations to model irradiation creep. The new model consists of three creep regimes, primary, recoverable, and steady state, which came from observations that strain-induced changes in CTE is not a function of steady state creep, recoverable strain is several times larger than the primary creep strain, and the dose where recoverable strain saturates is very near the dose where the CTE change saturates. The resulting equation for creep is:

$$\varepsilon = \underbrace{\frac{\alpha k_1}{E_0} \exp\left(-k_1\gamma_1\right) \int_0^{\gamma_1} \frac{\sigma}{SW} \exp\left(k_1\gamma\right) d\gamma}_{\text{Primary Creep}} + \underbrace{\frac{\omega k_2}{E_0} \exp\left(-k_2\gamma_1\right) \int_0^{\gamma_1} \frac{\sigma}{SW} \exp\left(k_2\gamma\right) d\gamma}_{\text{Recoverable Creep}} + \underbrace{\frac{\beta}{E_0} \int_0^{\gamma_1} \frac{\sigma}{SW} d\gamma}_{\text{Steady State Creep}} \,. \tag{2.16}$$

Burchell [41] instead utilized Equation (2.15) from [38, 39] and applied the analysis to the same data as Davies and Bradford. Tensile data from experiments conducted at Petten, 500°C for Davies and Bradford, and 900°C for Burchell. Figure 2.14a shows the fit from of the 500°C data by Davies and Bradford [40] and Figure 2.14b shows the fit from the 900°C data by Burchell [41]. The Davies Bradford model appears to fit the tensile creep data better than the Burchell model.

2.6.2 Transient Irradiation Creep in Graphite

The irradiation creep experiments for nuclear graphite were performed under a wide array of experimental conditions and are difficult to analyze to determine a controlling mechanism. Many of the experiments were not analyzed in the transient regime so there are only two theories for transient creep. Kelly and Brocklehurst [42] presented these two transient theories. The first is a shear deformation mode where dislocation pins are destroyed and the transient existence of the pins allows dislocation bowing and recovery occurs from the line tension of the dislocations. The other is a climb and glide mode where edge dislocations with line parallel to the c-axis, act as pins for basal dislocations, and the edge dislocations climb by absorption of point defects.

2.6.3 Steady-State Irradiation Creep in Graphite

In the same paper, where the transient creep mechanisms were discussed, Kelly and Brocklehurst [42] also discussed four mechanisms that were proposed to be controlling steady-state irradiation creep; the Cottrell model, diffusion of interstitial atoms between basal cracks, grain boundary sliding and pulling apart of crystals, and restraint of c-axis growth by stress. More recently these mechanisms have been changed to three: the Cottrell model, pinning-unpinning of dislocations, and grain rotation. These three mechanisms are presented individually below.

2.6.3.1 Cottrell Model

The first mechanism, called the Cottrell model, was first proposed by Roberts and Cottrell [43] as a way to describe creep of alpha uranium. The driving mechanism is that radiation-induced anisotropic growth of the uranium crystals cause internal stresses that approach the yield strength and the addition of an external stress results in surpassing the yield strength thus inducing creep. This mechanism has been discussed as it pertains to graphite in that the irradiation-induced growth of crystallites can cause stress build-up within grains and make the grains plastically deform.

In alpha uranium there was an initial time before creep began, which was time necessary to bring the grains to the plastic state (t_m), also called the relaxation time, given by [44]:

$$t_m \approx \frac{\sigma_y}{E}\dot{\varepsilon}_g \approx \frac{\sigma_y}{E}\left(\dot{\varepsilon}_c - \dot{\varepsilon}_a\right), \tag{2.17}$$

where σ_y is the yield stress, E is Young's modulus, and $\dot{\varepsilon}_g$ is the crystal growth rate. It was then found that the material is in a state of spontaneous plasticity and behaves like a Newtonian liquid when subjected to an external stress, which results in an overall flow approximately equal to the overall elastic strain divided by the relaxation time. The overall elastic strain is equivalent to the applied stress (σ) divided by Young's modulus, which results in a flow rate ($\dot{\varepsilon}_e$) given by:

$$\dot{\varepsilon}_e \approx \frac{\sigma / E}{t_m} \approx \frac{\sigma}{\sigma_y}\left(\dot{\varepsilon}_c - \dot{\varepsilon}_a\right). \tag{2.18}$$

This equation covers both the transient and steady-state behavior in that the change in crystallite size can behave differently with increasing dose. The dependencies of creep rate on stress, dose rate, and temperature are determined from Equation (2.18). The creep is linearly dependent on applied stress. The dependence on dose rate is linear because the growth rates change linearly with dose rate. The temperature dependence is inversely controlled because for graphite the yield stress increases with increasing temperature [17, 45-48], thus the creep rate should decrease with increasing temperature for graphite.

Kelly and Brocklehurst [42] discussed a few problems with the mechanism and how it relates to graphite. The first is that the dependence of the individual crystal yield stress on irradiation dose and temperature is unknown. In addition, this mechanism does not predict creep of HOPG because the crystallites are aligned in the same direction and thus would not cause these internal stresses, but irradiation creep in HOPG has been observed. Later, Kelly and Brocklehurst [49], added boron to increase the dimensional change rate, by a factor of 3, but the creep rate remained unchanged at 750°C, which disproved this as a possible mechanism.

2.6.3.2 Pinning-Unpinning of Basal Dislocations

The second model, called the pinning-unpinning mechanism, began with Kelly and Brocklehurst [42] postulating that irradiation creep is due to basal slip or an equivalent deformation mode. They discussed that basal slip is activated by irradiation not internal stress, and thus the basal creep rate is proportional to stress and independent of temperature from 350-600°C. They also discuss that basal glide only has 2 degrees of freedom, which doesn't fulfill the Taylor-Von Mises criterion, which is a possible contributing factor to the generation of porosity.

Kelly and Foreman [50] extended these postulations to result in the pinning-unpinning model as a possible description of the irradiation creep behavior of graphite. The model works under the assumption that graphite behaves as if it contains a high density of basal dislocations with a small concentration of pinning points. Irradiation can partially or completely pin dislocations, depending on temperature and dose. The pinning points are thought to be 2-6 atom clusters, which are created and have finite lifetime and are only temporary barriers to dislocation motion. To understand the complete theory the relationship between microscopic and macroscopic deformation, and the microscopic deformation must be understood. The relationship between microscopic and macroscopic deformation begins with the assumption that polycrystalline graphite consists of crystals of maximum density and an apparent density on the macroscopic level. The microscopic level only occurs within an individual crystal. The only deformation mode is basal slip with:

$$\begin{aligned} \left[\dot{\varepsilon}_{xz}\right]_r &= k\left[\sigma_{xz}\right]_r \phi \\ \left[\dot{\varepsilon}_{yz}\right]_r &= k\left[\sigma_{yz}\right]_r \phi \end{aligned}. \tag{2.19}$$

The macroscopic creep rate is given by:

$$\dot{\varepsilon}_m = \left[\frac{2C_{44}}{E_m}\left(\frac{\rho}{\rho_0}\right)\right]^{1/2} \dot{\varepsilon}, \tag{2.20}$$

where $\dot{\varepsilon}$ is the average rate of basal shear (microscopic). For typical reactor graphites ρ/ρ_0=0.8 and C_{44}/E_m~0.2, giving $\dot{\varepsilon}_m \sim 0.6\dot{\varepsilon}$. The microscopic deformation is given by:

$$\dot{\varepsilon} = \Omega b v = k\sigma\phi \tag{2.21}$$

where b is the Burger's vector, v dislocation velocity, Ω mobile dislocation density. Then a computer simulation was used to calculate the dislocation velocity. The result is the creep constant:

$$k = \frac{\dot{\varepsilon}}{\sigma\phi} = \frac{4\Omega L^2}{K_d \tau\phi} = 2.8x10^{-47}\,\frac{\Omega}{C_p} \tag{2.22}$$

where C_p is the pin concentration. The pin concentration increases under irradiation to a saturation value that is dependent on temperature and dose rate. If this theory is accurate then the linearity with stress fails at high and low stresses, the creep rate is proportional to the basal plane dislocation density, recovery creep is small since it only involves straightening of bowed dislocations, and for a dislocation density of 10^{12}cm/cm^3, to get a 1% macroscopic strain, requires an average dislocation displacement of 10^{-6}cm [50].

Veringa and Blackstone [51] extend the pinning-unpinning model to account for the effects of dose rate and the temperature, on C_p. They discussed that the creep rate should be inversely dependenct on C_p, which is co-dependent on dose rate and temperature, and should follow the trend of interstitial concentrations. Thus the pinning point concentration should have a direct dependent on dose rate and should decrease with increasing temperature due to the increased interstitial migration rate, which should result in the relationship of:

$$C_p \propto \frac{\phi}{\exp\left(-E_m \big/ kT\right)}, \tag{2.23}$$

and k should follows the form:

$$k = A\frac{\exp\left(-E_m \big/ kT\right)}{\phi}. \tag{2.24}$$

To support these dependencies, Veringa and Blackstone [51], plotted k versus temperature, for a number of different graphites irradiated at different conditions. They found that the minimum and maximum coefficients, at the same temperature, were found to be a factor of 7-10 different. Instead they found that plotting kE_0, where E_0 is the pre-

irradiation Young's modulus, versus temperature brings the data from different materials within a factor of 2. Instead of observing the dependence of *k* on temperature, following Equation (2.24), they observed a trend following:

$$kE_0 = \frac{f(T)}{\phi} + g(T), \tag{2.25}$$

where $g(T)$ is not dependent on flux, but it might be a contribution from Cottrell creep or pinning point density is not a simple dependence on temperature and flux as low flux experiments indicate. This results in a final creep equation of

$$\dot{\varepsilon} = k\sigma\phi = \left(\frac{f(T)}{\phi} + g(T) \right) \frac{\sigma\phi}{E_0} \tag{2.26}$$

All the graphites showed the same dependence of creep coefficient on temperature, neutron flux, and Young's modulus. From this correlation an estimate of creep behavior for any graphite from 350-1400°C and 0.2-2.5x10^{14}n/(cm^{2}s), or 2.6x10^{-8}dpa/s to 1.31x10^{-7}dpa/s, can be made as long as the pre-irradiation Young's modulus of the material is known. The plot in Figure 2.15 shows all the data Veringa and Blackstone analyzed to obtain this extension of the pinning-unpinning model.

Later, Kelly and Brocklehurst studied different graphites from 300°C-1100°C, up to doses of 7-8dpa, in tension and compression [49]. The data from their work supported Veringa and Blackstone that plotting strain divided by (initial strain) gives single curve for all the materials. They also discussed a short-coming in the pinning-unpinning mechanism because it requires that all materials contain essentially the same dislocation density. Instead they discuss that a model using groups of dislocation and twist boundaries, with similar pinning-unpinning, may be more suitable.

This mechanism should thus result in a linear dependence on applied tensile stress, because creep is controlled by basal slip. The creep rate should increase linearly with temperature due to a decrease in pinning points as the interstitials migrate faster, as shown by Veringa and Blackstone. Finally, the creep rate should be inversely dependent on dose rate, since the pinning point concentration is higher for higher dose rates and slows down the motion of the dislocations.

2.6.4 Steady-State Irradiation Creep Mechanisms in Metals

Thermal creep in metals is driven by either the motion of dislocations or by diffusion of defects. When irradiation is present to produce defects, the motion of dislocation can be enhanced by the higher defect concentration. The dislocation motion, in the presence of irradiation, results in four traditional mechanisms that describe the difference types of motion. These four mechanisms are the Stress-Induced Preferential Nucleation of loops (SIPN), Stress-Induced Preferential Absorption of defects (SIPA), Preferential Absorption Glide (PAG), and Climb and Glide from Dislocation Bias (CGDB). The thermal creep mechanisms driven by the diffusion of defects either through the bulk (Nabarro-Herring), or along grain boundaries (Coble), cannot be initiated or enhanced by irradiation because both mechanisms are driven by the difference of equilibrium defect concentrations at boundaries parallel and perpendicular to the applied stress rather than being driven by the total defect population [52].

Table 2.1. Summary of thermodynamic properties from Thrower and Mayer [7].

	Interstitial	Vacancy
S^f (k)	3	7
S^m (k)	4	7
E^f (eV)	7	7
E^{ma} (eV)	<0.1	3.1
E^{ca} (eV)	>5	>5.5
v (s^{-1})	$4x10^{12}$	$5x10^{13}$

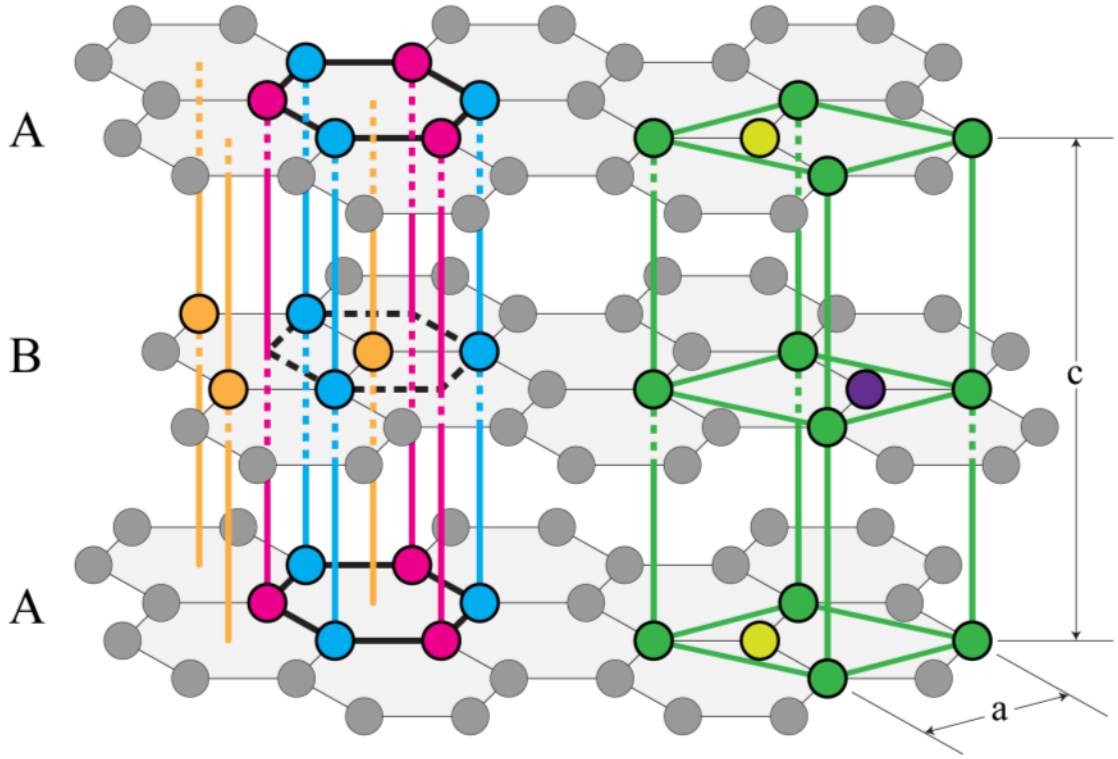

Figure 2.1 Illustration of the hexagonal microstructure of graphite. On left side, the blue atoms illustrate the three atoms in each A plane hexagon with atoms on those same sites in each plane, the pink atoms only have atoms in the location in the A planes, and the orange atoms only have atoms on the sites in the B planes. The right side is an outline of the unit cell for the hexagonal geometry. In the unit cell a=2.4612Å, c=6.7079Å, and there are 4 atoms in each cell [6].

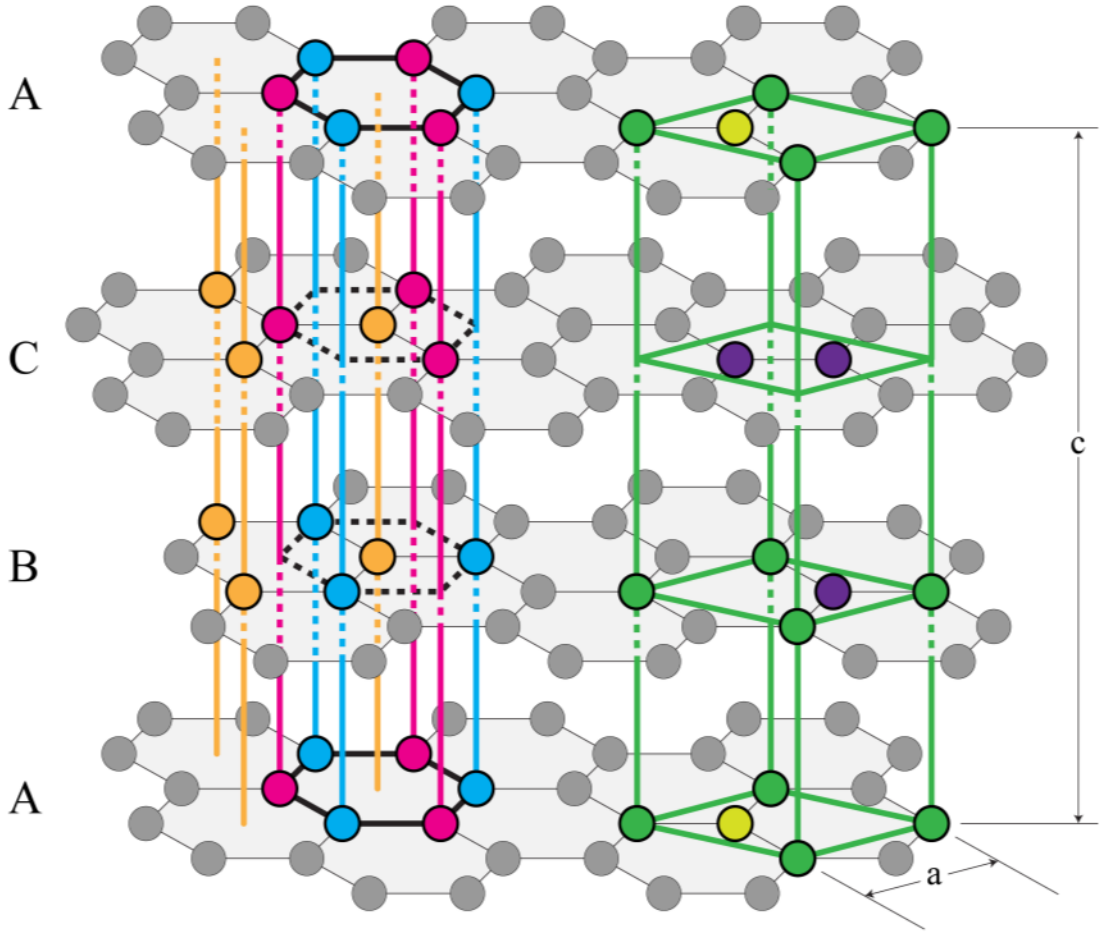

Figure 2.2 Illustration of the rhombohedral microstructure of graphite. On left side, the blue and pink atoms illustrate in the rhombohedral structure how every atom in an A plane hexagon has an atom above it in either the B plane (blue) or the C plane (pink), and how the other three atoms in the B and C planes are on the same site (orange). On the right side is an outline of the unit cell for the rhombohedral geometry. In the unit cell a=2.4612Å, c=10.0619Å, and there are 6 atoms in each cell [6].

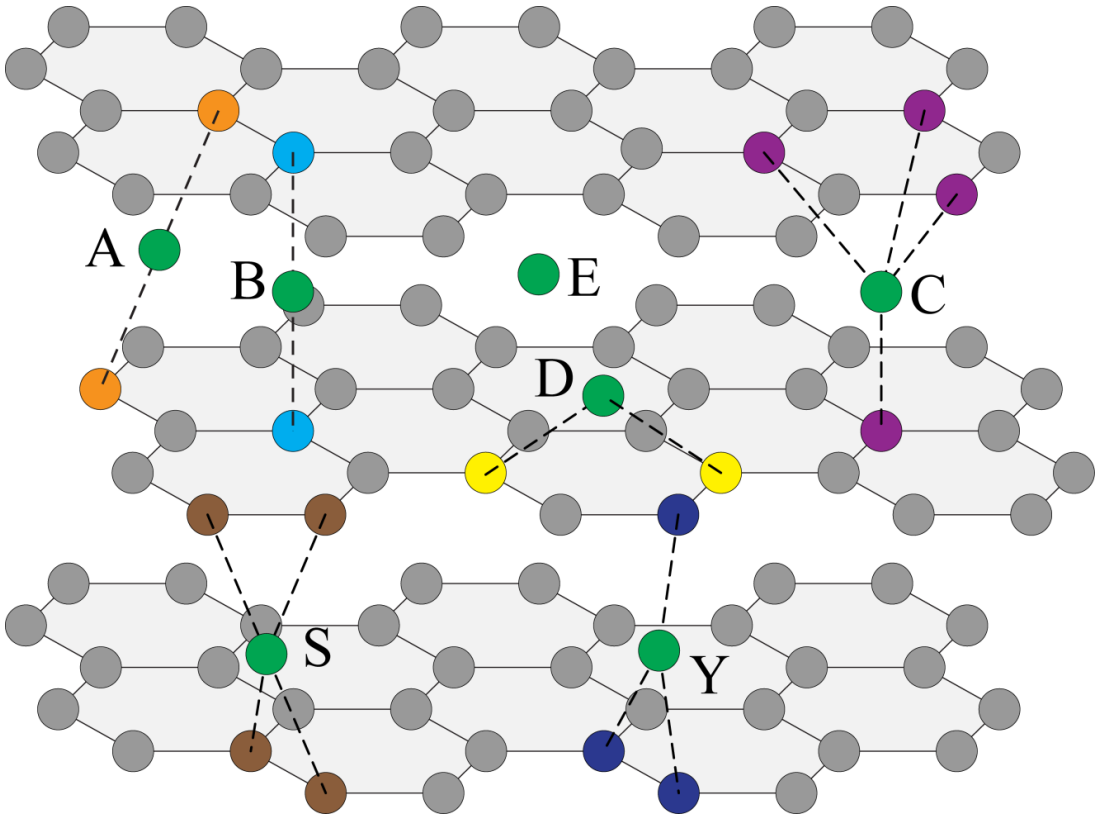

Figure 2.3. Schematic of proposed interstitial locations in graphite, locations A-E from [9], and spiro (S) and ylid (Y) from [10].

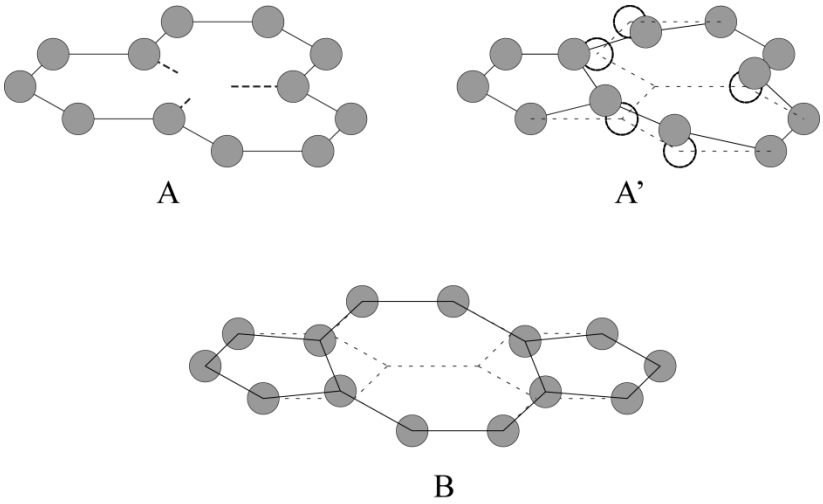

Figure 2.4. Schematic representation of the unreconstructed (A) and reconstructed(A') single vacancy, and schematic representation of di-vacancy (B), modified from [10].

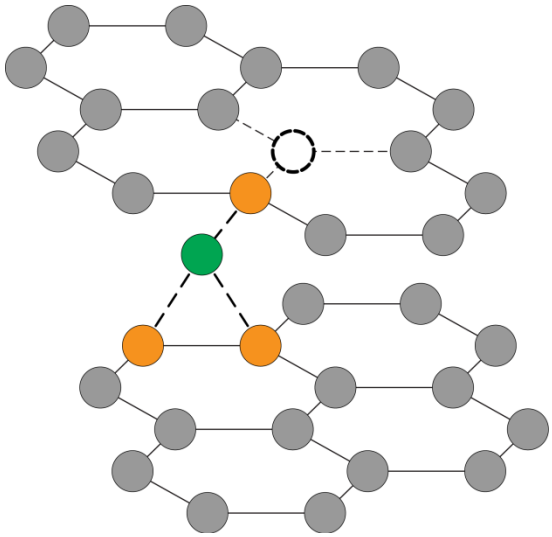

Figure 2.5. Schematic representation of the intimate Frenkel-pair defect in graphite, modified from [10].

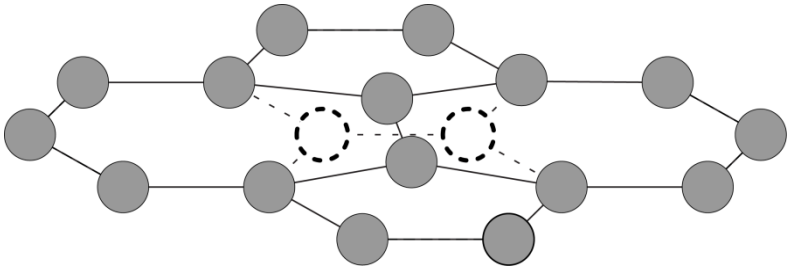

Figure 2.6. Schematic representation of the Stone-Wales defect, modified from [10], with the initial carbon locations outlined and bonds shown with dashed lines.

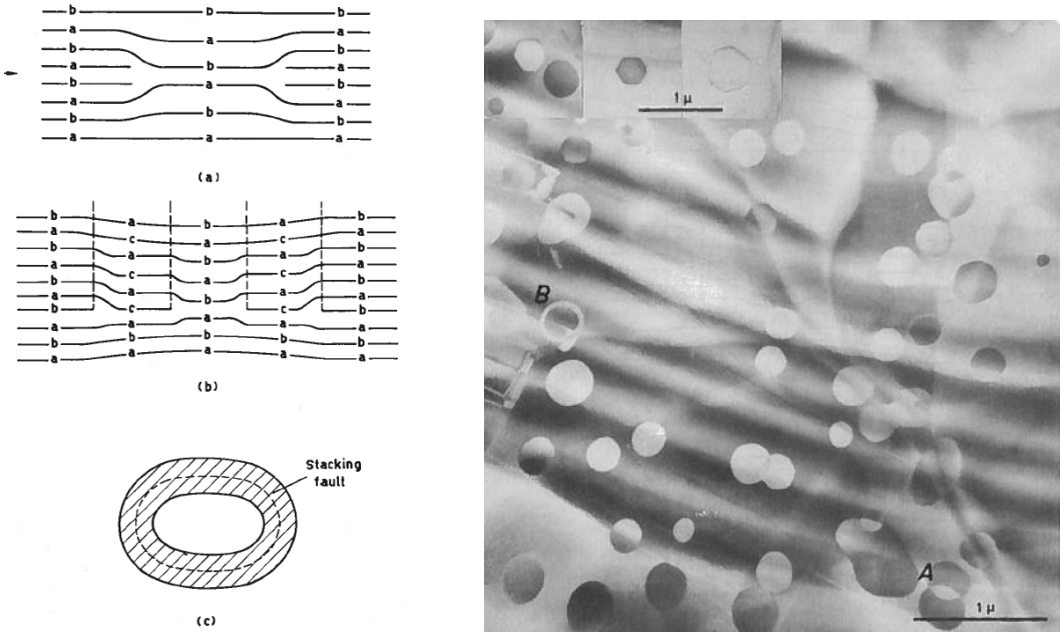

(a) (b)

Figure 2.7. (a) Schematic of two dislocation rings dissociating into two single layer and (b) is a micrograph of graphite with two dissociated dislocation rings (indicated by B in the image), from [15]

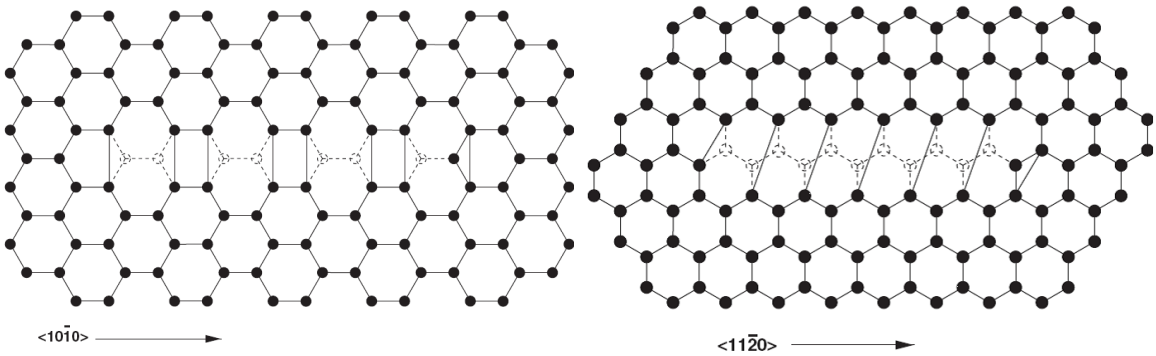

(a) (b)

Figure 2.8. Schematic of (a) boat edge line-like vacancy structure and the (b) zig-zag line-like vacancy structure, from [10].

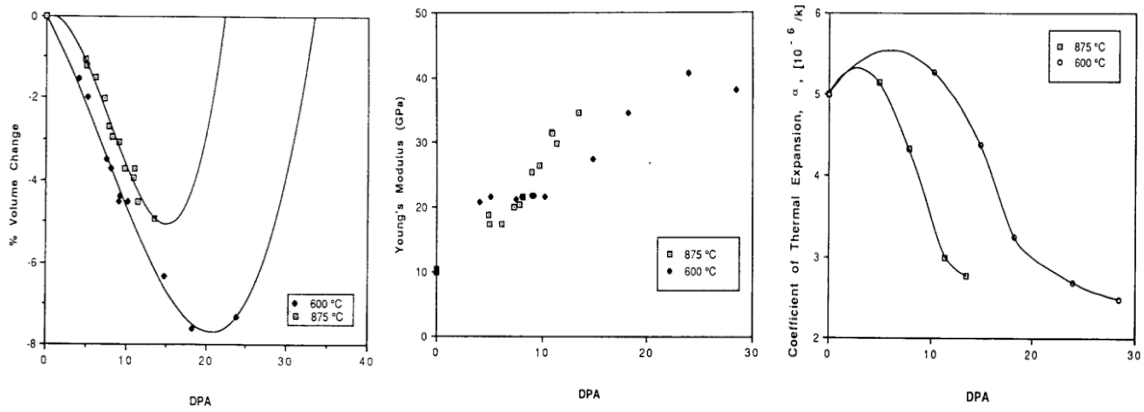

(a) (b) (c)

Figure 2.9. Plots of (a) volume change, (b) Young's modulus change, and (c) CTE change of GraphNOL versus total dose, irradiated at 600°C and 800°C, from [21].

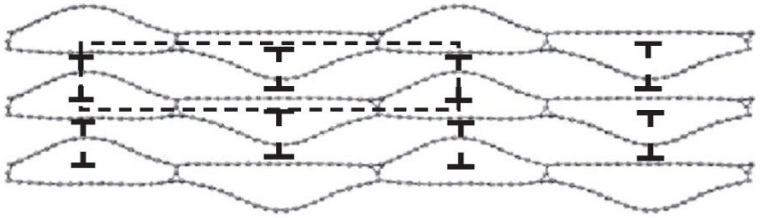

Figure 2.10. Computer model of buckled graphite, where the basal edge climb dislocations are held in place by interlayer pinning points, from [29].

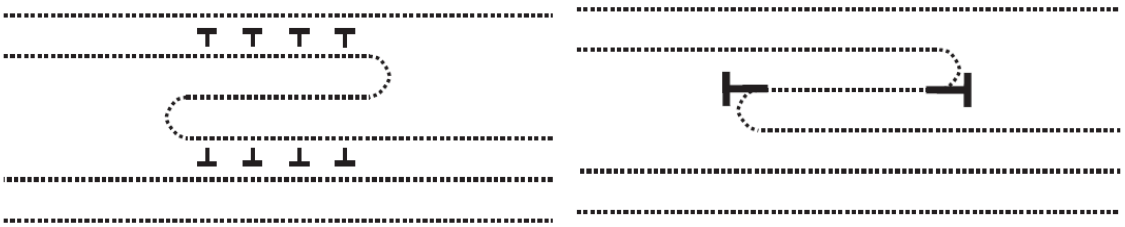

(a) (b)

Figure 2.11. Schematic of the Ruck and Tuck defect due to (a) pile up of climb dipoles or (b) an unfaulted climb dipole, from [29].

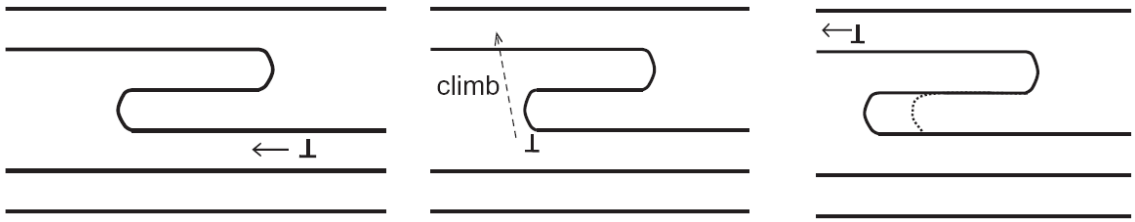

(a) (b) (c)

Figure 2.12. Schematic of the process (a to c) by which the passing of a single basal dislocation can extend the prismatic dipole since the passing dislocation deposits a segment of an extra half plane in the Ruck and Tuck defect, from [29].

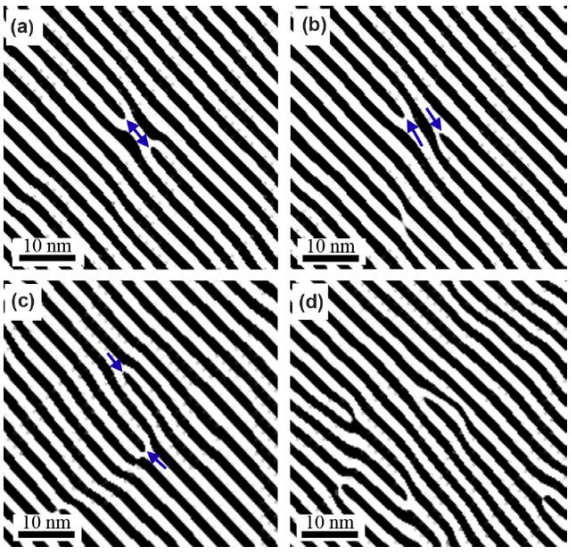

Figure 2.13. Images, from [30], showing the formation of the vacancy loop (a), the loop dissociating into two dislocations (b), dislocations undergoing positive climb (c), and multiple dislocations within a region (d).

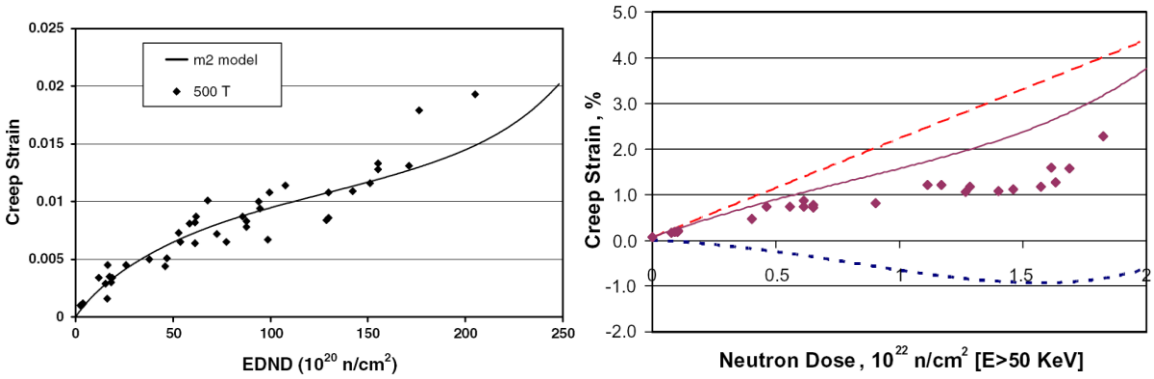

(a) (b)

Figure 2.14. Plots showing the fit of two new models (a) Davies and Bradford [40] fit, to 500°C tensile creep data from Petten and (b) Burchell [41] fit, purple line, to the 900°C tensile creep data, purple diamonds, from Petten.

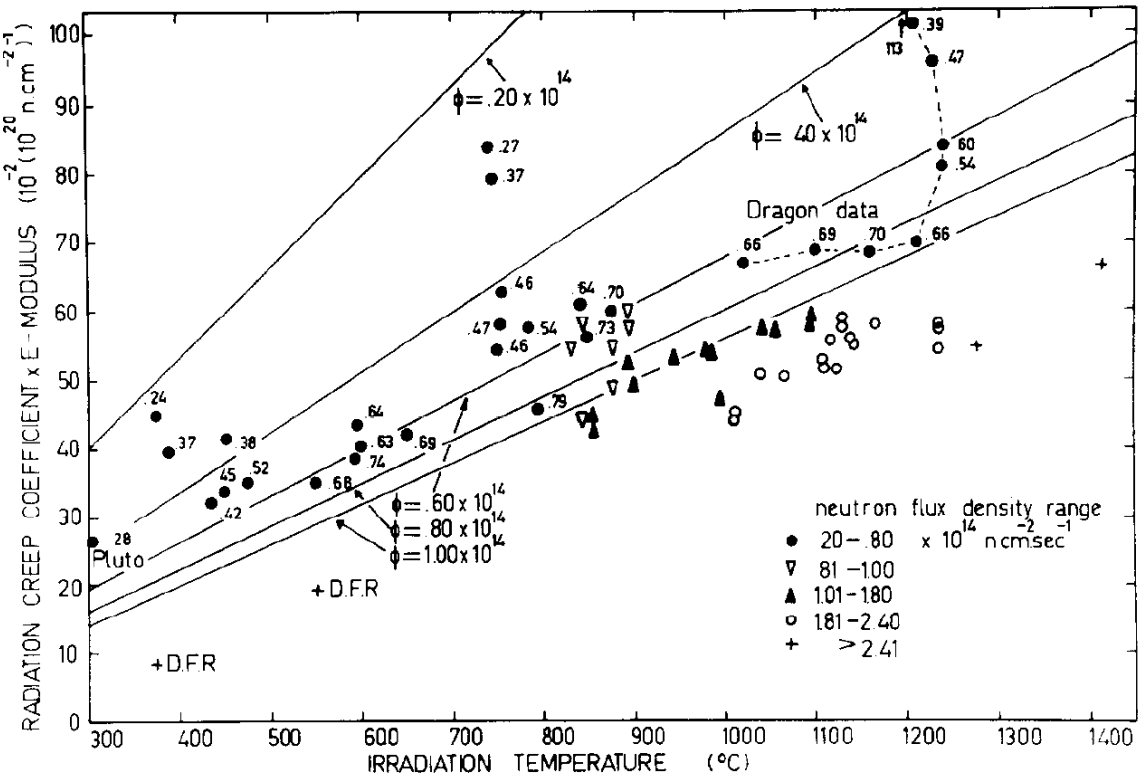

Figure 2.15. Plot of kE_0 versus irradiation temperature, which shows the dual dependence on irradiation temperature and dose rate, data from [51].

CHAPTER 3

EXPERIMENTAL PROCEDURE

This chapter covers the experimental techniques used in this research. Section 3.1 presents a description of the materials used in this research. Section 3.2 presents the design and characterization of the system used for the irradiation creep experiments. Section 3.3 presents the experimental procedure. Finally Section 3.4 presents the post irradiation analysis methodologies.

3.1 Materials

One grade of graphite is used in this work, ZXF-5Q grade from POCO Graphite Inc. The complete manufacturing process for this material is proprietary and not disseminated by the manufacturer. In a personal communication with a source not affiliated with POCO, it was mentioned that this material is manufactured from Green Pet Coke Filler (petroleum-produced coke that has not been calcined), which is milled to the desired particle size, the milled material is sieved to remove particles larger than the maximum size, then put into the press, and heat treated and isostatically formed into the final shape. Additionally there is no binder used in the production of this graphite, unlike the nuclear-grades, so essentially the formation of this material is similar to the sintering process used for ceramics. The physical and mechanical properties of this material, reported by the manufacturer, are listed in Table 3.1.

The structure of this material needs to be described on a macroscopic scale and on a microscopic scale. The macroscopic structure is comprised of randomly orientated and non-uniform size (no larger than 1μm) filler particles (grains), and the 20% porosity resulting from the forming process, shown schematically in Figure 3.1a. Within the filler particles there are two regions of interest, the crystallites and the Morovski cracks. A schematic representation of a filler particle is shown in Figure 3.1b. Each filler particle

has an overall c-axis direction (shown with the large arrow), but the Morovski cracks cause a break-up of the perfect structure. The crystallites (regions outlined with dashed lines) are regions within the filler particle, between the Morovski cracks, that have perfect graphite structures. The Morovski cracks cause curvature of the surrounding basal planes, which causes some tilting of the c-direction of the neighboring crystallite (red dashed arrow highlights tilted c-direction) and results in diffraction from the basal planes having an arc shape rather than a single spot. Transmission electron microscopy (TEM) of the material shows that most of the individual pores are smaller than the 300nm quoted by the manufacturer (Figure 3.2a) and the Morovski cracks in a filler particle (Figure 3.2b).

In both SEM and TEM it was difficult to find and image particle boundaries to determine the particle sizes. Instead the particle size can be inferred from an analysis of regions within the material with progressively smaller TEM diffraction apertures. A series of concentric SAED patterns, with progressively smaller apertures, are shown in Figure 3.3. The pattern taken with the 6.5μm diameter aperture shows a semi-uniform ring pattern expected for an isotropic polycrystalline material. The pattern taken with the 600nm diameter aperture has diffraction contribution from multiple crystallites within one to two particles, which result in the two bright arcs. The pattern taken with the 270nm diameter aperture shows diffraction from two slightly mismatched regions, most likely two crystallites within a single particle. This microscopy work has therefore shown that the grain size is smaller than the 1μm, but obtaining an exact measurement is still not possible with the available methodologies.

3.1.1 Sample Dimensions

The geometry of the samples in this work is strip shape that is 3mm in width, 35mm in length, and 0.07mm thick. The width of the samples was set by the design of the irradiation stage and clamping system. The irradiation stage was designed to allow the simultaneous irradiation of two samples, while keeping the total irradiation area at a minimum. The length of the samples is constrained by the dimensions of the heater used on the irradiation stage. The surface area of the heater is 25mm by 35mm and the samples must be longer than the shortest dimension of the heater face. This keeps the

clamps from being heated by the heater and allows for the samples to be within 1mm from the surface of the heater. The thickness of the sample was constrained by the minimum thickness that could be achieved during machining and by the maximum accelerating voltage of the linear accelerator while still allowing for the protons to pass through the sample and keeping a near-uniform irradiation damage profile through the sample thickness. The graphite samples were machined from a block of material using electrical discharge machining (EDM), and the minimum thickness that was reliably reproducible by the machinist was 0.07mm.

3.1.2 Proton Energy and Displacement Damage

To have uniform irradiation-induced creep, the protons must pass through the strip samples, and provide a near-uniform damage profile through the thickness. The graphite samples have average thickness of 70μm and an apparent density of 1.78g/cm^3. To determine the proton energy required, a stopping range table is created for protons with energy from 2MeV to 3.4MeV, using the Stopping and Range of Ions in Matter (SRIM) [53]. From the calculations, the minimum proton energy necessary to pass through the sample is 2.60MeV, which have an estimated range of 74.66μm with a straggle of ±3.04μm. The range and straggle calculated for protons with energy ranging from 2.00 to 3.40MeV are presented in Table 3.2. To ensure that all the protons pass through the sample, the minimum energy proton should have a range that is larger than 110% the sample thickness plus the range straggle, which results in a minimum proton range of 81μm for these graphite samples and this range corresponds to minimum proton energy of 2.75MeV.

After determining the necessary proton energy, the displacement damage was calculated using SRIM [53]. The displacement damage calculated by SRIM is defined as the number of displacements produced per ion per unit length (Å). These values are calculated as a function of depth into the material. Calculations in SRIM were performed in the detailed calculation with full damage cascades using a total of 1,000,000 simulated protons. This large number of protons was chosen because it provides a smooth, and more accurate, damage profile.

The displacement damage was calculated in SRIM using the full cascade calculation and a displacement energy of 33eV for the carbon atoms, as reported by Montet [8]. Figure 3.4 is a plot of the irradiation damage profile per incident proton versus depth into the sample computed by SRIM for 2.75MeV (red line) and 3.0MeV (blue line) protons in carbon with density and displacement values discussed previously in this section, while the thickness of the sample is indicated with the vertical black line. The output from SRIM gives the damage in units of displacements per ion per angstrom, which is converted into units of dpa per ion by:

$$\dot{d}\left(\frac{dpa}{proton}\right) = \frac{D_{SRIM}\left(\frac{displacements}{ion*Å}\right)}{N\left(\frac{atoms}{cm^3}\right)}, \tag{3.1}$$

where D_{SRIM} is the displacement rate calculated by SRIM and N is the atomic density of the material in units of atoms/cm^3. For the 70μm thick samples, the average displacement rate from 10μm to 70μm is 9.944x10^{-21} dpa per incident 2.75MeV proton, and 8.083x10^{-21} dpa per incident 3.0MeV proton. To achieve the near-uniform damage profile it was decided that a maximum of a factor of two increase of damage rate from the front to back surfaces was suitable, which occurs for a minimum proton energy of 3MeV, thus a proton energy of 3MeV was determined to be optimal for these experiments.

After determining the sample thickness and proton energy, the gradients through the samples can be better investigated. The electronic energy loss, due to interaction of the proton with the electron clouds, and the nuclear energy loss, due to collisions of protons and carbon atoms, can be iteratively calculated through the thickness of the sample. The results from this iterative calculation, and the SRIM calculated damage rate, are plotted in Figure 3.5, versus the sample thickness. All three sets of data plotted in Figure 3.5 show the increase of a factor of two from the front of the sample to the back.

The electronic energy loss through the sample can be used to calculate the heat generation because large number of free conduction electrons allows the electronic energy loss to be converted solely to heat [6]. A plot of heat production (q'') versus depth is plotted in Figure 3.6a. The temperature profile through the sample is calculated with 1-D heat transfer by:

$$\frac{\partial^2 T}{\partial x^2} + \frac{q'''}{k} = 0$$
$$\left.\frac{\partial T}{\partial x}\right|_{x=t} = 0 \quad T(x=0) = 1000^{\circ}C \qquad (3.2)$$

where the boundary conditions are listed below the equation and k is the thermal conductivity of the material. The first boundary condition sets the back surface with adiabatic conditions and the second condition sets the temperature of the front surface. The integration of Equation(3.2) requires a definition of q'''. The simplest definition is constant q''', the next logical step is q''' increasing linearly, followed by an exponential definition, lastly by a polynomial. The calculated q''' (red line) and the q''' with the different definitions of q''' are plotted in Figure 3.6b. The best approximation of q''' resulted from a third-order polynomial fit, shown by the equation in the bottom right corner of Figure 3.6b. The temperature profile through the sample is plotted in Figure 3.7a, for the various definitions of q'''. The temperature profiles for q''' defined as constant (green), q''' defined as linear (orange), and q''' defined as exponential (black) are plotted on the left y-axis and none show a temperature increase of more than 0.35ºC, while the profile for the polynomial definition (blue) is plotted on the right y-axis and shows an increase of ~11ºC. The assumption in Equation(3.2) is not accurate because it is a 1-D problem with only heat addition, which results in temperature continuously increasing over time therefore the temperature profiles plotted in Figure 3.7 are only transient profiles. A true steady-state 1-D representation requires the inclusion of a third term in Equation (3.2) that accounts for heat loss (q_0) in:

$$\frac{\partial^2 T}{\partial x^2} + \frac{q'''}{k} + q_0 = 0$$
$$\left.\frac{\partial T}{\partial x}\right|_{x=0} = 0 \quad \left.\frac{\partial T}{\partial x}\right|_{x=t} = 0 \quad T(x=0) = 1000^{\circ}C \qquad (3.3)$$

where the boundary conditions are listed below the equation. The first two boundary conditions set the front and back surfaces to adiabatic conditions and the third term sets the front surface temperature. The temperature profiles for q''' defined as linear (orange) and q''' defined as a polynomial (blue) are plotted in Figure 3.7b. The steady-state

temperature profile, calculated with the best-approximation of the q''', shows that at steady-state there is no temperature change through the sample thickness.

The non-steady-state temperature increase from the polynomial q''' fit (1.1%) can be considered a conservative estimation of the temperature profile through the samples, which is still a negligible temperature difference. But, as is shown with the steady-state calculation, the heat loss offsets the q''' gradient thus keeping the temperature through the sample thickness uniform.

The dose rate gradient will cause the defect population to increase through the sample thickness, and would be expected to affect to the creep rate and creep behavior. Because creep is dependent on the defect population, this gradient would cause the back surface to try to creep faster than the front surface. This cannot physically occur without the creation of an internal stress, which has been shown to occur in graphite that is experiencing non-uniform dimensional changes due to neutron irradiation. Since the entire sample is creeping at a given rate, and creep rate is assumed to be proportional to dose rate time stress, then for this relation to hold through the thickness of the sample, the dose rate gradient must be accompanied by a stress gradient. Figure 3.8, shows a schematic of the expected stress gradient (blue right y-axis), for a constant creep rate (green) and the known dose rate gradient (red line left y-axis).

3.2 Irradiation Experimental System

The irradiation creep experiments were performed using the 1.7MV Tandetron accelerator at the University of Michigan Ion Beam Laboratory. The samples were loaded on a custom designed stage, which is a portion of a larger irradiation chamber that incorporates the components necessary for experiments condition control and *in-situ* sample measurements. This section will describe the custom stage design, sample arrangement on the stage, stress application on the creep samples, dimensional change measurements, temperature measurement and control, dose determination and monitoring, and beam alignment using an aperture assembly.

3.2.1 Irradiation Chamber

The irradiation chamber was specially designed to accomplish four functions: load application and removal, temperature monitoring and control, proton flux monitoring and control, and *in-situ* measurement of dimensional change of the samples during the experiment. Figure 3.9 is a schematic of the irradiation chamber. The basic principle of operation is to apply a load to thin strip samples that are clamped on both top and bottom and are positioned close to a radiant heater. The temperature is monitored using a 2D infrared pyrometer and the elongation of the sample is measured by a laser speckle extensometer (LSE) (principle measurement technique), and a Differential Variable Reluctance Transducer (DVRT) (backup method). The proton beam is raster-scanned through an aperture over a small area on the sample in which the creep occurs. The following sections describe each of the major elements of the facility.

3.2.2 Irradiation Stage

The irradiation stage was specially designed to accomplish two tasks: securely mount two samples for irradiation creep studies and provide resistive heating to achieve the irradiation temperatures. Both samples are irradiated, but only one is loaded, and the unloaded sample serves as a reference to track dimensional changes. Figure 3.10 is a schematic of the irradiation stage and the dimensions of the assembled stage are shown in Figure 3.11 in (a) cross-sectional and (b) planar views. The stage consists of two 1/16 inch plates of alumina that are supported by four stainless steel posts connected to the vacuum flange. The alumina plates are used to insulate the vacuum flange and other metal components from the high temperatures generated by the heater and the proton beam. Connected to the stage is a pyrolytic coated boron nitride (PBN) heater that has an internal pyrolytic graphite (PG) heating element. A 250μm thick tantalum shield is placed between the PBN/PG heater and the samples, and serves two purposes; to prevent the protons from damaging the thin layer of PBN that covers the heating element, and to allow for the charge induced by the protons to be grounded to the vacuum chamber and measured for dose determination. The minimum thickness of tantalum necessary to stop

the protons is 43μm, but a 250μm thick shield was found to be optimal thickness based on mechanical stability and heat transfer considerations.

3.2.3 Sample Mounting

The samples are attached to the irradiation stage with a set of clamps for each sample. A schematic of the assembly of a graphite sample in the set of clamps is shown in Figure 3.12. The clamps consist of two stainless steel 304 clamp halves, two graphite spacers, and three stainless steel bolts. One clamp half has 0-80 size threaded holes, while the other has drilled holes. In each piece of the clamp is a recess that is thicker than the samples, which was included so that graphite foil can be included to account for thickness variation from sample-to-sample and to prevent crushing of the sample due to the clamping force applied when the clamp bolts are tightened. The three 0-80 bolts are tightened to apply the clamping force to the sample.

The threaded clamp pieces are placed first on a flat plate, a triple thick piece of the spacer graphite is placed in each recess of the clamp pieces, then the sample, followed by another triple thick piece of spacer graphite, followed by the non-threaded clamp pieces, and three bolts for each clamp assembly. The bolts are tightened evenly to induce a constant clamping force on the sample ends. Once assembled the plate and sample with two attached clamps is lifted and turned so the sample is in a vertical direction. Then the sample is pulled away from the plate and moved so the top clamp can be slid onto the sample mounting post until it touches the back clamp collet. The collets on the backside of the sample are positioned so that the samples are 1.5mm from the tantalum heater shield. The front collet is then slid onto the sample mounting post and the set screw is tightened to prevent the sample from moving. This process is repeated for the other sample. After both samples are hung on the stage the load-pin assembly is connected to the bottom clamp of the sample that will have the applied stress. The load-pin assembly is used to assure alignment of the tensile stress with the centerline of the sample and bottom clamp. The load-pin assembly is a two-piece system with a U-shape clevis with a channel cut in the bottom, and pin that connects the clevis to the hole in the sample clamp. The open channel in the load-pin assembly is always orientated away from the other sample; otherwise connecting the load inside the vacuum chamber is not possible.

3.2.4 Application of Stress

The tensile stress is applied by attaching a dead-weight to the load train, shown in Figure 3.13. The load train consists of the load-pin assembly, the weight post, ceramic insulator, and DVRT core. The mass of the bottom clamp, load-pin assembly, weight post, and DVRT core account for a fraction of the weight, while the majority of the weight is achieved with tungsten blocks of varying weight that can be combined to achieve the total weight required to apply the desired tensile stress. The weight required to achieve the target stress is determined by measuring the width and thickness of the sample with a micrometer. A triple beam scale is used to weigh the load train components and tungsten weights are added until the required weight is obtained. The load cell is not utilized in experiments above 600°C because the maximum operating temperature of the cell, 120°C, is exceeded.

3.2.5 Defining the Irradiation Area

A four plate aperture assembly is used to limit the region of the sample to be irradiated and to ensure that the samples are being evenly irradiated with the proton beam. A schematic of the assembled aperture is shown in Figure 3.14. The average aperture opening dimensions are on average 11mm x 11mm for a total area of 121mm^2. The slots in the left, right, and bottom aperture plates allow for adjustment of the aperture opening.

To ensure that the irradiation is uniform over the area of the samples the proton beam must extend past the sample region onto the apertures. The proton beam is focused to 3mm in diameter and a raster-scanner is used to sweep the beam over the sample. Rastering in the vertical direction is performed at 2061Hz and 0.48ms and scanning is in the horizontal direction at 255Hz and 3.9ms, vertical to horizontal ratio of 8.08. Keeping a non-integer ratio of the vertical-to-horizontal scanning cycles ensures the spatial uniformity of the irradiation because the path is always offset from the previous cycle. Figure 3.15 is a schematic representation of the beam path due to the raster scanner [54].

The primary difference that occurs with a raster-scanned beam, compared to a continuous beam, is that within a discrete region the defect production occurs in a pulsed-

manor. When the beam is hitting this small volume the defect production rate is high, but when the beam is not hitting this volume the defects are lost via diffusion down the concentration gradient, recombination, or absorption at sinks. The way to determine the time-average production rate of a pulsed beam ($\bar{K}_0$) is [55]:

$$\bar{K}_0 = K_0 \frac{t_{on}}{t_{on} + t_{off}}, \tag{3.4}$$

where K_0 is the production rate within the area of the scanned beam, t_{on} and t_{off} are the time when the beam is or is not hitting a the discrete volume. For this specific raster scanner the values of t_{on} and t_{off} are 50μs and 2000μs, respectively [54]. Therefore for this raster scanner, the instantaneous production rate is a factor of 41 larger than if the same proton current was continuously hitting the same region. The primary effect that may be arising with this higher instantaneous production rate would be rather the defects undergo more recombination due to the higher defect density.

Additionally, the use of a raster-scanned beam would be expected to effect the defect population if there is overlap of the damage cascades, since overlap could increase the defect loss due to annihilation. To determine if this is, or is not, occurring in graphite we can use the material values to compare the average distance between collisions and the cascade volume. The values we need to make this comparison are: number density (N $8.96\text{x}10^{22}$ at/cm^3), irradiation volume (V $2.31\text{x}10^{-3}$ cm^3), proton beam current (φ 46 μA=$2.87\text{x}10^{14}$ p$^+$/s), beam size (0.071cm^2), scattering cross section (σ_s $1\text{x}10^{-20}$ cm^2), and displaced atoms per collision (5 at/coll). The reaction rate (R) is given by:

$$R = \sigma_s \phi N = \left(1x10^{-20} cm^2\right)\left(\frac{2.87x10^{14}\ {}^{p^+}\!/_{s}}{0.071cm^2}\right)\left(8.93x10^{22}\ {}^{at}\!/_{cm^3}\right) = 3.63x10^{18}\ {}^{coll}\!/_{cm^3 s}. \tag{3.5}$$

Then by assuming the collisions are uniformly spaced, the total number of collisions in a sample (C) is calculated by:

$$C = R*V = \left(3.63x10^{18}\ {}^{coll}\!/_{cm^3 s}\right)\left(2.31x10^{-3} cm^3\right) = 8.38x10^{15}\ {}^{coll}\!/_{s} \tag{3.6}$$

The number of atoms within the irradiation region is equal to N multiplied by V giving $2.06\text{x}10^{20}$at/sample. The ratio of NV to C gives number of atoms surrounding a collision

(~24500 at/coll). Then by using *N* and assuming a spherical region of interaction, the average distance between collisions can be calculated by:

$$\frac{NV}{C} = \frac{2.06x10^{20}\ \frac{at}{sample}}{8.38x10^{15}\ \frac{coll}{sample*s}} = 24583\frac{at}{coll} = N\frac{4}{3}\pi r^3 \Rightarrow \quad (3.7)$$
$$r^3 = 4.05x10^{-7}\,cm = 40.5\text{Å}$$

Therefore the average distance between collisions is 40.5Å, while the atomic spacing is ~1.4Å and only ~5 displacements occur per collision. This large cascade spacing, relative to atomic spacing, suggests that there should be little to no cascade overlap and therefore will not affect the defect population.

To ensure dose uniformity over the width of the samples the beam should be scanned at least one beam width onto each aperture. For the 1.21cm^2 aperture opening the total scanned area is 2.89cm^2 and the aperture scanned area is 1.68cm^2, resulting in a stage to aperture current ratio of approximately 1:1.4. A schematic of this over scan process is presented in Figure 3.16. The slots in the horizontal aperture plates allow for width adjustment but also mean that the width is difficult to set to the exact minimum width. To account for this the aperture opening is at least 1.5mm outside the edges of the samples. This practice accounts for a half beam width over scan. Thus a one half beam width scan onto the apertures is sufficient. For the same aperture opening the new total scanned area is 1.96cm^2 and the aperture scanned area is 0.75cm^2, resulting in a stage to aperture current ratio of 1.5:1.

3.2.6 Measuring Dimensional Change

Elongation in the samples is measured with two independent measurement systems. The first is a non-contact laser speckle extensometer (LSE), which continually measures the dimensional change of both the stressed and reference sample in the center 5mm of the irradiation region. The other system is a differential variable reluctance transducer (DVRT) that is used to measure the dimensional change of the stressed sample over the entire length of the irradiation region.

3.2.6.1 Laser Speckle Extensometer

The LSE is a measurement system purchased from MESSPHYSIK Materials Testing, Austria. The system consists of a 405nm laser, digital video camera, computer, and image analysis software. An illustration of the measurement methodology of the LSE is illustrated in Figure 3.17. The laser is directed so that it is incident on the surface of the sample. The roughness of the sample surface causes the laser light to scatter and some of the light is scattered back towards the digital video camera. An example of the speckle pattern, top left corner of Figure 3.17, shows how the amount of light scattered from each position of the sample changes the intensity of the image; more light scattered and recorded by the camera results in a lighter region on the image. The signal from the digital camera is sent to a computer where the analysis software uses the images to calculate the dimensional changes. An image of the samples is shown in the bottom right corner of Figure 3.17 in which the two samples are outlined by the two large dashed boxes.

The user defines locations within the image to be analyzed. These locations are selected with regions of interest (ROI) boxes, which are shown as the four small dashed boxes in the picture of the software, Figure 3.17. The software uses a Fast Fourier Transform (FFT) to convert the speckle patterns within each box into a three-dimensional surface function, and then applies an algorithm to determine the location of the center of mass of each peak, which is shown schematically in Figure 3.18. The distance between the center of mass peaks from each ROI pair, and the dimensional change within each ROI, is continuously tracked and converted to strain by dividing the displacement by initial distance between ROI's. The software is setup to output and save the time, displacement values, elongation amount, and calculated strain to a tab delimited file every 30 seconds throughout the experiment. The noise in the LSE strain measurement has been quantified for this specific setup and determined to be ±0.02%, which equates to ±1μm for a 5mm gauge length.

3.2.6.2 Differential Variable Reluctance Transducer

The DVRT used in this setup was obtained from MicroStrain® Inc. The DVRT coil is mounted in the bottom of the irradiation chamber approximately 20cm below the bottom of the stage. The coil is mounted on the position feed-through that raises and lowers the load train, and the core is on the end on the load train. The DVRT differs from a linear variable differential transformer in that it utilizes one coil rather than two. The output voltage, ranging from 0-5V, is read into a computer, converted into displacement by a LabVIEW® program using the linear calibration of the DVRT. The LabVIEW® program is set to output and save the time, voltage, and calculated values of displacement and strain to a tab delimited file every 30 seconds throughout the experiment. The noise in the DVRT output voltage is ±0.002V when the output voltage is in the range of 0-1V, and ±0.02V when the output voltage is in the range of 1-5V.

3.2.7 Temperature Monitoring

The temperature of the samples is monitored continuously with an IRCON® two dimensional infrared thermal imaging system (stinger). The monitoring software of the imaging system utilizes areas of interest (AOI) for measuring temperature within a desired area and temperature output. The sizes of the AOI's are defined by the user, in these experiments the AOI size was two pixels vertically and two pixels horizontally. The height of two pixels is used so 12 AOI's can be located within the irradiated region of each sample without overlap, and the two pixel width is used to keep the AOI within the width of the samples. In the software the AOI's are shown as green-outlined boxes. A picture of the Stinger software is shown in Figure 3.19, seen are the 24 AOI's on the two samples, plus the table that shows the measured temperature for each AOI.

The stinger measures temperature within each AOI by measuring the infrared emission of the sample surface, converting this amount of emission into the equivalent temperature of a black-body, and to the sample temperature by correcting for the emissivity difference between the sample surface and a black body. The emissivity of the sample surface is dependent on the surface finish and the geometry of the stinger relative to the sample surface. The emissivity of the graphite samples was determined for this

specific geometric setup with bench-top calibration experiment. Three samples were mounted on the irradiation stage, one in a set of clamps on the left mounting post and two samples were sandwiched together in a set of clamps on the right mounting post. A K-type bare wire thermocouple was positioned between the sandwiched samples. The system was heated with the PBN/PG heater, the temperature of the thermocouple was read, and the emissivity values for the AOI's were set so the left sample read the same temperature. This calibration was only performed up to 600°C, but it has been shown that the emissivity of graphite is constant over a temperature range of 250°C-1500°C [56, 57].

The temperature of each AOI is output to a LabVIEW program that is used to monitor temperature fluctuations and output time-averaged temperature to a tab delimited file. This monitoring method makes it possible to keep the sample temperature within ±8°C of the set irradiation temperature. The measurement error of the Stinger, from the manufacturer, is the larger value of ±2°C or ±2% of the measured temperature [58].

3.2.8 Irradiation Condition Monitoring

The irradiation conditions are monitored continuously with a LabVIEW® program. These conditions include the proton current that is incident on the stage, the proton current on the individual aperture plates, and the pressure within the chamber. Alarms are set to alert the user when the stage current decreases below the desired value, if the apertures become unbalanced, or if the pressure goes above $2x10^{-7}$Torr. This same program is set to output and save the time, stage current, individual aperture currents, total accumulated charge on the stage, and pressure, to a tab delimited file every 30 seconds throughout the experiment.

The irradiation chamber and stage are isolated from the rest of the accelerator so the charge induced by the proton beam can be measured and recorded. The continuously produced charge from the protons hitting the stage creates a current, called the stage current, therefore a change in proton flux changes the total current produced. This current is passed through a charge integrator and then sent to a computer that records the current. Besides just recording the stage current, measurements from the charge integrator are recorded for a cumulative measurement of radiation dose, which

accumulates charge and outputs one count for every micro Coulomb of charge collected. The dose received by the samples at a given time can be calculated from the amount of charge the samples have received up to that point. This is achieved by determining a ratio that relates dose to the number of counts from the charge integrator. The equation for calculating dose from counts is:

$$\frac{Counts}{dpa} = \frac{N\left(\frac{at}{cm^3}\right) * Area(cm^2) * q\left(\frac{C}{proton}\right) * cts\left(\frac{count}{\mu C}\right) * 10^6\left(\frac{\mu C}{C}\right)}{Damage\ Rate\left(\frac{displacements}{ion * Å}\right) * 10^8\left(\frac{Å}{cm}\right)}, \qquad (3.8)$$

where N is the atomic density of the material, q is the Coulomb charge per ion ($1.602 \times 10^{-19} C/p^+$), *Area* is the area of the stage being irradiated, *cts* is the output of the charge integrator (1 count per 1μC of charge), and *Damage Rate* is the value calculated from SRIM. This ratio is input into a monitoring program so during the irradiation the accumulated dose it being constantly displayed.

3.3 Experimental Procedure

This section will present and discuss the experiment procedure for performing the irradiation creep experiments. The first section will discuss the assembly of the irradiation stage and chamber. Next will be a discussion of the process of conditioning the vacuum before starting the irradiation. The third section will discuss the process of starting the experiment. The fourth section will discuss the process of monitoring and controlling the experiment. Finally the experimental conditions used in this research will be presented.

3.3.1 Irradiation Stage Assembly

Prior to mounting the samples it is necessary to assemble the heater and heater shield. The power for the heater is passed into the chamber by a four-pin feedthrough, and then passed through two ceramic insulated copper wires, where finally it is connected to the two chuck assemblies of the heater. The chuck assembly consists of two 0.75 inch long threaded tantalum rods, six molybdenum nuts, four grafoil washers, and four

pyrolytic graphite (PG) washers. The electrical connection is achieved by placing a grafoil washer, a PG washer, and then the Mo nut on the front electrical connection point of the heater, threading the rod through the nut until the top faces are flush and then tightening a second Mo nut, PG washer, and grafoil washer on from the back side of the heater, see Figure 3.20 for a schematic of the assembled heater. The heater is fragile so the nuts should never be tightened more than one quarter of a turn tighter than finger-tight. Once both connections are made the resistance should be around 8Ω. Then the heater is mounted on the stage by passing the threaded rods through two holes on the alumina stage and then secured with the last two Mo nuts, see Figure 3.21. The copper wires have pins on both ends one of which goes onto the back of the threaded rod and the other goes onto the pin of the electrical feedthrough. After the connection is complete, the resistance of the system is tested with an ohm meter from the outside pins of the feedthrough. This resistance should still be around 8Ω. Then the feedthrough is connected to the power supply, and the current is raised to 0.25A to assure that all connections and the heater are working. Then the feedthrough is disconnected for moving the stage into the vacuum chamber.

Once the heater is assembled then the tantalum heater shield needs to be attached to the stage. The shield mounts to the stage in a manner similar to the heater. There are two mounting holes in the heater that are only for mounting (no power supply). The tantalum shield has corresponding holes. The shield is attached to the stage with two more molybdenum rods, four nuts, and a small piece of tantalum that electrically connects the shield to the stage. The shield is held on the stage by threading the rod through the nut until the top faces are flush, then passed through the hole in the shield, the hole in the heater, and another hole in the alumina stage. The small tantalum piece is tightened between the top nut and the heater shield in the upper corner of the heater and is connected to one of the four stage posts.

After the heater and shield are assembled the samples can be mounted on the stage following the process presented in Section 3.2.3. The tensile stress is applied to the sample outside the vacuum chamber to assure that the sample is clamped tightly and can hold the necessary stress. If the sample slips out of the clamps or cannot hold the stress a

new sample must be remounted and tested. Once a sample holds the stress on the bench top then the aperture can be connected to the stage.

The apertures are held on the stage with three 8in long posts. The posts must be at least 8in so that the apertures will not interfere with the LSE line-of-sight of the samples. Near the end of the aperture posts is a ceramic insulator that keeps the apertures isolated from the stage. These insulators need to be below the height of the stage to keep the ceramic pieces from producing interference in the Stinger temperature measurement. There are four wires that connect the aperture plates to an electrical feed through. The wires for the left and top aperture plates must be wound over the top aperture posts and around the back on the stage to reach the feedthrough to prevent them from interfering with the LSE, while the right and bottom wires do not need any special considerations. The aperture wires have female connectors that have corresponding male connectors that are soldered on the four feedthrough pins. An ohm meter is then used to check that none of the aperture plates are in electrical contact with the stage. The aperture feedthrough is then connected to the monitoring computer and setup so the top aperture plate is read into the computer as aperture 1, the bottom aperture plate is read as aperture 2, the left aperture plate is read as aperture 3, and the right aperture plate is read as aperture 4. This arrangement is utilized to aid in aligning the beam on the stage and apertures during startup. Then the feedthrough is disconnected for moving the stage into the vacuum chamber.

It is necessary to align the opening of the aperture with the samples. The width of the aperture opening can be increased, decreased, or shifted side-to-side during the alignment process because of the slots cut into the two horizontal plates. Alignment is performed with a bench-top setup shown in Figure 3.25. The assembled stage is at the right end of the laboratory bench, a laser that is mounted on an adjustable hand jack on the left end, and in the middle is the alignment jack that has two holes drilled through it to ensure the laser is aligned perpendicular to the stage. The first step of the alignment process is to center the laser through the alignment jack, the apertures, and on the stage (solid red line in Figure 3.25). After the laser is centered a piece of plastic is placed over the hole on the alignment jack closest to the stage to diffuse the laser and allow for the diffuse laser to completely cover the aperture opening. A picture highlighting this

process is shown in Figure 3.26. After alignment has been achieved, small scratches are made on the heater shield to indicate the top and bottom of the irradiation area, which are used as indicators for adjusting the vertical alignment of the LSE to the center of the irradiation region.

3.3.2 Irradiation Chamber Assembly

The main irradiation chamber is attached to the end of the accelerator 15° beam line. The orientation of the chamber must be kept so that the LSE nipple is orientated to the right and the Stinger nipple is orientated up and to the left. Before tightening the chamber on the beam line it is necessary to check that the top flange of the chamber is level. A picture of the chamber attached to the beam line is shown in Figure 3.27.

Next the bottom chamber, Figure 3.28, is connected to the bottom of the main chamber. This portion of the chamber houses the linear positioning feethrough. On the top of the feedthrough is the DVRT tower assembly that holds the DVRT cylinder. There are two ports on the sides of the nipple, one large port that has a hinged access window for positioning the DVRT tower and a small port that has the electrical feedthrough for the DVRT and load cell.

After tightening the bottom chamber, the feedthrough for the DVRT and load cell is connected to the monitoring computer. Next the load assembly, Figure 3.13, is placed in the DVRT tower. The weight assembly is lifted and lowered by hand to check that the monitoring computer reads the motion of the DVRT.

Next the irradiation stage is inserted into the irradiation chamber. The stage is lightly tightened to keep it secure and then adjusted until the stage is level. An ohm meter is used to double check that the aperture plates are not electrically grounded to the chamber or each other. Then the stage flange is tightened to the irradiation chamber. After tightening the stage, the DVRT positioning feedthrough is lifted to bring the bolt, at the top of the weight post, to a level that it can be inserted into the load-pin assembly without stressing the sample. Next the feedthrough is lowered until the bolt settles in the channel at the bottom of the load-pin assembly, then lowered until the DVRT starts to show motion, which means that the stress has been applied to the sample, and then lifted back to the position where the stress has been removed.

At this point the LSE is aligned and focused so the samples are centered within the width of the camera viewing region and so the vertical viewing region is located within the irradiation region. The chamber is sealed, all necessary electrical connections are made, and then the load positioning feedthrough is lowered to reapply the stress to the sample. The final step in assembling the chamber is to attach and tighten a blank flange to the top port of the chamber. The top port is left open during the loading process to allow access to the stage during the assembly process. Once the top flange is tight the DVRT feedthrough is lowered again to apply the stress to the sample.

3.3.3 Pre-irradiation Vacuum Conditioning

Once the chamber is sealed, the conditioning of the vacuum can begin. The first step in the process is to pull intermediate vacuum, below 100mTorr, on the irradiation chamber with a turbo pump, at which point the chamber is opened to the beam line and the vacuum quickly comes into the range of $3\text{-}4\text{x}10^{-6}$Torr. If the pressure inside the chamber does not achieve this range in half an hour there is a leak on one of the flanges.

With the experiments being performed at very high temperatures, and with the high oxidation rate of graphite, it is necessary to bake out the stage and chamber before starting the irradiation. Baking out the system helps released gasses trapped in the stage and chamber, and by doing so in a controlled manner prevents the graphite samples from oxidizing. The process of baking out this system is an incremental process of increasing the heater current and waiting for the vacuum pressure to recover. The first part of this process involves increasing the heater in steps of 0.5A and usually requires 45-90 minutes for the vacuum pressure to recover, up to 3A total going to the heater. The last part calls for increases in the heater in steps of 0.75A and usually requires 30-45 minutes for the vacuum pressure to recover. Once the heater current is above 5A the system is allowed to sit for a minimum of 8 hours, until the total vacuum pressure is below $7\text{x}10^{-8}$Torr. After this pressure has been attained, the heater is adjusted to the settings to be used for the experiment.

An example of the heater current, heater temperature, sample temperature, and chamber pressure during bake out is shown in Figure 3.29. In this example the experiment was conducted with pre-irradiation sample temperature of 475°C, but most

experiments required turning the heater off and returning the samples to room temperature. During the bake out process, the Stinger software is setup for the experiment and begins recording the sample temperature during the rest of the bake out process.

3.3.4 Irradiation Startup

The conditions of the experiment, dose rate and temperature, determine the total amount of beam current that is necessary. The total amount of current is obtained in the high energy faraday cup, at which time the low energy faraday cup is inserted, the high energy faraday cup and all the gate valves between the source and irradiation stage are removed and opened.

Next the steerer scanner is turned on, and the scanner amplitude is increased so the beam scan area is much larger than the aperture opening to prevent exceeding the desired irradiation temperature. At this point the low energy faraday cup is removed and allows the beam through the accelerator. The sample temperature will rise instantaneously when the beam is applied. The positioning and amplitude of the raster scanned beam is controlled by the steerer scanner. The settings for the steerer scanner are determined by monitoring the current on each aperture and stage with a LabView based monitoring system. The steerer controls are used to center the scanning beam over the area and the scanner controls are used to adjust the amplitude of the scanned region. These settings are adjusted until the desired stage to aperture ratio is achieved and the current is evenly distributed between the apertures. At this point the amplitude of the scanner is decreased, while continuously watching the sample temperature, until the desired temperature is obtained.

3.3.5 Experiment Monitoring

Throughout the experiment the sample temperature, stage current, aperture currents, chamber pressure, and LSE and DVRT elongation measurements are continuously monitored. The stage current is the only adjustment that is made to maintain irradiation temperature during the experiment, because it was determined that

the DVRT undergoes a thermal transient that lasts 10 hours after the beam has been initially applied to the samples or for a few hours anytime the PBN heater power is changed, but slight changes in the stage current after the initial transient have not been observed to affect the DVRT.

3.3.6 Creep Rate Determination

Throughout the experiment, the strain versus time data, from the LSE and DVRT for the stressed sample only, are analyzed with GraphPad® Prism5 statistical software to determine the linear fit and the 95% confidence interval of the slope. A constant initial length is used to convert displacement to strain, so the error of these values is not significant. The experiment is continued until the 95% confidence interval of the slope is less than 1% of the slope of the linear fit, but in some cases the experiment is continued past the point to achieve a desired final dose.

3.3.7 Stopping an Experiment

Once one or both of these final conditions are achieved, the faraday cup is inserted to end the irradiation. The system is cooled back to room temperature, the monitoring programs are stopped, the load positioning feed through is raised to remove the stress from the sample, the chamber is vented, the stage removed from the chamber, and the samples are removed from the stage. The samples are put into individual boxes and labeled with the irradiation conditions and whether the sample was the stress or reference sample for later analysis.

3.3.8 Experimental Conditions Used

There are three experimental conditions that can be changed for these experiments; applied stress, dose rate, temperature. For graphite the stress dependence is investigated at 1000°C, 1.15×10^{-6}dpa/s, with stresses of 5MPa, 10MPa, 20MPa, and 40MPa. The temperature range for the graphite experiments is 700°C to 1200°C, all at 20MPa applied stress, but the dose rates vary due to the coupling of temperature and dose rate. The dose rate dependence is investigated at 700°C, where some dose rate and

temperature decoupling is obtainable with the PBN/PG heater, with a 20MPa stress, and a dose rate range of 2.95×10^{-7}dpa/s to 5.51×10^{-7}dpa/s.

3.4 Post-Experimental Data Analysis of Creep Tests

This section will present and discuss the post-experimental data analysis of the creep tests, including how the final creep rates are calculated for each experiment, plus the creep rate error. The creep rate and error of the creep rate, for an experiment, are determined by performing a χ^2–analysis for of the LSE and DVRT data, for a linear fit. The χ^2 theorem is defined as:

$$\chi^2 = \sum_{i=1}^{N} \frac{\left(y_i - A - Bx_i\right)^2}{V_i}, \tag{3.9}$$

where y_i is the observed strain (dependent variable), A is the intercept for the best-fit line, B is the slope of the best-fit line, x_i is the time a given y_i is recorded (independent variable), V_i is the variance of y_i, and N is the number of data points [59]. During a given experiment it is acceptable to assume that the variance for all data points is constant, which simplifies Equation (3.9) to:

$$\chi^2 = \frac{1}{V_L} \sum_{i=1}^{N} \left(y_i - A - Bx_i\right)^2, \tag{3.10}$$

where V_L is defined to be the variance of the linear model. The intercept and slope of the best-fit line are determined by taking the partial derivative of Equation (3.10) with respect to A and B, setting both equations equal to 0, and solving for A and B :

$$\begin{aligned} \frac{\partial \chi^2}{\partial A} &= 0 = \frac{1}{V_L} \sum_{i=1}^{N} 2\left(y_i - A - Bx_i\right)(-1) \\ \frac{\partial \chi^2}{\partial B} &= 0 = \frac{1}{V_L} \sum_{i=1}^{N} 2x_i\left(y_i - A - Bx_i\right)(-1) \end{aligned} . \tag{3.11}$$

These two partial derivatives must be solved simultaneously and the resulting solutions are:

$$A=\frac{\sum_{i=1}^{N}x_i^2\sum_{i=1}^{N}y_i-\sum_{i=1}^{N}x_i\sum_{i=1}^{N}x_iy_i}{N\sum_{i=1}^{N}x_i^2-\left(\sum_{i=1}^{N}x_i\right)^2}$$
$$B=\frac{N\sum_{i=1}^{N}x_iy_i-\sum_{i=1}^{N}x_i\sum_{i=1}^{N}y_i}{N\sum_{i=1}^{N}x_i^2-\left(\sum_{i=1}^{N}x_i\right)^2} \quad . \tag{3.12}$$

The variance of the linear model (V_L) is then calculated using Equation (3.10). The value of χ^2 is obtained from a table, where the probability is set to 0.5, which means that the next measurement has a 50/50 chance of being above or below the fit, and the number of degrees of freedom (*DF*), defined as *N* minus the number of terms used in the fit (*P*). For a linear fit the value of *P* is two. For large values of *N*, the value of χ^2 approaches the number of degrees of freedom. V_L is thus determined by:

$$V_L=\frac{1}{N-2}\sum_{i=1}^{N}\left(y_i-A-Bx_i\right)^2 . \tag{3.13}$$

The variance of the intercept, *V*[*A*], and slope, *V*[*B*] are calculated using error propagation by:

$$V[A]=\sum\left[V_L\left(\frac{\partial A}{\partial y_i}\right)\right]=\frac{V_L\sum_{i=1}^{N}x_i^2}{N\sum_{i=1}^{N}x_i^2-\left(\sum_{i=1}^{N}x_i\right)^2}$$
$$V[B]=\sum\left[V_L\left(\frac{\partial B}{\partial y_i}\right)\right]=\frac{NV_L}{N\sum_{i=1}^{N}x_i^2-\left(\sum_{i=1}^{N}x_i\right)^2} \quad . \tag{3.14}$$

The variance of the intercept and slope for the best-fit line are a measure of the certainty of the values, hence the more data points the smaller the variance of either term. Traditionally the certainty is presented in terms of the standard deviation, σ, which is defined as the square root of the variance. The standard deviation of the intercept and slope are given by

$$\sigma_A = \sqrt{V[A]}$$
$$\sigma_B = \sqrt{V[B]}. \tag{3.15}$$

In section 3.3.6, it was stated that the experiments were run until the 95% confidence interval of the slope as calculated by PRISM was less than 1% of the slope. The 95% confidence interval from PRISM is defined as 1.96σ.

A similar analysis can be used on the temperature and stage data for each experiment to determine the standard deviation of the temperature and dose rate. Instead of defining a linear model for the fit a constant value model is used (zero slope). The resulting model is:

$$\chi^2 = \frac{1}{V_C}\sum_{i=1}^{N}\left(y_i - M\right)^2, \tag{3.16}$$

where M is the constant value, and V_C is the variance of the constant model. The same process of taking the partial derivative with respect to M:

$$\frac{\partial \chi^2}{\partial M} = 0 = \frac{1}{V_c}\sum_{i=1}^{N} 2\left(y_i - M\right)(-1), \tag{3.17}$$

setting equal to zero, and solving for M results in:

$$M = \frac{\frac{1}{V_c}\sum_{i=1}^{N} y_i}{\frac{N}{V_c}} = \frac{\sum_{i=1}^{N} y_i}{N}, \tag{3.18}$$

which is the equation for the arithmetic mean. The variance of the constant model is the calculated the same way as the linear model variance by:

$$V_C = \frac{1}{N-1}\sum_{i=1}^{N}\left(y_i - M\right)^2, \tag{3.19}$$

except that the number of terms used in the fit is only one, so the degrees of freedom is equal to N minus one. The variance of the constant, $V[M]$, is calculated by:

$$V[M] = \frac{V_C}{N}, \tag{3.20}$$

and the standard deviation of the constant is given by:

$$\sigma_M = \sqrt{V[M]}. \tag{3.21}$$

3.5 Atomic Spacing, Lattice Strain, and Crystallite Dimensions

This section presents the methodology used to measure and determine the atomic spacing and crystallite dimensions for the samples. These measurements and calculations were performed using X-ray diffraction (XRD). The XRD measurements were performed using the Rigaku Rotating Anode X-ray Diffractometer at the University of Michigan Hanawalt X-ray Microanalysis Laboratory. This diffractometer uses a copper source to produce X-rays with a wavelength of 1.540598Å and 1.544418Å for the $K_{\alpha 1}$ and $K_{\alpha 2}$ X-rays, respectively. A monochromator is used to limit the beam to contain only the $K_{\alpha 1}$ and $K_{\alpha 2}$ X-rays. All the XRD measurements were performed with the system in the $\theta/2\theta$ reflection mode, which rotates the sample θ degrees relative to the incident X-rays and the detector is at 2θ degrees relative to the incident X-rays. All of the spectra are recorded as counts versus 2θ.

Traditionally samples are held on an aluminum sample holder using a glass slide and clay compound, as shown in Figure 3.30a, but the diffraction peaks that arise from the clay that sticks out around the sides of the sample overlap with the peaks of interest for graphite. To remove the overlap a new sample holder was developed that eliminates the need for the glass and clay, Figure 3.30b.

The full spectrum for the as-received sample was taken for a 2θ range from 20-80°, with a scan rate of 0.80°/min, and a step size of 0.020°/step. This initial scan was used to determine scan rates for the different peaks of interest, because the scan rate directly affects the number of counts for each step. The initial scan showed a high intensity of the 0002 peak, while the other peaks were relatively weak, so to account for these lower intensity peaks the scan rates were decreased to increase the number of counts for each peak. For statistical measurements, the standard deviation is equal to the square root of the number of counts. The scan rates were decreased until the standard

deviation of the statistical measurements was less than 5% of the total number of counts at the peak maximum, thus requiring a minimum of 400 counts.

The primary peaks of interest are the [0002], [0004], and $[11\bar{2}0]$ peaks, because they are resulting from diffraction from one direction and do not have overlap with other peaks. The [0002] and [0004] peaks are used to analyze the c-axis spacing, plus the c-axis lattice strain and the c-direction size of the crystallites. The $[11\bar{2}0]$ peak is used to analyze the a-axis spacing and the a-direction crystallite size. The [0002] peak occurs for a 2θ of ~26°, [0004] occurs for a 2θ of ~54°, and the $[11\bar{2}0]$ peak occurs for a 2θ of ~76.5°. The scans for the [0002] peak was performed over the 2θ range of 24°-28°, the range for the [0004] peak was 53°-56°, and the $[11\bar{2}0]$ peak was 76°-79°, and all the scans were performed with a step size of 0.01°/step and a scan rate of 0.04°/minute. In addition, scans over the range of 32°-48° were performed with a step size of 0.01°/step and a scan rate of 0.20°/minute, to investigate the occurrence of rhombohedral structure in the irradiated samples.

The atomic spacing is obtained from the location of the diffraction peaks, while the lattice strain and crystallite dimensions are obtained from the width of the diffraction peaks. Crystalline graphite has a macroscopic grain structure and a microscopic crystallite structure. Each grain has an overall c-axis orientation, but the grains are all comprised of a large number of crystallites. The crystallites are defined as small volumes within a grain, which have a perfect hexagonal graphite crystal structure. The c-axis of the crystallites within a particular grain are all aligned with the macroscopic c-axis orientation of the grain, but the basal planes from one crystallite to another have different rotations around the c-axis [60].

3.6 Measurement of Young's Modulus and Hardness

The Young's modulus of the graphite samples is of interest in that it can directly relate to the elasticity of the material, which is highly dependent on the defect structure. Determining the Young's modulus allows a method to directly compare the graphite experiments by comparing the elastic strain unit of each experiment, where an elastic

strain unit is defined as the tensile stress divided by the Young's modulus. The hardness of the material is also of interest because it relates to the defect structure within the material and changes in the plastic behavior.

The Young's modulus and hardness measurements are performed using a TI-950 TriboIndenter, from Hysitron Inc., at the University of Michigan Orthopaedic Research Laboratories. This nano indenter uses a Berkovich tip, which results in equilateral triangle shaped indents. The samples are mounted on 0.5 inch diameter AFM specimen discs with crystal bond. The indentation process is controlled by a three-plate capacitive force/displacement transducer [61], patented design of Hysitron. The displacement of the indenter tip is determined with fixed top and bottom AC electrodes, which are 180° out of phase for their AC signals, and an electrode attached to the indenter tip. The sum of the two output signals is the resulting measure of the displacement, and is recorded in volts and converted into depth within the software. The indentation force is created by creating an electrostatic force between the bottom electrode, with an applied DC bias, and the electrode attached to the indenter tip, which pulls the indenter tip electrode down towards the bottom electrode. The force is recorded in units of volts, and converted to force within the software.

Prior to indentation, the samples were polished by hand with 0.5μm diamond lapping film until a mirror-like finish was achieved, which was done to remove the surface roughness that resulted from the EDM machining. For each sample, 50 indents were performed to provide better statistics for the measurements. The indents were aligned in a 10x5 indent array with 150μm spacing in both directions. The indents for this work were performed to maximum load of the indenter, 10mN, and were controlled with the force displacement mode. The loading process was: loading 0mN-10mN in 10 seconds, hold for 5 seconds, and unloading 10mN-0mN in 10 seconds. The force versus depth measurements are recorded for the entire loading and unloading process.

The indenter software fits the load versus depth data using a power law defined by:

$$P = A\left(h - h_f\right)^m, \tag{3.22}$$

where P is the force, A is indentation area, h is the depth, h_f is the post-load displacement, and m is a constant, for the unloading range from 98%-20%. The derivative of load versus depth results in the contact stiffness, S, defined by:

$$S = \frac{dP}{dh}. \tag{3.23}$$

The contact depth (h_c) is calculated by:

$$h_c = h_{\max} - 0.75 * \frac{P_{\max}}{S}, \tag{3.24}$$

where h_{max} is the maximum depth, P_{max} is the maximum force, S is stiffness, and the second term in the equation is the elastic depth. The Young's modulus is calculated by:

$$E_r = \frac{\sqrt{\pi}}{2\sqrt{A(h_c)}} S, \tag{3.25}$$

where S is the stiffness, and $A(h_c)$ is the calculated area of the indent from the geometry of the Berkovich tip at the contact depth. The hardness (H) is calculated by:

$$H = \frac{P_{\max}}{A(h_c)}, \tag{3.26}$$

where P_{max} is the maximum applied load and $A(h_c)$ is the same area of the tip used in Equation (3.25).

3.7 Experimental Determination and Analysis of Anisotropy

The change in anisotropy of the graphite samples is also being studied. The historical method for determining anisotropy of graphite utilized transmitted X-rays to obtain 0002 diffraction patterns, which were analyzed to determine an anisotropy value, now termed the Bacon Anisotropy Factor (BAF) [62] and the orientation parameter (R) [63]. It was determined that transmission electron microscopy (TEM) can be used in place of the historical method to determine the anisotropy of these ultra-fine grain graphites.

The anisotropy measurement from TEM uses selected area electron diffraction (SAED) to obtain the 0002 diffraction pattern from the sample. These patterns are then analyzed with the Graphite Anisotropy Analysis Program (GAAP) [64], which was specially written to extract the necessary data from the SAED patterns and then perform the numerical integrations to calculate the BAF and R values.

3.7.1 TEM Sample Preparation

To perform the SAED analysis the TEM samples need to be prepared so the sample is electron transparent, while obtaining a large thin region. The samples were prepared with a traditional mechanical polishing technique. First the samples were polished on both sides with 0.5μm diamond lapping film until a mirror-like finish was achieved. Next the samples were adhered, using M-Bond^{TM} 610 adhesive, to molybdenum support grids with a 1.5mm center hole. Lastly the samples were thinned using a Gatan Inc. Precision Ion Polishing System. The first thinning step used two 4.5keV argon ion beams 4° off the bottom of the sample, until a visible hole was formed. The final polish was performed with 2keV argon ions 2° off the bottom of the sample for 15 minutes.

3.7.2 SAED Pattern Collection

The SAED patterns are obtained using a 300kV JOEL 3011 TEM at the University of Michigan Electron Microbeam Analysis Laboratory. An SAED aperture with a 300μm physical opening, which results in a 6.5μm diameter circle when incident on the sample, is used to allow for a large area of the sample to be analyzed. The TEM is used with the 300kV accelerating voltage. First the sample to be analyzed is found in the microscope and then brought into focus. Next the desired SAED aperture is inserted and centered over the sample. Then the TEM is switched from imaging to diffraction mode to obtain the diffraction pattern. The diffraction pattern is recorded with a CCD camera as an 8-bit TIFF image, where the gain and exposure time of the camera are set so the [0002] diffraction ring in not saturated or covered by the transmitted spot. This was

repeated with each sample until 37 SAED patterns were recorded, which covered a total area of ~1200μm^2.

Table 3.1. Material properties of ZXF-5Q from [65].

Particle Size <1μm	Pore Size <0.3μm
Total Porosity 20% (volume)	Open Porosity 80%
Apparent Density 1.78g/cm^3	Compressive Strength 175MPa
Flexural Strength 112MPa	Tensile Strength 79MPa
Modulus of Elasticity 14.5GPa	Thermal Conductivity 70W/mK

Table 3.2. SRIM estimated range and straggle of protons with energy of 2.00 to 3.40 MeV, calculated by SRIM [53].

Proton Energy (MeV)	Range (μm)	Straggle (μm)
2.00	48.15	1.88
2.25	58.58	2.43
2.50	69.89	2.95
2.60	74.66	3.04
2.70	79.57	3.28
2.75	82.08	3.45
2.80	84.62	3.48
2.90	89.8	3.65
3.00	95.13	3.96
3.10	100.58	4.05
3.20	106.17	4.29
3.25	109.02	4.46
3.30	111.9	4.49
3.40	117.76	4.66

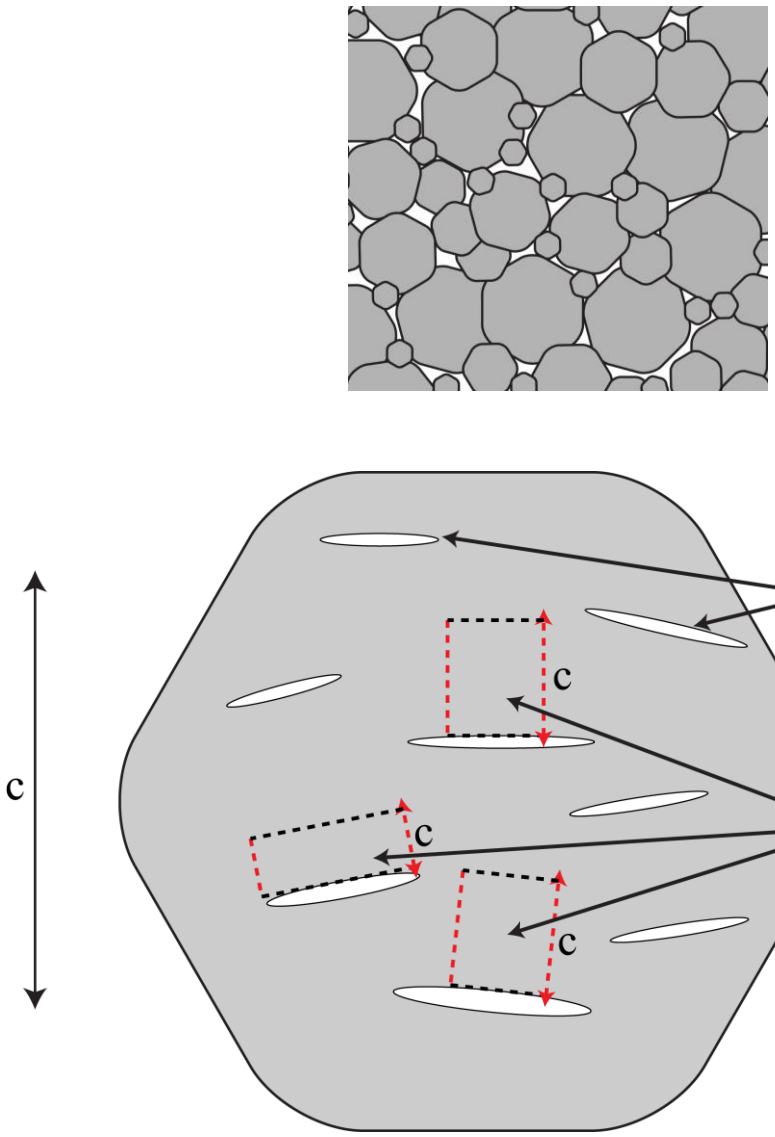

Figure 3.1. Schematic representation of the (a) randomly-orientated macroscopic structure (grey filler particles and white porosity) and (b) filler particle showing particle c-direction, Morovski cracks, and crystallites.

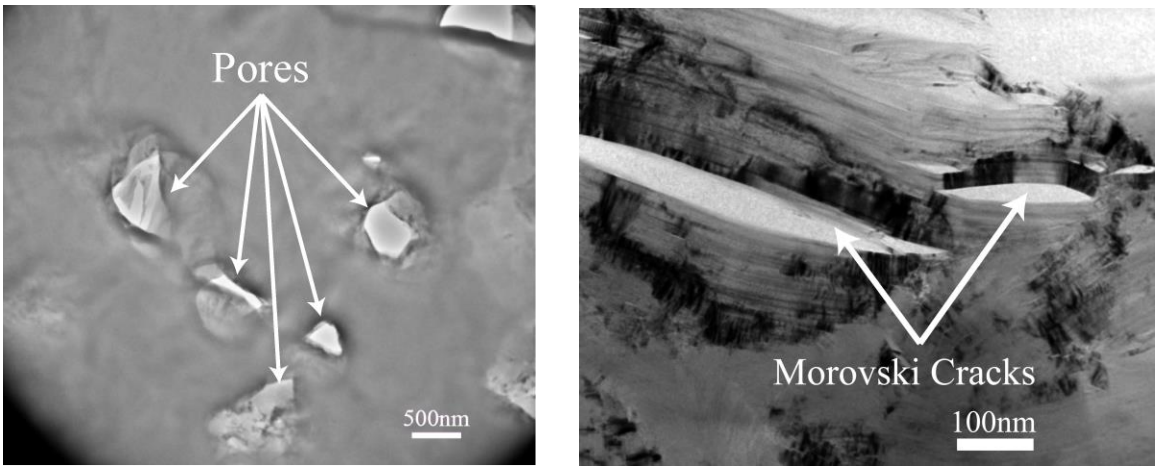

(a) (b)

Figure 3.2. TEM images of ZXF-5Q showing pore structure (a) and Morovski cracks (b).

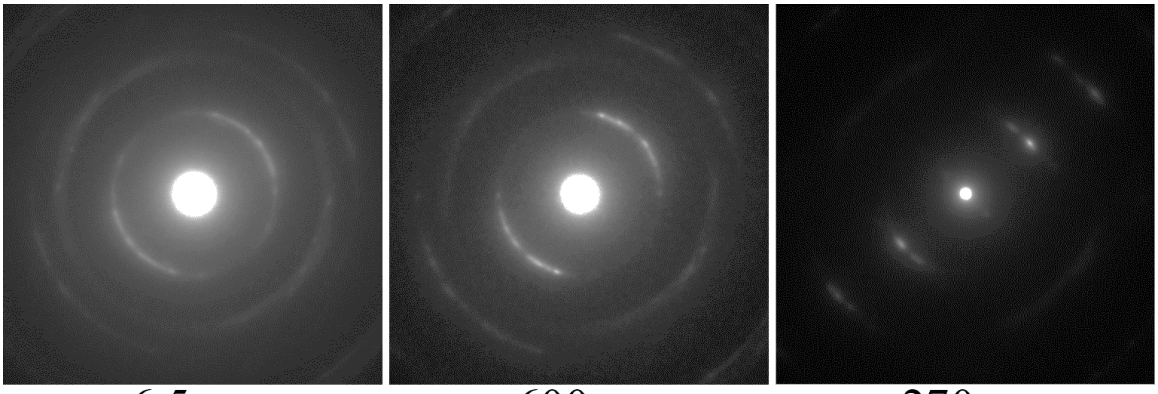

Figure 3.3. TEM SAED patterns with progressively smaller aperture diameters from left-to-right.

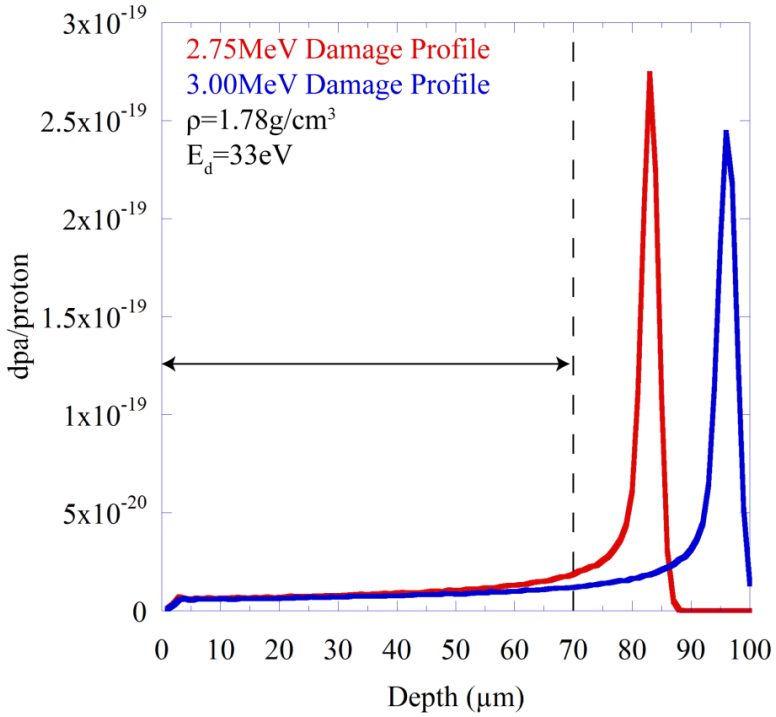

Figure 3.4. SRIM calculated displacement damage as a function of depth for 2.75MeV protons (red curve) and 3.0MeV protons (blue curve). The surface of the sample is located at the left side of the plot and the thickness of the sample is indicated with the dashed black line.

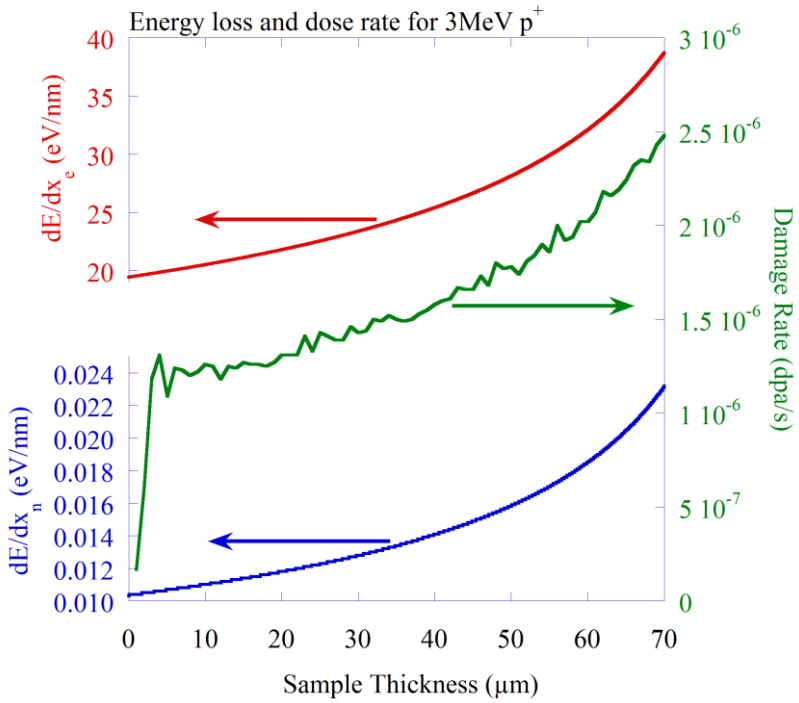

Figure 3.5. Plot of electronic energy loss (red), nuclear energy loss (blue), and damage rate (green), through the thickness of the sample.

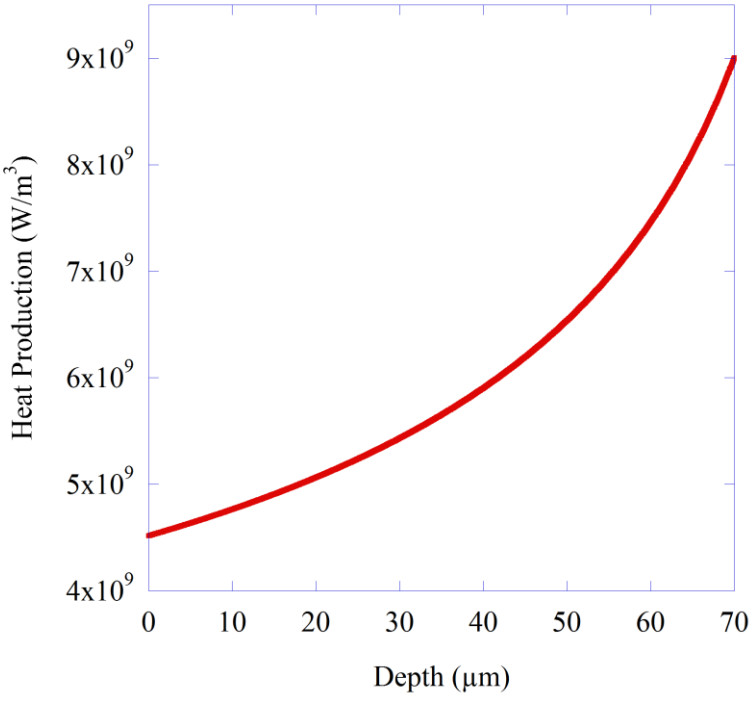

(a)

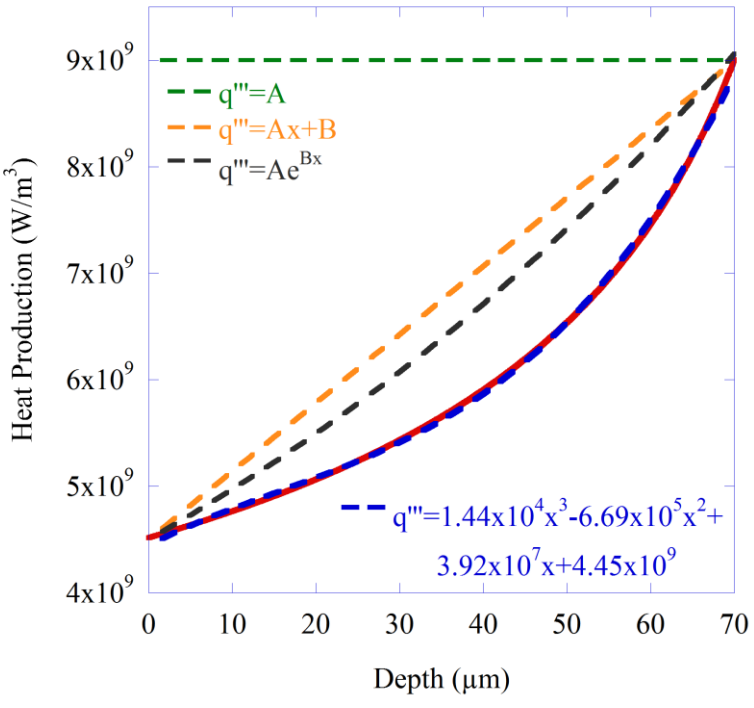

(b)

Figure 3.6. Heat generation (red) and sample temperature (blue) for a sample irradiated with a 3MeV proton beam and stage current of 23μA/cm^2.

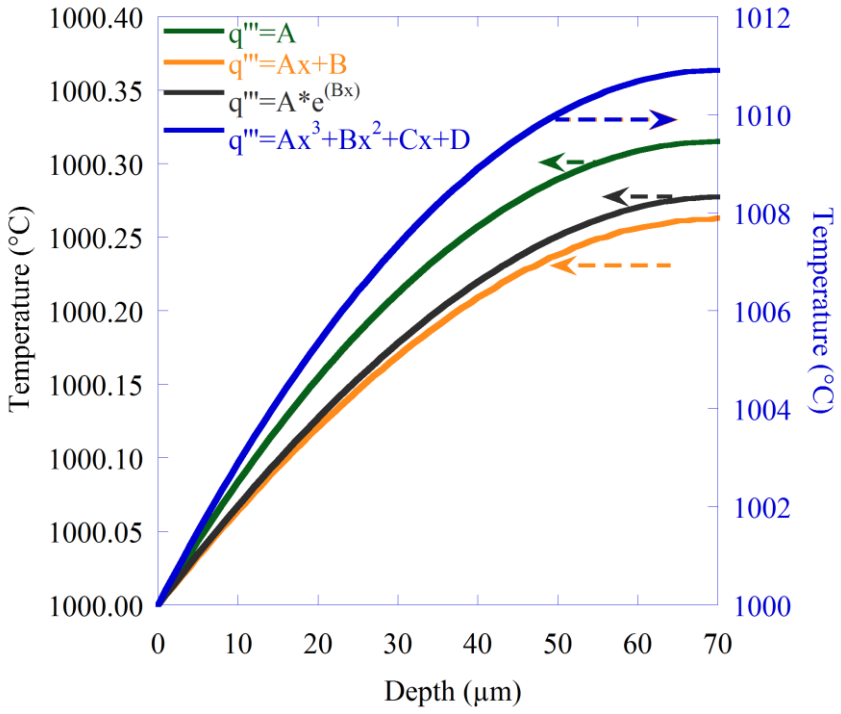

(a)

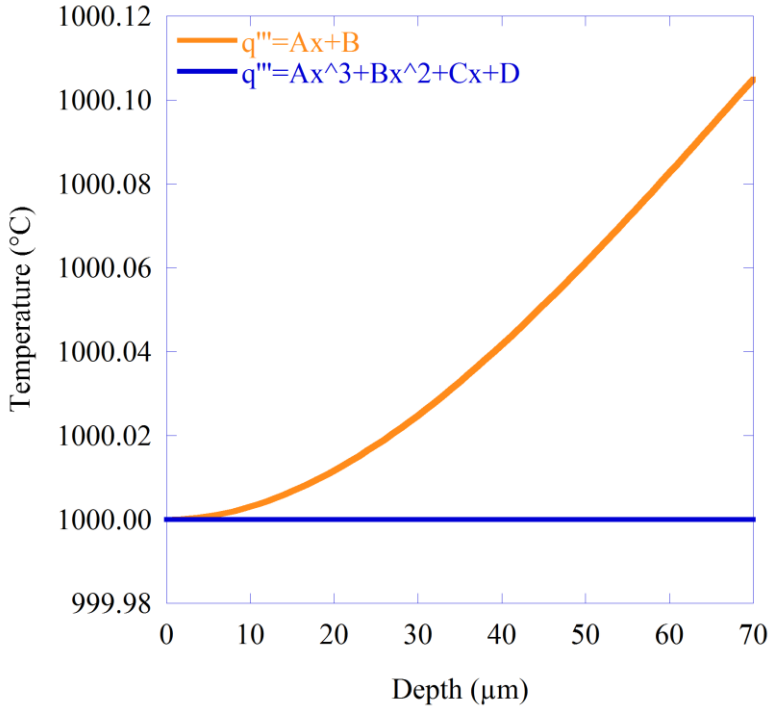

(b)

Figure 3.7. Plot of temperature profiles through sample for different definitions of q''', (a) without heat loss and (b) with heat loss.

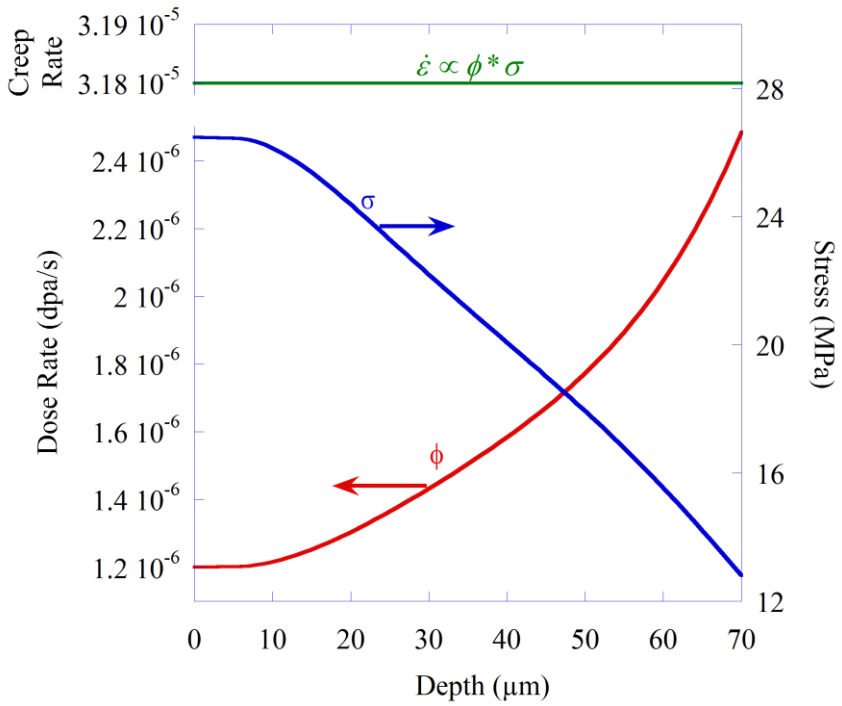

Figure 3.8. Schematic of the expected stress gradient (blue) for a constant creep rate (green) and the known dose rate gradient (red)

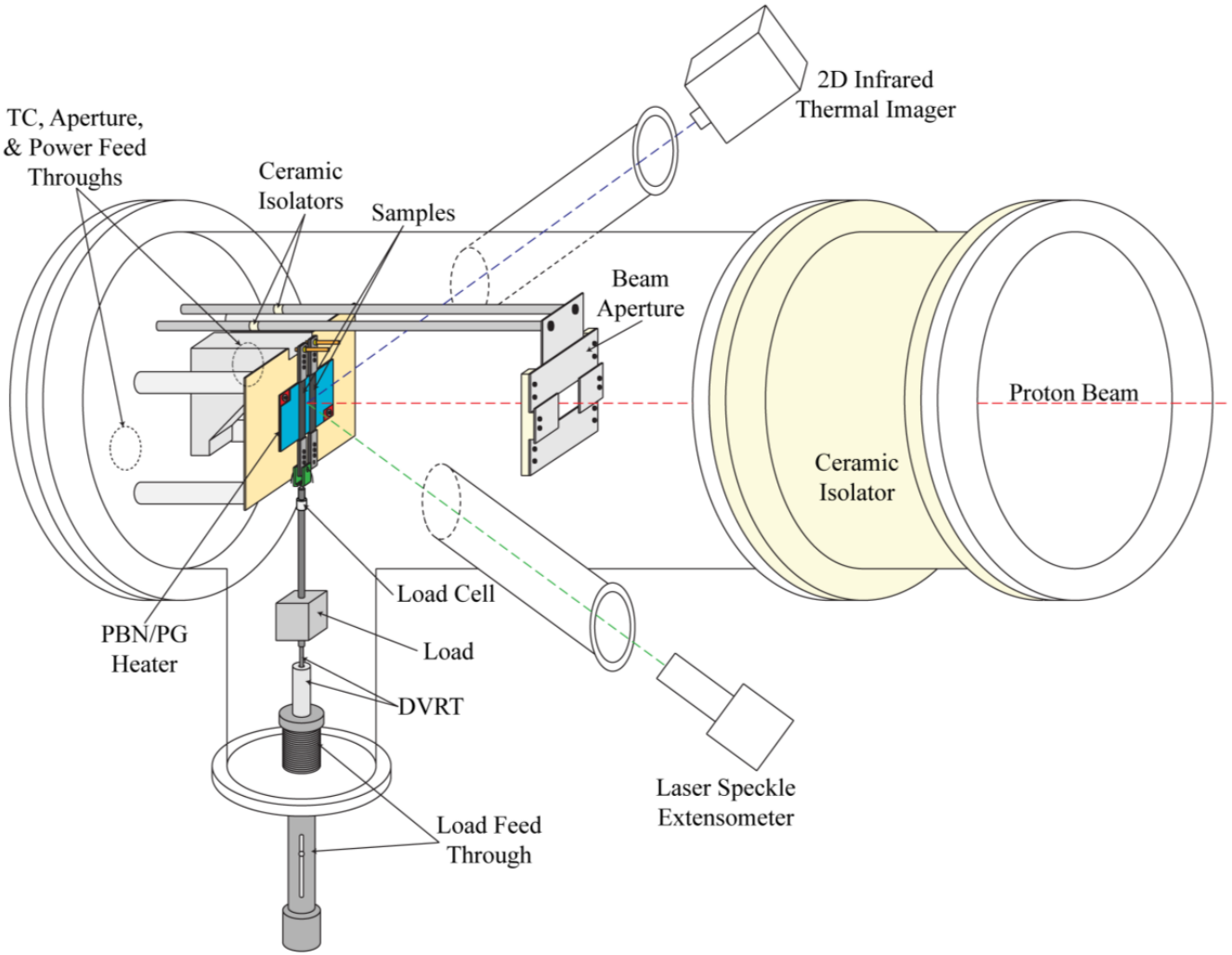

Figure 3.9. Schematic of irradiation chamber, showing the locations of the primary components of the system.

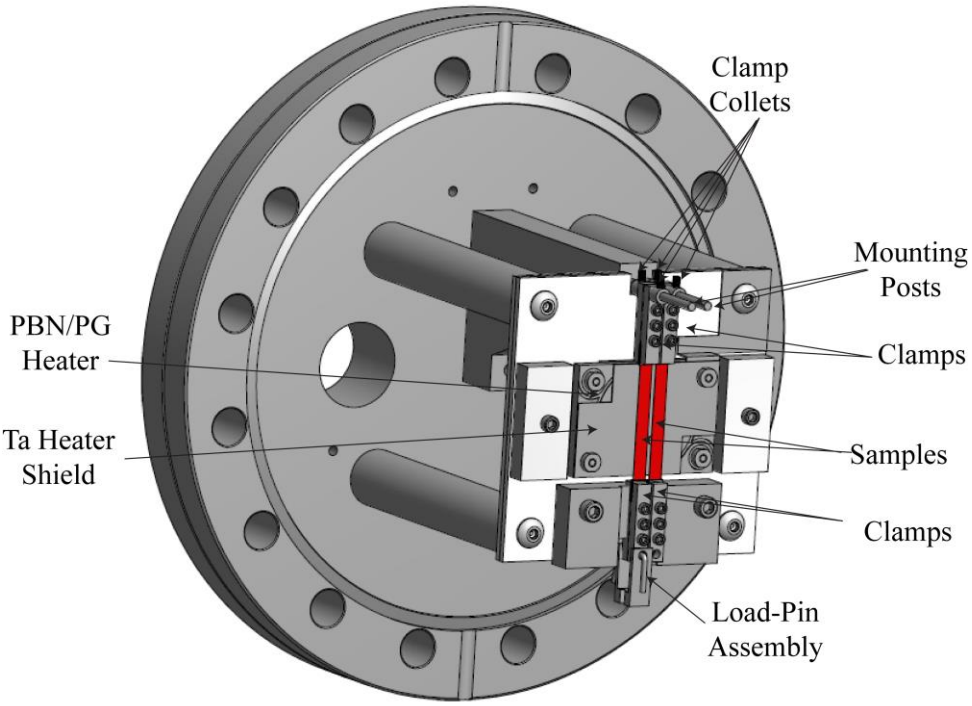

Figure 3.10. Schematic of the irradiation stage, showing the primary components used for load application and sample temperature control.

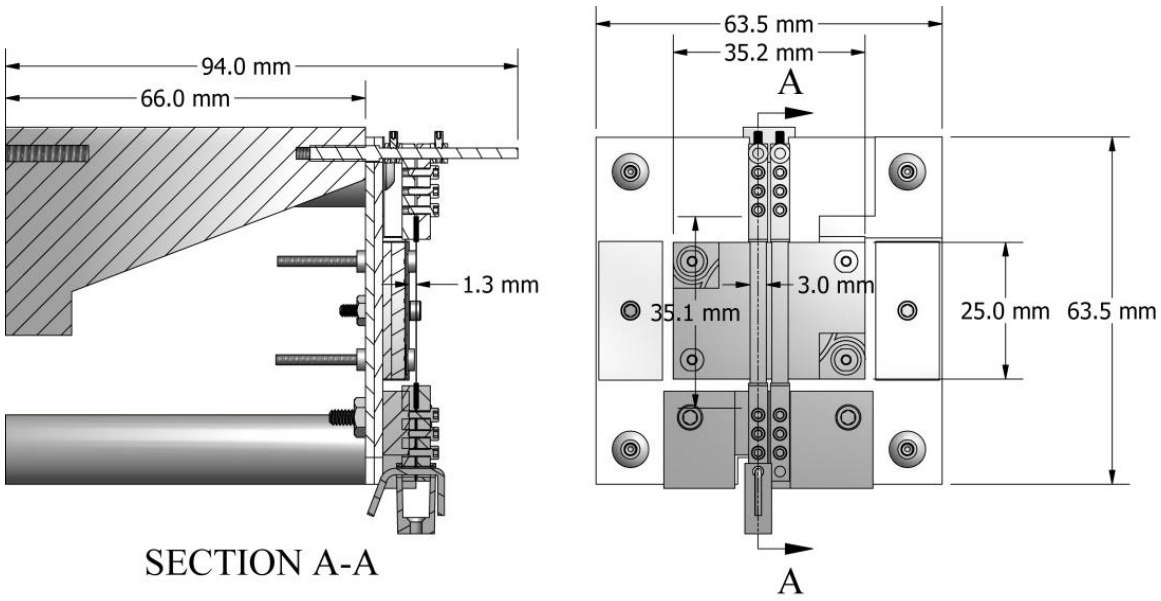

Figure 3.11. (a) Cross-sectional and (b) planar drawings of the assembled stage, with some of the primary dimensions marked. The cross-section is taken along the line A-A in the planar drawing. Note that the components in the drawing are to scale.

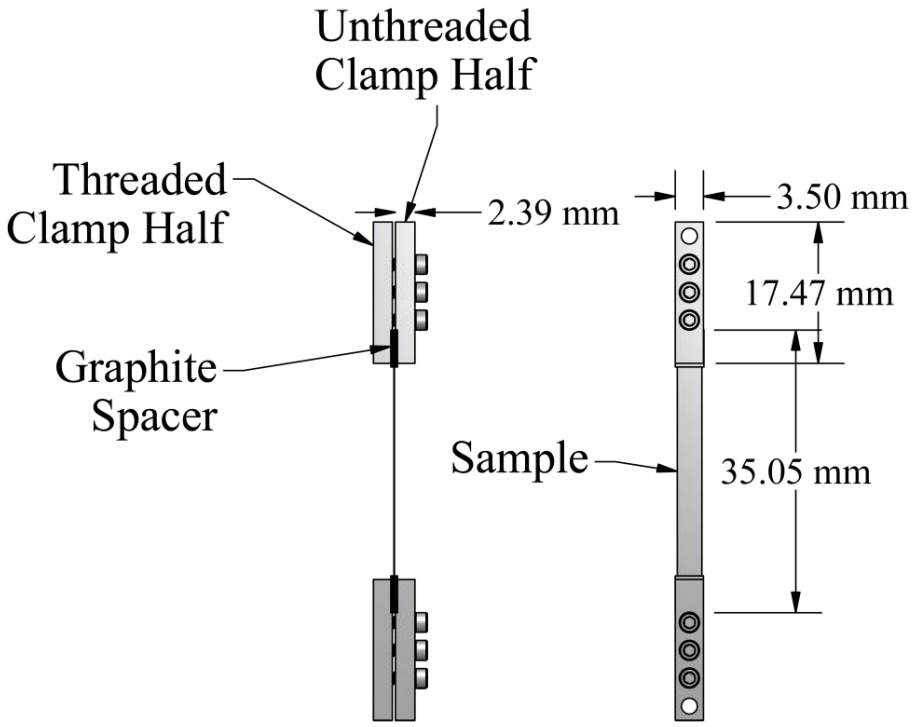

Figure 3.12. Schematic of a sample assembled in the set of clamps. Each clamps consist of two halves, one threaded the other not, two graphite spacers, and three bolts.

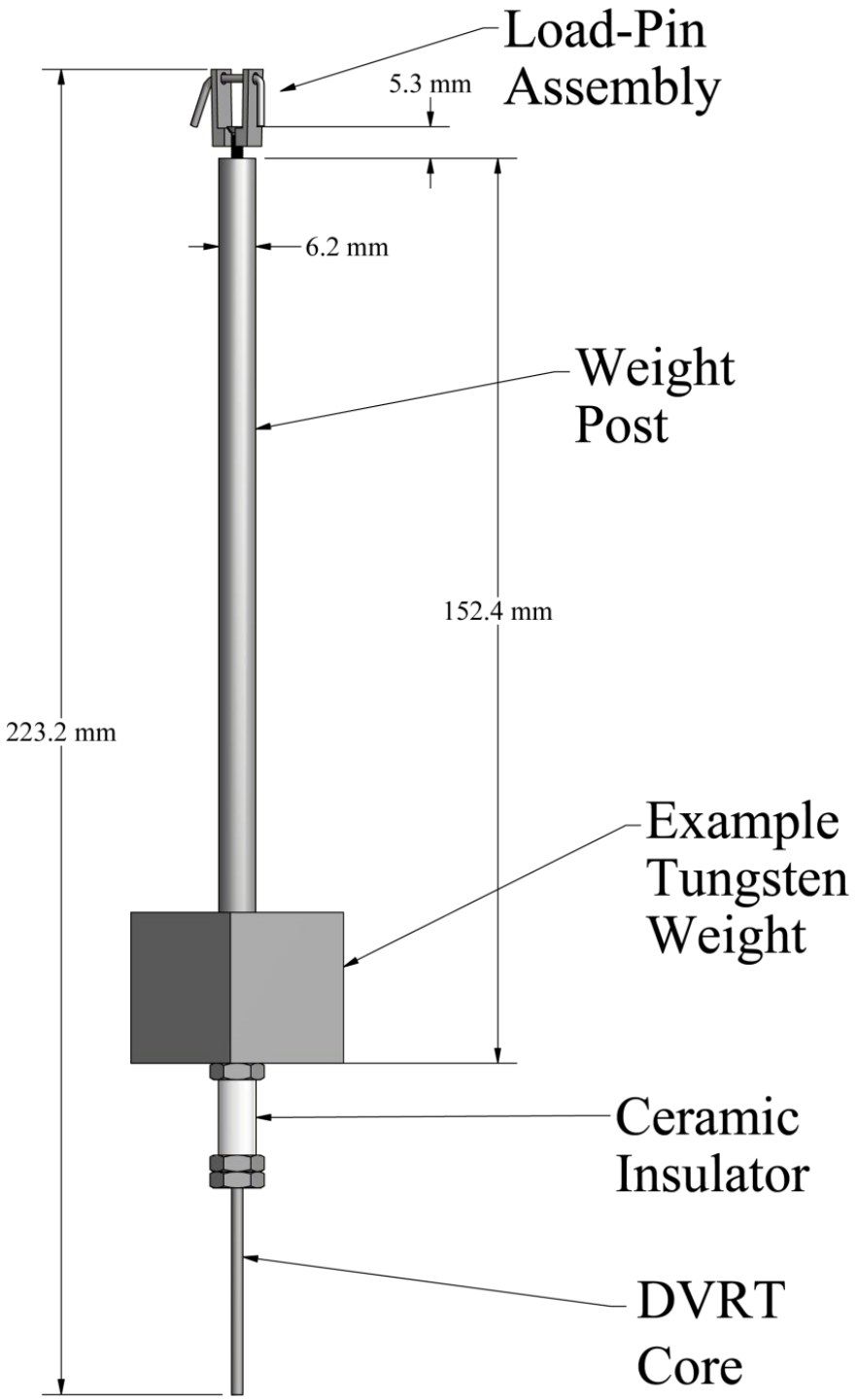

Figure 3.13. Schematic of the load train including the load-pin assembly for reference to location relative to Figure 3.10, the weight post, DVRT core, and an example tungsten weight.

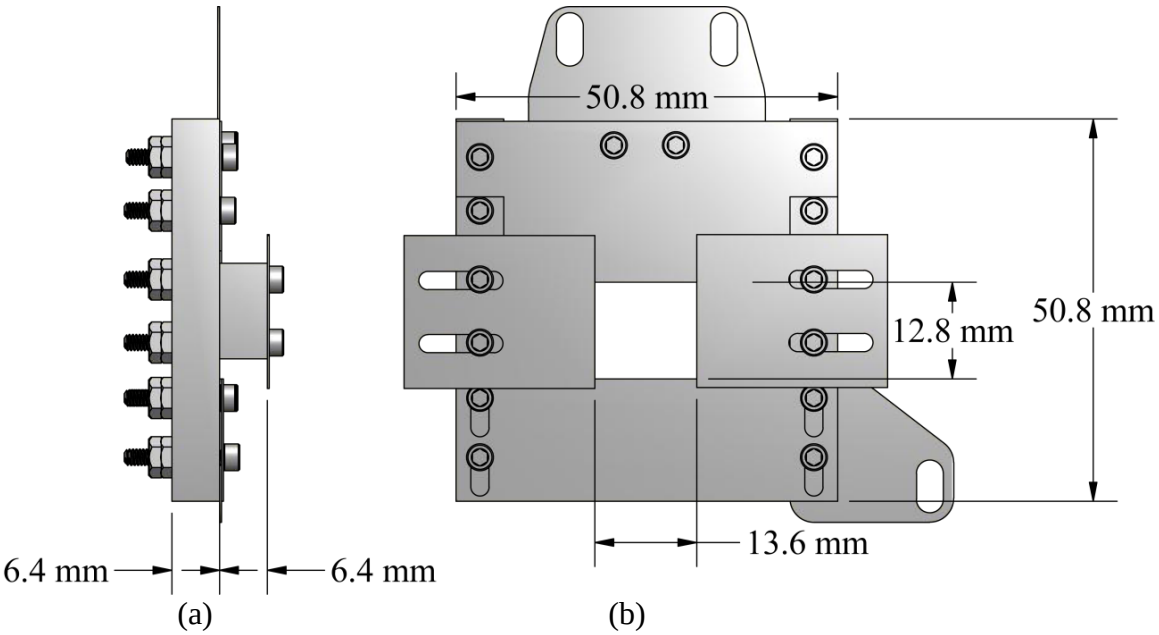

Figure 3.14. (a) Cross-sectional and (b) planar schematics of the aperture assembly. The assembly is comprised of four electrically isolated tantalum plates and the four boron nitride pieces that support and isolate the plates.

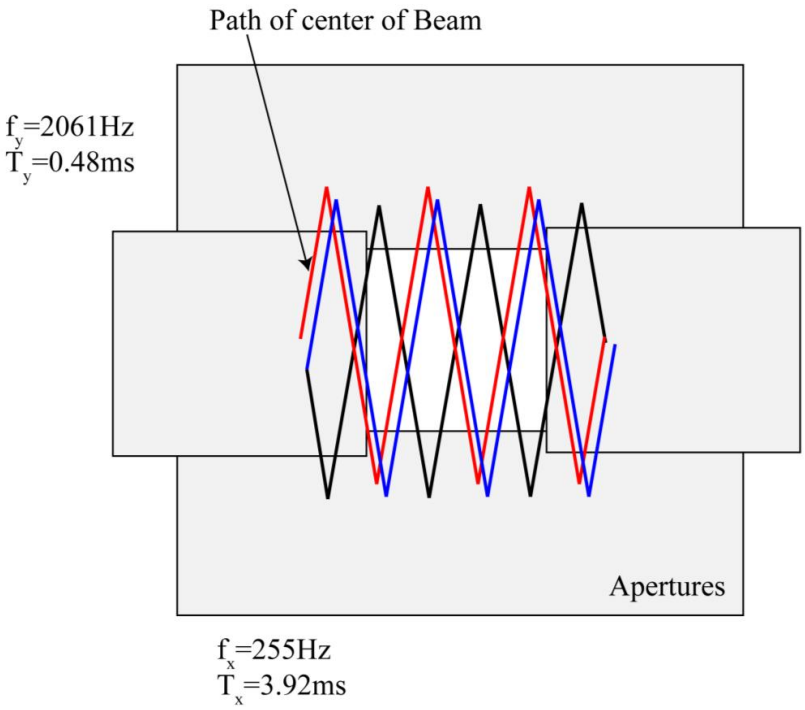

Figure 3.15. Pattern the beam traces due to the raster scanner during the proton irradiations, adapted from [54]. The grey boxes represent the aperture plates, while a representation of the raster-scanned beam path is shown by the red path from left-to-right, then black from right-to-left, and blue again from left-to-right

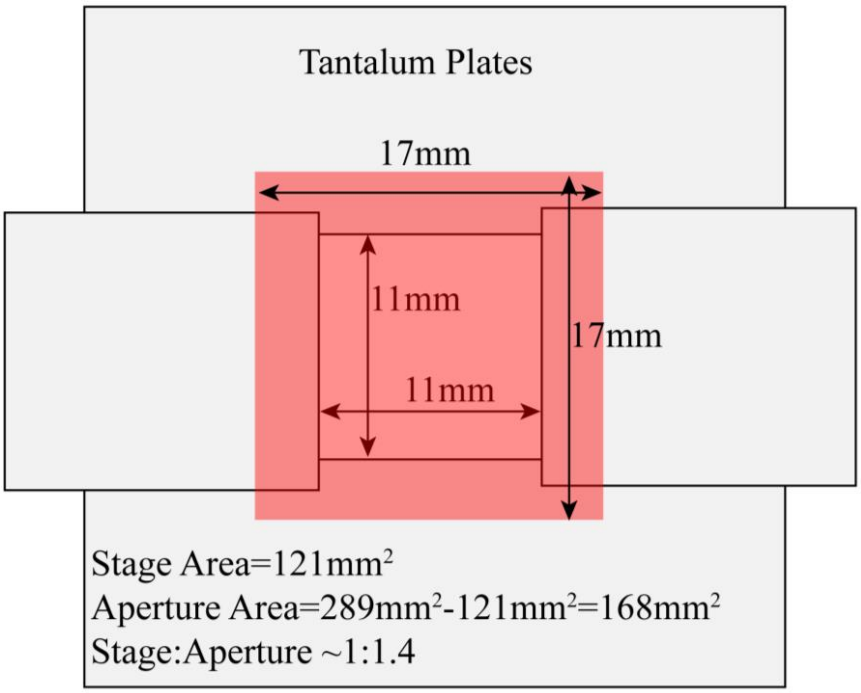

Figure 3.16. Schematic showing the process of over scanning the beam onto the apertures, and the resulting stage to aperture current ratio when a 3mm over scan is utilized.

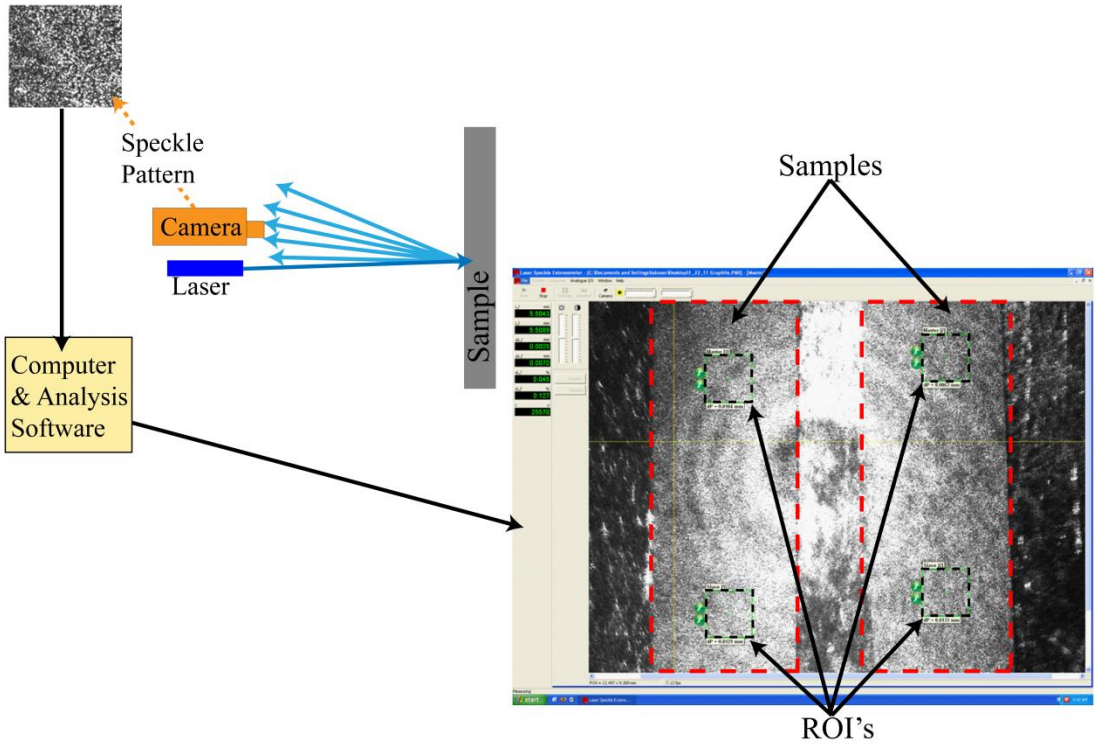

Figure 3.17. Schematic representation of the principle of operation of the LSE. The 405nm (blue) laser in incident of the surface of the sample, some light is scattered back to the 405nm filtered video camera, the speckle patter is transferred to the computer, and the computer software analyzes the speckle pattern to continuously measure the dimensional change. In the image at right, the two samples are outlined with the two large dash boxes, and the regions of interest (ROI's) are the two sets of small dashed boxes on each sample.

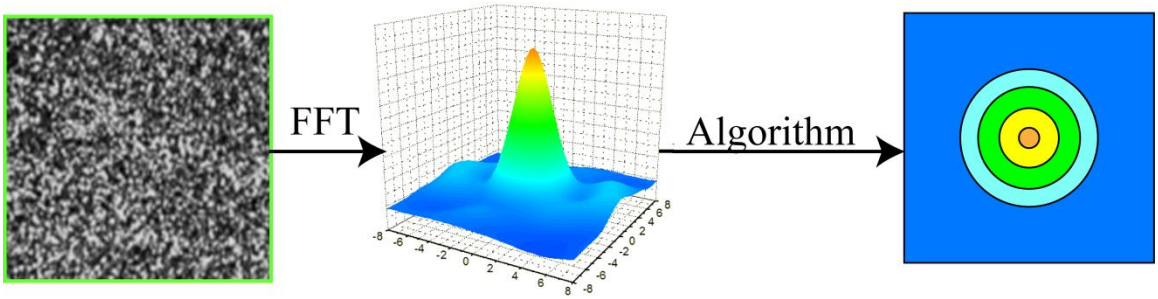

Figure 3.18. Schematic representation of the conversion of the speckle pattern (left), by FFT into the three-dimensional surface function (center), and the center of mass by algorithm (right).

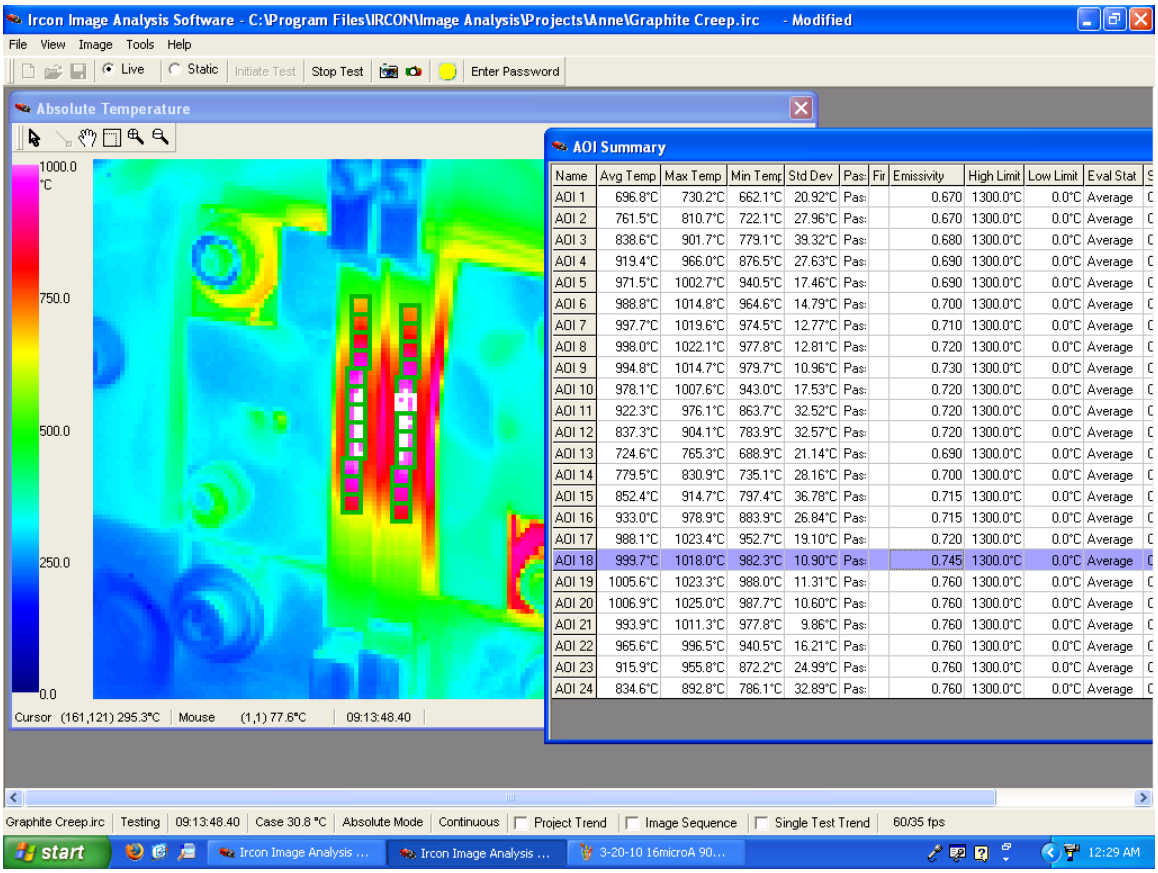

Figure 3.19. Picture of the Stinger software, on the left is the image from the camera, which is colorized relative to the surface temperature and on the right is the table that lists the temperatures within each AOI.

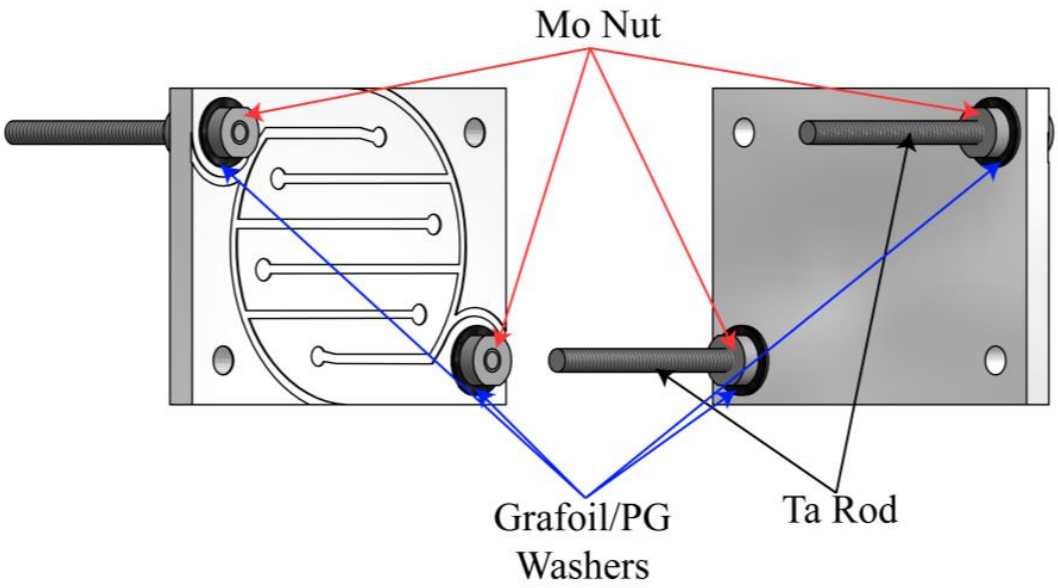

(a) (b)

Figure 3.20. Schematic drawing of the (a) front and (b) back sides of the assembled heater.

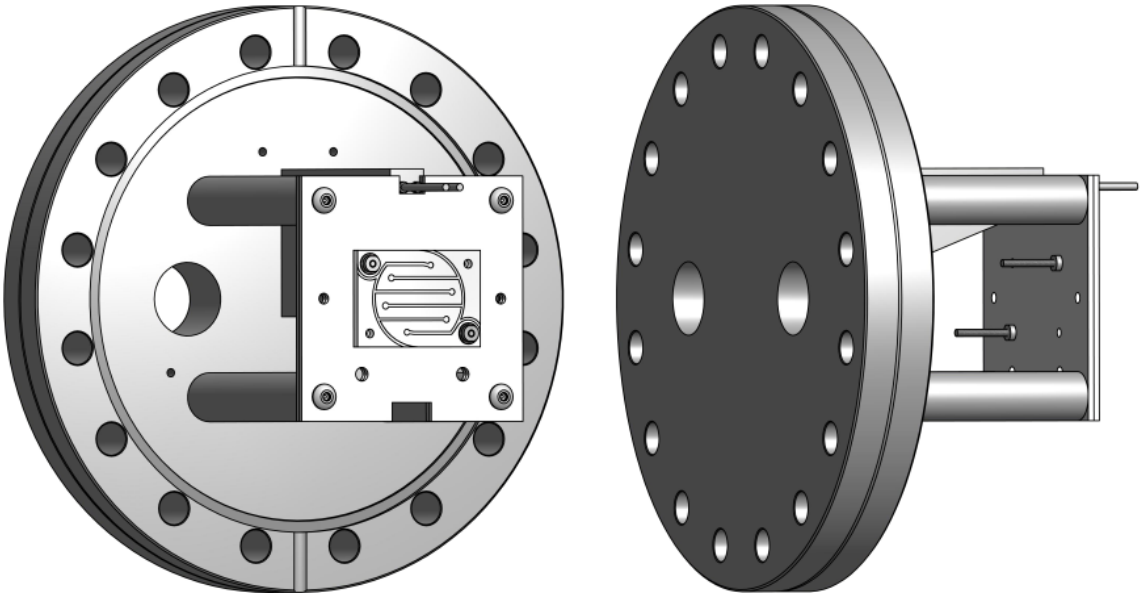

(a) (b)

Figure 3.21. Schematic of assembled heater on stage (a) front and (b) back views. In (b) the last two Mo nuts that hold the heater on the alumina stage are seen.

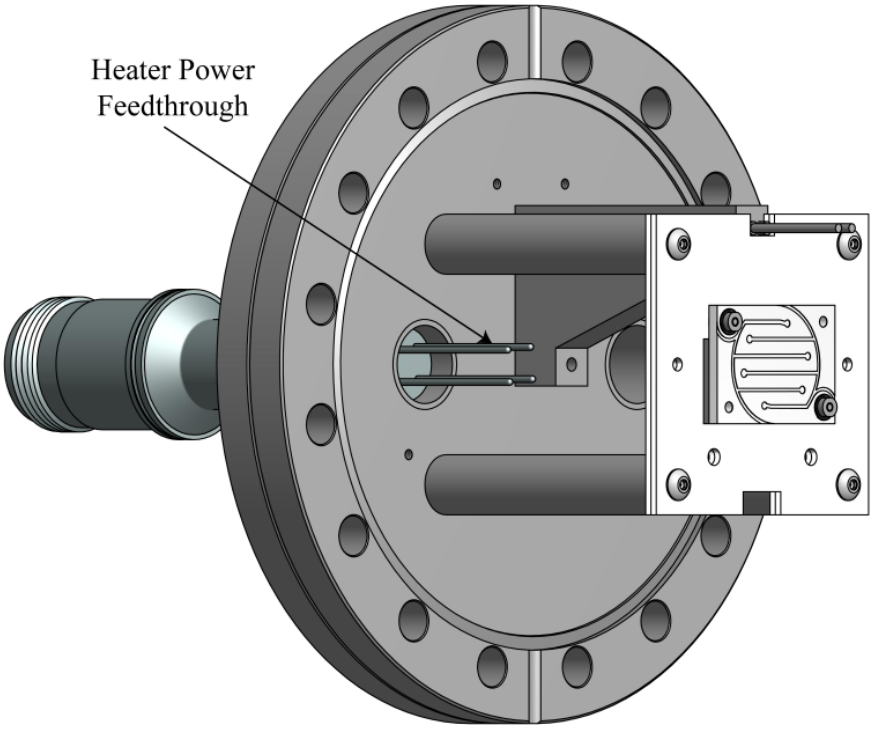

Figure 3.22. Schematic of assembled heater on stage and corresponding electrical feedthrough used to supply power to the heater. The wires connecting the feedthrough and the heater are not shown.

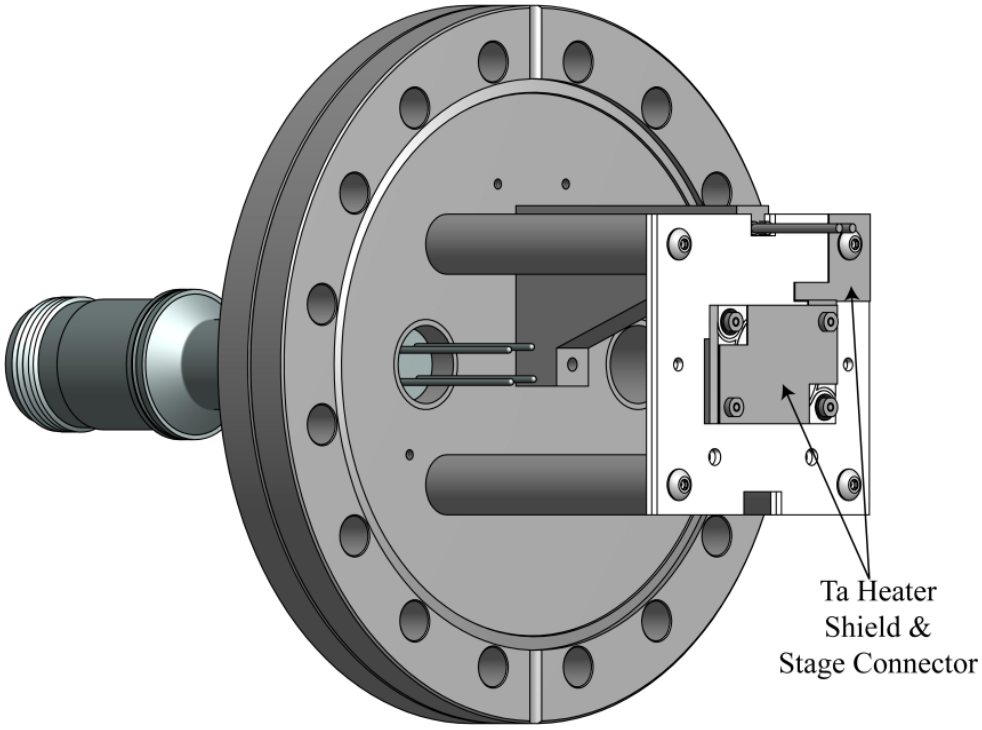

Figure 3.23. Schematic of assembled heater shield on stage.

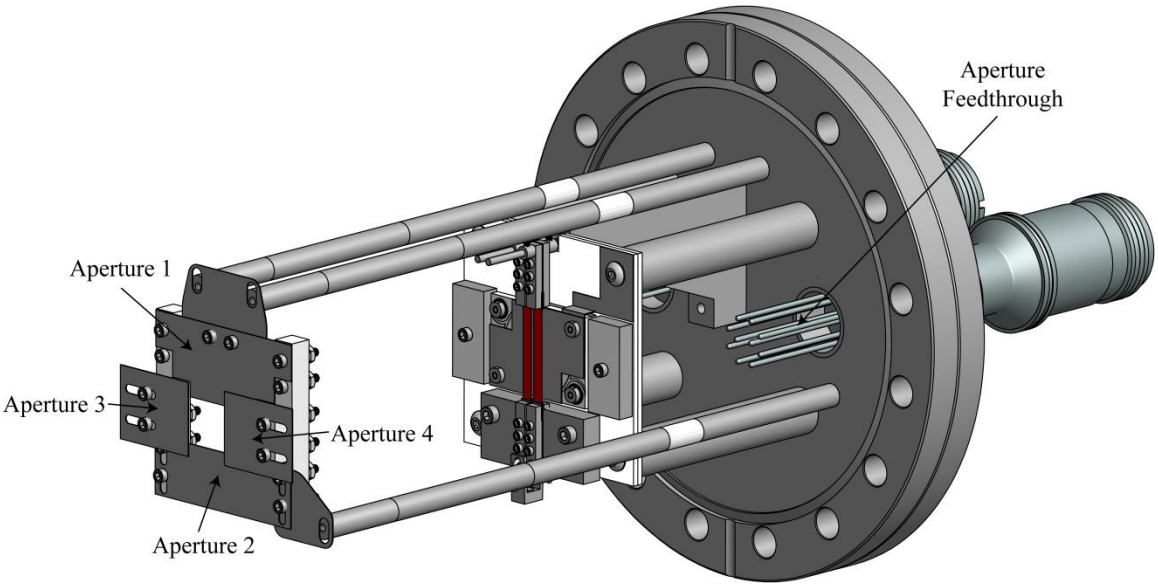

Figure 3.24. Schematic of assembled stage with apertures attached. The wires that connect the apertures to the feedthrough are not shown.

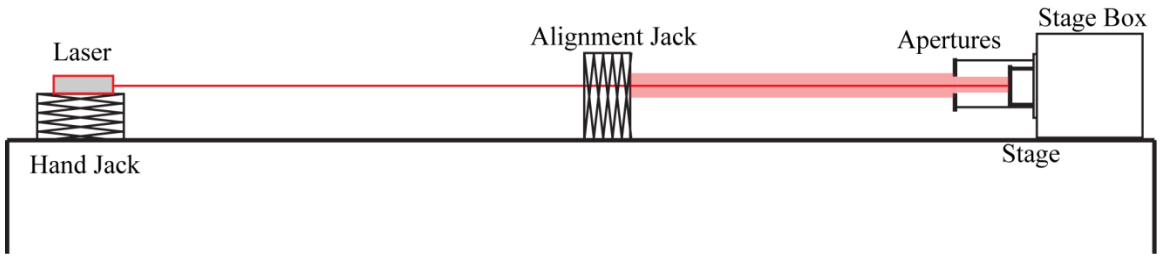

Figure 3.25. Schematic of bench-top aperture alignment.

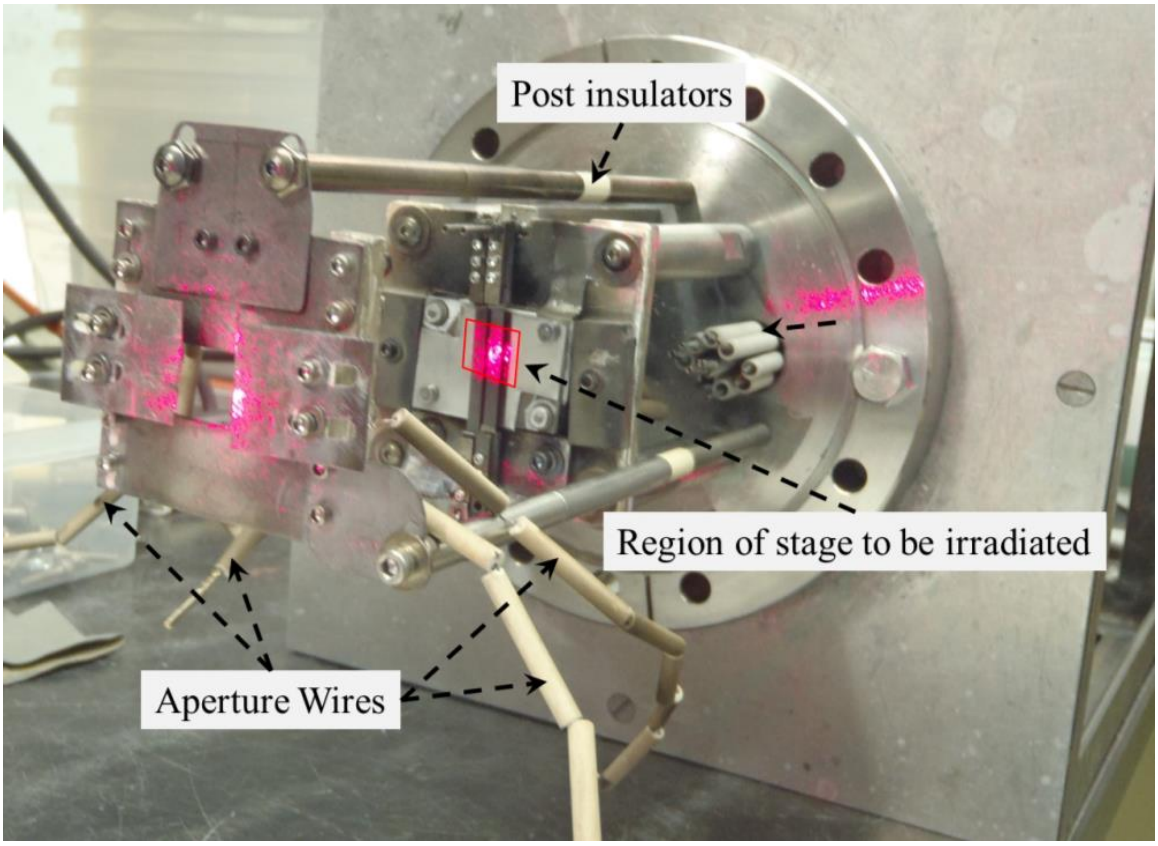

Figure 3.26. View of the irradiation stage while it is being check for aperture alignment. The diffuse laser that shows where the irradiation will be incident on the stage is outlined in red.

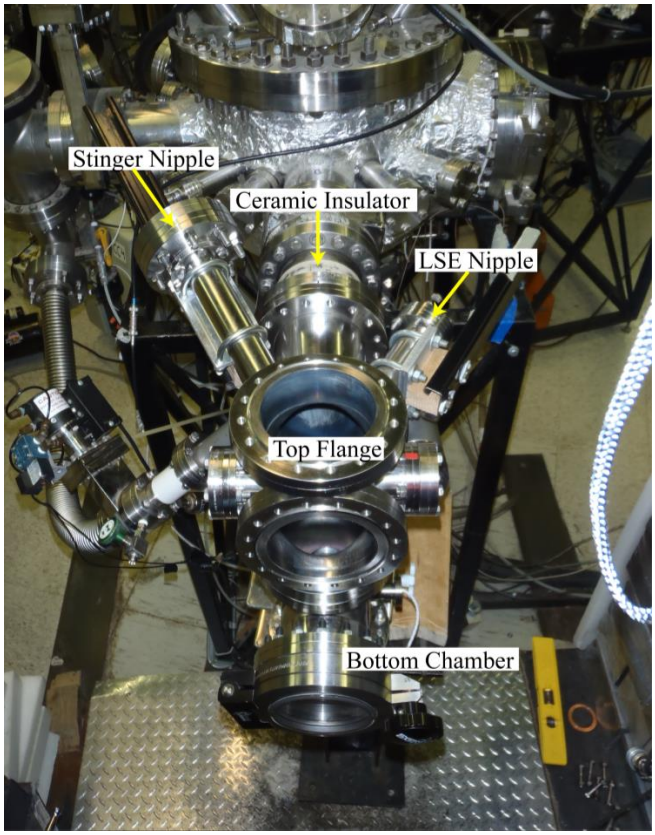

Figure 3.27. Picture of the chamber on the beam-line, with a top-down perspective.

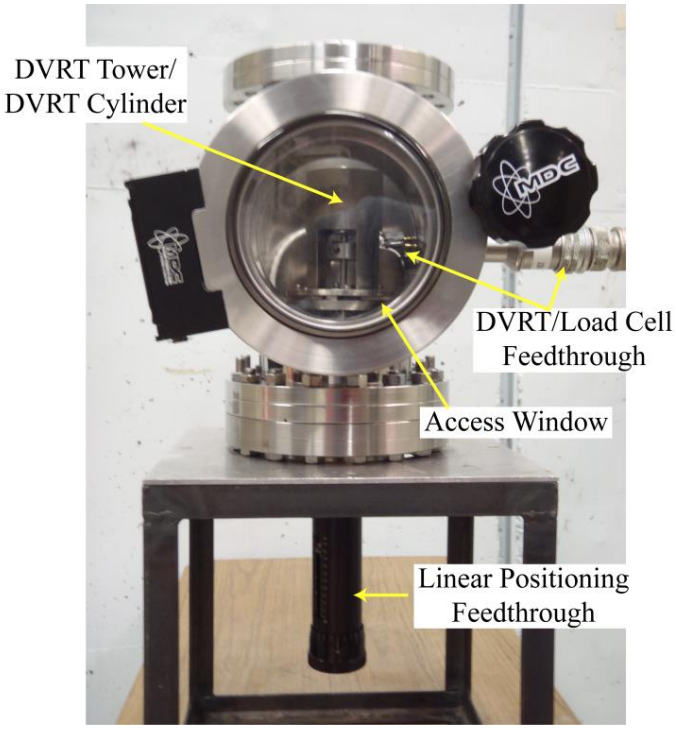

Figure 3.28. Picture of the assembled bottom flange.

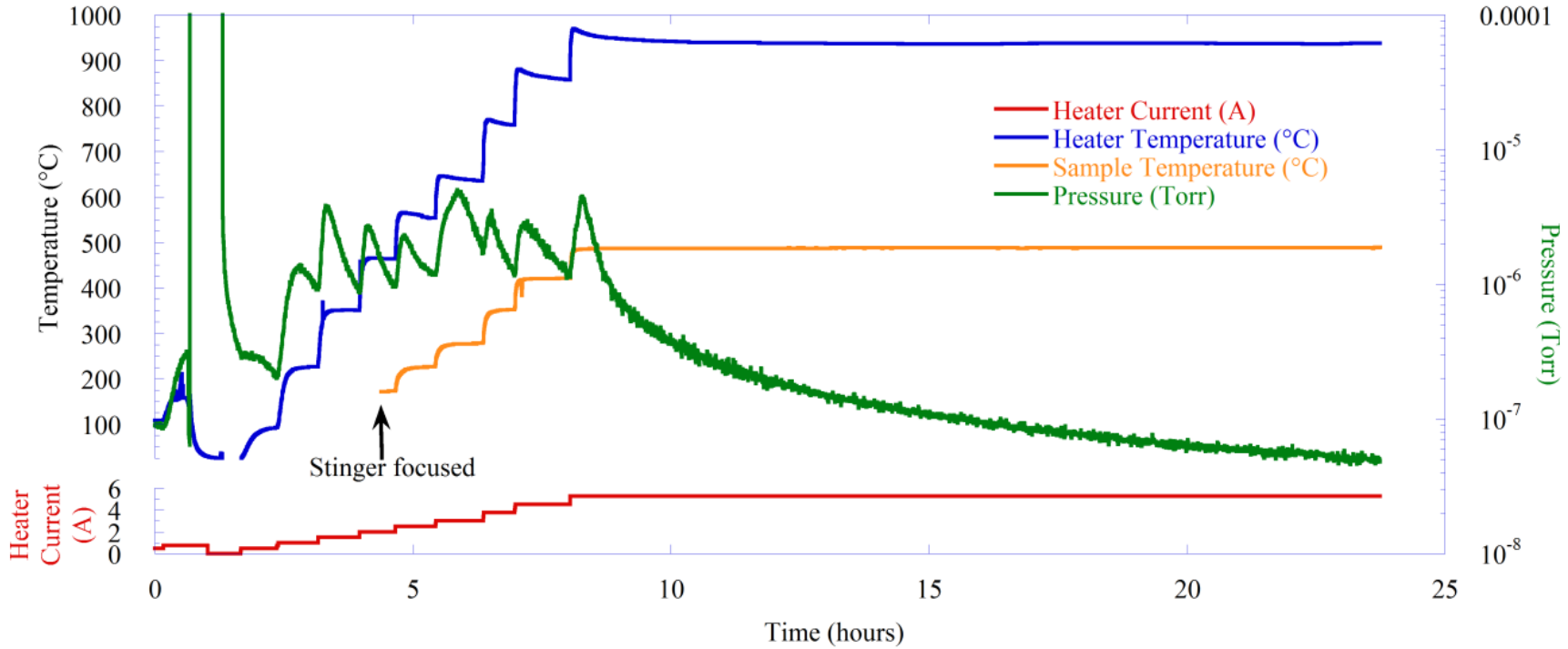

Figure 3.29. Plot of heater current (red), heater temperature (blue), sample temperature (orange), and pressure (green), for a typical bake out process.

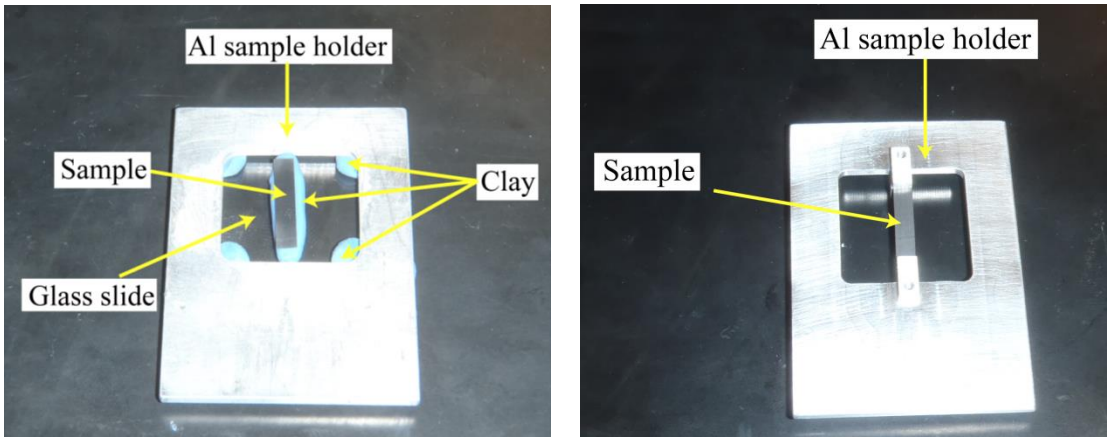

(a) (b)

Figure 3.30. Picture of graphite sample for XRD analysis in the (a) old sample holder and (b) redesigned sample holder.

CHAPTER 4

RESULTS

This chapter presents the results of the proton irradiation-induced creep experiments and post-irradiation analysis. The first section will present the data from the proton irradiation-induced creep experiments for graphite. The second section will present the irradiation creep dependencies on the experimental parameters. The third section will present the effects of the irradiation experimental parameters on the different material properties.

4.1 Irradiation Creep Results for POCO Graphite

This section presents twelve proton irradiation-induced creep experiments that were performed on the POCO ZXF-5Q graphite samples. A summary of the experimental conditions are presented in Table 4.1. Experiments 1, 2 and 3, were performed at 1000°C, ~0.1dpa/day, and 20MPa tensile stress, to quantify the experimental reproducibility. Experiments 1, 2, and 4, were performed at 1000°C, ~0.1dpa/day, and 20MPa tensile stress, to investigate the effect of final dose on the post-irradiation material properties. Experiments 1, 5, 6, and 7 were performed at 1000°C and a dose rate of ~0.1dpa/day, to investigate the effect of applied tensile stress on creep rate. Experiments 8 and 9 were performed at 700°C with a 20MPa applied stress to investigate the effect of dose rate on creep rate. These experiments had to be performed at a lower temperature because the coupling of temperature and dose rate cannot be removed with the addition of heating from the PBN/PG heater. Experiments 4, 10, 11, and 12, were performed with the 20MPa tensile stress to investigate the effect of temperature on creep rate.

An example of the experimental data is shown in Figure 4.1 for experiment #7. The strain measured by the LSE for the stressed (red data) and reference sample (blue

data) along with the strain measured by the DVRT for the stressed sample (green data) are plotted on the left y-axis, the sample temperature (black data) and stage current (pink data) are plotted on the right y-axis. The linear fit of the stressed sample LSE strain is shown with the orange line, the linear fit of the reference sample LSE strain is shown with the bright blue line, and the linear fit of the stressed sample DVRT strain is shown with the bright green line. The analyses are separated into the LSE measured strain of the stressed sample and the DVRT strain from the same sample. These are separated because the LSE was measuring strain in the center 5mm of the sample where the temperature is quite uniform, while the DVRT strain was measured over the entire length of the irradiated region which had a significant temperature gradient due to the heat loss. The dose, in dpa, at the time intervals is listed along the top x-axis. The linear fit analysis of the LSE and DVRT for the stressed sample and the constant fit analysis of the stage current and temperature, according to Section 3.4, are listed in Table 4.2. All of the experimental data from the creep experiments are presented in Appendix B, including all the statistical and error analysis. Throughout the rest of this section the data of interest for comparison will be plotted and listed in comparison tables.

For all the experiments the time is in units of hours, the strain measurements from the LSE and DVRT are in units of percent, the temperature has units of degrees Celsius, and the stage current is in units of microamperes. When the creep rates are determined with the process outlined in Section 3.4, the resulting units of creep rate are %/hr, and are summarized with the same units. The later analyses use creep rates in units of s^{-1}, which is a simple conversion from %/hr. The stage current is converted into dose rate ($\dot{d}$) by:

$$\dot{d}\left(\frac{dpa}{day}\right)=\frac{SC(\mu A)*Damage\ Rate\left(\frac{displacements}{ion*\text{Å}}\right)*10^{8}\left(\frac{\text{Å}}{cm}\right)*10^{-6}\left(\frac{C/s}{\mu A}\right)}{N\left(\frac{at}{cm^{3}}\right)*Area(cm^{2})*q\left(\frac{C}{proton}\right)*\frac{1}{86400}\left(\frac{day}{s}\right)}, \quad (4.1)$$

where *SC* is the stage current, *Damage Rate* is the value calculated from SRIM, *N* is the atomic density of the material, *Area* is the area of the stage being irradiated, and *q* is the Coulomb charge per ion ($1.602\text{x}10^{-19}C/p^{+}$). The later analyses use dose rates in units of dpa/s, which is a simple conversion from dpa/day.

4.1.1. Experimental Reproducibility

One of the key components of experimental observations and experiments is how accurately an experiment can be reproduced. Experiments 1, 2, and 3 were performed under similar conditions to quantify the reproducibility and confidence of these experiments. The strain measured by the LSE and DVRT from these experiments are plotted versus time in Figure 4.2. Even though the ending dose of experiment 2 was 1dpa, the data was analyzed out to a final dose of 0.421dpa, to compare with that from experiment 1. The same analysis was performed with the data from experiment 2, in regime 1.

The creep rate, creep rate variance, and dose rate, for each set of data plotted in Figure 4.2, is presented in Table 4.3. There was a slight difference in dose rate for these three experiments, and to correctly analyze the reproducibility it is necessary to normalize to the same dose rate. This was done by dividing the LSE and DVRT creep rates by the experimental dose rate and then multiplying by 0.100dpa/day. The normalized creep rates are also presented in Table 4.3.

Since the variances of the creep rates for all three experiments are similar, the reproducibility analysis can be performed assuming a constant variance for the three experiments. With this assumption, the reproducibility analysis is performed with the same methodology in Section 3.4, for a constant (zero slope) fit. The average creep rate (M) for the three experiments is calculated from Equation (3.12). The LSE M is 0.02108 %/hr, and the DVRT M is 0.02283 %/hr. After calculating M for each measurement, the χ^2 value of these three data sets is calculated according to:

$$\chi^2 = \sum_{i=1}^{N} \frac{\left(y_i - M\right)^2}{V_i}, \tag{4.2}$$

resulting in 6.51×10^5 for the LSE data and 8.90×10^4 for the DVRT data. For three experiments, with two degrees of freedom and a probability of 0.5, the χ^2 value should be 1.3862. The difference in the calculated χ^2 and the correct χ^2 results from the reproducibility of the experiments. The reproducibility of the experiments is then calculated by including a reproducible variance term (V_R) into Equation (4.2) resulting in:

$$\chi^2 = \sum_{i=1}^{N} \frac{\left(y_i - M\right)^2}{V_i + V_R}, \tag{4.3}$$

and using the correct χ^2 to solve for V_R. This calculation results in a V_R of 1.989×10^{-5} ($\%^2/hr^2$) for the LSE and 6.017×10^{-6} ($\%^2/hr^2$) for the DVRT. The standard deviation of the reproducibility (σ_R) is 4.459×10^{-3} (%/hr) for the LSE and 2.453×10^{-3} (%/hr) for the DVRT. The reproducibility of these experiments is described as a confidence percentage of the creep rate defined as σ_R/M, resulting in 21.1% for the LSE, and 10.7% for the DVRT.

4.1.2. Error Analysis of Creep Rates

As discussed in Section 3.3.6, the irradiation creep experiments were continued until the 95% confidence interval of the creep rate was less than 1% of the creep rate (B). With the 95% confidence interval being equal to $1.96\sigma_B$, the error of the creep rate (σ_B/B) is less than 0.5%. The error of the creep rates for each experiment is negligible when compared to how accurately these experiments can be reproduced. The previous section showed that the reproducible confidence percentage of the creep rate is 21.1% and 10.7% of the creep rate, for the LSE and DVRT respectively, and these percentages are used to show the confidence of the creep rate for all the experiments. The resulting error bars, for each creep rate, is equal to the creep rate multiplied by the confidence percentage.

4.2 Effect of Irradiation Parameters on Irradiation Creep Behavior

This section will present the dependencies of creep rate on the experimental conditions. The first section will discuss the effect of applied tensile stress on apparent creep rate. The second section will discuss the effect of dose rate on apparent creep rate. The third section will discuss the effect of temperature on apparent creep rate. The fourth section will discuss the effect of accumulated dose on apparent creep rate. The reason for discussing only the apparent creep rate, rather than the true creep rate, is that the EDM cutting of the graphite samples produced curvature in the samples. When the reference

samples were irradiated with no applied stress the irradiation caused relaxation of the curvature, which was observed by the LSE as elongation.

4.2.1 Stress Dependence

Experiments 1 and 4-7 were performed at 1000°C and ~0.1dpa/day dose rate to investigate the effect of applied tensile stress on the apparent creep rate. The strain versus time data for different applied tensile stress experiments are plotted in Figure 4.3. The top graph is the LSE data and the bottom graph is the DVRT data. A summary of the applied stress, linear fit slope (*B*), strain rate, dose rate, final dose, and normalized strain rate, are presented in Table 4.4. The apparent strain rate versus applied tensile stress is plotted in Figure 4.4, with the LSE strain rates plotted as red circles and the DVRT creep rates plotted as blue squares. The linear fit of the LSE values is shown with the red dashed line and the DVRT linear fit is shown with the blue dashed line. The equations of fit and R^2's are listed in red in the bottom right corner for the LSE and blue for the DVRT. The linear fit is forced through the origin of the plot since the apparent creep rate should be zero with no applied stress. These results show a linear dependence of apparent strain rate on applied tensile stress.

The tensile stress was obtained by measuring sample thickness, in the area to be irradiated, with a micrometer that has a spindle/anvil radius of 6mm. This large diameter spindle/anvil on the micrometer provides an average thickness of the sample. There is surface roughness of ~1μm from the machining process, but other sources of non-uniformity may cause the sample to be thicker or thinner than the measured thickness. A region that is 10% thinner would result in the stress being 11% larger, while 10% thicker would result in the stress being 9% lower. Then a triple beam scale was used to achieve the load-train assembly mass to cause the desired stress to within 1 gram. The deviation of ±1g results in a difference of less than 0.3% of the desired stress. Thus the only source of substantial variation of stress would be non-uniformities in sample thickness which were not quantified, so the average value of stress is used.

4.2.2 Dose Rate Dependence

Experiments 8 and 9 were performed at 700°C with a 20MPa stress to investigate the effect of dose rate on the apparent creep rate. The DVRT readings in the second and third regimes in experiment 8 were unreliable because the stage was initially at high temperature in the first regime, and then decreased for each consecutive regime. The DVRT readings are highly affected by the thermal conditions of the stage and require a long period of time to reach thermal equilibrium. Every time the condition was changed the DVRT strain was affected by continuous thermal contraction of the load assembly. To prevent this thermal effect, experiment 9 was performed by increasing stage heating for each consecutive regime. A plot of strain versus time for the LSE and DVRT data from the dose rate experiments are plotted in Figure 4.5. The LSE data is plotted as the red data for experiment #8 and blue data for experiment #9, while the DVRT data for the first regime of experiment #9 is plotted as the orange data and the light blue data is for experiment #9. The dose rates of the corresponding regimes are also labeled. A summary of the experimental regimes, dose rates (dpa/day and dpa/s), and corresponding linear fit slopes and creep rates is presented in Table 4.5, for reference, the two unreliable DVRT values are highlighted. The apparent strain rate versus dose rate is plotted in Figure 4.6, with the LSE strain rates plotted as red circles, the DVRT creep rates plotted as blue squares, and the two unreliable DVRT points are plotted as open blue squares. The linear fit of the LSE values is shown with the red dashed line and the DVRT linear fit is shown with the blue dashed line. The equations of fit and R^2's are listed in red in the top left corner for the LSE and blue for the DVRT. The linear fit is forced through the origin of the plot since the apparent creep rate should be zero with no irradiation. These results show a linear dependence of apparent strain rate on dose rate. The slope from the DVRT is one half the LSE slope, but of all the experiments this had the most changes to the non-irradiation thermal properties thus this difference is not surprising.

4.2.3 Temperature Dependence

Experiments 1, 4, and 10-12 were performed to investigate the effect of irradiation temperature on apparent creep rate. The data from the first regime of the two

700°C experiments 8 and 9 are also included. The LSE is an optically-based measurement system that was initially outfitted with a green laser, with a 535nm wavelength. The problem that arose at temperatures above 900°C is that the black-body emission from the graphite samples and tantalum heater shield began emitting light in the same wavelength as the laser and caused errors with the LSE measurements. It was found that a violet, 405nm wavelength, laser was a better option because the intensity of black-body emission in the 405nm range is much less than in the 535nm range. The 405nm laser was sufficient for the 1000°C irradiations, but the same interference was observed for the 1100°C and 1200°C irradiations. This interference was confirmed with the second and third regimes in experiment 3, where the LSE and DVRT strain rates matched in the 1000°C regime but in the 1100°C and 1200°C regimes the strain rates drastically diverged. Due to the interference, the LSE strain rates in the 1100°C and 1200°C, are not included in the temperature dependence analysis.

The temperature dependence experiments were all performed at different dose rates, so it is necessary to compare a value other than strain rate to account for the different dose rates. The creep compliance, *k*, is used instead of strain rate, which is defined by

$$k\left(\tfrac{1}{dpa*MPa}\right)=\frac{\dot{\varepsilon}\left(s^{-1}\right)}{\sigma(MPa)*\dot{d}\left(\tfrac{dpa}{s}\right)}, \tag{4.4}$$

where $\dot{\varepsilon}$ is the strain rate, σ is the applied tensile stress, and $\dot{d}$ is the dose rate.

The strain versus time data for different temperature experiments are plotted in Figure 4.7. The top graph is the LSE data and the bottom graph is the DVRT data. A summary of the experiment temperature, linear fit slope (*B*), strain rate, dose rate (dpa/day and dpa/s), applied stress, and compliance, are presented in Table 4.6, for reference the two unreliable LSE values are highlighted. The creep compliance versus temperature is plotted in Figure 4.8, with the LSE compliance plotted as red circles, the DVRT compliance plotted as blue squares, and the two LSE points, at 1100°C and 1200°C, are plotted as open red circles. The linear fit of the LSE values is shown with the red dashed line and the DVRT linear fit is shown with the blue dashed line. The

equations of fit and R^2's are listed in red in the bottom right corner for the LSE and blue for the DVRT. These results show a linear dependence of compliance on temperature.

4.2.4 Accumulated Dose Dependence

Experiments 1 and 2 were analyzed to determine whether accumulated dose caused a change of the instantaneous creep rate. The strain versus time data, used for this analysis, is plotted in Figure 4.9. The analysis was performed by taking the strain versus time data, breaking the data into 15 minute intervals, and then performing the same linear fit to determine creep rate over these short time intervals, as presented in Section 3.4. The discrete creep rates, plotted versus dose, are shown in Figure 4.10, with LSE data in red and DVRT data in blue.

This data was numerically analyzed to determine if there is any effect due to accumulated dose by performing an analysis, of strain rate as a function of dose, using the same methodologies from Section 3.4. The analysis was performed for two line fits: the first with zero slope (constant) and the second with a non-zero slope. A summary of the constant (M), constant fit variance (V_C), linear slope (B), linear intercept (A), and linear fit variance (V_L) of the LSE and DVRT date are listed in Table 4.7. A comparison of the variance of the two fits indicates whether the constant fit or linear fit is the better definition of the data. When another fit parameter is added to the analysis, the variance of the fit should decrease, but unless the variance decreases by at least an order of magnitude the simpler fit is the best to describe the data. The analysis shows that the LSE and DVRT creep rate versus dose, for both experiments, are best described with the zero slope fit, which indicates that there is no effect of accumulated dose on strain rate.

4.2.5 Comparison of Creep Rates from LSE and DVRT

The LSE and DVRT measured different physical creep rates. The LSE measured the creep rate in the center 5mm of the irradiation region, while the DVRT measured the total elongation due to irradiation. In the region where the LSE measured creep rate the temperature was approximately constant, while heat generation and transfer caused the temperature of the entire irradiated region to decrease towards the edges, sometimes as

much as 200ºC. Therefore it is expected that the LSE should be the correct creep rate for the quoted temperature and should be higher than the DVRT. The creep rates from the LSE are plotted versus the DVRT creep rate for the same experiment in Figure 4.11, along with the 1:1 ratio line. Most of these experiments show the expectation that the LSE creep rate is higher than the DVRT creep rate, but there are a few outliers that need to be addressed (circled in black). The outlier points for Experiments #11 and #12 are due to the LSE measurements being unreliable due to interference of blackbody radiation at the 1100ºC and 1200ºC. The outlier points for Experiments #8b and #8c were due to the DVRT continuously showing contraction due to the cooling of the system from the reduction of the heat contribution from the PBN heater. Other than these outliers, only the data from Experiments #3 and #7 do not go above the 1:1 line, when including measurement error.

The DVRT was included as a backup measurement technique in the event that there were unforeseen problems with the LSE, such as what occurred in Experiments #11 and #12. Therefore throughout the later analyses the trends of importance are from the LSE measurements, but in cases where the LSE measurements are invalid then the DVRT trends will be used.

4.3 Effects of Irradiation Conditions on Material Properties

This section presents the post-irradiation analysis of the samples. The first section will present the results of the XRD measurements. The second section will present the results of the TEM SAED anisotropy measurements. The third section will present the results of the nanoindenter measurements of Young's modulus and hardness.

4.3.1 XRD Measurements

The XRD measurements were performed according to the methodology described in the experimental chapter. The overlap of the graphite spectrum and the spectrum from the original aluminum, glass, and clay, sample holder is shown in Figure 4.12. Figure 4.12 is a plot of the XRD spectrum for a 2θ range of 20-80°, showing the spectrum for the as-received graphite sample in the original sample holder (red) and the spectrum for

the original sample holder (blue). This shows the amount of overlap of both spectra, which was the cause for designing a new sample holder. Figure 4.13 shows the same XRD spectra as Figure 4.12 with the new sample holder, which removed all background peaks due to the sample holder.

The spectra for the 0002, 0004, $11\bar{2}0$ peaks, and the range from 32-48° were collected with the procedure presented in the experimental chapter. The first set of spectra, Figure 4.14 through Figure 4.17, show the effect of total dose on the peak shape, for samples irradiated at 1000°C, 20MPa, and 0.1dpa/day. The second set of spectra, Figure 4.18 through Figure 4.21, show the effect of total dose on the peak shape, for samples irradiated at 1000°C, 0MPa, and 0.1dpa/day. The third set of spectra, Figure 4.22 through Figure 4.25, show the effect of applied stress on the peak shape, for samples irradiated at 1000°C, 0.1dpa/day, to a final dose of 0.25dpa. The fourth set of spectra, Figure 4.26 through Figure 4.29 , show the effect of irradiation temperature on the peak shape, for samples irradiated with a 20MPa tensile stress. The fifth set of spectra, Figure 4.30 through Figure 4.33, show the effect of irradiation temperature on the peak shape, for samples irradiated with a 0MPa tensile stress.

4.3.2 Anisotropy

The anisotropy measurements were performed according to the methodology described in the experimental chapter. The samples used for this measurement were the as-received material and the sample irradiated at 1000°C, 20MPa, 0.095dpa/day, to a dose of 1dpa. Of the samples that underwent creep strain at constant conditions, only the sample irradiated out to 1dpa underwent ~4.5% creep strain, while the rest underwent ~1-1.5% creep strain. It was decided that interrogating the anisotropy change from these extremes would indicate if the anisotropy changes were occurring and whether the time to perform sample preparation and measurement were necessary.

For both samples, 37 diffraction patterns were obtained, to interrogate a total area of greater than $1200\mu m^2$. The as-recorded diffraction patterns are presented in Appendix C. The final combined patterns are shown in Figure 4.34 for the as-received sample (a) and the crept sample (b). These combined patterns were analyzed using the GAAP

program [64]. The resulting average BAF for the as-received sample was 1.01, and the crept sample was 1.02.

In addition to analyzing the combined patterns, the individual patterns were analyzed to determine if there was any significant anisotropy that was lost when the individual images were combined. The BAF and R values for each image (numerically integrated over 90° interval so there are 4 R and BAF values per image) are plotted in Figure 4.35a. In this plot isotropic is when BAF=1 and R=0.667. The reason some of the BAF values are less than 1 is because instead of the value being maximum at 0° and decreasing to 90° there are some that have a minimum before 90° and then increase again (4 rather than 2 intense arcs around ring). An example of this occurrence in a pattern is shown in Figure 4.35b, for image #20 from the 1dpa sample. The average BAF and R values show that, as was seen with the combined images, that there is no significant texturing in the 1dpa sample, when compared to the as-received material. During analysis, the azimuthal angle location, around the [0002] ring, of the highest intensity is recorded. These values, for all the images, are plotted as a histogram in Figure 4.36, which again shows a random scatter in the angular location of the peaks.

Limited TEM imaging was done on the 1dpa sample to observe if there was any observable change to the microstructure. The pore size distribution and Morovski cracks showed no discernable change. A TEM micrograph of some pores from the 1dpa sample is shown in Figure 4.37, and a micrograph of Morovski cracks is shown in Figure 4.38.

4.3.3 Young's Modulus and Hardness

The Young's modulus and hardness measurements were performed according to the methodology described in the experimental chapter. The values of Young's modulus determined with nanoindentation (8GPa) is lower than the value reported by the manufacturer (14.5GPa), but that is because the manufactured used ultra-sonic wave propagation. Nanoindentation interrogated a much smaller volume and therefore had a smaller number of grains used for each measurement, hence why the final results are presented as change from the measured as-received value. These measurements were performed on nine samples from the set of experiments: as-received, 1000°C 20MPa 0.42dpa (experiment #1), 1000°C 20MPa 1.0dpa (experiment #2), 1000°C 40MPa

0.25dpa (experiment #5), 1000°C 5MPa 0.21dpa (experiment #7), 1000°C 0MPa 0.21dpa (experiment #7 reference), 900°C 20MPa 0.19dpa (experiment #10), 1200°C 20MPa 0.34dpa (experiment #12), and 1200°C 0MPa 0.34dpa (experiment #12 reference). Each sample was indented 50 times. The stress versus displacement plots for each indent for each sample is presented in Appendix D. The load versus depth plots of the representative indents, which were the indents that had the Young's modulus closest to the average value for the set, for each sample is presented in Figure 4.39 through Figure 4.43. A summary of the average Young's modulus, hardness, and the respective standard deviations for each sample are presented in Table 4.8.

The first plot shows the effect of accumulated dose, for samples irradiated at 1000°C with dose rate of ~0.1dpa/day, Figure 4.44. The second plot shows the effect of applied tensile stress, for samples irradiated at 1000°C with dose rate of ~0.1dpa/day to a total dose of 0.25dpa, except the 20MPa sample that was at 0.42dpa, Figure 4.45. The third plot shows the effect of irradiation temperature, Figure 4.46. In all of these plots the as-received values are indicated with green markers, the samples irradiated with applied stress are filled markers, and samples irradiated without stress are open markers. The error bars correspond to one standard deviation.

Table 4.1. Summary of POCO ZXF-5Q proton irradiation-induced creep experimental parameters.

Experiment Reference Number	Temperature (°C)	Stress (Mpa)	Dose Rate (dpa/day)	Total Dose (dpa)
1	1000	20	0.101	0.421
2	1000	20	0.095	1.001
3	1000 1100 1200 1000	20	0.093 0.126 0.153 0.090	0.727
4	1000	20	0.092	0.250
5	1000	40	0.103	0.250
6	1000	10	0.103	0.212
7	1000	5	0.090	0.212
8	700	20	0.0255 0.0433 0.0477	0.284
9	700	20	0.0379 0.0317 0.0255	0.189
10	900	20	0.070	0.139
11	1100	20	0.135	0.250
12	1200	20	0.176	0.340

Table 4.2. Summary of the linear fit to the LSE and DVRT data for the stressed sample, and the constant fit to the stage current and sample temperature from Experiment #7.

Linear Fit Values	LSE Stressed Sample	DVRT Stressed Sample	Constant Fit Values	Stage Current	Constant Fit Values	Temperature
A (%)	2.53	4.97	M (μA)	29.53	M (°C)	1001.38
B (%/hr)	$5.31\text{x}10^{-3}$	$1.08\text{x}10^{-2}$	V_C (μA^2)	0.15	V_C (°C^2)	7.80
V_L (%^{2})	$9.82\text{x}10^{-4}$	$6.79\text{x}10^{-4}$	$\sigma[M]$ (μA)	$4.90\text{x}10^{-3}$	$\sigma[M]$ (°C)	$3.40\text{x}10^{-2}$
$V[B]$ (%^{2}/hr^2)	$5.49\text{x}10^{-10}$	$6.91\text{x}10^{-10}$				
$V[A]$ (%^{2})	$5.97\text{x}10^{-7}$	$8.96\text{x}10^{-7}$				
$\sigma[B]$ (%/hr)	$2.34\text{x}10^{-5}$	$2.63\text{x}10^{-5}$				
$\sigma[A]$ (%)	$7.73\text{x}10^{-4}$	$9.46\text{x}10^{-4}$				

Table 4.3. Summary of LSE and DVRT slopes (B), the dose rate of each experiment, and the creep rate and variance of the creep rate after being normalized to a dose rate of 0.100dpa/day.

Exp #	LSE B (%/hr)	LSE $V[B]$ ($\%^2/hr^2$)	Dose Rate (dpa/day)	LSE B normalized to 0.100 dpa/day dose rate (%/hr)
1	2.574×10^{-2}	3.290×10^{-11}	0.1013	2.542×10^{-2}
2	1.908×10^{-2}	3.494×10^{-10}	0.0975	1.958×10^{-2}
3	1.723×10^{-2}	9.040×10^{-11}	0.0927	1.853×10^{-2}
LSE average B (M)				2.108×10^{-2}
LSE standard deviation (σ_R)				4.459×10^{-3}
σ_R/M				21.1%

Exp #	DVRT B (%/hr)	DVRT $V[B]$ ($\%^2/hr^2$)	Dose Rate (dpa/day)	DVRT B normalized to 0.100 dpa/day dose rate (%/hr)
1	2.218×10^{-2}	1.414×10^{-10}	0.1013	2.190×10^{-2}
2	2.088×10^{-2}	5.832×10^{-11}	0.0975	2.142×10^{-2}
3	2.340×10^{-2}	1.126×10^{-10}	0.0927	2.517×10^{-2}
DVRT average B (M)				2.283×10^{-2}
DVRT standard deviation (σ_R)				2.453×10^{-3}
σ_R/M				10.7%

Table 4.4. Summary of analysis values for stress dependence.

Exp #	Stress (MPa)	LSE *B* (%/hr)	LSE Strain Rate (s^{-1})	Dose Rate (dpa/day)	Final Dose (dpa)	Strain Rate normalized to 0.100 dpa/day (s^{-1})
7	5	5.31×10^{-3}	1.47×10^{-8}	0.090	0.212	1.64×10^{-8}
6	10	1.60×10^{-2}	4.44×10^{-8}	0.103	0.212	4.31×10^{-8}
1	20	2.57×10^{-2}	7.15×10^{-8}	0.101	0.421	7.10×10^{-8}
4	20	3.03×10^{-2}	8.41×10^{-8}	0.092	0.250	9.15×10^{-8}
5	40	5.38×10^{-2}	1.50×10^{-7}	0.103	0.250	1.45×10^{-7}

Exp #	Stress (MPa)	DVRT *B* (%/hr)	DVRT Strain Rate (s^{-1})	Dose Rate (dpa/day)	Final Dose (dpa)	Strain Rate normalized to 0.100 dpa/day (s^{-1})
7	5	1.08×10^{-2}	3.00×10^{-8}	0.090	0.212	3.34×10^{-8}
6	10	1.57×10^{-2}	4.37×10^{-8}	0.103	0.212	4.24×10^{-8}
1	20	2.48×10^{-2}	6.88×10^{-8}	0.101	0.421	6.83×10^{-8}
4	20	1.79×10^{-2}	4.96×10^{-8}	0.092	0.250	5.39×10^{-8}
5	40	4.82×10^{-2}	1.34×10^{-7}	0.103	0.250	1.30×10^{-7}

Table 4.5. Summary of analysis values for dose rate dependence.

Exp #	Dose Rate (dpa/day)	Dose Rate (dpa/s)	LSE *B* (%/hr)	LSE Strain Rate (s^{-1})
8-1	0.0255	$2.95x10^{-7}$	$1.21x10^{-3}$	$3.36x10^{-9}$
8-2	0.0433	$5.01x10^{-7}$	$5.42x10^{-3}$	$1.51x10^{-8}$
8-3	0.0477	$5.52x10^{-7}$	$8.24x10^{-3}$	$2.29x10^{-8}$
9-1	0.0378	$4.38x10^{-7}$	$7.14x10^{-3}$	$1.98x10^{-8}$
9-2	0.0317	$3.67x10^{-7}$	$4.85x10^{-3}$	$1.35x10^{-8}$
9-3	0.0255	$2.95x10^{-7}$	$4.43x10^{-3}$	$1.23x10^{-8}$

Exp #	Dose Rate (dpa/day)	Dose Rate (dpa/s)	DVRT *B* (%/hr)	DVRT Strain Rate (s^{-1})
8-1	0.0255	$2.95x10^{-7}$	$8.86x10^{-4}$	$2.46x10^{-9}$
8-2	0.0433	$5.01x10^{-7}$	$2.26x10^{-4}$	$6.28x10^{-10}$
8-3	0.0477	$5.52x10^{-7}$	$1.74x10^{-4}$	$4.84x10^{-10}$
9-1	0.0378	$4.37x10^{-7}$	$2.53x10^{-3}$	$7.02x10^{-9}$
9-2	0.0317	$3.67x10^{-7}$	$3.30x10^{-3}$	$9.17x10^{-9}$
9-3	0.0255	$2.95x10^{-7}$	$1.59x10^{-3}$	$4.40x10^{-9}$

Table 4.6. Summary of analysis values for temperature rate dependence.

Exp #	Temp (°C)	LSE *B* (%/hr)	LSE Strain Rate (s^{-1})	Dose Rate (dpa/day)	Dose Rate (dpa/s)	Stress (MPa)	Compliance $(MPa^{*}dpa)^{-1}$
8-1	700	$1.21x10^{-3}$	$3.36x10^{-9}$	0.0255	$2.95x10^{-3}$	20	$5.70x10^{-4}$
9-1	700	$7.14x10^{-3}$	$1.98x10^{-8}$	0.0378	$4.38x10^{-3}$	20	$2.27x10^{-3}$
10	900	$9.29x10^{-3}$	$2.58x10^{-8}$	0.070	$8.10x10^{-3}$	20	$1.59x10^{-3}$
1	1000	$2.57x10^{-2}$	$7.15x10^{-8}$	0.101	$1.17x10^{-3}$	20	$3.06x10^{-3}$
4	1000	$3.03x10^{-2}$	$8.41x10^{-8}$	0.092	$1.06x10^{-3}$	20	$3.95x10^{-3}$
11	1100	$8.86x10^{-3}$	$2.46x10^{-8}$	0.135	$1.56x10^{-3}$	20	$7.87x10^{-4}$
12	1200	$-3.39x10^{-3}$	$-9.42x10^{-9}$	0.176	$2.04x10^{-3}$	20	$-2.31x10^{-4}$

Exp #	Temp (°C)	DVRT *B* (%/hr)	DVRT Strain Rate (s^{-1})	Dose Rate (dpa/day)	Dose Rate (dpa/s)	Stress (MPa)	Compliance $(MPa^{*}dpa)^{-1}$
8-1	700	$8.86x10^{-4}$	$2.46x10^{-9}$	0.0255	$2.95x10^{-3}$	20	$4.17x10^{-4}$
9-1	700	$2.53x10^{-3}$	$7.02x10^{-9}$	0.0378	$4.38x10^{-3}$	20	$8.02x10^{-4}$
10	900	$1.11x10^{-2}$	$3.08x10^{-8}$	0.070	$8.10x10^{-3}$	20	$1.90x10^{-3}$
1	1000	$2.22x10^{-2}$	$6.16x10^{-8}$	0.101	$1.17x10^{-3}$	20	$2.64x10^{-3}$
4	1000	$1.79x10^{-2}$	$4.96x10^{-8}$	0.092	$1.06x10^{-3}$	20	$2.33x10^{-3}$
11	1100	$4.00x10^{-2}$	$1.11x10^{-7}$	0.135	$1.56x10^{-3}$	20	$3.55x10^{-3}$
12	1200	$4.61x10^{-2}$	$1.28x10^{-7}$	0.176	$2.04x10^{-3}$	20	$3.14x10^{-3}$

Table 4.7. Summary of the line fit parameters and resulting variance of the fits for experiments #1 and #2.

	Experiment #1		Experiment #2	
Linear Fit Variables	LSE	DVRT	LSE	DVRT
M (%/hr)	0.023081	0.024096	0.012742	0.019142
V_C (%^{2}/hr^2)	0.001108	0.001324	0.065819	0.016969
B (%/hr-dpa)	0.009344	0.011723	-0.015417	-0.020573
A (%/hr)	0.021047	0.021296	0.020475	0.029617
V_L (%^{2}/hr^2-dpa^2)	0.001109	0.001327	0.065865	0.016951

Table 4.8. Summary the nanoindentation measurements of Young's modulus and hardness.

Experiment Reference Number	Temperature (°C)	Stress (Mpa)	Total Dose (dpa)	Average Young's Modulus (GPa)	Average Hardness (MPa)
As-Received				8.058 ± 1.182	593.9 ± 139.9
1	1000	20	0.421	6.998 ± 0.963	544.1 ± 145.9
2	1000	20	1.001	8.732 ± 0.949	690.3 ± 153.8
5	1000	40	0.250	5.609 ± 0.991	403.5 ± 135.3
7	1000	5	0.212	8.259 ± 0.997	647.0 ± 93.0
7	1000	0	0.212	7.893 ± 1.337	531.1 ± 160.9
10	900	20	0.139	4.307 ± 0.672	313.1 ± 62.6
12	1200	20	0.340	7.550 ± 0.982	590.5 ± 107.5
12	1200	0	0.34	8.065 ± 1.063	661.3 ± 132.1

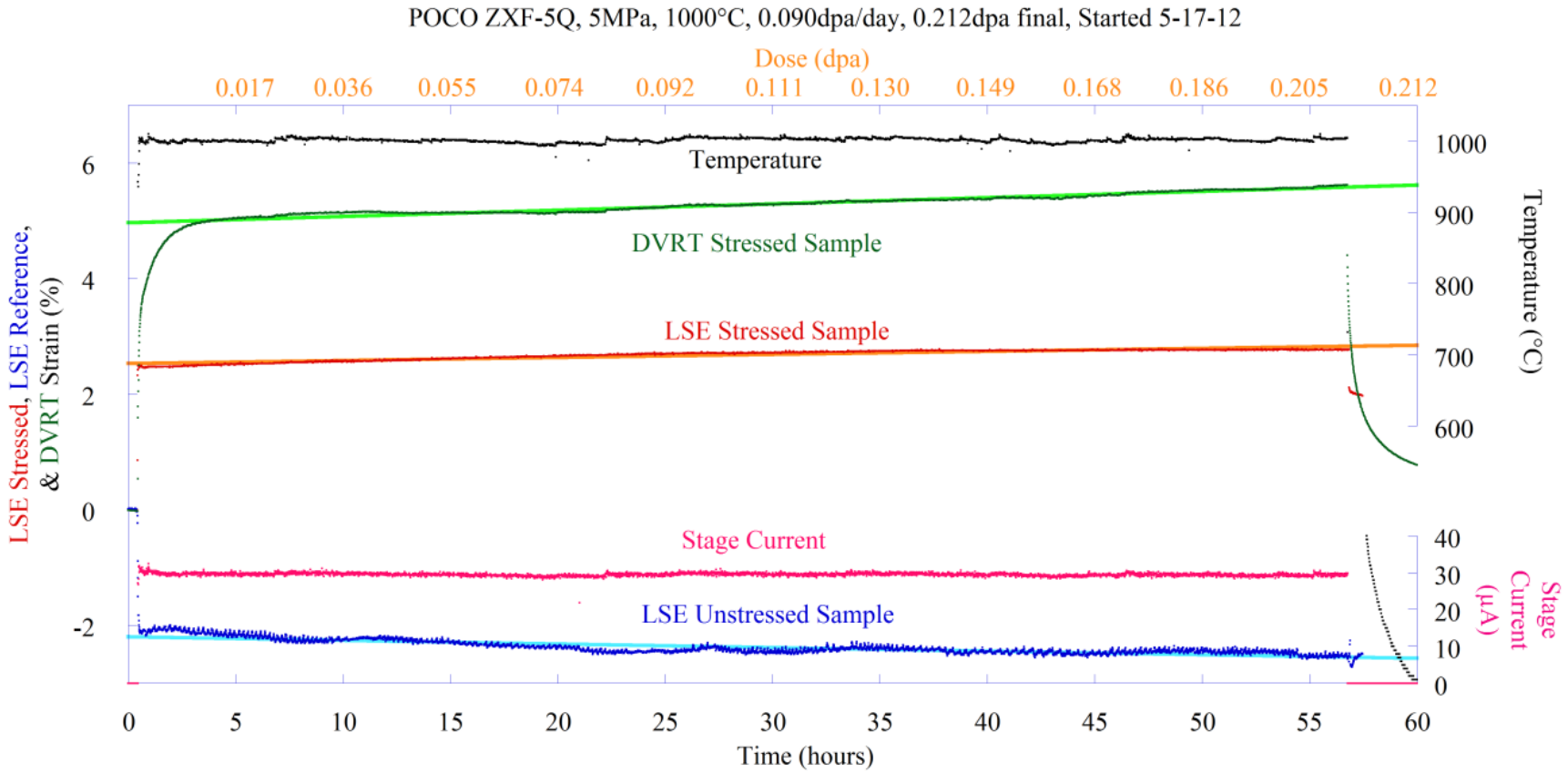

Figure 4.1. Experimental data from Experiment #7, performed at 1000°C, 0.090dpa/day, 5MPa stress, to a final dose of 0.212dpa.

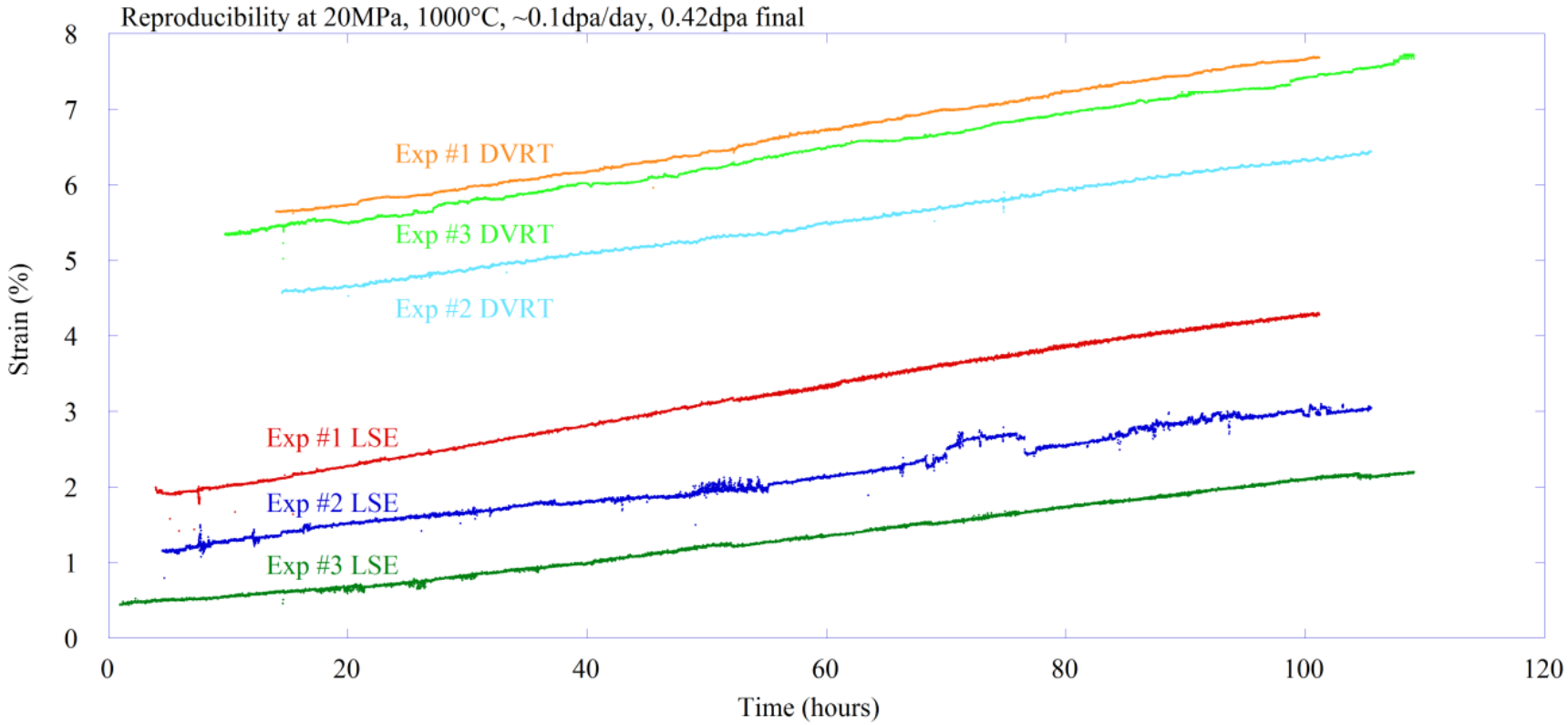

Figure 4.2. Plot of LSE and DVRT strain versus time, for the reproducibility derived from Experiments #1-3.

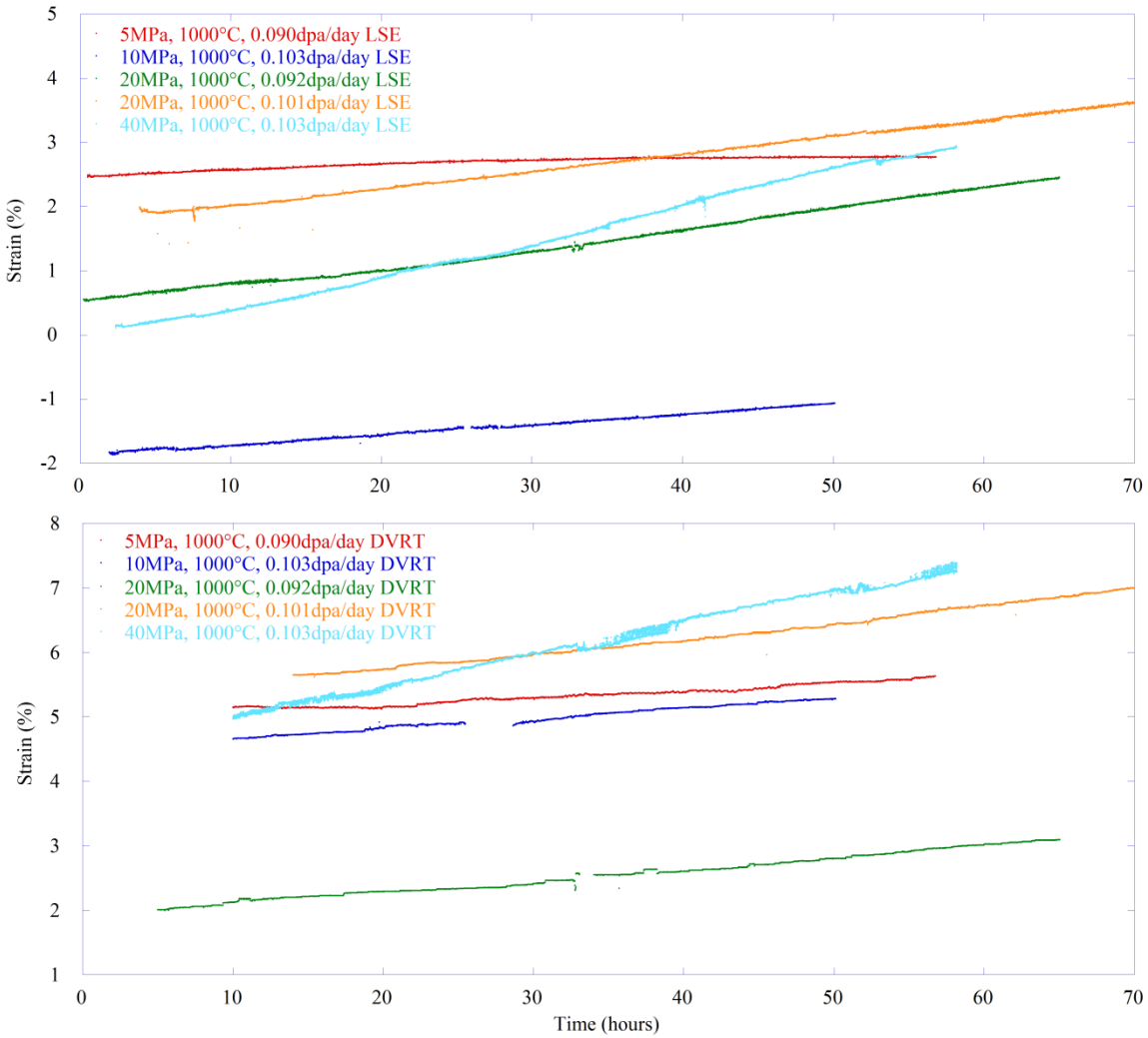

Figure 4.3. Plots of strain versus time for the LSE (top graph) and DVRT (bottom graph) for the stress dependence analysis. All the experiments were performed out to a dose of ~0.25 dpa, except for Experiment #1 (orange data), but the data past 70 hours does not differ from the data shown.

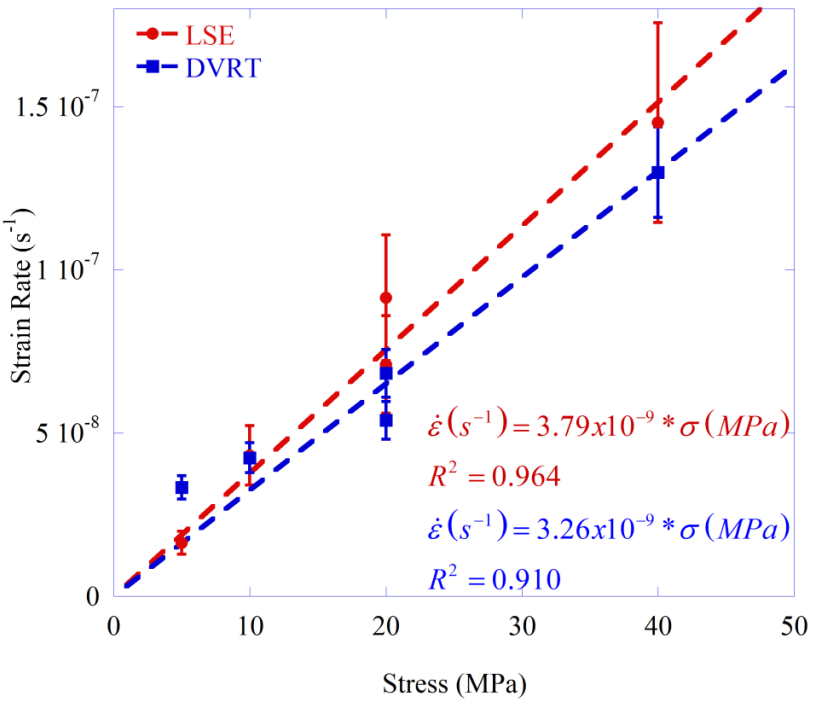

Figure 4.4. Plot of LSE (red circles) and DVRT (blue squares) apparent strain rates versus applied tensile stress. The dashed lines are the linear fit of the LSE (red line) and DVRT (blue line), when forced through the origin. The equations of the linear fit and the R^2 of the fit (LSE in red and DVRT in blue) are given in the bottom right corner of the plot.

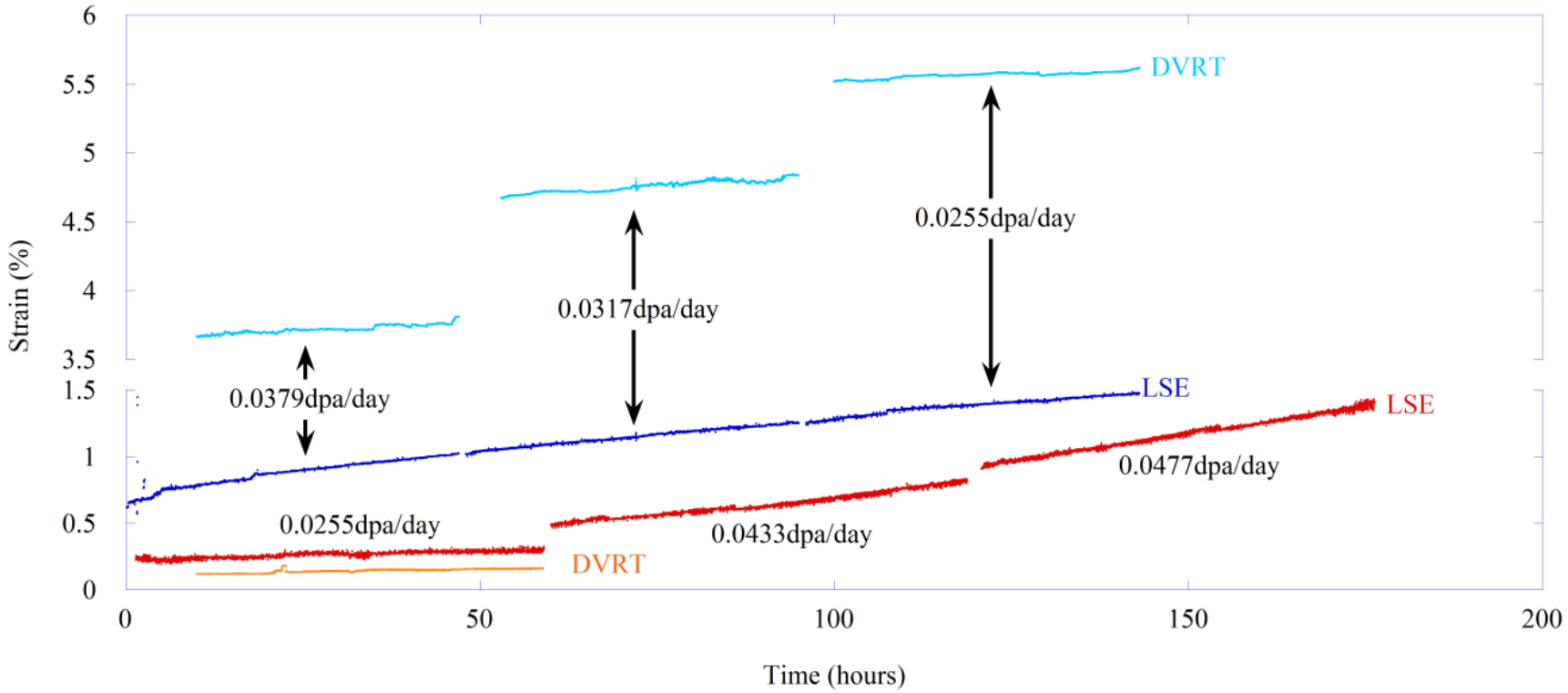

Figure 4.5. Plot of strain versus time, for the 700°C 20MPa dose rate dependence experiments, of the LSE and DVRT data from experiment #8 (red and orange data respectively) and experiment #9 (blue and light blue respectively).

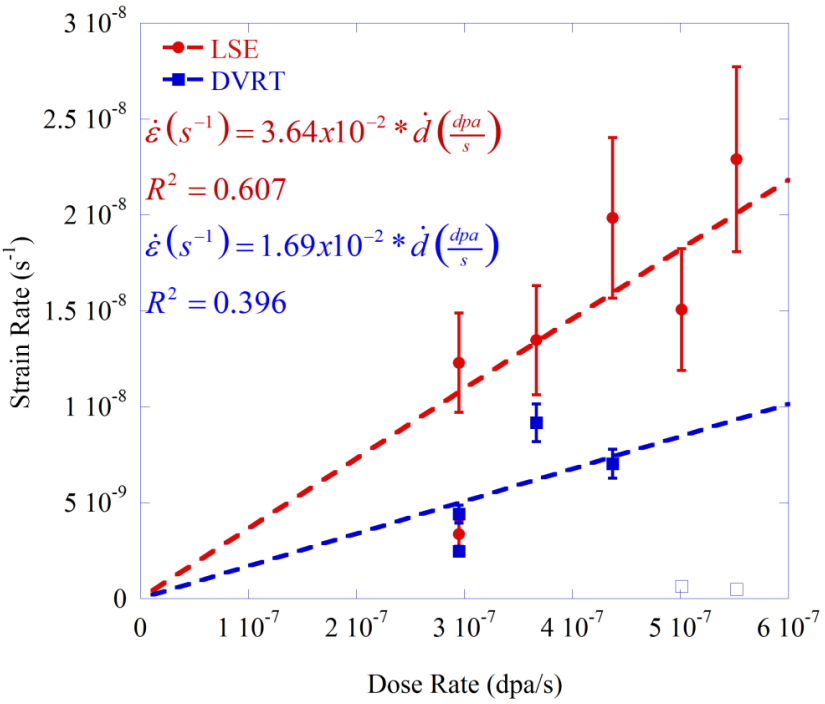

Figure 4.6. Plot of LSE (red circles) and DVRT (blue squares) apparent strain rates versus dose rate. The dashed lines are the linear fit of the LSE (red line) and DVRT (blue line), when forced through the origin. The equations of the linear fit and the R^2 of the fit (LSE in red and DVRT in blue) are given in the top left corner of the plot.

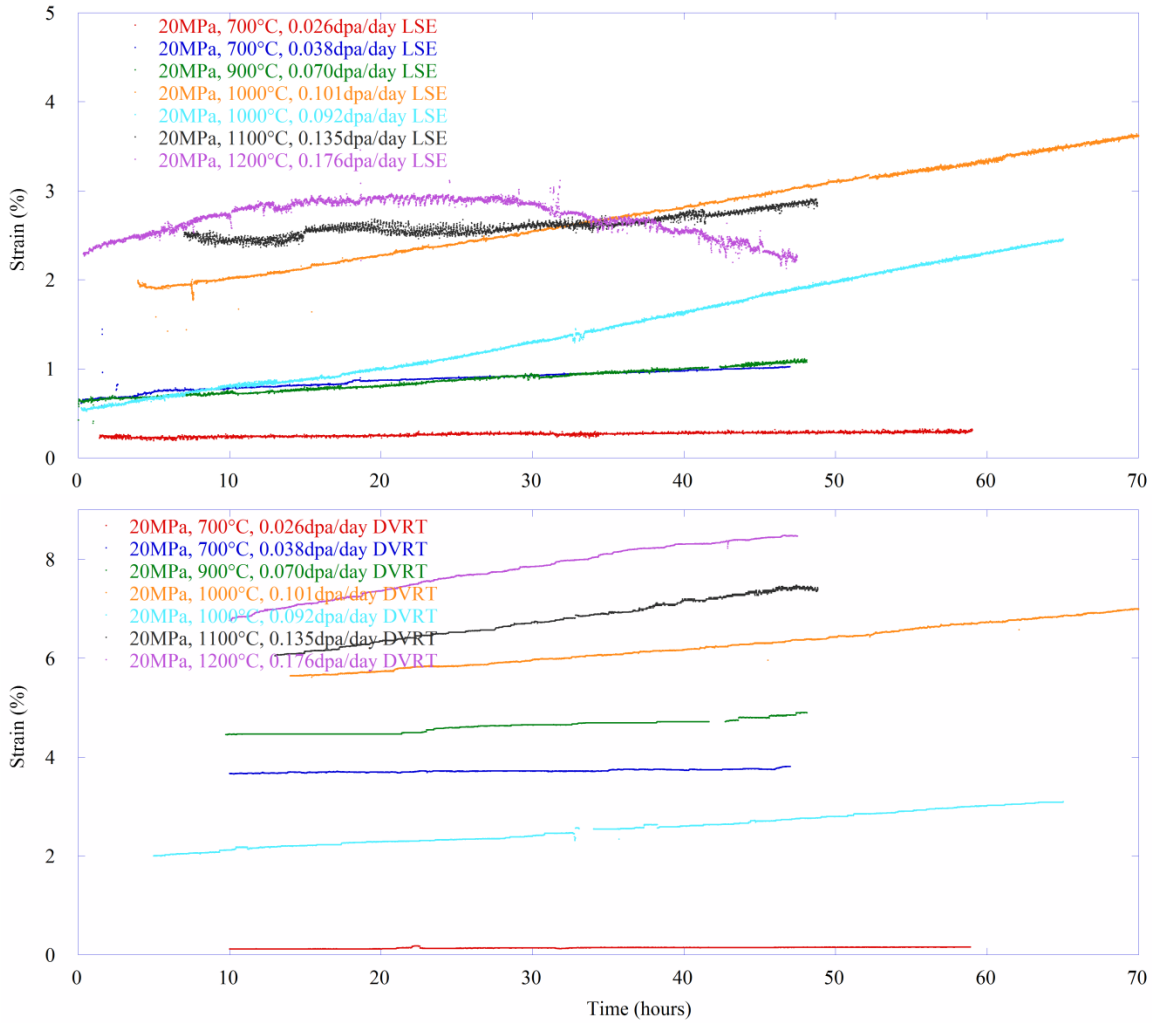

Figure 4.7. Plots of strain versus time for the LSE (top graph) and DVRT (bottom graph) for the temperature dependence analysis. Experiment #1 (orange data) was continued past hour 70, but the data past 70 hours does not differ from the data shown.

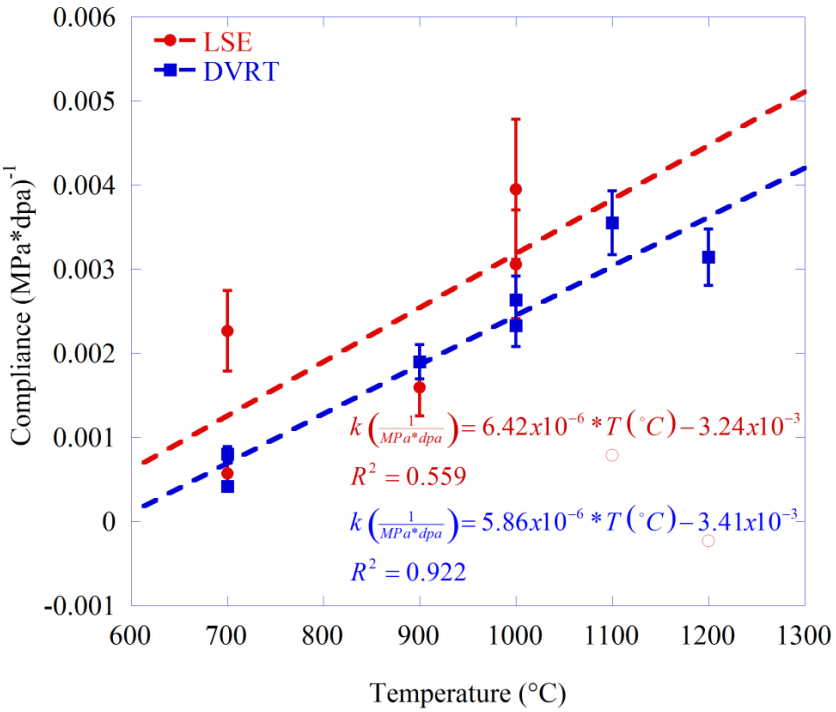

Figure 4.8. Plot of LSE (red circles) and DVRT (blue squares) compliance versus dose rate. The dashed lines are the linear fit of the LSE (red line) and DVRT (blue line). The equations of the linear fit and the R^2 of the fit (LSE in red and DVRT in blue) are given in the bottom right corner of the plot.

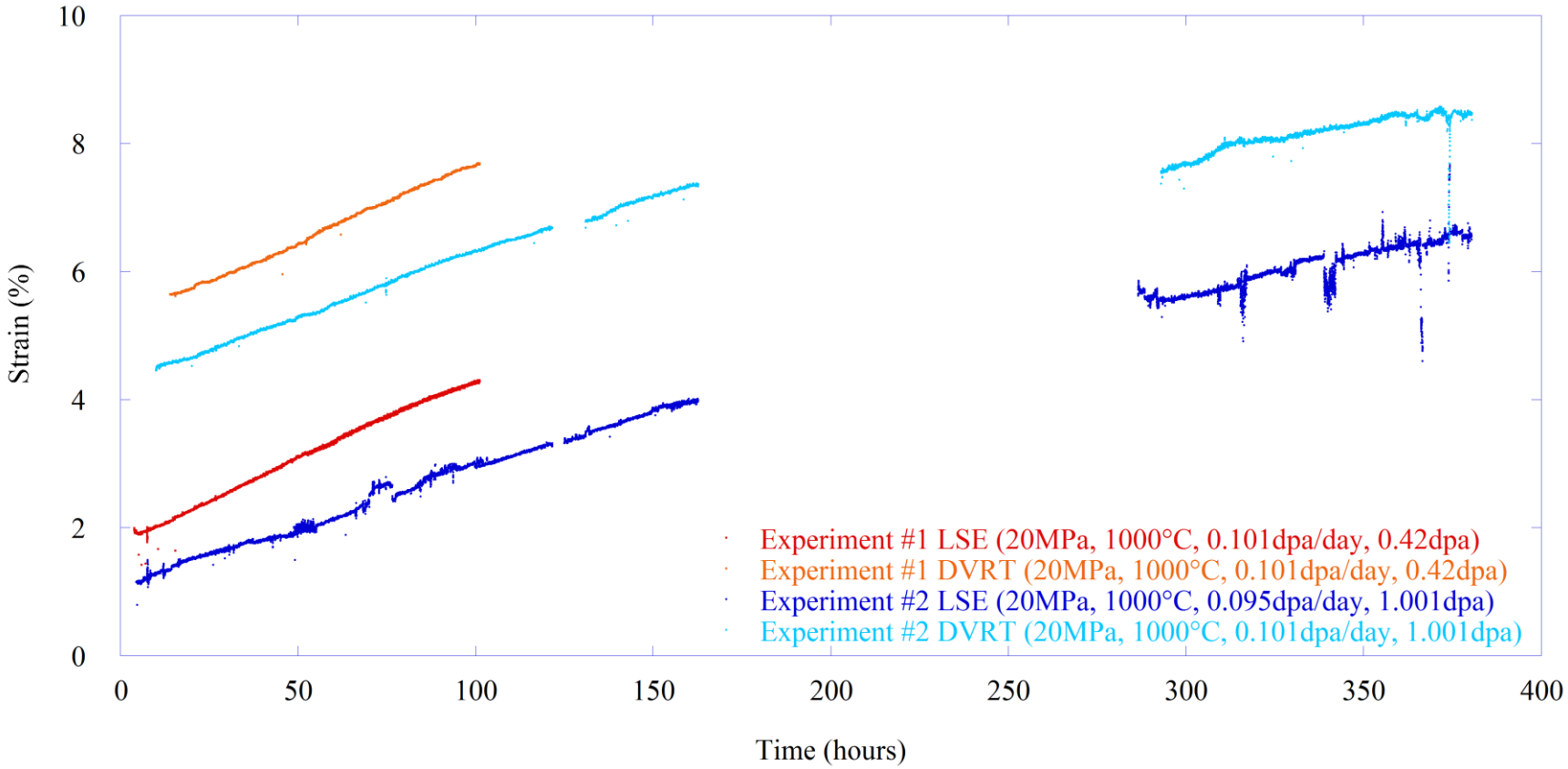

Figure 4.9. Plot of strain versus time, for the 1000°C 20MPa accumulated dose analysis, of the LSE and DVRT data from experiment #1 (red and orange data respectively) and experiment #2 (blue and light blue respectively).

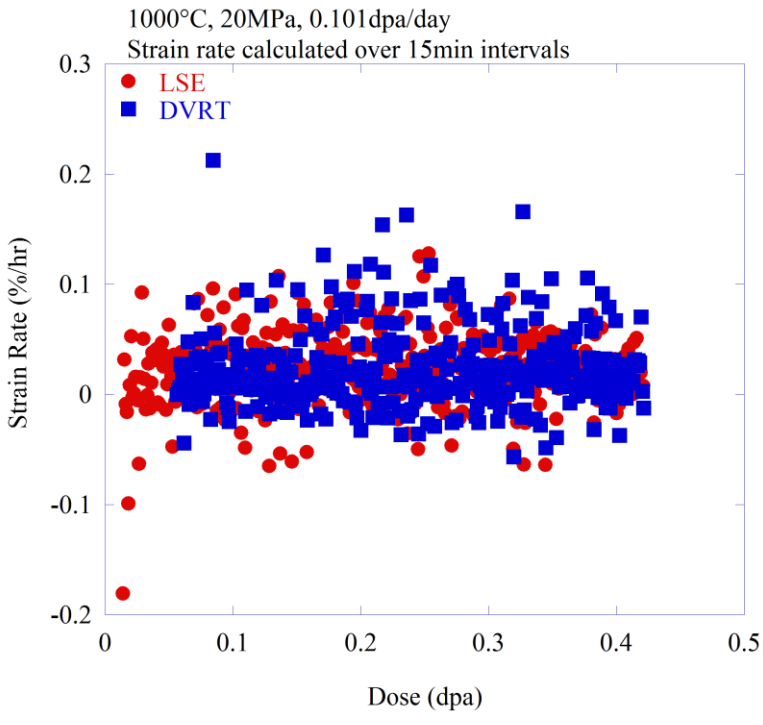

(a)

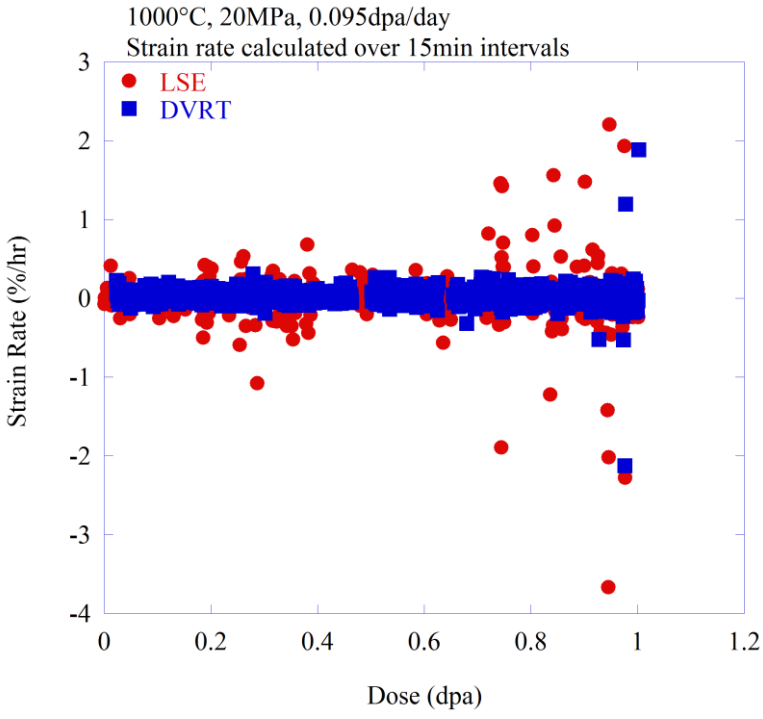

(b)

Figure 4.10. Plot of instantaneous creep rates from the LSE (red) and DVRT (blue), in 15 minute intervals, versus dose for experiment #1 (a) and #2 (b).

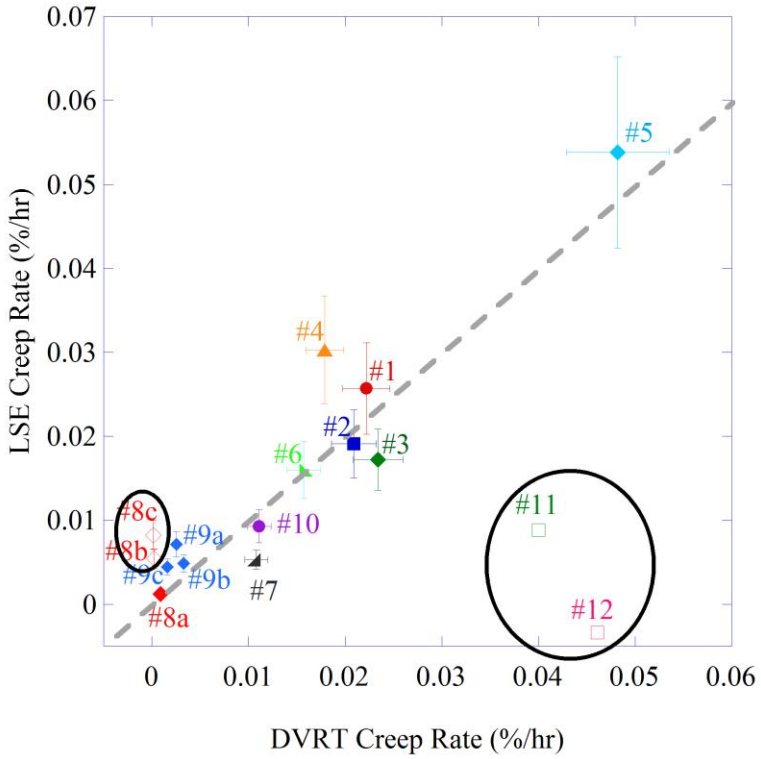

Figure 4.11. Plot of LSE vs. DVRT creep rate. Dashed line represents a 1:1 ratio.

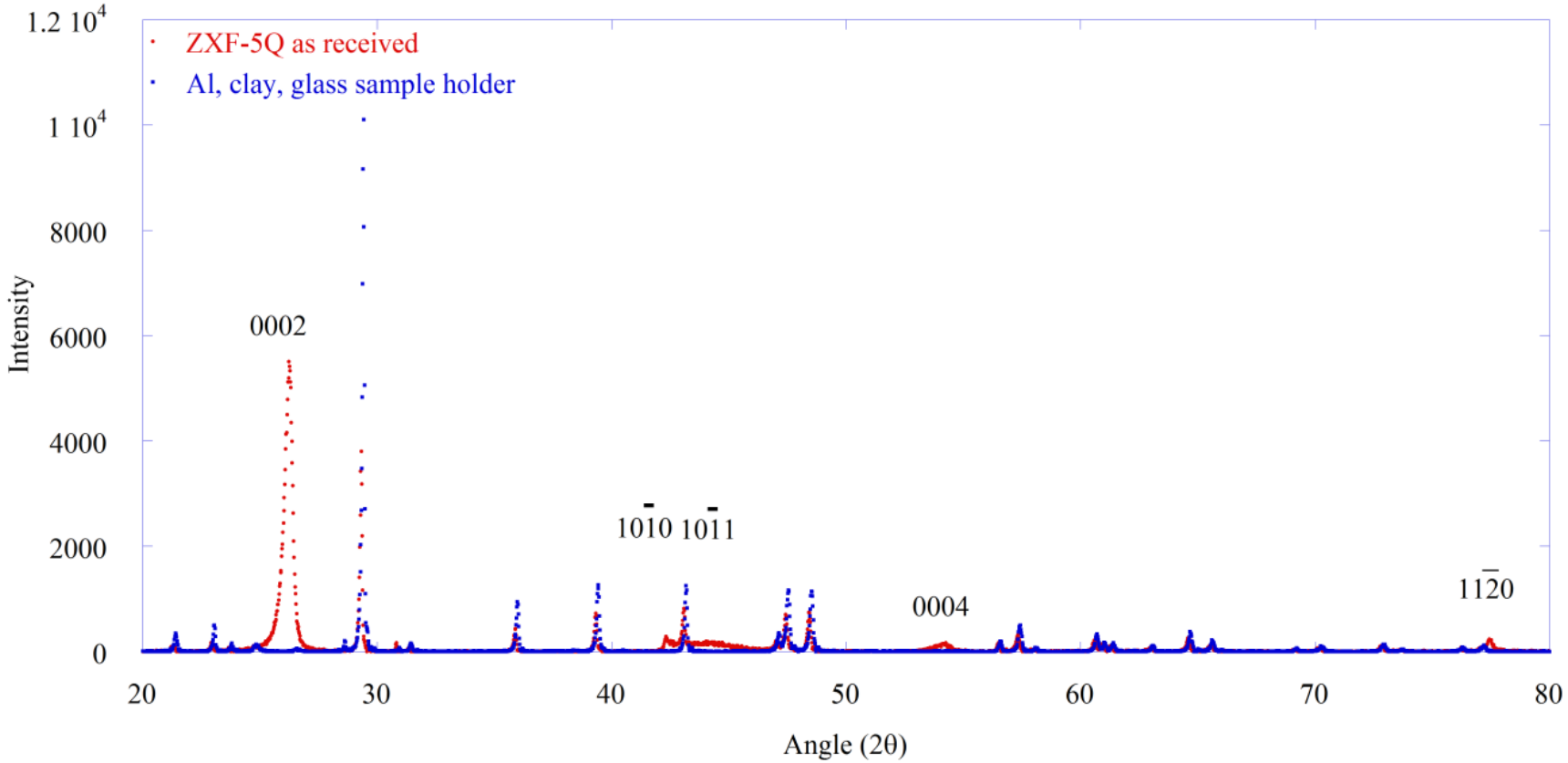

Figure 4.12. XRD spectrum of as-received graphite sample (red) using the original aluminum, glass and clay sample holder, and the spectrum arising from the original sample holder (blue).

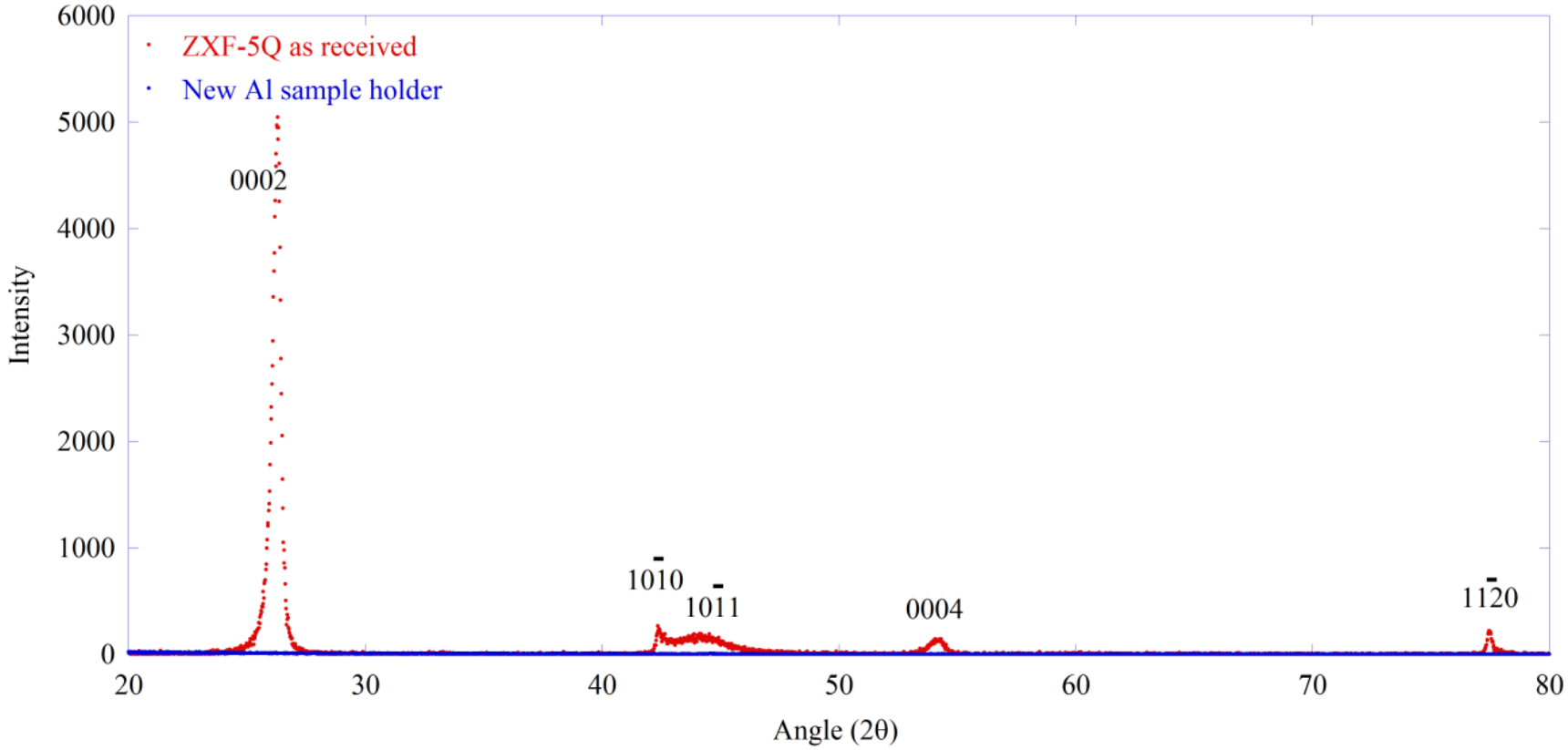

Figure 4.13. XRD spectrum of as-received graphite sample (red) using the new aluminum sample holder, and the spectrum arising from the sample holder (blue).

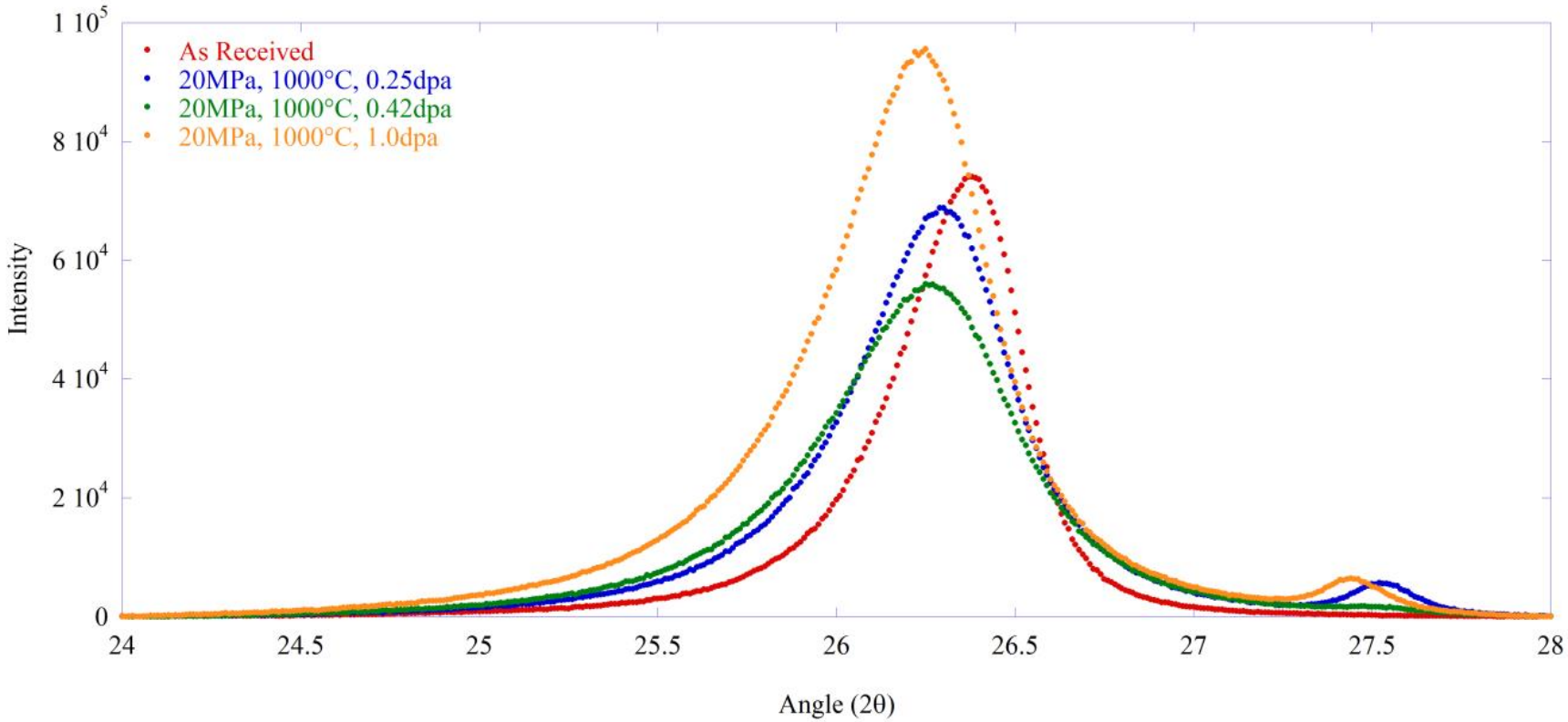

Figure 4.14. XRD of 0002 peak with changing total dose for as-received sample (red), 0.25dpa (blue), 0.421dpa (green), and 1.0dpa (orange). All irradiated samples were irradiated at 1000°C, ~0.1dpa/day, and 20MPa stress.

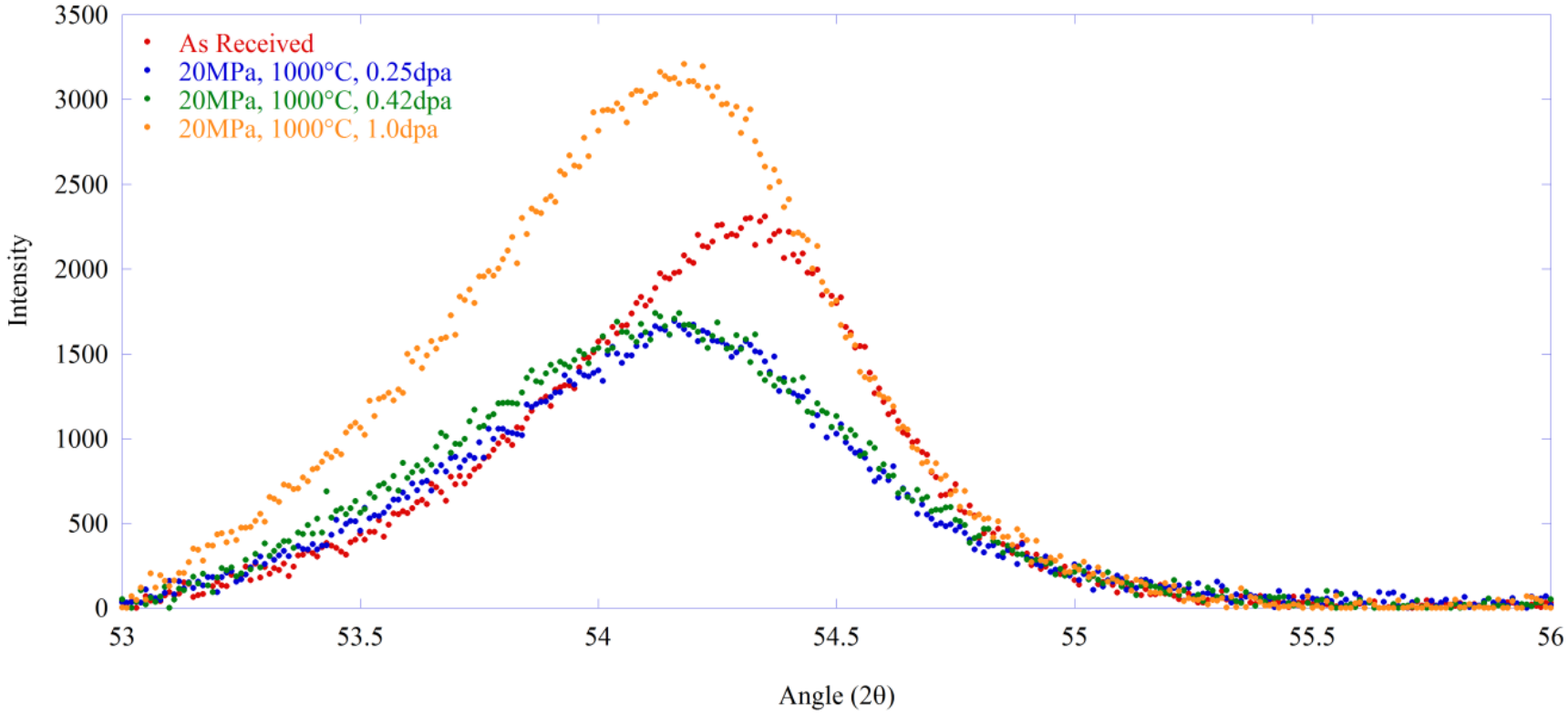

Figure 4.15. XRD of 0004 peak with changing total dose for as-received sample (red), 0.25dpa (blue), 0.421dpa (green), and 1.0dpa (orange). All irradiated samples were irradiated at 1000°C, ~0.1dpa/day, and 20MPa stress.

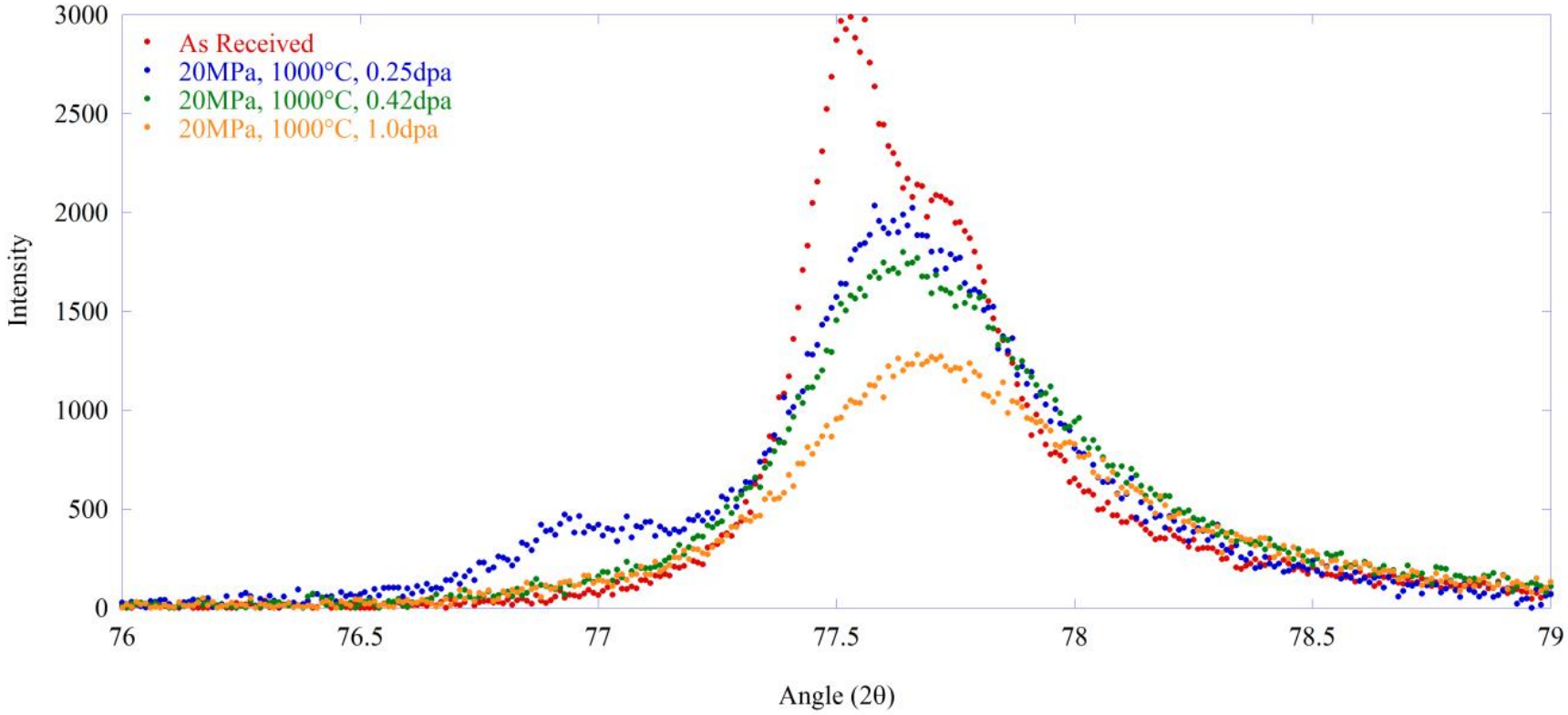

Figure 4.16. XRD of $11\bar{2}0$ peak with changing total dose for as-received sample (red), 0.25dpa (blue), 0.421dpa (green), and 1.0dpa (orange). All irradiated samples were irradiated at 1000°C, ~0.1dpa/day, and 20MPa stress.

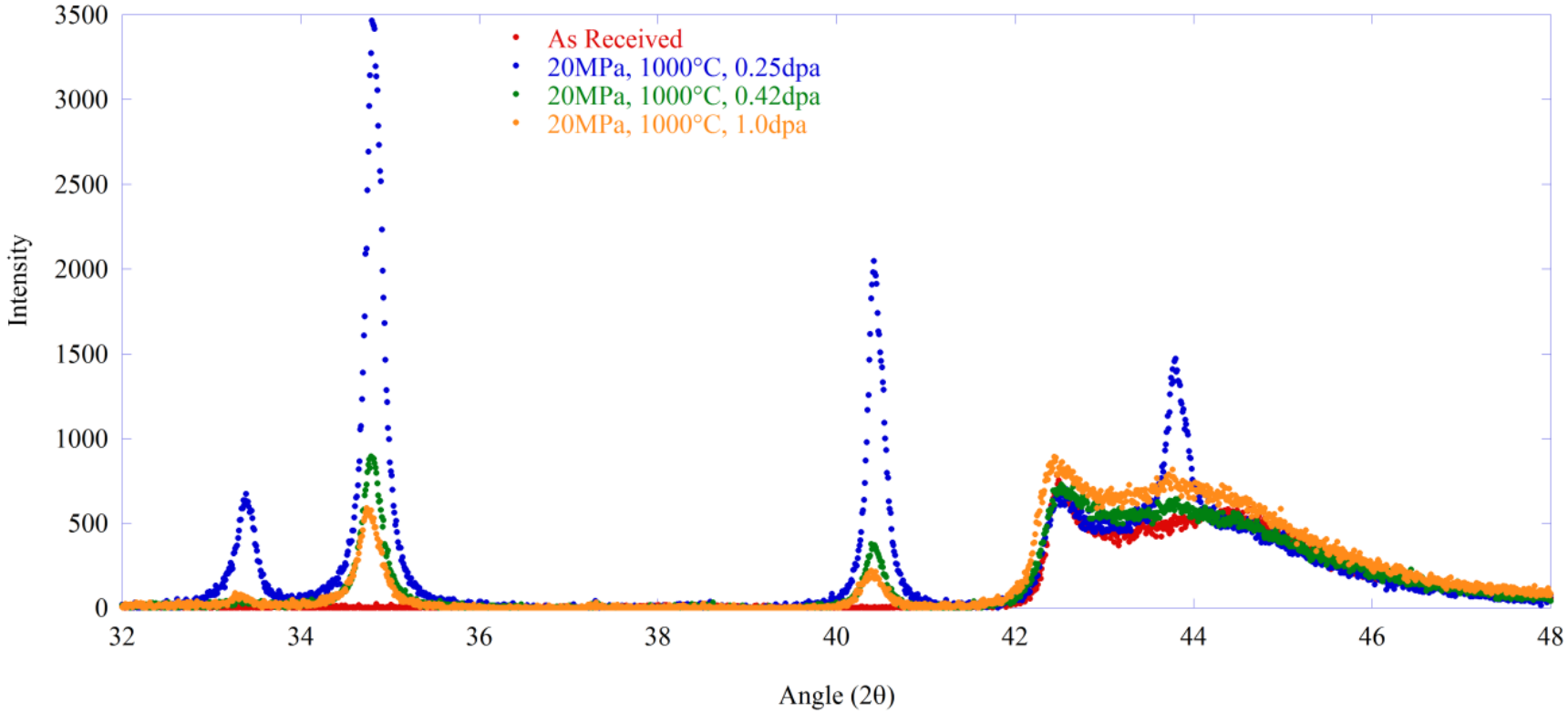

Figure 4.17. XRD of 32-48° range with changing total dose for as-received sample (red), 0.25dpa (blue), 0.421dpa (green), and 1.0dpa (orange). All irradiated samples were irradiated at 1000°C, ~0.1dpa/day, and 20MPa stress.

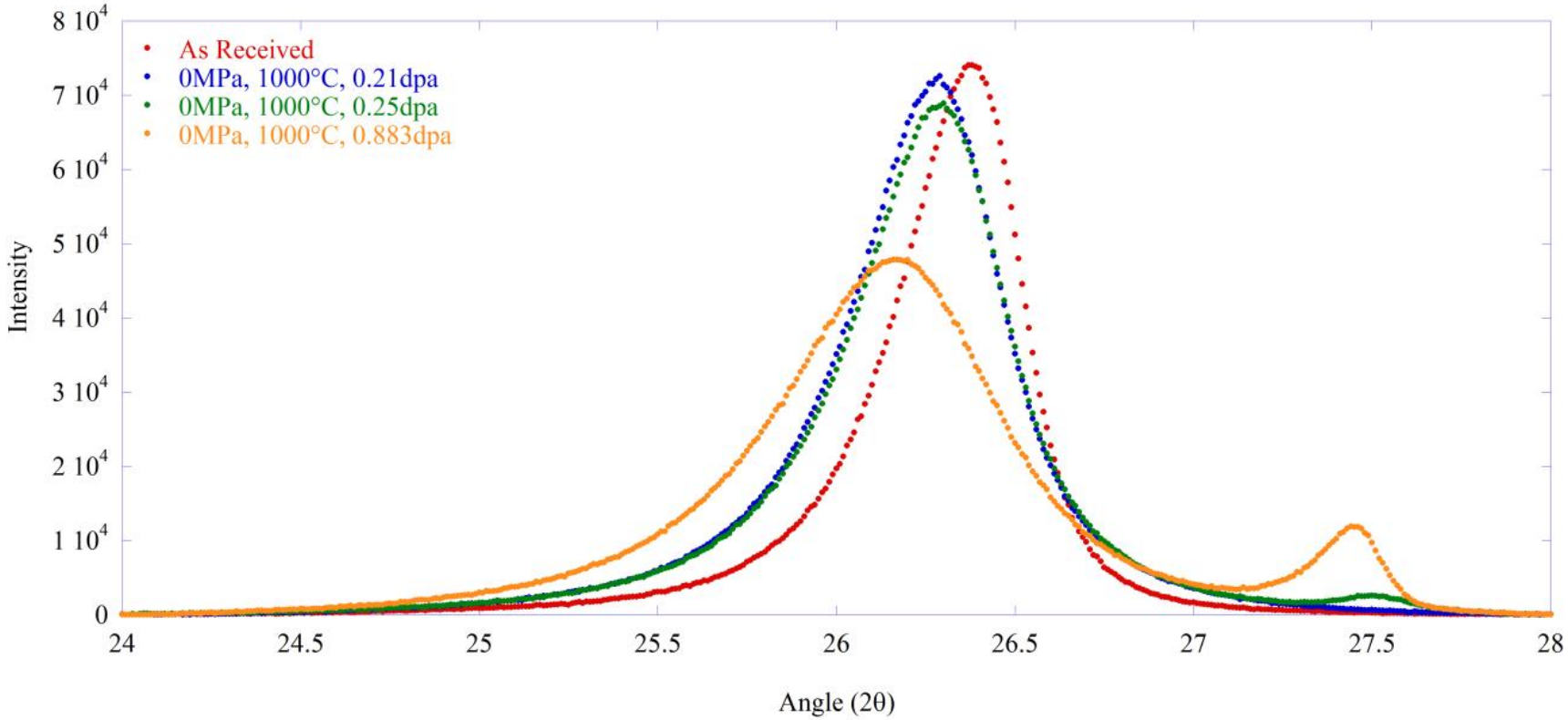

Figure 4.18. XRD of 0002 peak with changing total dose for as-received sample (red), 0.21dpa (blue), 0.25dpa (green), and 0.883dpa (orange). All irradiated samples were irradiated at 1000°C, ~0.1dpa/day, and 0MPa stress.

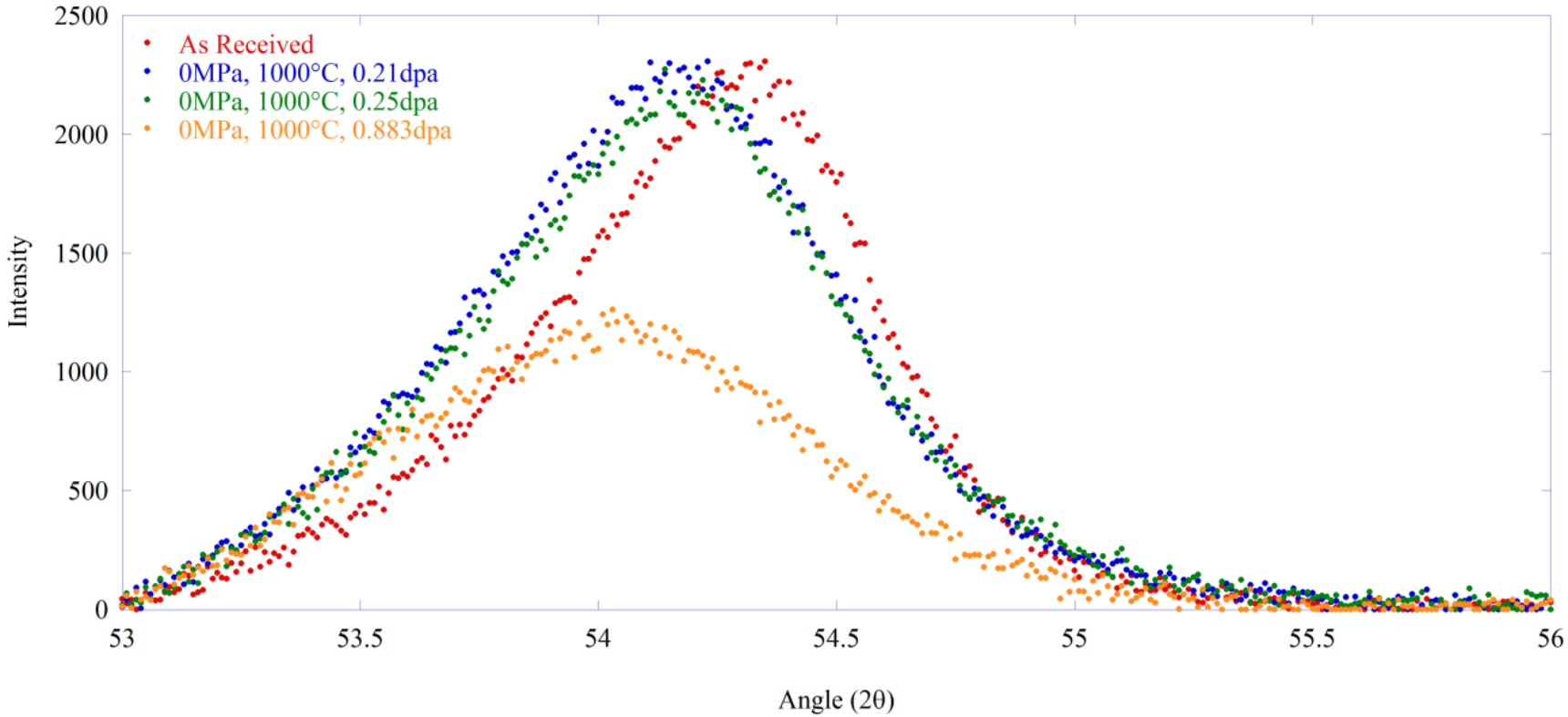

Figure 4.19. XRD of 0004 peak with changing total dose for as-received sample (red), 0.21dpa (blue), 0.25dpa (green), and 0.883dpa (orange). All irradiated samples were irradiated at 1000°C, ~0.1dpa/day, and 0MPa stress.

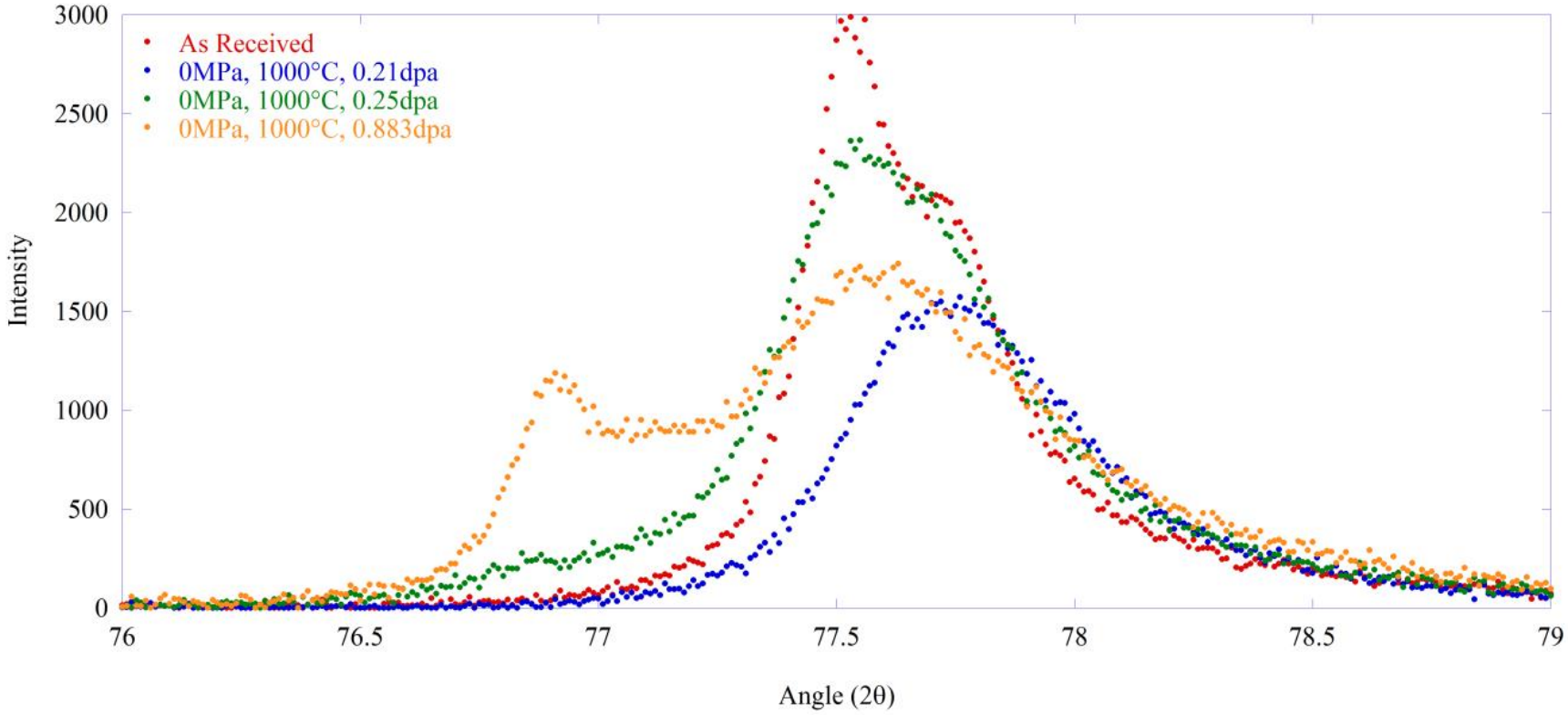

Figure 4.20. XRD of $11\bar{2}0$ peak with changing total dose for as-received sample (red), 0.21dpa (blue), 0.25dpa (green), and 0.883dpa (orange). All irradiated samples were irradiated at 1000°C, ~0.1dpa/day, and 0MPa stress.

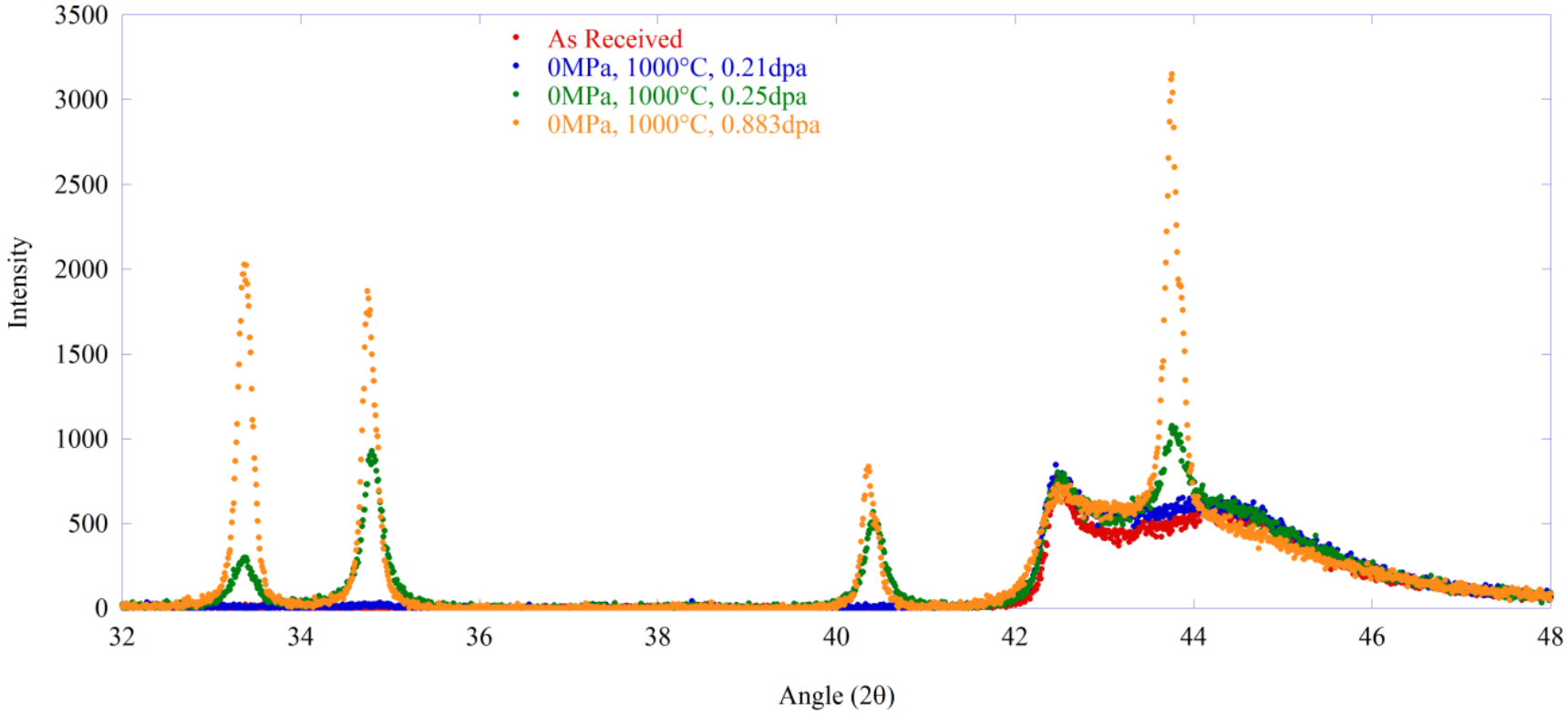

Figure 4.21. XRD of 32-48° range with changing total dose for as-received sample (red), 0.21dpa (blue), 0.25dpa (green), and 0.883dpa (orange). All irradiated samples were irradiated at 1000°C, ~0.1dpa/day, and 0MPa stress.

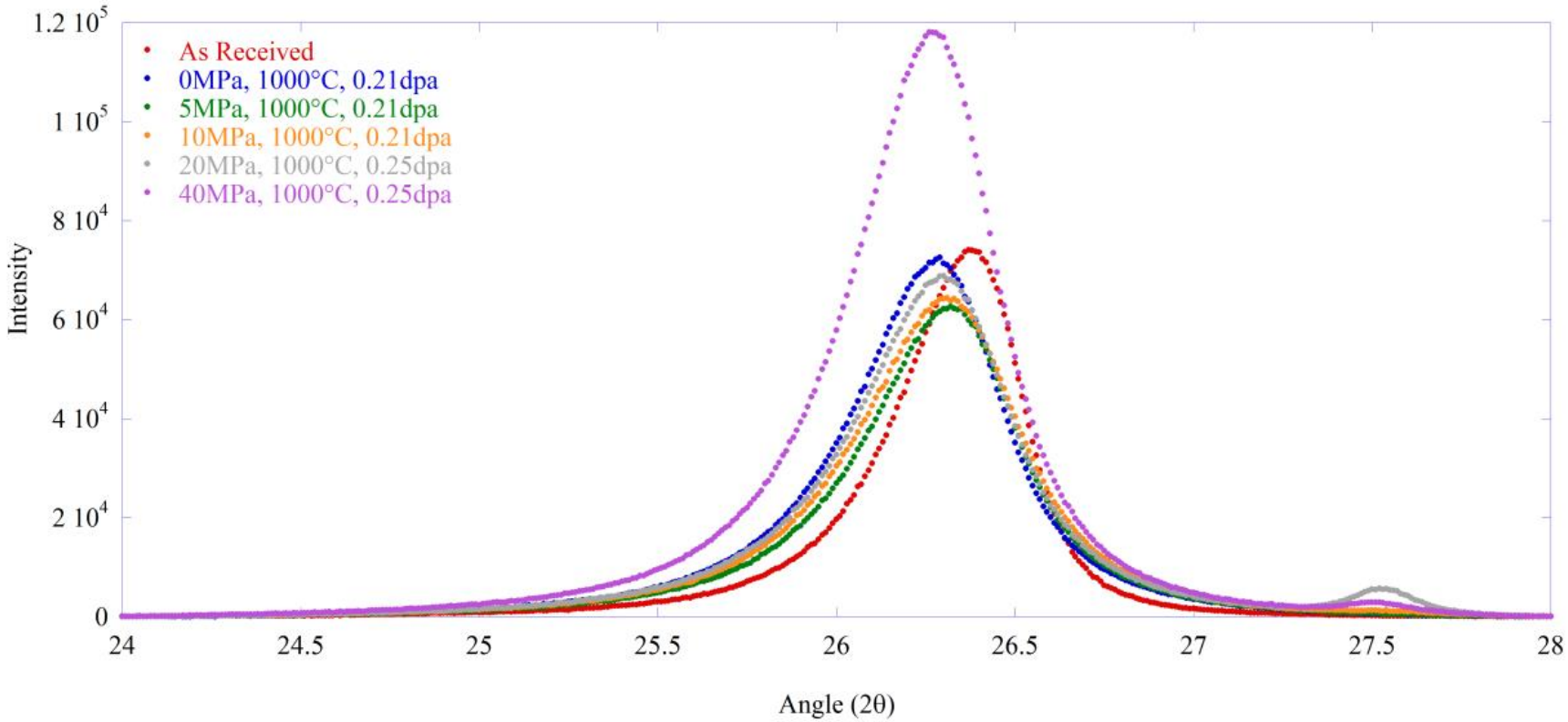

Figure 4.22. XRD of 0002 peak with different applied tensile stress for as-received sample (red), 0MPa (blue), 5MPa (green), 10MPa (orange), 20MPa (grey), and 40MPa (purple). All irradiated samples were irradiated at 1000°C, ~0.1dpa/day, and to a final dose around 0.25dpa.

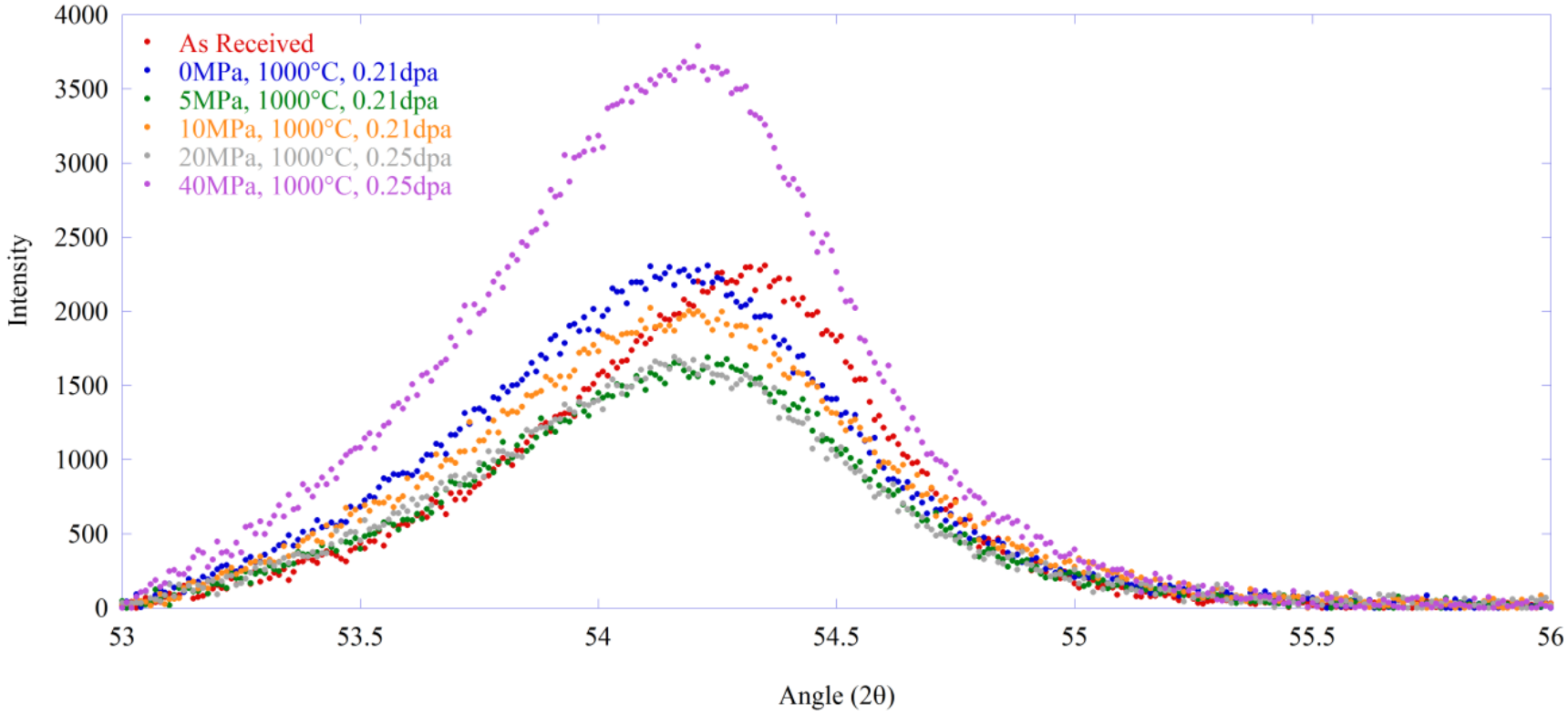

Figure 4.23. XRD of 0004 peak with different applied tensile stress for as-received sample (red), 0MPa (blue), 5MPa (green), 10MPa (orange), 20MPa (grey), and 40MPa (purple). All irradiated samples were irradiated at 1000°C, ~0.1dpa/day, and to a final dose around 0.25dpa.

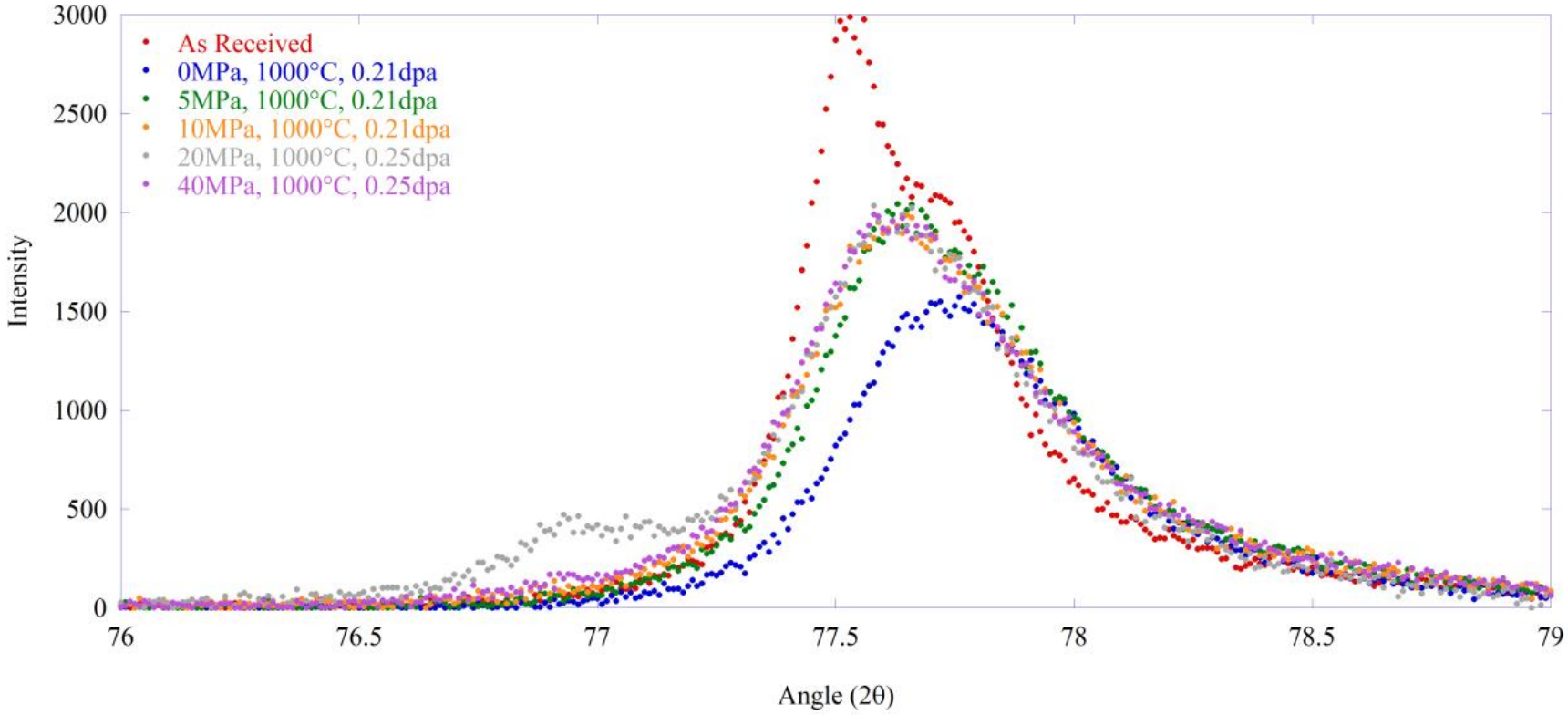

Figure 4.24. XRD of $11\bar{2}0$ peak with different applied tensile stress for as-received sample (red), 0MPa (blue), 5MPa (green), 10MPa (orange), 20MPa (grey), and 40MPa (purple). All irradiated samples were irradiated at 1000°C, ~0.1dpa/day, and to a final dose around 0.25dpa.

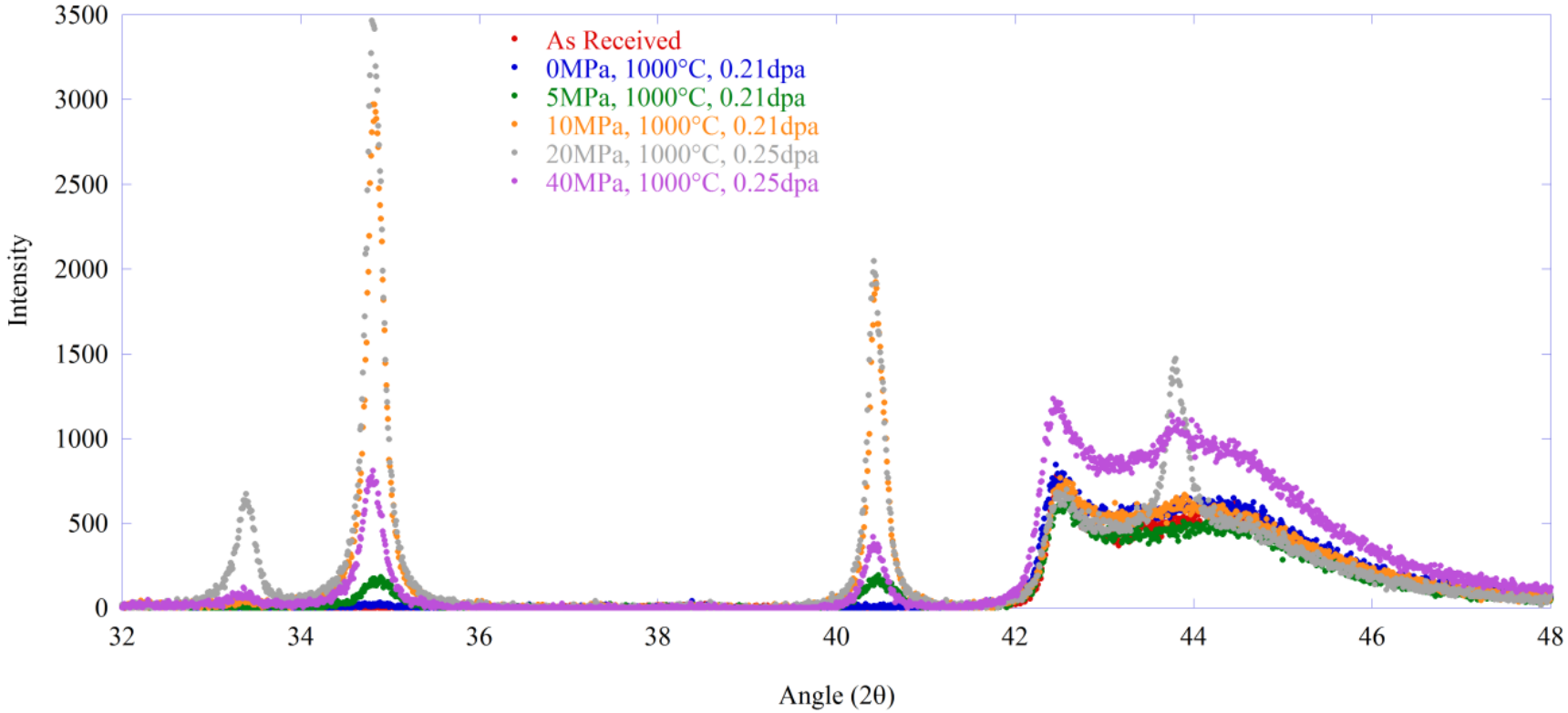

Figure 4.25. XRD of 32-48° range with different applied tensile stress for as-received sample (red), 0MPa (blue), 5MPa (green), 10MPa (orange), 20MPa (grey), and 40MPa (purple). All irradiated samples were irradiated at 1000°C, ~0.1dpa/day, and to a final dose around 0.25dpa.

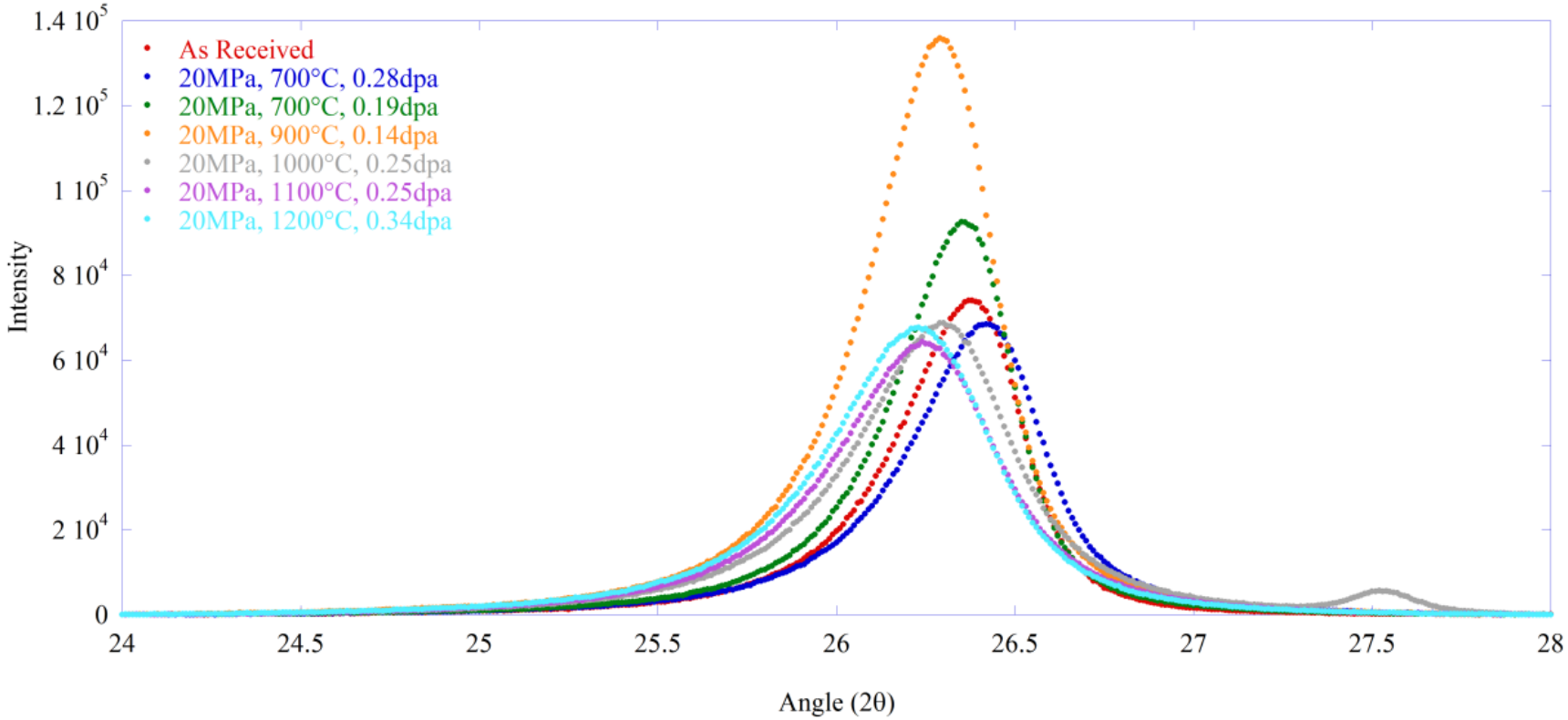

Figure 4.26. XRD of 0002 peak for different irradiation temperatures for as-received sample (red), 700°C to 0.28dpa (blue), 700°C to 0.19dpa (green), 900°C to 0.14dpa (orange), 1000°C to 0.25dpa (grey), 1100°C to 0.25dpa (purple), and 1200°C to 0.34dpa (bright blue). All irradiated samples were irradiated with a 20MPa stress.

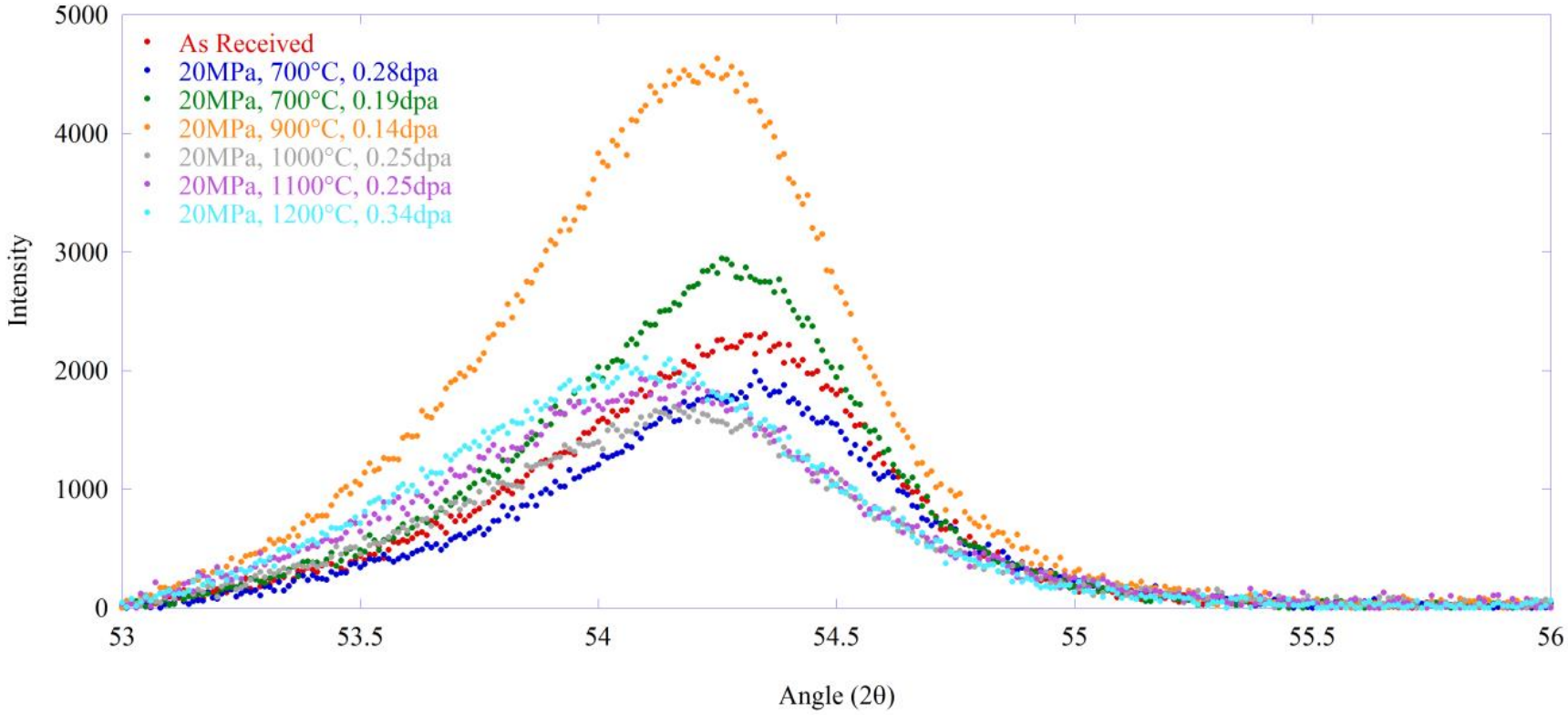

Figure 4.27. XRD of 0004 peak for different irradiation temperatures for as-received sample (red), 700°C to 0.28dpa (blue), 700°C to 0.19dpa (green), 900°C to 0.14dpa (orange), 1000°C to 0.25dpa (grey), 1100°C to 0.25dpa (purple), and 1200°C to 0.34dpa (bright blue). All irradiated samples were irradiated with a 20MPa stress.

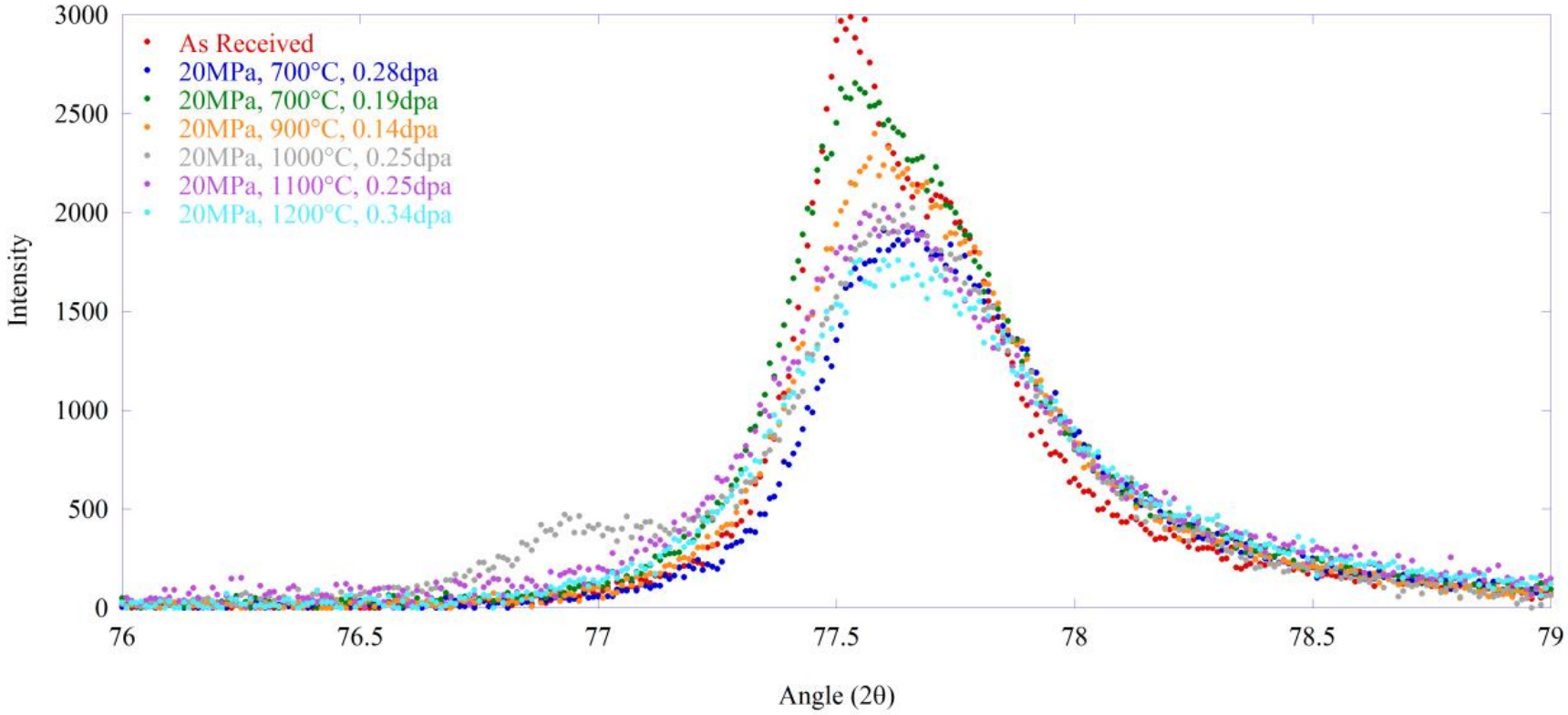

Figure 4.28. XRD of $11\bar{2}0$ peak for different irradiation temperatures for as-received sample (red), 700°C to 0.28dpa (blue), 700°C to 0.19dpa (green), 900°C to 0.14dpa (orange), 1000°C to 0.25dpa (grey), 1100°C to 0.25dpa (purple), and 1200°C to 0.34dpa (bright blue). All irradiated samples were irradiated with a 20MPa stress.

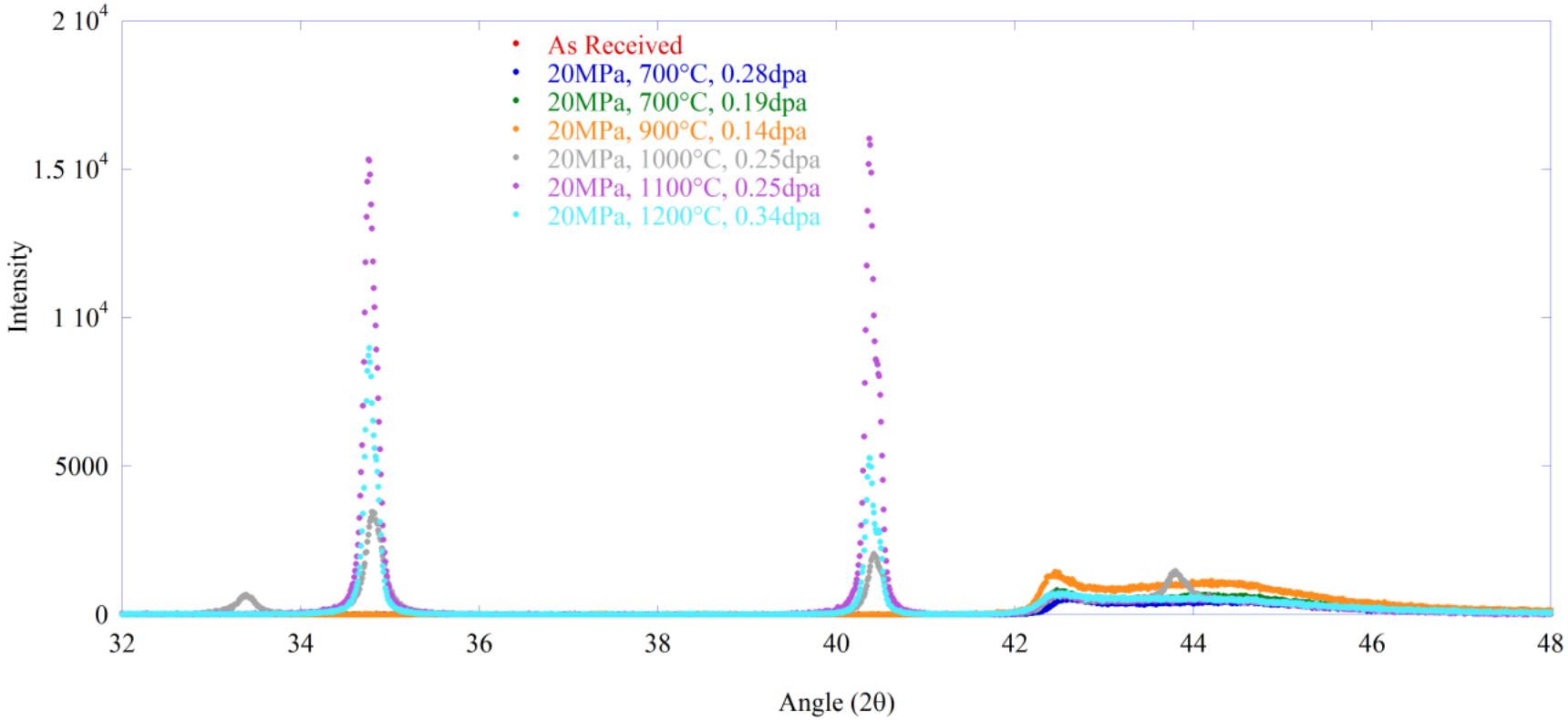

Figure 4.29. XRD of 32-48° range for different irradiation temperatures for as-received sample (red), 700°C to 0.28dpa (blue), 700°C to 0.19dpa (green), 900°C to 0.14dpa (orange), 1000°C to 0.25dpa (grey), 1100°C to 0.25dpa (purple), and 1200°C to 0.34dpa (bright blue). All irradiated samples were irradiated with a 20MPa stress.

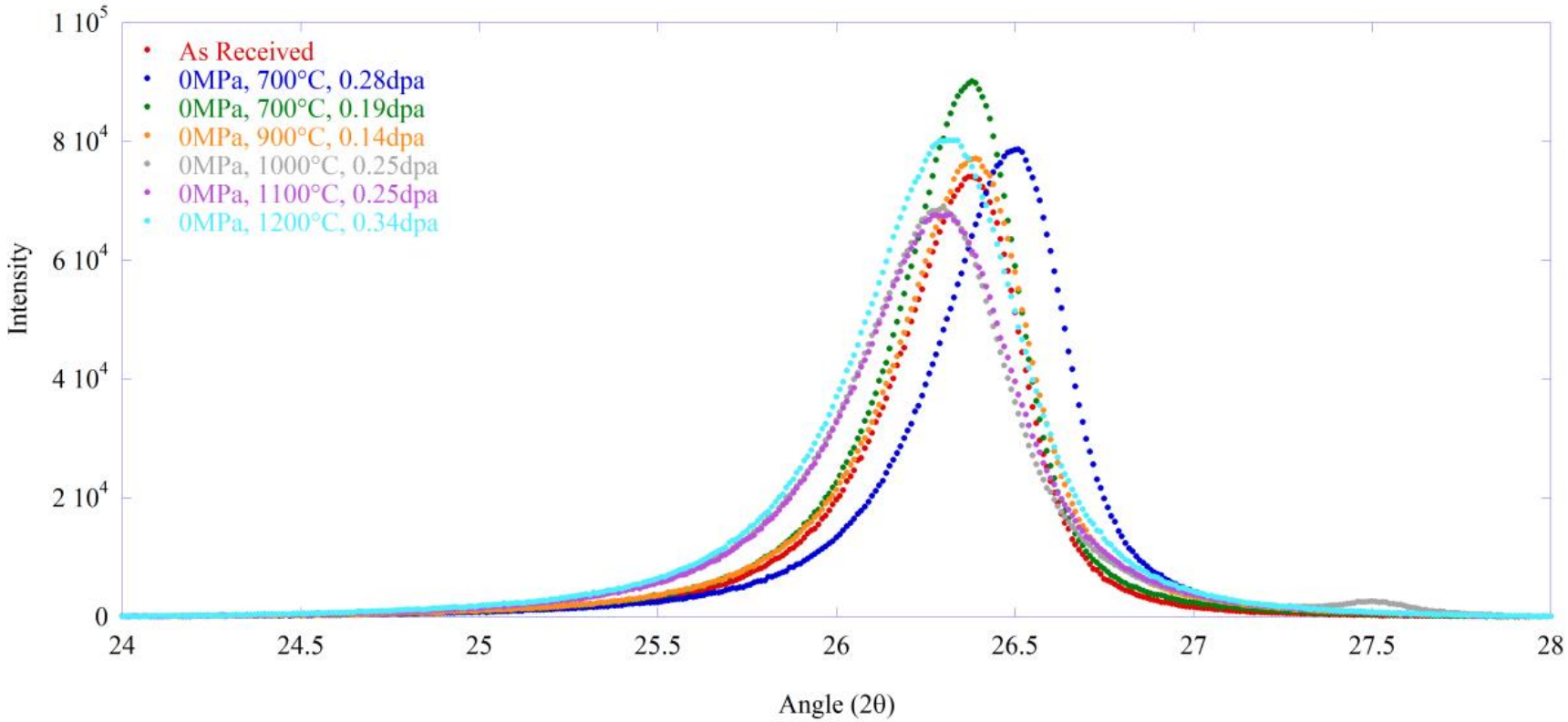

Figure 4.30. XRD of 0002 peak for different irradiation temperatures for as-received sample (red), 700°C to 0.28dpa (blue), 700°C to 0.19dpa (green), 900°C to 0.14dpa (orange), 1000°C to 0.25dpa (grey), 1100°C to 0.25dpa (purple), and 1200°C to 0.34dpa (bright blue). All irradiated samples were irradiated with a 0MPa stress.

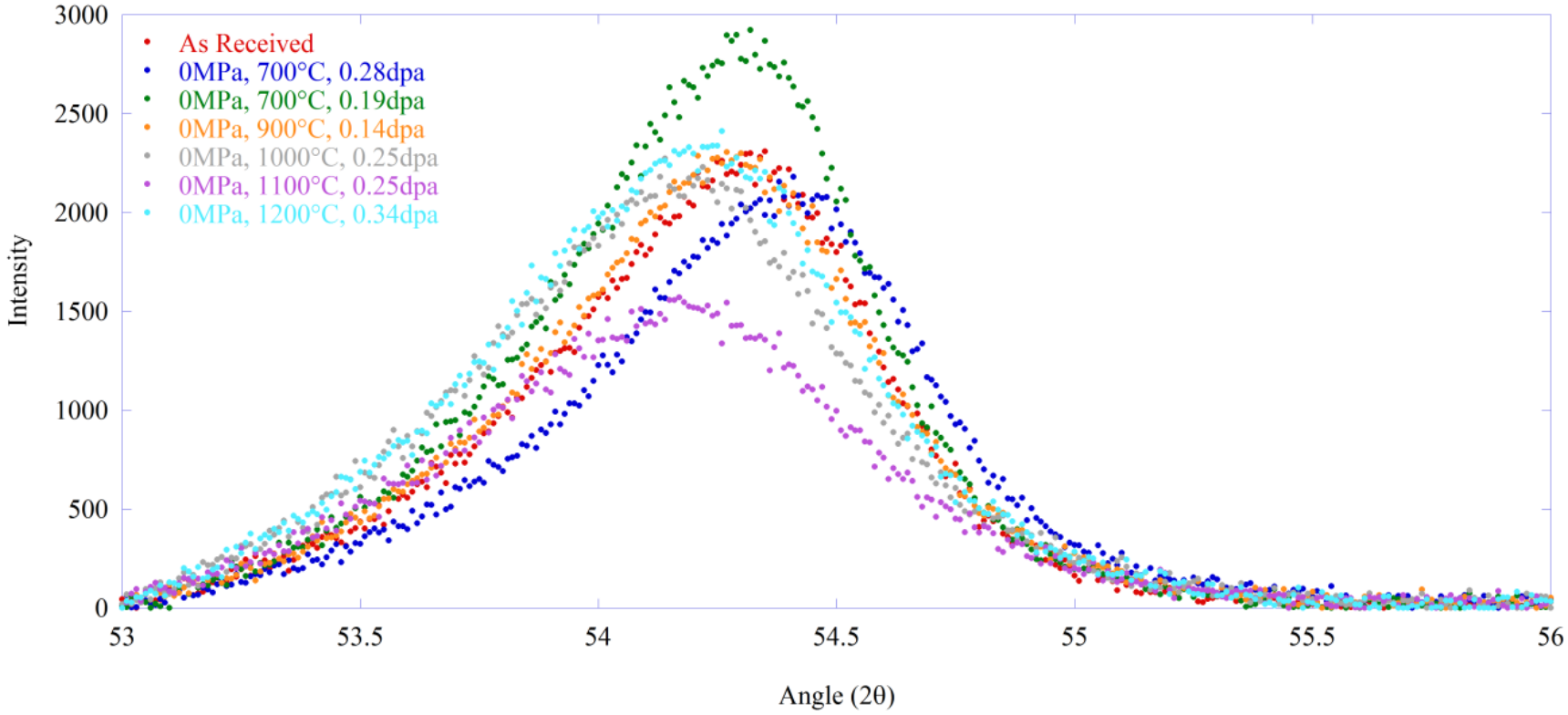

Figure 4.31. XRD of 0004 peak for different irradiation temperatures for as-received sample (red), 700°C to 0.28dpa (blue), 700°C to 0.19dpa (green), 900°C to 0.14dpa (orange), 1000°C to 0.25dpa (grey), 1100°C to 0.25dpa (purple), and 1200°C to 0.34dpa (bright blue). All irradiated samples were irradiated with a 0MPa stress.

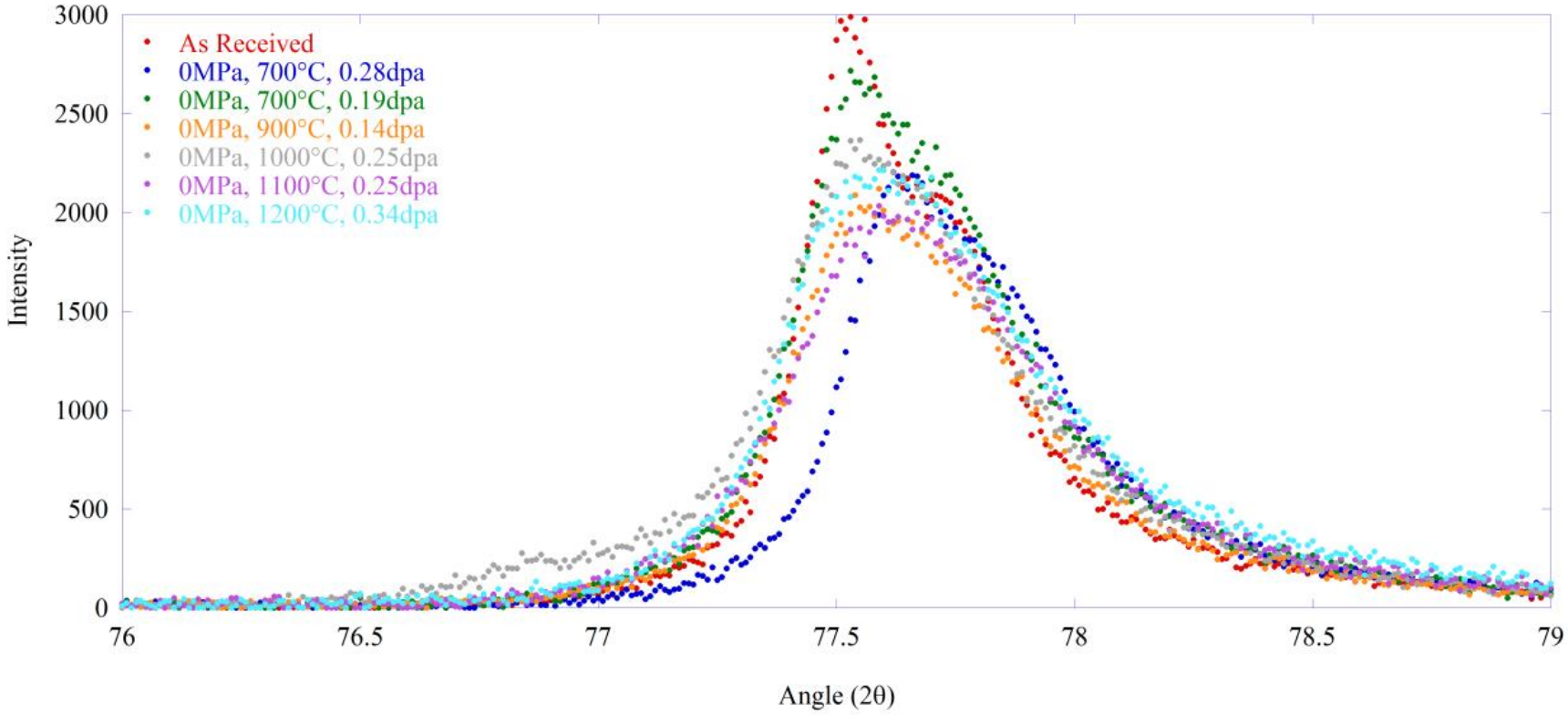

Figure 4.32. XRD of $11\bar{2}0$ peak for different irradiation temperatures for as-received sample (red), 700°C to 0.28dpa (blue), 700°C to 0.19dpa (green), 900°C to 0.14dpa (orange), 1000°C to 0.25dpa (grey), 1100°C to 0.25dpa (purple), and 1200°C to 0.34dpa (bright blue). All irradiated samples were irradiated with a 0MPa stress.

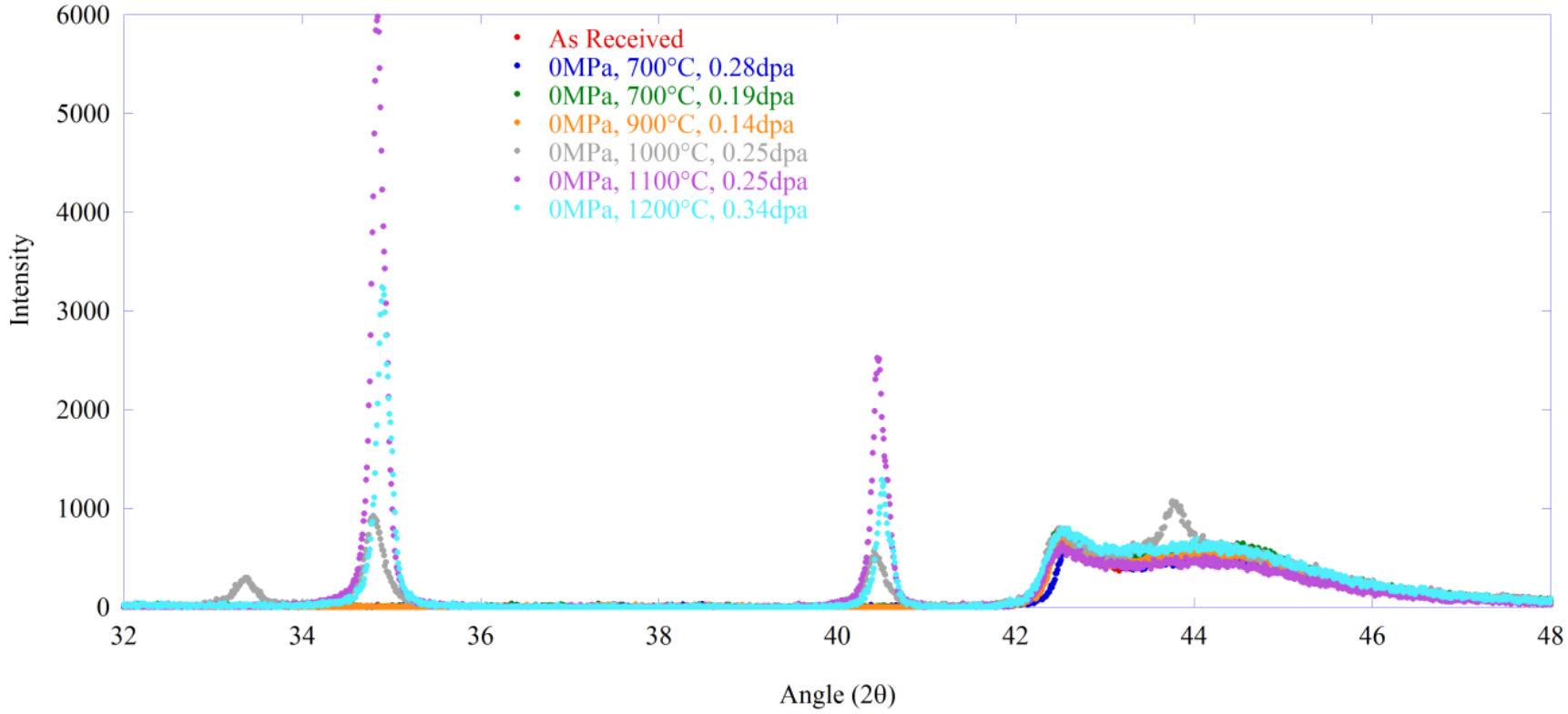

Figure 4.33. XRD of 32-48° range for different irradiation temperatures for as-received sample (red), 700°C to 0.28dpa (blue), 700°C to 0.19dpa (green), 900°C to 0.14dpa (orange), 1000°C to 0.25dpa (grey), 1100°C to 0.25dpa (purple), and 1200°C to 0.34dpa (bright blue). All irradiated samples were irradiated with a 20MPa stress.

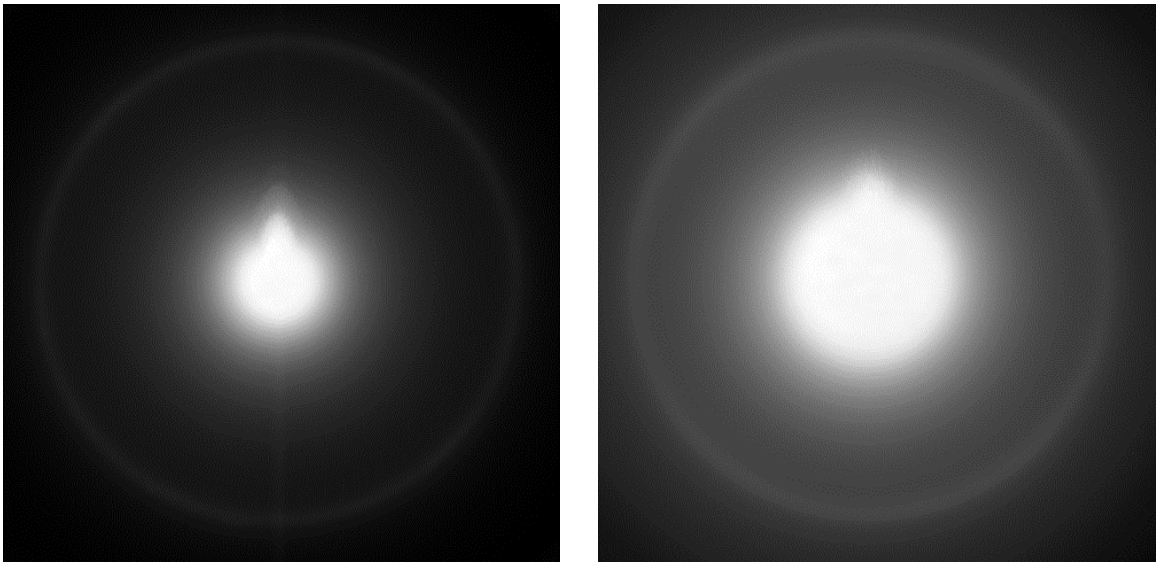

(a) (b)

Figure 4.34. Combined TEM SAED patterns for the as-received sample (a) and the sample irradiated at 1000°C, 0.095dpa/day, 20MPa, to 1dpa (b).

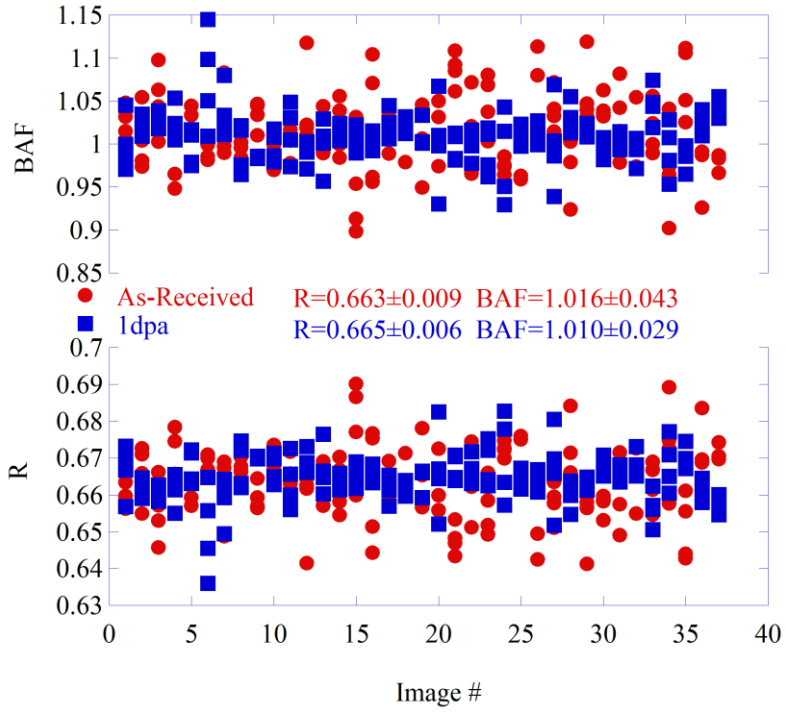

(a)

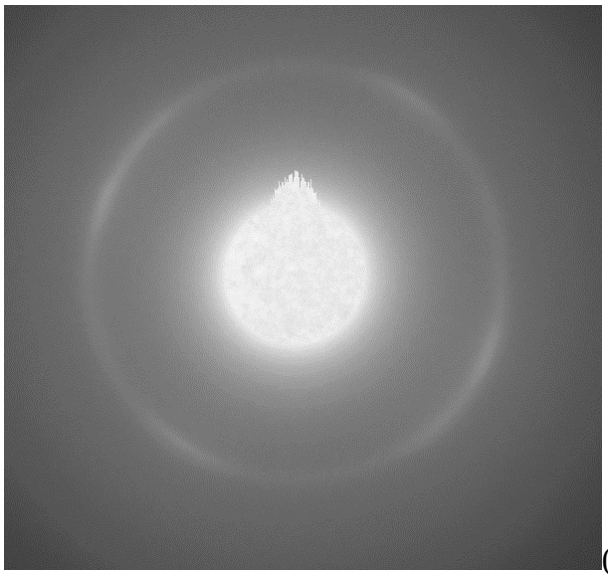

(b)

Figure 4.35. Plot of (a) the four individual BAF and R values from each TEM SAED pattern recorded for the as-received sample (red) and the sample irradiated to 1dpa (blue). (b) SAED pattern #20 for the 1dpa sample showing the 4 intense regions that skew the BAF calculations.

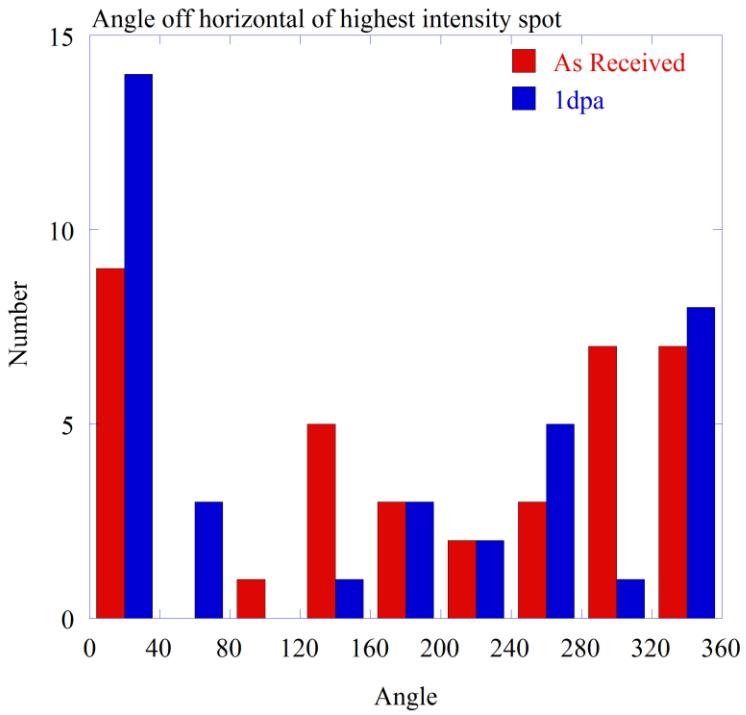

Figure 4.36. Histogram plot of the azimuthal angle around the [0002] ring where the intensity was highest.

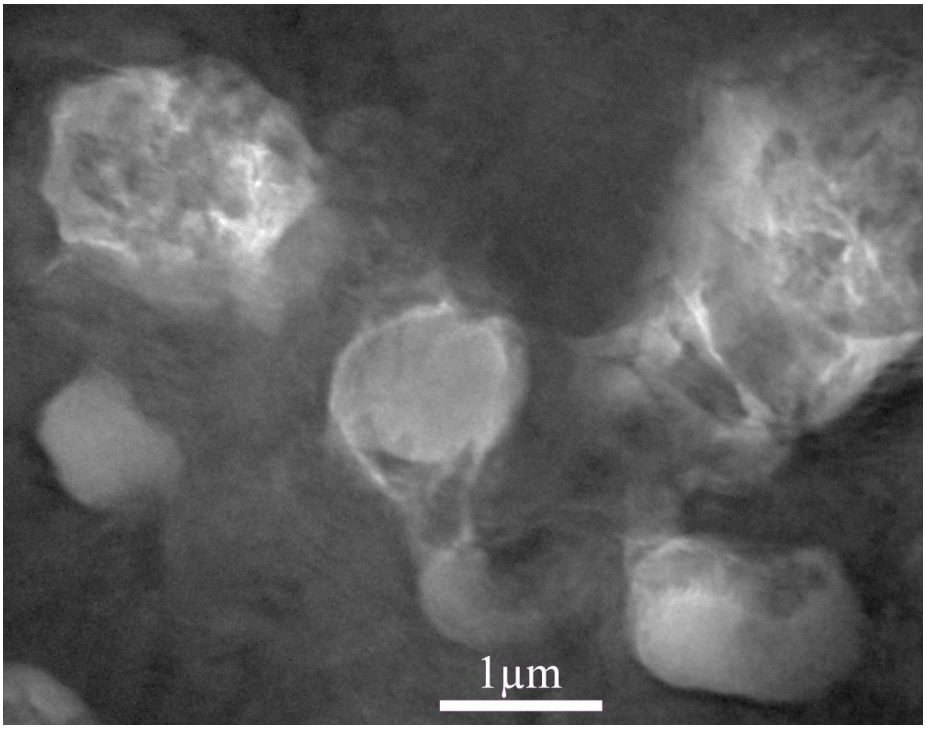

Figure 4.37. TEM micrograph of pores in sample irradiated to 1dpa.

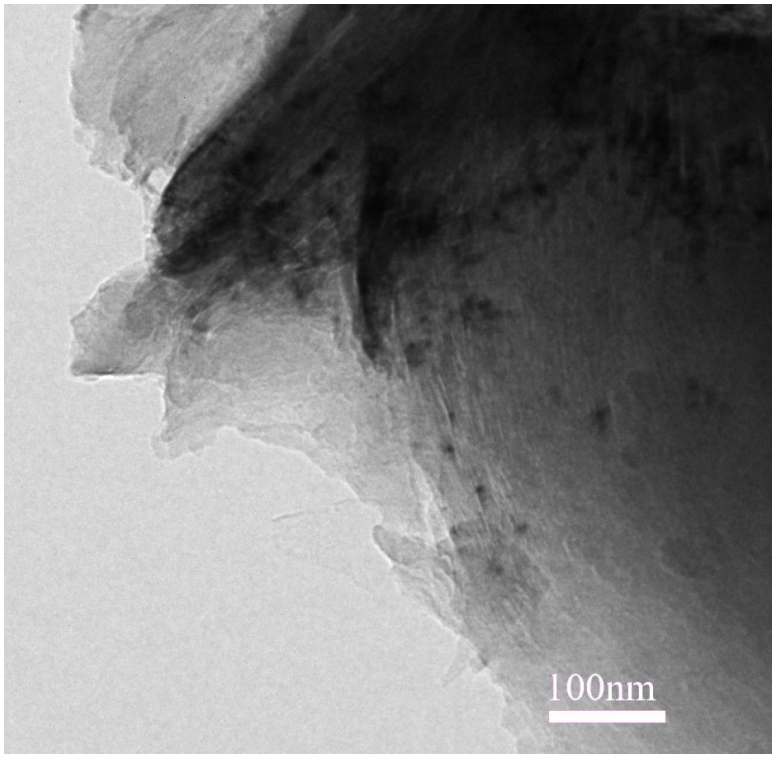

Figure 4.38. TEM micrograph of Morovski cracks in sample irradiated to 1dpa.

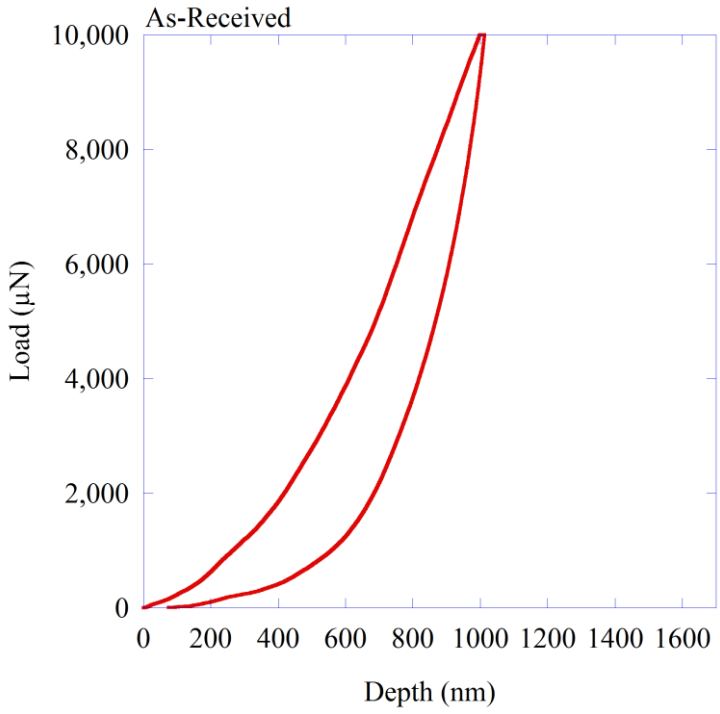

(a)

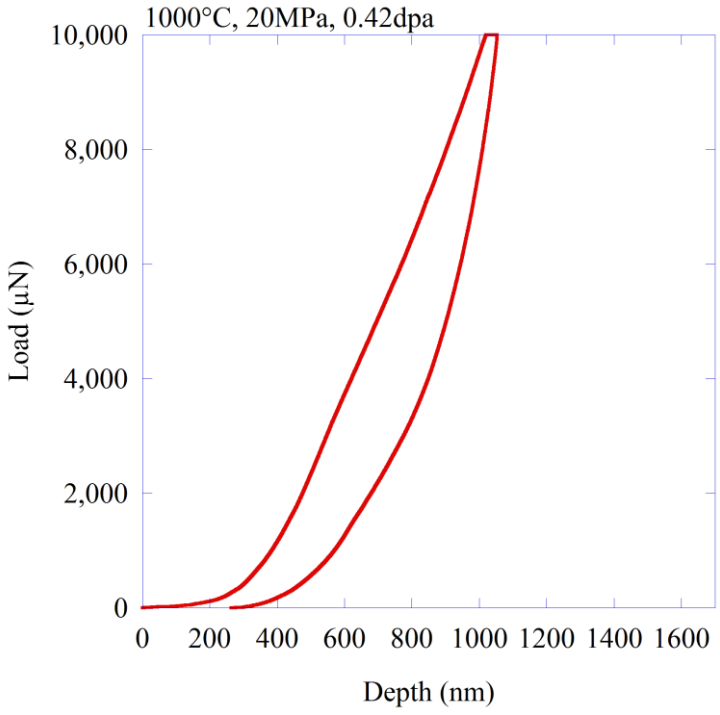

(b)

Figure 4.39. Representative load versus depth plot for the (a) as-received sample and (b) the sample irradiated at 1000°C 20MPa to 0.42dpa.

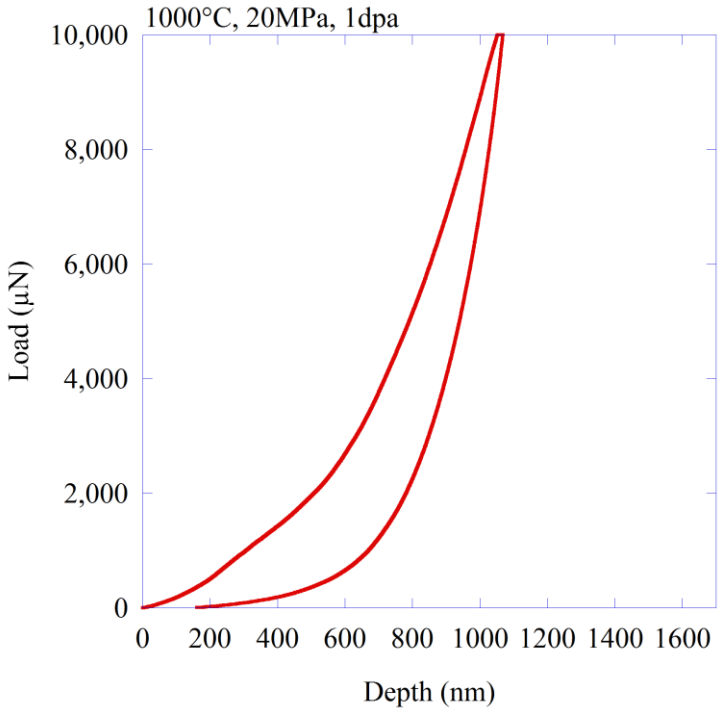

(a)

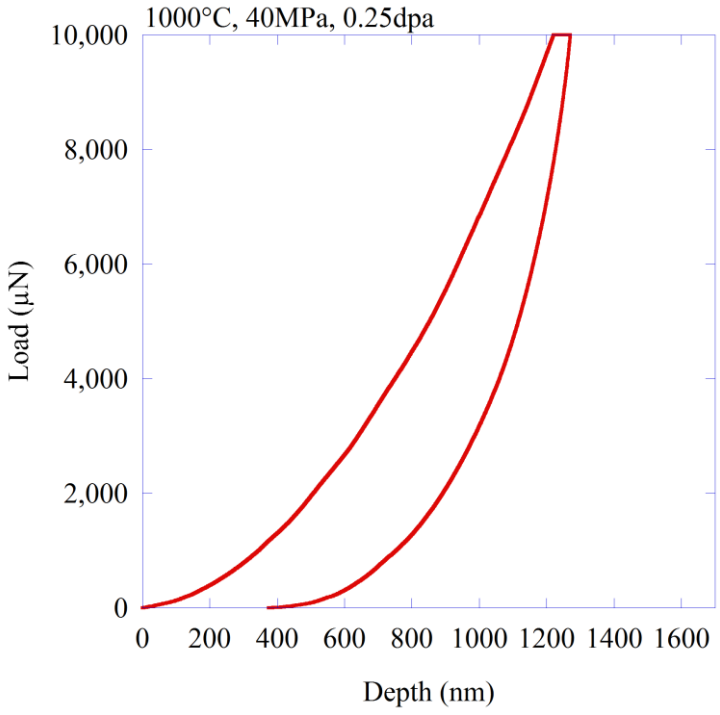

(b)

Figure 4.40. Representative load versus depth plot for the (a) sample irradiated at 1000°C 20MPa to 1.0dpa and (b) the sample irradiated at 1000°C 40MPa to 0.25dpa.

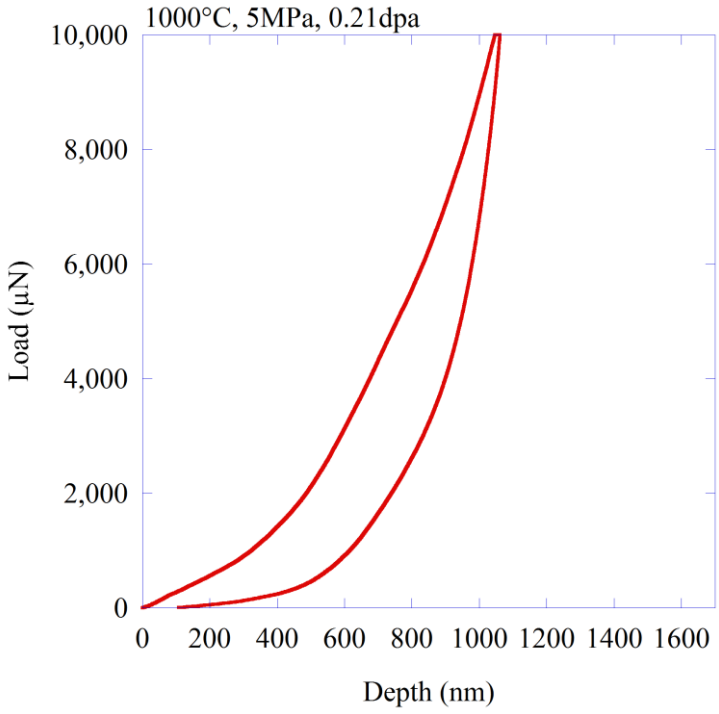

(a)

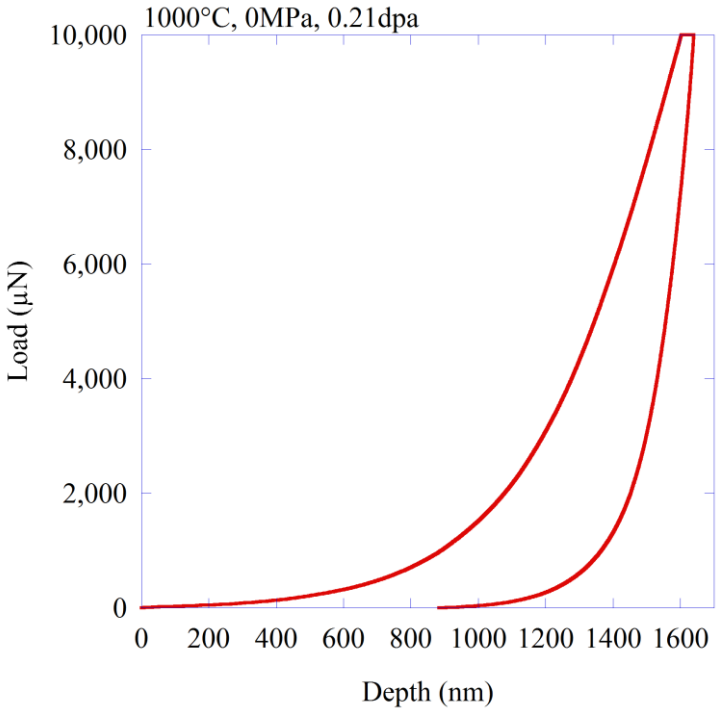

(b)

Figure 4.41. Representative load versus depth plot for the (a) sample irradiated at 1000°C 5MPa to 0.21dpa and (b) the sample irradiated at 1000°C 0MPa to 0.21dpa.

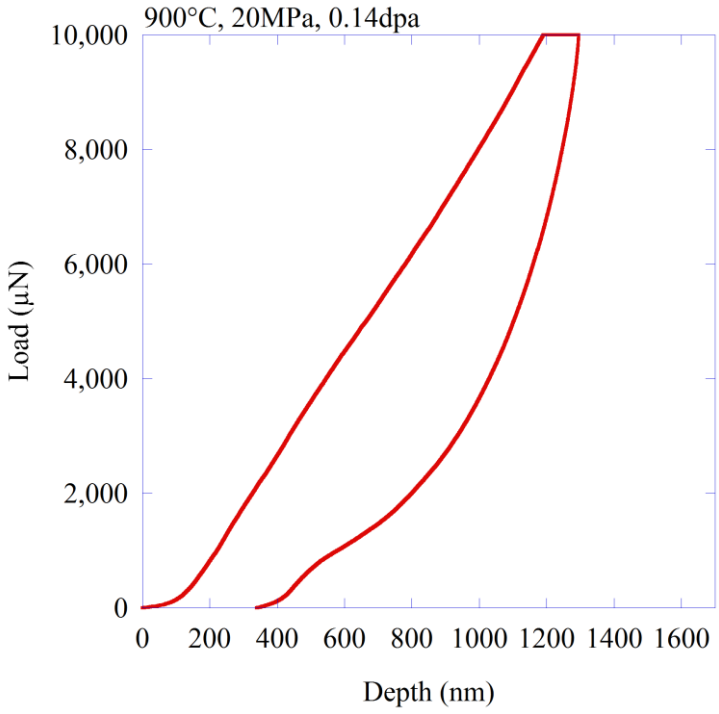

(a)

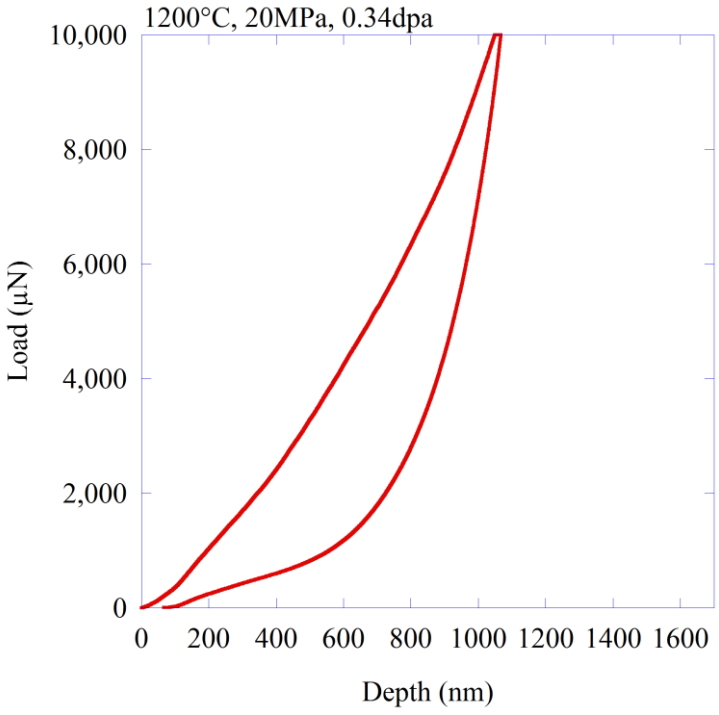

(b)

Figure 4.42. Representative load versus depth plot for the (a) sample irradiated at 900°C 20MPa to 0.14dpa and (b) the sample irradiated at 1200°C 20MPa to 0.34dpa.

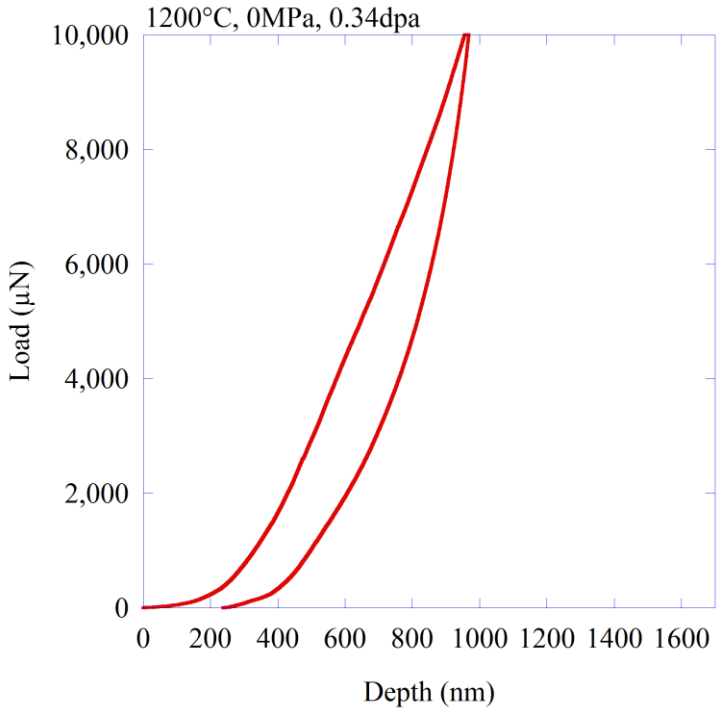

Figure 4.43. Representative load versus depth plot for the sample irradiated at 1200°C 0MPa to 0.34dpa.

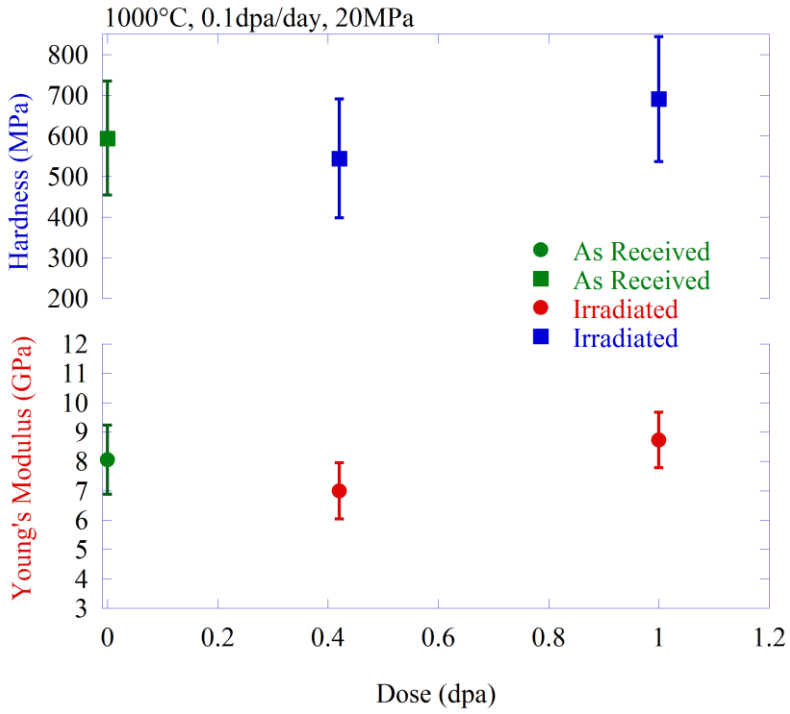

Figure 4.44. Effect of total accumulated dose on Young's modulus and hardness, for samples irradiated at 1000°C, 0.1dpa/day, and 20MPa stress.

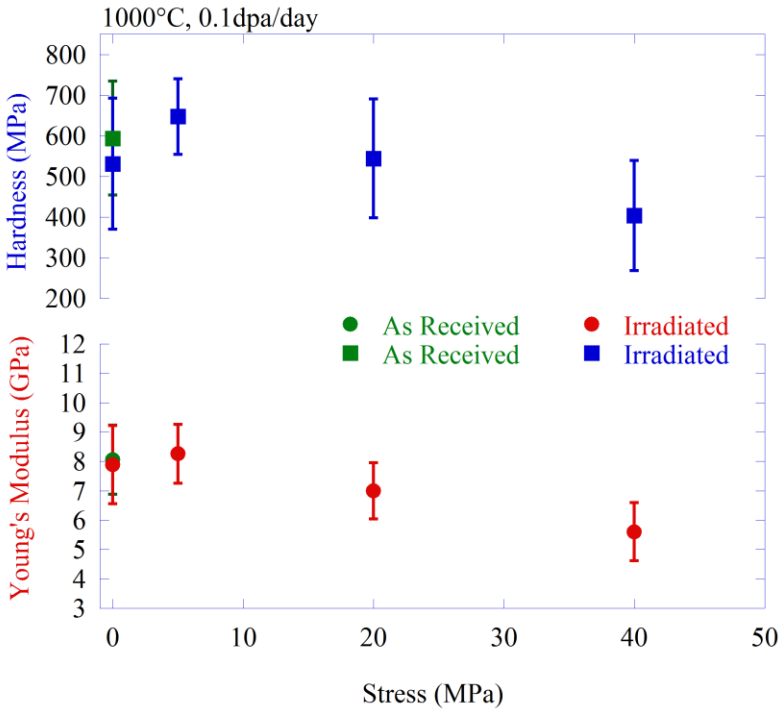

Figure 4.45. Effect of applied tensile stress on Young's modulus and hardness, for samples irradiated at 1000°C 0.1dpa/day, all samples were irradiated to a final dose of 0.25dpa except the 20MPa sample that was 0.42dpa.

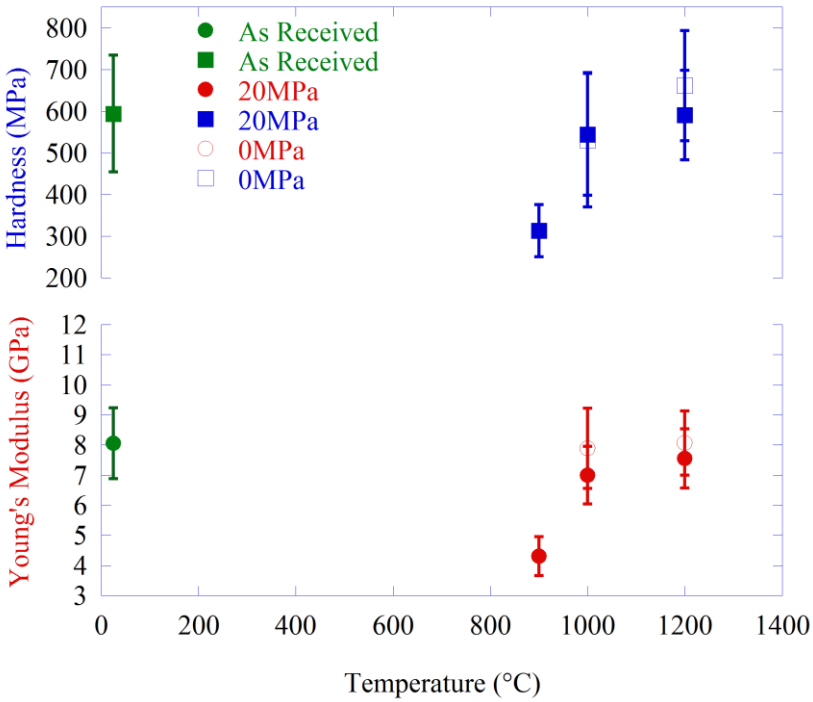

Figure 4.46. Effect of irradiation temperature on Young's modulus and hardness.

CHAPTER 5

DISCUSSION

This chapter will present the analyses necessary to determine the mechanism of proton-irradiation induced creep in ultra-fine grain graphite. First an in-depth statistical analysis of the irradiation creep experiments and the microstructural changes from the post-experimental analysis will be presented. These experimental results will then be compared with literature results for neutron irradiation-induced creep in graphite and the resulting microstructural changes to determine if proton irradiations resulted in similar behavior. Lastly these experimental dependencies and microstructural changes will be used to determine the mechanism of irradiation-induced creep in ultra-fine grain graphite.

5.1 Statistical Analysis of Experimental Results

This section presents the statistical analysis of the experimental results to investigate the dependence of several variables on experimental parameters. The analyses presented here follow the χ^2–analysis methodology presented in Section 3.4. The analyses in this section are being performed so the dependencies of creep rate on the experimental conditions can be used to compare with and determine the creep mechanism. First to be discussed is the analysis of the creep rate dependence on the applied stress, dose rate, temperature, and accumulated dose. Next the XRD spectra analysis methodology will be presented followed by the analysis of the calculated crystal structure parameters on accumulated dose, stress, and temperature. The analysis of the measured Young's modulus and hardness on accumulated dose, stress, and temperature will be presented. Finally the conclusions from these analyses will be presented.

There are six equations that will be used throughout these analyses. Throughout the analyses the variables *A* and *B* will be different terms in each fit, so each equation is listed for reference. The equations of fit are:

- Constant $y = A$ (5.1)
- Linear $y = Ax + B$ (5.2)
- Squared $y = Ax^2$ (5.3)
- Power $y = Ax^B$ (5.4)
- Arrhenius $y = A\exp\left(-B/x\right)$ (5.5)
- Plateau $y = A - A*\exp(B*x)$. (5.6)

Some of the linear analyses (Equation (5.2)) will be performed with the intercept set to zero (B=0), and the reasons for this use will be given.

The non-linear regression fitting (same methodology as the χ^2–analysis) of these equations to the data was performed with the GrahpPad PRISM© software. The software calculates the parameters, the standard deviation of each parameter, the R^2 of the fit (for all the non-constant equations), and the variance of the fit.

The criterion for determining the best-fit equation will be the magnitude of the variance. This will be the defining litmus because the variance is dependent on both the sum of the squares (how much the data and fit agree) and the degrees of freedom (number of data points minus number of constants in the fit equation). R^2 is not the optimal value for comparison because it is calculated by [66]:

$$R^2 = 1 - \frac{\sum (y_i - Y_i)^2}{\sum (y_i - M)^2}, \tag{5.7}$$

where the term in the numerator is the sum of the squares of the data (y_i) of the fit line (Y_i), the denominator is the sum of the squares of the data off the mean value (M), and it should be noted that the definition of R^2 results in fits with Equation (5.1) having a value of zero.

Not every equation will be used for analysis of each data set. When performing non-linear regression analysis it is important to understand the equations of fit and whether they are physically meaningful for the analysis. For example, the Arrhenius equation, Equation (5.5), describes how reaction rates change with increasing

temperature, so it will be a logical fit-equation to investigate temperature effects but not for dose effects.

5.1.1 Determination of Creep Rate Dependencies

The experimental parameters that can affect creep rate are applied stress, dose rate, temperature, and accumulated dose. This section will investigate the dependence of creep rate on these individual parameters. The first analysis will be on the effect of applied stress, followed next by dose rate, temperature, and finally accumulated dose. Throughout this section the creep rates from the LSE measurements are used for the dependence analyses because the LSE provides an instantaneous measurement of creep rate and were measured within regions of uniform temperature. The dependencies of the DVRT measurements will also be presented, but the thermal gradients, time necessary for it to reach thermal equilibrium, and estimated gauge length, have significant effect on the magnitude of the measurements. Therefore the dependencies from the DVRT will be listed with the LSE values, but the trends from the DVRT will only be used when LSE measurements were invalid, specifically for the temperature dependence.

5.1.1.1 Applied Stress

The analysis of stress dependence was done with the constant, linear, square, and power-law equations, Equations (5.1) through (5.4), with the intercepts set equal to zero since creep cannot occur without an applied stress. These are the only equations used because the physical models that best describe the expected dependences rely on stress raised to a power. The fit parameters for this analysis are presented in Table 5.1. The best-fit for the data is the linear dependence of creep rate on applied stress, which has the lowest variance and is confirmed by the power fit with a power value close to 1.0. The creep rate versus stress data are plotted with the linear fit in Figure 5.1.

5.1.1.2 Dose Rate

The analysis of dose rate dependence was done with the constant, linear, square, and power equations, Equations (5.1) through (5.4), with the intercepts set equal to zero

since creep cannot occur without irradiation . These are the only equations used because the physical models that best describe the expected dependences rely on dose rate raised to a power. The fit parameters for this analysis are presented in Table 5.2. The best-fit for the LSE data is the linear dependence of creep rate on dose rate, which has the lowest variance. The best-fit for the DVRT data is the square equation, but with having data at three dose rate values, in a narrower range than the LSE, it is logical to assume that the same equation of best-fit for the LSE should be applicable for DVRT. The creep rate versus dose rate data are plotted with the best-fit trend lines in Figure 5.2.

5.1.1.3 Temperature

The analysis of temperature dependence was done with the constant, linear, and Arrhenius equations, Equations (5.1) (5.2) and (5.5) respectively. The DVRT measurements are used for the temperature dependence because the LSE measurements were invalid due to sample blackbody emission at the two highest temperatures. These equations were used to investigate whether the appropriate temperature dependence is linear or Arrhenius. The fit parameters for this analysis are presented in Table 5.3. The best-fit for the data could be argued as either the linear dependence or the Arrhenius dependence because both have approximately the same variance. From a physical sense the Arrhenius should be the preferred model, but it is possible that the Arrhenius fit can be approximated by a linear fit within this limited temperature range, thus explaining why both equations best-fit the data. The creep compliance versus temperature data are plotted with the best-fit trend lines in Figure 5.3.

5.1.1.4 Accumulated Dose

The analysis of accumulated dose was done with the constant and linear equations, Equations (5.1) and (5.2). These equations were used to investigate whether the creep rate was affected as the accumulated dose increased, which indicates whether the creep experiment was in the primary or steady-state creep regime. The fit parameters for this analysis are presented in Table 5.4. The best-fit indicates that the creep rate does

not change with increasing dose, thus indicating that the experiments are in the steady-state regime. The creep rate versus accumulated dose is plotted in Figure 5.4.

5.1.2Analysis of XRD Spectra

This section will present the analysis of the X-ray diffraction data presented in the results chapter starting with the methodology used to analyze the XRD spectra that is to determine the crystal unit cell dimensions, atomic spacing, crystallite size, and variation in lattice spacing. The crystallite size is a measure of the dimensions of regions in the material that have perfect crystallographic ordering. Then the analysis and discussion of the effects of dose, applied tensile stress, and irradiation temperature on the calculated structure parameters will be discussed.

5.1.2.1 XRD Spectra Analysis

This work utilizes the Williamson-Hall methodology [67, 68] to analyze the XRD spectra for the purpose of determining how the crystal structure changes due to the irradiation conditions. The first step in the analysis is to convert the data from the recorded spectra, with units of 2θ, into the reciprocal lattice. Conversion into the reciprocal lattice allows for a simplified analysis of the spectra. The conversion from the recorded spectra into the reciprocal lattice is achieved by calculating S (reciprocal lattice spacing in units of nm^{-1}) for every value of 2θ by:

$$S = \frac{2\sin\theta}{\lambda} \tag{5.8}$$

where λ is the wavelength of the X-Ray used for analysis (0.154059nm for the CuKα). Then the peaks are fit with a Cauchy distribution, using GrahpPad PRISM© software [69]:

$$f(A,C,W) = \frac{A}{1+\left(\frac{S-C}{W}\right)^2} \tag{5.9}$$

where A is the amplitude, $S(nm^{-1})$ is the independent variable, $C(nm^{-1})$ is the position of the center of the peak, and $W(nm^{-1})$ is the width of the peak (the full-width at half

maximum). Examples of the (0002) peak and (0004) peak, in *S* space, for the as-received sample (red) and the sample from experiment #2 (blue) are presented in Figure 5.5. The centroid and widths of the (0002) and (0004) spectra for all samples measured are summarized in Table 5.5, and the values for the $(11\bar{2}0)$ spectra are summarized in Table 5.6.

The d-spacing, *d*(nm), of the corresponding diffraction planes is equal to 1/*C*. The unit cell dimensions are related to *d* by:

$$\frac{1}{d^2} = \frac{4}{3a^2}\left(h^2 + hk + k^2\right) + \frac{1}{c^2}l^2 \tag{5.10}$$

where *a* is the lattice parameter in the basal plane, *c* is the lattice parameter in the c-direction, both indicated in Figure 2.1, *h k* and *l* are three independent components of the Miller-Bravais system, [*hkil*], used for indexing diffraction patterns of materials with a hexagonal structure. The spacing between atoms in each graphite hexagon (a_0), in the basal planes, is related to *a* from a geometric relationship of a hexagon by:

$$a_0 = \frac{a}{2\sin\left(60^\circ\right)}. \tag{5.11}$$

The calculated values of the *d*-spacing, unit cell dimensions *a* and *c*, atomic spacing a_o, and the relative change from the as-received sample for all samples measured are listed in Table 5.7 for the c-direction and in Table 5.8 for the a-direction.

The crystallite dimensions and lattice strains are calculated from an analysis of the full-width at half maximum of the Cauchy fit of peaks from the same direction family. There are few diffraction peaks that arise for graphite, and even fewer that are multiples from the same family. From this work, two peaks from the [0001] family are measured, (0002) and (0004), which provide an analysis for only the c-direction. Only one peak from the $[11\bar{2}0]$ family was available to be easily measured and analyzed for the a-direction. When multiple measurements from a single family are available, then both the crystallite size and lattice strain can be determined by performing a linear fit of *W* versus *C*. This linear fit was performed using the inverse variance weighting methodology as to determine the standard deviations for both the slope and intercept for continued error

propagation. The values of the crystallite dimension (L), and the lattice strain (ε) are then determined from the linear fit equation using [67]:

$$W = \frac{1}{L} + 2\varepsilon C, \tag{5.12}$$

where L is equal to the inverse of the intercept of the linear fit and ε is equal to one half of the slope of the linear fit. The lattice strain (ε) is the variation of the spacing around the average value ($\varepsilon=\Delta d/d$), and the approximate maximum spread of the spacing is defined as $2\Delta d$, which is equal to $2\varepsilon_c d$. An example of W plotted versus C for the (0002) and (0004) peaks from Figure 5.5, is shown in Figure 5.6 along with the linear fit for the two samples. For the as-received example the intercept was calculated to be $6.08\text{x}10^{-3} \pm 1.58\text{x}10^{-3}$ nm^{-1}, which translates into L_c of 164.49 ± 42.75 nm, and the calculated slope was $4.66\text{x}10^{-3} \pm 9.23\text{x}10^{-5}$, which translates into ε_c of $2.33\text{x}10^{-3} \pm 4.62\text{x}10^{-5}$. For the 1dpa example the intercept was calculated to be $1.81\text{x}10^{-2} \pm 1.64\text{x}10^{-3}$ nm^{-1}, which translates into L_c of 55.18 ± 4.99 nm, and the calculated slope was $3.35\text{x}10^{-3} \pm 9.99\text{x}10^{-5}$, which translates into ε_c of $1.67\text{x}10^{-3} \pm 4.99\text{x}10^{-5}$. This analysis was performed on all the samples to determine the L_c and ε_c for all the samples. The contribution of peak broadening, from lattice strain, is small compared to the contribution from decreasing crystallite size. Since two points are not available for the linear fit for the a-direction, it will be assumed that the all of the broadening of the $11\bar{2}0$ peak is from decreasing crystallite size. The calculated values of the c-direction crystallite size (L_c), c-direction lattice strain (ε_c), and relative change from the as-received value are listed in Table 5.9, and the a-direction crystallite size (L_a) and the relative change from the as-received sample Table 5.10.

5.1.2.2 Effect of Experiment Parameters on Crystal Lattice Spacing and Size

This section discusses how the experimental parameters affect the crystal structure parameters (lattice spacing, c-axis spacing spread, and crystallite sizes) that were calculated from the XRD spectra. Figure 5.7 to Figure 5.9 show the effect of

accumulated dose, for samples irradiated at 1000°C with dose rate of ~0.1dpa/day, on atomic spacing, c-axis spread in spacing ($2\varepsilon_c d$), and crystallite size, respectively. Figure 5.10 to Figure 5.12 show the effect of applied tensile stress, for samples irradiated at 1000°C with dose rate of ~0.1dpa/day to a total dose of 0.25dpa, on atomic spacing, c-axis spread in spacing ($2\varepsilon_c d$), and crystallite size, respectively. Figure 5.13 to Figure 5.15 show the effect of irradiation temperature on atomic spacing, c-axis spread in spacing ($2\varepsilon_c d$), and crystallite size, respectively. In all of these plots, the values corresponding to the c-direction with stress are shown as red circles, the a-direction with stress are shown as blue squares, the c-direction without stress are shown as orange circles, and the a-direction without stress are shown as light blue squares. The error bars correspond to one standard deviation, resulting from error propagation of the standard error of the peak centroid and width from the XRD spectra fits. It should be noted in the plots of atomic spacing changes, that the standard deviation of the values are a factor of 100 smaller than the values (see Table 5.7 and Table 5.8), and as a result of being that small the error bars are hidden behind the data points.

5.1.2.3Analysis of Crystal Parameter Changes

The effects of dose, stress, and temperature, on the crystal parameters for the stressed samples are investigated using the same methodology and equations used for the creep rate dependencies. These dependencies will be compared with results from literature analysis of neutron irradiation effects.

5.1.1.1.1 Microstructure Changes with Increasing Dose

The accumulation of dose has the largest effect on the crystal parameters. The non-linear regression of the dose effects were performed with the constant, linear, and plateau equations. The summaries of dose effects on the crystal parameters are listed in Table 5.11 through Table 5.13. This analysis shows that the c-spacing exponentially increases to a plateau value, while the a-spacing, c-spacing spread, and L_c and L_a all exponentially decrease to a plateau values.

The increase in c-spacing can be caused by single interstitials, interstitial clusters between basal planes, and interstitial loops. In the temperature regimes for these experiments, single interstitials should not be contributing to the observed expansion because single interstitials are only stable when irradiated at -196ºC [70], due to the high diffusion coefficient. Reynolds and Thrower [71] observed large interstitial loops in graphite, via TEM, but found that the c-spacing only increased around the edge of the loops and these loops were not sufficient to cause the total increase of c-spacing. In the temperature range of interest for the experiments performed in this work, the observed loop diameters were 70-80nm with average spacing of 3.8-5.6μm, while the graphite used in these experiments have crystallites with an average pre-irradiation size of 56nm and the average grain is less than 1μm in size, thus it is unlikely that the loops observed by Reynolds and Thrower would be occurring in the samples for this work.

Reynolds and Thrower [71] postulated that the primary source of c-spacing change is due to small interstitial clusters that are too small to observe with a TEM. They determined that these clusters must have a stable configuration, have a low diffusibility, no tendency to grow, and are subject to irradiation annealing, thus leading them to propose that these small clusters are single hexagons of six atoms [71]. They also state that the concentration of these small clusters reach an equilibrium population that is characteristic of flux and irradiation temperature. These six-atom hexagonal clusters that reach an equilibrium population, are in agreement with this work where it is observed that c-spacing increases to a plateau value and the plateau value is reached once the equilibrium population has been achieved.

The decrease of the interatomic spacing (a_0) can result from two sources, the elastic response to the c-axis expansion (Poisson ratio effect) and the effect of vacancies. The change of a_0 due to Poisson's ratio is calculated by [72]:

$$\frac{\Delta a_0}{a_{0_i}} = \frac{S_{13}}{S_{33}} \frac{\Delta c}{c_i}, \tag{5.13}$$

where S_{13} and S_{33} are the elastic compliances of perfect graphite crystals, $-3.3\text{x}10^{-13}\text{Pa}^{-1}$ and $275\text{x}10^{-13}\text{Pa}^{-1}$ respectively [9]. From this comparison, a_0 should decrease by -0.012% for every 1% increase of c-spacing, which does not adequately explain the

contraction in this work (-0.14% a_0 contraction with 0.54% c-spacing expansion) or the contraction observed with neutron irradiation [72]. Therefore the primary source of contraction of a_0 should result from vacancies.

In graphite, vacancies occur as single vacancies, di-vacancies, lines, collapsed lines, and loops [24, 73]. Single and di-vacancies can cause a-axis contraction from lattice relaxation into the vacant sites [70, 74], but this relaxation is expected to be minimal because the surrounding covalent bonds are stiff and hard to elongate, thus the primary effect is electrons undergo rearrangement from a single shared electron covalent bond
(C-C with 1.542Å atom spacing) to sharing two electrons in the covalent bond (C=C with 1.334Å atom spacing) [72], like the lattice rearrangements shown in Figure 2.6. Vacancies become mobile around 500ºC, and as such for irradiations above this temperatures the vacancies can still occur as single and di-vacancies, albeit at a lower percentage, and also begin to form lines and loops [24].

Vacancy lines have been shown to occur in irradiations below 500ºC, but only for high doses where the chance encounter of vacancies occurs [24]. At higher temperatures, vacancy lines begin forming with the onset of irradiation and the average number of vacancies in a line increases with increasing temperature [24]. For an uncollapsed vacancy line, the same changes in covalent bonding observed for atoms surrounding single and di-vacancies, will affect the atoms surrounding the line. As vacancy lines form, some will tend to collapse to allow for atoms on either side of the line to covalently bond, this collapse does not contribute to a change of a_0 since the original structure will be restored, but does contribute to the reduction of the length of the basal plane [73]. The concentration of uncollapsed vacancy lines should saturate with dose, and the saturation concentration should decrease with increasing irradiation temperature [24]. Vacancy loops have been observed at temperatures above 650ºC with the average number of vacancies in the loop increasing for increasing temperature, but the loops only form if the initial vacancy cluster can relax into circular form before collapsing into a line [24]. The formation of vacancy loops does not affect a_0 [70].

Kelly et al. [73] investigated the effect of annealing, at temperatures below 2000ºC, of graphite irradiated at temperatures above 350ºC and to high doses, which are

cases where most vacancies are in lines and loops. They observed no recovery of the a_0 at these annealing temperatures, which suggests that most of the vacancies are in collapsed lines, instead of loops, and cannot be annealed out at these temperatures. These results suggest that the primary source of contraction of a_0, observed in this work, is due to the formation and saturation of uncollapsed vacancy lines.

The measurement of a decreasing c-spacing variation with increasing dose may at first seem counter-intuitive; because as the 6-atom hexagon interstitial clusters are formed they cause the c-spacing to increase, but only in the localized region around the clusters. Work by Bacon and Warren [28], is some of the only crystal parameter analysis that discuss the effect of interstitials on the variation of the c-spacing. They proposed that in the immediate vicinity of a cluster, the increase of the c-spacing is significantly greater than the average increase, and decreases towards the average value as the distance from the cluster becomes large, where the average is calculated from the shift of the XRD peaks. Additionally they propose that the distribution of the clusters should have a fairly uniform distribution. They support this uniform distribution with a thought experiment as follows. An interstitial cluster already exists at point *P*, in Figure 5.16, and another cluster tries to form at point *Q'*, but the planes at this point are in a compressive state and thus not energetically favorable so instead the new cluster forms at point *Q*. Therefore as the interstitial clusters reach saturation density, the c-spacing stops increasing, but the uniform distribution of the clusters has resulted in an overall decrease of the variation of the spacing.

The crystallite dimensions are the measure of the length of regions within the material that have perfect graphite structure. The interstitial clusters that cause the c-spacing increase are also the features that cause the break-up of the crystallites in both the c-direction and in the basal planes. The fact that the clusters reach a saturation point agrees with the fact that L_c and L_a decrease to plateau values. The accumulation of vacancy lines that decrease a_0 and vacancy loops that don't affect a_0 are other possible sources of the break-up of the crystallites. It is unknown, and not easily determined, whether the interstitial clusters or vacancy structures control this break-up of the structure. Additionally, the fact that the crystallite volume does not continually decrease

suggests that the material will maintain some structural ordering instead of becoming amorphous.

5.1.1.1.2 Microstructure Changes with Applied Stress

The stress effects were analyzed with the constant and linear equations. The summaries of stress effects on the crystal parameters are listed in Table 5.14 through Table 5.16. Applied stress showed no effect on any of the calculated parameters since the data is best-fit by a constant, except for L_a that decreases linearly with increasing stress.

The samples for the stress analysis only received a total dose of 0.25dpa, so the crystal parameter changes have not reached the plateau values, which may result in an incomplete understanding of changes due to stress. Work from Richards and Kellett [74], observed that stress reduced the amount of c-axis spacing increase. With this observation they postulated that the stress reduction could be due to a smaller population of interstitials or a smaller density of interstitial clusters without a change of interstitial concentration. The decrease of interstitial population could arise from stress increasing the recombination rate or stress increasing the interstitial mobility, while the decrease of cluster density was proposed as the clusters being swept together by gliding basal dislocations. Unfortunately none of the measurements in this work agree with this postulation from Richards and Kellett.

5.1.1.1.3 Microstructure Changes with Irradiation Temperature

The temperature effects were analyzed with the constant, linear, and Arrhenius equations. The samples irradiated at 700ºC were irradiated with three different conditions each and had lower final doses than the other samples, so data at 700ºC was excluded from the statistical analyses. The summaries of stress effects on the crystal parameters are listed in Table 5.17 through Table 5.19.

The temperature effects on $\Delta c/c_i$ agree best with the Arrhenius dependence. As discussed in Section 5.1.1.1.1, in the temperature range for these experiments, the primary source of increase of c-spacing should be due to the six-atom hexagonal clusters.

As temperature is increased the interstitials should be more mobile and therefore the interstitial population should decrease thus decreasing the cluster density. But, in these experiments it was necessary to increase the dose rates to achieve the higher temperatures, so it is possible that increase in dose rate overcame the increased mobility thus causing the higher cluster concentration, therefore resulting in the c-spacing increase as temperature increased.

This analysis also showed there was not temperature effect on a_0. As discussed in Section 5.1.1.1.1, the primary source of the change of a_0 should be due to uncollapsed vacancy lines. It was also mentioned that as irradiation temperature increases the concentration of these uncollapsed lines should decrease, but the length should increase. There are two possible sources that can be causing the a_0 spacing to remain unchanged in these temperature ranges: the higher dose rates offset the increased vacancy mobility thus keeping the vacancy concentration constant, or the lengthening of the uncollapsed lines offsets the decrease of the number of uncollapsed lines.

The c-spacing variation also showed no effect of temperature. As shown in Section 5.1.1.1.1, as the interstitial clusters become evenly spaced the variation reduces. This suggests that even though average c-spacing is increasing, with increasing temperature, that the clusters still have a uniform distribution thus causing the variation to remain constant.

The analysis of L_c and L_a, showing that both decrease as temperature increases, agrees with the increase of interstitial clusters that cause the increase c-spacing. As the concentration of these clusters increase, the spacing between clusters will decrease resulting in the decreasing dimensions of the regions with perfect ordering. The variance is a quantification of the spread of a data set and is equal to the average of the total square distance between the data points and the equation of fit. In this case, the variance of the linear fit of L_c versus temperature is 277, therefore the data points are, on average, 16.6nm away from the fit equation.

5.1.1.1.4 Comparison of Crystal Changes with Mechanism of Radiation Damage in Graphite

An analysis of the mechanism of radiation damage in graphite should provide some additional insight into the changes of crystal parameters due to irradiation. As discussed in Section 2.6 the historical view of radiation effects in graphite is that interstitials coalesce between basal planes to form interstitial loops, that grow until they essentially become new basal planes, which cause the grains to grow in the c-direction, and vacancy coalescence in the basal planes cause the grains to shrink in the a-direction [75]. Recent *in-situ* TEM analysis [30] has shown results that are in disagreement with the historical view of radiation damage in graphite. In that study, researchers observed that interstitial loops are not the cause of the radiation-induced changes and instead vacancy loops form and dissociate into two dislocations that increase in length by positive climb.

This newly-observed mechanism of radiation effects in graphite can explain some of the trends of the irradiation effects on the crystal parameters. The changes in c-spacing are neither supported nor disproven by these newer observations because the initial postulation about the existence of these clusters was because they were not observed with TEM. The reduction of a_0 from vacancy lines is in agreement with this mechanism since it shows the formation of vacancy lines and loops. The variation of the c-spacing spread, like the change in c-spacing is not affected by this mechanism since it is the uniform distribution of interstitial clusters that decreases the variation. The decrease of crystallite dimensions is in agreement with this damage mechanism in that the formation and climb of the dislocation are additional sources that result in breaking-up regions of perfect structure.

Likewise, this damage mechanism should be able to give an idea as to why applied stress did not have an effect on the crystal parameters. The driving force for the damage mechanism is the formation and dissociation of vacancy lines and loops. The anisotropy of graphite limits vacancy motion to within a single basal plane. The application of a stress should not enhance the rate at which vacancies interact to form loops because basal plane covalent bonding is stiff and limits the stress effects within

plane. Therefore, the formation of lines and loops is only a function of vacancy concentration and diffusion coefficient.

Finally, this mechanism explains some of the temperature effects on crystal parameters. As with dose, the c-spacing and c-spacing spread are not affected by this mechanism. The fact that a_0 is not effected by temperature suggests that the density of rearranged covalent bonds is not changing. The only crystal parameter that can be effected by this damage mechanism, for increasing temperature, is the crystallite size. The cause for this is that at higher temperatures the vacancies are more mobile and thus the vacancy lines and loops can form and dissociate at a higher rate, thus producing more dislocations that act as additional features that can break-up the region of perfect structure.

5.1.1.1.5 Conclusions from Analysis of Crystal Parameter Changes

These analyses have presented and discussed the possible causes of the dramatic changes of the crystal parameters. The c-spacing changes are caused by the formation of six-atom hexagonal clusters between basal planes. The formation of these clusters is not affected by an applied stress. The temperature should decrease the density of these clusters, but this may be offset by the higher temperature experiments having a higher damage rate. These same clusters are also the source of the c-spacing variation, but it has been shown that the decrease of variation with dose is due to these clusters being evenly spaced throughout the material. The applied stress cannot prevent this uniform spacing, hence why stress does not change the variation. And the same competing temperature effects on the clusters are the reason why variation does not change as temperature changes. The decrease of in-plane atomic spacing is a result of the rearrangement of the covalent bonds of atoms surrounding uncollapsed vacancy lines. The lack of stress and temperature affecting a_0 suggests that the total number of rearranged bonds does not change, even at higher temperatures where the uncollapsed line density should be less but the length of each line is increased. The decrease of crystallite sizes are primarily driven by the same interstitial clusters that effect c-spacing and variation, where the cluster density saturates with dose, is not affected by stress, and temperature and dose rate have a competing effect.

The vacancy dissociation driven irradiation damage mechanism generally agrees with the changes in crystal parameters that are not solely affected by the interstitial clusters. The mechanism shows that the vacancy line necessary to affect a_0 are forming. Additionally this mechanism provides another microstructural feature that can be contributing to the decreasing crystallite dimensions.

5.1.2.4 Additional Peaks in XRD Spectra

In Section 4.3.1, it was shown that additional peaks begin to appear in the XRD spectra that cannot be indexed for hexagonal graphite. These peaks occur for angles around 33.4º, 34.8º, 40.4º, and 43.8º. Figure 4.24 and Figure 4.28 show that the 33.4º and 43.8º peaks only occur together, and the 34.8º and 40.4º occur together and are not dependent on the presence of the 33.4º and 43.8º peaks. The occurence of these two sets are not correlated with each other implying that the two sets of peaks are from different structures.

No combination of crystallographic directions in either the hexagonal or rhombohedral stacking can account for the peak at 33.4º, but the planar spacing does show a correspondence to the [200] crystallographic direction for the diamond lattice structure (cubic system). Likewise the 43.8º can correspond to the [111] crystallographic direction in diamond. A summary of the 2θ values, the d-spacing for each angle, the diamond cubic pattern index, and resulting d-spacing for the diamond structure are given in Table 5.20. The ideal crystal parameter for diamond is 3.57Å, which results in fair agreement with the d-spacing values calculated from the peak locations, whereas a crystal parameter of 3.7Å, which is less than ideal for diamond gives a better agreement between the actual and calculated d-spacing ($d_{Diamond}$ * in Table 5.20).

This same analysis was used to confirm whether the peaks at 33.4º and 43.8º can be attributed to graphite structures, and also to index the patterns at 34.8º and 40.4º, summarized in Table 5.21. The 43.8º peak can be indexed with [10-11] planes for rhombohedral graphite, but the 33.4º peak can only be indexed for an h or k of 0.8, which is not physically possible. Therefore the 33.4º and 43.8º peaks are most likely arising from the formation of a region with diamond structure. The peak at 34.8º only corresponds to diffraction from the [0004] direction for rhombohedral graphite, and the

40.4º peak only corresponds to diffraction from the [0003] direction for hexagonal graphite. These directions are generally forbidden for diffraction, but localized changes of the structure due to irradiation may result in these directions becoming visible.

5.1.3 Analysis of Young's Modulus

The effects of dose, stress, and temperature, on the Young's modulus and hardness of the stressed samples were investigated using the same methodology and equations used for the creep rate dependencies. It should be noted that the variance of the hardness fit may appear large, but in actuality it shows that the data is on average 73MPa different from the best-fit line for stress dependence. The plot of Young's modulus versus accumulated dose is given in Figure 5.17. The effect of accumulated dose was analyzed with the constant and linear equations, and the summary of this analysis is listed in Table 5.22. The plot of Young's modulus versus stress is plotted in Figure 5.18. The effect of stress was analyzed with the constant and linear equations, and the summary of this analysis is listed in Table 5.23. The plot of Young's modulus versus temperature is shown in Figure 5.19. The effect of temperature was analyzed with the constant, linear, and Arrhenius equations, and the summary of this analysis is listed in Table 5.24.

This analysis shows that accumulated dose, to 1dpa, does not affect the Young's modulus. It is of importance to note that the Young's modulus measurements in graphite are primarily from the elastic response due to the porosity and microstructure rather than the true elastic response of the grains. In single crystal graphite the Young's modulus is just as anisotropic as the crystal structure, with the Young's modulus in the direction in the basal planes is 1060GPa, while perpendicular to the basal planes is 36.5GPa [9], while most graphites average between 8 and 15GPa. In neutron irradiation of graphite there are three stages where Young's modulus changes with dose. The first stage occurs generally at doses below 1 dpa, where it is believed that the formation of defects pin the edge dislocations and can cause increases of 20-80% [75], but the motion or lack of motion of dislocations is a plastic behavior and should not change the elastic response. The second stage occurs in conjunction with the first stage but continues until the turn-around dose is reached. In this region the Young's modulus increases because the closure of the pre-existing porosity increases the sample density, which is known to cause

an increase of Young's modulus [76]. In this region increases of over 400% from pre-irradiation have been observed. The third stage occurs when the material begins to swell after turn-around, which creates new porosity and thus rapidly decreases Young's modulus [75]. The most likely reason for there being no dose effect in this work is because the graphite in this work does not have a binder phase. The binder phase is usually less graphitic than the filler particles, so it is possible that the low-dose increase seen from neutron irradiations is due to a stiffening of the binder phase rather than the current idea being due to the pinning of dislocations.

This analysis also showed that Young's modulus decreased with increased tensile stress. This indicates that the highest stress (40MPa), which is half the yield strength, most likely opened new porosity, thus reducing the Young's modulus below the pre-irradiation value, whereas the lower stress samples were not significantly different from the pre-irradiation. If these experiments were performed to doses where the porosity closure began to have a significant effect, it would be expected that Young's modulus, for all samples with stress, would be less that the unstressed sample. This is due to the fact that neutron irradiations have shown that a tensile stress reduces both the rate and total densification of a sample, and increasing the tensile stress provides further reduction [77].

Finally, it was determined that the Arrhenius fit best described the effect of temperature on Young's modulus. This is counter-intuitive, because neutron irradiation experiments have found that as temperature increases the rate and amount of densification decreases [75], similar to increasing tensile stress. The source of the disagreement is unknown and difficult to speculate. It is possible that the dislocations being created by the irradiation damage mechanism are causing some of these increases, but is difficult to prove.

The lack of dose effects on Young's modulus suggests that there has not been a sufficient structural change in these samples to increase the Young's modulus. For the stress effects, the fact that the sample subjected to the highest stress had a significant decrease of Young's modulus, suggests that this sample may have had an increase in porosity. The increase of Young's modulus with increasing temperature cannot be explained since it does not agree with current understanding.

5.1.4 Conclusions from Statistical Analysis of Experimental Results

The statistical analyses of the creep rate dependences determined that creep rate is linearly dependent on stress and dose rate. It was also determined that temperature affects creep rate with an Arrhenius dependence that can be approximated as linear in the temperature range investigated. Lastly, it was determined that creep rate did not change with increasing dose, indicating that the creep was in the steady-state regime.

The statistical analyses of the crystal parameters determined that the c-direction lattice spacing increases to a plateau value with increasing dose, is not affected by stress, and increases for higher irradiation temperatures. The a-direction lattice spacing decreases to a plateau value with increasing dose and is not affected by stress or temperature. The crystallite sizes, in both directions, exponentially decay to a plateau value with increasing dose, are not affected by stress, and decrease in size at higher temperatures. The Young's modulus analyses determined there is no effect of accumulated dose, increasing stress decreases the post-irradiation Young's modulus, and increasing temperature increases the post-irradiation Young's modulus.

The changes in the crystal parameters are consistent with the hypothesis that six-atom interstitial clusters between basal planes are the source of c-spacing increase, c-spacing variation, and the primary source of decrease of the crystallite sizes. The decrease in a_0 is due to rearrangement of the covalent bonds around uncollapsed vacancy lines, while the collapse of lines and loops adds to the decrease of the crystallite dimension in the basal planes. The Young's modulus analysis shows that there is not sufficient densification of the samples to cause a measurable change in the dose ranges from these experiments. Incidentally, the stress effects suggested that a sufficiently high stress could not be completely overcome with creep, thus resulting in pore formation that reduces Young's modulus.

5.2 Comparison of Experimental Creep Results with Neutron Results

As was discussed in the background chapter, the mechanism of irradiation-induced creep in graphite is not fully understood. This is because only a handful of neutron experiments have been performed and none have systematically investigated all

of the effects of stress, dose rate, and temperature. This lack of data primarily results from the cost, time, and experimental difficulty of performing creep experiments in-reactor. This work has been able to successfully determine the effects of experimental conditions on the irradiation creep behavior, and these dependencies will be used to determine the mechanism of proton irradiation-induced creep. The primary question that needs to be addressed is whether this mechanism is the same no matter if the radiation source is protons or neutrons, which will be addressed in this section.

The first step in answering the question of interest is to compare the radiation damage mechanisms for neutrons and protons to determine if the processes are similar. The next step will be to compare the experimental dependences of creep rate on the experimental parameters (stress, dose rate, temperature, accumulated dose). A discussion of the possible source of discrepancy in the creep rates for proton and neutron experiments will then be presented. In addition to the creep rate dependencies, a comparison of the effects of proton and neutron irradiations on the microstructural parameters will be presented. Finally, this section will be concluded with a summary of these comparisons and a summary as to whether the mechanism of proton irradiation-induced creep is also the best description for neutron irradiation-induced creep.

5.2.1 Comparison of Damage Mechanisms in Graphite for Protons versus Neutrons

The damage mechanism for neutrons and protons involves the creation of primary knock-on atoms (PKA). The PKA travel through the material losing energy by both electronic energy losses from interaction of the moving atom and the electron clouds of lattice atoms and from nucleus interaction collisions with atoms [78]. The large spacing between basal planes makes it favorable for displaced atoms to be channeled so a majority of the energy loss of the moving atom can result from glancing-angle collisions and it is more likely for channeled atoms to collide with interstitials [79]. In addition, graphite has a large number of free conduction electrons, like metals, so energy transferred to the lattice from electronic energy loss will only result in heating the sample [6].

5.2.1.1 Collision Kinematics – PKA Formation

The maximum energy of a PKA (T) is equal to the incident particle energy (E_i) multiplied by the energy transfer efficiency factor (γ), given by [52]:

$$\gamma = \frac{4M_1M_2}{\left(M_1 + M_2\right)^2}, \tag{5.14}$$

where M_1 is the mass of the incoming particle, and M_2 is the mass of the target atom. The value of γ, for both neutrons and protons in carbon, is 0.284. The average PKA energy, with isotropic neutron scattering, is equal to one-half of the maximum transferred energy, therefore the average energy of the PKA can be on the order of 300keV from a 2MeV neutron. The average PKA energy from a proton collision has to be determined from the scattering potential, which is determined by comparing the distance of closest approach and the screening radius. The distance of closest approach (ρ) is defined by [52]:

$$\rho = \frac{Z_1Z_2\varepsilon^2}{\left(\frac{M_2}{M_1 + M_2}\right)E_i}, \tag{5.15}$$

where Z and M are the atomic number and mass of the incident ion (1) and target atom (2), ε^2 is the electronic charge constant equal to 1.44 eV*nm. The target atom screening radius (a) is defined by:

$$a = \frac{0.8853a_0}{\left(Z_1^{2/3} + Z_2^{2/3}\right)^{1/2}}, \tag{5.16}$$

where a_0 is the Bohr radius (0.05292nm) and results in a screening radius of $2.26\text{x}10^{-2}$ nm for carbon. If $\rho << a$, then Rutherford scattering can be used to describe the atom-target collisions [52]. In these experiments, the proton energy entering the samples was 3MeV and the exiting proton energy was ~1.3MeV, resulting in ρ values in the range $3.12\text{x}10^{-6}$ to $7.2\text{x}10^{-6}$ nm. Thus Rutherford scattering is the appropriate model to describe these interactions, and can be used until the proton energy is less 5000eV (ρ=$2.2\text{x}10^{-3}$nm). The maximum PKA energy, for head-on collisions, is the same as that for neutrons (γE_i). When the collision of the charged particle is glancing, i.e., when the

impact parameter (*b*) is equal to the screening radius, then as long as the energy transferred is greater than the displacement energy, then Rutherford scattering can be used for all collisions [52], and in graphite the proton energy must be greater than 120eV for Rutherford scattering to be applicable for all collisions. For all Rutherford scattering collisions, average energy of the PKA ($\bar{T}$) from a proton collision is given by [52]:

$$\bar{T} = E_d \ln\left(\frac{\gamma E_i}{E_d}\right), \tag{5.17}$$

where E_d is the displacement energy (33eV in carbon [8]). The resulting average energy of the PKA is 335eV from a 3MeV proton and 307eV from a 1.3MeV proton.

The production rate of PKA's is dependent on the scattering cross-section. The neutron scattering cross-section is energy dependent above 0.01MeV, and is shown in Figure 5.20 [79]. The proton scattering cross-section (σ_d) is also energy dependent, but Rutherford scattering results in an inverse dependence on E_i, and is given by [52]:

$$\sigma_d\left(E_i\right) = \frac{\pi\gamma\left(Z_2 e^2\right)^2 [0.156]}{4\left(\frac{12}{13}\right)^2 E_i}, \tag{5.18}$$

where the term in [] is from the Kinchin and Pease displacement function approximation. The Kinchin and Pease approximation is used to predict the number of displacements produced by a PKA over all the possible values of *T*. The approximations are [80]:

- $T < E_d$ - there are no atoms displaced
- $E_d < T < 2E_d$ - there is one displaced atom
- $2E_d < T < E_c$ - the number of atoms displaced is equal to $T/2E_d$
    - E_c is the cut-off energy where the approximation is that above E_c only electronic energy loss occurs (375keV)
- $E_c < T$ - the number of displaced atoms is equal to $E_c/2E_d$

and result in a piece-wise integration equal to:

$$\int_0^{E_d} 0\,dT + \int_{E_d}^{2E_d} 1\,dT + \int_{2E_d}^{E_c} \frac{T}{2E_d}\,dT + \int_{E_c}^{\gamma E_i} \frac{E_c}{2E_d}\,dT\,. \tag{5.19}$$

For the proton energies of interest, the resulting scattering cross-sections range from $1.0\text{x}10^{-20}\text{cm}^2$ for a 3MeV proton to $3.0\text{x}10^{-20}\text{cm}^2$ for a 1MeV proton.

5.2.1.2 PKA Interactions with Lattice

Simmons [78] provides a good description of the interaction of PKA's with the lattice and will be summarized here. For collisions of like-atoms, the Bohr interatomic potential is used, and is given by:

$$V(r) = \frac{Z^2 e^2}{r} \exp\left(-\frac{r}{a}\right), \tag{5.20}$$

where r is the distance between interacting atoms and the screening radius (a Equation (5.16)) is now equal to 1.82×10^{-2}nm. The differential cross-section is given by:

$$d\sigma_a = 2\pi b db, \tag{5.21}$$

where b is the impact parameter, and the differential cross-section as a function of energy transferred (T_2) to the secondary knock-on atoms (SKA) is given by:

$$d\sigma_a = W_a(T_1, T_2)\, dT_2, \tag{5.22}$$

where W_a is the energy transfer probability, and is dependent on the PKA and SKA energy (T_1 and T_2 respectively) to define the interaction potentials. When the PKA energy is above 50keV, Rutherford scattering can be used, but at lower energies the Bohr potential must be used. The calculations of W_a, for multiple values of T_1 and T_2, show that at higher PKA energies it is more probable that a small fraction of energy is transferred to the SKA.

Next, Simmons [78] performed calculations to determine, as a function of PKA energy (T_1), the average SKA energy ($\overline{T_2}$), the energy lost to lattice vibrations per displacement ($\overline{T_L}$), the electronic energy loss between PKA collisions (R^*), the mean free path between PKA collisions (λ), and the range of the PKA (R_{PKA}), which are listed in Table 5.25. What these calculations show is that for PKA's with energy above 1keV the distance between collisions is large, compared to the atomic spacing, and the average resulting SKA energy is less than 500eV. When the energy (of either PKA or SKA) is less than 500eV the next collision results in a damage cascade that involves a maximum of 7 atoms, from $T/(2E_d)$, termed a displacement group. Thus a PKA causes widely-spaced displacement groups until it has lost significant energy via collisions and

electronic energy loss and causes the final displacement group. A schematic of this process was presented by Simmons, but the schematic recreated in [79] is shown in Figure 5.21a.

As calculated previously, the average energy of the proton-produced PKA's is 300-340eV. This PKA energy is below the 500eV threshold from Simmons' calculations, and as such, each proton collision will result in the production of one displacement group involving a maximum of 5 atoms, shown in Figure 5.21b. This PKA energy is much smaller than the PKA energy from neutron collisions, but is the same energy as the SKA's produced from the neutron-produced PKA collisions. But, since each neutron collision produces a PKA, which travels through the matrix causing multiple discrete displacement groups, it can be thought of as if the PKA is behaving like a proton, where each collision produces a displacement group. A 2MeV neutron creates an average PKA with 568keV energy, and the slowing down of this PKA results in 610 total displaced atoms. A 2MeV proton produces 5 displacements per collision, therefore 122 proton collisions are required to create the same total number of displacements that occur for one neutron collision.

5.2.1.3 Conclusion from Damage Mechanism Analysis

The analysis has shown that the initial interactions of neutrons and protons with graphite are different; the average PKA energy from neutron collisions is 300keV while the average PKA from proton collisions is 340eV. The similarity of the damage mechanism arises when comparing the damage process of the neutron-produced PKA and the damage process of protons. The neutron PKA travels long distances between collisions, relative to the atomic spacing, and when a collisions does occur the average energy transferred from the neutron-PKA to the SKA is less than 500eV, which is similar to the 300-340eV transferred from the proton to the proton-PKA. Thus even though the respective PKA's are not comparable, the neutron-SKA's and proton-PKA's (both moving carbon atoms) have similar energies and therefore should result in single displacement groups.

5.2.2 Comparison of Creep Rate Dependencies

This section will present a comparison of the creep rate on different parameters for protons vs. neutrons. Next a comparison of the measured creep rates from this work will be compared to values for neutrons from the literature. Finally a discussion of the possible reasons for discrepancy between proton and neutron irradiation will be presented.

The most suitable method of comparing the results from this work with neutron irradiation is to compare the values of kE_0, as was done in [51]. The creep compliance, Equation (4.4), has units of (stress*dose)$^{-1}$ so when multiplied by the pre-irradiation Young's modulus (E_0), the resulting unit for kE_0 is dose^{-1} or dpa^{-1}. Burchell [75] presented a concise summary of the conversion factors from neutron fluence to dose, depending on the neutron energy cutoff or other definitions used quantifying fluence, for the fluence values traditionally reported in the literature, which are listed in Table 5.26.

5.2.2.1 Stress Dependence

As shown in Section 5.1.1.1, the proton irradiation-induced creep experiments exhibited a linear dependence of creep rate on applied tensile stress. The literature for neutron irradiation-induced creep experiments observed the same linear stress dependence [35-37]. The comparison of the stress dependence for protons and neutrons is plotted in Figure 5.22, where the proton irradiation creep rate (in units of s^{-1}) is plotted on the left axis, and the neutron irradiation creep rates are plotted on the right axis (in units of cycle^{-1} since some of the irradiation times were unknown). This comparison shows that for both protons and neutrons, the stress dependence is linear.

5.2.2.2 Dose Rate Dependence

As shown in Section 5.1.1.2, the proton irradiation-induced creep experiments exhibited a linear dependence of creep rate on dose rate. Three sets of neutron data utilized different dose rates. The first set was restrained shrinkage experiments from Veringa [51], and the other sets were tensile experiments on SM1-24 [36] and IG-110 [37]. The comparison of kE_0 versus dose rate, for the proton and neutron results, is

plotted in Figure 5.23. The data from Veringa all show that kE_0 decreases with increasing dose rate, but it is difficult to trust in this data because of how the determinations of stress and creep rate were made. The first problem is that the stress was always changing and the only way stress was determined was with reheating the samples and restrainers after irradiation. The problem, with determining stress with this process, is that it has been shown that radiation damage, and resulting changes in thermal expansion coefficients, can be annealed out at temperatures as low as 350ºC [73, 81-83], which could greatly influence the calculation of stress. In addition, the steady state creep rates were not explicitly calculated and instead were iteratively calculated from limited dimensional measurements with a series of differential equations. These two analyses are the possible source of those samples having an inverse dependence of kE_0 on dose rate. The creep compliance (k), calculated via Equation (4.4), is the term that accounts for only the temperature dependence, thus kE_0 plotted verses dose rate should be constant. The proton results, and the results for SM1-24 and IG-110 were analyzed with the same methodology from Section CHAPTER 5, and the results from this analysis are presented in Table 5.27. For the proton data and the SM1-24 4.5MPa data, the fit of kE_0 versus dose rate is best described with the constant model, while the SM1-24 3.3MPa and 6.4MPa data are best-fit with the linear fit with negative slope, and the IG-110 data sets are ambiguous since each only has two data points. Therefore this analysis shows that proton irradiation creep rate is linearly dependent on dose rate, while the neutron irradiation creep rate dependence on dose rate is still uncertain. Temperature Dependence

As shown in Section 5.1.1.3, the proton irradiation-induced creep experiments exhibited an Arrhenius dependence of creep compliance on temperature. Numerous neutron creep experiments were performed at a range of temperatures. The comparison of kE_0 versus temperature, for the proton and neutron results, is plotted in Figure 5.24. The neutron data is separated according to graphite grade and stress state (restrained shrinkage labeled RS, tension labeled T, and compression labeled C).

Much of the neutron creep data in Figure 5.24 were only performed at one or two temperatures (Burchell, Gray, Mitchell, and Perks). The data with only two temperatures all show a higher value of kE_0 for the higher temperature, but two data points are not

sufficient for an analysis. The Veringa, Dragon, SM1-24 and IG-110 experiments were performed at multiple temperatures, and are re-plotted with the proton data in Figure 5.25, where the proton data is plotted against the left y-axis and the neutron data sets are plotted against the right y-axis to provide a better visual comparison the temperature dependence. These data sets were analyzed, with the Section CHAPTER 5 methodology, with the constant, linear, and Arrhenius equations, and summary of this analysis is given in Table 5.28. The proton LSE and Veringa data are best-fit with the Arrhenius dependence, the proton DVRT and Dragon data are best-fit with the linear dependence, while the SM1-24 and IG-110 data is best described with a constant. Accumulated Dose Dependence

As shown in Section 5.1.1.4, the proton irradiation-induced creep experiments exhibited no effect of accumulated dose on creep rate (out to 1dpa). The literature results from irradiation creep of H-451 [41] show no effect of accumulated dose out to 2dpa from the compression creep experiments (irradiated in ORR) and no effect until 4dpa for the tension experiment (irradiated in HFR in Petten). The creep strain versus dose for the proton and H-451 neutron experiments are plotted in Figure 5.26. For the neutron data, the dashed lines are the steady-state best-fit lines that were determined in [41], which are included to assist with viewing how the creep strain begins to deviate off linearity above the respective doses.

5.2.2.3 Conclusions from Creep Rate Dependencies Comparisons

In general the creep rate dependencies, on the experimental conditions, agree fairly well between the proton and neutron irradiations. Both types of experiments exhibited a linear dependence of creep rate on applied stress, no matter if the stress is tension or compression. The analysis of the creep rate dependence on dose rate was in less agreement, because some of the neutron data showed a linear dependence on dose rate while other showed no dose rate effect. From the temperature comparison, the proton experiments and restrained shrinkage neutron experiments kE_0 had a combination of Arrhenius and linear dependences, while the neutron samples in tension showed no temperature effect. The cause of the disagreement of temperature effects is not currently known. Lastly, it was shown that creep rate was not affected by accumulated dose for

either protons or neutrons, in ranges where the dose was low enough to not cause significant microstructure changes (i.e. 2dpa for neutron in compression and 4dpa for neutrons in tension).

5.2.3 Possible Source of Compliance Value Disagreement

From the temperature dependence analysis, it was shown that the kE_0 values from the proton creep experiments were an order of magnitude larger than neutron experiments at similar temperatures. It was shown in Section 5.2.1 that the inherent damage mechanism for neutrons and protons is similar. One major difference between the experiments is that in the reactor experiments the graphite is exposed to both neutrons and gamma-rays.

Very little work has been done to understand the effects of gamma-rays in graphite. Work from Russia [84, 85] found that the ratio of neutron and gamma-ray fluxes had a significant effect on the turn-around dose, defined as the dose where the graphite stops densification and begins to swell. The ratio of neutron flux to gamma-ray flux is termed the Radiation Composition Factor (RCF), and from multiple experiments in reactors with different RCF's, over a range of temperatures an empirical equation [85] for the turn-around fluence (in units of 10^{21}n/cm^2 E>0.18MeV) is given by:

$$F_{turn-around} = 19.85 + 0.0721T_{irr} - 7.49x10^{-5}T_{irr}^2 - \frac{2.44}{\phi_n/\phi_\gamma}, \qquad (5.23)$$

where T_{irr} is the irradiation temperature and the denominator of the last term is the RCF. It was proposed that the mechanism driving this gamma-ray effect is the gamma-ray interaction within the graphite producing fast electrons that stimulate diffusional processes. If this were the case, it would be expected that enhanced diffusional processes would result in a higher creep rate than for proton experiments (provided that irradiation creep is diffusion driven), which is the opposite of what is observed.

This empirical dependence on temperature and RCF can be utilized to compare the neutron and proton experiments, which requires calculating the RCF for one of the neutron creep experiments. H-451 underwent irradiation creep in compression at 600ºC and 900ºC in the Oak Ridge Research Reactor (ORR), "Burchell H-451 C" data in Figure

5.24. The same graphite was irradiated at 600ºC and 900ºC, without stress in High Flux Isotope Reactor (HFIR) [86]. The results for these irradiations are shown in Figure 5.27, and it was stated that the densification of the sample at 600ºC was similar to that at the same temperature in ORR. Thus with the data in Figure 5.27, the RCF for ORR and HFIR can be calculated. The turn-around dose for the 600ºC sample is $2.5 \times 10^{26} n/m^2$ and the turn-around dose for the 900ºC sample is $1 \times 10^{26} n/m^2$. Inserting the turn-around dose value and irradiation temperature into Equation (5.23) results in an RCF of 0.155 for these reactors.

Given the RCF, Equation (5.21) can be used to determine an equivalent for the case in which the gamma-ray flux is zero. The equivalent temperature, if gamma-rays were not present, for the 600ºC sample is 950ºC, and the equivalent temperature for the 900ºC experiment is 1100ºC. A summary of the values from these calculations, and the corresponding kE_0 for the creep experiments, are listed in Table 5.29

Proton creep experiments were performed at both 900ºC and 1100ºC, and a value at 950ºC can be calculated by linear interpolation between the 900ºC and 1000ºC experiments; the experimental results are summarized in Table 5.30. The data necessary for the comparison of the neutron and proton data are summarized in Table 5.31, the final column in the table is the ratio of kE_0 at the equivalent temperature divided by the kE_0 for the neutron results. The comparison of the kE_0 ratios show that for both the 600ºC and 900ºC neutron experiments, the kE_0 values at the equivalent temperatures are an order of magnitude higher, which supports the assertion that the gamma-rays are a significant contribution in the discrepancy between this work and the neutron experiments.

Recently two groups in China [87, 88] observed that room temperature gamma-ray exposure increased the crystallinity of graphite. Specifically it was found that gamma-ray irradiation decreased the c-axis spacing, increased c-direction crystallite size, and increased the amount of graphitized material. What is surprising about these observations is that these increases in crystallinity can only occur thermally when graphite is heated to temperatures above 2000ºC in the graphitization process [75]. Essentially this work showed that gamma-rays are allowing the sources of structural imperfections (defects) to be removed from the system at temperatures well below the necessary thermal conditions. This suggests that from the crystallite size measurements

versus dose, Figure 5.9, if gamma-rays were to be present the crystallite dimensions would not decrease as quickly with dose and the plateau size would be larger.

It is possible, but needs to be investigated, that the gamma-rays are annealing a portion of the irradiation defects in reactor experiments, and that this decrease in defect population is the cause of the order-of-magnitude difference between the proton and neutron irradiation-induced creep experiments. This annealing of defects could be part of the discrepancy observed in the comparison of the dose rate and temperature effects on creep rate. For the graphite irradiated at constant stress, SM1-24 and IG-110, these samples were stacked in their respective irradiation capsules. The neutron fluxes were shown to vary over the length of the irradiation capsule, and it is likely that the gamma-ray fluxes also vary, but differently than the neutron flux, over the same length. Therefore it is possible that the calculated dose rates, for the neutron samples, are not correct because the RCF is not uniform over the capsule length.

5.2.4 Comparison of Microstructure Results with Neutron Results

The effects of irradiation parameters on the crystal properties, Young's modulus, and anisotropy, of the proton irradiated samples have been discussed previously in this chapter. This section will compare those observed effects with results from measurements on graphite samples irradiated with neutrons. All of the crystal parameters, from both proton and neutron samples, were determined from XRD spectra, but none of the historical XRD work utilized the Williamson-Hall analysis so the c-spacing spread has never been determined for neutron irradiated graphite.

5.2.4.1 Comparison of Dose Effects on Crystal Parameters

The first analysis was the effect of dose on the lattice parameters and crystallite dimensions. When the samples underwent proton irradiation with constant stress and temperature, the changes in $\Delta c/c_0$ and $\Delta a/a_0$ exponentially approached a plateau value (positive for $\Delta c/c_0$, and negative for $\Delta a/a_0$), and this same behavior has been observed for graphite irradiated with neutrons [24, 81, 89]. A comparison of $\Delta c/c_0$ and $\Delta a/a_0$ from this work and neutron measurements on samples irradiated at 650ºC [89] are plotted

in Figure 5.28. The trends of $\Delta c/c_0$ increasing to a plateau and $\Delta a/a_0$ decreasing to a plateau are similar for both, but the magnitude of the neutron plateau values were a factor of five lower. This difference may stem from the neutron irradiation having a lower concentration of defects due to the gamma-rays, which would then decrease the density of interstitial clusters resulting in a smaller increase of c-spacing and a lower uncollapsed line density resulting in fewer C-C bonds rearranging to a smaller spacing. Additionally it was observed that the crystallite sizes, both L_c and L_a, decreased exponentially with dose, to a plateau value. The only observations noted in neutron literature is that severe deterioration of crystal perfection has been observed [74].

5.2.4.2 Comparison of Stress Effects on Crystal Parameters

The second analysis was the effect of applied stress on the lattice parameters and crystallite dimensions. When the samples underwent proton irradiation to a constant final dose and temperature, there were no significant effects of applied tensile stress on changes in $\Delta c/c_0$ and $\Delta a/a_0$. For neutrons samples, that underwent restrained shrinkage at 300ºC, the increase in $\Delta c/c_0$ was less than in the unrestrained sample [74]. A comparison of results from this work and the neutron results are plotted in Figure 5.29. The samples with the most disparity between proton and neutron irradiations were at doses around 2-2.5dpa, around the plateau values, but for samples at doses around 0.4dpa the difference was within experimental error (unstressed 1.05% ± 0.11% and 0.92% ± 0.11% restrained). This indicates that the applied stress may have an effect on the plateau and exponential decay values in the dose dependence. When the samples underwent proton irradiation to a constant final dose and temperature, there were no observed effects of applied tensile stress on changes in L_c and L_a, while the neutron irradiated samples, that underwent restrained shrinkage tests, L_c did not decrease as quickly compared to the unrestrained sample [74].

5.2.4.3 Comparison of Temperature Effects on Crystal Parameters

The third analysis was the effect of irradiation temperature on the lattice parameters and crystallite dimensions. When the samples underwent proton irradiation with the same applied tensile stress, but with different dose rates and final doses, it was observed that $\Delta c/c_0$ was higher at higher irradiation temperatures and the change of $\Delta a/a_0$ was within experimental error. For graphite irradiated with neutrons, it has been observed that $\Delta c/c_0$ and $\Delta a/a_0$ decrease for higher irradiation temperatures [24, 81, 89]. A plot of the changes of $\Delta c/c_0$ and $\Delta a/a_0$ versus irradiation temperature, for samples irradiated to different doses, is shown in Figure 5.30 [24]. This plot shows that for the neutron samples, the change in spacing at a constant temperature increases with dose as expected, and that increasing temperature reduces the amount of change. The proton samples show the expected decrease of a_0 for increasing temperature at the same dose, but the opposite for c-spacing, which may be an artifact of the higher temperature experiments having a higher dose rate. When the samples underwent proton irradiation, with the same applied tensile stress to a constant final dose, it was observed that L_c and L_a were not affected by temperature. The effect of temperature on these values in neutron irradiated graphite has not been measured.

5.2.4.4 Comparison of Experimental Conditions on Young's Modulus

The fourth analysis was the effects of irradiation conditions on Young's modulus. It should be noted that the measurements in this work were done with nanoindentation, while measurements on the neutron irradiated samples were calculated from ultrasonic wave propagation measurements. When the samples underwent proton irradiation, with constant stress and temperature, there was no observed effect of dose, out to 1dpa, on Young's modulus. For graphite irradiated with neutrons an increase of Young's modulus with dose has been observed [21, 26, 81], but as mentioned in Section 5.1.3 Young's modulus primarily increases as the porosity of the sample is removed and in the nuclear grades it is most likely that the low-dose increase is due to a stiffening of the binder phase and therefore should not occur for the material from this work. A plot of Young's

modulus versus dose, for proton and neutron irradiations, is shown in Figure 5.31, where the blue and orange neutron data are from [21] and the gray date is from [26]. It should be noted that in the neutron irradiated samples, Young's modulus increased by 75-100% at a dose of 1dpa. When the samples underwent proton irradiation to a constant final dose and temperature, it was observed that Young's modulus decreased for the highest stress sample. It was observed with neutron irradiations that the Young's modulus still increased with applied tensile stress, but with an applied tensile stress it only increased by 10%-20% while the unstressed samples increased 80% [36]. A comparison of the change of Young's modulus, due to stress, is plotted versus dose in Figure 5.32. When the samples underwent proton irradiation with the same applied tensile stress to a constant final dose (0.25dpa 1000ºC-1200ºC samples only) it was found that temperature had no effect on Young's modulus. In neutron irradiations, the percent increase of Young's modulus, at turn-around dose, decreases with increasing temperature [21, 81], as is seen with the 600ºC (blue data) and 875ºC (orange data) in Figure 5.31, where turn-around for the 600ºC data is at 25dpa and increased Young's modulus by over 300%, while at 875ºC turn-around is 12dpa and increased Young's modulus by 250%, which is to be expected since the sample irradiated at 600ºC undergoes more densification at turn-around than the 875ºC.

5.2.4.5 Comparison of Irradiation Creep Effects on Anisotropy

The final analysis was the effect of 4.5% irradiation creep strain on the anisotropy. This analysis found no change between the unirradiated sample and the sample that experienced proton irradiation-induced creep. The only work that investigated anisotropy in neutron irradiated graphite [74] also exhibited no change in anisotropy due to irradiation with stress.

5.2.4.6 Conclusions from Microstructure Comparisons

The effects of accumulated dose on the crystal parameters showed the same behavior, albeit the changes for the proton samples were larger than for the neutrons. At similar total dose, both proton and neutron samples showed negligible effect of stress on

crystal parameters. The temperature effects on crystal parameters had a slight disagreement between proton and neutron experiments, but this difference was in the c-spacing change where the proton samples irradiated at higher temperature showed larger expansion, which may be a result of higher dose rates as temperature increased.

The Young's modulus comparisons were not as straightforward as other comparisons. At low doses, the dose effects on Young's modulus mostly agree in that there is little-to-no change. Neutron experiments showed that Young's modulus still increases, but to a lesser extent, when irradiated with applied tensile stress, whereas the proton results showed the highest tensile stress showed a significant decrease of Young's modulus. The effects of temperature found that the extent of Young's modulus increase at turn-around decreases with increasing temperature, while the proton results showed no temperature effect. The Young's modulus comparisons highlight that the closure and/or formation of porosity are the primary source of change, and for the proton experiments the samples shouldn't reach turn-around until dose approaches 15dpa (calculated at 1000ºC from Equation(5.23)).

5.2.5 Conclusions from Neutron Comparisons

The analysis showed that the fundamental damage mechanism in graphite is the same for neutrons and protons, the only difference being that neutron-created PKA's produce multiple discrete displacement groups while the proton-created PKA's produces one displacement group. Next it was shown that the irradiation creep rate dependence on experimental parameters (stress, dose rate, temperature, and accumulated dose) for proton irradiation agree fairly well with those observed for neutron irradiation creep experiments, though there are some differences that need to be investigated further. Thirdly, the effect of gamma-rays was discussed and it was shown that gamma-rays are potentially annealing out defects, which could explain the lower creep rates in-reactor compared to those with proton irradiation. Lastly, it was shown that the irradiation experimental parameters for protons have similar effects on the microstructure, but some of the discrepancies may be due to the possibility of lower defect concentrations for the neutron samples. Overall, it has been shown in this section that irradiation of graphite

with protons is a suitable proxy for neutron irradiations, as long as the effect of gamma-rays can be determined.

5.3 Analysis of Irradiation Creep Mechanisms

This section will utilize the experimental conditions and results to determine the irradiation-induced creep mechanism. The first part will present calculations of the thermal and irradiation-produced defects. The second part will present a comparison of the experimental creep rate dependences with the potential irradiation creep mechanisms, which will utilize the calculations in the first section for part of this comparison. In addition a comparison of the microstructure changes will be compared with changes expected for each mechanism. Lastly, a summary of the comparisons will be presented and used to determine the mechanism of irradiation creep.

5.3.1 Defect Calculations

To compare the experimental results with the irradiation creep mechanisms, it is first necessary to investigate the effects of temperature and irradiation on the defect populations. This section will first present the calculations of thermal defect properties, specifically the thermal concentrations of interstitials and vacancies and the diffusion coefficients of interstitials and vacancies. Then the concentrations of irradiation-produced interstitials and vacancies will be presented.

5.3.1.1 Thermal Defect Properties

The review article by Thrower and Mayer [7] provided a thorough discussion of current experiments that resulted in the thermodynamic properties of defect production. These values included the entropy of formation (S^f), entropy of migration (S^m), energy of formation (E^f), energy of migration (E^f), and jump frequency (v), which are listed for both interstitials and vacancies in Table 5.32.

The thermal interstitial concentration (C_i^0) is calculated by:

$$C_i^0 = \exp\left(\frac{S_i^f}{k}\right)\exp\left(\frac{-E_i^f}{kT}\right) = \exp\left(\frac{3k}{k}\right)\exp\left(\frac{-7.0eV}{\left(8.617x10^{-5}\frac{eV}{K}\right)*T(K)}\right), \quad (5.24)$$

and the thermal vacancy concentration (C_v^0) is calculated by:

$$C_v^0 = \exp\left(\frac{S_v^f}{k}\right)\exp\left(\frac{-E_v^f}{kT}\right) = \exp\left(\frac{7k}{k}\right)\exp\left(\frac{-7.0eV}{\left(8.617x10^{-5}\frac{eV}{K}\right)*T(K)}\right). \quad (5.25)$$

A plot of the thermal defect concentrations versus temperature are plotted in Figure 5.33. The similarities of the thermal concentrations result from similar formation energies for interstitials and vacancies.

The thermal diffusion coefficient for interstitials (D_i) is given by:

$$D_i = \underbrace{\tfrac{1}{6} z_i \lambda^2 \nu_i \exp\left(\frac{S_i^m + S_i^f}{k}\right)}_{D_0} \exp\left(\frac{-E_i^m}{kT(K)}\right), \quad (5.26)$$

where z_i is the number of nearest sites, which is equal to 6 since interstitials have been shown to move between the basal planes and have 6 energetically favorable nearest-neighbor sites, and the terms without temperature dependence constitute the pre-exponential diffusion coefficient (D_0). The jump distance, λ_i, is equal to the spacing between atoms in the basal plane (a_0=1.419Å) resulting in:

$$\begin{aligned} D_i &= \tfrac{1}{6} 6\left(1.42x10^{-8}cm\right)^2 \left(4x10^{12}s^{-1}\right)\exp\left(\frac{7k}{k}\right)\exp\left(\frac{-0.1eV}{kT}\right) \\ &= 0.885\frac{cm^2}{s}\exp\left(\frac{-0.1eV}{\left(8.617x10^{-5}\frac{eV}{K}\right)*T(K)}\right) = 0.885\frac{cm^2}{s}\exp\left(\frac{-1160.5K}{T(K)}\right) \end{aligned} \quad (5.27)$$

In the Thrower and Mayer [7] article, a value of D_0 for interstitial diffusion, calculated from a ^{14}C tracer diffusion experiment, was reported as 0.91cm^2/s, which is close to the value of 0.885cm^2/s calculated with Equation (5.27). The thermal diffusion coefficient for vacancies (D_v) is calculated by:

$$D_v = \tfrac{1}{6} z_v \lambda^2 \nu_v \exp\left(\frac{S_v^m}{k}\right)\exp\left(\frac{-E_v^m}{kT}\right), \quad (5.28)$$

where z_v is the number of nearest neighbor sites, which is equal to 3 since vacancies only move within the basal plane. The jump distance, λ_i, is equal to the spacing between atoms in the basal plane (a_0=1.419Å) resulting in:

$$D_v = \tfrac{1}{6}3\left(1.42x10^{-8}cm\right)^2\left(5x10^{13}s^{-1}\right)\exp\left(\frac{7k}{k}\right)\exp\left(\frac{-3.1eV}{kT}\right)$$
$$= 5.528\tfrac{cm^2}{s}\exp\left(\frac{-3.1eV}{\left(8.617x10^{-5}\tfrac{eV}{K}\right)*T(K)}\right) = 5.528\tfrac{cm^2}{s}\exp\left(\frac{-35975.4K}{T(K)}\right). \quad (5.29)$$

The diffusion coefficients are plotted versus temperature in Figure 5.34. Unlike defect concentrations, the interstitial diffusion coefficient is many orders of magnitude higher than that for vacancies, which results from the differences in migration energies.

5.3.1.2 Irradiation Production of Point Defects

Under irradiation, the point defect balance equations are given by the chemical rate equations:

$$\frac{dC_i}{dt} = K_0 - K_{iv}C_iC_v - K_{is}C_iC_s$$
$$\frac{dC_v}{dt} = K_0 - K_{iv}C_iC_v - K_{vs}C_vC_s \quad , \quad (5.30)$$

where K_0 is the defect production rate (in dpa/s), K_{iv} is the is the recombination rate constant, K_{is} is the interstitial loss to sinks rate constant, K_{vs} is the vacancy loss to sinks rate constant, C_i is the interstitial concentration, C_v is the vacancy concentration, and C_s is the sink concentration. During steady state, the concentrations are not changing, and thus the simultaneous equations can be solved to investigate the effects of temperature on the steady-state interstitial concentration:

$$C_i^{SS} = \frac{-K_{vs}C_s}{2K_{iv}} + \left[\frac{K_0K_{vs}}{K_{iv}K_{is}} + \frac{K_{vs}^2C_s^2}{4K_{iv}^2}\right]^{0.5}$$
$$C_i^{SS} = \frac{-4\pi r_{vs}D_vC_s}{2\left(4\pi r_{iv}\left(D_i+D_v\right)\right)} + \left[\frac{K_0 4\pi r_{vs}D_v}{\left(4\pi r_{iv}\left(D_i+D_v\right)\right)\left(4\pi r_{is}D_i\right)} + \frac{\left(4\pi r_{vs}D_v\right)^2C_s^2}{4\left(4\pi r_{iv}\left(D_i+D_v\right)\right)^2}\right]^{0.5} \quad , \quad (5.31)$$

and steady-state vacancy concentration:

$$C_v^{SS} = \frac{-K_{is}C_s}{2K_{iv}} + \left[\frac{K_0 K_{is}}{K_{iv}K_{vs}} + \frac{K_{is}^2 C_s^2}{4K_{iv}^2} \right]^{0.5}$$

$$C_v^{SS} = \frac{-4\pi r_{is} D_i C_s}{2\left(4\pi r_{iv}\left(D_i + D_v\right)\right)} + \left[\frac{K_0 4\pi r_{is} D_i}{\left(4\pi r_{iv}\left(D_i + D_v\right)\right)\left(4\pi r_{vs} D_v\right)} + \frac{\left(4\pi r_{is} D_i\right)^2 C_s^2}{4\left(4\pi r_{iv}\left(D_i + D_v\right)\right)^2} \right]^{0.5} \quad . \quad (5.32)$$

There are four time constants from these defect balance equations that help determine the appropriate labeling of the irradiation regime. These time constants are [52]:

$$\tau_1 = \frac{1}{\sqrt{K_0 K_{iv}}} \quad (5.33)$$

$$\tau_2 = \frac{1}{K_{is}C_s} \quad (5.34)$$

$$\tau_3 = \frac{1}{K_{vs}C_s} \quad (5.35)$$

$$\tau_4 = \frac{\tau_1^2}{\tau_2} = \frac{K_{is}C_s}{K_0 K_{iv}}, \quad (5.36)$$

where τ_1 is the time it takes for recombination to begin, τ_2 is the time for interstitials to begin to annihilate at sinks, τ_3 is the time for vacancies to begin to annihilate at sinks, and τ_4 is when recombination overtakes interstitial loss to sinks.

The first step in determining the irradiation regime is comparing τ_1 and τ_2; if $\tau_1 < \tau_2$ then the sink density is low and the first defect loss will be due to recombination, if $\tau_1 \approx \tau_2$ then the sink density is intermediate, and if $\tau_1 > \tau_2$ then the sink density is high. To compare these values it is necessary to determine an approximate sink density. Interstitials and vacancies only move in directions parallel to the basal planes [10], therefore the sink density can be calculated using a 2-dimensional analysis. In Section 5.1.2.3 it was shown that the pre-irradiation crystallite size of the basal planes is 56.8nm, so assuming the crystallite boundaries are the primary sinks, the crystallites are square shaped, and the average boundary between crystallites is one atomic spacing wide. This results in a basal plane area of 3226 nm^2, boundary area of 16.1 nm^2, and sink density of

$4.99x10^{-3}$. This is for theoretical density, but the graphite samples used are 78% theoretical density thus giving a final sink density of $3.93x10^{-3}$, or $3.5x10^{20}$ sinks/cm^3. Using this sink density, and the diffusion coefficients and damage rates from the 700ºC and 1000ºC experiments result in:

$$\tau_1^{700^\circ C} = 8.90x10^{-6}\,s \qquad \tau_1^{1000^\circ C} = 3.88x10^{-6}\,s$$
$$\tau_2^{700^\circ C} = 5.97x10^{-15}\,s \qquad \tau_2^{1000^\circ C} = 4.50x10^{-15}\,s$$
$$\tau_3^{700^\circ C} = 3.31s \qquad \tau_3^{1000^\circ C} = 5.44x10^{-4}\,s$$
$$\tau_4^{700^\circ C} = 1.33x10^{4}\,s \qquad \tau_4^{1000^\circ C} = 3.35x10^{3}\,s\,.$$

In both cases $\tau_1 >>> \tau_2$, which indicates that the experiments are in the high sink density regime, additionally experimental work has shown that vacancies become mobile in graphite around 500ºC [24], therefor these experiment are also in the high temperature regime. This regime has three regions, the first being from time zero to τ_2 where interstitial and vacancy concentrations buildup, at τ_2 the interstitials begin to annihilate at sinks while the vacancy concentration continues to build-up until τ_3, when the vacancies begin to annihilate at sinks. In this regime recombination is negligible and vacancies and interstitials are primarily annihilated at sinks, which results in the steady state concentrations of interstitials and vacancies given by:

$$C_i^{SS} = \frac{K_0}{K_{is}C_s} = \frac{K_0}{4\pi r_{is} D_i C_s} \tag{5.37}$$

$$C_v^{SS} = \frac{K_0}{K_{vs}C_s} = \frac{K_0}{4\pi r_{vs} D_v C_s}\,. \tag{5.38}$$

An example of the vacancy and interstitial concentrations versus irradiation time are plotted in Figure 5.35.

In Section 3.2.5 it was suggested that the higher defect density, due to the raster scanned beam, may increase the recombination of defects. The calculations of the loss terms, for the 1000ºC and 700ºC irradiations, from Equation (5.30) are listed in Table 5.33, including the loss term for recombination ($K_{iv}C_iC_v$), interstitial loss to sinks

($K_{is}C_iC_s$), vacancy loss to sinks ($K_{vs}C_vC_s$), calculated for the for both continuous and pulsed beam irradiations, and the last column lists the fraction of defect lost to recombination. These calculations show that for the pulsed beam there is a larger percentage of defects loss to recombination, but the loss to sinks is still the dominant mechanism by at least two orders of magnitude.

The steady-state defect concentrations are affected by irradiation temperature and can be influenced by the thermal contribution of defect creation. By using the average damage rate of the 700ºC and 1200ºC experiments (8.7×10^{-7}dpa/s), the steady-state irradiation Equations (5.37) and (5.38), and the thermal concentration Equations (5.24) and (5.25), the total steady-state defect concentrations as a function of temperature can be plotted, as shown in Figure 5.36. It is interesting to note from these figures that the vacancy concentration, in the temperature regime of these experiments, is strongly temperature dependent while the interstitial concentration is nearly flat.

The concentrations, calculated in Figure 5.36, used a constant dose rate to calculate the change of steady-state defect concentrations due to changing temperature. It is then necessary to calculate the discrete concentrations using the dose rates at the actual temperatures. The steady-state concentrations of defects are calculated using these discrete values and plotted in Figure 5.37, overlaid on the data from Figure 5.36. Each successively higher temperature irradiation required a higher dose rate. The higher dose rates did not significantly affect the vacancy concentration, but the higher dose rates dramatically changed the interstitial concentrations. Over this temperature range the interstitial concentration was not dramatically affected by temperature, while the dose rate increased by an order of magnitude, which resulted in the steady-state concentration going from decreasing with increasing temperature (at constant dose rate) to increasing with increasing temperature. Many of the mechanisms are controlled by the defect concentration and diffusion coefficients, so the discrete values of D_iC_i and D_vC_v are plotted versus temperature in Figure 5.38. A statistical analysis of C_v, C_i, D_vC_v, and D_iC_i versus 10^3/T was performed with a linear (Equation (5.2)) and Arrhenius dependence given by:

$$y = A * \exp(B * x). \tag{5.39}$$

The Arrhenius dependence was adjusted from earlier to account for the *x* term being 1/T. The constants, error of the constants, R^2, and variance of the fits are listed in Table 5.34. From this analysis, C_v is best-fit with the inverse Arrhenius dependence, while C_i, D_vC_v, and D_iC_i are all best-fit with Arrhenius but could also be described approximately with a linear dependence.

5.3.1.3 Conclusions from Defect Calculations

The calculations in this section have been used to examine both the thermal and irradiation produced defects. First the thermal concentrations and diffusion coefficients were calculated. The sink density was calculated from the pre-irradiation crystallite size. Then the diffusion coefficients and sink density were used to determine that the irradiation regime throughout this work is in the high temperature high sink density regime, which was then used to calculate the time-dependent concentration profiles. The irradiation experimental conditions were used to compare the steady-state irradiation concentrations with the trends expected for constant dose rate. This analysis showed that even though the interstitial concentration should decrease with increasing temperature, the increased dose rate overcame this and resulted in higher interstitial concentrations for experiments with increasing irradiation temperature. Lastly, it was shown that C_v has an inverse Arrheius dependence, while C_i, D_vC_v, and D_iC_i all have an Arrhenius dependence but can be approximated by a linear fit in this temperature range.

The calculation and analysis shows C_i increases with temperature, which relates back to the XRD analysis, Section 5.1.1.1.3, where the increase of c-spacing increases and crystallite sizes decrease, for samples irradiated at higher temperature. This agrees with the previous statement that a higher interstitial concentration will increase the cluster density and therefore increases the c-spacing and decreases the crystallite size.

5.3.2 Comparison of Experimental Dependencies with Expected Trends from Mechanisms

As described in the background chapter, there are two mechanisms, which have been suspected to be the controlling irradiation-induced creep mechanism in graphite, Pinning-Unpinning and the disproven Cottrell mechanism. This section will re-

summarize the possible Pinning-Unpinning mechanism, and will also briefly re-discuss the traditional irradiation-induced creep mechanisms in other materials. Then the experimental dependencies will be used in a process of elimination methodology to narrow down the potential controlling mechanism.

5.3.2.1 Pinning-Unpinning of Basal Dislocations

The proposed mechanism was the Pinning-Unpinning mechanism. The theory behind this mechanism is that graphite has a high density of basal dislocations that are only lightly pinned and that irradiation will continuously create and destroy these pinning points, thus allowing the dislocations to move before being pinned again for a discrete amount of time. This mechanism is physically represented by [50]:

$$\dot{\varepsilon}_{SS} = k\phi\frac{\sigma}{E_0}, \tag{5.40}$$

where k is the creep coefficient, σ is applied stress, ϕ is the dose rate, and E_0 is the pre-irradiation Young's modulus. Analysis of restrained shrinkage experiments [51] revealed that k has a linear dependence on temperature and an inverse dependence on dose rate, which arises from the creep rate being inversely controlled by the concentration of pinning points (i.e. the higher the pinning point concentration the lower the creep rate), and resulting in the following form of the creep rate:

$$\dot{\varepsilon}_{SS} = \underbrace{\left(\frac{f(T)}{\phi} + g(T)\right)}_{k}\frac{\sigma\phi}{E_0}. \tag{5.41}$$

This analysis from Veringa [51], which has shown that k is inversely dependent on dose rate effectively determined that creep rate is independent of dose rate, because k being inversely dependent on dose rate cancels out the dose rate component in the numerator in Equation(5.41). In Section 5.2.2.2, it was shown that, for both proton and neutron creep experiments at constant stress state, creep rate is linearly dependent on dose rate. Therefore the dose rate dependence of this mechanism does not agree with the experimental results.

This mechanism requires single interstitials and interstitial clusters to pin the dislocations. In Section 5.1.1.1.1, it was shown that single interstitials are unlikely to occur at these experimental temperatures, and instead the c-spacing increase is due to the increasing interstitial cluster density, which reaches a maximum value around 1 dpa. If this mechanism is occurring, then as the cluster density increases and then plateaus, the creep rate should initially be high and then decrease to a constant, but instead the creep rate was shown to be constant out to 1dpa. Further analysis found that c-spacing increases with higher irradiation temperature, due to a higher concentration of interstitials, which should result in the creep rate being lower at higher temperatures for this mechanism.

This mechanism disagrees with three of the dependences from these experiments. The first is this mechanism should have no dependence on dose rate, while this work showed linear dose rate dependence. The second is that this mechanism should have a decreasing creep rate as the cluster density increases, but these experiments did not show an effect of cluster density on creep rate. The disagreement of this mechanism with the dose rate dependence suggests that this is not the irradiation creep mechanism occurring in this work.

5.3.2.2 Stress-Induced Preferential Nucleation (SIPN) of Loops

There are four other steady-state irradiation-induced creep mechanisms that need to be considered for this analysis. The first is the Stress-Induced Preferential Nucleation of loops (SIPN). This mechanism consists of preferential formation of interstitial loops between basal planes that are orientated perpendicular to the applied tensile stress, while vacancy loops form on basal planes orientated parallel to the applies stress. The formation of both types of loops will cause the sample to lengthen in the direction of the applied stress. SIPN is physically represented by [52]:

$$\dot{\varepsilon}_{SIPN} = \frac{2}{3} b \rho_L \dot{r}_L \frac{\exp\frac{\sigma n \Omega}{kT} - 1}{\exp\frac{\sigma n \Omega}{kT} + 2}, \tag{5.42}$$

where b is the Burger's vector of the loop, ρ_L is the loop density, $\dot{r}_L$ is the loop growth rate, n is the number of atoms needed to form a loop, k is the Boltzmann constant, T is the temperature, and Ω is the volume of an atom. The dose rate dependence lies in the loop growth rate, which is given by [52]:

$$\dot{r}_L = \frac{K_0}{(\rho_N - \rho_L)b}\left(\frac{k_V^2(\varepsilon_i - \varepsilon_v')}{k^2} + \frac{k_d^2(1-\varepsilon_i)}{k^2}\frac{z_d k_c^2}{(k^2 + z_d k_d^2)} - \frac{K^e}{K_0}\right), \tag{5.43}$$

where K_0 is the dose rate, ρ_N is the network dislocation density, k_V^2 is the void sink strength (equal to zero in graphite), ε_i is the fraction of interstitials immobilized by the cascades, ε_v is the fraction of vacancies immobilized by the cascades, k_d^2 is the dislocation sink strength, k^2 is the total sink strength, z_d is the dislocation bias factor, k_c^2 is the dislocation core sink strength, and K^e is the vacancy thermal emission rate. In the temperature regimes of interest, there is no thermal vacancy production ($K^e = 0$), and all other values are physical constants in the material so they will not change. Thus Equations (5.42) and (5.43) can be combined to give:

$$\dot{\varepsilon}_{SIPN} = \frac{2}{3}\underbrace{\left(\frac{\exp\frac{\sigma n\Omega}{kT} - 1}{\exp\frac{\sigma n\Omega}{kT} + 2}\right)}_{G}\underbrace{\left(\frac{\rho_L K_0}{(\rho_N - \rho_L)}\right)}_{H}\underbrace{\left(\frac{k_d^2(1-\varepsilon_i)}{k^2}\frac{z_d k_c^2}{(k^2 + z_d k_d^2)}\right)}_{J}. \tag{5.44}$$

This mechanism has an approximate linear dependence of creep rate on applied stress and a linear dependence on dose rate, which both agree with the experimental results, but a 1/T dependence. The portion of Equation (5.44) labeled *G* decreases by a factor of 1.5 when the temperature is increased from 700ºC to 1200ºC. The *H* term is strongly dependent on the loop and dislocation densities, and the *J* term is not affected by irradiation conditions. For term *H*, when $\rho_N >> \rho_L$, as ρ_L increases the creep rate should increase, but when $\rho_L >> \rho_N$, as ρ_L increases the creep rate remain constant. Graphite has been shown to have a high concentration of dislocations [50], so it is expected that $\rho_N >> \rho_L$ so as loops are nucleated the creep rate should increase, but in Section 5.1.1.4

it was shown that creep rate is not changing with dose. There are a few other limitations that have been noted in previous work about this mechanism. The first being that once loops have been nucleated, the strain is controlled by dose so if the stress is removed creep should continue [90]. The other is that loops with preferred orientation have been observed in metals, but the creep strain rate is still significantly larger than predicted by this mechanism [52].

In Section 2.6, it was shown that the damage mechanism of graphite is due to the disassociation of vacancy lines and loops into two dislocations, rather than the formation of interstitial loops. In addition, interstitial loops have only been observed in natural single crystals of graphite [71], but not in manufactured graphite. This mechanism is difficult to compare with the microstructure changes, because the formation of interstitial loops should not affect the c-spacing, except for the region around the loop circumference, and the formation of vacancy loops would not affect the atomic spacing (a_0) .

This mechanism disagrees with two of the dependences from these experiments. The first is this mechanism should cause creep rate to decrease with increasing irradiation temperature, while this work showed an Arrhenius increase with increasing temperature. The second is that this mechanism should cause creep rate to increase as the loop density increases with accumulated dose, but these experiments showed no effect of dose on creep rate. Finally, the only time interstitial loops have been observed is in naturally occurring single crystals of graphite. The disagreement of this mechanism with the temperature dependence, in addition to interstitial loops having not been observed in manufactured graphite, suggests that this is not the irradiation creep mechanism occurring in this work.

5.3.2.3 Stress-Induced Preferential Absorption (SIPA)

The next irradiation-induced creep mechanism is Stress-Induced Preferential Absorption (SIPA) of defects at dislocations. In this mechanism, strain occurs via dislocation climb, where the climb occurs when defects are preferentially absorbed at dislocations. SIPA is represented by [52]:

$$\dot{\varepsilon}_{SIPA} = \frac{2}{9}\Omega\rho_d \frac{\sigma}{E}\left(\Delta z_i' D_i C_i - \Delta z_v' D_v C_v\right), \tag{5.45}$$

where Ω is the atomic volume, ρ_d is the dislocation density, σ is applied stress, E is Young's modulus, $\Delta z_i'$ is the interstitial capture efficiency, $\Delta z_v'$ is the vacancy capture efficiency, D_i is the interstitial diffusion coefficient, C_i is the steady-state interstitial concentration, D_v is the vacancy diffusion coefficient, and C_v is the steady-state vacancy concentration. This mechanism is linearly dependent on stress, and the dependencies on dose rate and temperature arise from the term in parentheses in Equation(5.45). It was shown in Section 5.3.1.2 that C_i and C_v are linearly dependent on dose rate, at a constant temperature, since these experiments were performed in a high temperature regime where the defects are primarily annihilated at sinks. In addition, calculations in Section 5.3.1.2 showed that, for the conditions used in these experiments, $D_i C_i$ and $D_v C_v$ have an Arrhenius temperature dependence, which can be approximated as linear in the temperature range applicable to this work.

The linear dependence on stress and dose rate, and Arrhenius temperature dependence, are all in agreement with the experimental dependencies from this work. Finally this mechanism should not be affected by accumulated dose, assuming that the dislocation density does not change. The radiation damage mechanism shows that dislocations are being created, but as long as the pre-existing dislocations are being annihilated at a similar rate there should be no dose effects. This continuity of dislocation density is also in agreement with the Young's modulus not changing with dose, because if the dislocation density were to decrease the Young's modulus would increase because there would be a lower total elastic response.

SIPA has a higher creep rate with higher stress, which can result from stress increasing the dislocation sink strength or stress increasing defect diffusion rates by stretching the lattice thus reducing the energy needed for interstitials to move from site-to-site [90]. Therefore, this mechanism should be in agreement with the microstructure changes due to applied stress. The stress effects of the crystal parameters were measured on samples, which were at doses where the changes had not plateaued; therefore some of

the changes expected from higher stress may be obscured. But, when stress enhances sink strength or diffusion rates, more interstitials will diffuse to the dislocations thus reducing the concentration of interstitial clusters, which would cause a reduction of the c-spacing increase, and would keep the c-spacing variation and crystallite sizes larger than without stress.

This mechanism agrees with all four experimentally observed creep rate dependencies. The only potential source of disagreement comes from there being no noticeable effect of stress on crystal parameters, but these differences may be obscured by the samples being at a relatively low dose compared to the doses necessary for the crystal changes to reach their plateau values. The agreement of this mechanism with all the creep rate dependencies suggests that SIPA is the irradiation creep mechanism occurring in this work.

5.3.2.4 Preferential Absorption Glide (PAG)

The third irradiation-induced creep mechanism is Preferential Absorption Glide (PAG). This mechanism works in an additive fashion with SIPA, but instead of strain being primarily due to dislocation climb, this mechanism produces strain primarily by the glide of dislocations, when dislocation climb over an obstacle in the glide plane has been enabled by preferential absorption. PAG is described by [52]:

$$\dot{\varepsilon}_{PAG} = \frac{4}{9b}\left(\frac{\sigma}{E}\right)^2 \Omega\left(\pi\rho_d\right)^{1/2}\left(\Delta z_i' D_i C_i\right), \tag{5.46}$$

where b is the Burgers vector, the Ω is the atomic volume, ρ_d is the dislocation density, σ is applied stress, E is Young's modulus, $\Delta z_i'$ is the interstitial capture efficiency, D_i is the interstitial diffusion coefficient, and C_i is the steady-state interstitial concentration. This mechanism has squared stress dependence, and the dependencies on dose rate and temperature arise from the term in parentheses in Equation(5.46). It was shown in Section 5.3.1.2 that C_i is linearly dependent on dose rate since these experiments were performed in a high temperature regime where the defects are primarily annihilated at sinks. In addition, calculations in Section 5.3.1.2 showed that, for the conditions used in

these experiments, D_iC_i has an Arrhenius temperature dependence, which is approximately linear in the temperature range for this work.

This mechanism has a square dependence on stress, which does not agree with the experimental results. In Section 5.1.1.1, it was attempted to fit a square dependence to the creep rate versus stress results, but the fit was two orders of magnitude larger than the linear fit. Otherwise, the linear dependence on dose rate, and Arrhenius temperature dependence, are all in agreement with the experimental dependencies from this work. Finally this mechanism, like SIPA, should not be affected by accumulated dose, assuming that the dislocation density does not change. The radiation damage mechanism shows that dislocations are being created, but as long as the pre-existing dislocations are being annihilated at a similar rate there should be no dose effects. This mechanism should have similar crystal parameter dependencies as SIPA since both are driven by dislocation motion, but as with SIPA the stress effects are obscured by the low sample doses.

This mechanism disagrees with one, possibly two, of the dependences from these experiments. The first is that creep rate from this mechanism has a square stress dependence, but this work cannot be described with this dependence. The other potential source of disagreement comes from there being no noticeable stress effect to crystal parameters, but these differences may be obscured by the samples being at a relatively low dose compared to the doses necessary for the crystal changes to reach their plateau values. The disagreement of this mechanism with the stress dependence suggests that this is not the irradiation creep mechanism occurring in this work.

5.3.2.5 Climb and Glide from Dislocation Bias (CGDB)

The fourth irradiation-induced creep mechanism is Climb and Glide from Dislocation Bias (CGDB) for interstitials. This mechanism is similar to PAG, but instead of preferential absorption of all defects at dislocations, dislocations have a bias for interstitials while the vacancies are absorbed at voids. CGDB is represented by [52]:

$$\dot{\varepsilon}_{CGDB} = \frac{\rho_m l^2 \Omega 8\pi^2 (1-\nu)^2 \sigma_{xy}^2}{(\mu b)^2}\left(z_i^d D_i C_i - z_v^d D_v C_v\right), \tag{5.47}$$

where ρ_m is the mobile dislocation density, l is the glide length on the slip plane, Ω is the atomic volume, v is Poisson's ratio, σ_{xy} is stress, μ is the shear modulus, b is the Burgers vector, z_i^d and z_v^d are the dislocation capture efficiencies for interstitials and vacancies, D_i is the interstitial diffusion coefficient, C_i is the steady-state interstitial concentration, D_v is the vacancy diffusion coefficient, and C_v is the steady-state vacancy concentration. This mechanism has a squared stress dependence, and the dependencies on dose rate and temperature arise from the term in parentheses in Equation(5.47). It was shown in Section 5.3.1.2 that C_i and C_v are linearly dependent on dose rate, since these experiments were performed in a high temperature regime where the defects are primarily annihilated at sinks. In addition, calculations in Section 5.3.1.2 showed that, for the conditions used in these experiments, D_iC_i and D_vC_v have an Arrhenius temperature dependence.

This mechanism has the same square dependence on stress as PAG, but as with PAG this dependence does not agree with the experimental results. Otherwise, the linear dependence on dose rate, and Arrhenius temperature dependence, are all in agreement with the experimental dependencies from this work. Finally this mechanism, like SIPA and PAG, should not be affected by accumulated dose, assuming that the dislocation density does not change. And again like SIPA and PAG, this dislocation movement-driven mechanism should have similar crystal parameter dependencies on stress, but the stress effects are obscured by the low sample doses.

This mechanism disagrees with one, possibly two, of the dependences from these experiments. The first is that creep rate from this mechanism has a square stress dependence, but this work cannot be described with this dependence. The other potential source of disagreement comes from there being no noticeable stress effect to crystal parameters, but these differences may be obscured by the samples being at a relatively low dose compared to the doses necessary for the crystal changes to reach their plateau values. The disagreement of this mechanism with the stress dependence suggests that this is not the irradiation creep mechanism occurring in this work.

5.3.2.6 Summary of Mechanism Agreement with Experimental Results

The analyses in Section 5.1.1 determined that the irradiation creep experiments in this work have a linear dependence on applied stress and dose rate, and an Arrhenius dependence on temperature. Calculations in Section 5.3.1.2 determined that the interstitial and vacancy concentrations are linearly dependent on dose rate, and that values of D_iC_i and D_vC_v, calculated for the experimental conditions increase with temperature via an Arrhenius dependence.

The primary litmus for determining the mechanism of irradiation creep is the comparison of the experimental creep rate dependencies and the mechanism-predicted dependencies. The linear stress dependence agrees with the Pinning-Unpinning, SIPN, and SIPA mechanisms, while PAG and CGDB require a square dependence. The linear dose rate dependence agrees with the SIPN, SIPA, PAG, and CGDB, while pinning-unpinning is independent of dose rate. The Arrhenius temperature dependence agrees with the Pinning-Unpinning, SIPA, PAG, and CGDB, while SIPN should decrease at higher temperatures. The constant creep rate, with increasing accumulated dose, agrees with the Pinning-Unpinning, SIPA, PAG, and CGDB, whereas SIPN should decrease as loops are formed with increasing dose. These agreements and disagreements are summarized in Table 5.35.

PAG and CGDB are in disagreement with the stress dependence and it was shown in Section 5.1.1.1 that the creep rate dependence on stress cannot be described with a square stress dependence, thus these two mechanisms are not likely controlling creep. Pinning-Unpinning is in disagreement with the dose rate dependence in that is has no dose rate dependence, in contradiction to Section 5.1.1.2 where it was shown that creep rate is linearly dependent on dose rate, therefore this is not the controlling mechanism. SIPN disagrees with both the temperature dependence and the accumulated dose not effect on creep rate, in addition to the fact that loops have not been observed in manufactured graphite, which suggests that SIPN is not the mechanism. The only mechanism that agrees with all the experimental trends is SIPA.

The comparison of the mechanisms and the crystal parameter changes was limited because in Section 5.1.2.3 it was shown that the majority of the changes occurred only due to the radiation damage mechanism, and this was supported by the interstitial

concentration calculations in Section 5.3.1.2 that showed why the counterintuitive temperature changes in c-spacing and crystallite size were caused by the higher interstitial concentrations. The only microstructural change that would be expected with the SIPA mechanism is changes resulting from the applied stress. Primarily the c-spacing plateaued increase should be lower for the higher stressed samples since more interstitials would be absorbed at the dislocations thus leaving fewer to form the six-atom clusters that are the proposed source of the c-spacing increase. Additionally, if stress reduces the cluster density then it would be expected that the crystallite sizes would be larger, and the c-spacing variation would be larger, for the higher stressed samples. Unfortunately the samples with different stressed were not irradiated out to a dose level where the plateau is reached, but these dependencies have been observed for graphite irradiated with neutrons. Additionally, the comparison of creep mechanisms and Young's modulus was limited because the primary source of change in Young's modulus is the closure of the pre-existing porosity.

5.3.3 Conclusions from Analysis of Irradiation Creep Mechanism

SIPA was the only mechanism, of the five investigated, that had significant agreement for all the experimentally-determined and mechanism-predicted creep rate dependencies on stress, dose rate, temperature, and accumulated dose. The only possible source of discrepancy could arise when dislocations are annihilated at crystallite and grain boundaries. But, the vacancy disassociation mechanism of radiation damage in graphite provides a potential continuous source of dislocations, thus allowing for the dislocation density to remain approximately constant.

Table 5.1. Creep rate and stress dependence analysis

	$A \pm \sigma[A]$	$B \pm \sigma[B]$	R^2	Variance
LSE Constant	$7.34 \times 10^{-8} \pm 2.20 \times 10^{-8}$			2.41×10^{-15}
LSE Linear	$3.79 \times 10^{-9} \pm 1.85 \times 10^{-10}$		0.964	8.59×10^{-17}
LSE Square	$1.05 \times 10^{-10} \pm 2.09 \times 10^{-11}$		0.475	1.27×10^{-15}
LSE Power	$5.37 \times 10^{-9} \pm 1.96 \times 10^{-9}$	0.897 ± 0.108	0.973	8.81×10^{-17}
DVRT Constant	$6.56 \times 10^{-8} \pm 1.71 \times 10^{-8}$			1.46×10^{-15}
DVRT Linear	$3.26 \times 10^{-9} \pm 2.28 \times 10^{-10}$		0.910	1.31×10^{-16}
DVRT Square	$9.06 \times 10^{-11} \pm 1.78 \times 10^{-11}$		0.377	9.13×10^{-16}
DVRT Power	$5.40 \times 10^{-9} \pm 2.80 \times 10^{-9}$	0.851 ± 0.154	0.928	1.41×10^{-16}

Table 5.2. Creep rate and dose rate dependence analysis

	$A \pm \sigma[A]$	$B \pm \sigma[B]$	R^2	Variance
LSE Constant	$1.45 \times 10^{-8} \pm 2.77 \times 10^{-9}$			4.59×10^{-17}
LSE Linear	$3.64 \times 10^{-2} \pm 4.13 \times 10^{-3}$		0.607	1.80×10^{-17}
LSE Square	78517 ± 9223		0.581	1.92×10^{-17}
LSE Power	17.68 ± 148.3	1.423 ± 0.575	0.660	1.95×10^{-17}
DVRT Constant	$5.76 \times 10^{-9} \pm 1.47 \times 10^{-9}$			8.64×10^{-18}
DVRT Linear	$1.69 \times 10^{-2} \pm 3.23 \times 10^{-3}$		0.396	5.22×10^{-18}
DVRT Square	45413 ± 8330		0.439	4.85×10^{-18}
DVRT Power	151.2 ± 3015	1.614 ± 1.348	0.464	6.95×10^{-18}

Table 5.3. Creep rate temperature dependence analysis

	A ± σ[A]	B ± σ[B]	R^2	Variance
LSE Constant	$2.29x10^{-3} \pm 5.83x10^{-4}$			$1.70x10^{-6}$
LSE Linear	$2.75x10^{-6} \pm 5.31x10^{-7}$		0.372	$1.07x10^{-6}$
LSE Linear	$6.42x10^{-6} \pm 3.30x10^{-6}$	$3.24x10^{-3} \pm 2.87x10^{-3}$	0.559	$9.99x10^{-7}$
LSE Arrhenius	$3.52x10^{-2} \pm 5.44x10^{-2}$	2383 ± 1444	0.573	$9.68x10^{-7}$
DVRT Constant	$2.11x10^{-3} \pm 4.39x10^{-4}$			$1.35x10^{-6}$
DVRT Linear	$2.36x10^{-6} \pm 2.96x10^{-7}$		0.582	$5.64x10^{-7}$
DVRT Linear	$5.86x10^{-6} \pm 7.64x10^{-7}$	$3.41x10^{-3} \pm 7.33x10^{-4}$	0.922	$1.27x10^{-7}$
DVRT Arrhenius	$2.84x10^{-2} \pm 1.35x10^{-2}$	2470 ± 495.1	0.905	$1.54x10^{-7}$

Table 5.4. Creep rate accumulated dose analysis

	$A \pm \sigma[A]$	$B \pm \sigma[B]$	R^2	Variance
1 dpa LSE Constant	$1.27\text{x}10^{-2} \pm 8.13\text{x}10^{-3}$			$6.58\text{x}10^{-2}$
1 dpa LSE Linear	$1.51\text{x}10^{-2} \pm 1.40\text{x}10^{-2}$		$-1.30\text{x}10^{-3}$	$6.59\text{x}10^{-2}$
1 dpa LSE Linear	$-1.54\text{x}10^{-2} \pm 2.79\text{x}10^{-2}$	$2.05\text{x}10^{-2} \pm 1.62\text{x}10^{-2}$	$3.06\text{x}10^{-4}$	$6.59\text{x}10^{-2}$
0.42 dpa LSE Constant	$2.31\text{x}10^{-2} \pm 1.69\text{x}10^{-3}$			$1.11\text{x}10^{-3}$
0.42 dpa LSE Linear	$8.41\text{x}10^{-2} \pm 7.12\text{x}10^{-3}$		$-8.97\text{x}10^{-2}$	$1.21\text{x}10^{-3}$
0.42 dpa LSE Linear	$9.34\text{x}10^{-3} \pm 1.43\text{x}10^{-2}$	$2.11\text{x}10^{-2} \pm 3.55\text{x}10^{-3}$	$1.10\text{x}10^{-3}$	$1.11\text{x}10^{-3}$
1 dpa DVRT Constant	$1.91\text{x}10^{-2} \pm 4.28\text{x}10^{-3}$			$1.70\text{x}10^{-2}$
1 dpa DVRT Linear	$2.32\text{x}10^{-2} \pm 7.34\text{x}10^{-3}$		$-1.07\text{x}10^{-3}$	$1.72\text{x}10^{-2}$
1 dpa DVRT Linear	$-2.06\text{x}10^{-2} \pm 1.47\text{x}10^{-2}$	$2.96\text{x}10^{-2} \pm 8.61\text{x}10^{-3}$	$2.13\text{x}10^{-3}$	$1.70\text{x}10^{-2}$
0.42 dpa DVRT Constant	$2.41\text{x}10^{-2} \pm 1.95\text{x}10^{-3}$			$1.32\text{x}10^{-3}$
0.42 dpa DVRT Linear	$8.63\text{x}10^{-2} \pm 7.66\text{x}10^{-3}$		$-5.51\text{x}10^{-2}$	$1.40\text{x}10^{-3}$
0.42 dpa DVRT Linear	$1.17\text{x}10^{-2} \pm 1.85\text{x}10^{-2}$	$2.13\text{x}10^{-2} \pm 4.82\text{x}10^{-3}$	$1.16\text{x}10^{-3}$	$1.33\text{x}10^{-3}$

Table 5.5. Summary of Cauchy fit centroid (C) and width (W) for the (0002) and (0004) peaks.

	As Received	1000°C 20MPa 0.25dpa	1000°C 20MPa 0.42dpa	1000°C 20MPa 1.00dpa	1000°C 0MPa 0.21dpa	1000°C 0MPa 0.25dpa	1000°C 5MPa 0.21dpa
C_{0002} (nm^{-1})	2.959 ± $1.8x10^{-4}$	2.951 ± $1.5x10^{-4}$	2.947 ± $1.8x10^{-4}$	2.943 ± $1.8x10^{-4}$	2.949 ± $1.5x10^{-4}$	2.950 ± $1.5x10^{-4}$	2.953 ± $1.5x10^{-4}$
W_{0002} (nm^{-1})	0.0199 ± $2.6x10^{-4}$	0.0263 ± $2.1x10^{-4}$	0.0308 ± $2.5x10^{-4}$	0.0280 ± $2.6x10^{-4}$	0.0249 ± $2.1x10^{-4}$	0.0255 ± $2.1x10^{-4}$	0.0254 ± $2.1x10^{-4}$
C_{0004} (nm^{-1})	5.920 ± $3.8x10^{-4}$	5.909 ± $3.6x10^{-4}$	5.906 ± $4.5x10^{-4}$	5.905 ± $4.2x10^{-4}$	5.907 ± $3.6x10^{-4}$	5.908 ± $3.6x10^{-4}$	5.911 ± $3.8x10^{-4}$
W_{0004} (nm^{-1})	0.0337 ± $5.5x10^{-4}$	0.0396 ± $5.3x10^{-4}$	0.0420 ± $6.6x10^{-4}$	0.0379 ± $6.2x10^{-4}$	0.0382 ± $5.3x10^{-4}$	0.0386 ± $5.2x10^{-4}$	0.0392 ± $5.6x10^{-4}$

	1000°C 10MPa 0.21dpa	1000°C 40MPa 0.25dpa	700°C 20MPa 0.28dpa	700°C 20MPa 0.19dpa	900°C 20MPa 0.14dpa	1100°C 20MPa 0.25dpa	1200°C 20MPa 0.34dpa
C_{0002} (nm^{-1})	2.952 ± $1.5x10^{-4}$	2.948 ± $1.5x10^{-4}$	2.964 ± $1.5x10^{-4}$	2.957 ± $1.6x10^{-4}$	2.950 ± $1.6x10^{-4}$	2.945 ± $1.6x10^{-4}$	2.943 ± $1.8x10^{-4}$
W_{0002} (nm^{-1})	0.0268 ± $2.2x10^{-4}$	0.0242 ± $2.1x10^{-4}$	0.0221 ± $2.2x10^{-4}$	0.0192 ± $2.3x10^{-4}$	0.0208 ± $2.3x10^{-4}$	0.0267 ± $2.3x10^{-4}$	0.0267 ± $2.5x10^{-4}$
C_{0004} (nm^{-1})	5.909 ± $3.8x10^{-4}$	5.908 ± $3.7x10^{-4}$	5.921 ± $3.4x10^{-4}$	5.918 ± $3.4x10^{-4}$	5.911 ± $3.6x10^{-4}$	5.903 ± $3.8x10^{-4}$	5.900 ± $4.1x10^{-4}$
W_{0004} (nm^{-1})	0.0407 ± $5.6x10^{-4}$	0.0372 ± $5.4x10^{-4}$	0.0345 ± $5.0x10^{-4}$	0.0317 ± $5.0x10^{-4}$	0.0336 ± $5.2x10^{-4}$	0.0410 ± $5.7x10^{-4}$	0.0396 ± $6.0x10^{-4}$

	700°C 0MPa 0.28dpa	700°C 0MPa 0.19dpa	900°C 0MPa 0.14dpa	1100°C 0MPa 0.25dpa	1200°C 0MPa 0.34dpa	1000°C 0MPa 0.88dpa
C_{0002} (nm^{-1})	2.972 ± $1.7x10^{-4}$	2.959 ± $1.6x10^{-4}$	2.960 ± $1.6x10^{-4}$	2.951 ± $1.6x10^{-4}$	2.952 ± $1.7x10^{-4}$	2.936 ± $3.1x10^{-4}$
W_{0002} (nm^{-1})	0.0207 ± $2.5x10^{-4}$	0.0193 ± $2.3x10^{-4}$	0.0215 ± $2.2x10^{-4}$	0.0261 ± $2.3x10^{-4}$	0.0260 ± $2.4x10^{-4}$	0.0368 ± $4.4x10^{-4}$
C_{0004} (nm^{-1})	5.929 ± $3.5x10^{-4}$	5.919 ± $3.7x10^{-4}$	5.918 ± $3.3x10^{-4}$	5.908 ± $3.8x10^{-4}$	5.911 ± $3.9x10^{-4}$	5.895 ± $5.0x10^{-4}$
W_{0004} (nm^{-1})	0.0348 ± $5.0x10^{-4}$	0.0324 ± $5.3x10^{-4}$	0.0347 ± $4.7x10^{-4}$	0.0411 ± $5.6x10^{-4}$	0.0382 ± $5.7x10^{-4}$	0.0437 ± $7.5x10^{-4}$

Table 5.6. Summary of Cauchy fit centroid (C) and width (W) for the $(11\bar{2}0)$ peaks.

	As Received	1000°C 20MPa 0.25dpa	1000°C 20MPa 0.42dpa	1000°C 20MPa 1.00dpa	1000°C 0MPa 0.21dpa	1000°C 0MPa 0.25dpa	1000°C 5MPa 0.21dpa
$C_{11\bar{2}0}$ (nm^{-1})	8.135 ± $3.1x10^{-4}$	8.140 ± $1.8x10^{-4}$	8.143 ± $2.6x10^{-4}$	8.147 ± $2.8x10^{-4}$	8.149 ± $2.4x10^{-4}$	8.136 ± $1.9x10^{-4}$	8.144 ± $2.5x10^{-4}$
$W_{11\bar{2}0}$ (nm^{-1})	0.0176 ± $4.3x10^{-4}$	0.0246 ± $2.6x10^{-4}$	0.0258 ± $3.7x10^{-4}$	0.0293 ± $4.0x10^{-4}$	0.0220 ± $3.5x10^{-4}$	0.0230 ± $2.7x10^{-4}$	0.0221 ± $3.6x10^{-4}$

	1000°C 10MPa 0.21dpa	1000°C 40MPa 0.25dpa	700°C 20MPa 0.28dpa	700°C 20MPa 0.19dpa	900°C 20MPa 0.14dpa	1100°C 20MPa 0.25dpa	1200°C 20MPa 0.34dpa
$C_{11\bar{2}0}$ (nm^{-1})	8.142 ± $2.5x10^{-4}$	8.141 ± $2.4x10^{-4}$	8.143 ± $2.6x10^{-4}$	8.136 ± $2.6x10^{-4}$	8.139 ± $2.4x10^{-4}$	8.138 ± $2.4x10^{-4}$	8.141 ± $2.9x10^{-4}$
$W_{11\bar{2}0}$ (nm^{-1})	0.0233 ± $3.5x10^{-4}$	0.0239 ± $3.4x10^{-4}$	0.0216 ± $3.8x10^{-4}$	0.0206 ± $3.7x10^{-4}$	0.0206 ± $3.5x10^{-4}$	0.0253 ± $3.5x10^{-4}$	0.0262 ± $4.2x10^{-4}$

	700°C 0MPa 0.28dpa	700°C 0MPa 0.19dpa	900°C 0MPa 0.14dpa	1100°C 0MPa 0.25dpa	1200°C 0MPa 0.34dpa	1000°C 0MPa 0.88dpa
$C_{11\bar{2}0}$ (nm^{-1})	8.146 ± $2.8x10^{-4}$	8.138 ± $2.8x10^{-4}$	8.138 ± $2.6x10^{-4}$	8.141 ± $2.5x10^{-4}$	8.139 ± $3.1x10^{-4}$	8.135 ± $6.6x10^{-4}$
$W_{11\bar{2}0}$ (nm^{-1})	0.0196 ± $4.1x10^{-4}$	0.0204 ± $3.9x10^{-4}$	0.0211 ± $3.6x10^{-4}$	0.0238 ± $3.6x10^{-4}$	0.0241 ± $4.5x10^{-4}$	0.0337 ± $9.7x10^{-4}$

Table 5.7. Summary of d-spacing for the (0002) and (0004) peaks, the c-axis crystal lattice parameter and % change from as-received.

	As Received	1000°C 20MPa 0.25dpa	1000°C 20MPa 0.42dpa	1000°C 20MPa 1.00dpa	1000°C 0MPa 0.21dpa	1000°C 0MPa 0.25dpa	1000°C 5MPa 0.21dpa
d_{0002} (Å)	3.380 ± 2.1x10^{-4}	3.389 ± 1.7x10^{-4}	3.393 ± 2.1x10^{-4}	3.398 ± 2.1x10^{-4}	3.391 ± 1.7x10^{-4}	3.390 ± 1.7x10^{-4}	3.386 ± 1.7x10^{-4}
d_{0004} (Å)	1.689 ± 1.1x10^{-4}	1.692 ± 1.0x10^{-4}	1.693 ± 1.3x10^{-4}	1.693 ± 1.2x10^{-4}	1.693 ± 1.0x10^{-4}	1.693 ± 1.0x10^{-4}	1.692 ± 1.1x10^{-4}
c (Å)	6.759 ± 4.2x10^{-4}	6.777 ± 3.4x10^{-4}	6.787 ± 4.1x10^{-4}	6.796 ± 4.2x10^{-4}	6.782 ± 3.5x10^{-4}	6.780 ± 3.4x10^{-4}	6.773 ± 3.4x10^{-4}
$\Delta c/c_i$ (%)	0.000 ± 8.7x10^{-3}	0.271 ± 8.0x10^{-3}	0.407 ± 8.7x10^{-3}	0.544 ± 8.8x10^{-3}	0.339 ± 8.0x10^{-3}	0.305 ± 7.9x10^{-3}	0.203 ± 8.0x10^{-3}

	1000°C 10MPa 0.21dpa	1000°C 40MPa 0.25dpa	700°C 20MPa 0.28dpa	700°C 20MPa 0.19dpa	900°C 20MPa 0.14dpa	1100°C 20MPa 0.25dpa	1200°C 20MPa 0.34dpa
d_{0002} (Å)	3.386 ± 1.8x10^{-4}	3.388 ± 1.7x10^{-4}	3.392 ± 1.8x10^{-4}	3.374 ± 1.9x10^{-4}	3.382 ± 1.8x10^{-4}	3.390 ± 1.9x10^{-4}	3.396 ± 2.0x10^{-4}
d_{0004} (Å)	1.692 ± 1.1x10^{-4}	1.692 ± 1.1x10^{-4}	1.693 ± 9.8x10^{-5}	1.689 ± 9.8x10^{-5}	1.690 ± 1.0x10^{-4}	1.692 ± 1.1x10^{-4}	1.694 ± 1.2x10^{-4}
c (Å)	6.773 ± 3.4x10^{-4}	6.775 ± 3.5x10^{-4}	6.784 ± 3.4x10^{-4}	6.748 ± 3.6x10^{-4}	6.764 ± 3.7x10^{-4}	6.780 ± 3.6x10^{-4}	6.791 ± 3.8x10^{-4}
$\Delta c/c_i$ (%)	0.203 ± 8.0x10^{-3}	0.237 ± 8.1x10^{-3}	0.373 ± 8.0x10^{-3}	-0.169 ± 8.1x10^{-3}	0.068 ± 8.3x10^{-3}	0.305 ± 8.2x10^{-3}	0.475 ± 8.3x10^{-3}

	700°C 0MPa 0.28dpa	700°C 0MPa 0.19dpa	900°C 0MPa 0.14dpa	1100°C 0MPa 0.25dpa	1200°C 0MPa 0.34dpa	1000°C 0MPa 0.88dpa
d_{0002} (Å)	3.365 ± 2.0x10^{-4}	3.380 ± 1.8x10^{-4}	3.378 ± 1.8x10^{-4}	3.389 ± 1.8x10^{-4}	3.388 ± 2.0x10^{-4}	3.406 ± 3.5x10^{-4}
d_{0004} (Å)	1.687 ± 9.8x10^{-5}	1.689 ± 1.1x10^{-4}	1.690 ± 9.3x10^{-5}	1.693 ± 1.1x10^{-4}	1.692 ± 1.1x10^{-4}	1.696 ± 1.4x10^{-4}
c (Å)	6.729 ± 3.9x10^{-4}	6.759 ± 3.7x10^{-4}	6.757 ± 3.6x10^{-4}	6.777 ± 3.7x10^{-4}	6.775 ± 3.9x10^{-4}	6.812 ± 7.1x10^{-4}
$\Delta c/c_i$ (%)	-0.437 ± 8.4x10^{-3}	0.000 ± 8.2x10^{-3}	-0.034 ± 8.1x10^{-3}	0.271 ± 8.2x10^{-3}	0.237 ± 8.5x10^{-3}	0.783 ± 1.2x10^{-2}

Table 5.8. Summary of d-spacing for the $(11\bar{2}0)$ peaks, the a-axis lattice parameter, and atomic spacing and % change from as-received.

	As Received	1000°C 20MPa 0.25dpa	1000°C 20MPa 0.42dpa	1000°C 20MPa 1.00dpa	1000°C 0MPa 0.21dpa	1000°C 0MPa 0.25dpa	1000°C 5MPa 0.21dpa
$d_{11\bar{2}0}$ (Å)	1.229 ± 4.6×10^{-5}	1.229 ± 2.8×10^{-5}	1.228 ± 3.9×10^{-5}	1.227 ± 4.2×10^{-5}	1.227 ± 3.7×10^{-5}	1.229 ± 2.8×10^{-5}	1.228 ± 3.8×10^{-5}
a (Å)	2.459 ± 9.2×10^{-5}	2.457 ± 5.6×10^{-5}	2.456 ± 7.8×10^{-5}	2.455 ± 8.4×10^{-5}	2.454 ± 7.3×10^{-5}	2.458 ± 5.7×10^{-5}	2.456 ± 7.6×10^{-5}
a_0 (Å)	1.419 ± 5.3×10^{-5}	1.419 ± 3.2×10^{-5}	1.418 ± 4.5×10^{-5}	1.417 ± 4.8×10^{-5}	1.417 ± 4.2×10^{-5}	1.419 ± 3.3×10^{-5}	1.418 ± 4.4×10^{-5}
$\Delta a_0/a_{0_i}$ (%)	0.000 ± 5.3×10^{-3}	-0.061 ± 4.4×10^{-3}	-0.098 ± 4.9×10^{-3}	-0.147 ± 5.1×10^{-3}	-0.172 ± 4.8×10^{-3}	-0.012 ± 4.4×10^{-3}	-0.111 ± 4.9×10^{-3}

	1000°C 10MPa 0.21dpa	1000°C 40MPa 0.25dpa	700°C 20MPa 0.28dpa	700°C 20MPa 0.19dpa	900°C 20MPa 0.14dpa	1100°C 20MPa 0.25dpa	1200°C 20MPa 0.34dpa
$d_{11\bar{2}0}$ (Å)	1.228 ± 3.7×10^{-5}	1.228 ± 3.6×10^{-5}	1.228 ± 4.0×10^{-5}	1.229 ± 4.0×10^{-5}	1.229 ± 3.7×10^{-5}	1.229 ± 3.6×10^{-5}	1.228 ± 4.4×10^{-5}
a (Å)	2.456 ± 7.4×10^{-5}	2.457 ± 7.2×10^{-5}	2.456 ± 7.9×10^{-5}	2.458 ± 7.9×10^{-5}	2.457 ± 7.3×10^{-5}	2.458 ± 7.3×10^{-5}	2.457 ± 8.8×10^{-5}
a_0 (Å)	1.418 ± 4.3×10^{-5}	1.418 ± 4.1×10^{-5}	1.418 ± 4.6×10^{-5}	1.419 ± 4.6×10^{-5}	1.419 ± 4.2×10^{-5}	1.419 ± 4.2×10^{-5}	1.418 ± 5.1×10^{-5}
$\Delta a_0/a_{0_i}$ (%)	-0.086 ± 4.8×10^{-3}	-0.074 ± 4.8×10^{-3}	-0.098 ± 5.0×10^{-3}	-0.012 ± 5.0×10^{-3}	-0.049 ± 4.8×10^{-3}	-0.037 ± 4.8×10^{-3}	-0.074 ± 5.2×10^{-3}

	700°C 0MPa 0.28dpa	700°C 0MPa 0.19dpa	900°C 0MPa 0.14dpa	1100°C 0MPa 0.25dpa	1200°C 0MPa 0.34dpa	1000°C 0MPa 0.88dpa
$d_{11\bar{2}0}$ (Å)	1.228 ± 4.3×10^{-5}	1.229 ± 4.2×10^{-5}	1.229 ± 3.9×10^{-5}	1.228 ± 3.8×10^{-5}	1.229 ± 4.7×10^{-5}	1.229 ± 1.0×10^{-4}
a (Å)	2.455 ± 8.6×10^{-5}	2.458 ± 8.4×10^{-5}	2.458 ± 7.7×10^{-5}	2.457 ± 7.6×10^{-5}	2.457 ± 9.4×10^{-5}	2.459 ± 2.0×10^{-4}
a_0 (Å)	1.418 ± 5.0×10^{-5}	1.419 ± 4.8×10^{-5}	1.419 ± 4.5×10^{-5}	1.418 ± 4.4×10^{-5}	1.419 ± 5.5×10^{-5}	1.419 ± 1.2×10^{-4}
$\Delta a_0/a_{0_i}$ (%)	-0.135 ± 5.1×10^{-3}	-0.037 ± 5.1×10^{-3}	-0.037 ± 4.9×10^{-3}	-0.074 ± 4.9×10^{-3}	-0.049 ± 5.4×10^{-3}	0.000 ± 8.9×10^{-3}

Table 5.9. Summary of c-axis crystallite size and % change from as-received, c-axis lattice strain and % change from as-received.

	As Received	1000°C 20MPa 0.25dpa	1000°C 20MPa 0.42dpa	1000°C 20MPa 1.00dpa	1000°C 0MPa 0.21dpa	1000°C 0MPa 0.25dpa	1000°C 5MPa 0.21dpa
L_c (nm)	164.49 ± 42.75	77.45 ± 8.18	51.08 ± 4.34	55.18 ± 4.99	85.54 ± 10.08	79.78 ± 8.57	86.86 ± 10.60
$\Delta L_c / L_{c_i}$ (%)	0.00 ± 36.75	-52.92 ± 13.21	-68.94 ± 8.49	-66.46 ± 9.23	-48.00 ± 14.84	-51.50 ± 13.64	-47.20 ± 15.16
ε_c (%)	0.233 ± 4.6x10^{-3}	0.226 ± 4.2x10^{-3}	0.190 ± 5.2x10^{-3}	0.167 ± 5.0x10^{-3}	0.225 ± 4.3x10^{-3}	0.220 ± 4.2x10^{-3}	0.234 ± 4.4x10^{-3}
$\Delta\varepsilon_c / \varepsilon_{c_i}$ (%)	0.000 ± 2.80	-3.09 ± 2.64	-18.70 ± 2.75	-28.27 ± 2.57	-3.69 ± 2.64	-5.55 ± 2.58	0.464 ± 2.75

	1000°C 10MPa 0.21dpa	1000°C 40MPa 0.25dpa	700°C 20MPa 0.28dpa	700°C 20MPa 0.19dpa	900°C 20MPa 0.14dpa	1100°C 20MPa 0.25dpa	1200°C 20MPa 0.34dpa
L_c (nm)	77.20 ± 8.49	89.18 ± 10.91	103.84 ± 14.94	147.34 ± 30.72	124.11 ± 21.71	79.79 ± 9.42	72.20 ± 8.25
$\Delta L_c / L_{c_i}$ (%)	-53.07 ± 13.24	-45.78 ± 15.57	-36.87 ± 18.75	-10.42 ± 29.85	-24.55 ± 23.64	-51.49 ± 13.85	-56.11 ± 12.46
ε_c (%)	0.235 ± 4.4x10^{-3}	0.220 ± 4.3x10^{-3}	0.210 ± 4.1x10^{-3}	0.210 ± 4.1x10^{-3}	0.216 ± 4.2x10^{-3}	0.241 ± 4.6x10^{-3}	0.218 ± 4.9x10^{-3}
$\Delta\varepsilon_c / \varepsilon_{c_i}$ (%)	0.715 ± 2.76	-5.76 ± 2.62	-9.80 ± 2.51	-9.78 ± 2.52	-7.53 ± 2.58	3.36 ± 2.83	-6.39 ± 2.79

	700°C 0MPa 0.28dpa	700°C 0MPa 0.19dpa	900°C 0MPa 0.14dpa	1100°C 0MPa 0.25dpa	1200°C 0MPa 0.34dpa	1000°C 0MPa 0.88dpa
L_c (nm)	154.84 ± 35.67	162.48 ± 38.27	119.03 ± 19.28	89.60 ± 11.68	72.16 ± 7.99	33.37 ± 2.74
$\Delta L_c / L_{c_i}$ (%)	-5.87 ± 32.69	-1.22 ± 34.65	-27.64 ± 22.16	-45.53 ± 15.84	-56.13 ± 12.39	-79.71 ± 5.53
ε_c (%)	0.239 ± 4.3x10^{-3}	0.222 ± 4.4x10^{-3}	0.222 ± 4.0x10^{-3}	0.253 ± 4.5x10^{-3}	0.206 ± 4.6x10^{-3}	0.117 ± 6.8x10^{-3}
$\Delta\varepsilon_c / \varepsilon_{c_i}$ (%)	2.60 ± 2.73	-4.82 ± 2.65	-4.90 ± 2.54	8.47 ± 2.88	-11.67 ± 2.64	-50.00 ± 3.06

Table 5.10. Summary of a-axis crystallite size and % change from as-received.

	As Received	1000°C 20MPa 0.25dpa	1000°C 20MPa 0.42dpa	1000°C 20MPa 1.00dpa	1000°C 0MPa 0.21dpa	1000°C 0MPa 0.25dpa	1000°C 5MPa 0.21dpa
L_a (nm)	56.85 ± 1.40	40.73 ± 0.44	38.71 ± 0.56	34.18 ± 0.47	45.37 ± 0.71	43.50 ± 0.51	45.23 ± 0.74
$\Delta L_a / L_{a_i}$ (%)	0.00 ± 3.49	-28.35 ± 1.93	-31.90 ± 1.95	-39.88 ± 1.70	-20.19 ± 2.34	-23.49 ± 2.09	-20.44 ± 2.35

	1000°C 10MPa 0.21dpa	1000°C 40MPa 0.25dpa	700°C 20MPa 0.28dpa	700°C 20MPa 0.19dpa	900°C 20MPa 0.14dpa	1100°C 20MPa 0.25dpa	1200°C 20MPa 0.34dpa
L_a (nm)	42.84 ± 0.64	41.91 ± 0.60	46.34 ± 0.80	48.54 ± 0.88	48.59 ± 0.82	39.46 ± 0.54	38.11 ± 0.60
$\Delta L_a / L_{a_i}$ (%)	-24.64 ± 2.18	-26.28 ± 2.10	-18.49 ± 2.46	-14.61 ± 2.62	-14.53 ± 2.55	-30.58 ± 1.96	-32.96 ± 1.97

	700°C 0MPa 0.28dpa	700°C 0MPa 0.19dpa	900°C 0MPa 0.14dpa	1100°C 0MPa 0.25dpa	1200°C 0MPa 0.34dpa	1000°C 0MPa 0.88dpa
L_a (nm)	51.12 ± 1.06	49.12 ± 0.95	47.35 ± 0.82	42.00 ± 0.64	41.55 ± 0.77	29.64 ± 0.86
$\Delta L_a / L_{a_i}$ (%)	-10.07 ± 2.90	-13.61 ± 2.71	-16.71 ± 2.51	-26.12 ± 2.14	-26.92 ± 2.26	-47.87 ± 1.98

Table 5.11. Lattice Parameters vs. Accumulated Dose Analysis

	A ± σ[A]	B ± σ[B]	R^2	Variance
$\Delta c/c_i$ (%) Linear	0.6316 ± 0.1046		0.748	1.36×10^{-2}
$\Delta c/c_i$ (%) Plateau	0.5893 ± 0.02252	2.627 ± 0.233	0.998	1.74×10^{-4}
$\Delta a_0/a_{0_i}$ (%) Linear	-0.1646 ± 0.02047		0.865	5.19×10^{-4}
$\Delta a_0/a_{0_i}$ (%) Plateau	$-0.1755 \pm 9.57 \times 10^{-3}$	1.851 ± 0.198	0.998	1.24×10^{-5}

Table 5.12. C-spacing variation vs. Accumulated Dose Analysis

	A ± σ[A]	B ± σ[B]	R^2	Variance
$2\varepsilon_c d$ (Å) Constant	$2.77\text{x}10^{-2}$ ± $2.08\text{x}10^{-3}$			$1.72\text{x}10^{-5}$
$2\varepsilon_c d$ (Å) Linear	$-9.20\text{x}10^{-3}$ ± $2.33\text{x}10^{-3}$	$3.15\text{x}10^{-2}$ ± $1.30\text{x}10^{-3}$	0.887	$2.93\text{x}10^{-6}$
$2\varepsilon_c d$ (Å) Plateau	$9.20\text{x}10^{-3}$ ± $4.62\text{x}10^{-2}$	0.513 ± 1.324	0.896	$2.70\text{x}10^{-6}$

Table 5.13. Crystallite Size vs. Accumulated Dose Analysis

	A ± σ[A]	B ± σ[B]	R^2	Variance
L_c (nm) Linear	-91.16 ± 59.98	125.10 ± 33.38	0.536	1948.5
L_c (nm) Plateau	51.25 ± 6.21	6.52 ± 1.55	0.990	43.2
L_a (nm) Linear	-19.48 ± 8.96	50.75 ± 4.99	0.703	43.5
L_a (nm) Plateau	34.34 ± 1.08	4.57 ± 0.695	0.993	0.965

Table 5.14. Lattice Parameters vs. Stress Analysis

	A ± σ[A]	B ± σ[B]	R^2	Variance
$\Delta c/c_i$ (%) Constant	$0.288 \pm 2.60\text{x}10^{-2}$			$4.04\text{x}10^{-3}$
$\Delta c/c_i$ (%) Linear	$1.79\text{x}10^{-3} \pm 1.86\text{x}10^{-3}$	$0.266 \pm 3.50\text{x}10^{-2}$	0.188	$4.10\text{x}10^{-3}$
$\Delta a_0/a_{0_i}$ (%) Constant	$-8.60\text{x}10^{-2} \pm 2.17\text{x}10^{-2}$			$2.83\text{x}10^{-3}$
$\Delta a_0/a_{0_i}$ (%) Linear	$7.22\text{x}10^{-4} \pm 1.69\text{x}10^{-3}$	$-9.50\text{x}10^{-2} \pm 3.18\text{x}10^{-2}$	0.044	$3.38\text{x}10^{-3}$

Table 5.15. C-spacing variation vs. Stress Analysis

	A ± σ[A]	B ± σ[B]	R^2	Variance
$2\varepsilon_c d$ (Å) Constant	$3.07\text{x}10^{-2} \pm 3.59\text{x}10^{-4}$			$7.73\text{x}10^{-7}$
$2\varepsilon_c d$ (Å) Linear	$-1.85\text{x}10^{-5} \pm 2.70\text{x}10^{-5}$	$3.10\text{x}10^{-2} \pm 5.08\text{x}10^{-4}$	0.105	$8.64\text{x}10^{-7}$

Table 5.16. Crystallite Size vs. Stress Analysis

	A ± σ[A]	B ± σ[B]	R^2	Variance
L_c (nm) Constant	82.67 ± 2.11			26.76
L_c (nm) Linear	0.103 ± 0.1597	81.38 ± 3.01	0.095	30.28
L_a (nm) Constant	43.26 ± 0.748			3.354
L_a (nm) Linear	$-8.35 \times 10^{-2} \pm 4.23 \times 10^{-2}$	44.31 ± 0.796	0.494	2.123

Table 5.17. Lattice Parameters vs. Temp Analysis

	A ± σ[A]	B ± σ[B]	R^2	Variance
$\Delta c/c_i$ (%) Constant	0.399 ± 0.0658			1.73×10^{-2}
$\Delta c/c_i$ (%) Linear	$9.20 \times 10^{-4} \pm 3.10 \times 10^{-4}$	-0.567 ± 0.328	0.815	1.07×10^{-2}
$\Delta c/c_i$ (%) Arrhenius	5.051 ± 4.242	2676 ± 916.4	0.825	4.54×10^{-3}
$\Delta a_0/a_{0_i}$ (%) Constant	$-5.53 \times 10^{-2} \pm 7.93 \times 10^{-3}$			2.51×10^{-4}
$\Delta a_0/a_{0_i}$ (%) Linear	$-4.91 \times 10^{-5} \pm 7.96 \times 10^{-5}$	$-3.73 \times 10^{-3} \pm 8.40 \times 10^{-2}$	0.160	3.17×10^{-4}
$\Delta a_0/a_{0_i}$ (%) Arrhenius	-0.1385 ± 0.2118	958.5 ± 1613	0.144	3.23×10^{-4}

Table 5.18. c-spacing variation vs. Temp Analysis

	A ± σ[A]	B ± σ[B]	R^2	Variance
$2\varepsilon_c d$ (Å) Constant	$3.06\text{x}10^{-2} \pm 7.79\text{x}10^{-4}$			$2.43\text{x}10^{-6}$
$2\varepsilon_c d$ (Å) Linear	$3.40\text{x}10^{-6} \pm 8.19\text{x}10^{-6}$	$2.70\text{x}10^{-2} \pm 8.65\text{x}10^{-3}$	0.079	$3.36\text{x}10^{-6}$
$2\varepsilon_c d$ (Å) Arrhenius	$3.51\text{x}10^{-2} \pm 9.63\text{x}10^{-3}$	144.8 ± 283.7	0.118	$3.21\text{x}10^{-6}$

Table 5.19. Crystallite Size vs. Temp Analysis

	A ± σ[A]	B ± σ[B]	R^2	Variance
L_c (nm) Constant	88.39 ± 12.01			577
L_c (nm) Linear	-0.1534 ± 0.0745	249.5 ± 78.68	0.679	277
L_c (nm) Arrhenius	11.63 ± 8.362	-2080 ± 709.9	0.801	169
L_a (nm) Constant	41.72 ± 2.351			22.1
L_a (nm) Linear	$-3.27\text{x}10^{-2} \pm 1.13\text{x}10^{-2}$	76.07 ± 11.95	0.807	6.40
L_a (nm) Arrhenius	17.63 ± 3.851	-889.6 ± 221	0.887	3.74

Table 5.20. Values used for indexing 33.4º and 43.8º peaks for the cubic diamond structure.

2θ	d (Å)	h	k	l	$d_{Diamond}$	$d_{Diamond}$*
33.4º	2.68	2	0	0	2.52	2.62
43.8º	2.07	1	1	1	2.06	2.13

Table 5.21. Values used for indexing XRD peaks for graphite.

2θ	d (Å)	h	k	l	$d_{Hexagonal}$	$d_{Rhombohedral}$
33.4º	2.68	0.8	0	0	2.66	2.66
43.8º	2.07	1	0	1	2.03	2.08
34.8º	2.58	0	0	4	1.68	2.52
40.4º	2.23	0	0	3	2.24	3.35

Table 5.22. Young's modulus dependence on accumulated dose analysis

	A ± σ[A]	B ± σ[B]	R^2	Variance
Young's (GPa) Constant	7.929 ± 0.505			0.765
Young's (GPa) Linear	0.817 ± 1.538	7.542 ± 0.963	0.220	1.193
Hardness (MPa) Constant	609.5 ± 42.92			5526
Hardness (MPa) Linear	105.9 ± 103.4	559.3 ± 64.76	0.512	5392

Table 5.23. Young's modulus dependence on stress analysis

	A ± σ[A]	B ± σ[B]	R^2	Variance
Young's (GPa) Constant	7.190 ± 0.5896			1.390
Young's (GPa) Linear	$-6.37 \times 10^{-2} \pm 1.12 \times 10^{-2}$	8.225 ± 0.251	0.942	0.121
Hardness (MPa) Constant	531.4 ± 49.90			9961
Hardness (MPa) Linear	-4.424 ± 2.375	603.3 ± 53.43	0.634	5463

Table 5.24. Young's modulus dependence on temperature analysis

	A ± σ[A]	B ± σ[B]	R^2	Variance
Young's (GPa) Constant	6.285 ± 1.002			3.011
Young's (GPa) Linear	9.66×10^{-3} ± 5.97×10^{-3}	-3.698 ± 6.218	0.723	1.665
Young's (GPa) Arrhenius	30.08 ± 28.61	1611 ± 1006	0.736	1.587
Hardness (MPa) Constant	482.6 ± 85.8			22087
Hardness (MPa) Linear	0.826 ± 0.514	-370.9 ± 535.2	0.721	12339
Hardness (MPa) Arrhenius	2712 ± 2918	1778 ± 1143	0.728	12007

Table 5.25. Calculated collision values for PKA interaction, from [78]

T_1 (eV)	T_2 (eV)	T_L (eV)	R^* (eV)	λ (nm)	R_{PKA} (nm)
500	136	11		0.98	
1,000	196	12		1.11	6.7
5,000	368	13	200	1.80	21.0
10,000	415	14	405	2.25	25.0
50,000	424	18	1600	4.52	130
100,000	382	22	3100	6.46	235
500,000	297	39	15,140	17.3	790
1,000,000	282	50	32,800	28.5	1365

Table 5.26. Conversion factors from neutron fluence (n/cm^2) to dose (dpa) for common fluence designations from [75].

Neutron Fluence for given energy	Conversion factor to dpa
n/cm^2 [E>50keV]	6.8×10^{-22}
n/cm^2 [E>0.1MeV]	7.3×10^{-22}
n/cm^2 [E>0.18MeV]	8.9×10^{-22}
n/cm^2 [E>1.0MeV]	14.5×10^{-22}
n/cm^2 [Equivalent DIDO Nickel Dose (EDN and EDND)]	13.1×10^{-22}
Calder Equivalent (MWd/Ate)	1.43×10^{-4}

Table 5.27. Statistical analysis results for dose rate effects on kE_0 for proton and neutron irradiations at constant stress.

	A ± σ[A]	B ± σ[B]	R^2	Variance
LSE Constant	24.97 ± 3.687			81.54
LSE Linear	$3.31x10^7$ ± $3.87x10^7$	11.47 ± 16.25	0.154	86.23
DVRT Constant	11.65 ± 2.482			24.63
DVRT Linear	$3.30x10^7$ ± $4.59x10^7$	0.1327 ± 16.21	0.206	29.33
SM1-24 3.3MPa Constant	2.505 ± 0.2464			0.243
SM1-24 3.3MPa Linear	$-4.21x10^7$ ± $1.27x10^7$	6.167 ± 1.106	0.847	0.056
SM1-24 4.5MPa Constant	2.910 ± 0.0620			0.023
SM1-24 4.5MPa Linear	$5.78x10^6$ ± $5.59x10^6$	2.399 ± 0.498	0.211	0.023
SM1-24 6.4MPa Constant	3.231 ± 0.397			0.472
SM1-24 6.4MPa Linear	$-6.75x10^7$ ± $4.11x10^7$	6.873 ± 2.239	0.729	0.256
IG-110 9MPa Constant	4.540 ± 0.31			
IG-110 9MPa Linear	$-3.7x10^7$	6.475		
IG-110 13.5MPa Constant	4.510 ± 0.81			
IG-110 13.5MPa Linear	$1.33x10^8$	-6.047		

Table 5.28. Summary of statistical analyses of temperature effects on kE_0

	A ± σ[A]	B ± σ[B]	R^2	Variance
LSE Constant	38.09 ± 5.673			257.4
LSE Linear	$9.33x10^{-2} \pm 2.97x10^{-2}$	-47.05 ± 27.36	0.622	113.6
LSE Arrhenius	486.9 ± 503.2	-2346 ± 998.5	0.632	110.5
DVRT Constant	39.53 ± 7.00			490.2
DVRT Linear	$9.83x10^{-2} \pm 3.54x10^{-2}$	-54.84 ± 34.41	0.491	280.9
DVRT Arrhenius	344.4 ± 365.7	-2072 ± 1083	0.477	288.8
Veringa Constant	3.96 ± 0.096			0.539
Veringa Linear	$1.49x10^{-3} \pm 3.50x10^{-4}$	2.62 ± 0.325	0.245	0.415
Veringa Arrhenius	5.30 ± 0.350	-241.4 ± 54.7	0.298	0.386
Dragon Constant	6.05 ± 0.365			1.065
Dragon Linear	$8.10x10^{-3} \pm 4.16x10^{-3}$	-3.488 ± 4.91	0.387	0.762
Dragon Arrhenius	29.2 ± 24.94	-1853 ± 1013	0.385	0.764
SM1-24 Constant	2.8670 ± 0.1224			0.210
SM1-24 Linear	$-3.01x10^{-3} \pm 4.63x10^{-3}$	5.51 ± 4.07	$3.40x10^{-2}$	0.219
SM1-24 Arrhenius	1.26 ± 1.70	720.7 ± 1182	$3.04x10^{-2}$	0.220
IG-110 Constant	4.400 ± 0.302			0.455
IG-110 Linear	$-1.61x10^{-3} \pm 4.11x10^{-3}$	5.87 ± 3.77	$4.86x10^{-2}$	0.576
IG-110 Arrhenius	3.104 ± 2.256	315.4 ± 649.6	$6.74x10^{-2}$	0.565

Table 5.29. Summary of neutron values corresponding to turn-around fluence, RCF, equivalent temperature, and kE_0 for the neutron creep experiments.

Temperature (ºC)	Fluence (n/m^2 E>0.1MeV)	Fluence (n/cm^2 E>0.18MeV)	RCF (ϕ_n/ϕ_γ)	Equivalent Temp ($\phi_\gamma=0$) (ºC)	kE_0 $(dpa)^{-1}$
600	$2.5x10^{26}$	$20.5x10^{21}$	0.156	950	2.65
900	$1x10^{26}$	$8.2x10^{21}$	0.154	1100	4.56

Table 5.30. Summary of proton creep experiment temperatures and kE_0 values. The value of kE_0 at 950ºC is linearly interpolated from experimental values at 900ºC and 1000ºC.

Temperature (ºC)	kE_0 $(dpa)^{-1}$ from DVRT
900	27.55
1100	51.51
950*	32.88

Table 5.31. Summary of comparison of neutron creep compliance and proton experiments at equivalent temperature.

Neutron Temperature (ºC)	Neutron kE_0 $(dpa)^{-1}$ f	Equivalent Temperature (ºC)	kE_0 $(dpa)^{-1}$ at Equivalent Temperature	Ratio kE_0^{ET}/ kE_0^{N}
600	2.65	950	32.88	12.41
900	4.56	1100	51.55	11.29

Table 5.32. Summary of thermodynamic quantities from Thrower and Mayer [7]

	Interstitial	Vacancy
S^f (k)	3	7
S^m (k)	4	7
E^f (eV)	7	7
E^m (eV)	0.1	3.1
v (s^{-1})	$4x10^{12}$	$5x10^{13}$

Table 5.33. Comparison of defect loss terms for the continuous and pulsed beam irradiations.

1000ºC	Damage Rate (dpa/s)	$K_{iv}C_iC_v$ (#/cm^{3}s)	$K_{is}C_iC_s$ (#/cm^{3}s)	$K_{vs}C_vC_s$ (#/cm^{3}s)	$\frac{K_{iv}C_iC_{vs}}{K_{is}C_iC + K_{iv}C_iC_{vs}}$
Constant Beam	1.17×10^{-6}	1.7×10^{10}	1.1×10^{17}	1.1×10^{17}	1.6×10^{-7}
Pulsed Beam	4.68×10^{-5}	2.7×10^{13}	4.2×10^{18}	4.2×10^{18}	6.5×10^{-6}
700ºC					
Constant Beam	4.38×10^{-7}	6.6×10^{12}	2.6×10^{16}	2.6×10^{16}	2.5×10^{-4}
Pulsed Beam	1.75×10^{-5}	1.0×10^{16}	1.0×10^{18}	1.0×10^{18}	9.8×10^{-3}

Table 5.34. Statistical analysis of defect concentrations and products of diffusion coefficients and concentrations.

	A ± σ[A]	B ± σ[A]	R^2	Variance
C_v Linear	$-1.9\times10^{-9} \pm 7.56\times10^{-10}$	$2.51\times10^{-6} \pm 9.57\times10^{-7}$	0.666	9.19×10^{-12}
C_v Arrhenius	$3.19\times10^{-20} \pm 2.54\times10^{-25}$	$30.21 \pm 8.90\times10^{-3}$	1	4.35×10^{-18}
C_i Linear	$1.27\times10^{-23} \pm 5.21\times10^{-25}$	$-1.1\times10^{-20} \pm 6.59\times10^{-22}$	0.995	4.27×10^{-40}
C_i Arrhenius	$1.44\times10^{-19} \pm 9.51\times10^{-22}$	-4235 ± 92.58	0.999	5.19×10^{-41}
D_vC_v Linear	$5.54\times10^{-24} \pm 4.36\times10^{-25}$	$-5.1\times10^{-21} \pm 5.51\times10^{-22}$	0.982	8.18×10^{-41}
D_vC_v Arrhenius	$1.25\times10^{-19} \pm 6.7\times10^{-22}$	-5361 ± 86.76	1	7.45×10^{-42}
D_iC_i Linear	$5.54\times10^{-24} \pm 4.36\times10^{-25}$	$-5.1\times10^{-21} \pm 5.51\times10^{-22}$	0.982	8.19×10^{-41}
D_iC_i Arrhenius	$1.25\times10^{-19} \pm 6.7\times10^{-22}$	-5361 ± 86.76	1	7.45×10^{-42}

Table 5.35. Tally of mechanisms and how they compare with macroscopic creep trends.

	Pinning-Unpinning	SIPN	SIPA	PAG	CGDB
$\dot{\varepsilon}$ linear with stress	Agree	Agree	Agree	Disagree	Disagree
$\dot{\varepsilon}$ linear with dose rate	Disagree	Agree	Agree	Agree	Agree
$\dot{\varepsilon}$ Arrhenius with temperature	Agree	Disagree	Agree	Agree	Agree
$\dot{\varepsilon}$ constant with dose	Disagree	Disagree	Agree	Agree	Agree

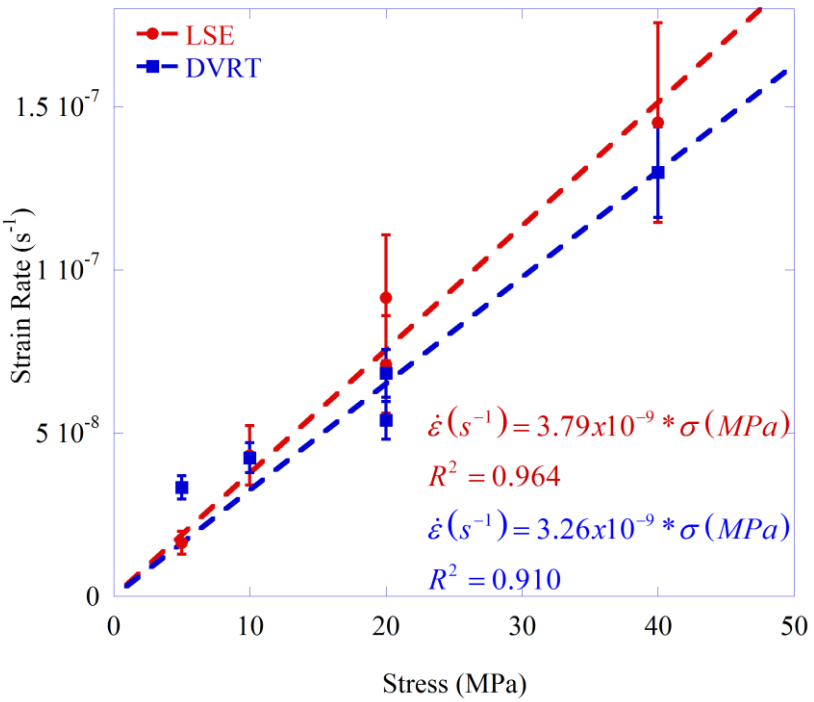

Figure 5.1. Plot of creep strain rate versus applied tensile stress data and linear fits.

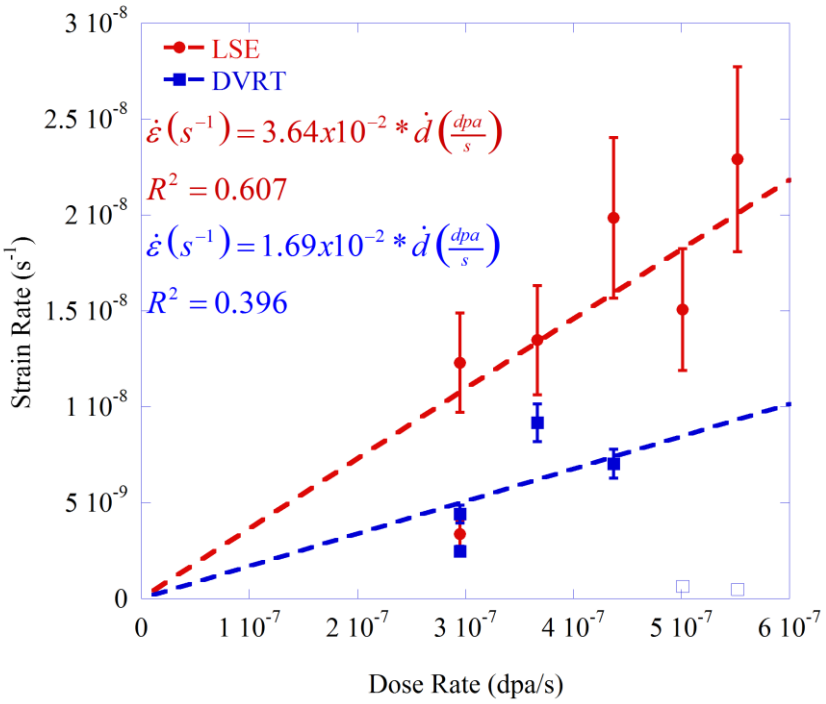

Figure 5.2. Plot of creep strain rate versus dose rate, with linear fits.

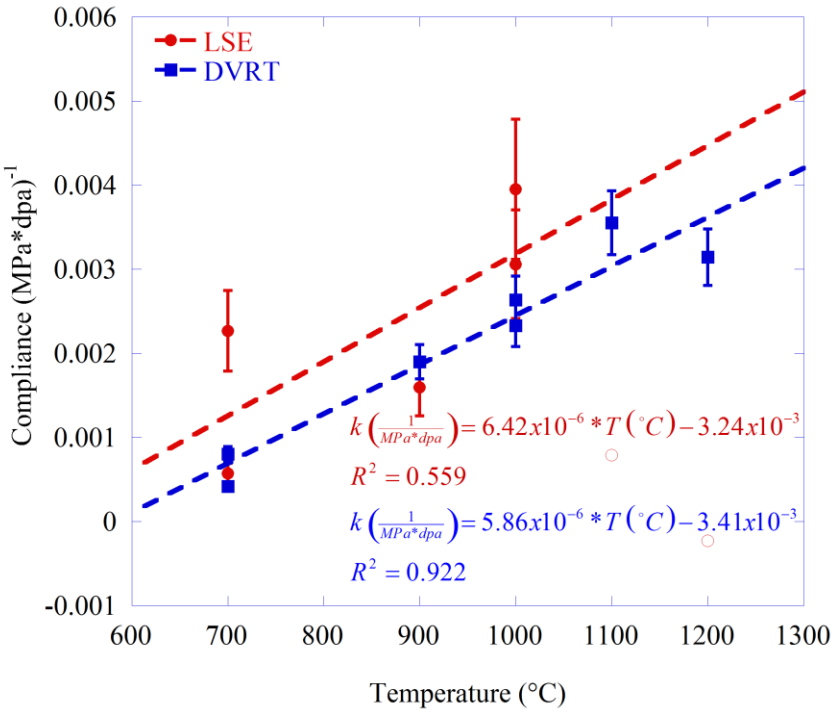

Figure 5.3. Plot of creep compliance versus temperatures, with best-fit trend lines and the equations of fit.

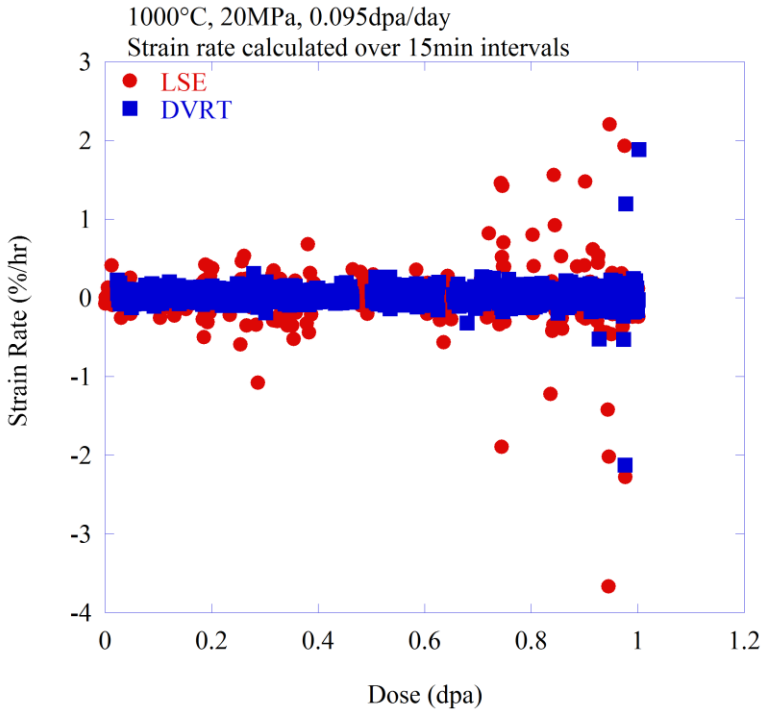

(a)

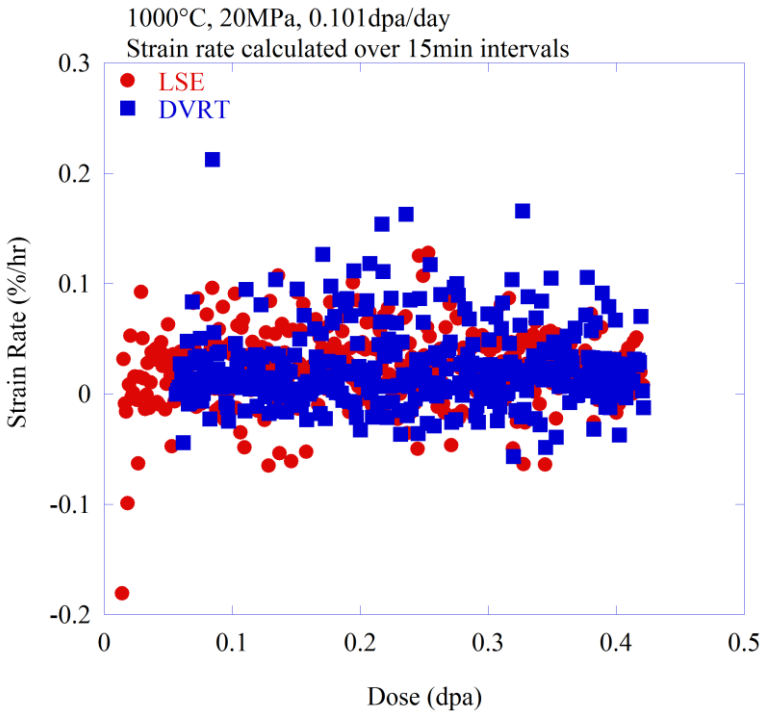

(b)

Figure 5.4. Strain rate versus dose from the experiments performed at 1000ºC, 20MPa stress, to final doses of 1.0 dpa (a) and 0.42 dpa (b).

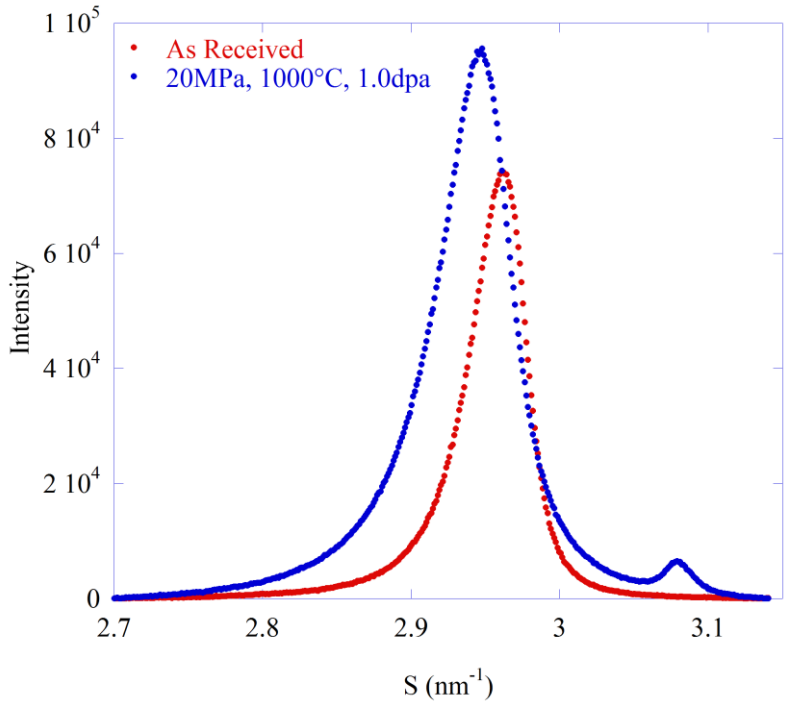

(a)

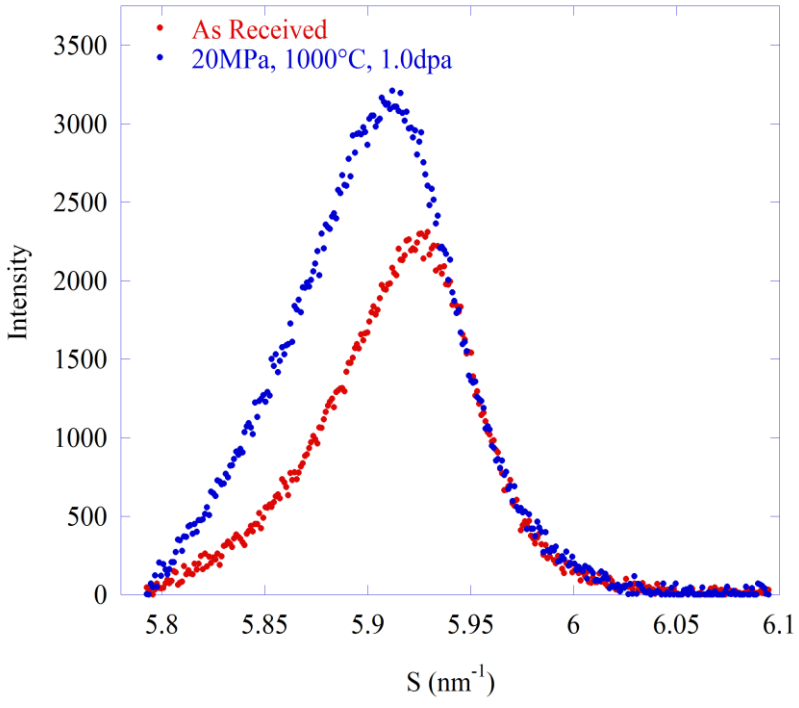

(b)

Figure 5.5. Example plots of the (0002) (a) and (0004) (b) peaks from the as-received sample (red) and the creep sample from experiment #2 (blue)

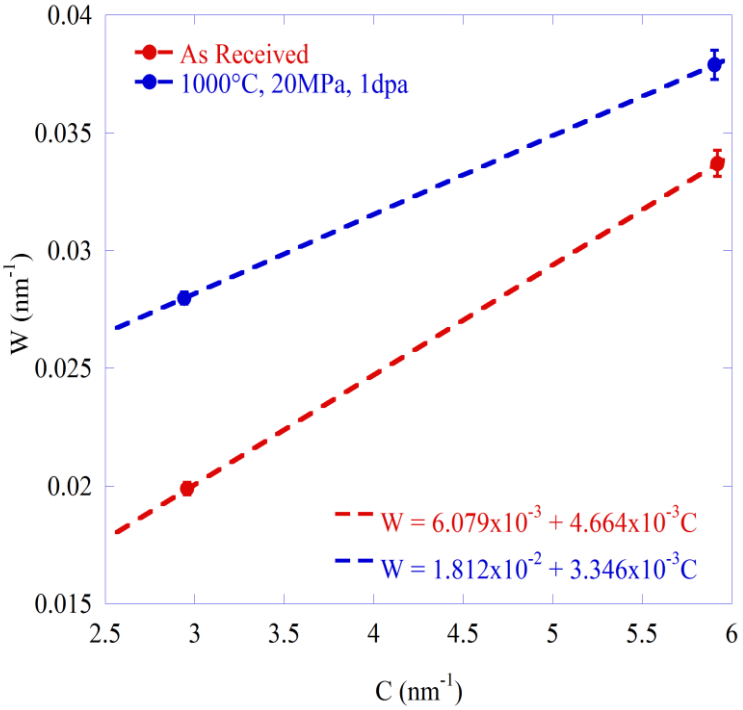

Figure 5.6. Example plot of *W* versus *C* from the (0002) and (0004) peaks for the as-received (red) and experiment #2 (blue) samples.

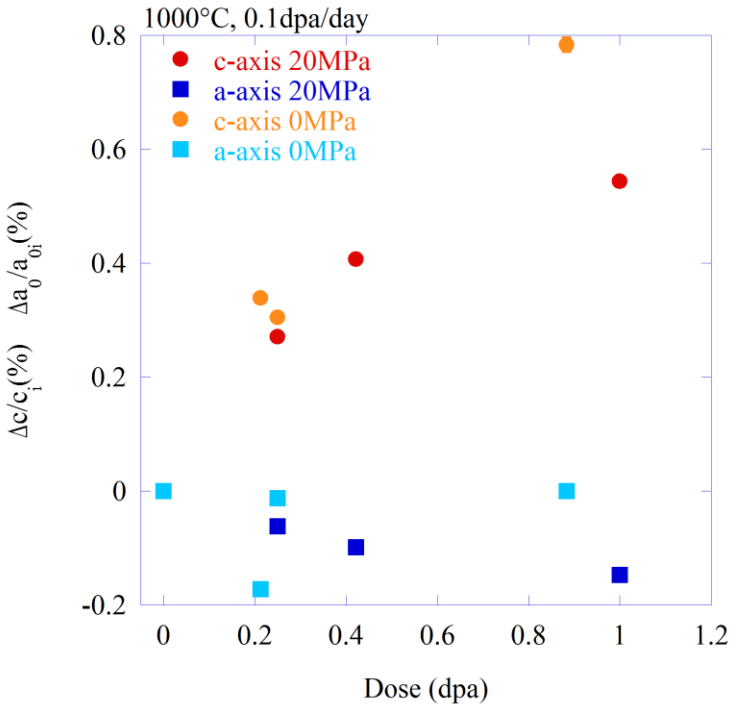

Figure 5.7. Plot of the change of planar and atomic spacing versus total accumulated dose.

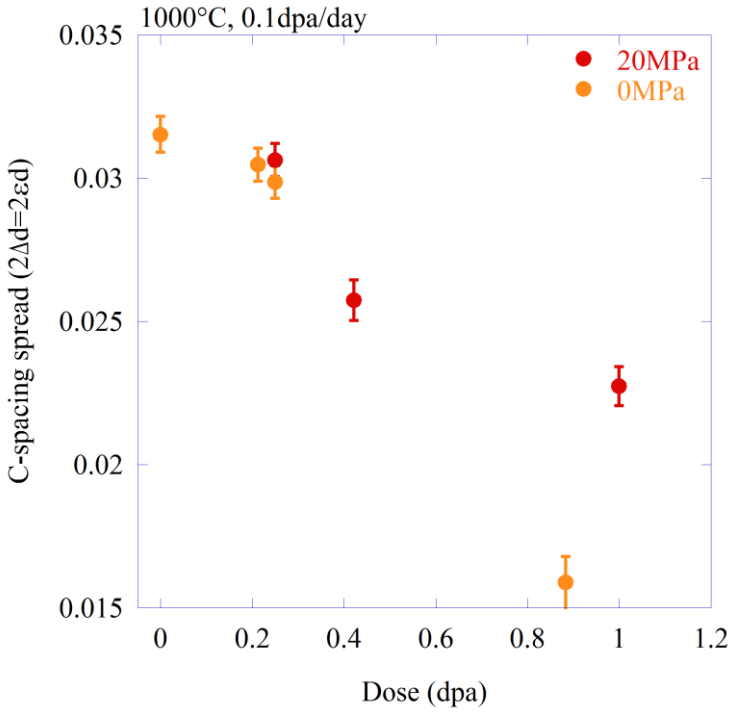

Figure 5.8. Plot of the change of c-axis lattice strain versus total accumulated dose.

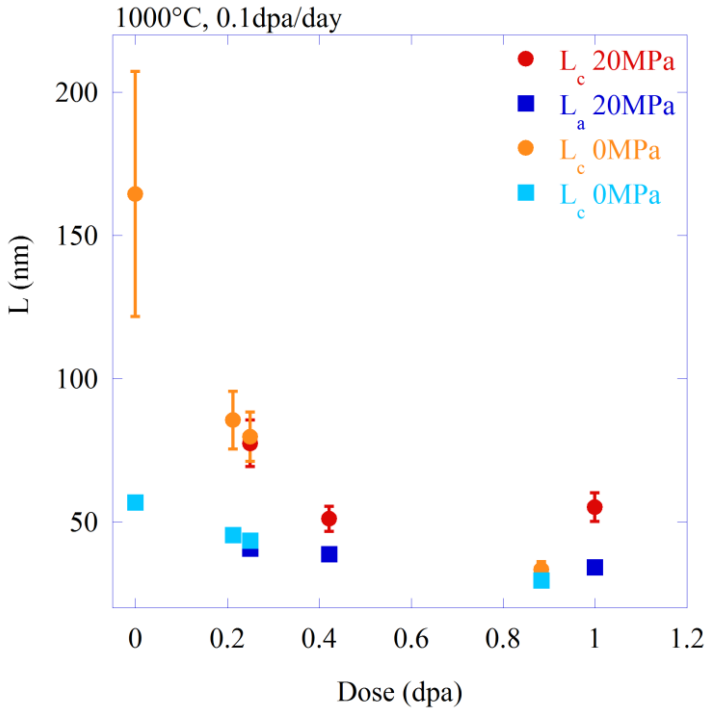

Figure 5.9. Plot of the change of crystallite size versus total accumulated dose.

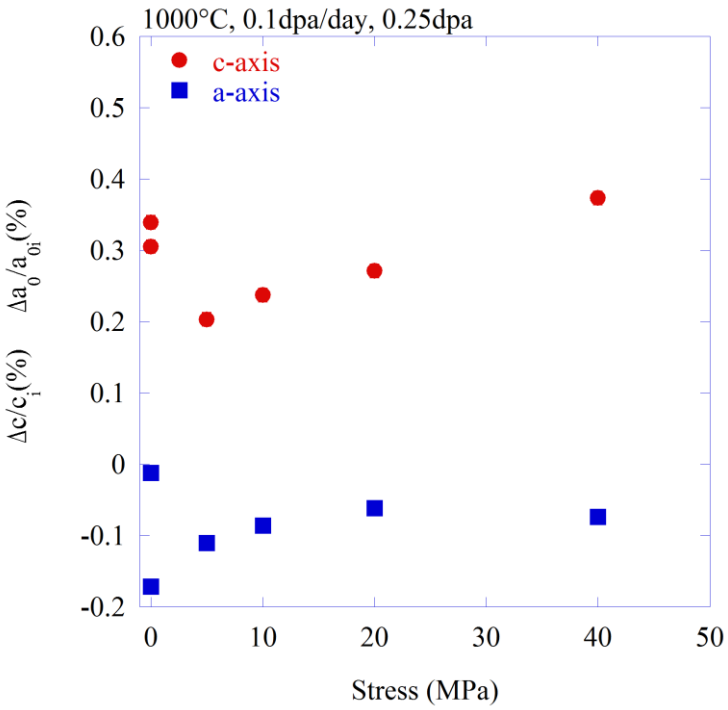

Figure 5.10. Plot of the change of planar and atomic spacing versus applied tensile stress.

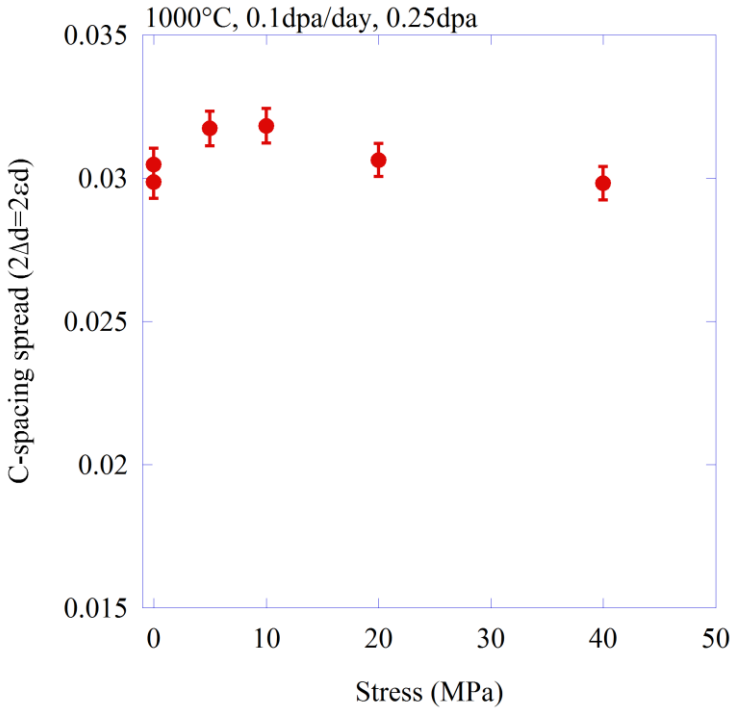

Figure 5.11. Plot of the change of c-axis lattice strain versus applied tensile stress.

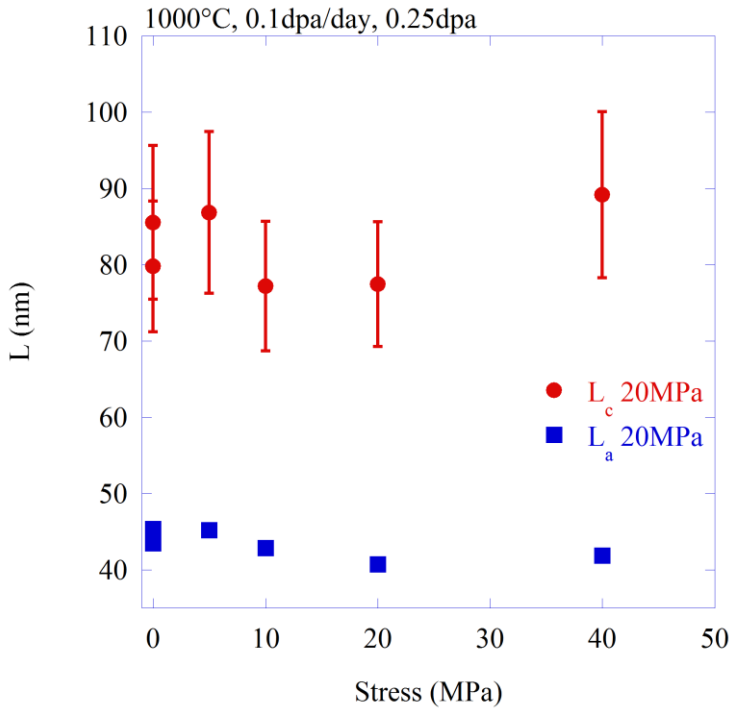

Figure 5.12. Plot of the change of crystallite size versus applied tensile stress.

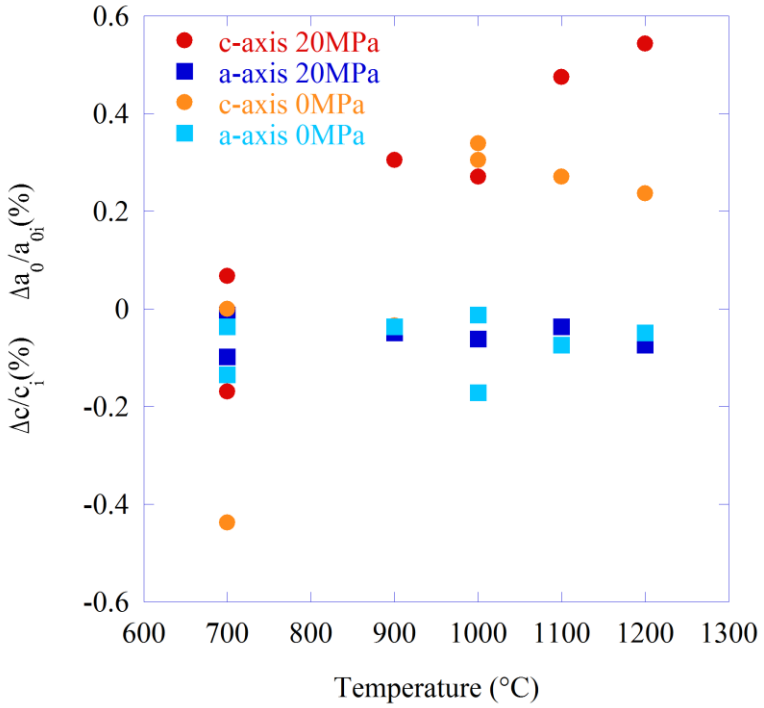

Figure 5.13. Plot of the change of planar and atomic spacing versus irradiation temperature.

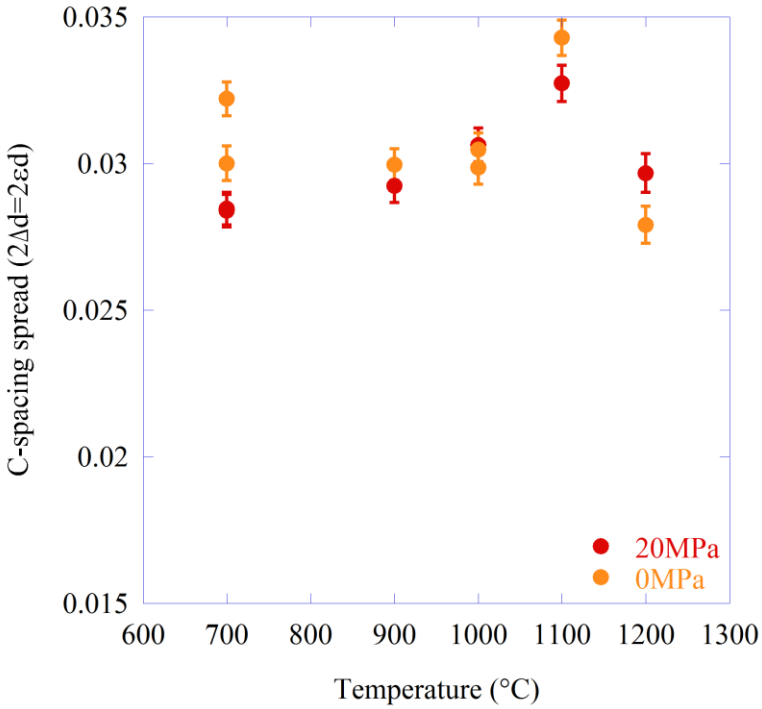

Figure 5.14. Plot of the change of c-axis lattice strain versus irradiation temperature.

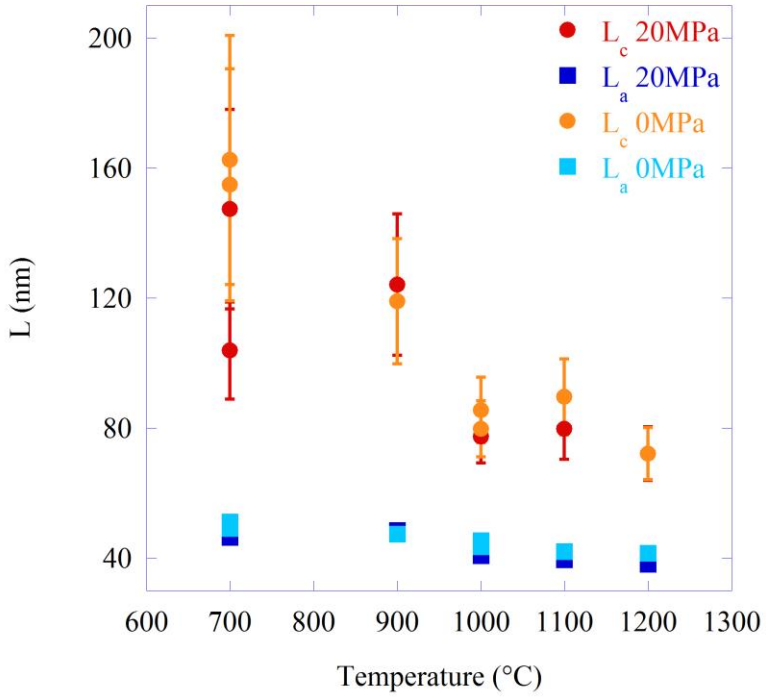

Figure 5.15. Plot of the change of crystallite size versus irradiation temperature.

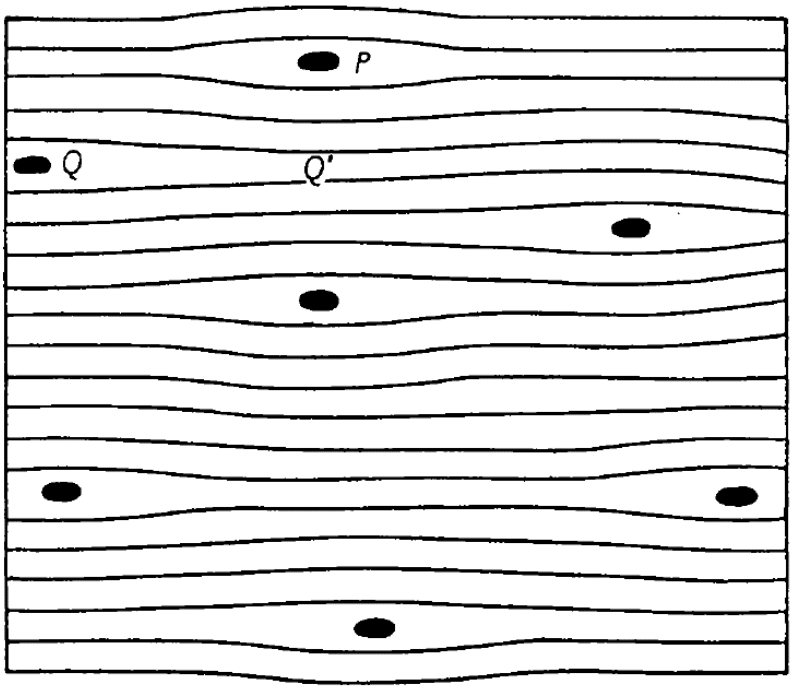

Figure 5.16. Schematic representation of the uniform distribution of interstitial clusters in graphite, from [28].

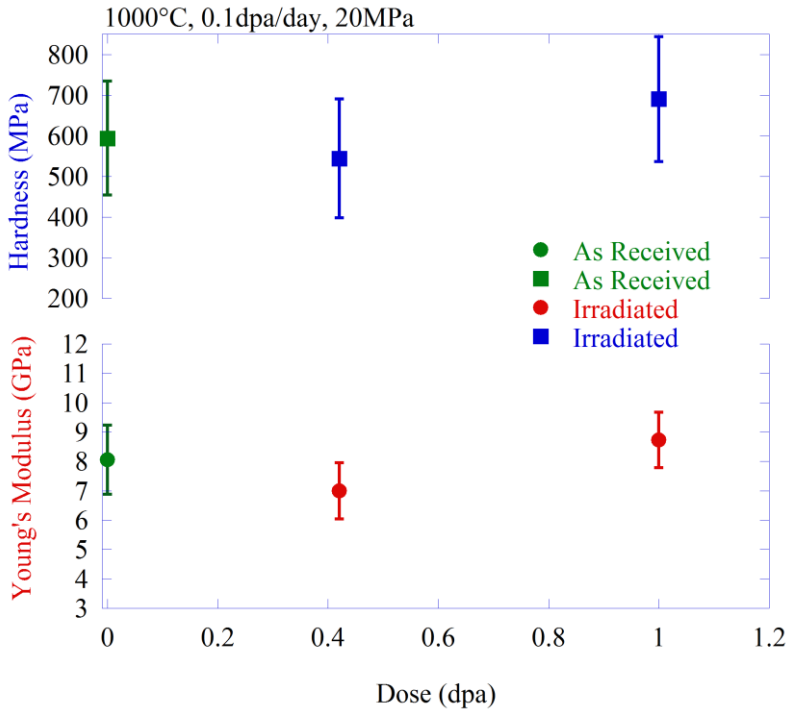

Figure 5.17. Plot of Young's modulus versus accumulated dose.

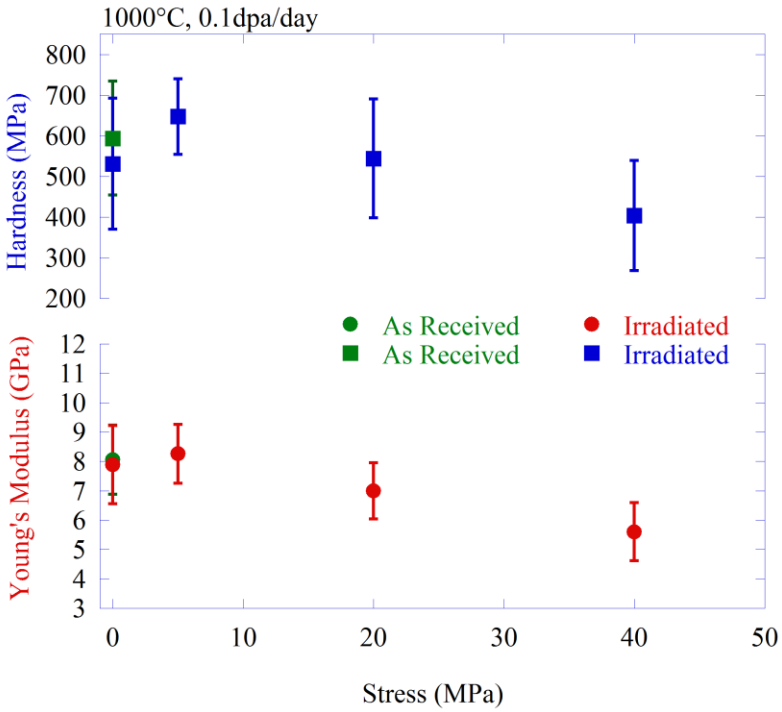

Figure 5.18. Plot of Young's modulus versus stress.

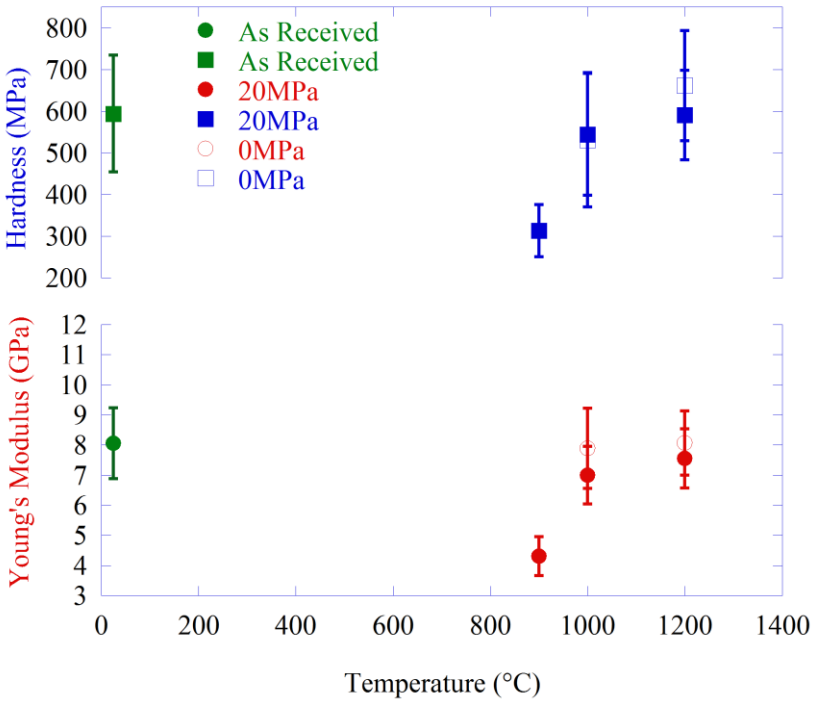

Figure 5.19. Plot of Young's modulus versus temperature.

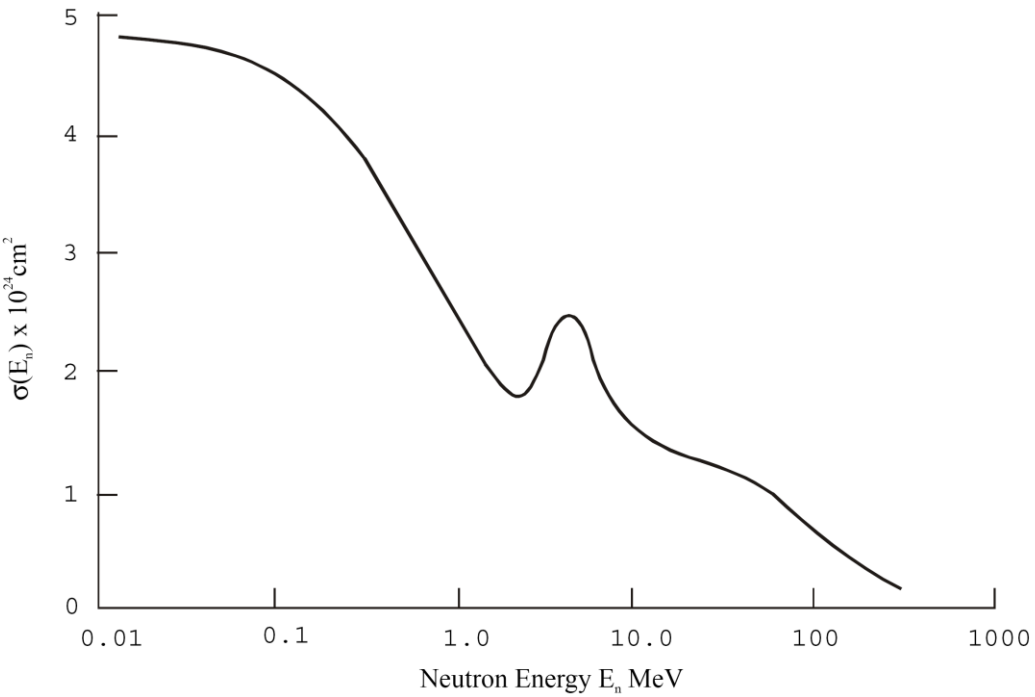

Figure 5.20. Elastic scattering cross-section vs. neutron energy, from [79]. Below 0.01MeV the cross-section is approximately constant at 4.71 barns.

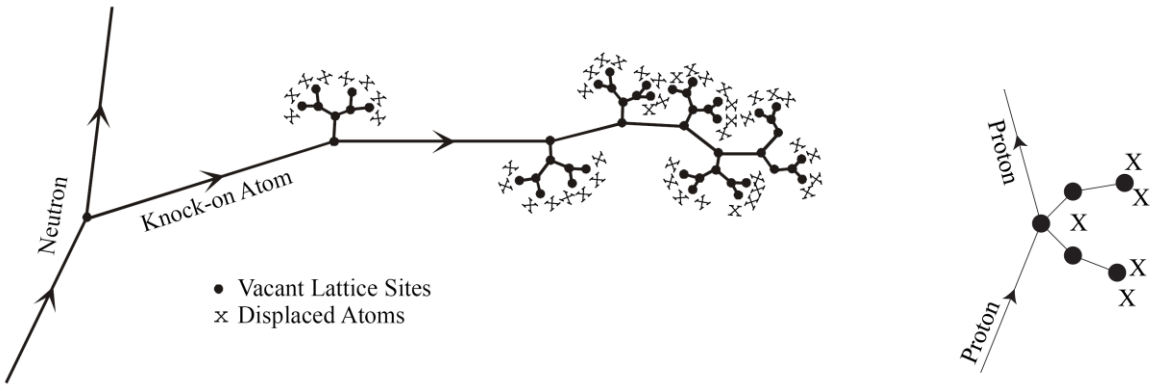

(a) (b)

Figure 5.21. Schematic representation of damage path of one PKA through graphite lattice (a), from [79], and proton damage (b).

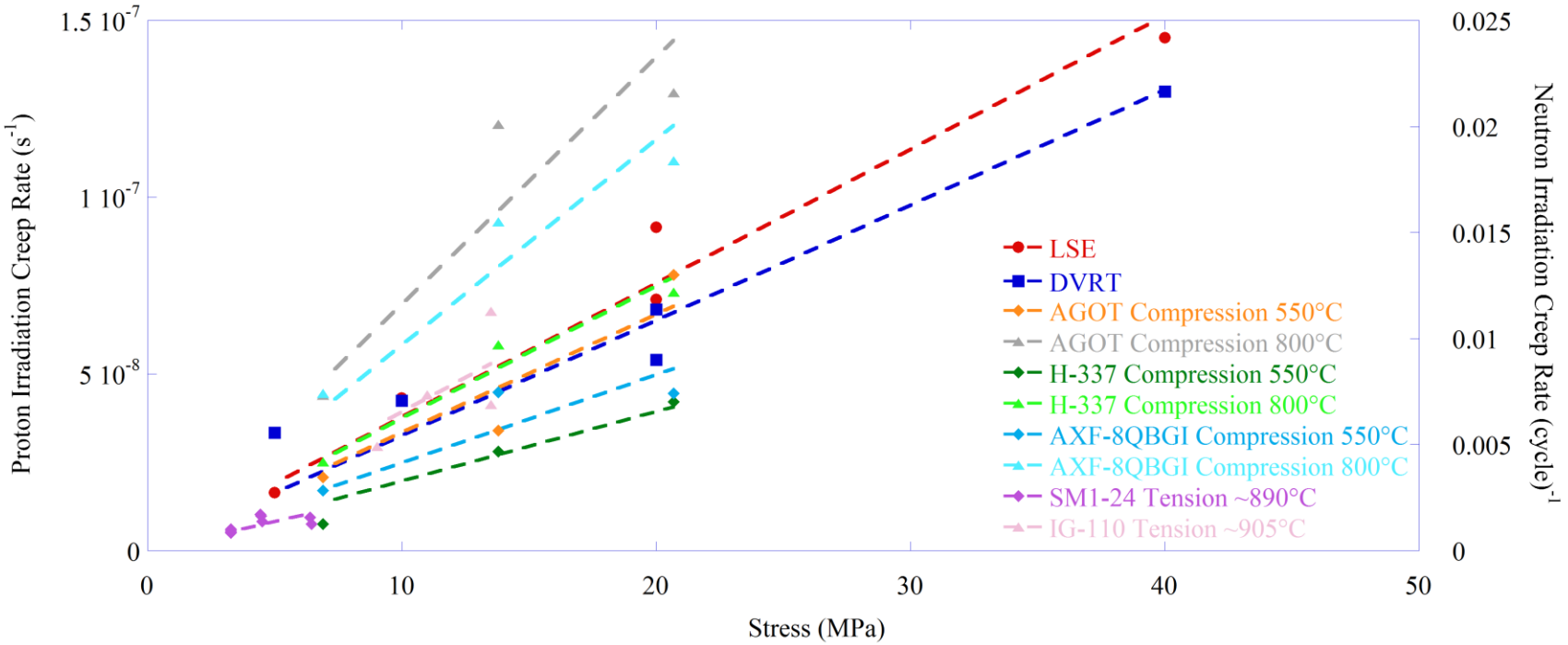

Figure 5.22. Comparison of stress dependence for proton irradiation creep experiments (red circles and blue squares on left axis) and stress dependence for neutron creep experiments. AGOT, H-337, and AXF-8QBGI from [35], SM1-24 data from [36], and data for IG-110 from [37].

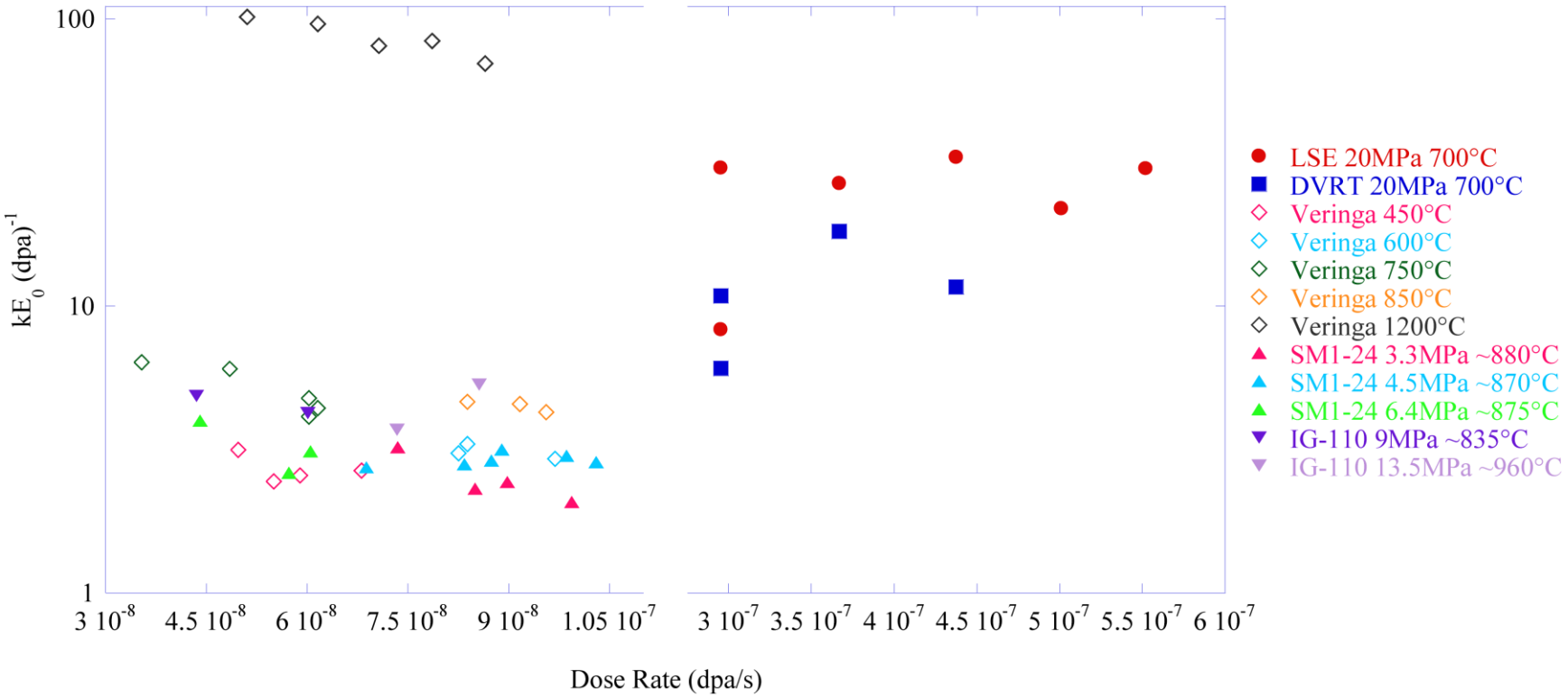

Figure 5.23. Comparison of dose rate dependence for proton irradiation creep experiments with 20MPa stress at 700ºC (red circles and blue squares) and neutron experiments. Veringa data [51] was obtained from restrained-shrinkage experiments. SM1-24 [36] and IG-110 [37] were performed with constant tensile load. The applied stress (if known) and average irradiation temperature are listed for the neutron data.

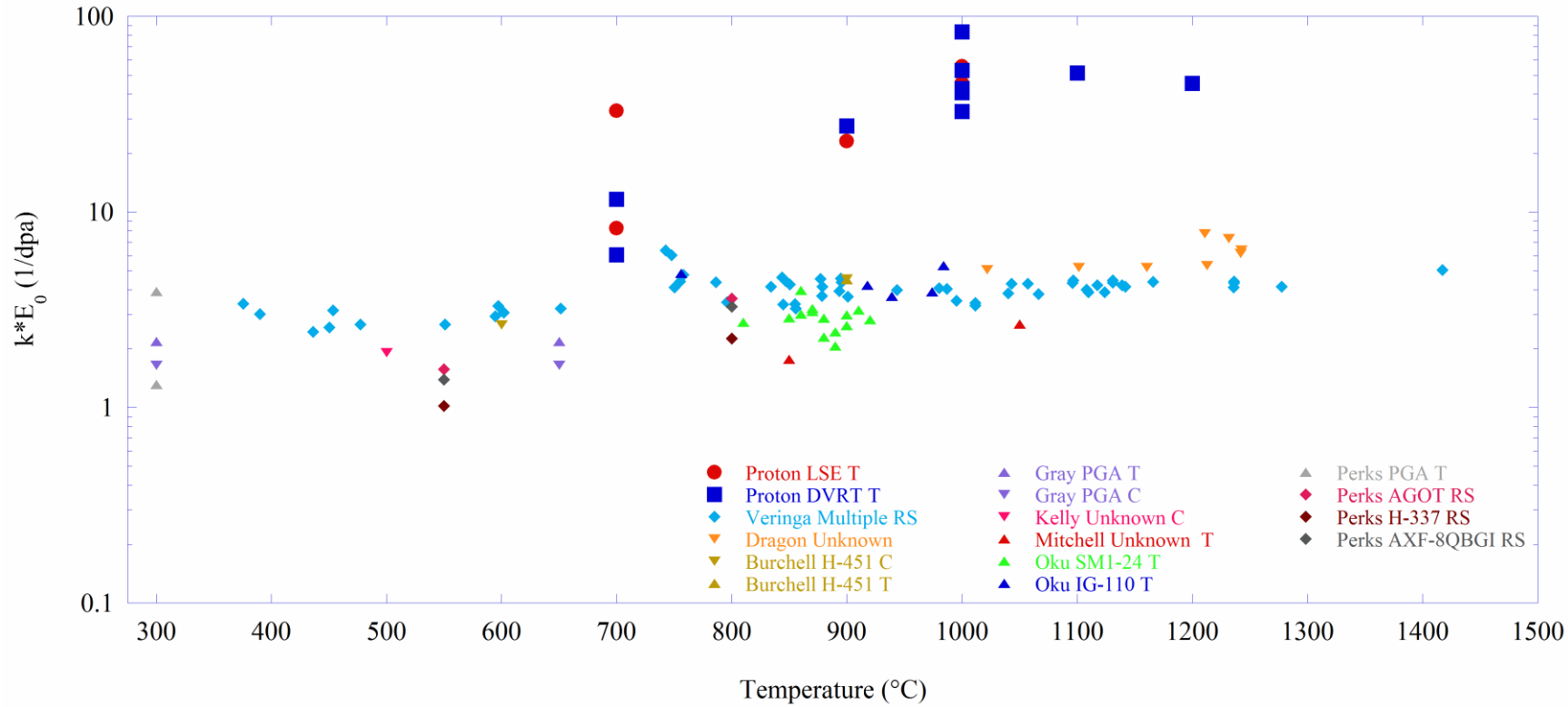

Figure 5.24. Comparison of temperature dependence of compliance, normalized for Young's modulus, (kE0) for proton irradiation creep experiments and neutron creep experiments. Veringa & Dragon data from [51], Burchell data from [41], Gray data from [33, 34], Kelly data from [39], Mitchell data from [91], Oku data from [36, 37], Perks PGA from [31], Perks AGOT H-337 and AXF-5QBGI from [92].

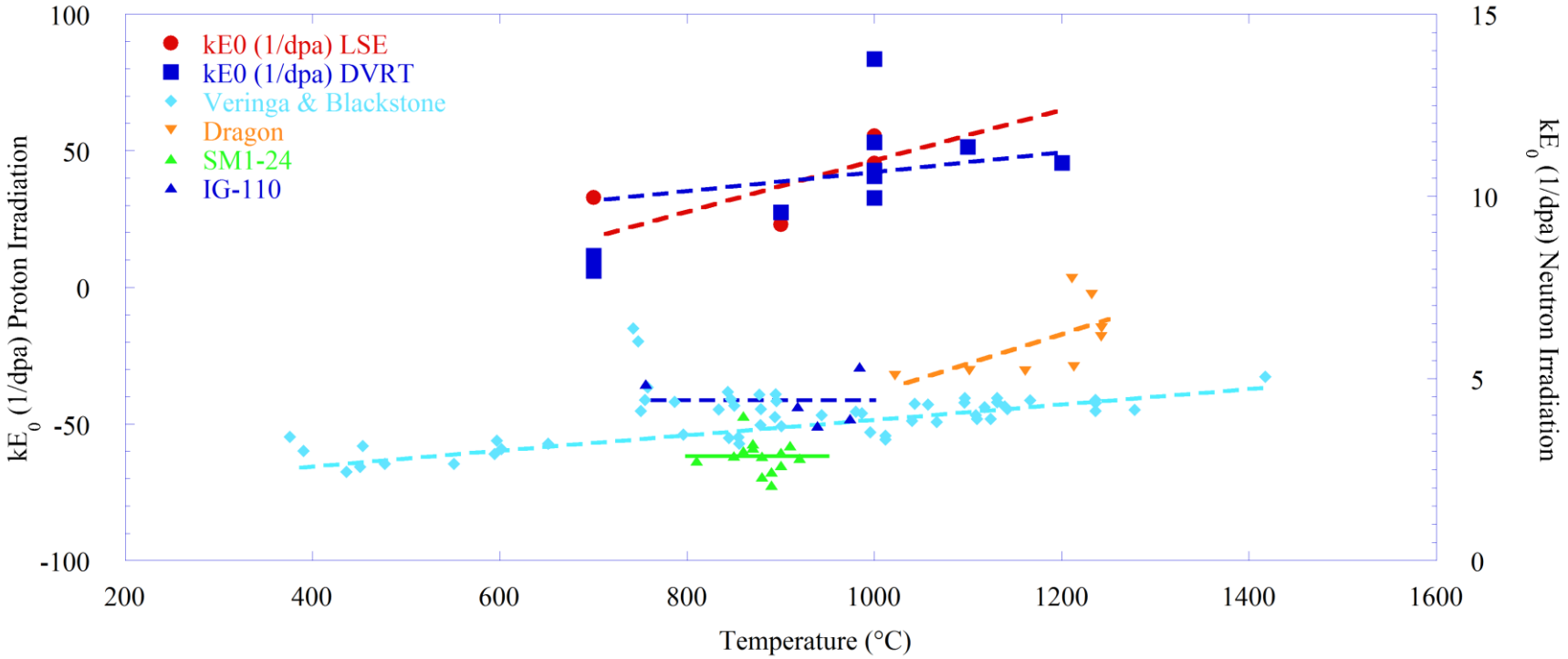

Figure 5.25. Plot of proton (left axis) and neutron (right axis) kE_0 versus temperature, where only neutron results with more than two temperature values were used.

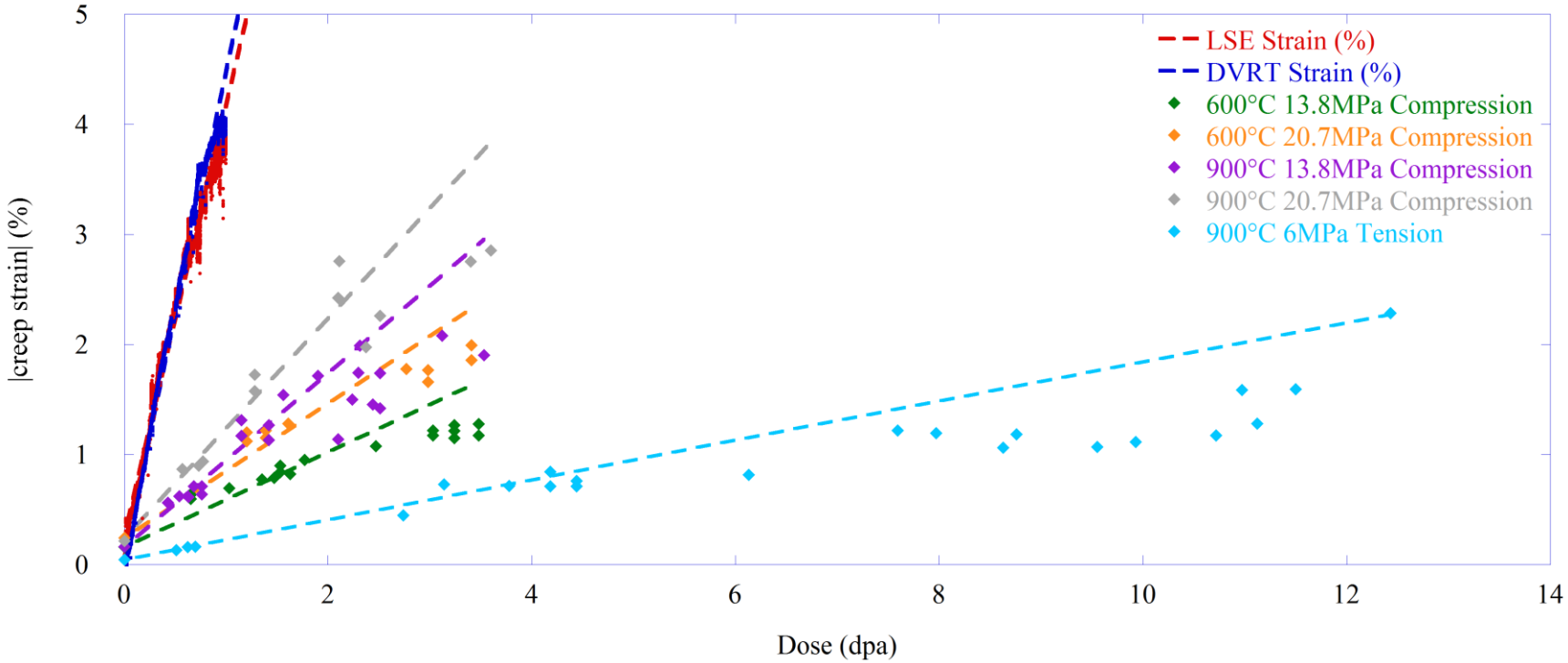

Figure 5.26. Comparison of accumulated dose dependence for proton irradiation creep experiments and neutron creep experiments, from [41]. Y-axis is the absolute value of creep strain to compare tensile and compression results.

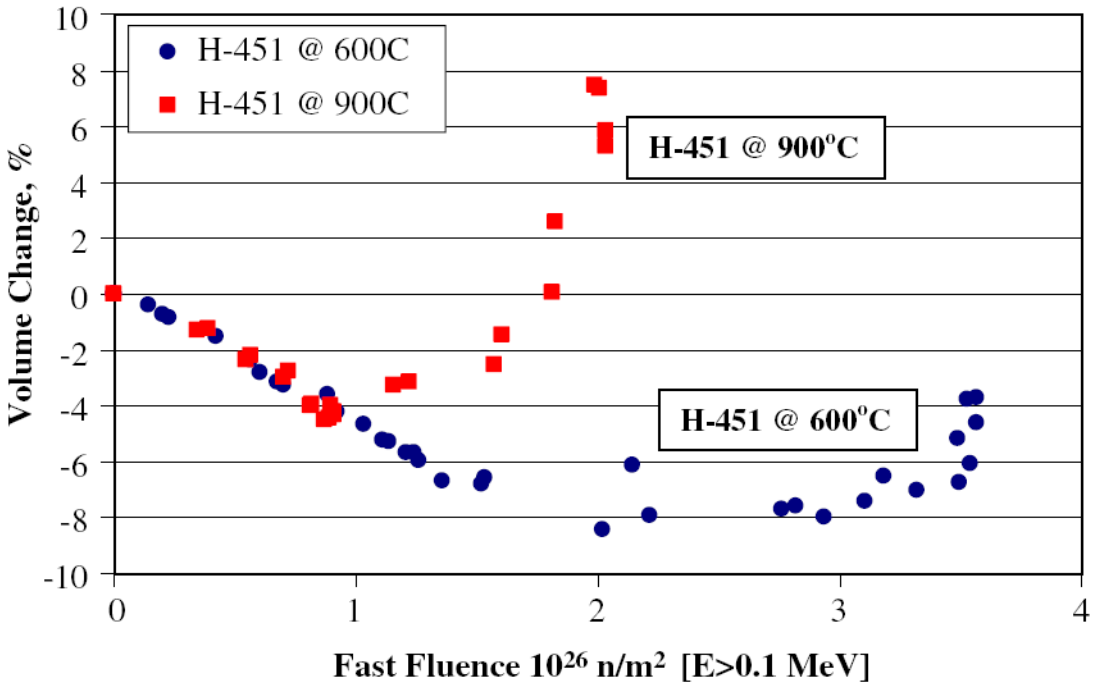

Figure 5.27 Neutron irradiation of H-451 without stress in HFIR [86], the data for 600ºC were found to be similar to the results at 600ºC from irradiations in ORR.

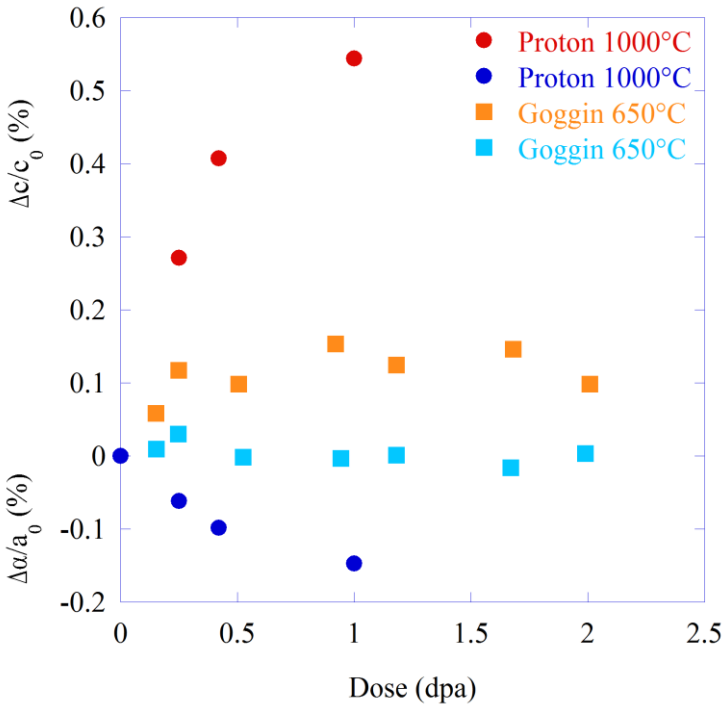

Figure 5.28. Plot of lattice parameter changes versus dose for the proton irradiations (circles) at 1000ºC and neutron irradiations (squares) at 650ºC [89]. The c-spacing change is shown with the red and orange data while the change of atomic-spacing is shown in blue and light blue.

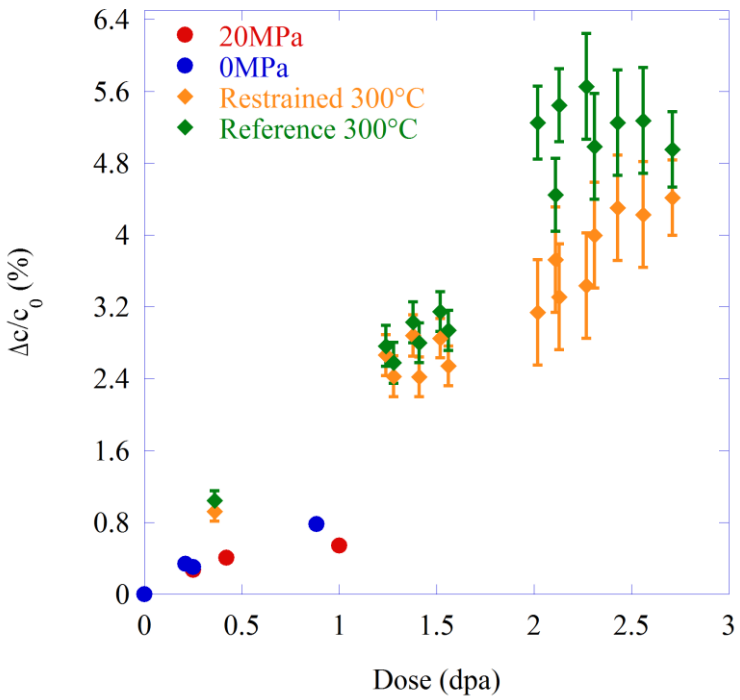

Figure 5.29. Plot of $\Delta c/c_0$ versus dose, showing the effects of stress for proton and neutron [74] irradiated graphite.

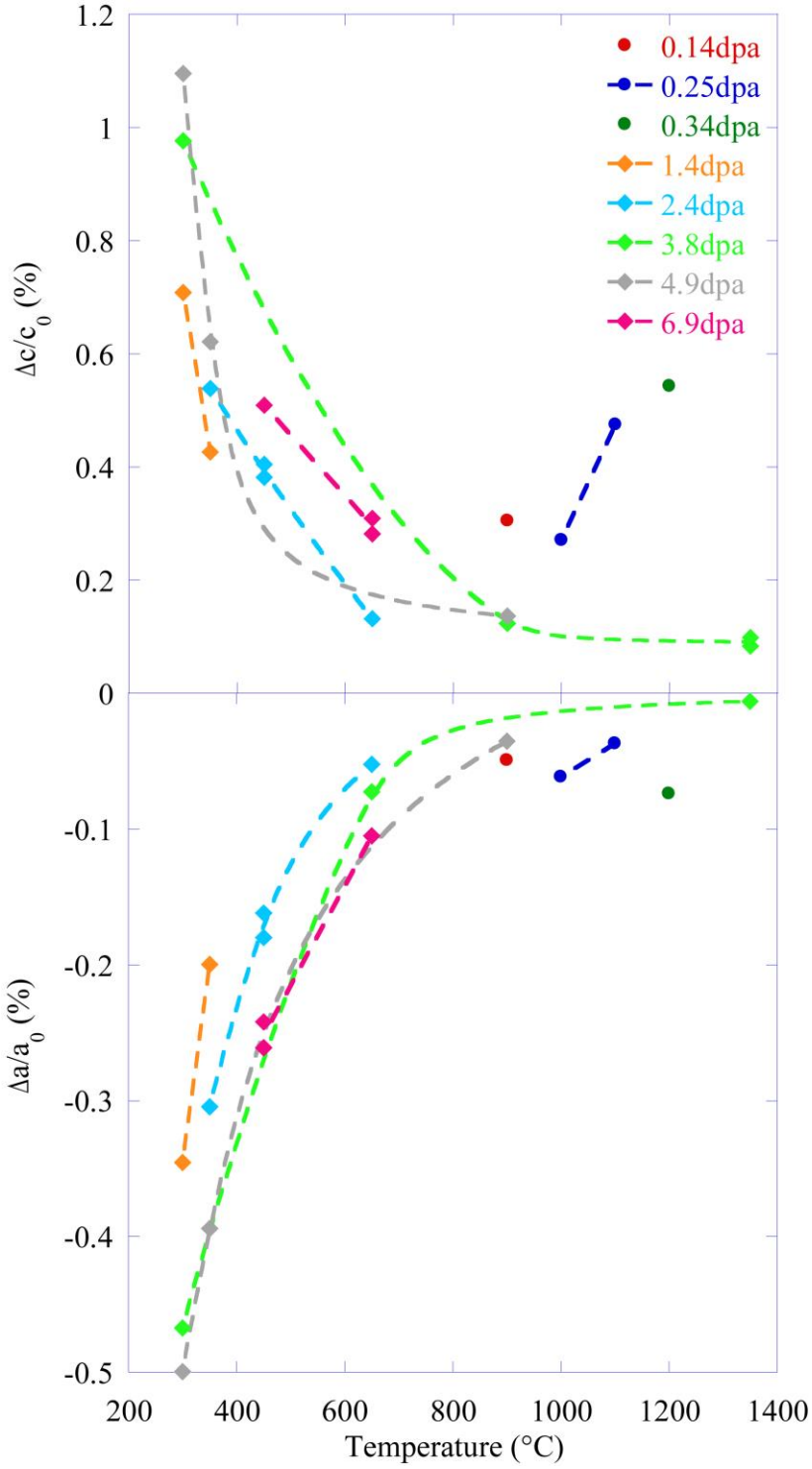

Figure 5.30. Plot of $\Delta c/c_0$ and $\Delta a/a_0$ versus temperature, at various total doses, showing how temperature effects the magnitude of the spacing changes for proton and neutron [24] irradiated graphite.

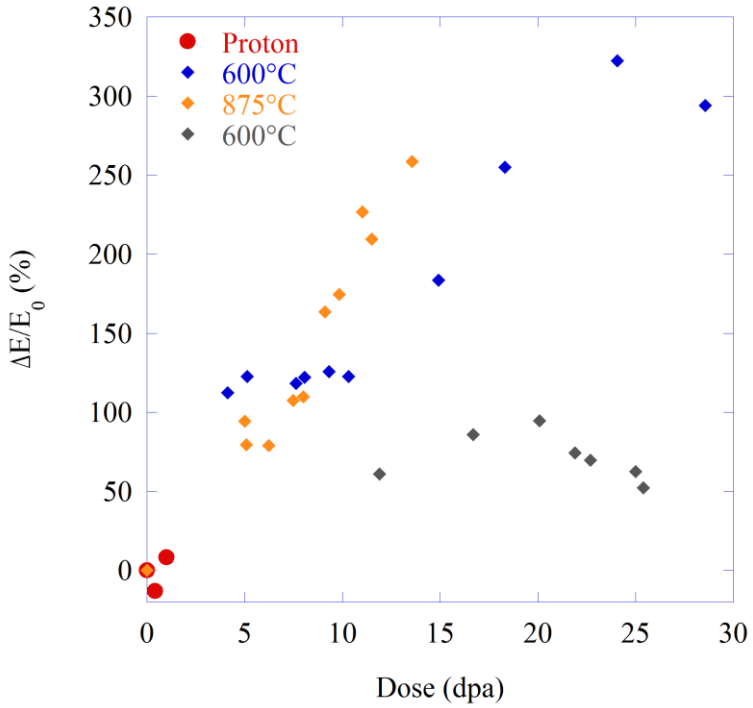

Figure 5.31. Plot of change of Young's modulus versus dose, including results from this work and neutron irradiations at 600ºC (blue) and 875ºC (orange) from [21] and 600ºC (gray) from [26].

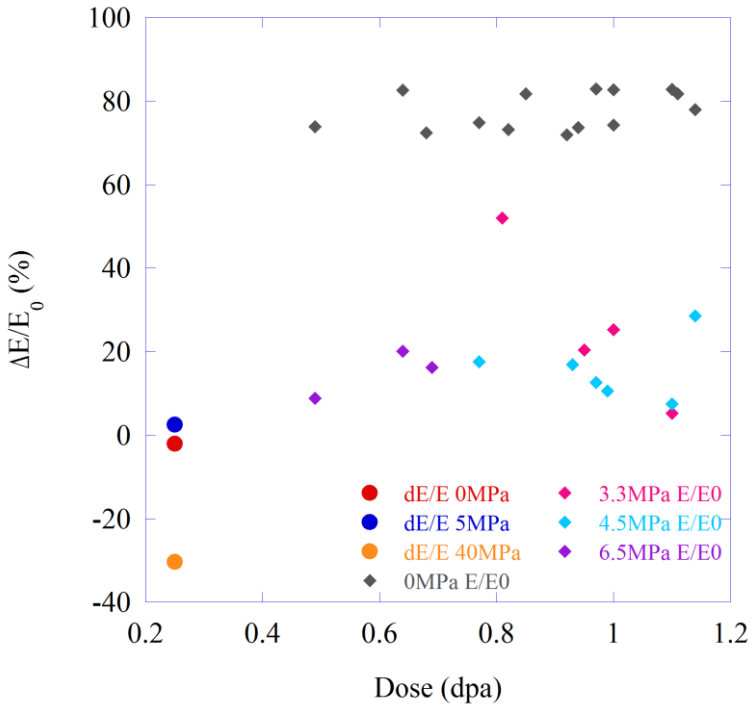

Figure 5.32. Plot of change of Young's modulus versus dose, showing how applied stress reduces the percent increase in neutron irradiations [36].

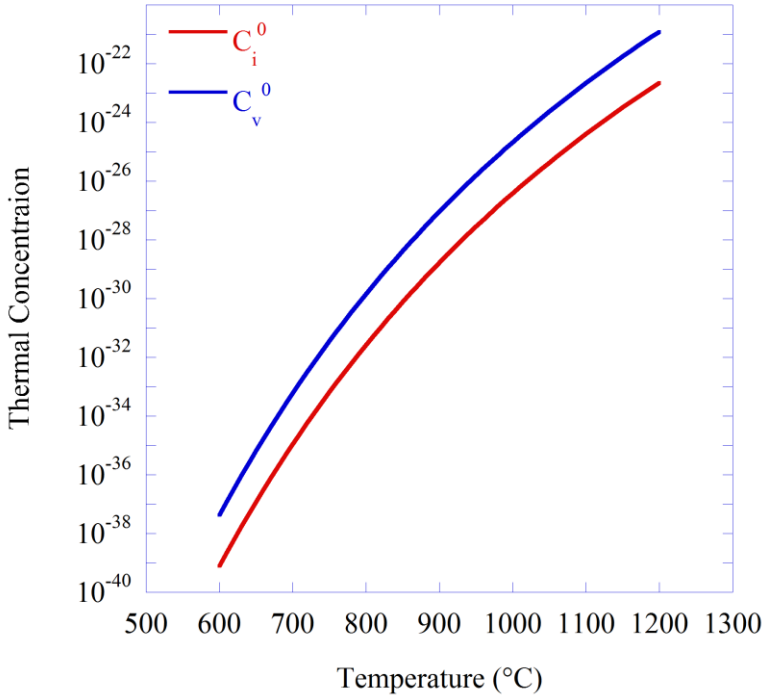

Figure 5.33. Plot of thermal interstitial and vacancy concentration versus temperature.

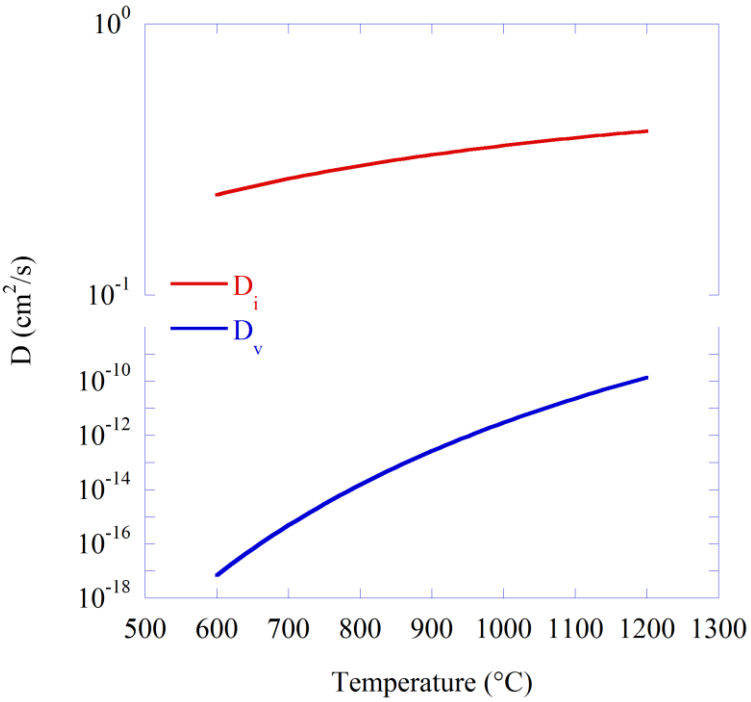

Figure 5.34. Plot of interstitial and vacancy diffusion coefficients versus temperature.

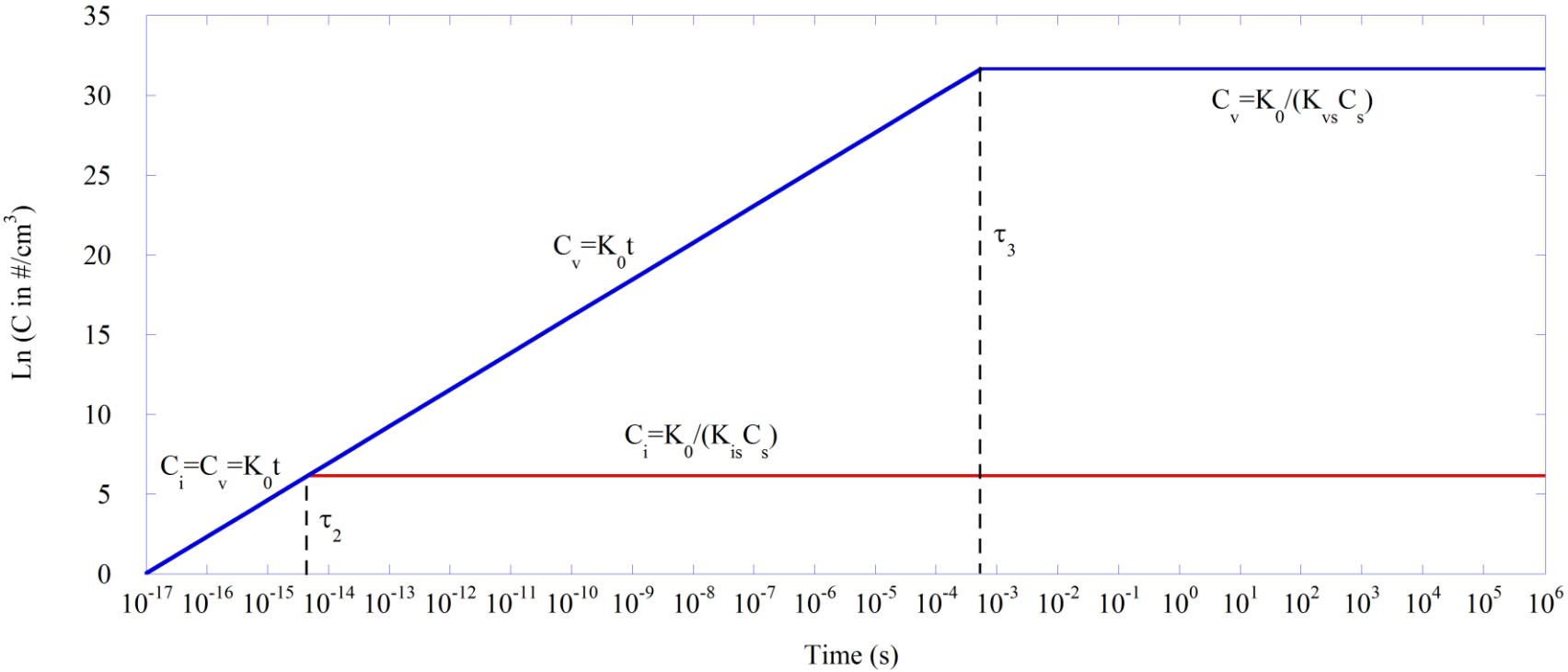

Figure 5.35. Plot of log of concentration versus irradiation time for the 1000ºC irradiation conditions, with interstitial concentration plotted in red and vacancy concentration plotted in blue.

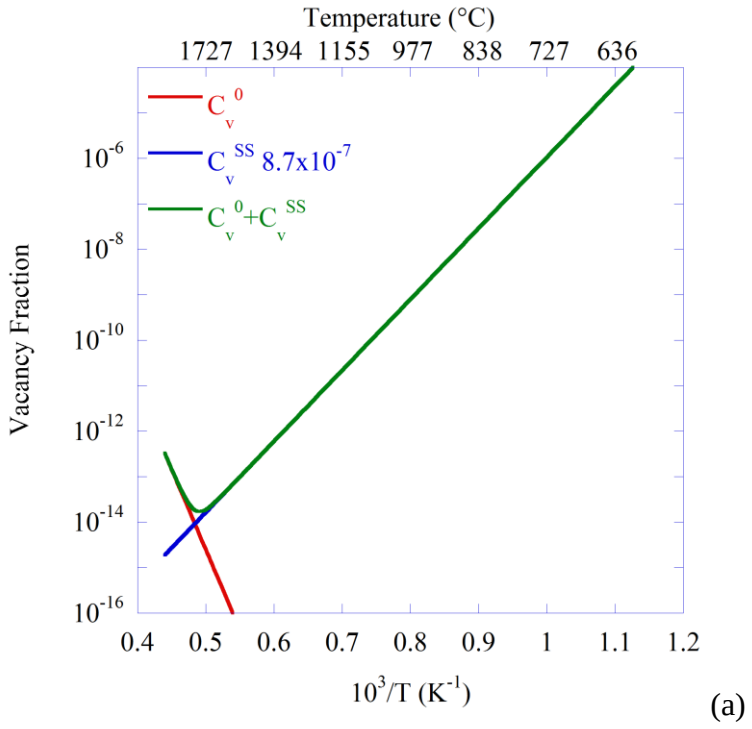

(a)

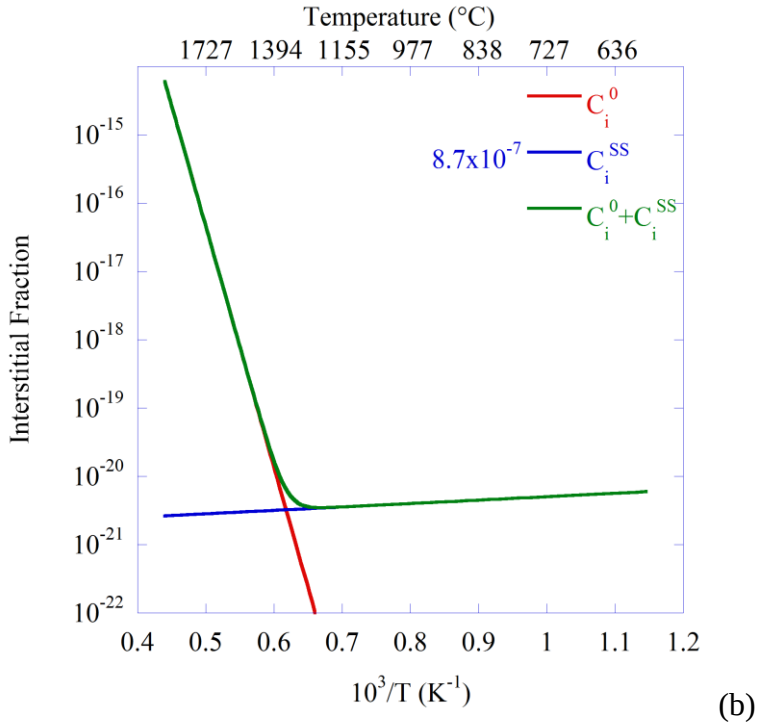

(b)

Figure 5.36. Steady-state vacancy (a) and interstitial (b) concentrations versus 1/T. In both plots the thermal equilibrium values are plotted in red, the irradiation steady-state values are plotted in blue, and the sum of the concentrations are plotted in green. Dose rate of $8.7x10^{-7}$dpa/s used to calculate the steady-state concentration.

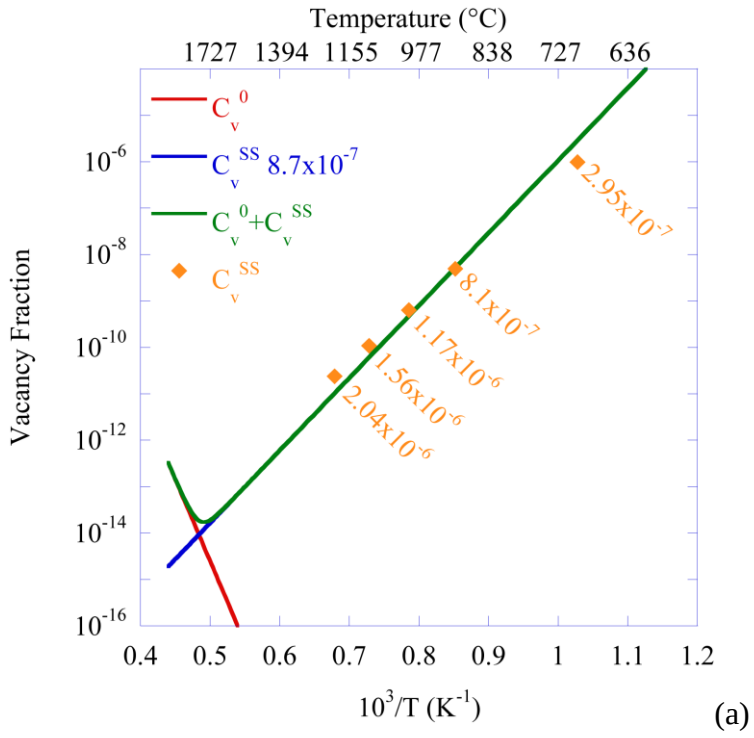

(a)

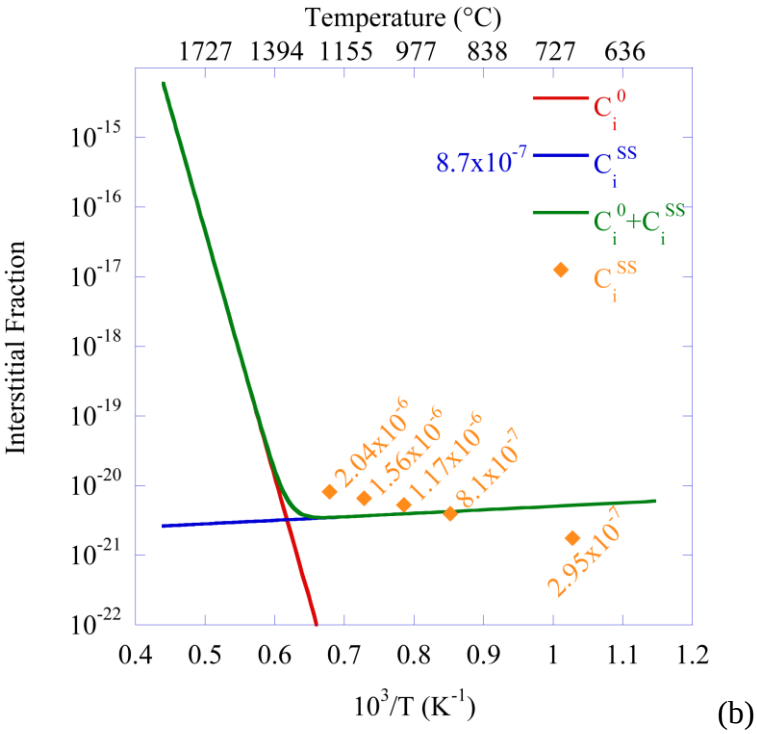

(b)

Figure 5.37. Steady-state defect concentrations (orange diamonds), calculated at the experimental temperatures and respective dose rates (in orange with units of dpa/s), overlaid on the concentrations plotted in Figure 5.36.

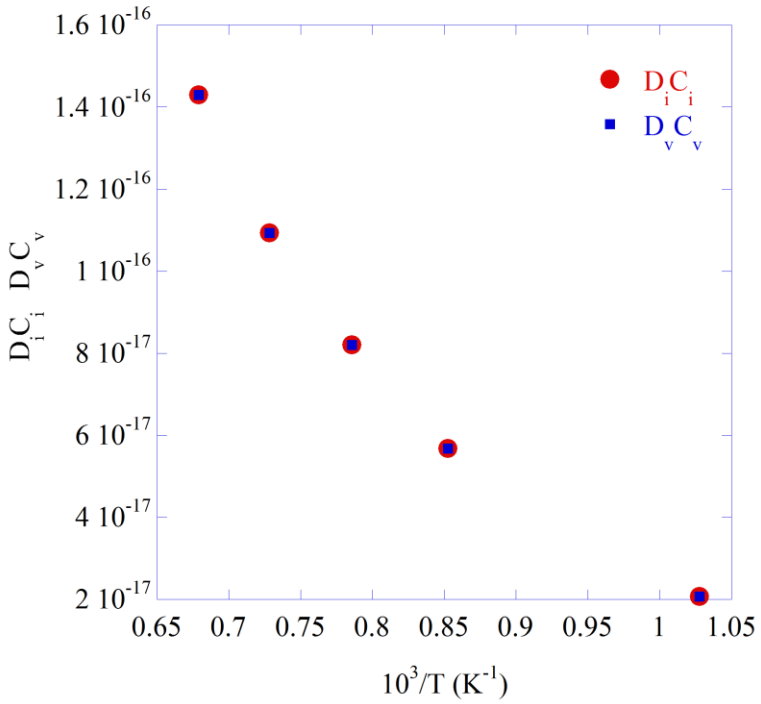

Figure 5.38. Plot of D_iC_i (red circles) and D_vC_v (blue squares) versus irradiation temperature. It is important to note that the calculated values are the same.

CHAPTER 6

CONCLUSIONS

The conclusions of this thesis are:

1. An experimental facility was developed to perform proton irradiation-induced creep experiments. Three experiments were performed with the same stress, dose rate, and temperature to determine the reproducibility and confidence of these experiments. These three experiments showed the creep rate measurements to be reproducible within a 20% certainty from the LSE measurements and 10% certainty from the DVRT. This facility was utilized to investigate the effects of applied tensile stress, irradiation dose rate, temperature, and accumulated dose, on the irradiation creep behavior of ultra-fine grain graphite ZXF-5Q.

2. The irradiation-induced creep rate was determined to have a linear dependence on applied stress and dose rate, an Arrhenius dependence on irradiation temperature (can be reliably fit with a linear fit in this temperature range), and no dependence on accumulated dose.

3. The creep rate dependencies from this work were shown to mostly agree with the dependencies observed for graphite that has undergone neutron irradiation-induced creep.

4. The primary difference was the creep compliance values from the proton experiments were an order of magnitude larger than the values from neutron irradiations. Limited literature on the effects of gamma-rays in graphite suggests that the gamma-rays are annealing the radiation defects and thus effectively reducing the actual damage rate from the neutrons.

5. The change in crystal structure, lattice parameters and crystallinity, were strongly affected by accumulated dose. The change of c-spacing, c-spacing variation, and crystallite dimensions were proposed to be caused by the formation of six-atom hexagonal clusters between the basal planes. The reduction of interatomic spacing was shown to be caused by the rearrangement of covalent bonds between atoms surrounding uncollapsed vacancy lines.

6. The increase of c-spacing, decrease of c-spacing variation, and decrease of crystallite sizes, with increasing temperature, were shown to have resulted from the higher dose rates, necessary to achieve the higher temperatures, causing an increase of interstitial concentrations and therefore having a higher density of the six-atom clusters.

7. The changes in crystal parameters showed good agreement overall with changes measured from graphite irradiated with neutrons. Specifically the trends of the changes in spacing and crystallinity agreed well, but the proton results showed larger change for the same dose, which may also be due to the reduction of defect concentrations from gamma-rays.

8. This work didn't observe a significant change of Young's modulus and did not agree with changes observed from neutron irradiations. It is possible that the source of this difference is the lack of binder phase in the material from this work, plus these experiments were not performed to dose levels where changes of the density would result in the increase of Young's modulus. The one sample that showed a significant change was the high-stress sample and it is postulated that irradiation creep was not sufficient to prevent this stress from producing new porosity.

9. The initial comparison of the mechanism of point defect production for neutrons and protons did not initially agree. It was determined that the point defect production from the neutron-created PKA and the proton did agree and resulted in discrete displacement groups of 4-8 atoms.

10. The similarities of creep rate dependencies, crystal structure changes, and radiation damage mechanism, show that protons can be used as a suitable proxy to study the neutron irradiation effects in graphite. The only difference between these irradiation sources is the lack of gamma-rays in the proton irradiations, but this could be accounted for by determining the effects of gamma-rays in graphite.

11. It was determined, via a process of elimination, that the most probable mechanism controlling irradiation-induced creep of graphite is SIPA. This was the only mechanism that showed agreement between both experimental creep rate dependencies and the creep rate dependencies predicted by the mechanism, and agrees with the stress effects on crystal parameters seen for neutron irradiations.

12. Lastly, this work can be used as a baseline study of the effects of radiation and applied stress on the filler phase of graphite. By combining this with a systematic study of the effect of irradiation on the binder phase it would become possible to tailor-make a nuclear graphite for use in nuclear reactors that would respond to irradiation in a pre-determined manor and have the desired mechanical properties.

FUTURE WORK

This work has identified a viable mechanism of proton irradiation-induced creep for ultra-fine grain graphite. The comparison of the experimental results with results from neutron irradiation-induced creep experiments show similar behavior but do not agree for all the comparisons. There are multiple experimental investigations that would assist in supporting that proton irradiation of graphite can be a suitable proxy for neutron irradiation.

The first investigation would focus on the effects of gamma-rays on the crystal parameters of graphite. The limited research available on this does not provide an understanding of these effects. This investigation would be most beneficial if it investigated the effects of a range of discrete gamma-ray energies on both as-manufactured graphite and graphite that has already been exposed to a radiation source. Additionally, investigating the effects of gamma-rays on graphite at high temperatures should be determined and compared with pure thermal effects from the same temperature. This investigation would then result in determining if the difference between the proton creep experiments and neutron creep experiments was due to the presence of gamma-rays.

The second investigation would be to perform a proton irradiation-induced creep experiment on a nuclear-grade graphite. The nuclear grade should be one that has already been subjected to irradiation creep with neutrons, preferably tensile creep. Then by performing the proton irradiation creep experiment at similar conditions, the comparison could be utilized to directly compare the results.

The third investigation would require performing a proton irradiation-induced creep experiment to a final dose between 10 and 15 dpa. This would bring the reference sample near the turn-around dose. Going to these significantly higher doses would result in the most significant crystal parameter and Young's modulus changes. The low dose of the stress effect samples possibly obscured the stress effects on crystal parameters, plus

these doses were not high enough to cause the density changes that would affect the Young's modulus.

The last analysis would be an investigation of the density of the samples irradiated in these experiments. The doses may not be high enough for the changes to be measured. Assuming the differences are sufficient to be measured, this would show whether the irradiation caused densification, whether tensile stress reduced the amount of densification, and could also show whether the high-stress experiment resulted in the generation of new porosity as postulated.

APPENDICES

APPENDIX A

CREEP STAGE PART DRAWINGS

This appendix presents annotated drawings of all the vacuum chamber components that were specially machined for this work. Table A.1 lists the name of each part that was machined and the number of each piece necessary to assemble the irradiation creep stage. Next are all the drawings of the parts that had to be machined. Lastly, a list of the hardware that can be purchased from a supplier is listed in Table A.2.

Table A.1. Machined part list with number of each part necessary to assemble creep stage.

Part Name	Number of Pieces Needed
Alumina Bottom Piece	1
Alumina Heater Standoff	1
Alumina Side Plates	2
Alumina Stage Plate	2
Aperture Boron Nitride Post	2
Aperture Boron Nitride Small Post	2
Aperture Bottom Mount	1
Aperture Bottom Plate	1
Aperture Side Plate	2
Aperture Top Mount	1
Aperture Top Plate	1
Clamp	4
Clamp Threaded	4
Feedthrough Base	1
Feedthrough Base-Tower Connect	1
Feedthrough Spring Top	1
Feedthrough Tower	1
Feedthrough Tower DVRT Holder	1
Load Post	1
Load-Pin Adapter	1
Load-Pin Pin	1
Mounting Post	2
Sample Collet	4
Sample Post Base	1
Stage Flange	1
Stage Post	4
Tantalum Link	1
Tantalum Shield	1

Front View

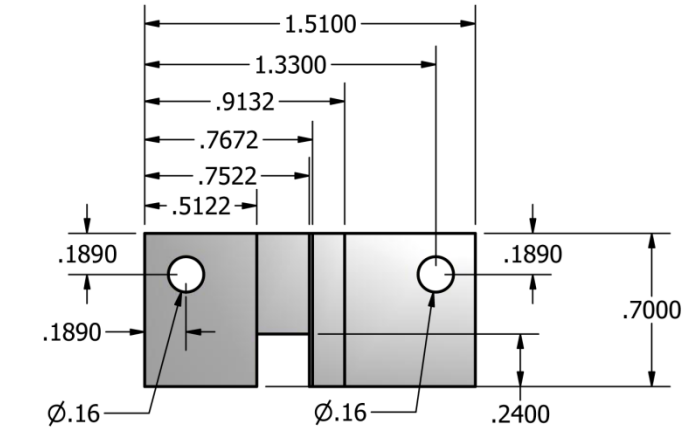

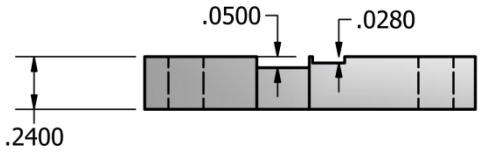

Edge View

Iso View

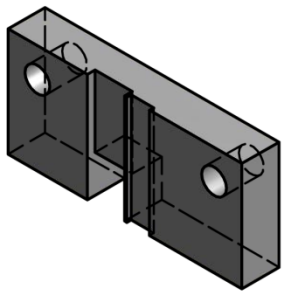

Part Name: Alumina Bottom Piece.ipt

Front View

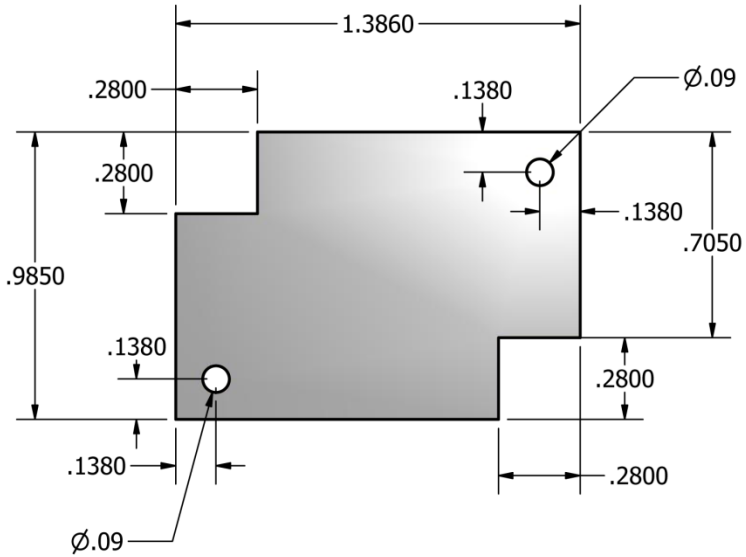

Side View

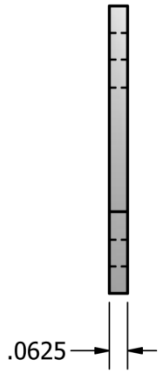

Iso View

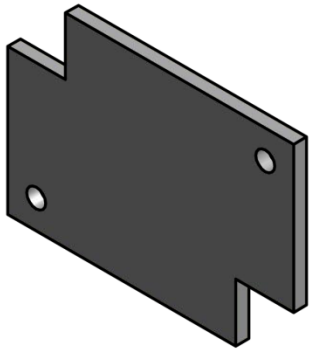

Part Name: Alumina Heater Stantoff.ipt

Front View

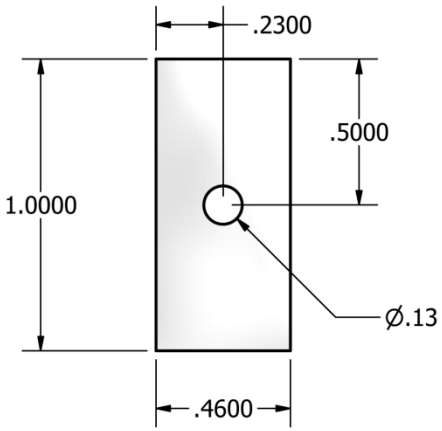

Side View

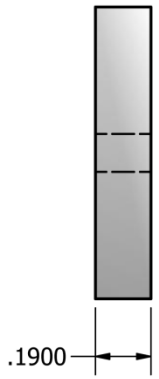

Iso View

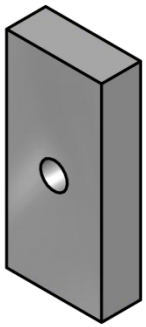

Part Name: Alumina Side Plates.ipt

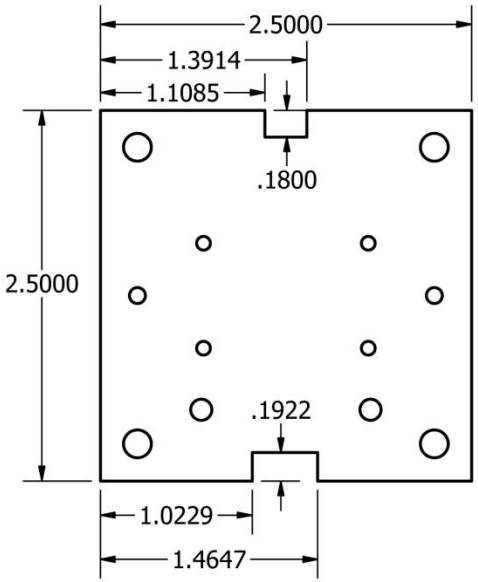

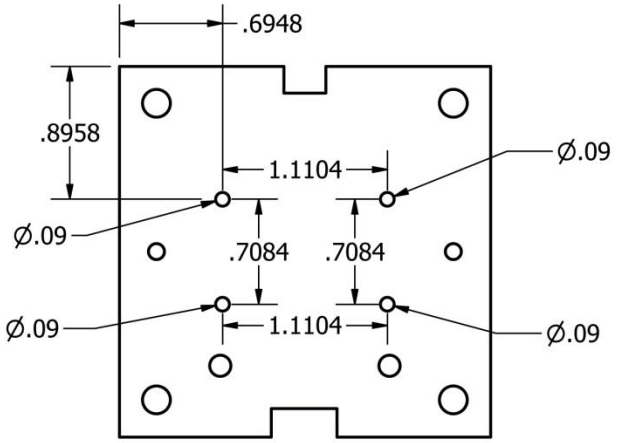

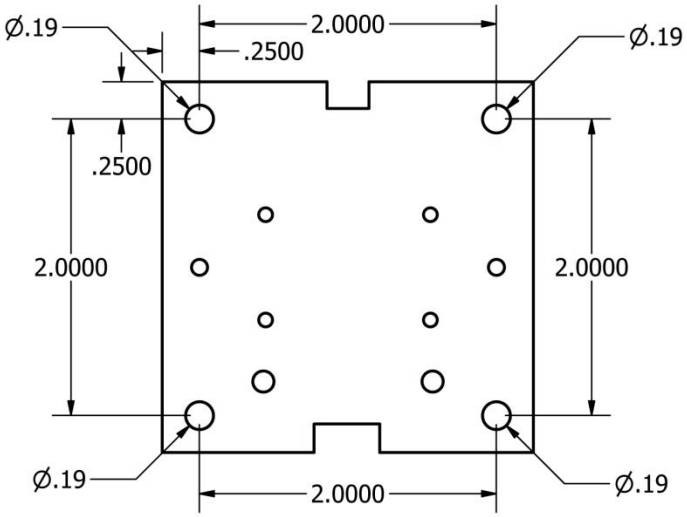

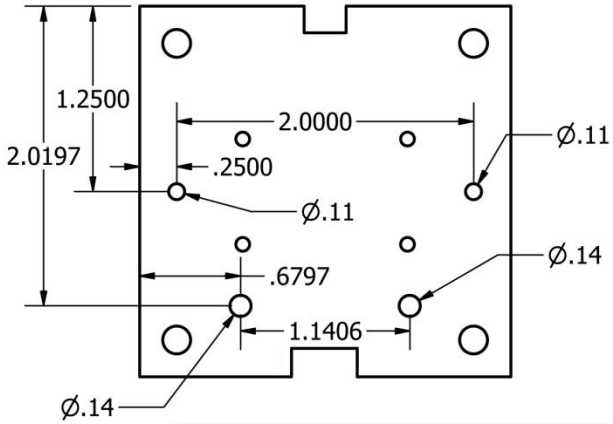

Part Name: Alumina Plate.ipt

Front View

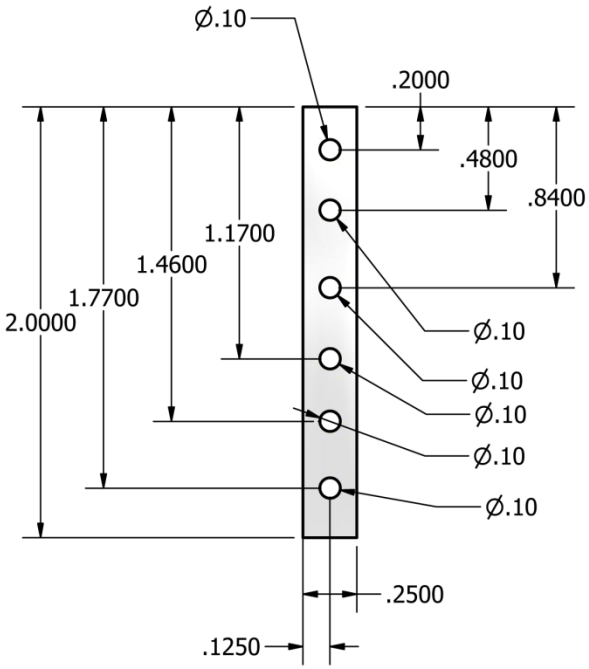

Side View

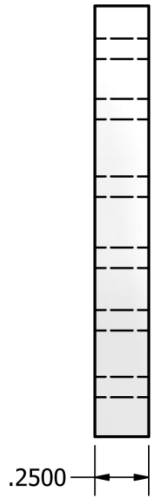

Iso View

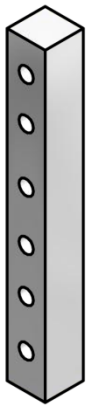

Part Name: Aperture Boron Nitride Post.ipt

Front View

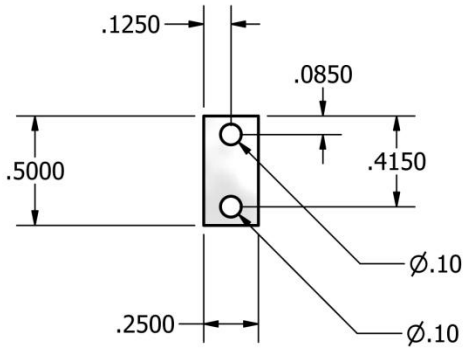

Side View

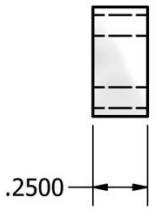

Iso View

Part Name: Aperture Boron Nitride Small Post.ipt

Front View

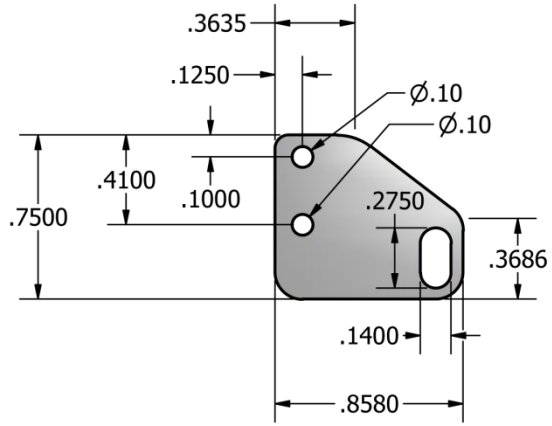

Side View

Iso View

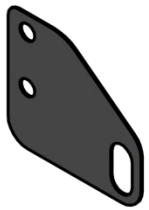

Part Name: Aperture Bottom Mount.ipt

Front View

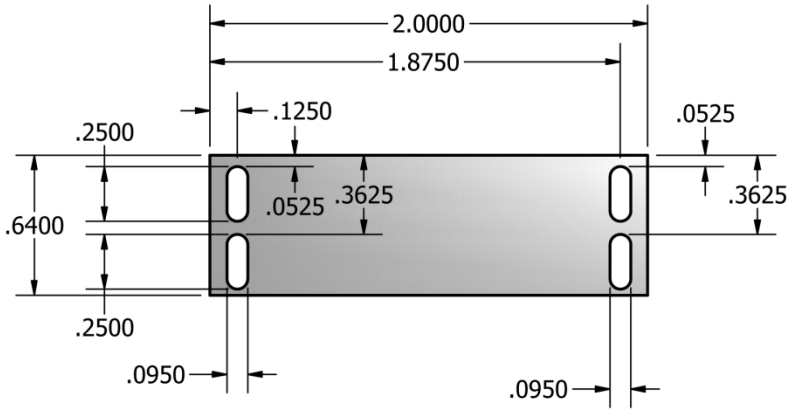

Side View

Iso View

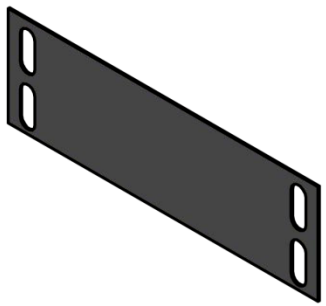

Part Name: Aperture Bottom Plate.ipt

Front View

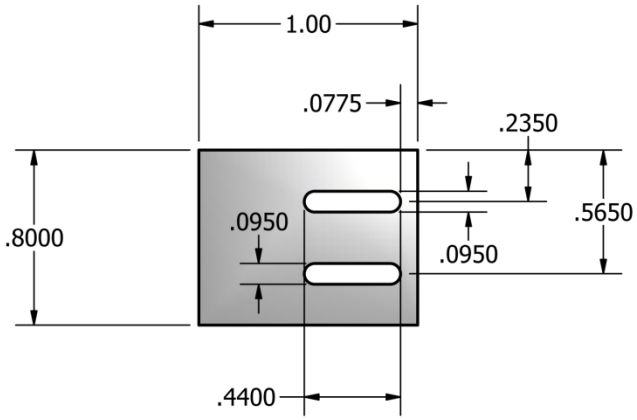

Side View

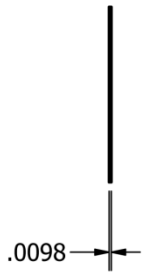

Iso View

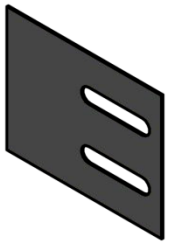

Part Name: Aperture Side Plate.ipt

Front View

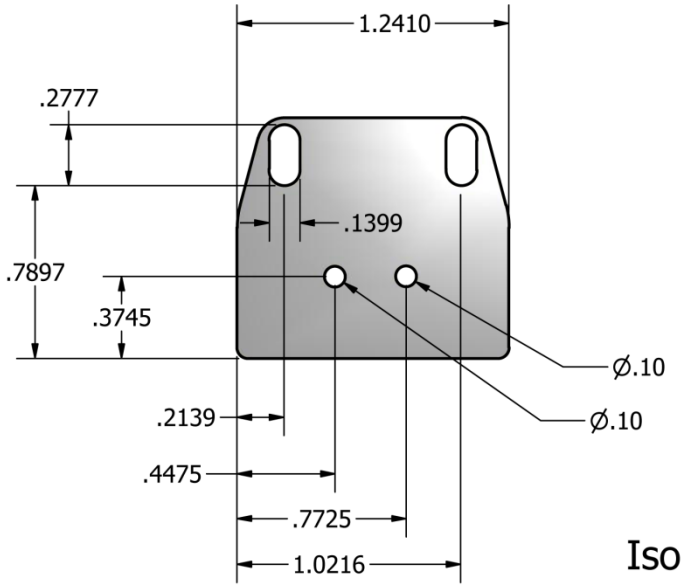

Side View

Iso View

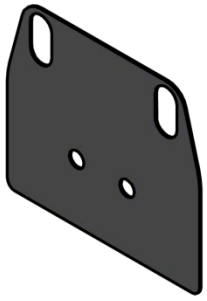

Part Name: Aperture Top Mount.ipt

Front View

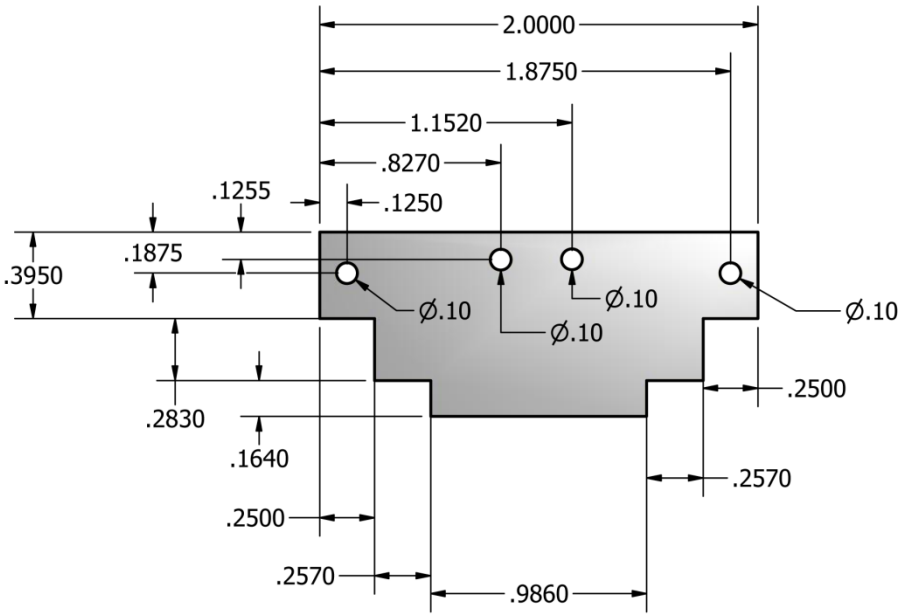

Side View

Iso View

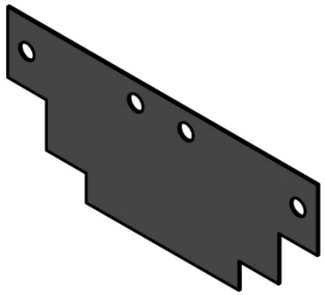

Part Name: Aperture Top Plate.ipt

Front View

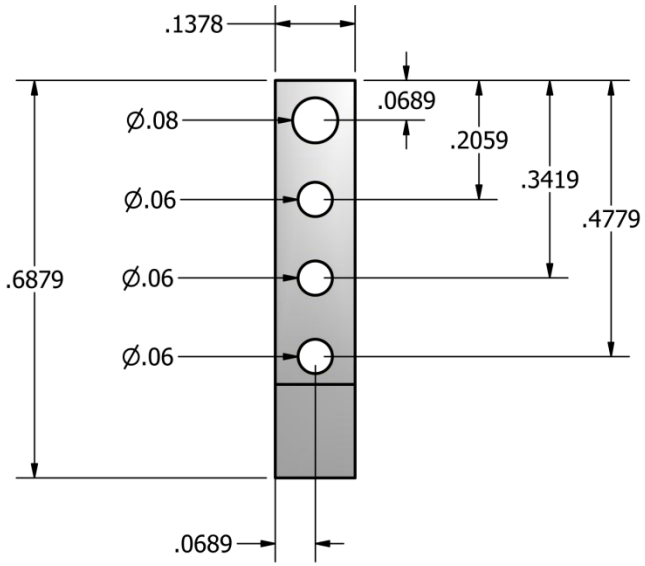

Side View

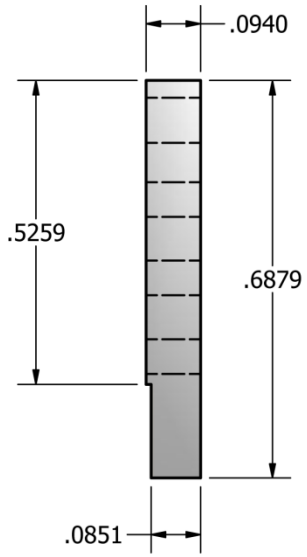

Iso View

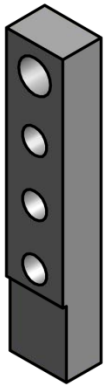

Part Name: Clamp.ipt

Front View

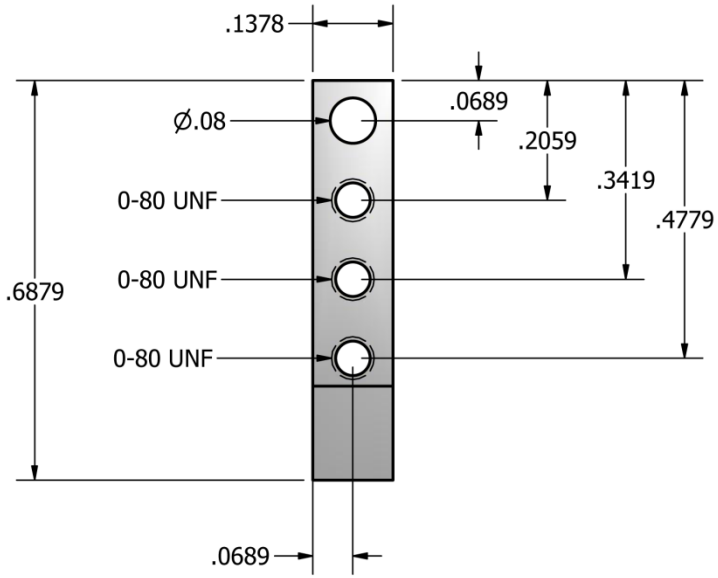

Side View

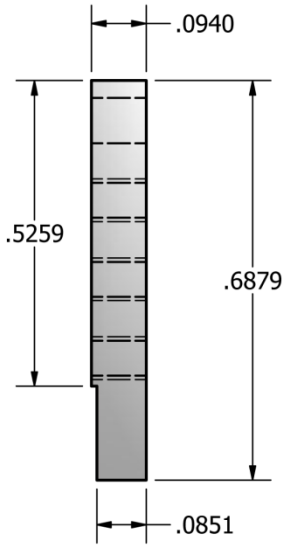

Iso View

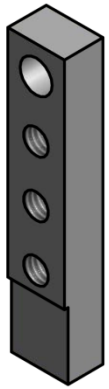

Part Name: Clamp Threaded.ipt

Front View

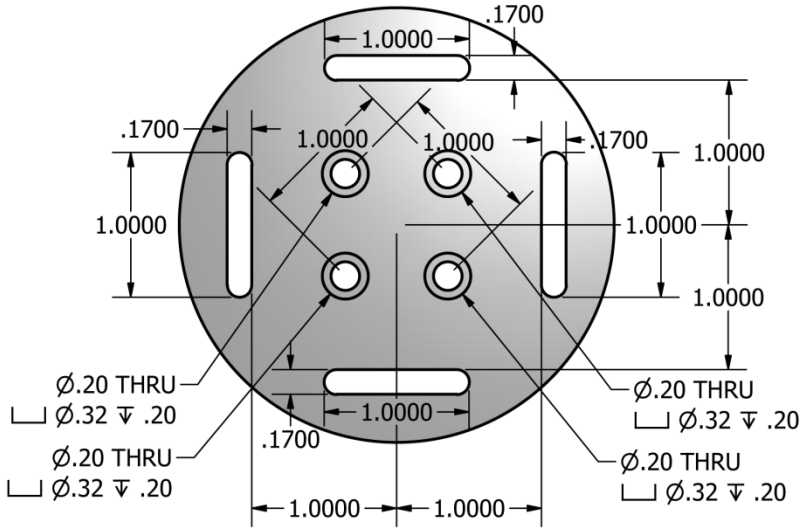

Side View

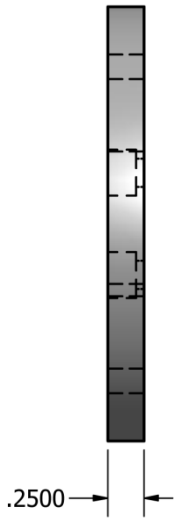

Iso View

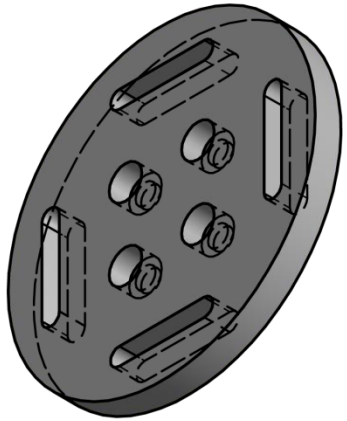

Part Name: Feedthrough Base.ipt

Front View

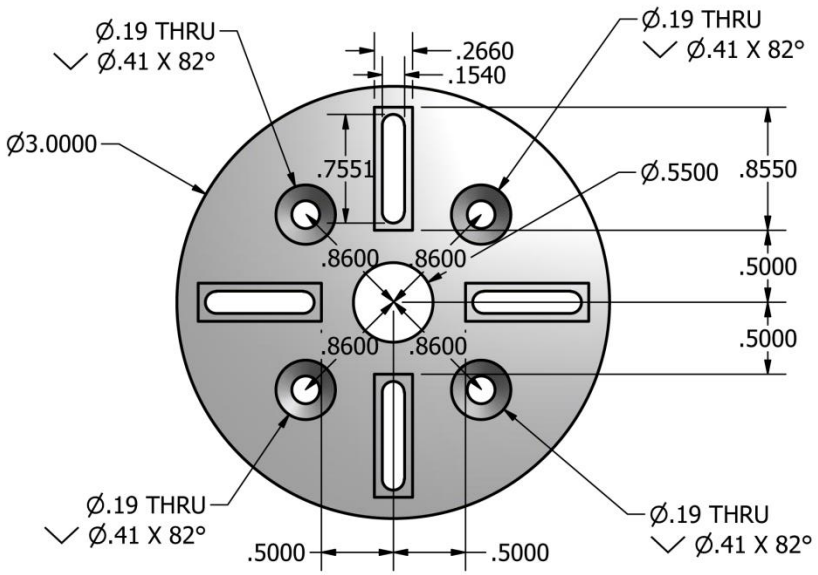

Side View

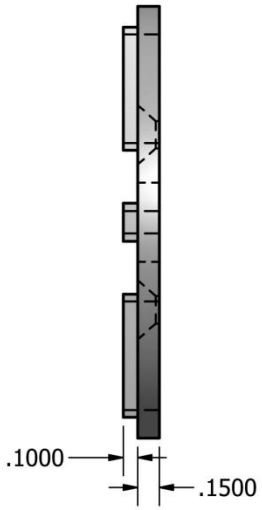

Iso View

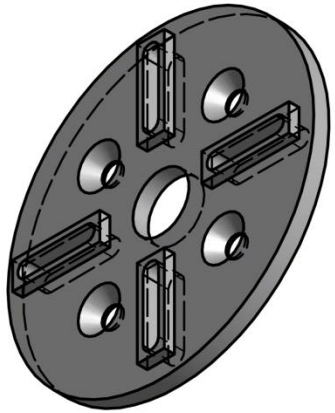

Part Name: Feedthrough Base-Tower Connect.ipt

Front View

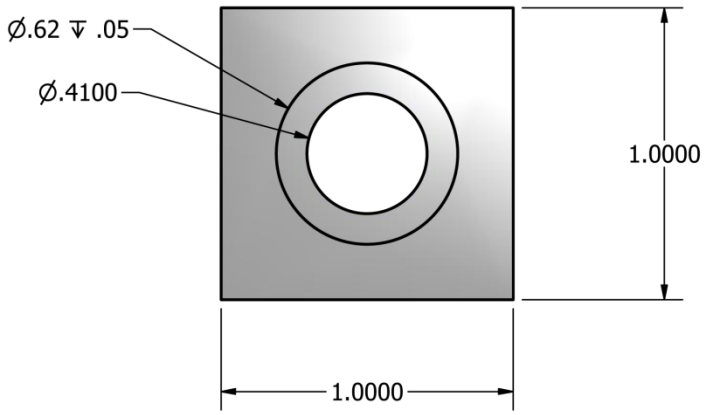

Side View

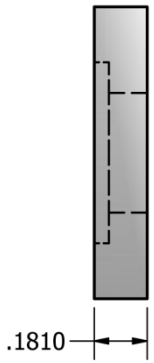

Iso View

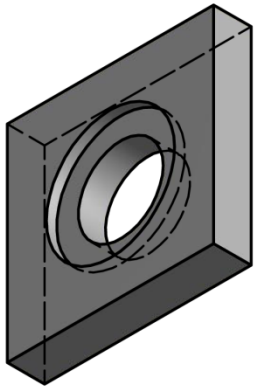

Part Name: Feedthrough Spring Top.ipt

Front View

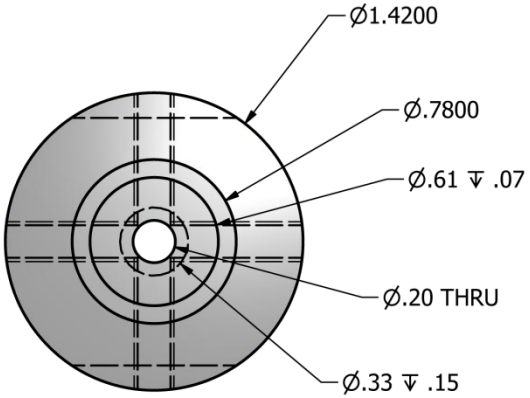

Side View

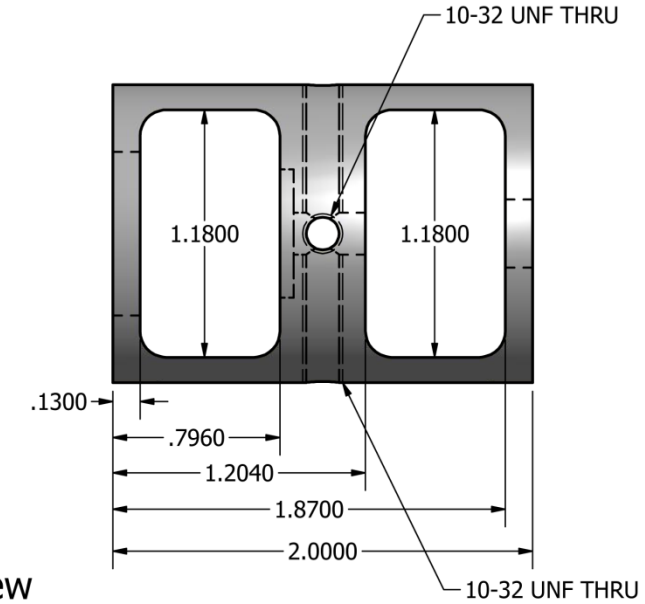

Iso View

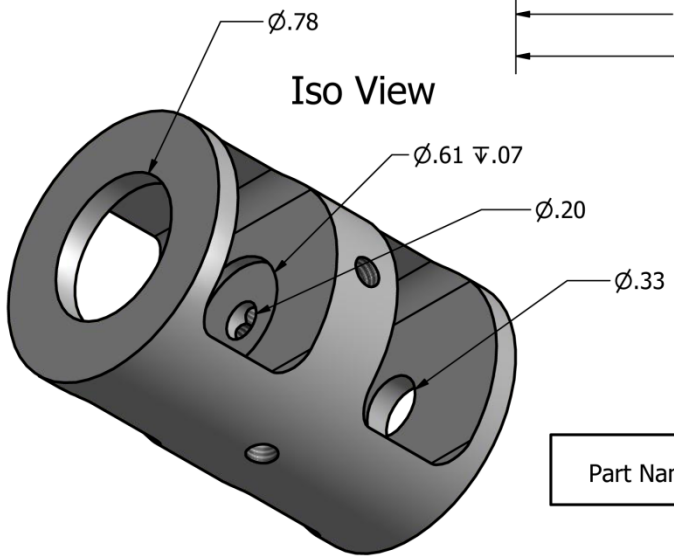

Part Name: Feedthrough Tower DVRT Holder.ipt

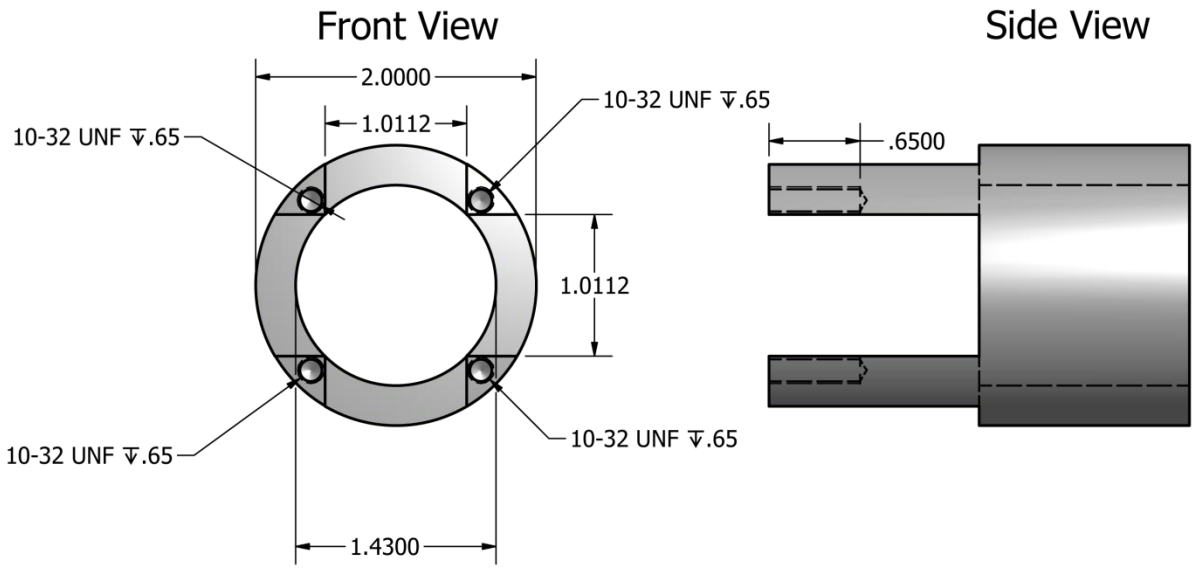

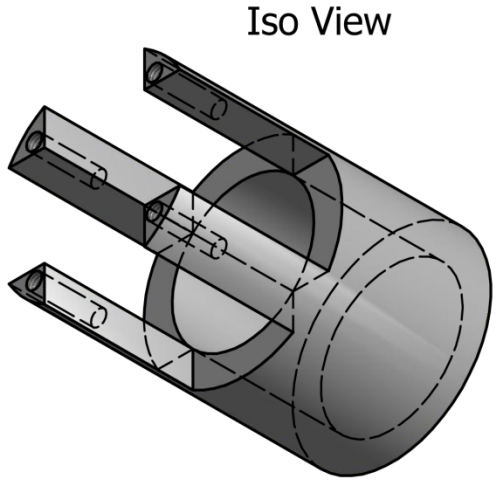

Part Name: Feedthrough Tower.ipt

Front View

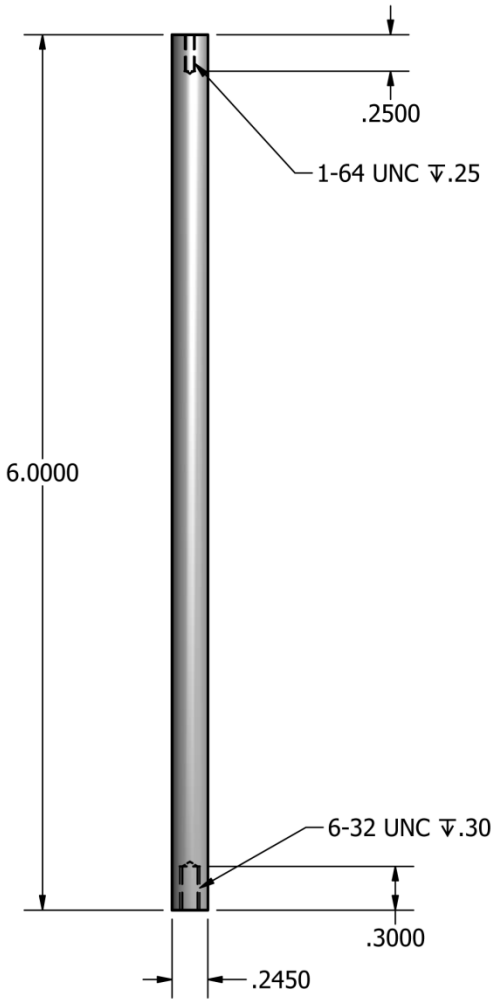

Iso View

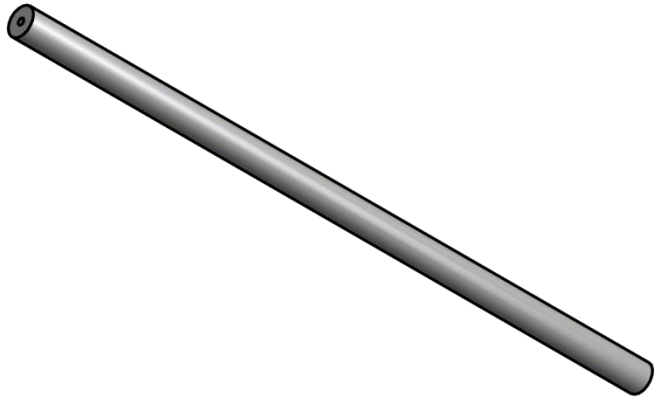

Part Name: Load Post.ipt

Front View

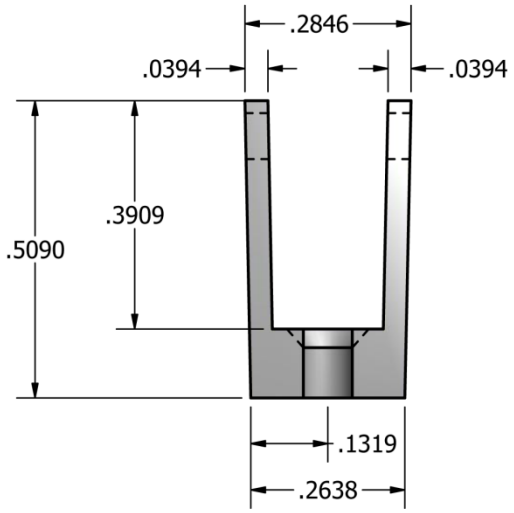

Side View

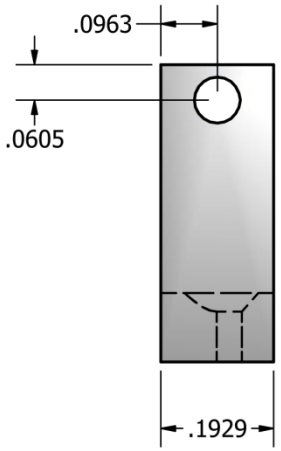

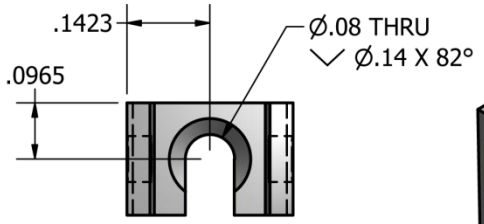

Iso View

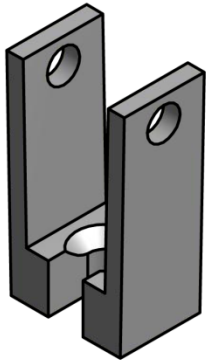

Part Name: Load-Pin Adapter.ipt

Front View

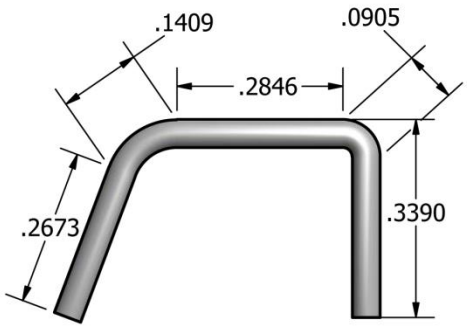

Side View

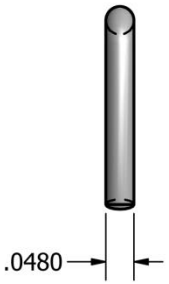

Iso View

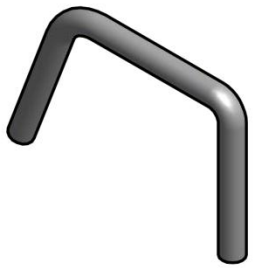

Part Name: Load-Pin Pin.ipt

Front View

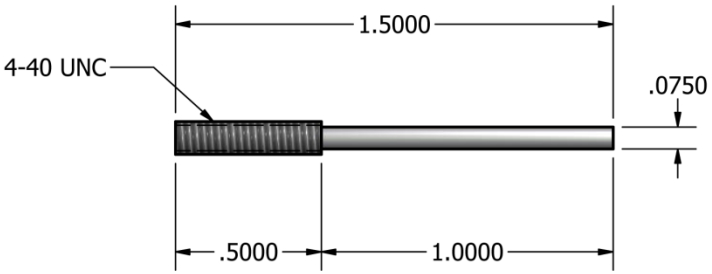

Iso View

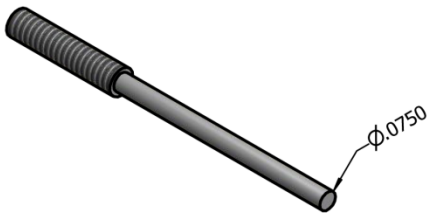

Part Name: Mounting Post.ipt

Front View

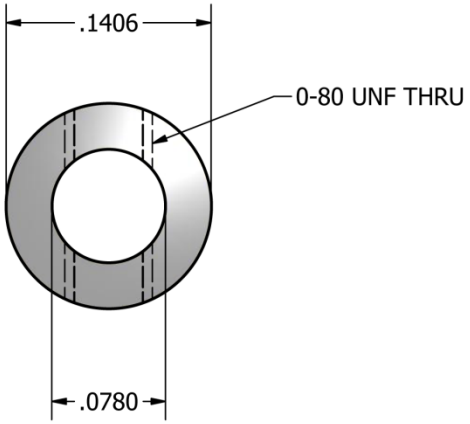

Side View

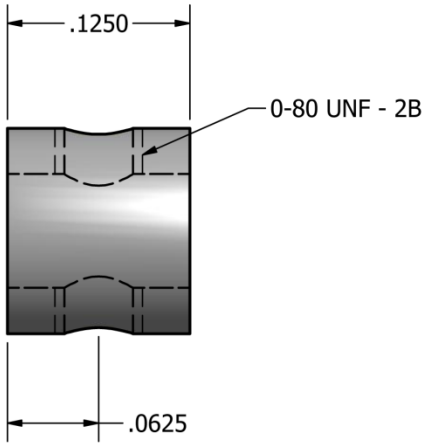

Iso View

Part Name: Sample Collet.ipt

Front View

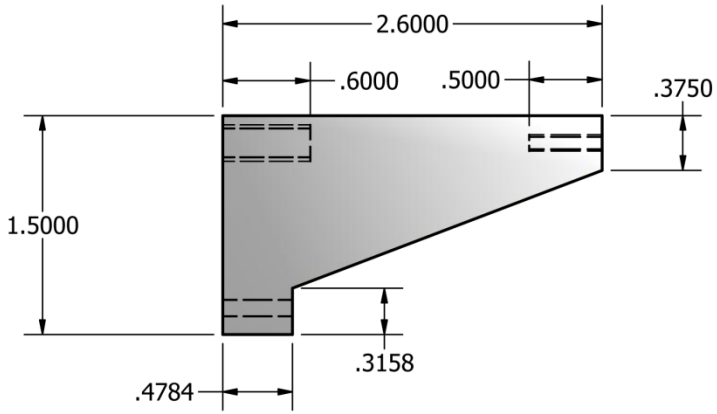

Side View

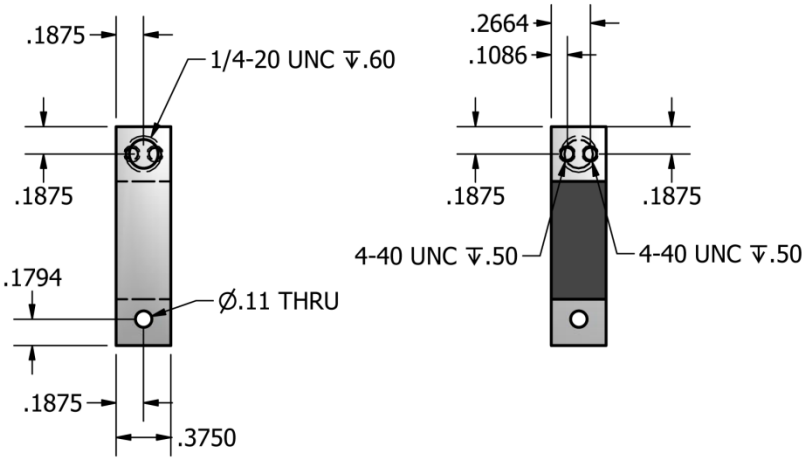

Iso View

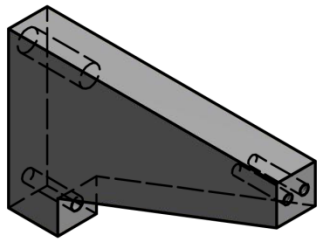

Part Name: Sample Post Base.ipt

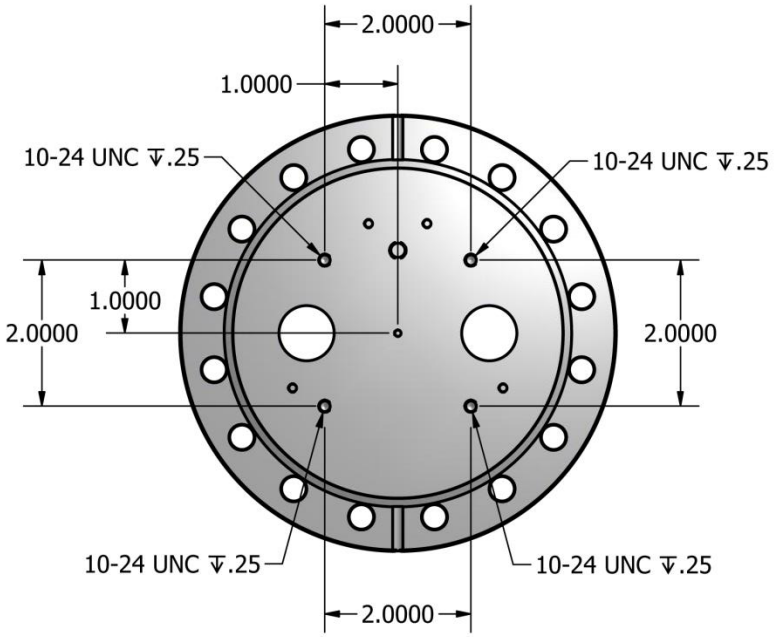

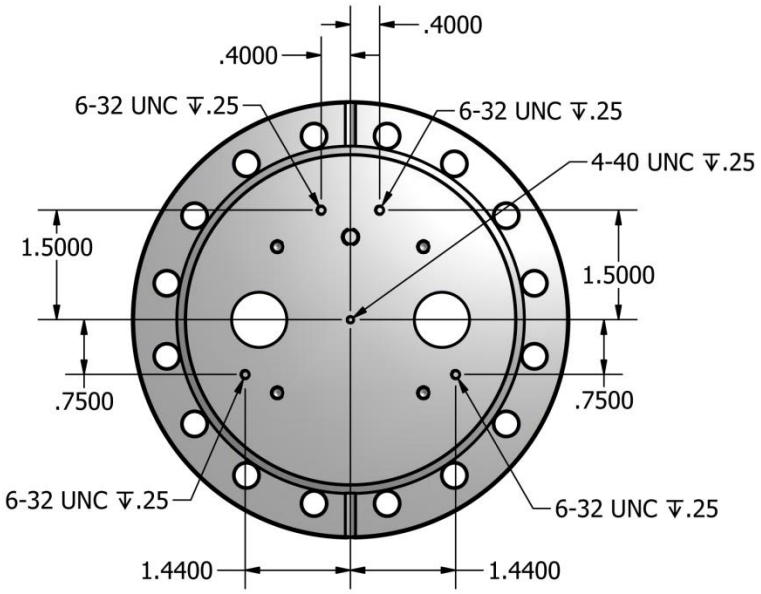

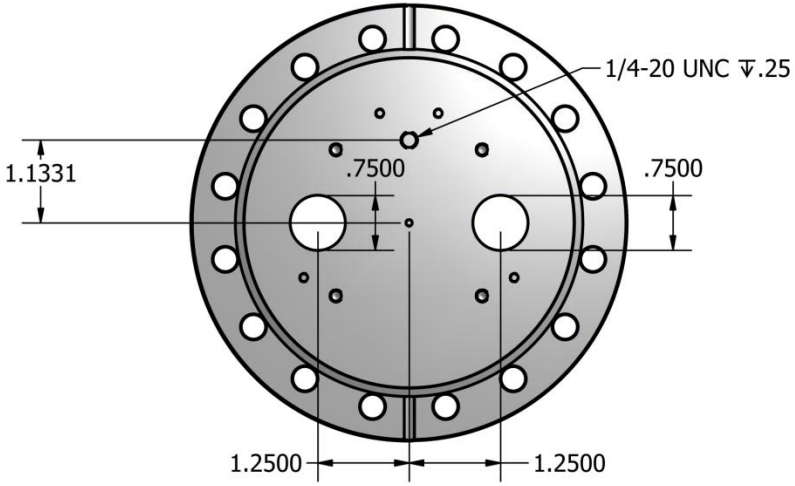

Part Name: Stage Flange.ipt

Front View

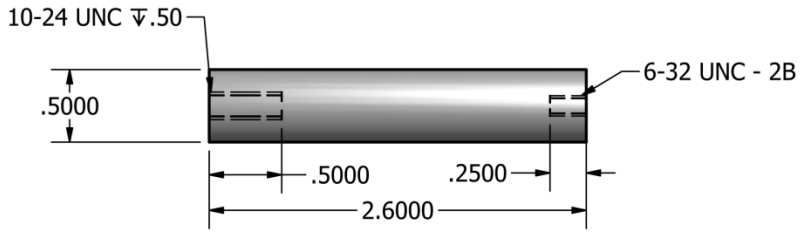

Side View

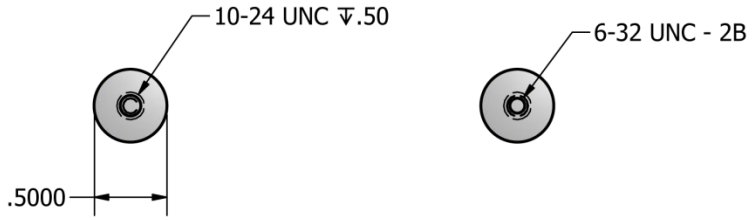

Iso View

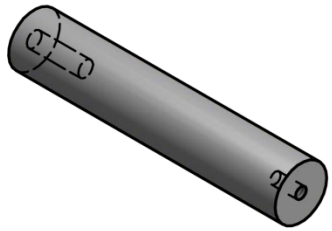

Part Name: Stage Post.ipt

Front View

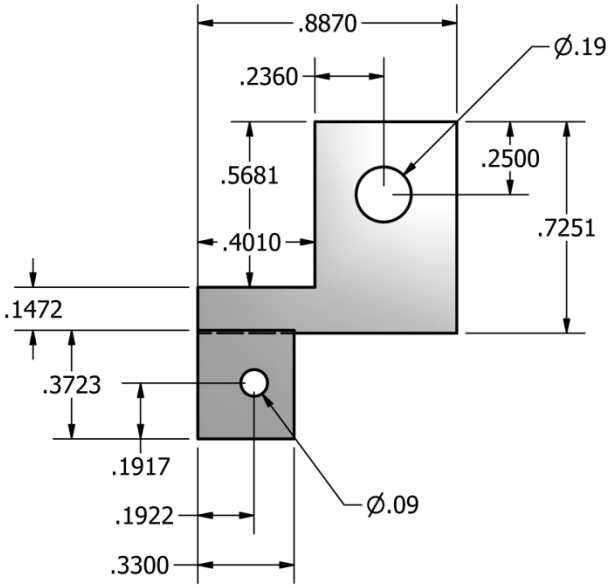

Side View

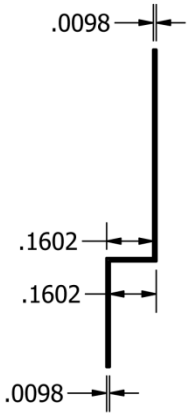

Iso View

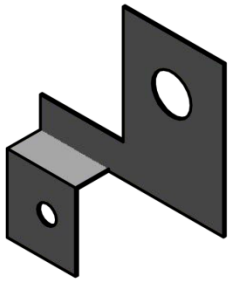

Part Name: Tantalum Link.ipt

Front View

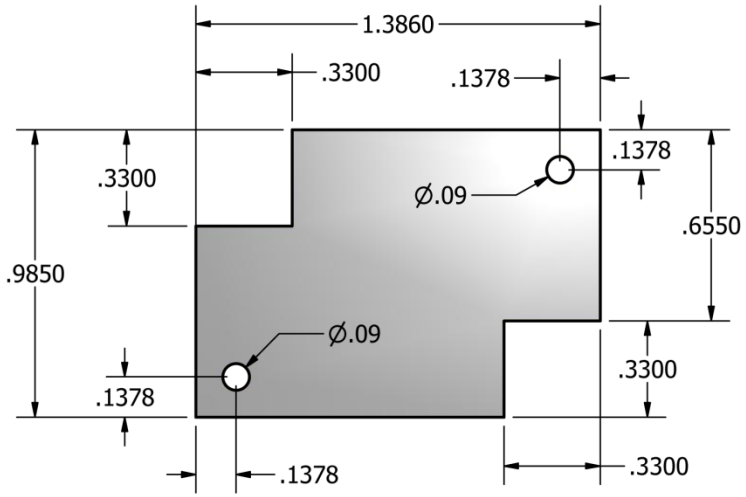

Side View

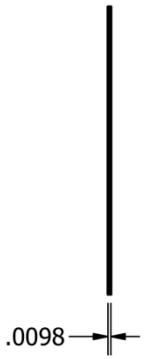

Iso View

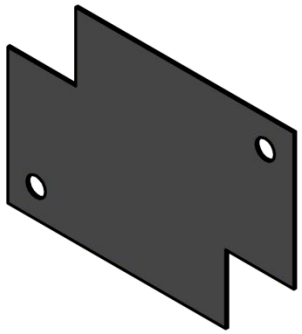

Part Name: Tantalum Shield.ipt

Tungsten loading weights were ordered from Midwest Tungsten Service, Inc. http://www.tungsten.com/. Six weights were machined with a 1.0" x 1.0"cross section, and a 0.25" hole drilled through the center. The heights of the blocks were 0.190", 0.378", 0.756", 1.512", 2.268", and 3.024" to achieve respective masses of 0.125, 0.250, 0.500, 1.000, 1.500, and 2.00 pounds.

The alumina for the stage pieces were ordered from ZIRCAR Refractory Composites, Inc. http://zrci.com/. All the pieces were made from Refractory Sheet Type RS-99R.

The graphite foil, used between the samples and the clamp pieces, was purchased from Alfa Aesar, http://www.alfa.com. The foil is 0.005" thick x 30cm x 100cm sheet, part number 43078. The tantalum used for the heater shield, tantalum link, and the aperture pieces were also purchased from Alfa Aesar. The tantalum is 0.01" thick x 200mm x 200mm sheets, part number 10353.

The boron nitride, used for the aperture posts, was purchased from McMaster-Carr Supply Company, http://www.mcmaster.com. These pieces are 0.25" x 0.25" x 12", part number 84995K52.

All the other pieces, from the drawings, were machined from 304 stainless steel. The parts of the stage that were pre-fabricated, and all the necessary hardware, were purchased from McMaster-Carr Supply Company. A list of all these items, part description and associated part numbers, are included in Table A.2. All the metal parts were ordered from 316 stainless steel, when available, otherwise 18-8 stainless steel parts were ordered.

Table A.2. Part list of pre-fabricated stage components and necessary hardware, including part description and McMaster-Carr Supply Company associated part numbers.

Part Description	Part #
Ceramic Female Threaded Round Standoff 1/4" OD, 1/2" Length, 6-32 Screw Size	94335A115
18-8 SS Female Threaded Round Standoff 1/4" OD, 1" Length, 6-32 Screw Size	91125A449
18-8 SS Female Threaded Round Standoff 1/4" OD, 2" Length, 6-32 Screw Size	91125A483
Type 316 SS Cup Point Set Screw 6-32 Thread, 1/2" Long	92313A148
Type 316 SS Button Head Socket Cap Screw 6-32 Thread, 1/4" Length	98164A106
Type 316 SS Cup Point Set Screw 10-24 Thread, 1/2" Long	92313A242
Type 316 SS Socket Head Cap Screw 4-40 Thread, 5/8" Length	92185A111
Type 316 SS Cup Point Set Screw 1/4"-20 Thread, 1/2" Long	92313A537
Type 316 SS Socket Head Cap Screw 4-40 Thread, 1/2" Length	92185A110
Type 316 SS General Purpose Flat Washer NO. 4 Screw Size, 5/16" OD, .02"-.04" Thick	90107A005
Type 316 SS Machine Screw Hex Nut 4-40 Thread Size, 1/4" Width, 3/32" Height	90257A005
Type 316 SS Socket Head Cap Screw 6-32 Thread, 1/2" Length	92185A148
Type 316 SS Machine Screw Hex Nut 6-32 Thread Size, 5/16" Width, 7/64" Height	90257A007
Type 316 SS General Purpose Flat Washer NO. 6 Screw Size, 3/8" OD, .02"-.04" Thick	90107A101
Type 316 SS Socket Head Cap Screw 2-56 Thread, 3/4" Length	92185A092
Type 316 SS Socket Head Cap Screw 2-56 Thread, 5/8" Length	92185A089
Type 316 SS Socket Head Cap Screw 2-56 Thread, 3/16" Length	92185A073
18-8 SS Machine Screw Hex Nut 2-56 Thread Size, 3/16" Width, 1/16" Height	91841A003
18-8 SS Socket Head Cap Screw 0-80 Thread, 3/16" Length	92196A054
18-8 SS Flat Head Phillips Machine Screw 1-64 Thread, 1/2" Length	91771A070
Type 316 SS Cup Point Set Screw 6-32 Thread, 3/8" Long	92313A146
18-8 SS Cup Point Set Screw 0-80 Thread, 1/8" Long	92311A052
Type 316 SS Flat Head Socket Cap Screw 10-32 Thread, 1/2" Length	90585A989
Type 316 SS Socket Head Cap Screw 10-24 Thread, 3/8" Length	92185A240
Type 316 SS Socket Head Cap Screw 6-32 Thread, 1" Length	92185A153
Type 316 SS Cup Point Set Screw 10-32 Thread, 1/4" Long	92313A825

APPENDIX B

CREEP EXPERIMENT DATA

This appendix presents the data from the proton irradiation-induced creep experiments, and the corresponding analysis that was preformed according to Section 3.4. In the data plots, the strain measurements (in %) from the LSE measurements for the stressed sample (red data) and unstressed sample (blue data) and the DVRT measurement for the stressed sample (green data) are plotted on the left y-axis, the temperature in degrees Celsius (black data) is plotted along the top of the graph on the right y-axis, and the stage current in micro Amperes (pink data) is plotted along the bottom of the graph on the right y-axis. The linear fit of the strain for the strain measurements are also plotted for the LSE stressed sample (orange), LSE unstressed sample (bright blue), and DVRT stressed sample (bright green). The calculated dose is included along the top axis, in orange.

Table B.1. Summary of the linear fit to the LSE and DVRT data for the stressed sample, and the constant fit to the stage current and sample temperature from Experiment #1.

Linear Fit Values	LSE Stressed Sample	DVRT Stressed Sample	Constant Fit Values	Stage Current	Constant Fit Values	Temperature
A (%)	1.78	5.30	M (μA)	33.18	M (°C)	1002.46
B (%/hr)	$2.57\text{x}10^{-2}$	$2.22\text{x}10^{-2}$	V_C (μA^2)	1.27	V_C (°C^2)	12.16
V_L (%^{2})	$9.13\text{x}10^{-4}$	$1.91\text{x}10^{-4}$	$\sigma[M]$ (μA)	$1.12\text{x}10^{-2}$	$\sigma[M]$ (°C)	$3.20\text{x}10^{-2}$
$V[B]$ (%^{2}/hr^2)	$3.33\text{x}10^{-11}$	$1.43\text{x}10^{-10}$				
$V[A]$ (%^{2})	$1.19\text{x}10^{-7}$	$1.75\text{x}10^{-7}$				
$\sigma[B]$ (%/hr)	$5.77\text{x}10^{-6}$	$1.20\text{x}10^{-5}$				
$\sigma[A]$ (%)	$3.44\text{x}10^{-4}$	$4.18\text{x}10^{-4}$				

Table B.2. Summary of the linear fit to the LSE and DVRT data for the stressed sample, and the constant fit to the stage current and sample temperature from Experiment #2.

Linear Fit Values	LSE Stressed Sample	DVRT Stressed Sample	Constant Fit Values	Stage Current	Constant Fit Values	Temperature
A (%)	1.08	4.25	M (μA)	44.08	M (°C)	997.63
B (%/hr)	$1.91\text{x}10^{-2}$	$2.09\text{x}10^{-2}$	V_C (μA^2)	29.55	V_C (°C^2)	10.84
V_L (%^{2})	$4.84\text{x}10^{-3}$	$3.97\text{x}10^{-4}$	$\sigma[M]$ (μA)	$5.03\text{x}10^{-2}$	$\sigma[M]$ (°C)	$2.99\text{x}10^{-2}$
$V[B]$ (%^{2}/hr^2)	$3.49\text{x}10^{-10}$	$5.68\text{x}10^{-11}$				
$V[A]$ (%^{2})	$1.18\text{x}10^{-6}$	$2.44\text{x}10^{-7}$				
$\sigma[B]$ (%/hr)	$1.87\text{x}10^{-5}$	$7.54\text{x}10^{-6}$				
$\sigma[A]$ (%)	$1.08\text{x}10^{-3}$	$4.94\text{x}10^{-4}$				

Table B.3. Summary of the linear fit to the LSE and DVRT data for the stressed sample, and the constant fit to the stage current and sample temperature from Experiment #3.

Linear Fit Values	LSE Stressed Sample	DVRT Stressed Sample	Constant Fit Values	Stage Current	Constant Fit Values	Temperature
A (%)	0.34	5.07	M (μA)	31.12	M (°C)	1002.54
B (%/hr)	$1.72\text{x}10^{-2}$	$2.34\text{x}10^{-2}$	V_C (μA^2)	0.34	V_C (°C^2)	14.14
V_L (%^{2})	$1.06\text{x}10^{-3}$	$9.87\text{x}10^{-4}$	$\sigma[M]$ (μA)	$5.32\text{x}10^{-3}$	$\sigma[M]$ (°C)	$3.30\text{x}10^{-2}$
$V[B]$ (%^{2}/hr^2)	$8.40\text{x}10^{-11}$	$1.05\text{x}10^{-10}$				
$V[A]$ (%^{2})	$3.36\text{x}10^{-7}$	$4.56\text{x}10^{-7}$				
$\sigma[B]$ (%/hr)	$9.17\text{x}10^{-6}$	$1.02\text{x}10^{-5}$				
$\sigma[A]$ (%)	$5.80\text{x}10^{-4}$	$6.75\text{x}10^{-4}$				

Table B.4. Summary of the linear fit to the LSE and DVRT data for the stressed sample, and the constant fit to the stage current and sample temperature from Experiment #4.

Linear Fit Values	LSE Stressed Sample	DVRT Stressed Sample	Constant Fit Values	Stage Current	Constant Fit Values	Temperature
A (%)	0.45	1.92	M (μA)	31.61	M (°C)	998.16
B (%/hr)	$3.03\text{x}10^{-2}$	$1.79\text{x}10^{-2}$	V_C (μA^2)	7.16	V_C (°C^2)	7.09
V_L (%^{2})	$2.35\text{x}10^{-3}$	$7.96\text{x}10^{-4}$	$\sigma[M]$ (μA)	$3.10\text{x}10^{-2}$	$\sigma[M]$ (°C)	$3.03\text{x}10^{-2}$
$V[B]$ (%^{2}/hr^2)	$8.64\text{x}10^{-10}$	$3.69\text{x}10^{-10}$				
$V[A]$ (%^{2})	$1.22\text{x}10^{-6}$	$5.66\text{x}10^{-7}$				
$\sigma[B]$ (%/hr)	$2.94\text{x}10^{-5}$	$1.92\text{x}10^{-5}$				
$\sigma[A]$ (%)	$1.11\text{x}10^{-3}$	$7.53\text{x}10^{-4}$				

Table B.5. Summary of the linear fit to the LSE and DVRT data for the stressed sample, and the constant fit to the stage current and sample temperature from Experiment #5.

Linear Fit Values	LSE Stressed Sample	DVRT Stressed Sample	Constant Fit Values	Stage Current	Constant Fit Values	Temperature
A (%)	-0.15	4.52	M (μA)	34.22	M (°C)	998.77
B (%/hr)	$5.38\text{x}10^{-2}$	$4.82\text{x}10^{-2}$	V_C (μA^2)	0.44	V_C (°C^2)	8.41
V_L (%^{2})	$2.91\text{x}10^{-3}$	$2.36\text{x}10^{-3}$	$\sigma[M]$ (μA)	$8.18\text{x}10^{-3}$	$\sigma[M]$ (°C)	$3.50\text{x}10^{-2}$
$V[B]$ (%^{2}/hr^2)	$5.60\text{x}10^{-10}$	$8.75\text{x}10^{-10}$				
$V[A]$ (%^{2})	$6.59\text{x}10^{-7}$	$1.19\text{x}10^{-6}$				
$\sigma[B]$ (%/hr)	$2.37\text{x}10^{-5}$	$2.96\text{x}10^{-5}$				
$\sigma[A]$ (%)	$8.12\text{x}10^{-4}$	$1.09\text{x}10^{-3}$				

Table B.6. Summary of the linear fit to the LSE and DVRT data for the stressed sample, and the constant fit to the stage current and sample temperature from Experiment #6.

Linear Fit Values	LSE Stressed Sample	DVRT Stressed Sample	Constant Fit Values	Stage Current	Constant Fit Values	Temperature
A (%)	-1.87	4.50	M (μA)	34.63	M (°C)	998.14
B (%/hr)	$1.60\text{x}10^{-2}$	$1.57\text{x}10^{-2}$	V_C (μA^2)	0.51	V_C (°C^2)	11.09
V_L (%^{2})	$1.44\text{x}10^{-4}$	$3.29\text{x}10^{-4}$	$\sigma[M]$ (μA)	$9.66\text{x}10^{-3}$	$\sigma[M]$ (°C)	$3.33\text{x}10^{-2}$
$V[B]$ (%^{2}/hr^2)	$1.29\text{x}10^{-10}$	$5.52\text{x}10^{-10}$				
$V[A]$ (%^{2})	$1.13\text{x}10^{-7}$	$5.87\text{x}10^{-7}$				
$\sigma[B]$ (%/hr)	$1.14\text{x}10^{-5}$	$2.35\text{x}10^{-5}$				
$\sigma[A]$ (%)	$3.36\text{x}10^{-4}$	$7.66\text{x}10^{-4}$				

Table B.7. Summary of the linear fit to the LSE and DVRT data for the stressed sample, and the constant fit to the stage current and sample temperature from Experiment #7.

Linear Fit Values	LSE Stressed Sample	DVRT Stressed Sample	Constant Fit Values	Stage Current	Constant Fit Values	Temperature
A (%)	2.53	4.97	M (μA)	29.53	M (°C)	1001.38
B (%/hr)	$5.31\text{x}10^{-3}$	$1.08\text{x}10^{-2}$	V_C (μA^2)	0.15	V_C (°C^2)	7.80
V_L (%^{2})	$9.82\text{x}10^{-4}$	$6.79\text{x}10^{-4}$	$\sigma[M]$ (μA)	$4.90\text{x}10^{-3}$	$\sigma[M]$ (°C)	$3.40\text{x}10^{-2}$
$V[B]$ (%^{2}/hr^2)	$5.49\text{x}10^{-10}$	$6.91\text{x}10^{-10}$				
$V[A]$ (%^{2})	$5.97\text{x}10^{-7}$	$8.96\text{x}10^{-7}$				
$\sigma[B]$ (%/hr)	$2.34\text{x}10^{-5}$	$2.63\text{x}10^{-5}$				
$\sigma[A]$ (%)	$7.73\text{x}10^{-4}$	$9.46\text{x}10^{-4}$				

Table B.8. Summary of the linear fit to the LSE and DVRT data for the stressed sample, and the constant fit to the stage current and sample temperature from Experiment #8.

Linear Fit Values	LSE Stressed Sample	DVRT Stressed Sample	Constant Fit Values	Stage Current	Constant Fit Values	Temperature
0.0255dpa/day Regime						
A (%)	0.23	0.11	M (μA)	7.18	M (°C)	702.47
B (%/hr)	1.21×10^{-3}	8.86×10^{-4}	V_C (μA^2)	0.04	V_C (°C^2)	6.93
V_L (%^{2})	7.26×10^{-5}	4.50×10^{-5}	$\sigma[M]$ (μA)	2.58×10^{-3}	$\sigma[M]$ (°C)	3.17×10^{-2}
$V[B]$ (%^{2}/hr^2)	3.79×10^{-11}	4.00×10^{-11}				
$V[A]$ (%^{2})	4.51×10^{-8}	5.55×10^{-8}				
$\sigma[B]$ (%/hr)	6.16×10^{-6}	6.33×10^{-6}				
$\sigma[A]$ (%)	2.12×10^{-4}	2.36×10^{-4}				
0.0433dpa/day Regime						
A (%)	0.15	-0.68	M (μA)	12.19	M (°C)	704.09
B (%/hr)	5.42×10^{-3}	2.26×10^{-4}	V_C (μA^2)	0.03	V_C (°C^2)	3.79
V_L (%^{2})	1.85×10^{-4}	5.50×10^{-6}	$\sigma[M]$ (μA)	2.27×10^{-3}	$\sigma[M]$ (°C)	2.32×10^{-2}
$V[B]$ (%^{2}/hr^2)	9.13×10^{-11}	4.94×10^{-12}				
$V[A]$ (%^{2})	7.55×10^{-7}	4.49×10^{-8}				
$\sigma[B]$ (%/hr)	9.55×10^{-6}	2.22×10^{-6}				
$\sigma[A]$ (%)	8.69×10^{-4}	2.12×10^{-4}				
0.0477dpa/day Regime						
A (%)	-0.07	-0.92	M (μA)	13.43	M (°C)	704.91
B (%/hr)	8.24×10^{-3}	1.74×10^{-4}	V_C (μA^2)	0.05	V_C (°C^2)	7.73
V_L (%^{2})	9.00×10^{-5}	8.89×10^{-6}	$\sigma[M]$ (μA)	2.86×10^{-3}	$\sigma[M]$ (°C)	3.41×10^{-2}
$V[B]$ (%^{2}/hr^2)	5.26×10^{-11}	7.86×10^{-12}				
$V[A]$ (%^{2})	1.17×10^{-6}	1.83×10^{-7}				
$\sigma[B]$ (%/hr)	7.26×10^{-6}	2.80×10^{-6}				
$\sigma[A]$ (%)	1.08×10^{-3}	4.27×10^{-4}				

Table B.9. Summary of the linear fit to the LSE and DVRT data for the stressed sample, and the constant fit to the stage current and sample temperature from Experiment #9.

Linear Fit Values	LSE Stressed Sample	DVRT Stressed Sample	Constant Fit Values	Stage Current	Constant Fit Values	Temperature
0.0379dpa/day Regime						
A (%)	0.71	3.65	M (μA)	10.91	M (°C)	703.09
B (%/hr)	7.14×10^{-3}	2.53×10^{-3}	V_C (μA^2)	0.08	V_C (°C^2)	5.17
V_L (%^{2})	5.57×10^{-4}	1.09×10^{-4}	$\sigma[M]$ (μA)	3.88×10^{-3}	$\sigma[M]$ (°C)	3.07×10^{-2}
$V[B]$ (%^{2}/hr^2)	5.43×10^{-10}	2.23×10^{-10}				
$V[A]$ (%^{2})	4.01×10^{-7}	2.06×10^{-7}				
$\sigma[B]$ (%/hr)	2.33×10^{-5}	1.49×10^{-5}				
$\sigma[A]$ (%)	6.33x10-4	4.54×10^{-4}				
0.0317dpa/day Regime						
A (%)	0.80	4.51	M (μA)	9.13	M (°C)	704.38
B (%/hr)	4.85×10^{-3}	3.30×10^{-3}	V_C (μA^2)	0.08	V_C (°C^2)	81.95
V_L (%^{2})	1.97×10^{-5}	1.57×10^{-4}	$\sigma[M]$ (μA)	4.09×10^{-3}	$\sigma[M]$ (°C)	1.21×10^{-1}
$V[B]$ (%^{2}/hr^2)	1.90×10^{-11}	2.20×10^{-10}				
$V[A]$ (%^{2})	1.01×10^{-7}	1.24×10^{-6}				
$\sigma[B]$ (%/hr)	4.36×10^{-6}	1.48×10^{-5}				
$\sigma[A]$ (%)	3.18×10^{-4}	1.11×10^{-3}				
0.0255dpa/day Regime						
A (%)	0.85	5.37	M (μA)	7.36	M (°C)	702.37
B (%/hr)	4.43×10^{-3}	1.59×10^{-3}	V_C (μA^2)	0.05	V_C (°C^2)	60.70
V_L (%^{2})	1.24×10^{-4}	8.89×10^{-5}	$\sigma[M]$ (μA)	3.29×10^{-3}	$\sigma[M]$ (°C)	1.04×10^{-1}
$V[B]$ (%^{2}/hr^2)	1.19×10^{-10}	1.16×10^{-10}				
$V[A]$ (%^{2})	1.72x10-6	1.73×10^{-6}				
$\sigma[B]$ (%/hr)	1.09×10^{-5}	1.08×10^{-5}				
$\sigma[A]$ (%)	1.31×10^{-3}	1.31×10^{-3}				

Table B.10. Summary of the linear fit to the LSE and DVRT data for the stressed sample, and the constant fit to the stage current and sample temperature from Experiment #10.

Linear Fit Values	LSE Stressed Sample	DVRT Stressed Sample	Constant Fit Values	Stage Current	Constant Fit Values	Temperature
A (%)	0.63	4.30	M (μA)	23.09	M (°C)	898.91
B (%/hr)	$9.29\text{x}10^{-3}$	$1.11\text{x}10^{-2}$	V_C (μA^2)	0.10	V_C (°C^2)	9.15
V_L (%^{2})	$1.48\text{x}10^{-4}$	$9.31\text{x}10^{-4}$	$\sigma[M]$ (μA)	$4.24\text{x}10^{-3}$	$\sigma[M]$ (°C)	$4.01\text{x}10^{-2}$
$V[B]$ (%^{2}/hr^2)	$1.37\text{x}10^{-10}$	$1.78\text{x}10^{-9}$				
$V[A]$ (%^{2})	$1.04\text{x}10^{-7}$	$1.67\text{x}10^{-6}$				
$\sigma[B]$ (%/hr)	$1.17\text{x}10^{-5}$	$4.22\text{x}10^{-5}$				
$\sigma[A]$ (%)	$3.22\text{x}10^{-4}$	$1.29\text{x}10^{-3}$				

Table B.11. Summary of the linear fit to the LSE and DVRT data for the stressed sample, and the constant fit to the stage current and sample temperature from Experiment #11.

Linear Fit Values	LSE Stressed Sample	DVRT Stressed Sample	Constant Fit Values	Stage Current	Constant Fit Values	Temperature
A (%)	2.37	5.52	M (μA)	44.42	M (°C)	1101.36
B (%/hr)	$8.86\text{x}10^{-3}$	$4.00\text{x}10^{-2}$	V_C (μA^2)	0.59	V_C (°C^2)	12.28
V_L (%^{2})	$2.45\text{x}10^{-3}$	$5.15\text{x}10^{-4}$	$\sigma[M]$ (μA)	$1.09\text{x}10^{-2}$	$\sigma[M]$ (°C)	$4.84\text{x}10^{-2}$
$V[B]$ (%^{2}/hr^2)	$3.36\text{x}10^{-9}$	$1.16\text{x}10^{-9}$				
$V[A]$ (%^{2})	$3.11\text{x}10^{-6}$	$1.23\text{x}10^{-6}$				
$\sigma[B]$ (%/hr)	$5.80\text{x}10^{-5}$	$3.41\text{x}10^{-5}$				
$\sigma[A]$ (%)	$1.76\text{x}10^{-3}$	$1.11\text{x}10^{-3}$				

Table B.12. Summary of the linear fit to the LSE and DVRT data for the stressed sample, and the constant fit to the stage current and sample temperature from Experiment #12.

Linear Fit Values	LSE Stressed Sample	DVRT Stressed Sample	Constant Fit Values	Stage Current	Constant Fit Values	Temperature
A (%)	2.77	6.44	M (μA)	50.25	M (°C)	1199.47
B (%/hr)	-3.39×10^{-3}	4.61×10^{-2}	V_C (μA^2)	0.55	V_C (°C^2)	17.92
V_L (%^{2})	4.00×10^{-2}	3.18×10^{-3}	$\sigma[M]$ (μA)	1.04×10^{-2}	$\sigma[M]$ (°C)	5.63×10^{-2}
$V[B]$ (%^{2}/hr^2)	3.82×10^{-8}	6.28×10^{-9}				
$V[A]$ (%^{2})	2.90×10^{-5}	5.93×10^{-6}				
$\sigma[B]$ (%/hr)	1.96×10^{-4}	7.93×10^{-5}				
$\sigma[A]$ (%)	5.38×10^{-3}	2.43×10^{-3}				

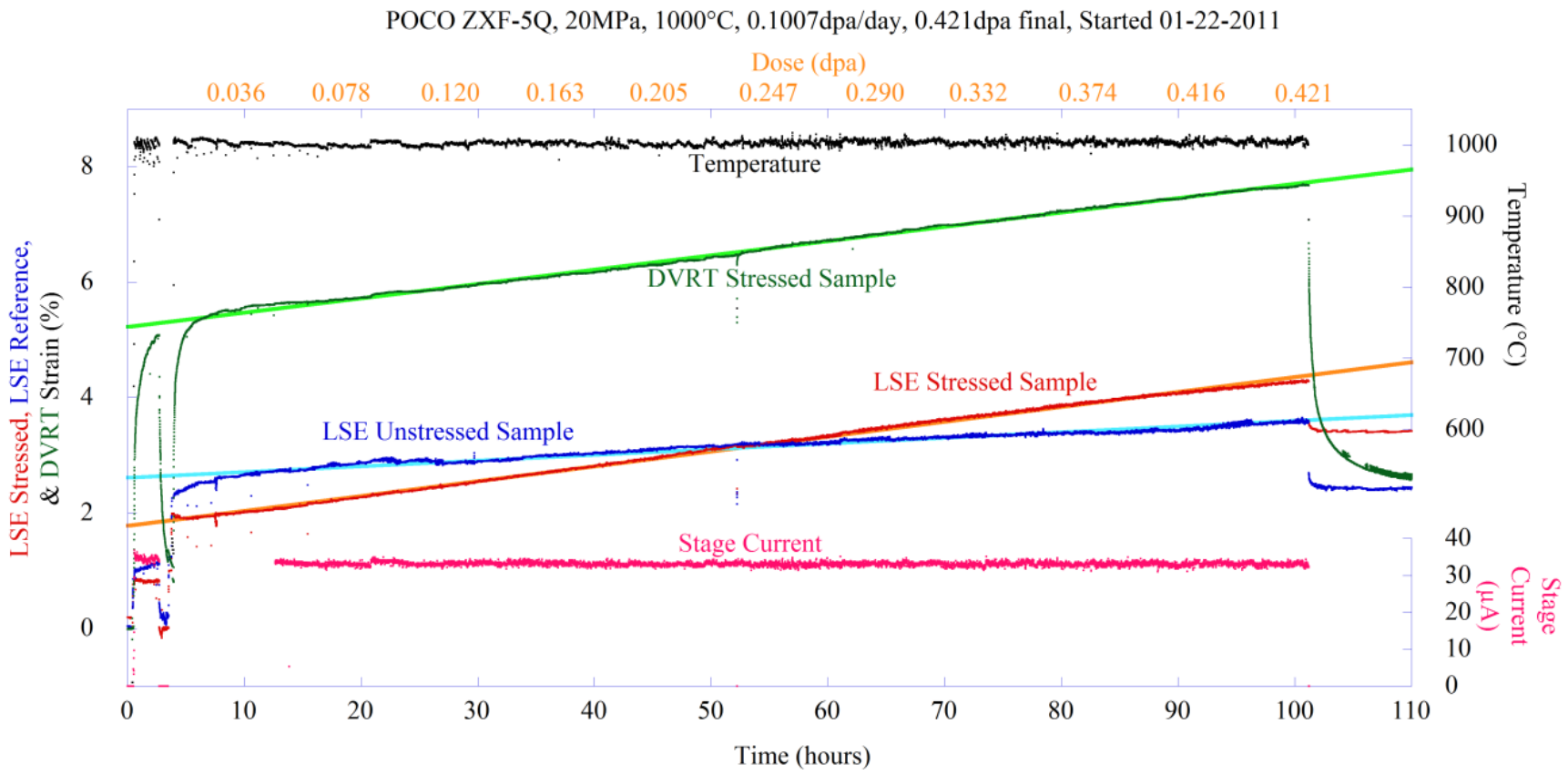

Figure B.1. Experimental data from Experiment #1, performed at 1000°C, 0.101dpa/day, 20MPa stress, to a final dose of 0.421dpa.

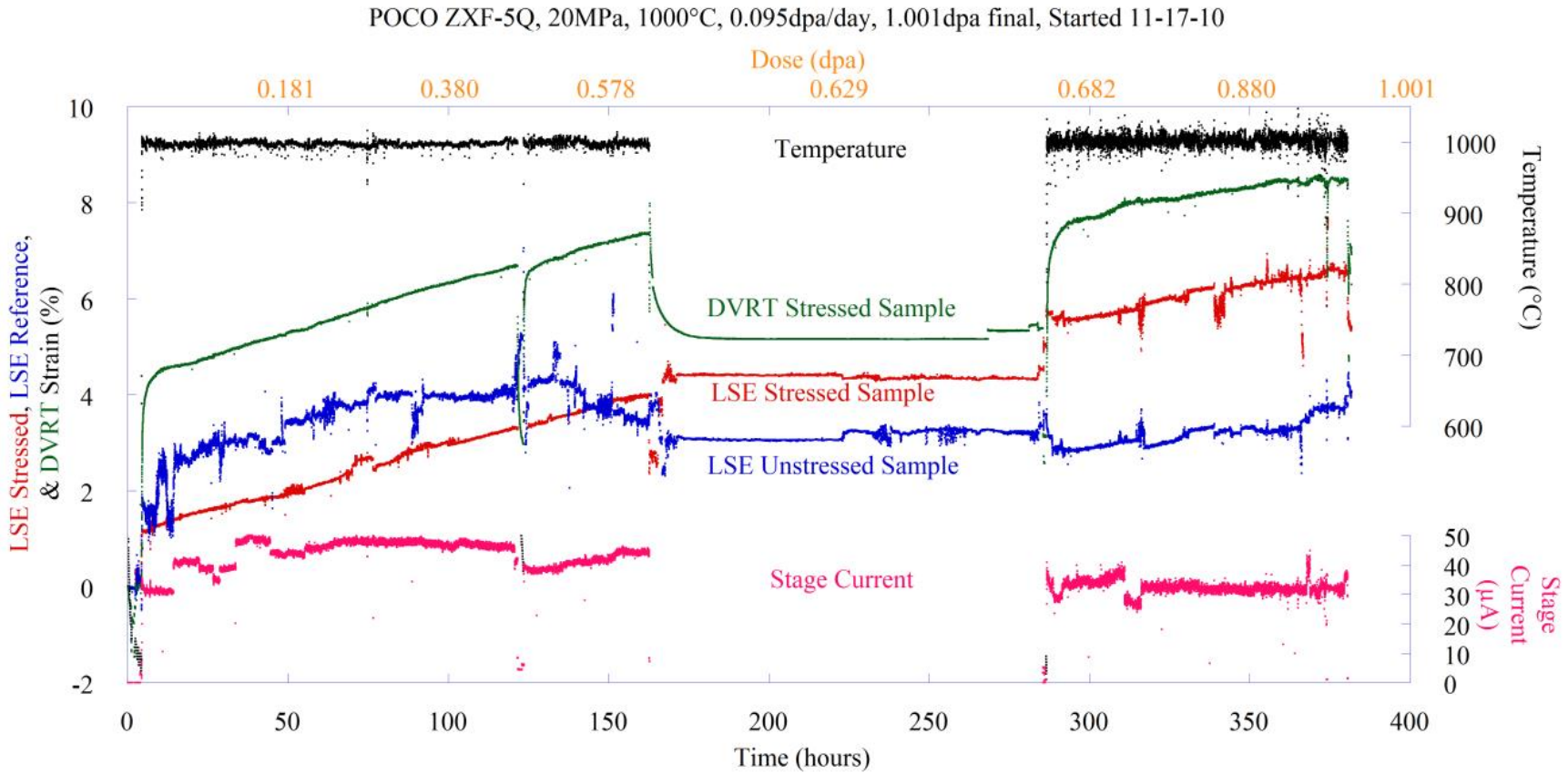

Figure B.2. Experimental data from Experiment #2, performed at 1000°C, 0.098dpa/day, 20MPa stress, to a final dose of 1.001dpa.

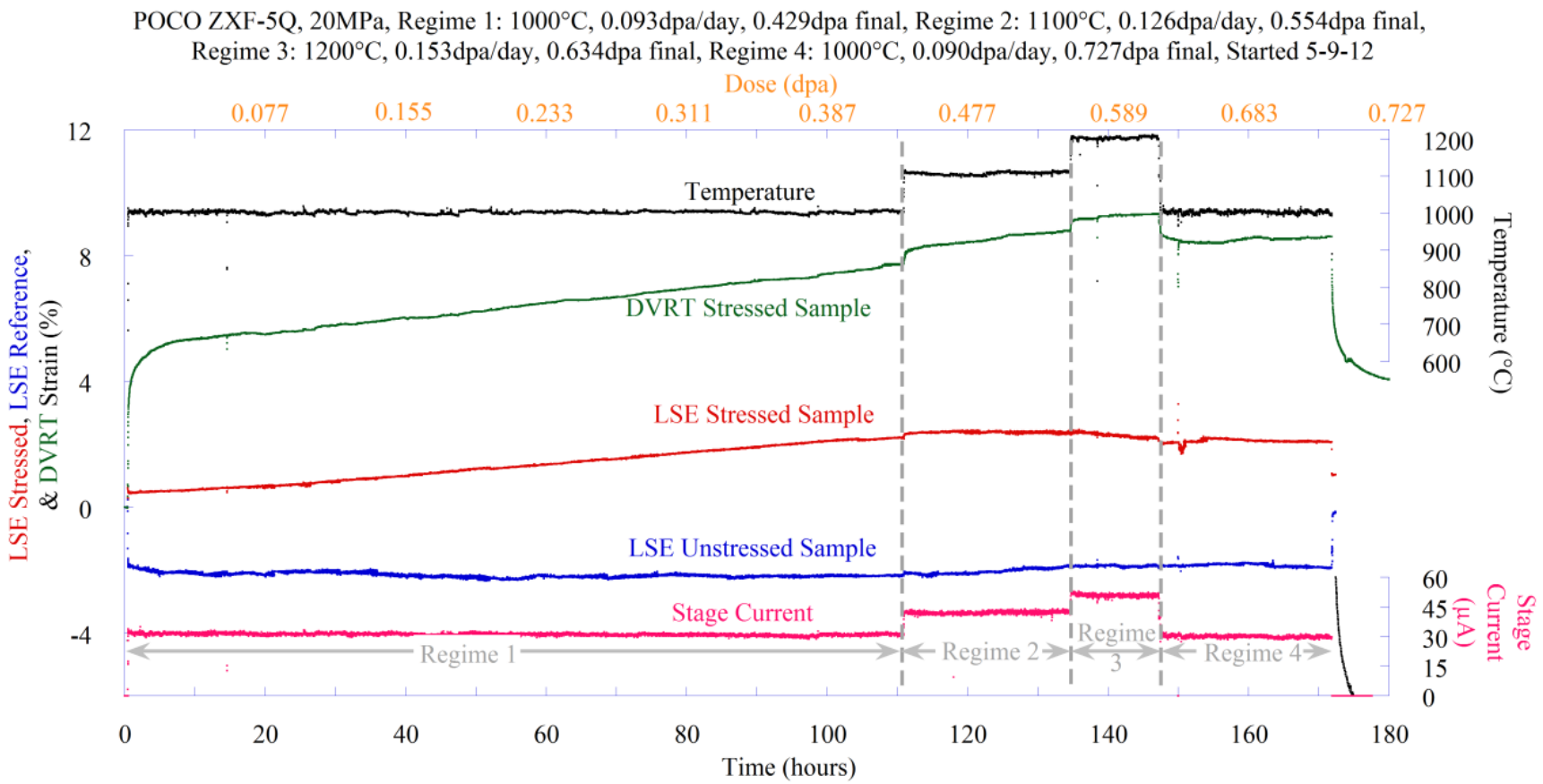

Figure B.3. Experimental data from Experiment #3 with a 20MPa stress. Regime 1 was performed at 1000°C and 0.093dpa/day until a final dose of 0.429dpa. Regime 2 was performed at 1100°C and 0.126dpa/day until a final dose of 0.554dpa. Regime 3 was performed at 1200°C and 0.153dpa/day until a final dose of 0.634dpa. Regime 4 was performed at 1000°C and 0.090dpa/day until a final dose of 0.727dpa.

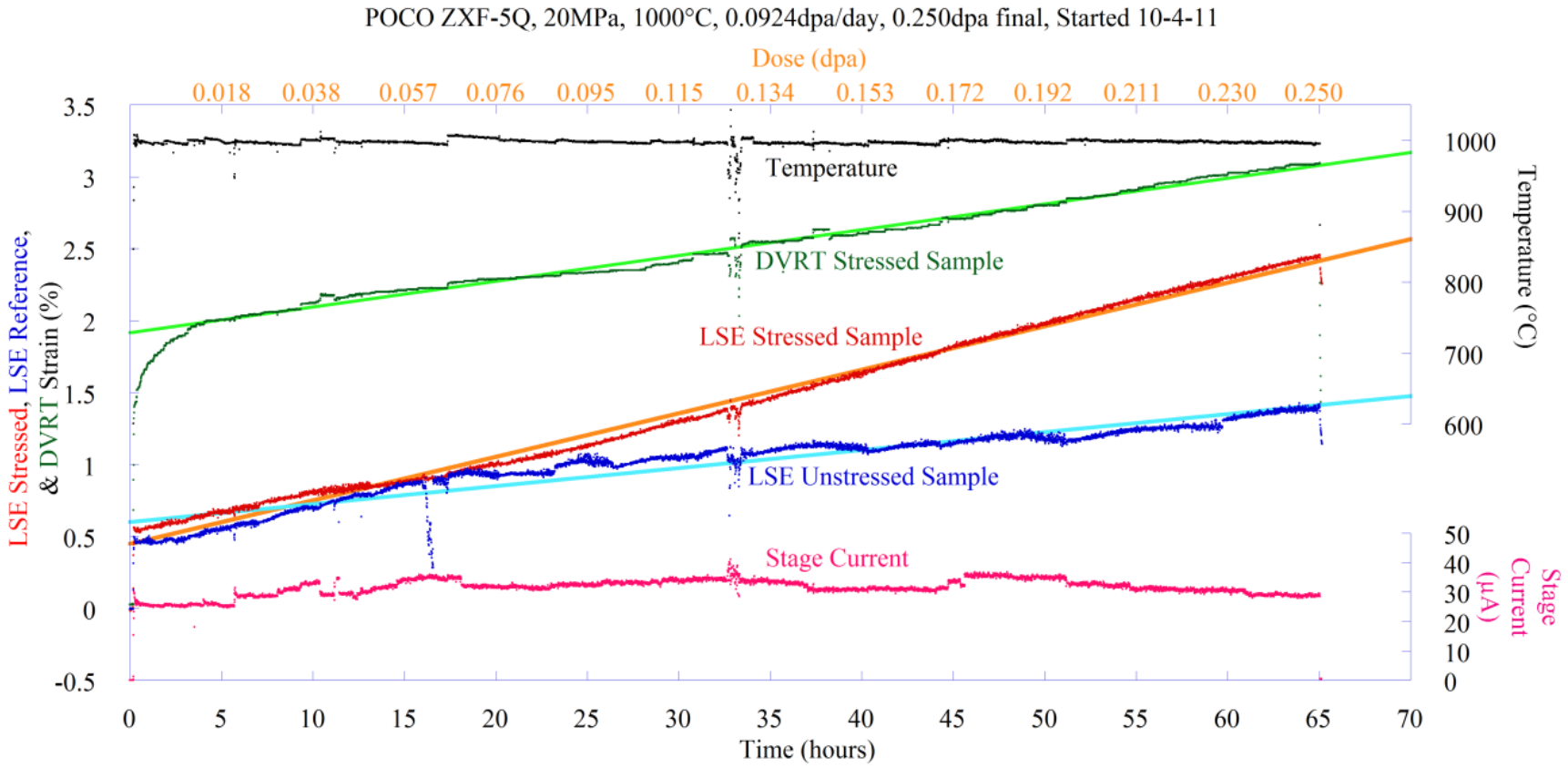

Figure B.4. Experimental data from Experiment #4, performed at 1000°C, 0.092dpa/day, 20MPa stress, to a final dose of 0.250dpa.

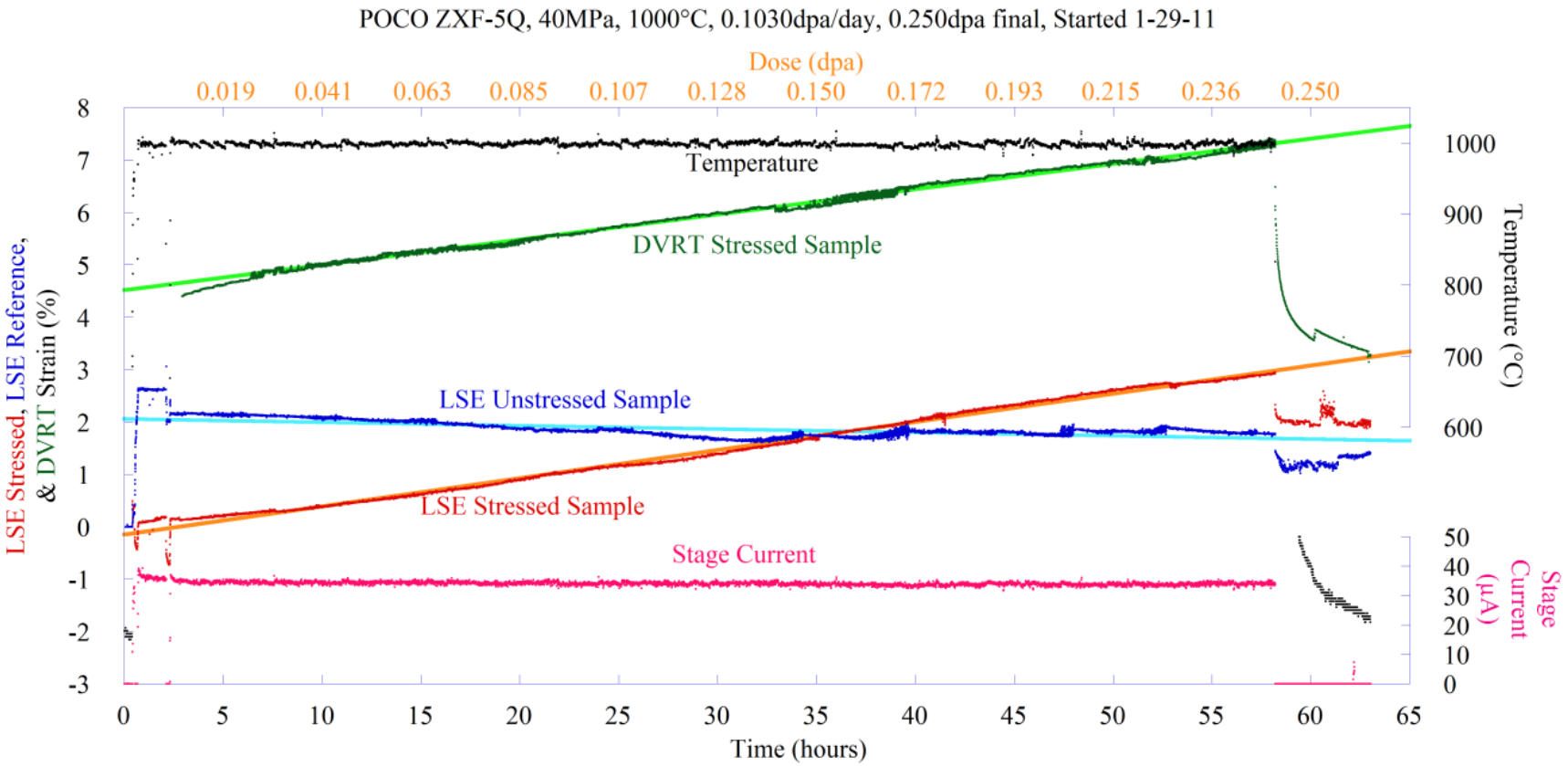

Figure B.5. Experimental data from Experiment #5, performed at 1000°C, 0.103dpa/day, 40MPa stress, to a final dose of 0.250dpa.

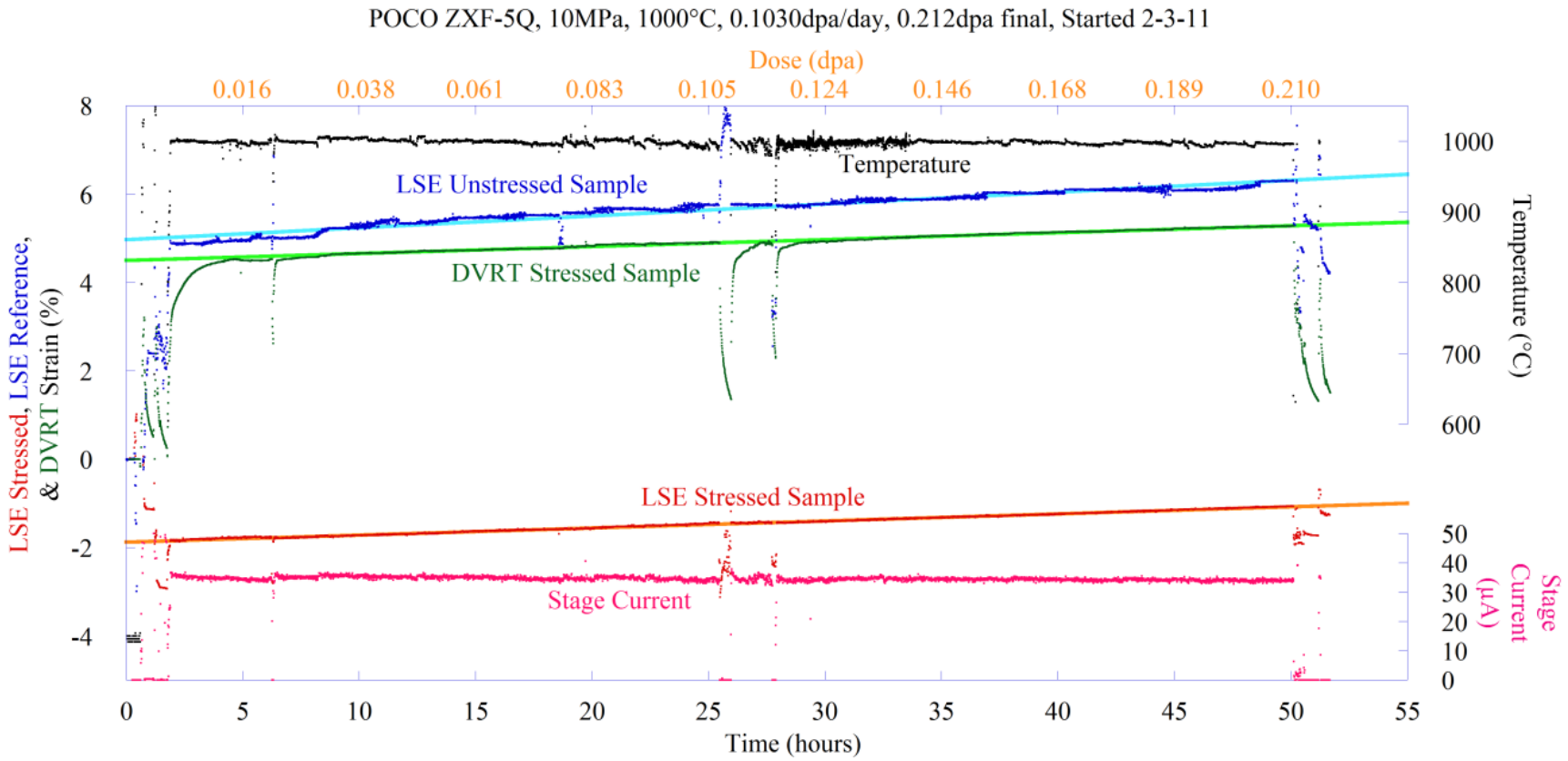

Figure B.6. Experimental data from Experiment #6, performed at 1000°C, 0.103dpa/day, 10MPa stress, to a final dose of 0.212dpa.

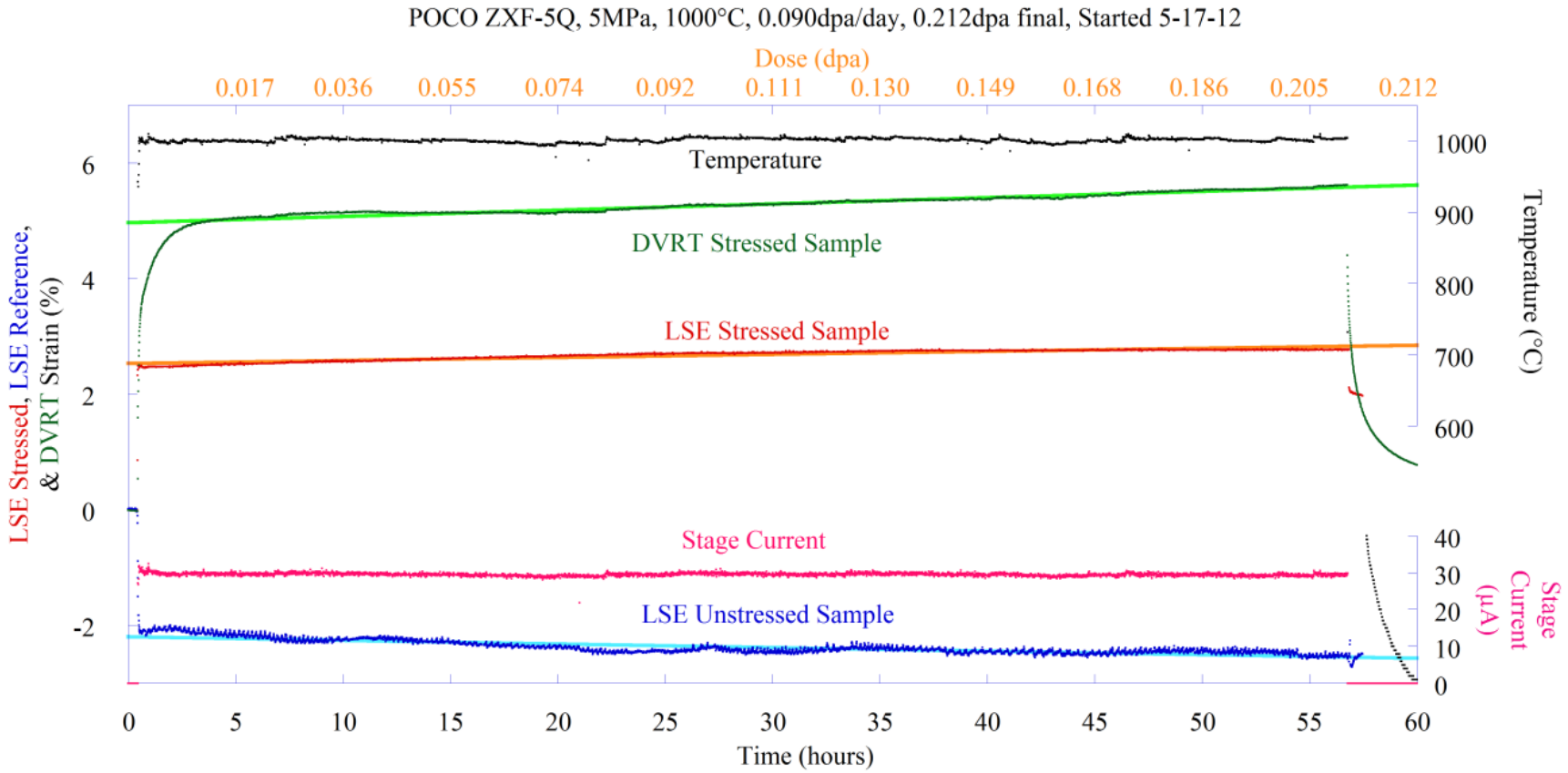

Figure B.7. Experimental data from Experiment #7, performed at 1000°C, 0.090dpa/day, 5MPa stress, to a final dose of 0.212dpa.

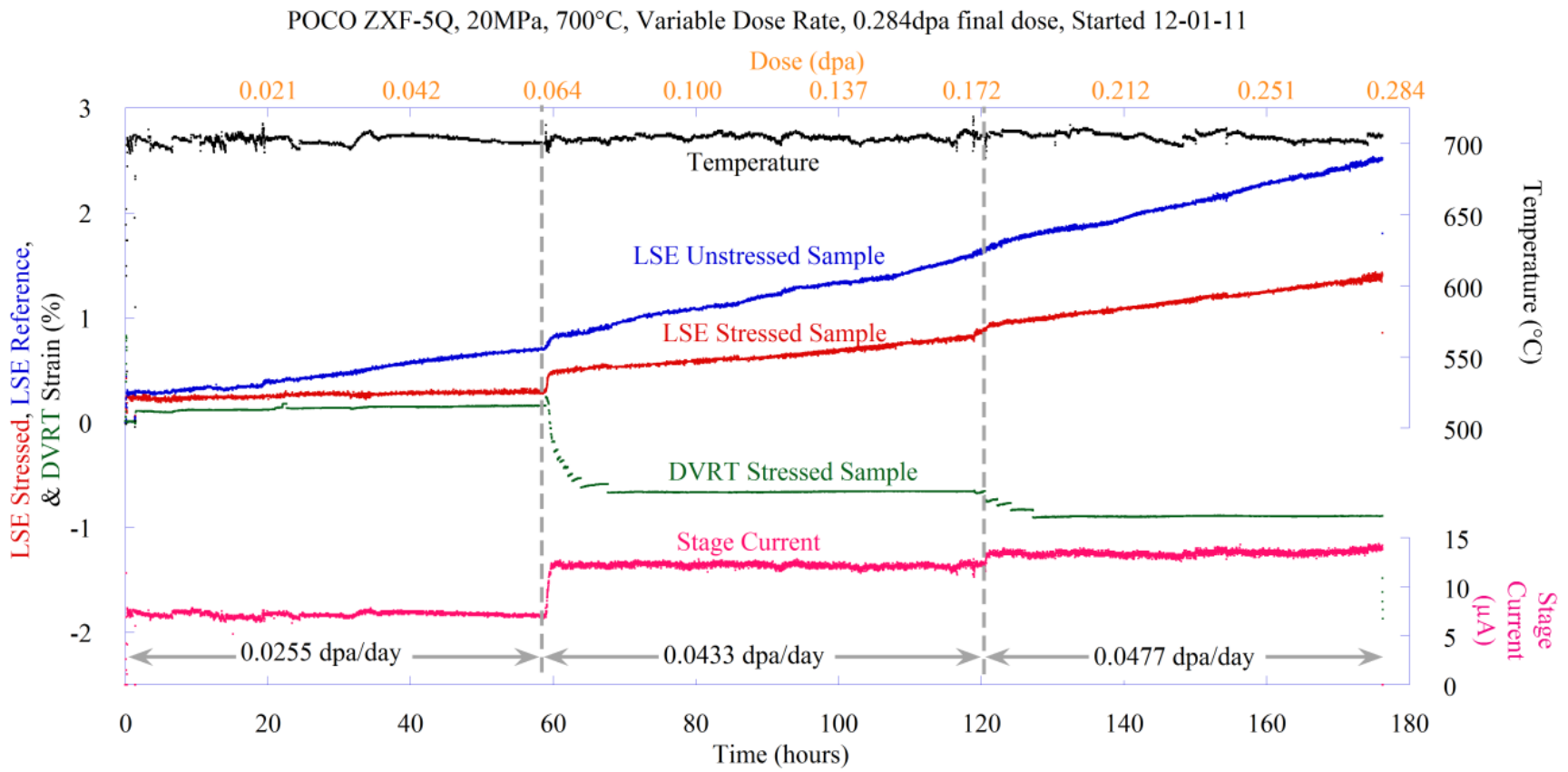

Figure B.8. Experimental data from Experiment #8, performed at 700°C and 20MPa stress. The experiment is broken into three sections, separated by the vertical grey dashed lines, according to the dose rate for that section. The dose rate for each section is listed along the bottom of the graph.

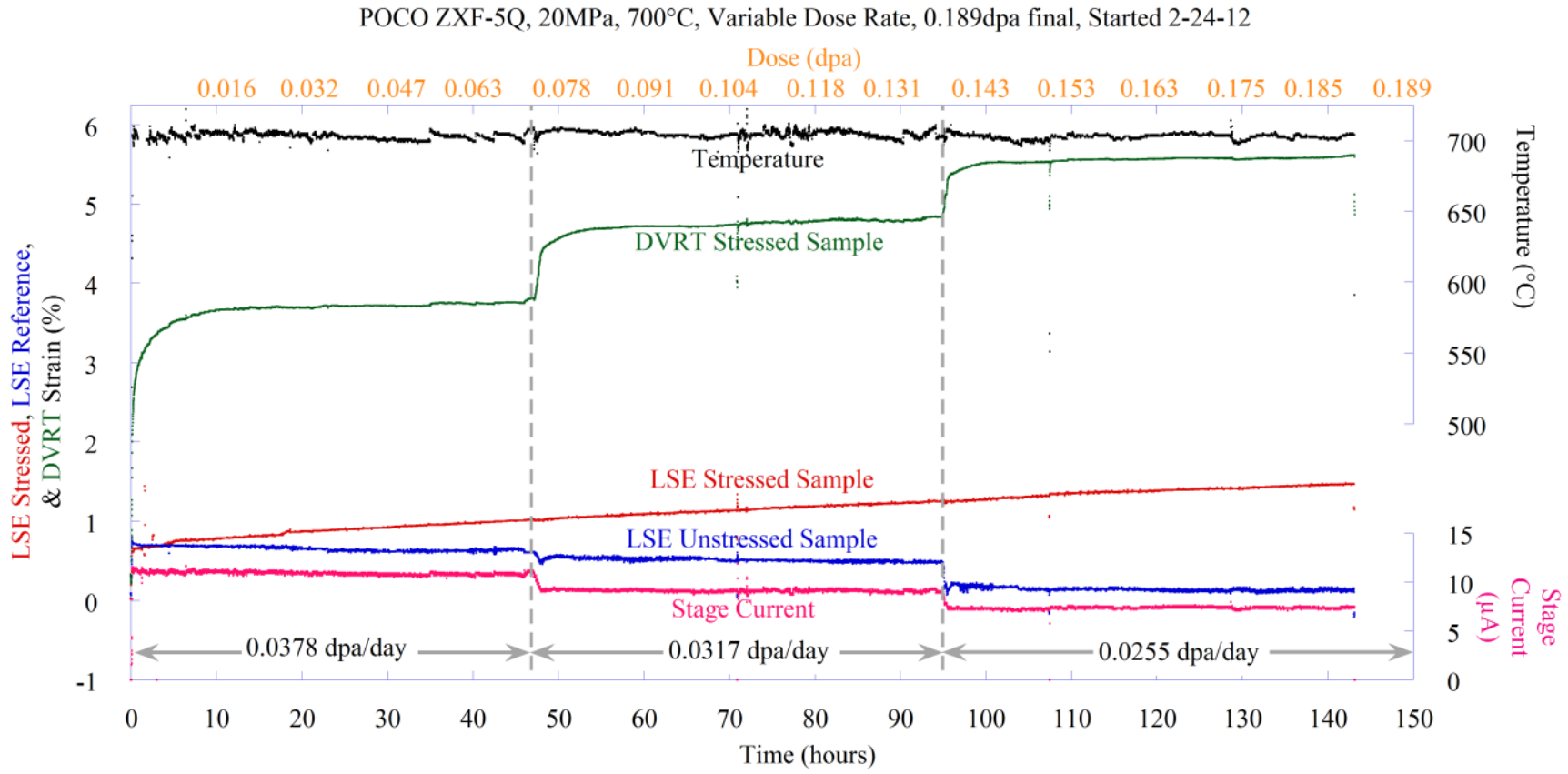

Figure B.9. Experimental data from Experiment #9, performed at 700°C and 20MPa stress. The experiment is broken into three sections, separated by the vertical grey dashed lines, according to the dose rate for that section. The dose rate for each section is listed along the bottom of the graph.

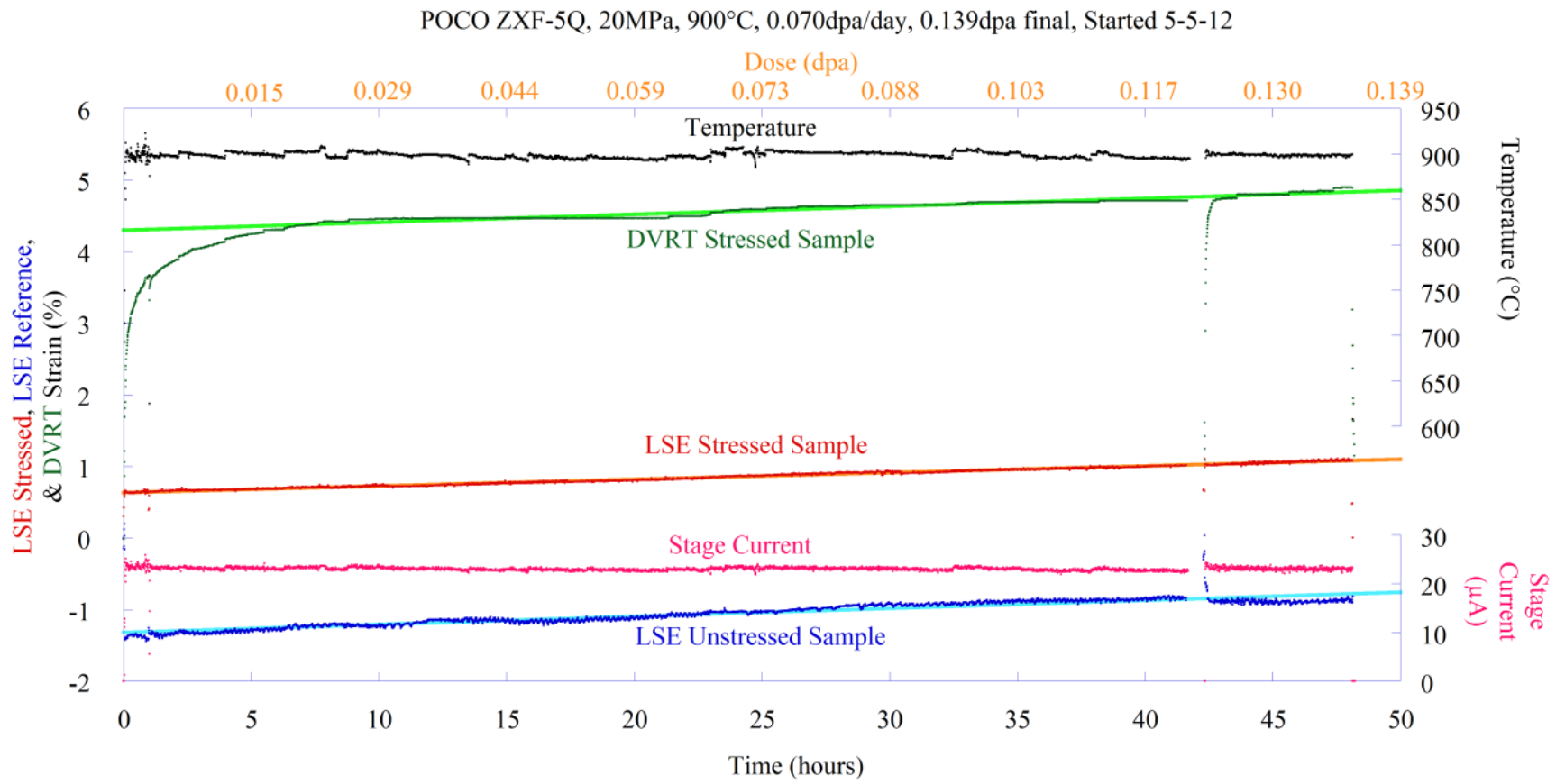

Figure B.10. Experimental data from Experiment #10, performed at 900°C, 0.070dpa/day, 20MPa stress, to a final dose of 0.139dpa.

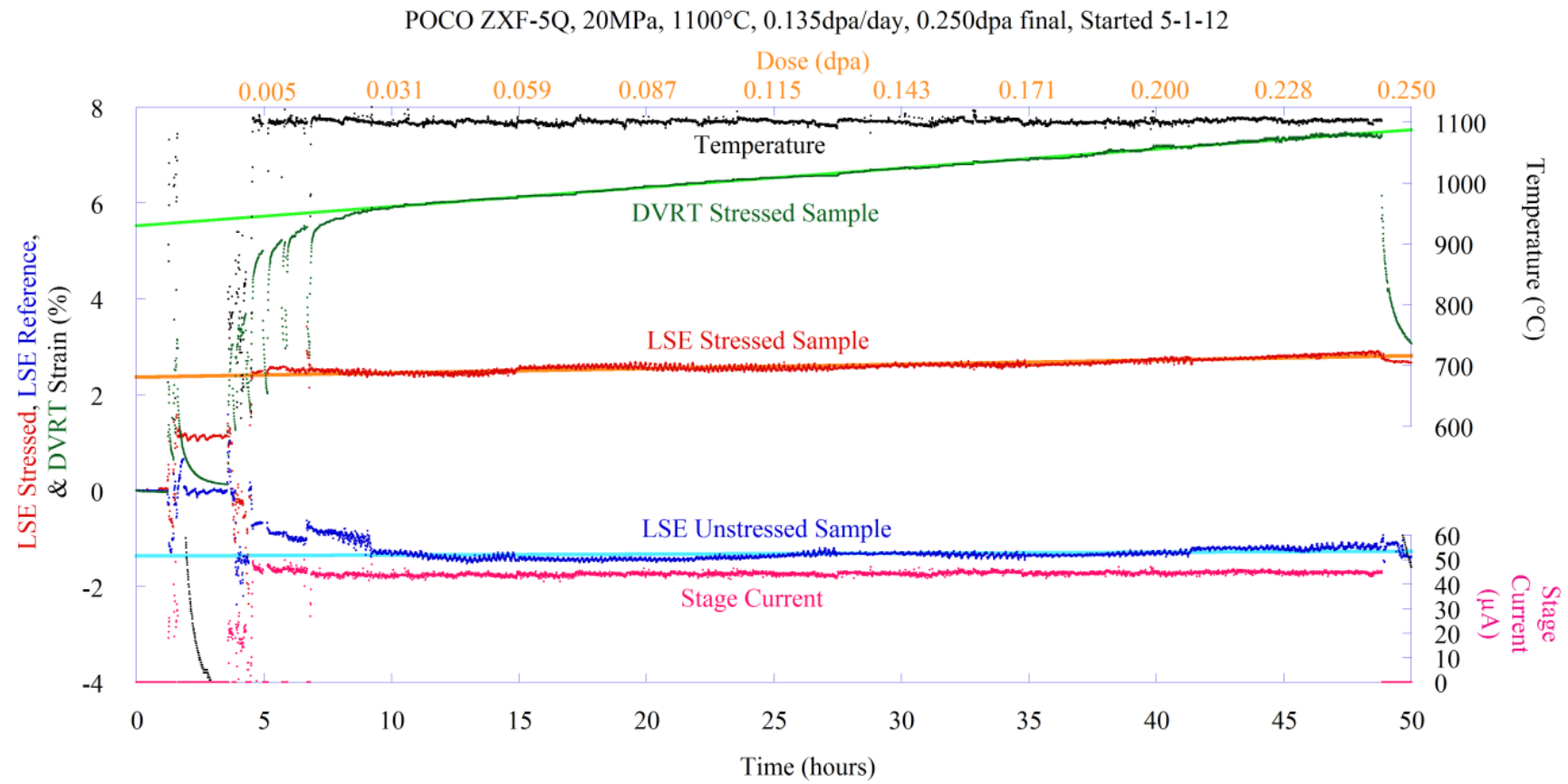

Figure B.11. Experimental data from Experiment #11, performed at 1100°C, 0.135dpa/day, 20MPa stress, to a final dose of 0.250dpa.

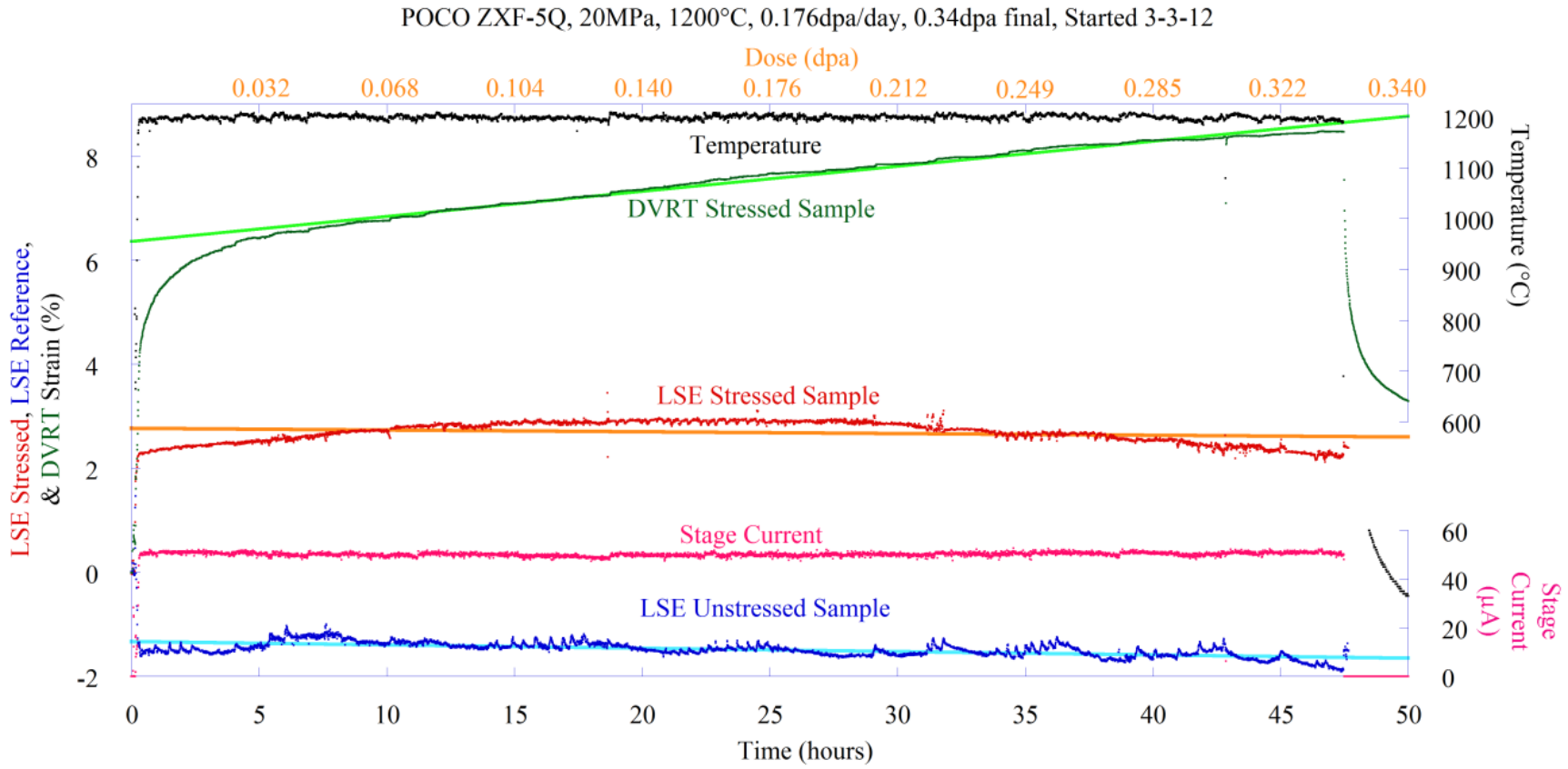

Figure B.12. Experimental data from Experiment #12, performed at 1200°C, 0.176dpa/day, 20MPa stress, to a final dose of 0.340dpa.

APPENDIX C

ANISOTROPY DATA

This appendix presents the TEM SAED patterns that were obtained for the as-received sample and the sample irradiated at 1000°C, 20MPa, to 1.0dpa. All of the patterns were recorded with a camera length of 600cm, and accelerating voltage of 300kV.

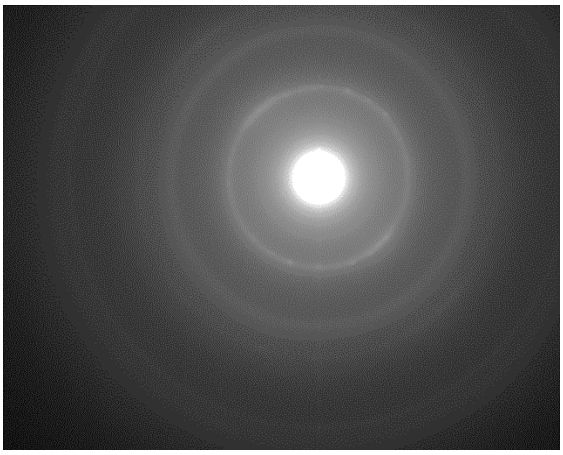

(1)

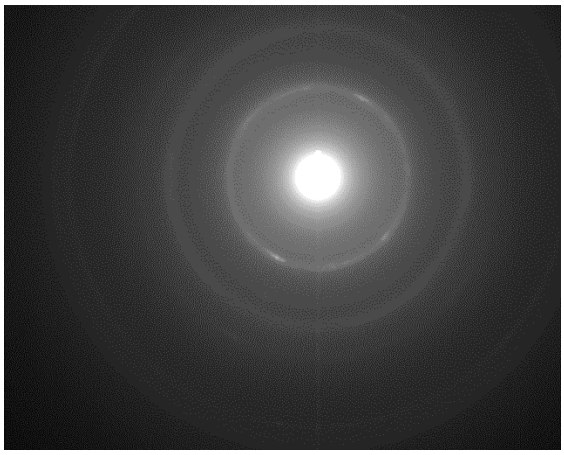

(2)

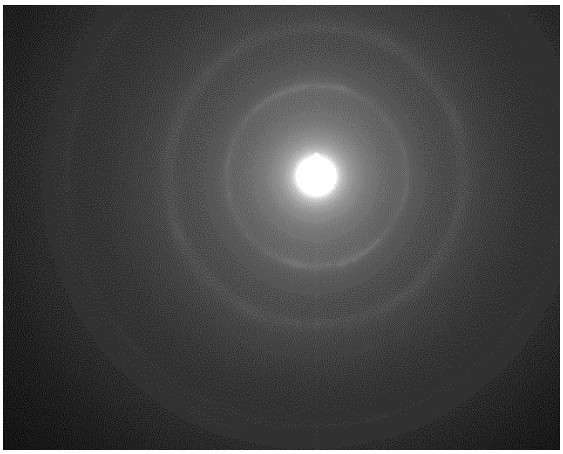

(3)

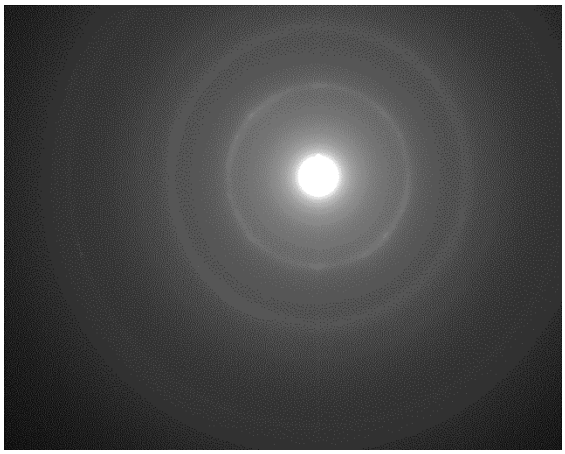

(4)

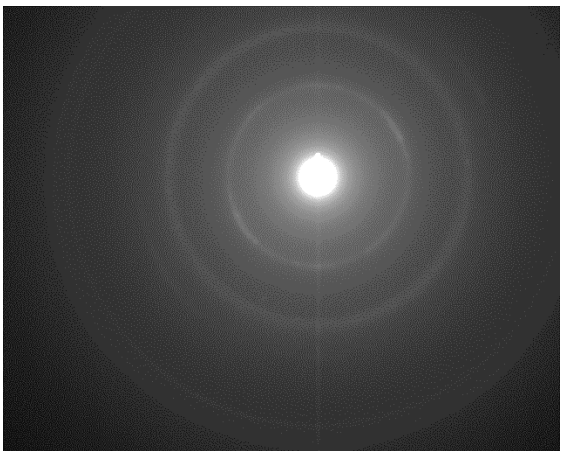

(5)

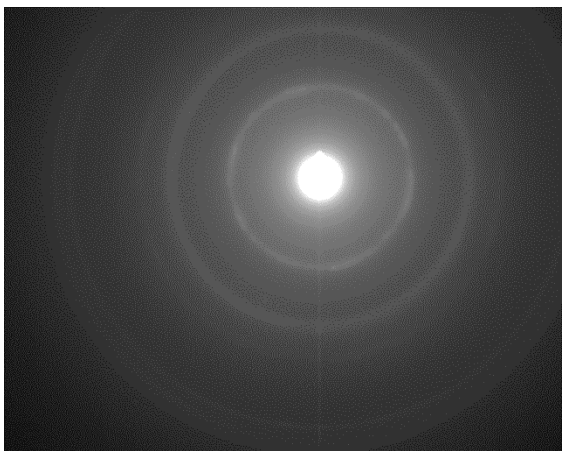

(6)

Figure C.1. Diffraction patterns 1-6 recorded for the as-received sample.

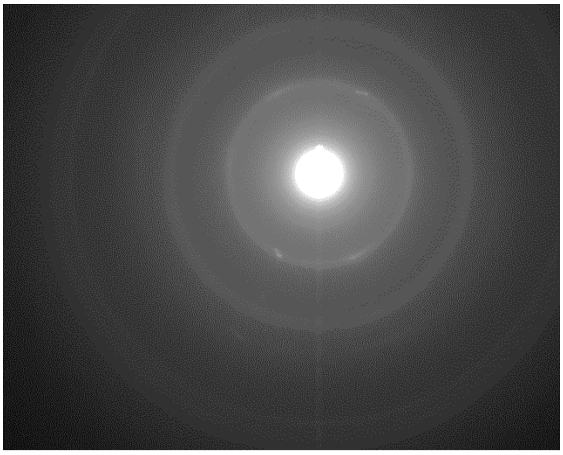

(7)

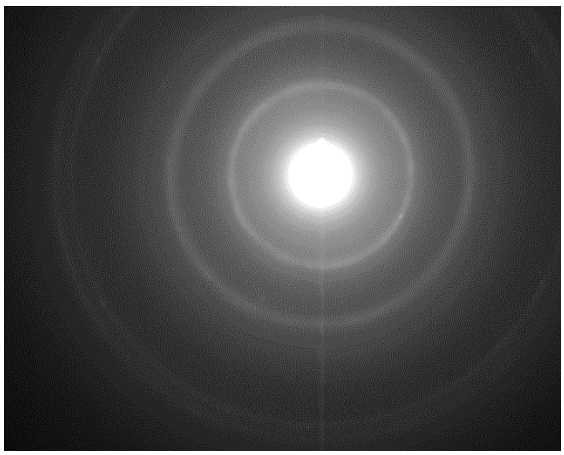

(8)

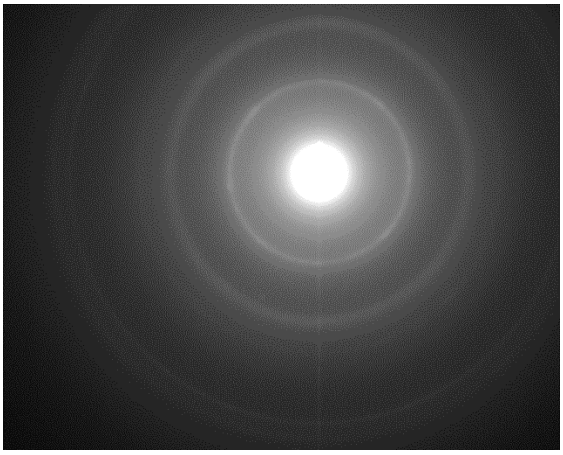

(9)

(10)

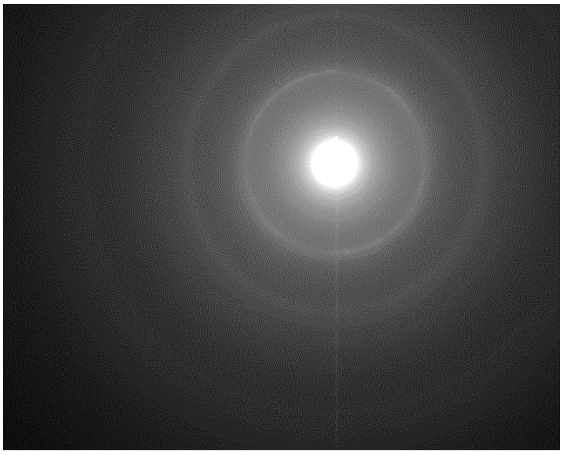

(11)

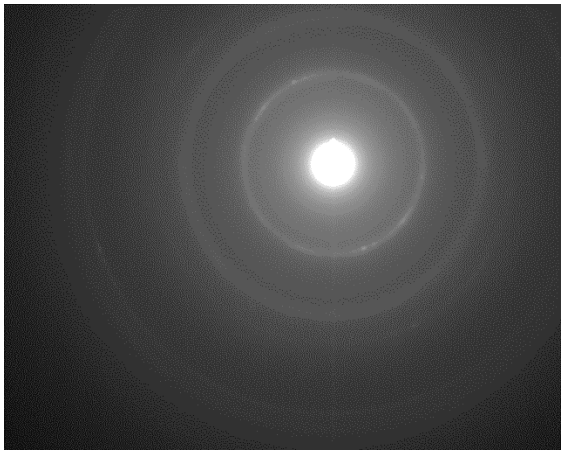

(12)

Figure C.2. Diffraction patterns 7-12 recorded for the as-received sample.

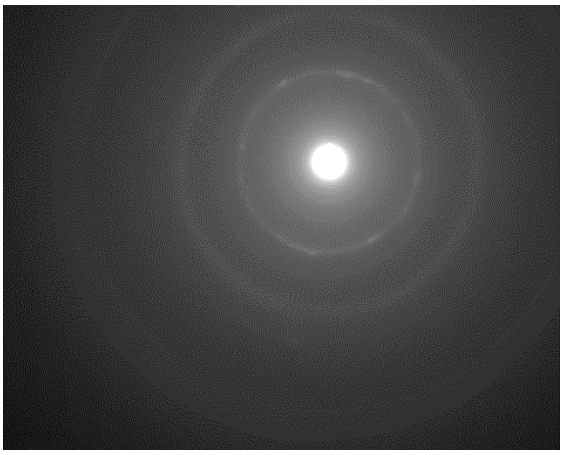

(13)

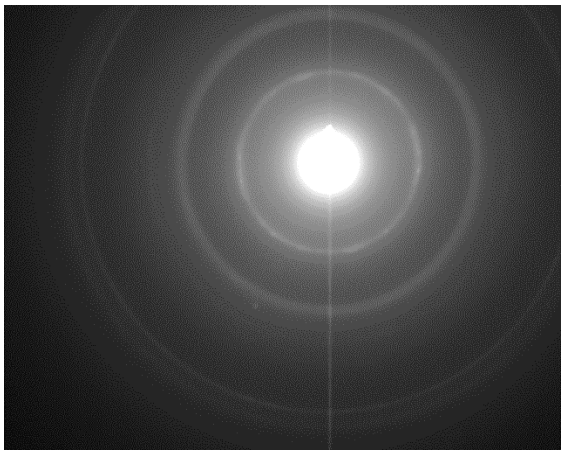

(14)

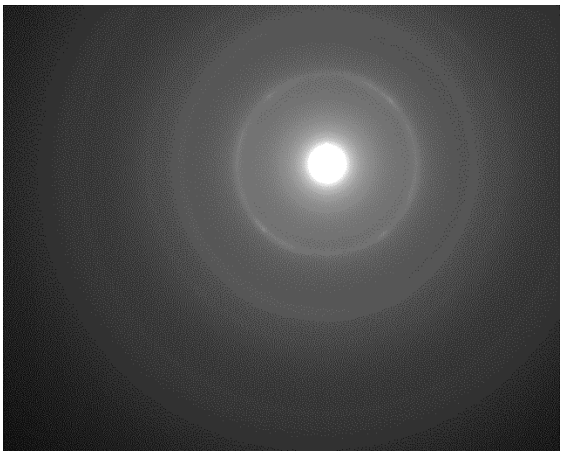

(15)

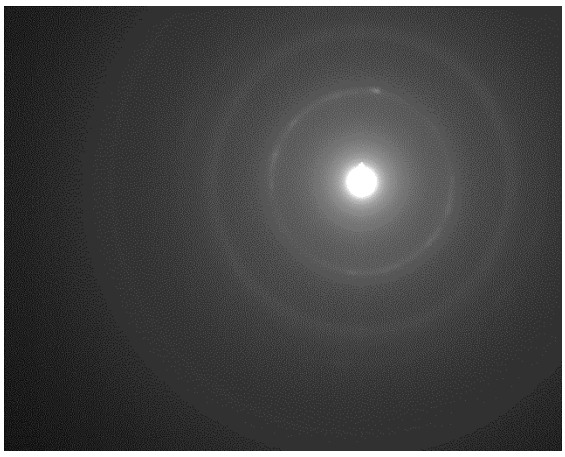

(16)

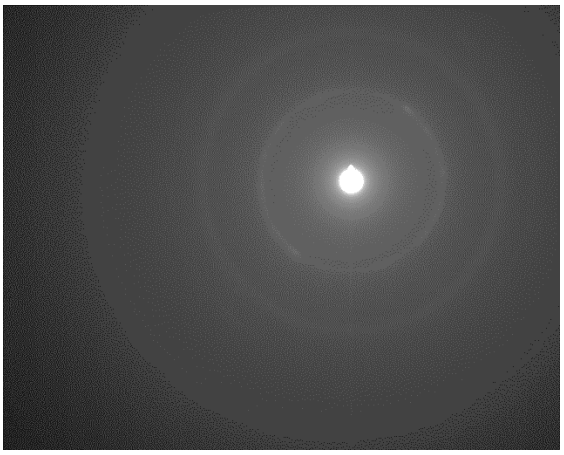

(17)

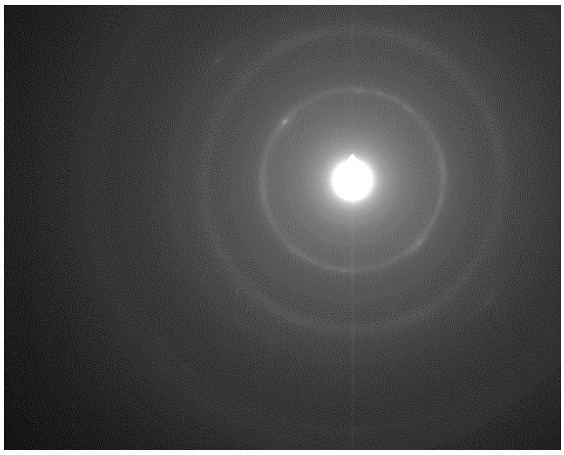

(18)

Figure C.3. Diffraction patterns 13-18 recorded for the as-received sample.

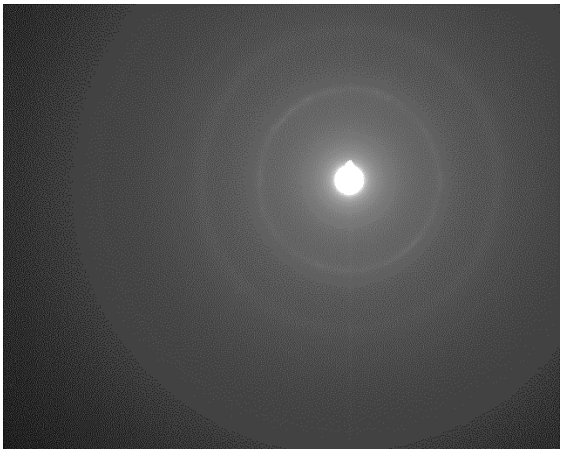

(19)

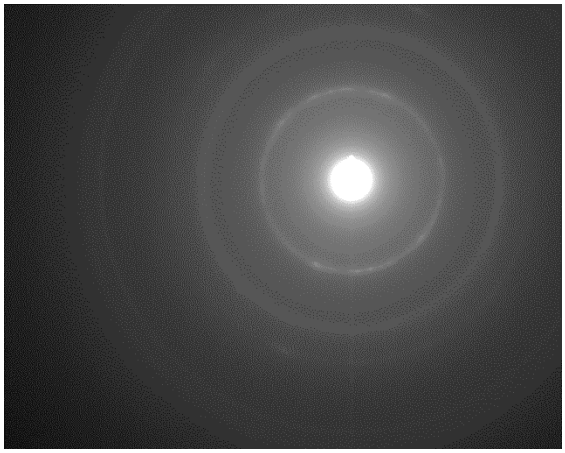

(20)

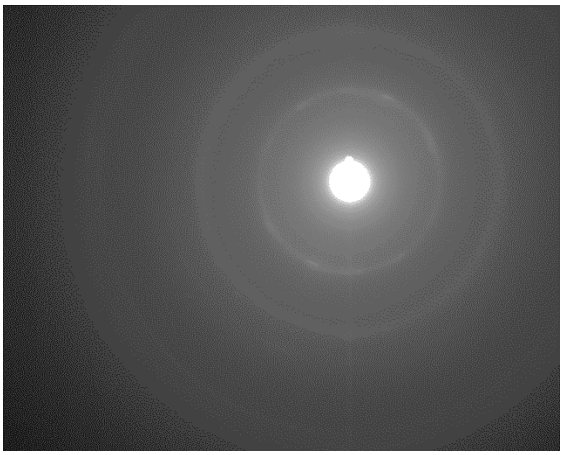

(21)

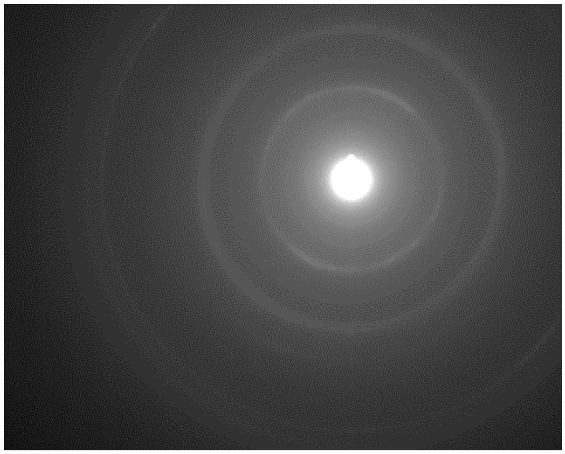

(22)

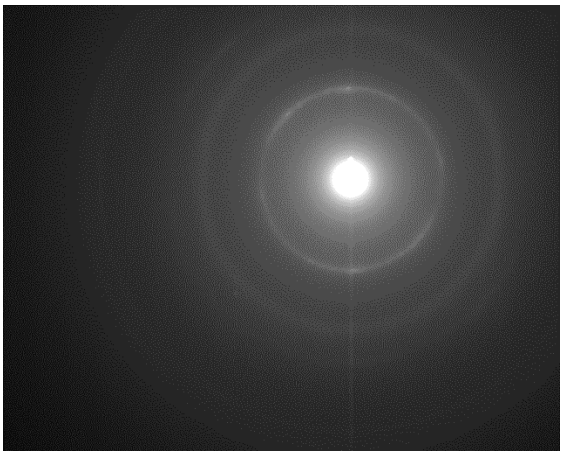

(23)

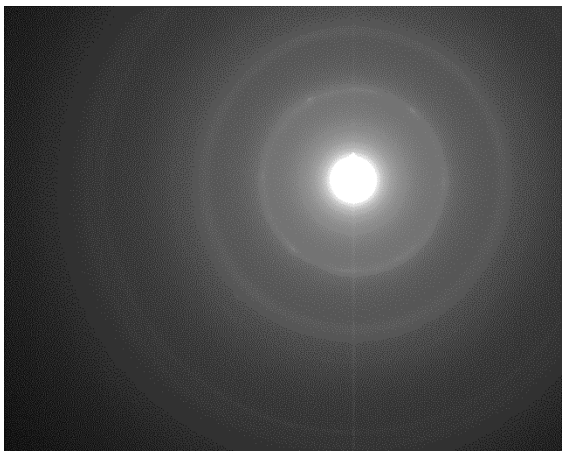

(24)

Figure C.4. Diffraction patterns 19-24 recorded for the as-received sample.

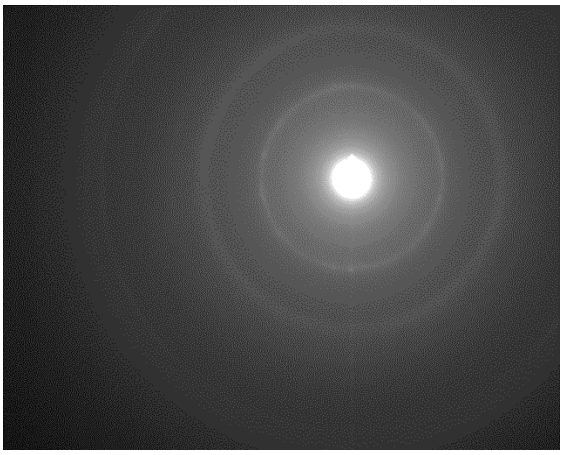

(25)

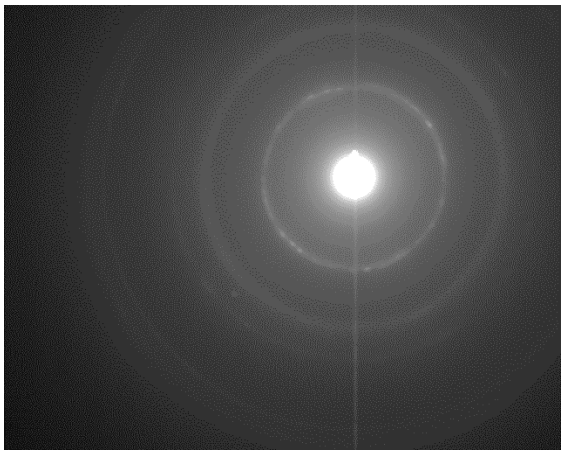

(26)

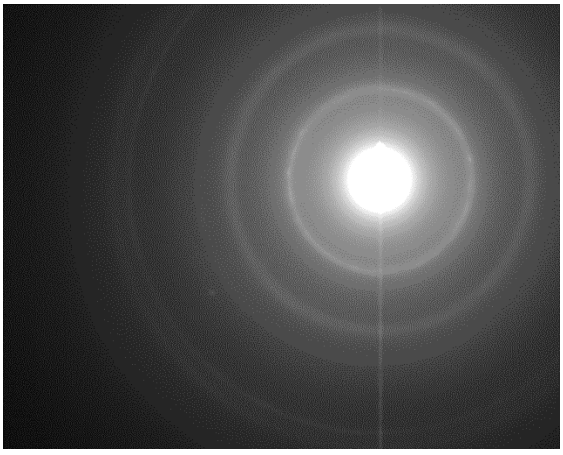

(27)

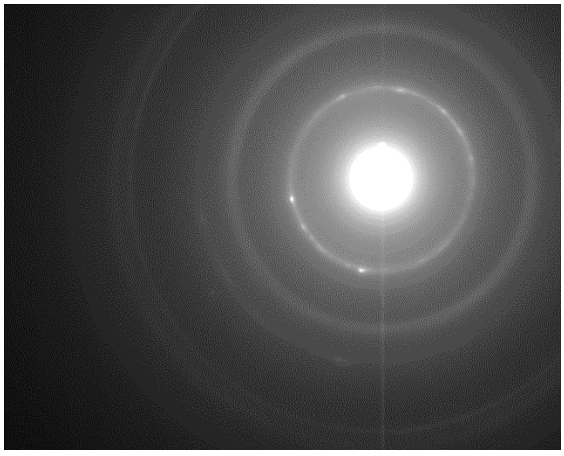

(28)

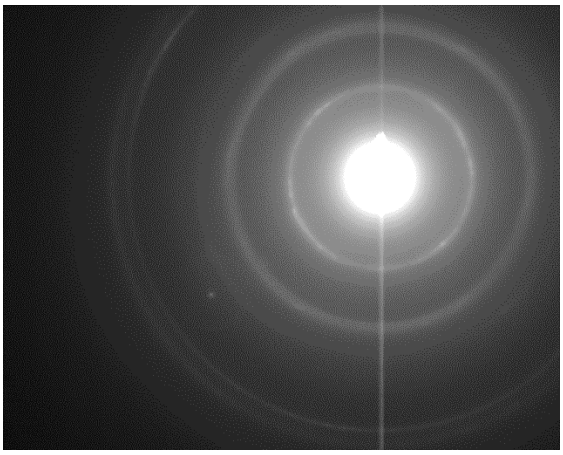

(29)

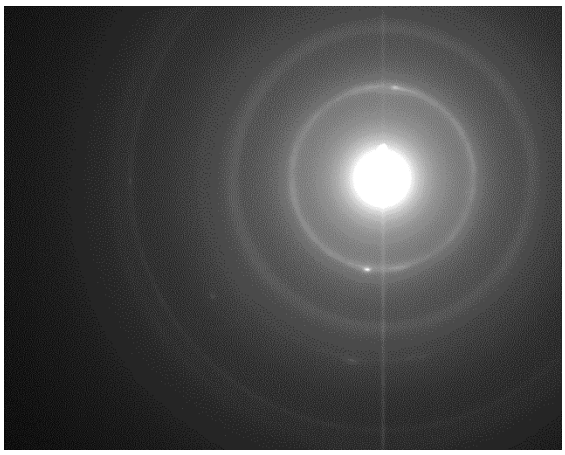

(30)

Figure C.5. Diffraction patterns 25-30 recorded for the as-received sample.

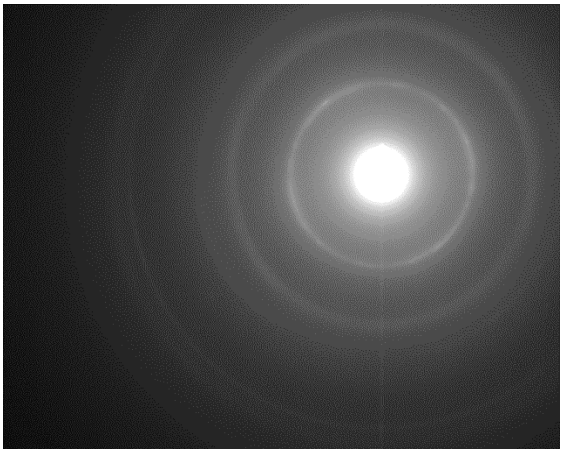

(31)

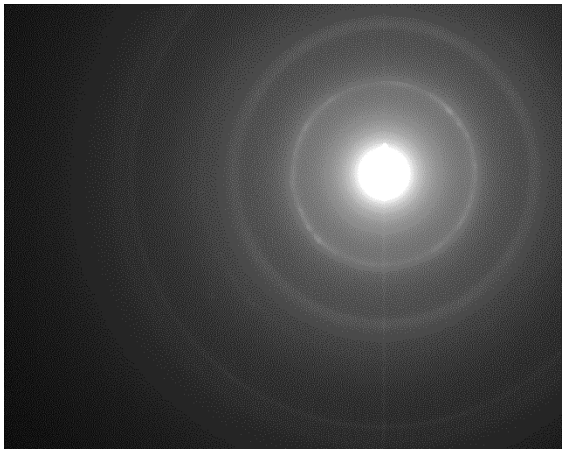

(32)

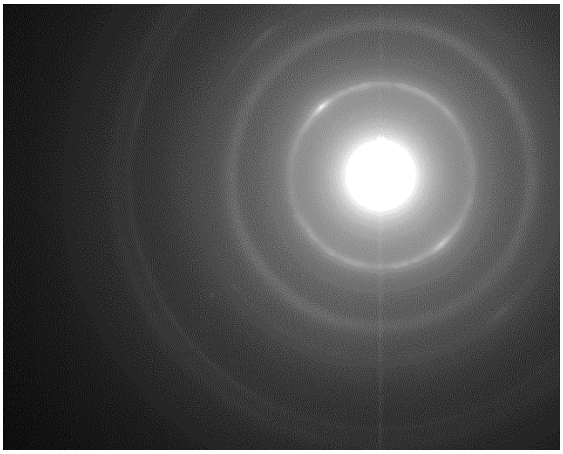

(33)

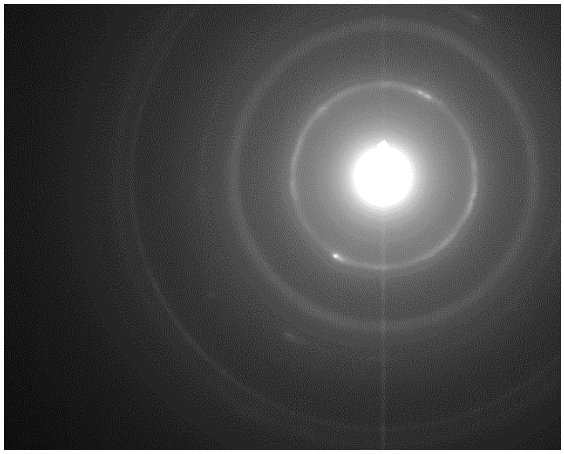

(34)

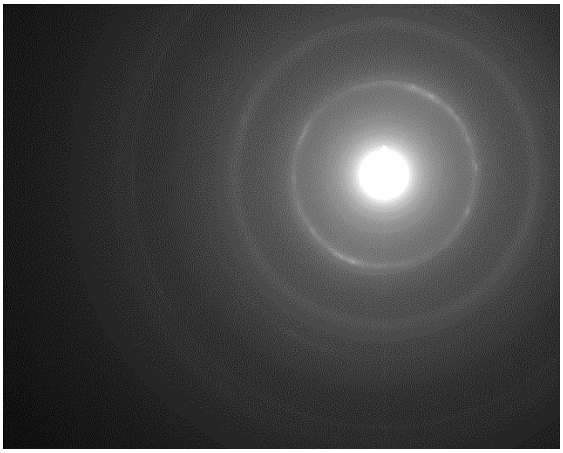

(35)

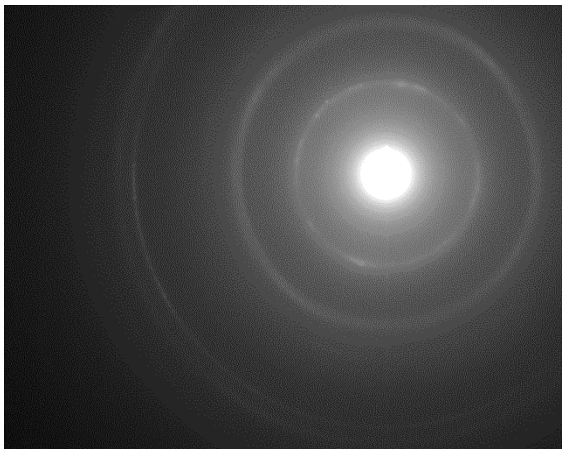

(36)

Figure C.6. Diffraction patterns 31-36 recorded for the as-received sample.

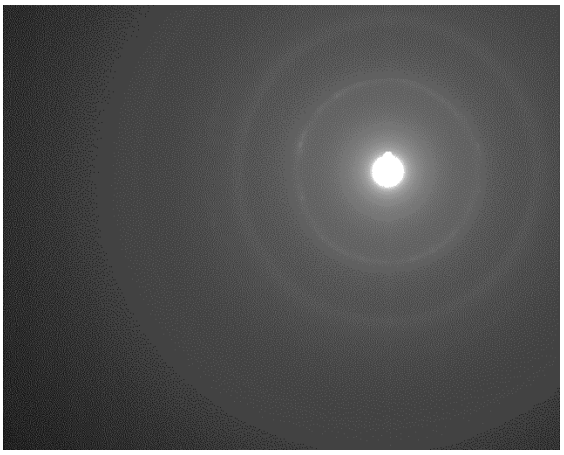

(37)

Figure C.7. Diffraction pattern 37 recorded for the as-received sample.

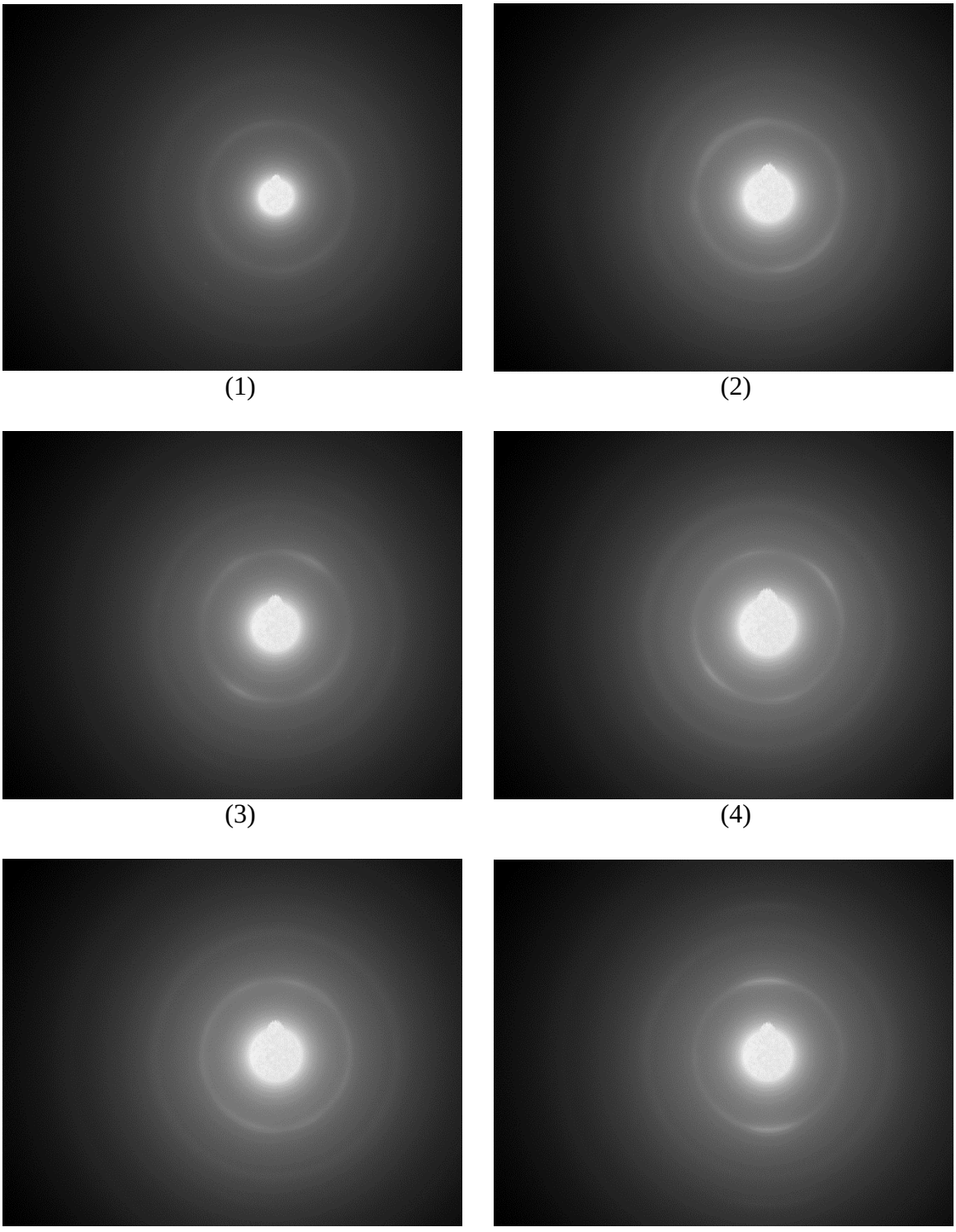

(1) (2)

(3) (4)

(5) (6)

Figure C.8. Diffraction patterns 1-6 recorded for the sample irradiated at 1000°C 20MPa to 1.0dpa.

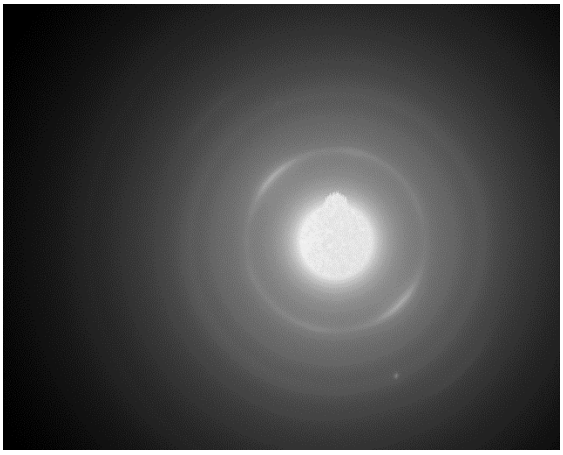

(7)

(8)

(9)

(10)

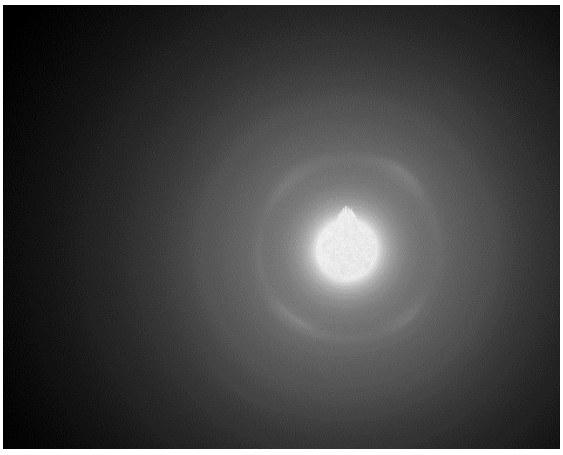

(11)

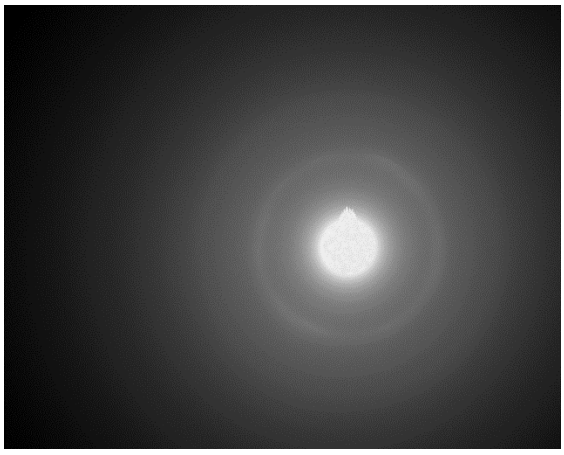

(12)

Figure C.9. Diffraction patterns 7-12 recorded for the sample irradiated at 1000°C 20MPa to 1.0dpa.

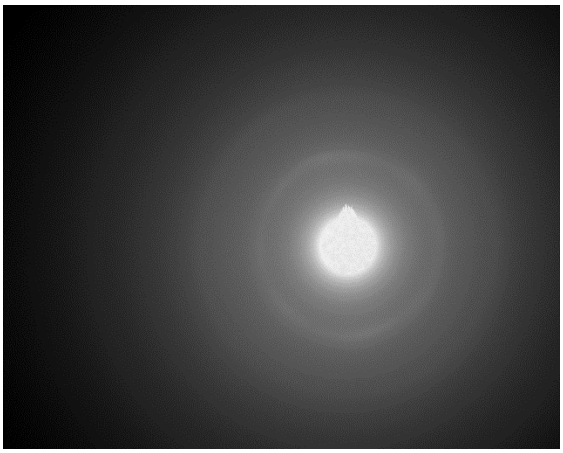

(13)

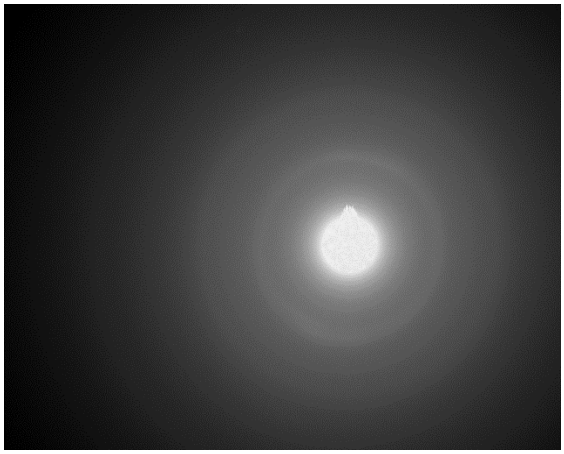

(14)

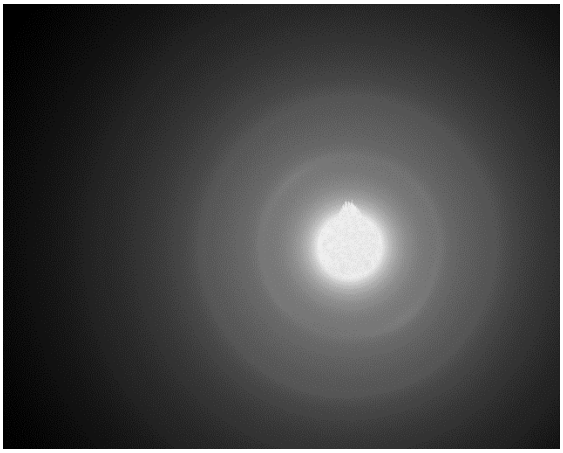

(15)

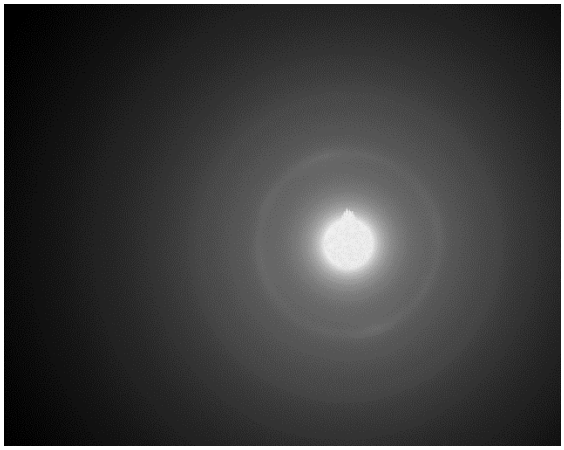

(16)

(17)

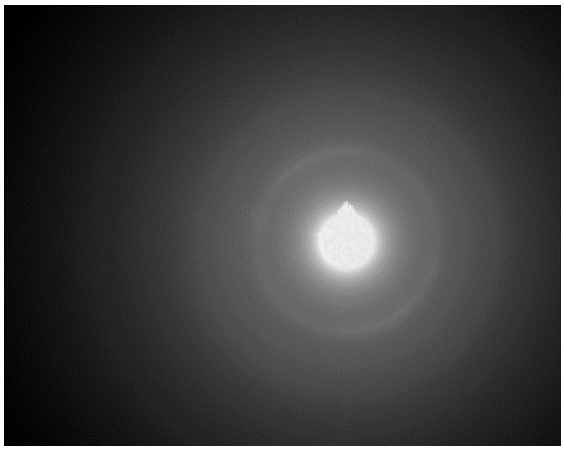

(18)

Figure C.10. Diffraction patterns 13-18 recorded for the sample irradiated at 1000°C 20MPa to 1.0dpa.

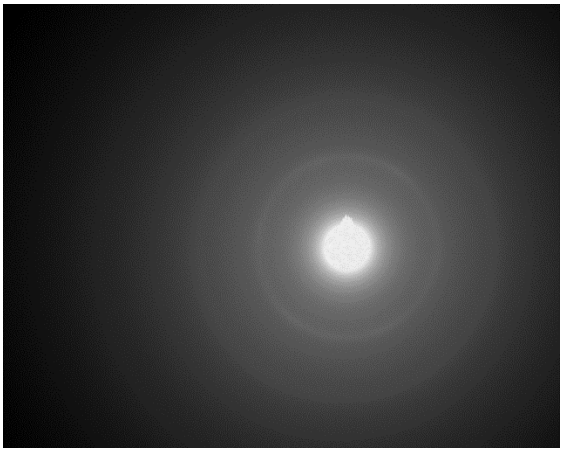

(19)

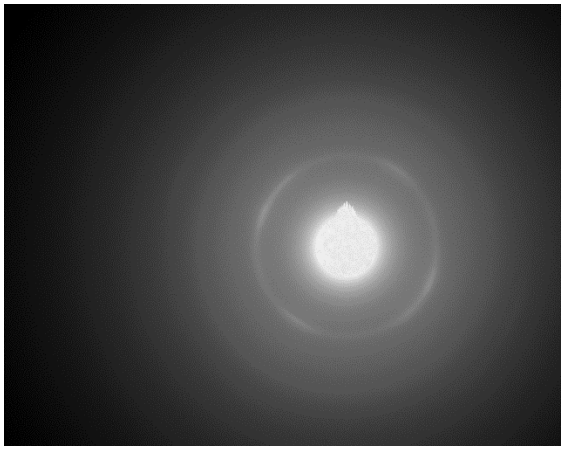

(20)

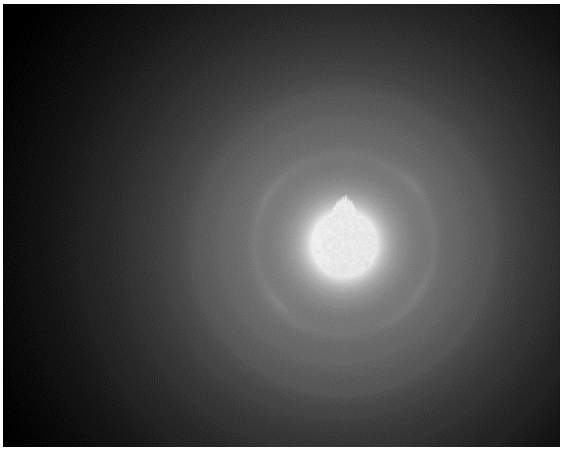

(21)

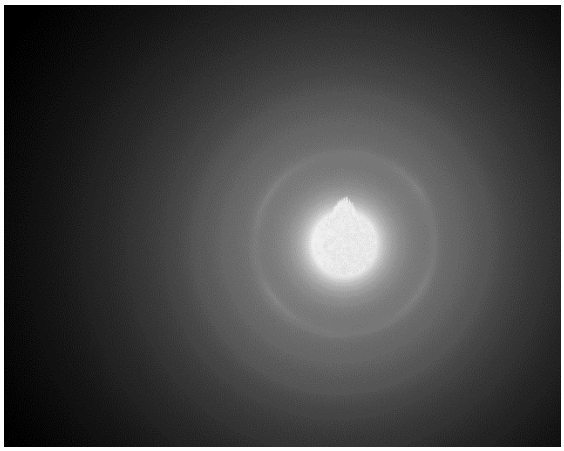

(22)

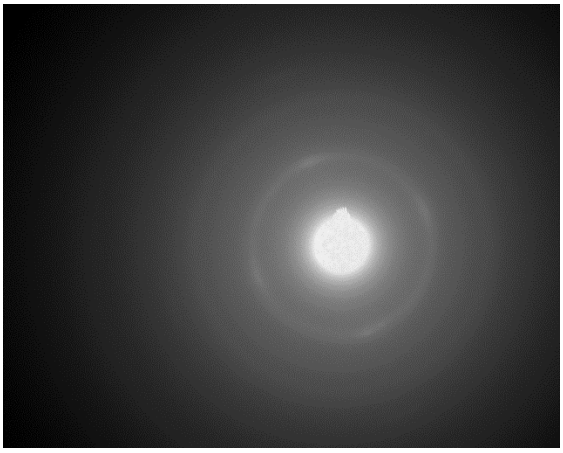

(23)

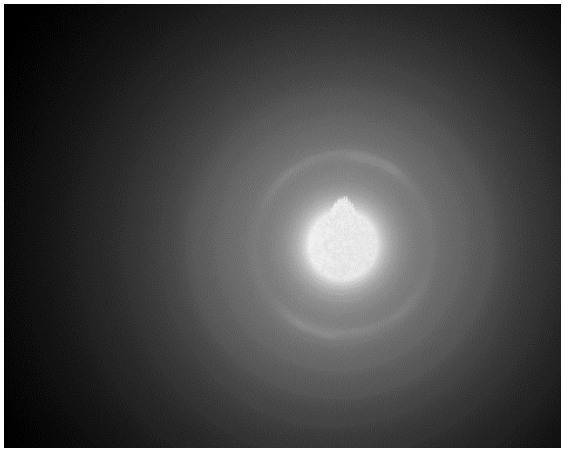

(24)

Figure C.11. Diffraction patterns 19-24 recorded for the sample irradiated at 1000°C 20MPa to 1.0dpa.

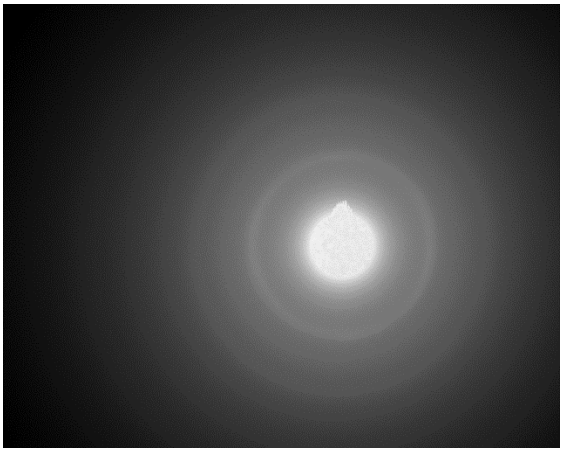

(25)

(26)

(27)

(28)

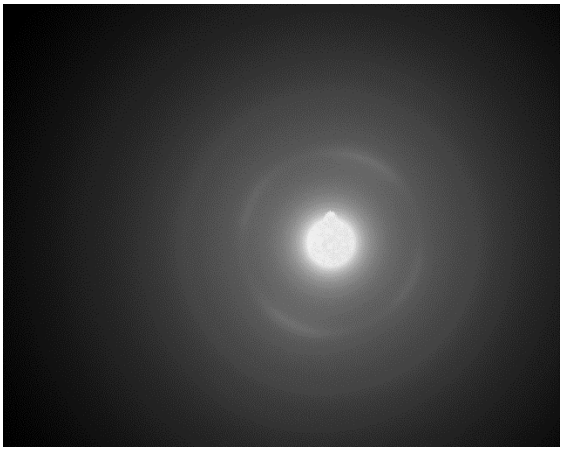

(29)

(30)

Figure C.12. Diffraction patterns 25-30 recorded for the sample irradiated at 1000°C 20MPa to 1.0dpa.

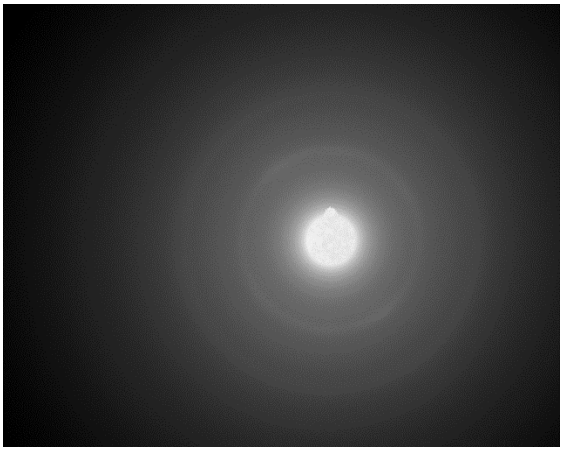

(31)

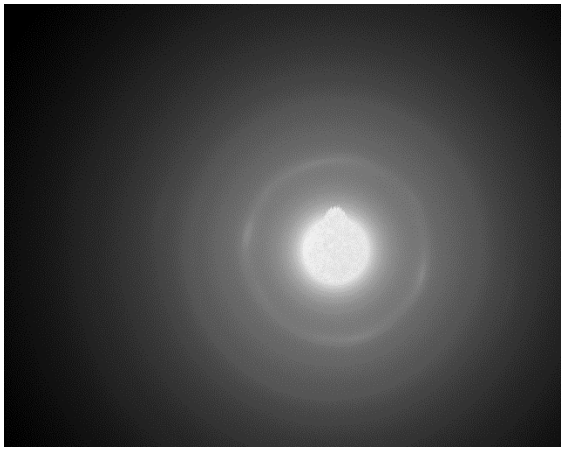

(32)

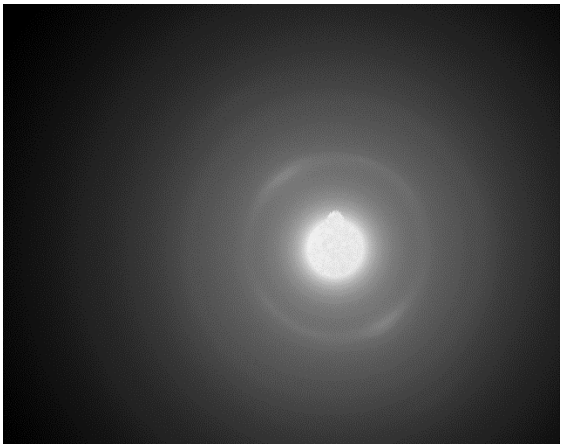

(33)

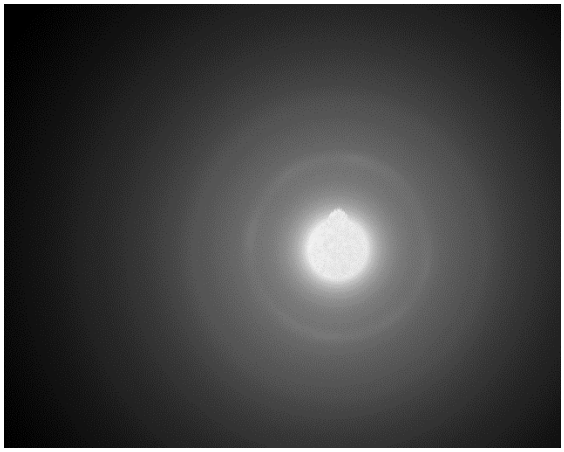

(34)

(35)

(36)

Figure C.13. Diffraction patterns 31-36 recorded for the sample irradiated at 1000°C 20MPa to 1.0dpa.

(37)

Figure C.14. Diffraction pattern 37 recorded for the sample irradiated at 1000°C 20MPa to 1.0dpa.

APPENDIX D

YOUNG'S MODULUS AND HARDNESS DATA

This appendix presents the load versus depth plots from the nanoindentation measurements used to determine the Young's modulus and hardness. Not all samples underwent nanoindentation, due to equipment availability. The samples investigated were the as-received material and the samples from the experiments listed in Table D.1; for the experiments where both the stressed and reference sample were measured there is an * next to the experiment number.

Table D.1. Summary of POCO ZXF-5Q proton irradiation-induced creep experimental parameters.

Experiment Reference Number	Temperature (°C)	Stress (Mpa)	Dose Rate (dpa/day)	Total Dose (dpa)
1	1000	20	0.101	0.421
2	1000	20	0.098	1.001
5	1000	40	0.103	0.250
7*	1000	5	0.090	0.212
10	900	20	0.070	0.139
12*	1200	20	0.176	0.340

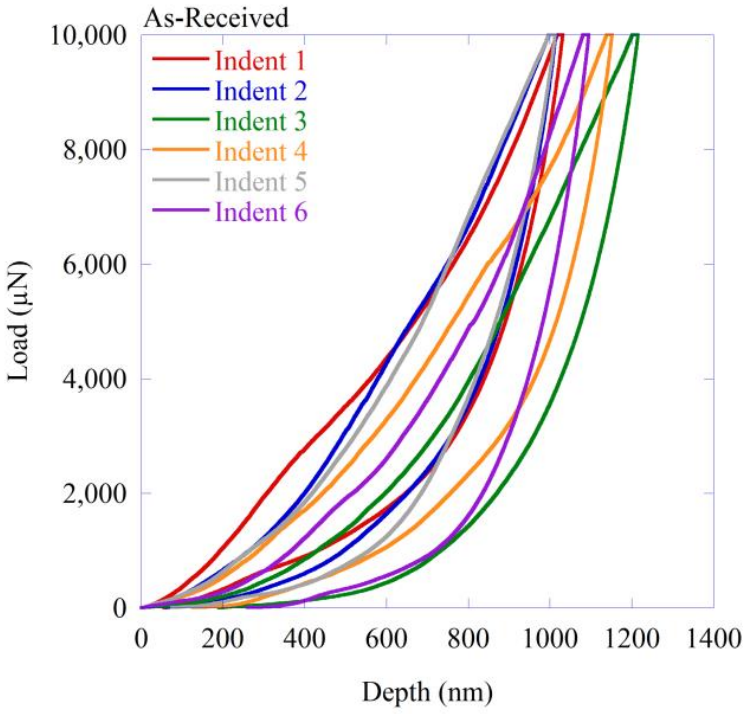

(a)

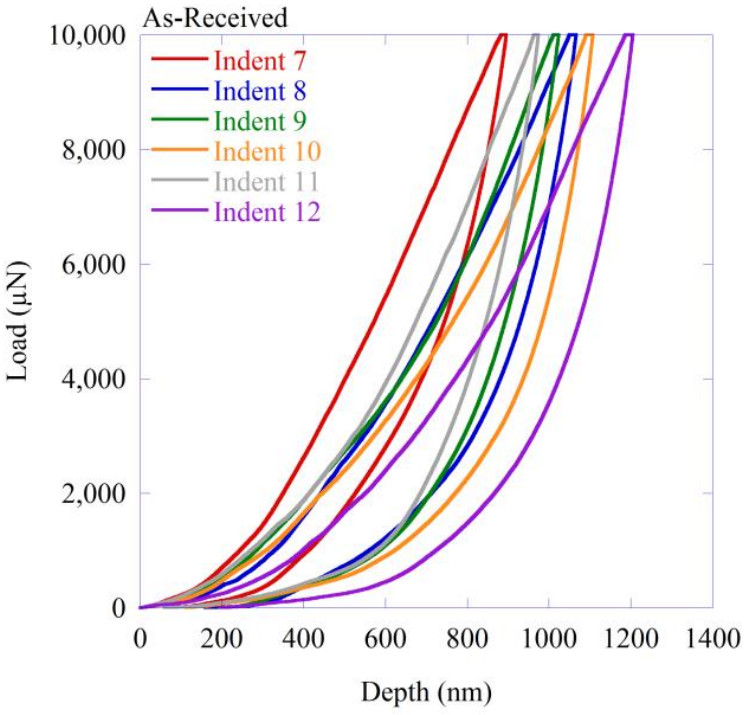

(b)

Figure D.1. Plots of load versus depth for nanoindentation #1-6 (a) and #7-12 (b) for the as-received material.

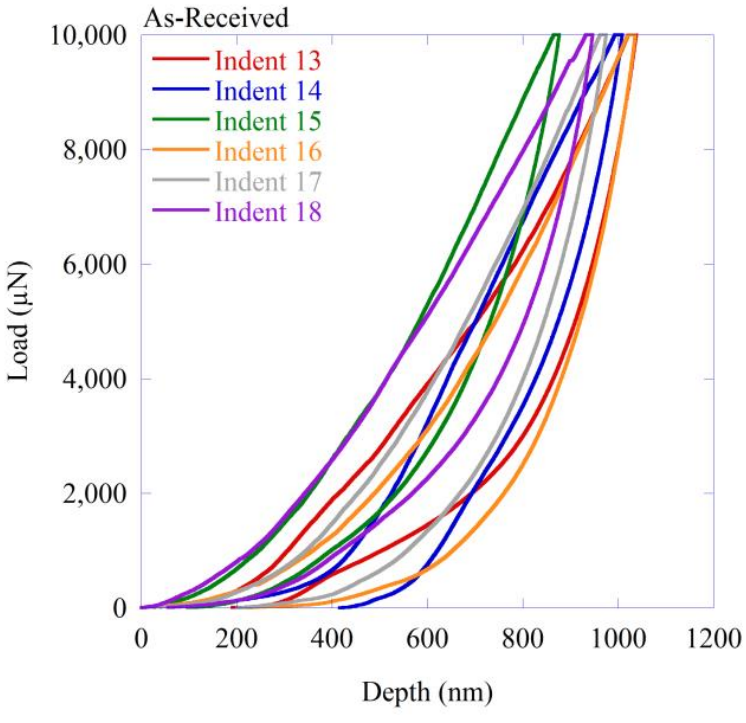

(a)

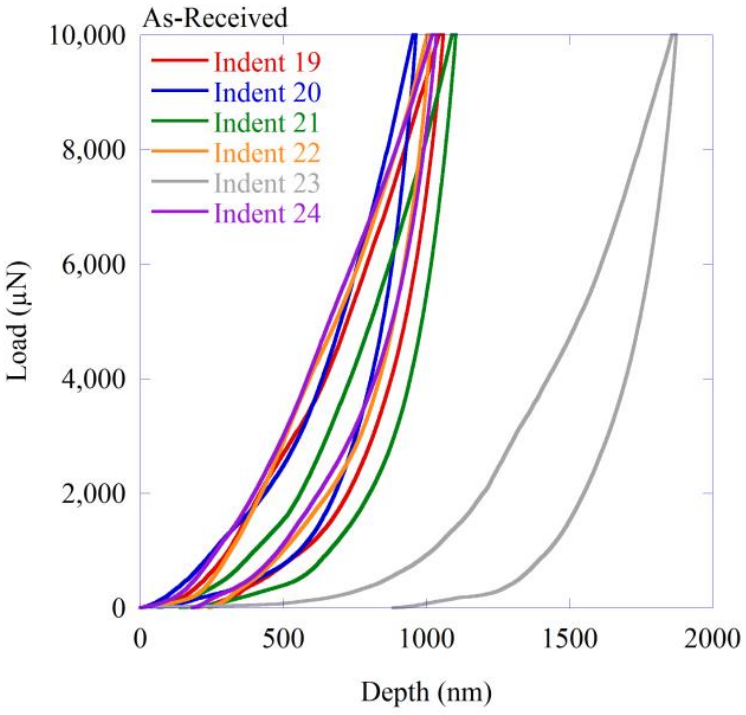

(b)

Figure D.2. Plots of load versus depth for nanoindentation #13-18 (a) and #19-24 (b) for the as-received material.

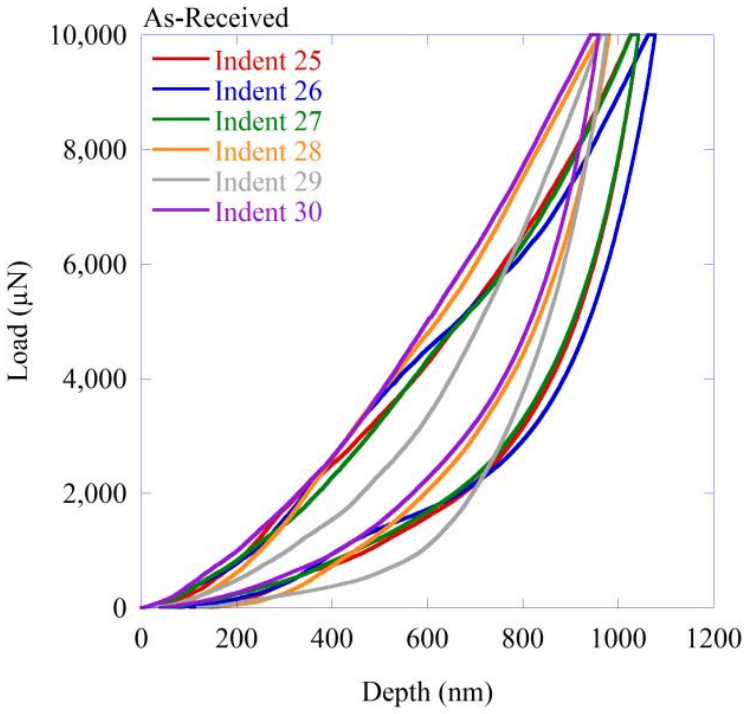

(a)

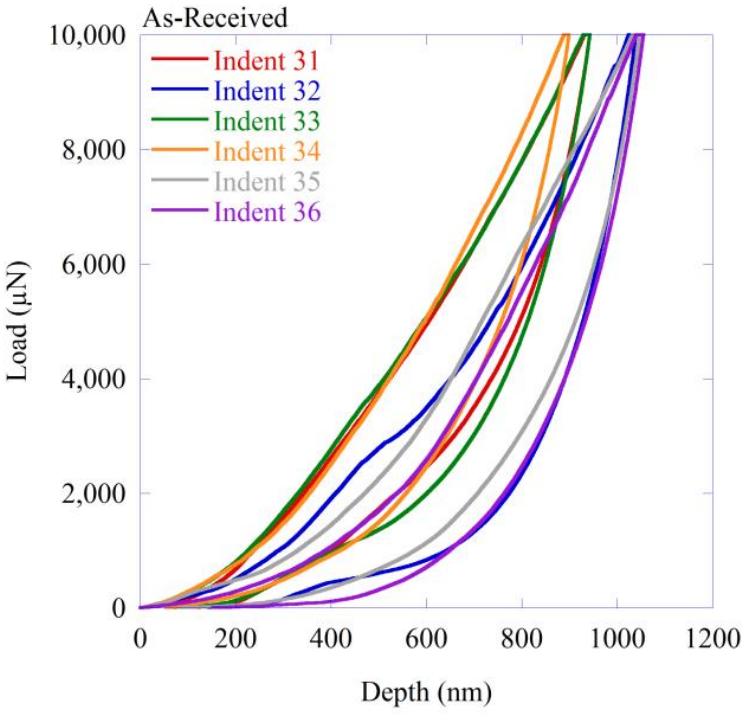

(b)

Figure D.3. Plots of load versus depth for nanoindentation #25-30 (a) and #31-36 (b) for the as-received material.

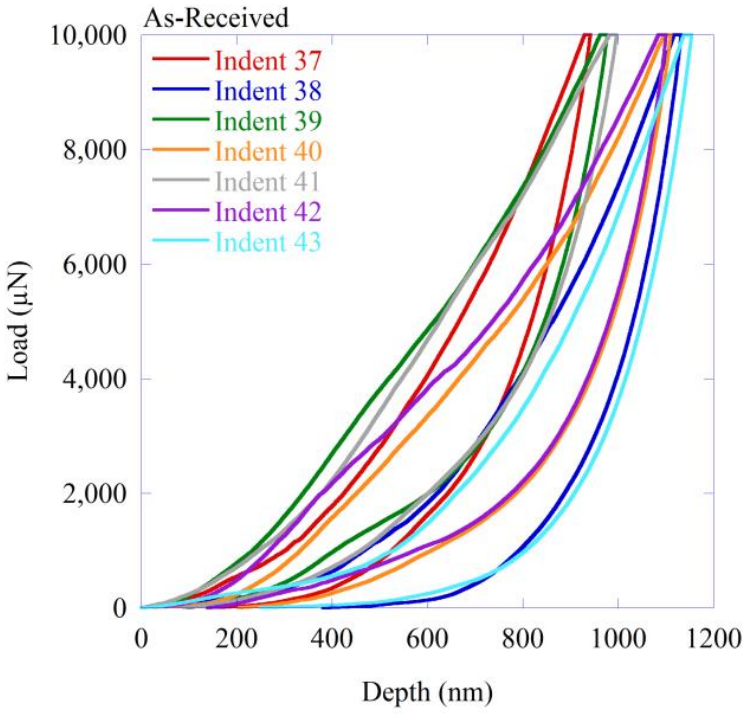

(a)

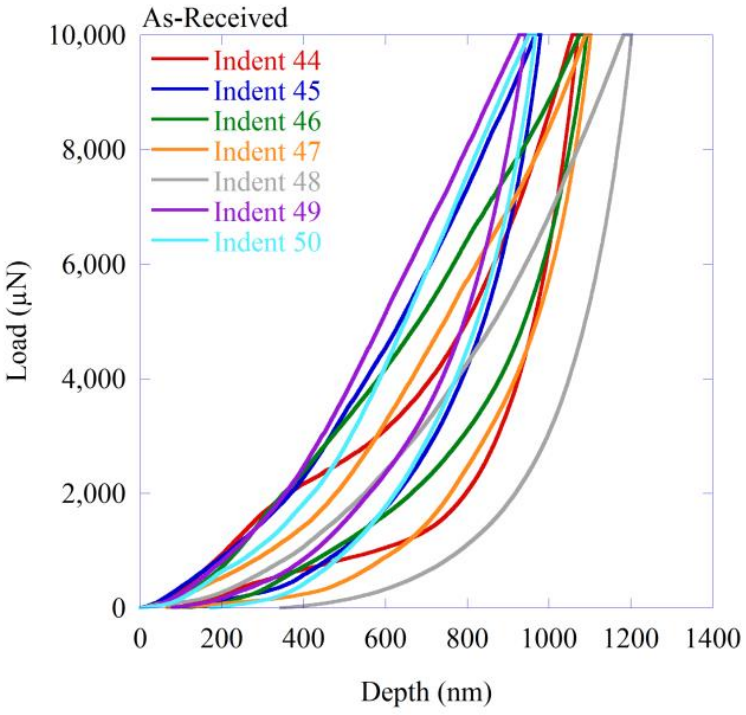

(b)

Figure D.4. Plots of load versus depth for nanoindentation #37-43 (a) and #44-50 (b) for the as-received material.

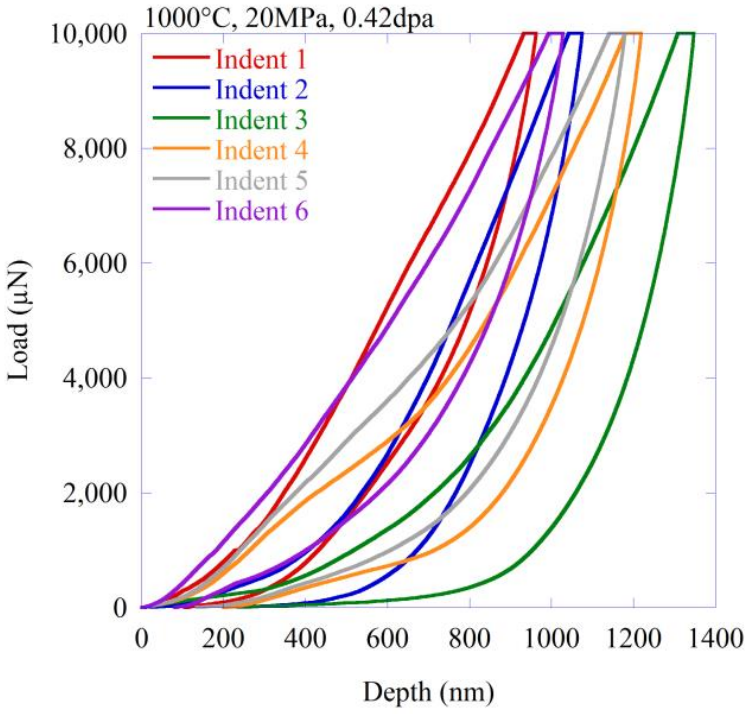

(a)

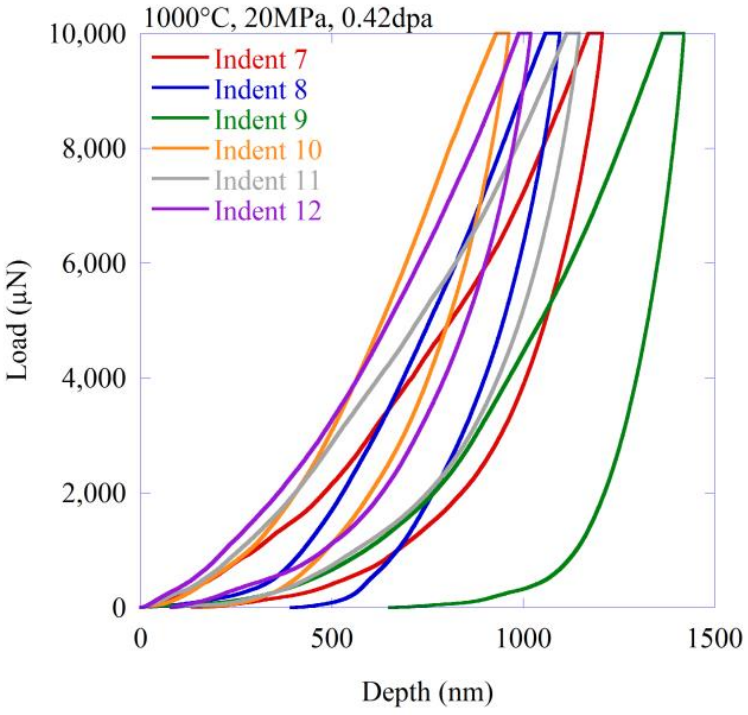

(b)

Figure D.5. Plots of load versus depth for nanoindentation #1-6 (a) and #7-12 (b) for the sample irradiated at 1000°C, 20MPa, to a final dose of 0.42dpa.

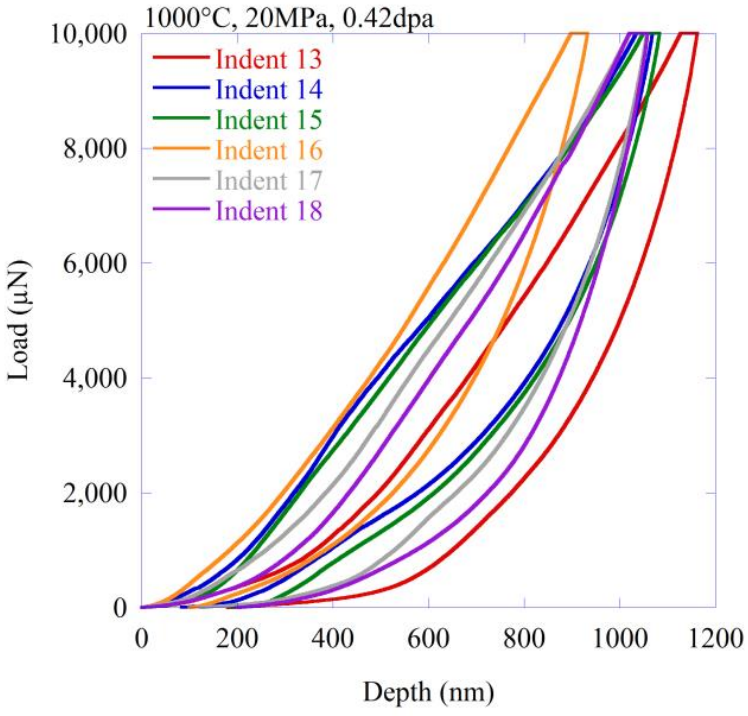

(a)

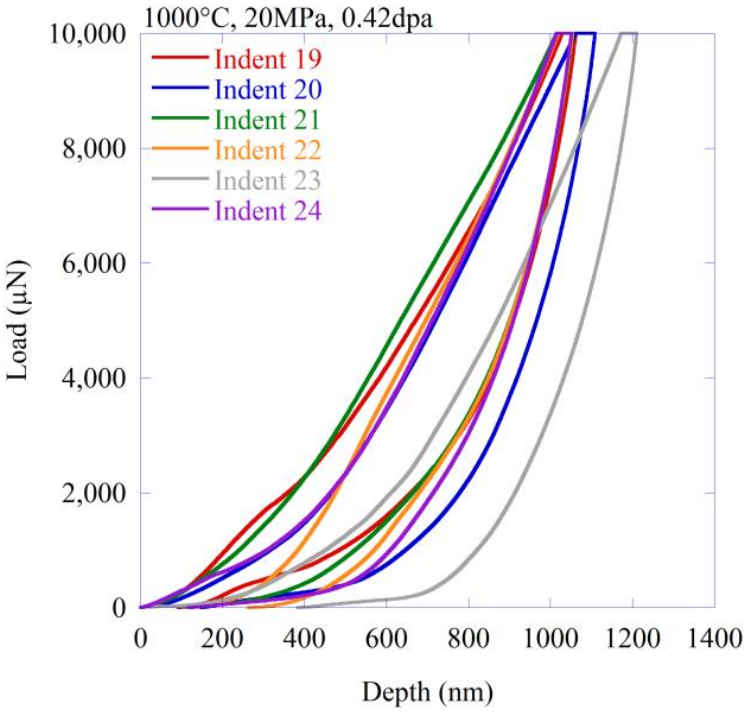

(b)

Figure D.6. Plots of load versus depth for nanoindentation #13-18 (a) and #19-24 (b) for the sample irradiated at 1000°C, 20MPa, to a final dose of 0.42dpa.

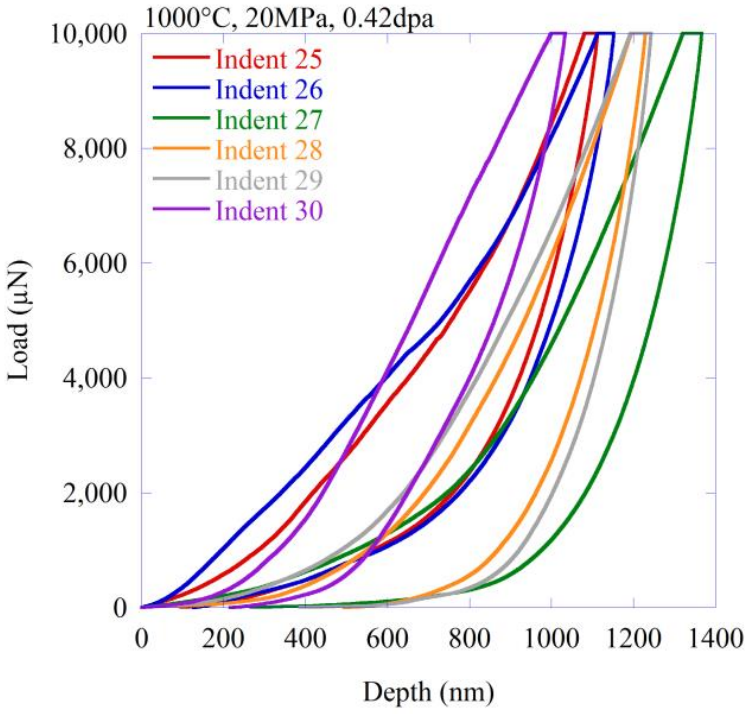

(a)

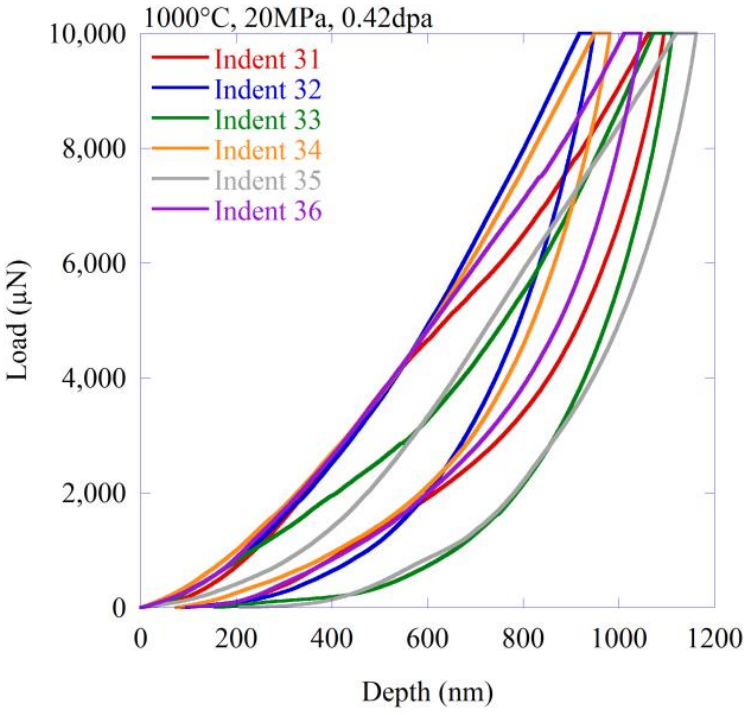

(b)

Figure D.7. Plots of load versus depth for nanoindentation #25-30 (a) and #31-36 (b) for the sample irradiated at 1000°C, 20MPa, to a final dose of 0.42dpa.

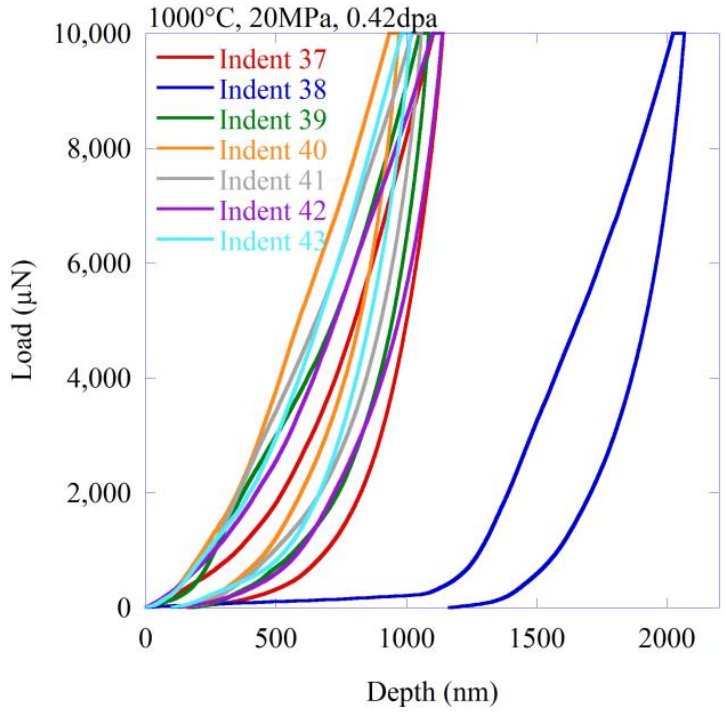

(a)

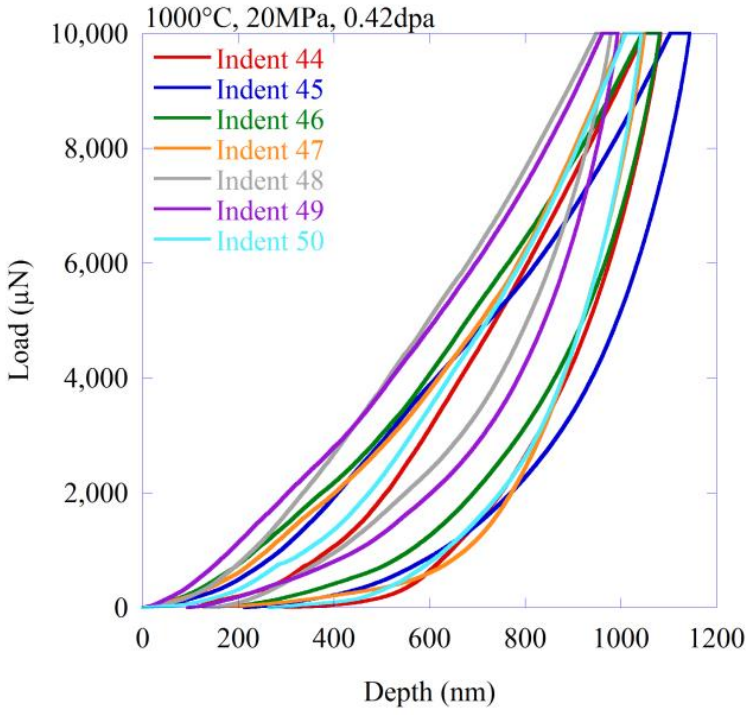

(b)

Figure D.8. Plots of load versus depth for nanoindentation #37-43 (a) and #44-50 (b) for the sample irradiated at 1000°C, 20MPa, to a final dose of 0.42dpa.

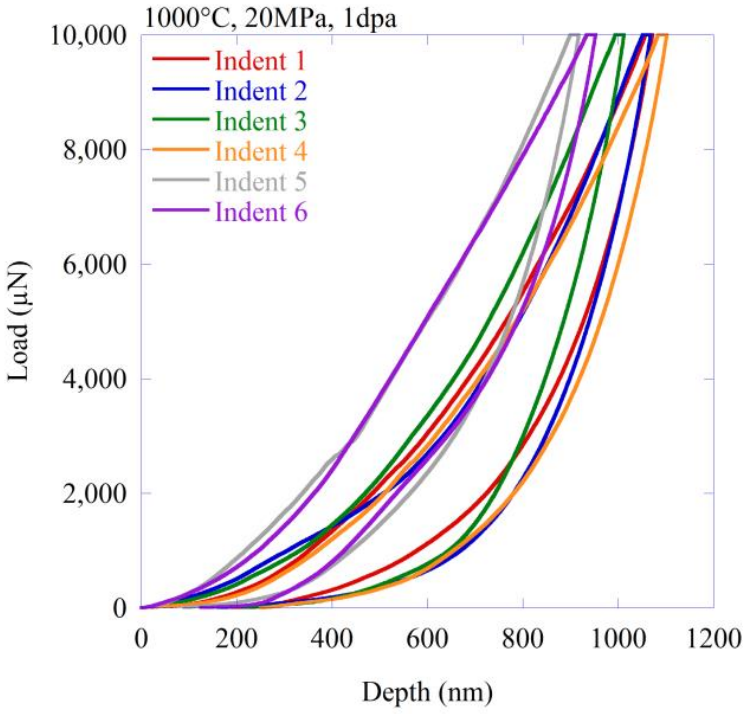

(a)

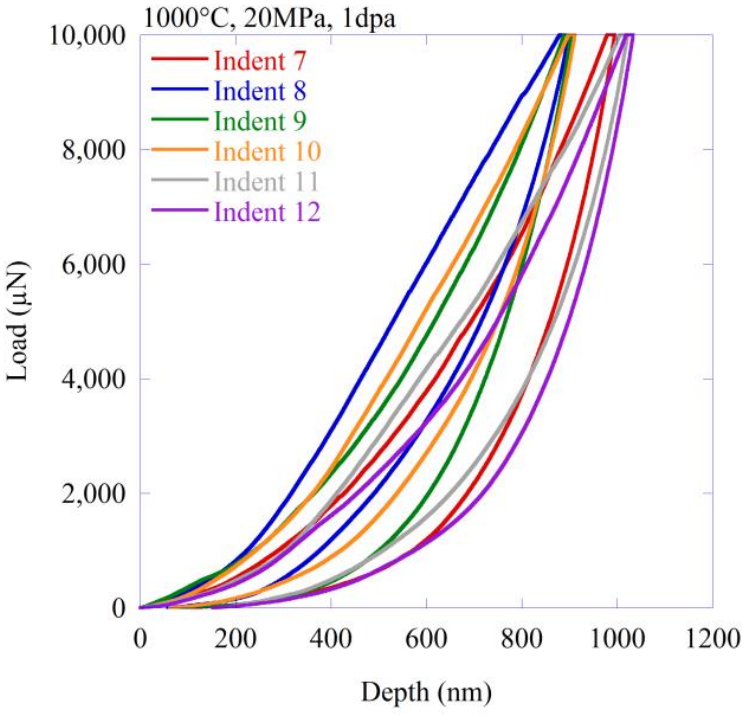

(b)

Figure D.9. Plots of load versus depth for nanoindentation #1-6 (a) and #7-12 (b) for the sample irradiated at 1000°C, 20MPa, to a final dose of 1.0dpa.

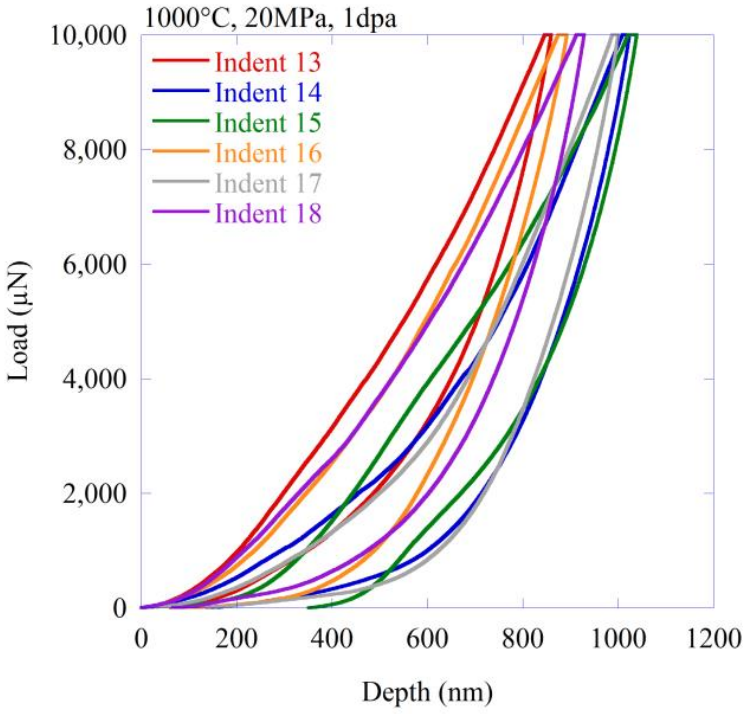

(a)

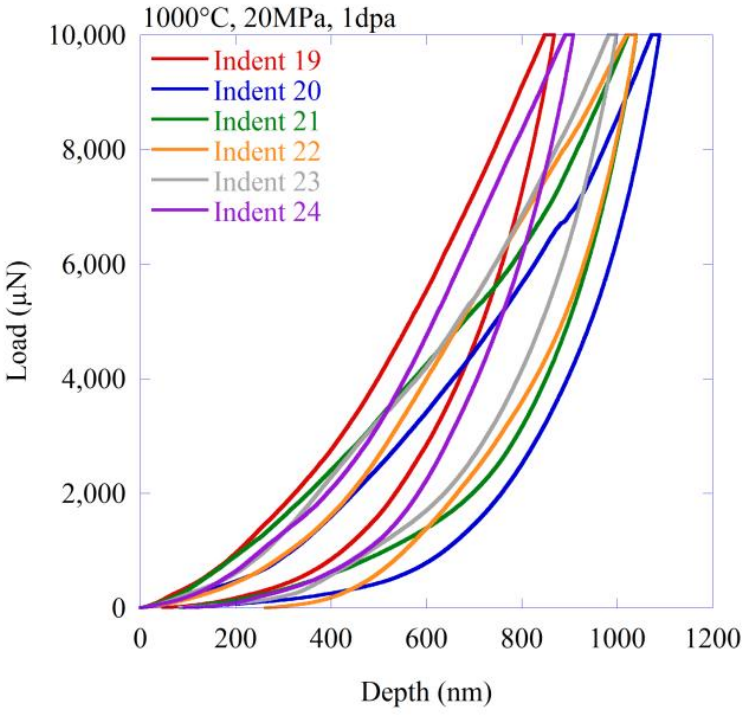

(b)

Figure D.10. Plots of load versus depth for nanoindentation #13-18 (a) and #19-24 (b) for the sample irradiated at 1000°C, 20MPa, to a final dose of 1.0dpa.

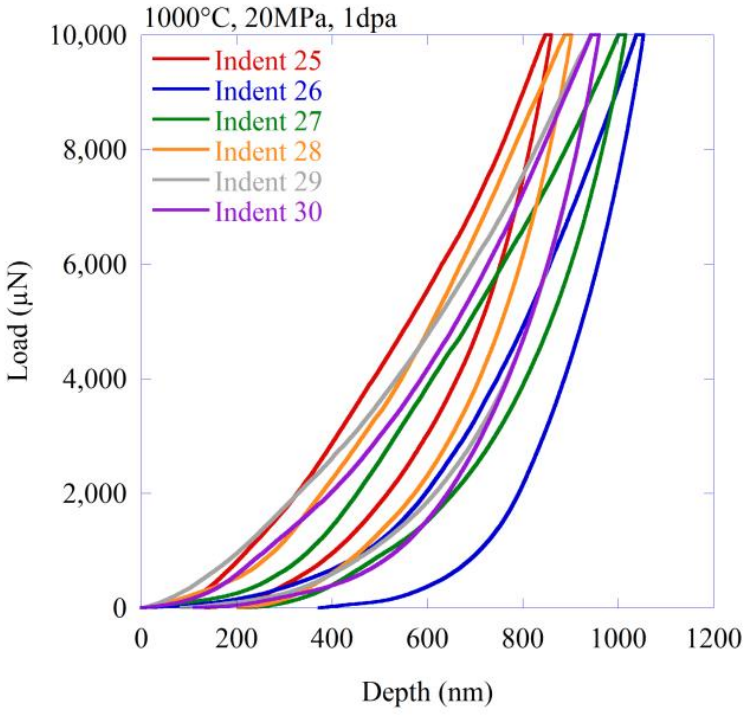

(a)

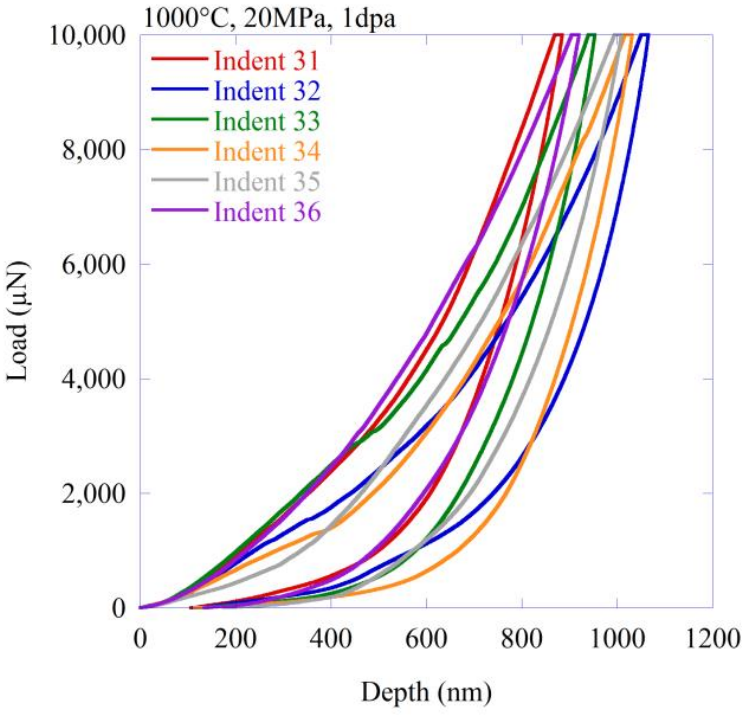

(b)

Figure D.11. Plots of load versus depth for nanoindentation #25-30 (a) and #31-36 (b) for the sample irradiated at 1000°C, 20MPa, to a final dose of 1.0dpa.

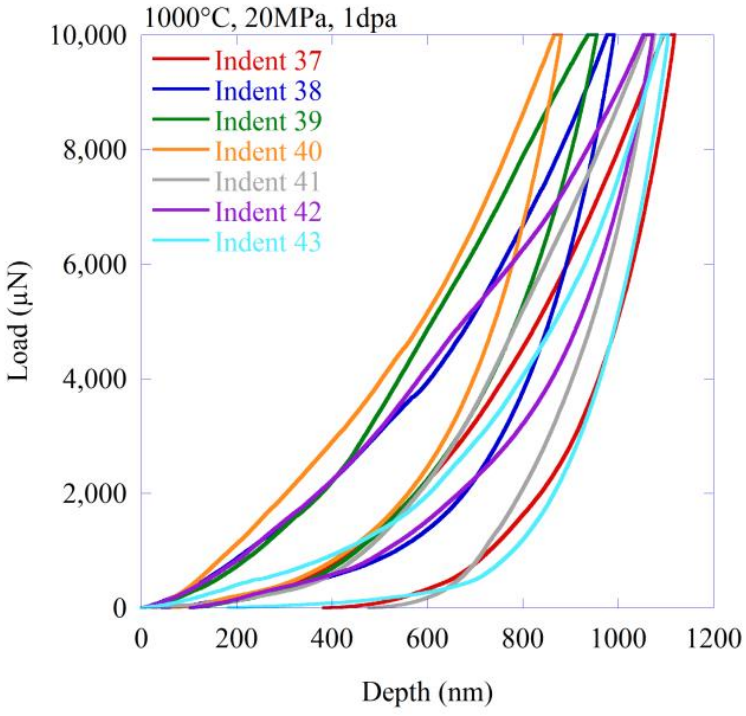

(a)

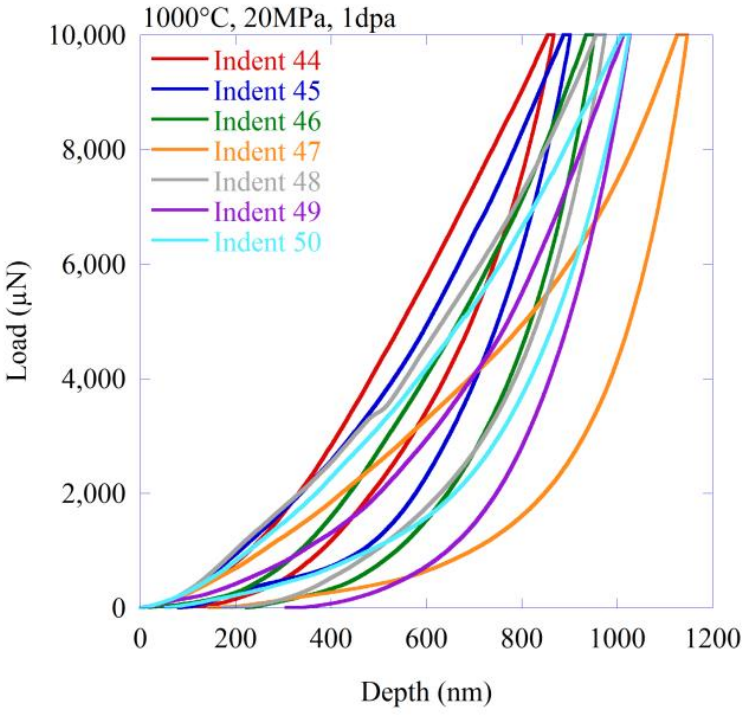

(b)

Figure D.12. Plots of load versus depth for nanoindentation #37-43 (a) and #44-50 (b) for the sample irradiated at 1000°C, 20MPa, to a final dose of 1.0dpa.

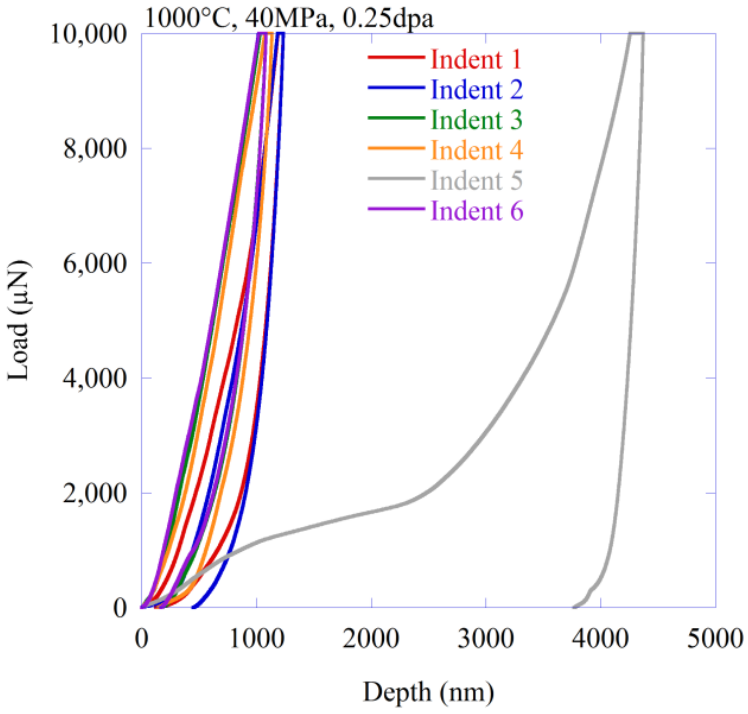

(a)

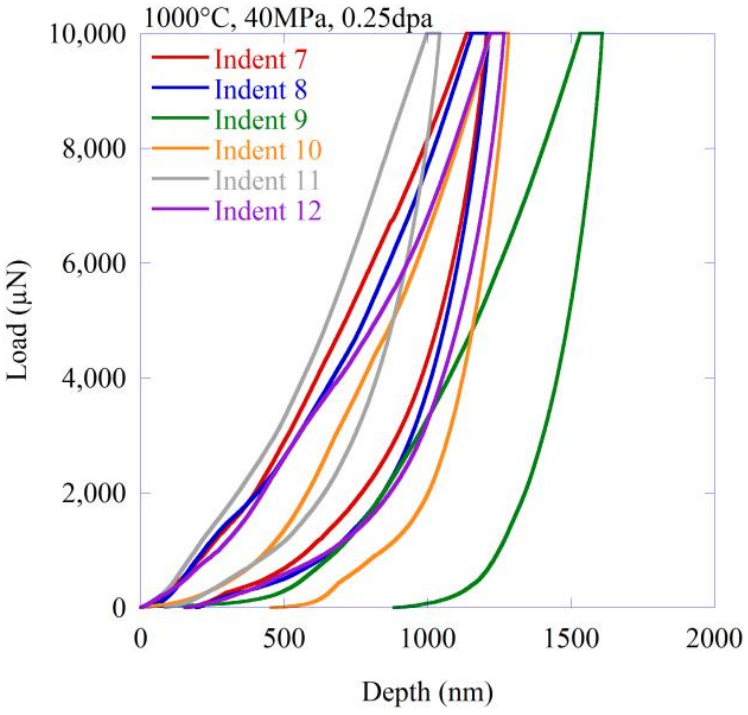

(b)

Figure D.13. Plots of load versus depth for nanoindentation #1-6 (a) and #7-12 (b) for the sample irradiated at 1000°C, 40MPa, to a final dose of 0.25dpa.

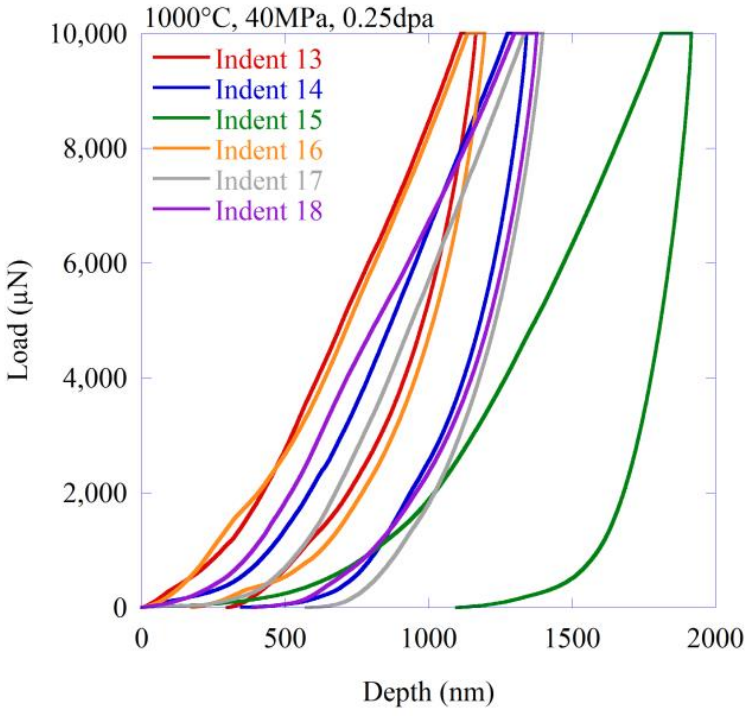

(a)

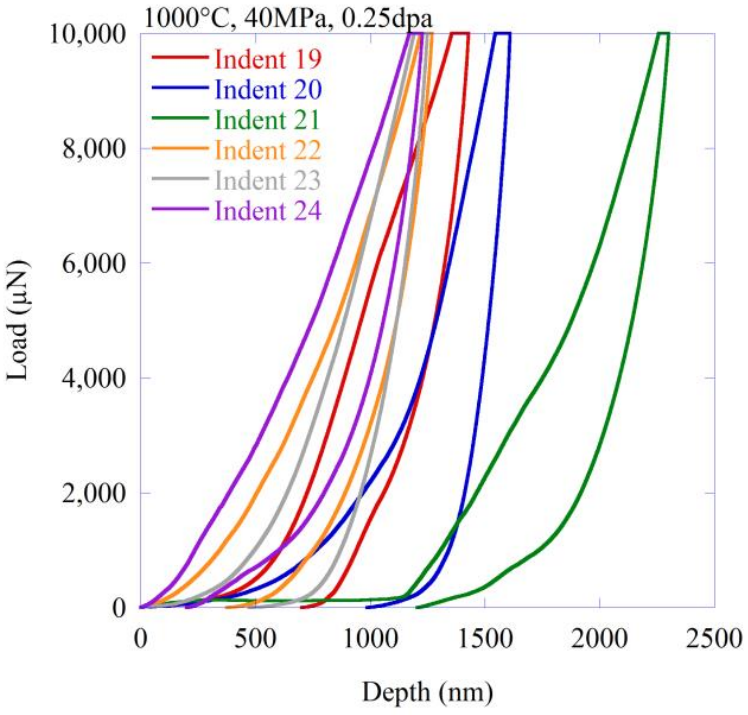

(b)

Figure D.14. Plots of load versus depth for nanoindentation #13-18 (a) and #19-24 (b) for the sample irradiated at 1000°C, 40MPa, to a final dose of 0.25dpa.

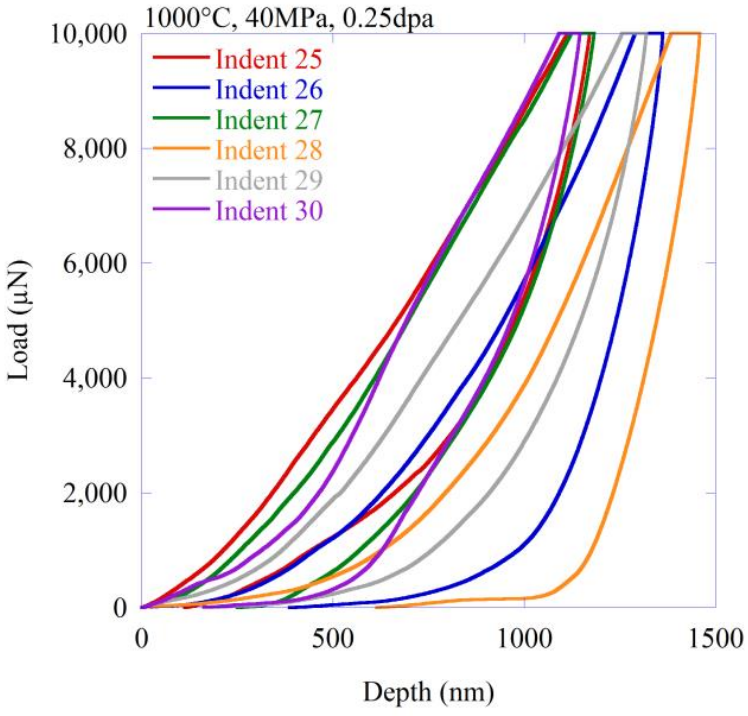

(a)

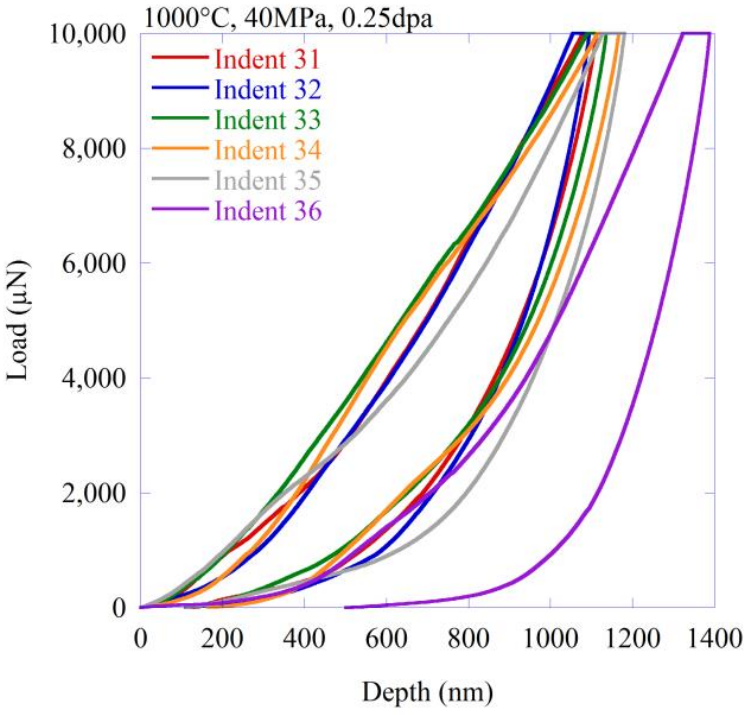

(b)

Figure D.15. Plots of load versus depth for nanoindentation #25-30 (a) and #31-36 (b) for the sample irradiated at 1000°C, 40MPa, to a final dose of 0.25dpa.

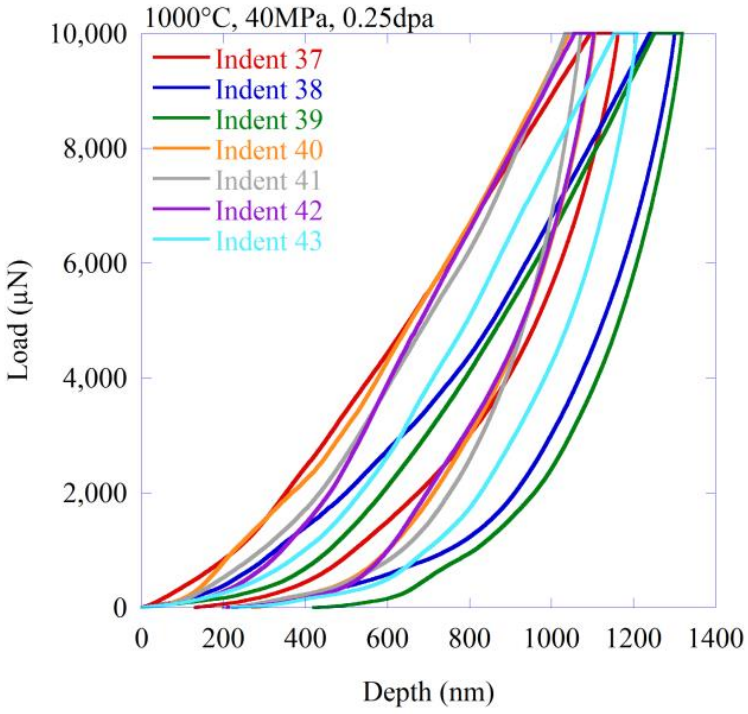

(a)

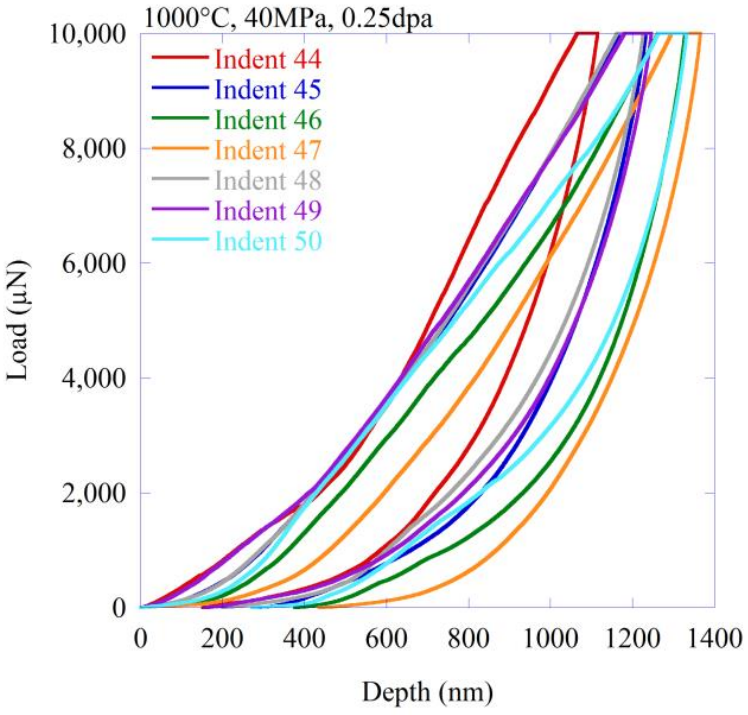

(b)

Figure D.16. Plots of load versus depth for nanoindentation #37-43 (a) and #44-50 (b) for the sample irradiated at 1000°C, 40MPa, to a final dose of 0.25dpa.

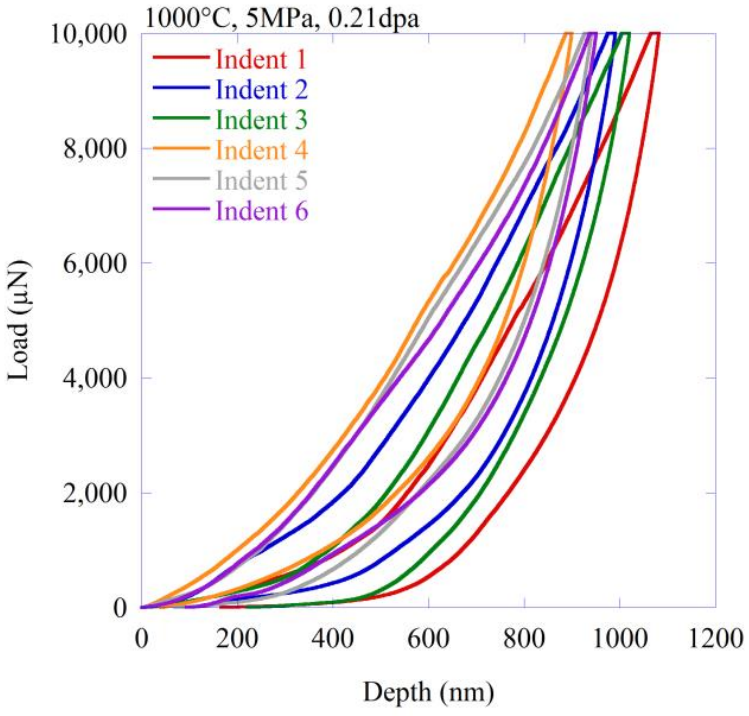

(a)

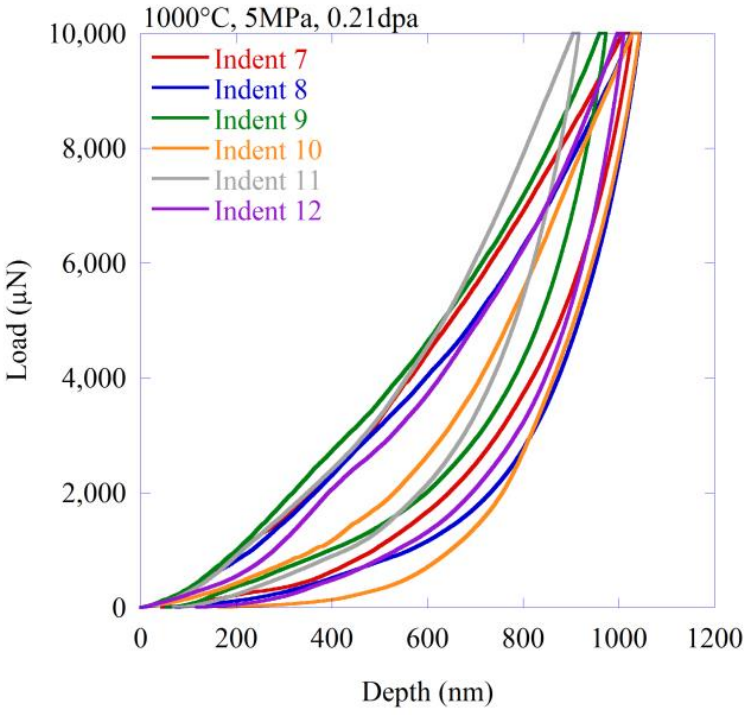

(b)

Figure D.17. Plots of load versus depth for nanoindentation #1-6 (a) and #7-12 (b) for the sample irradiated at 1000°C, 5MPa, to a final dose of 0.21dpa.

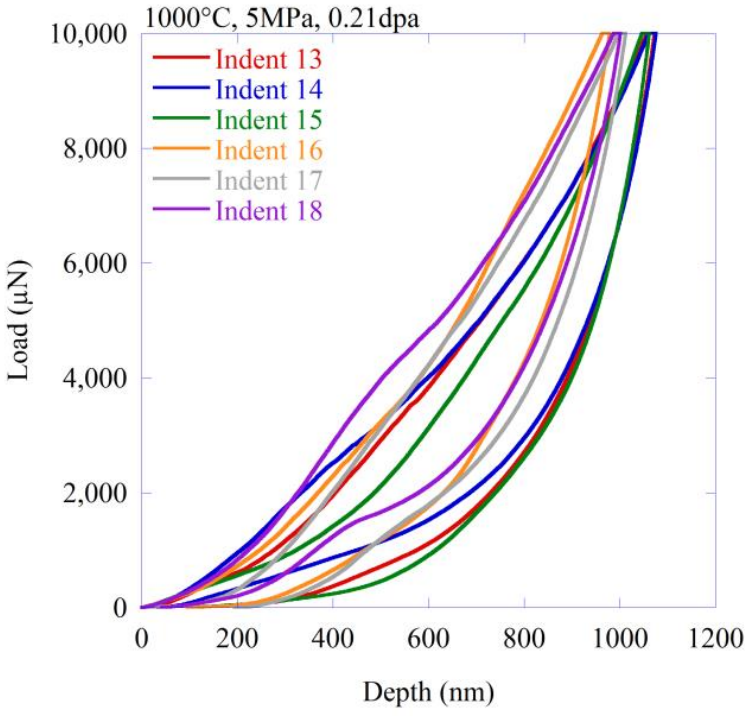

(a)

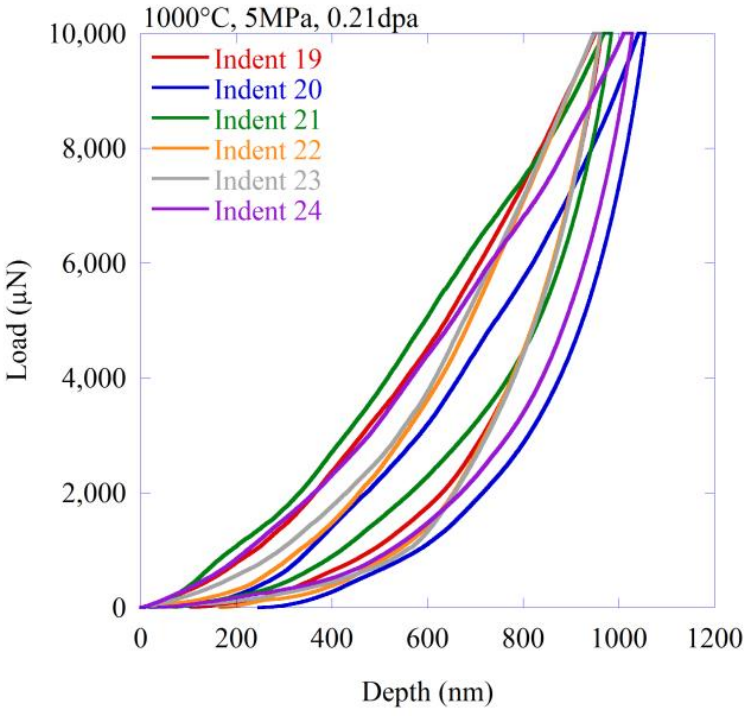

(b)

Figure D.18. Plots of load versus depth for nanoindentation #13-18 (a) and #19-24 (b) for the sample irradiated at 1000°C, 5MPa, to a final dose of 0.21dpa.

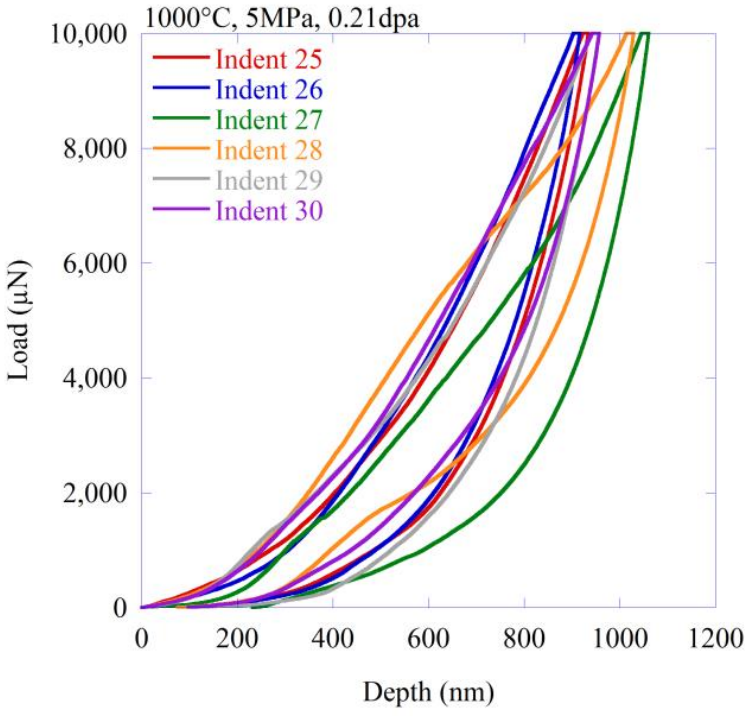

(a)

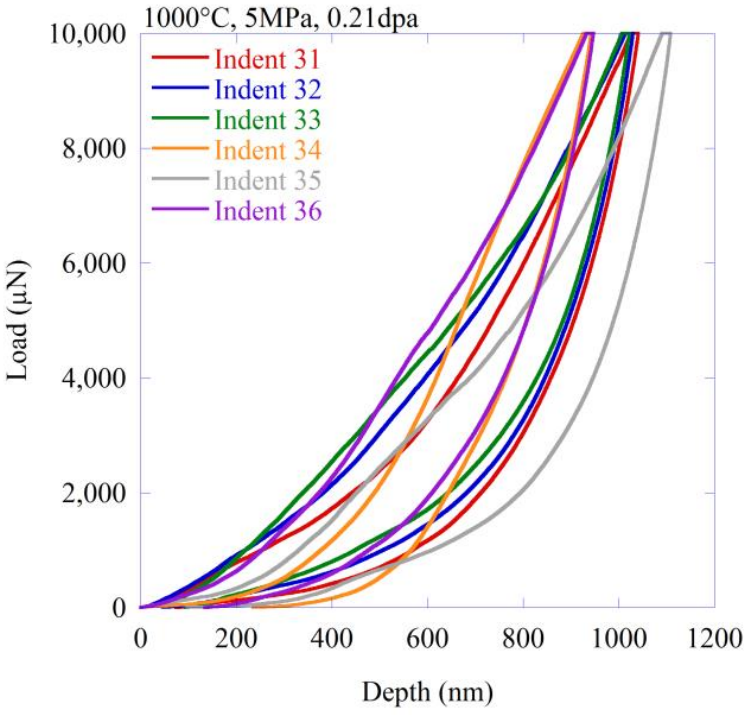

(b)

Figure D.19. Plots of load versus depth for nanoindentation #25-30 (a) and #31-36 (b) for the sample irradiated at 1000°C, 5MPa, to a final dose of 0.21dpa.

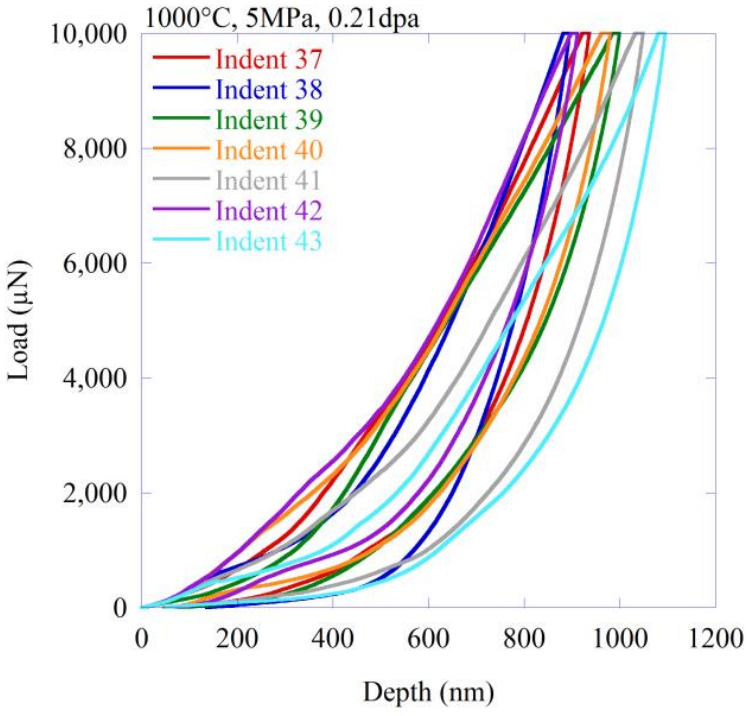

(a)

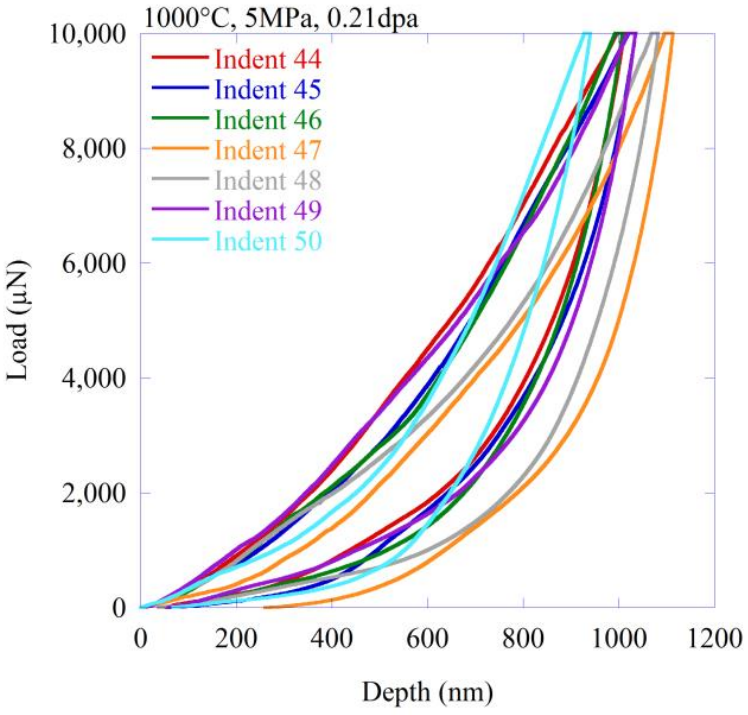

(b)

Figure D.20. Plots of load versus depth for nanoindentation #37-43 (a) and #44-50 (b) for the sample irradiated at 1000°C, 5MPa, to a final dose of 0.21dpa.

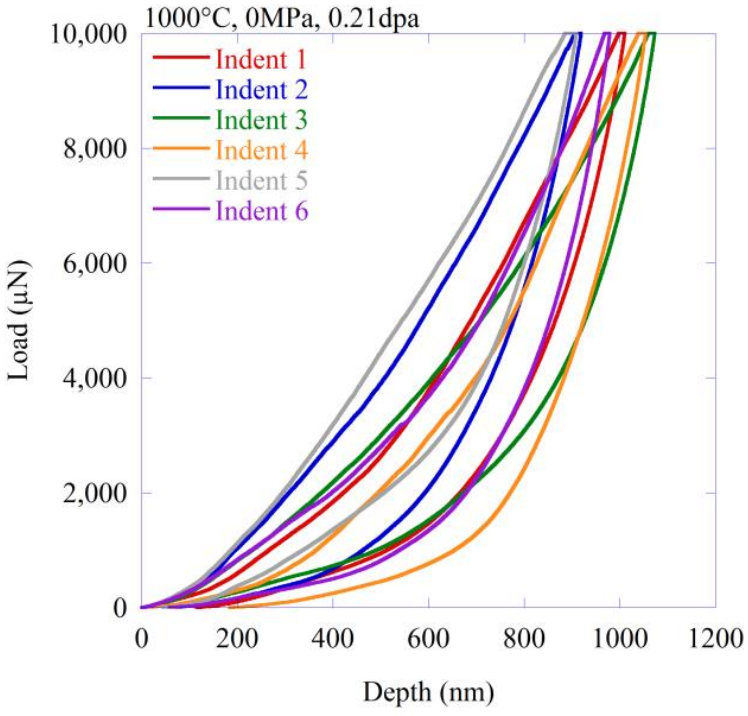

(a)

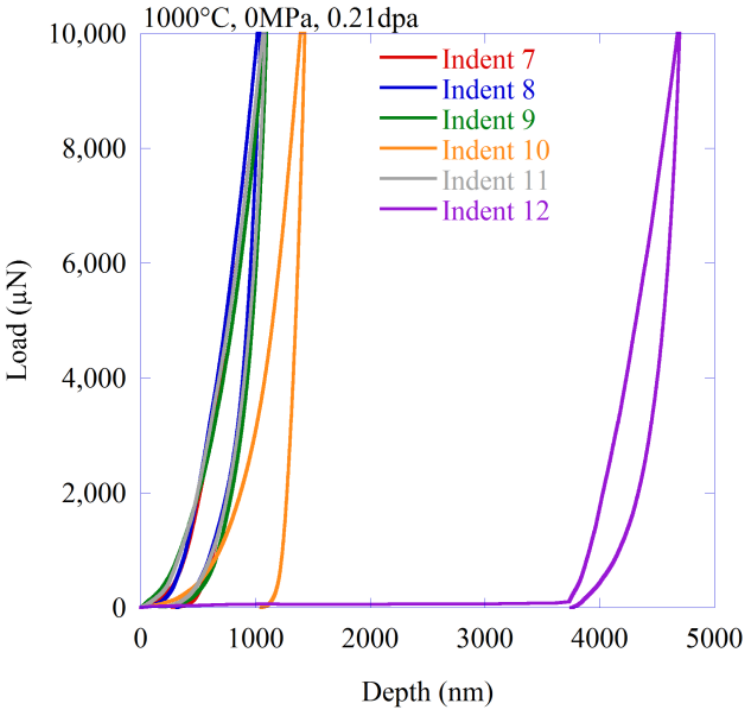

(b)

Figure D.21. Plots of load versus depth for nanoindentation #1-6 (a) and #7-12 (b) for the sample irradiated at 1000°C, 0MPa, to a final dose of 0.21dpa.

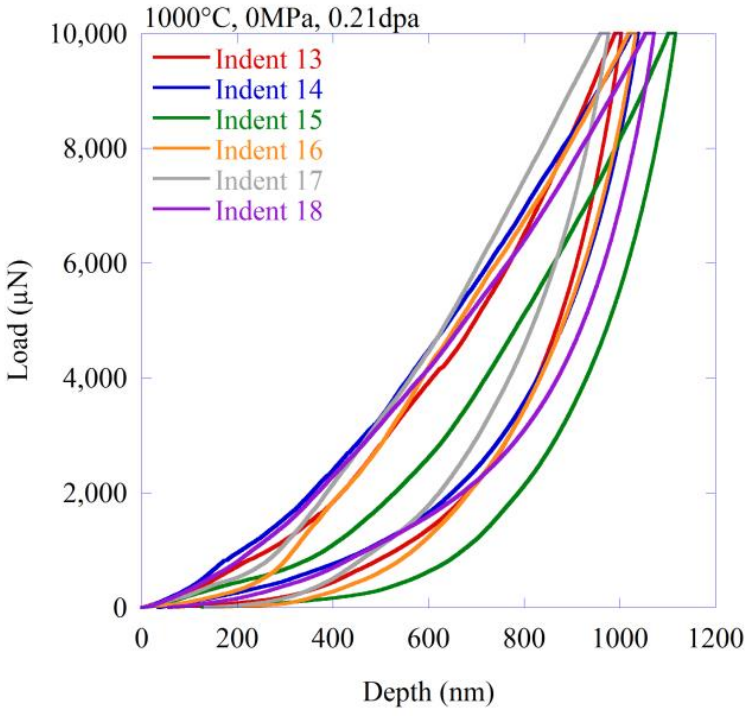

(a)

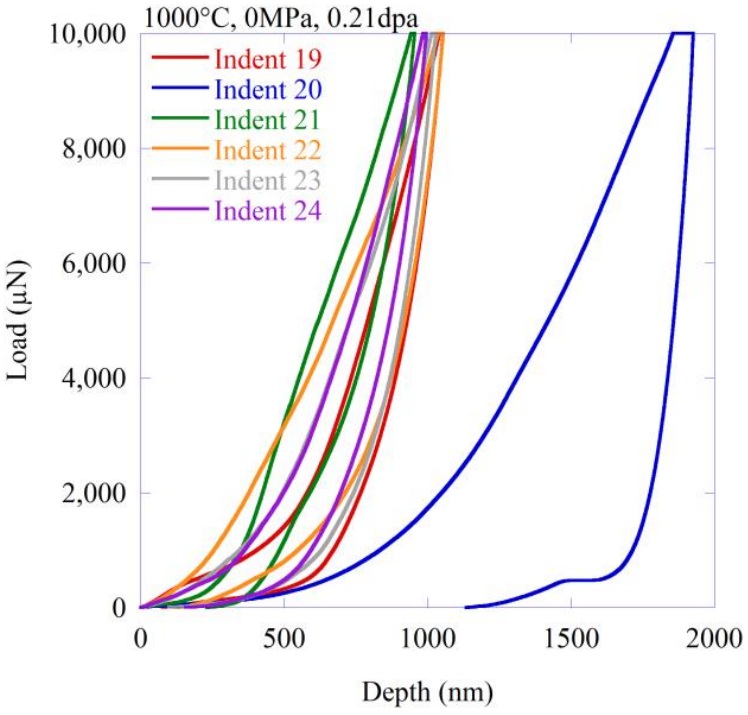

(b)

Figure D.22. Plots of load versus depth for nanoindentation #13-18 (a) and #19-24 (b) for the sample irradiated at 1000°C, 0MPa, to a final dose of 0.21dpa.

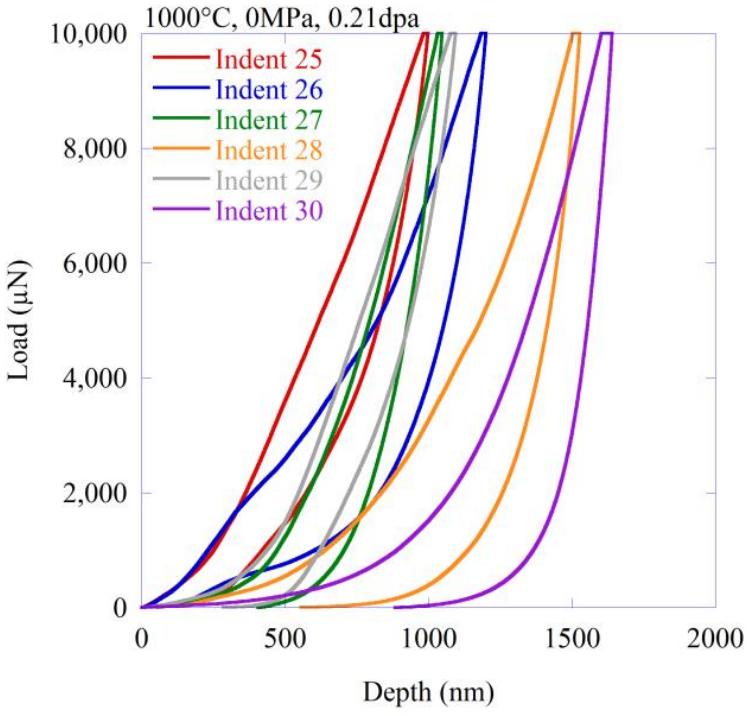

(a)

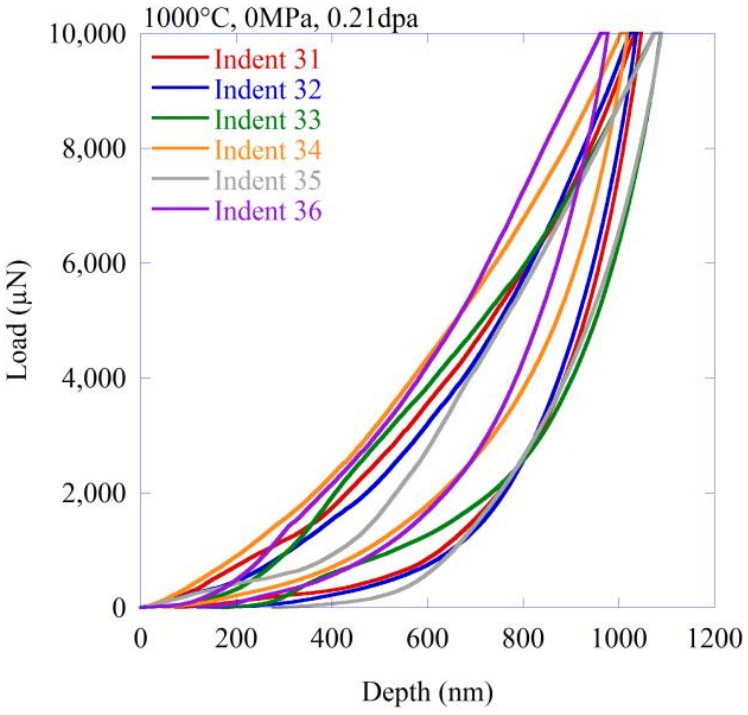

(b)

Figure D.23. Plots of load versus depth for nanoindentation #25-30 (a) and #31-36 (b) for the sample irradiated at 1000°C, 0MPa, to a final dose of 0.21dpa.

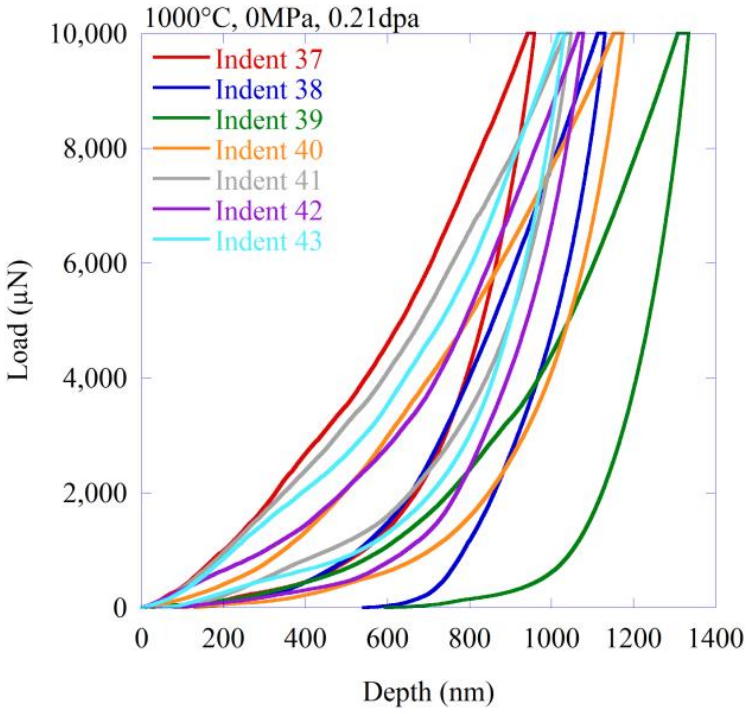

(a)

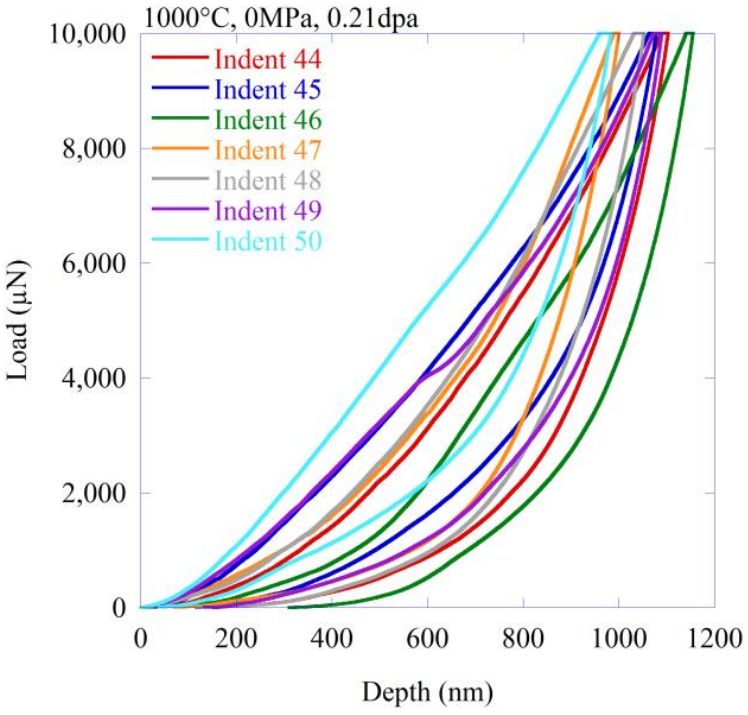

(b)

Figure D.24. Plots of load versus depth for nanoindentation #37-43 (a) and #44-50 (b) for the sample irradiated at 1000°C, 0MPa, to a final dose of 0.21dpa.

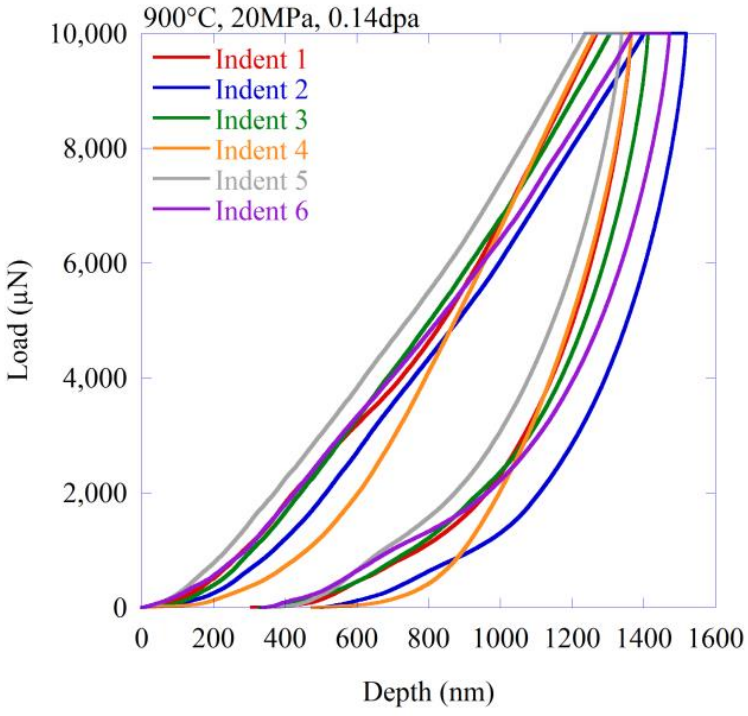

(a)

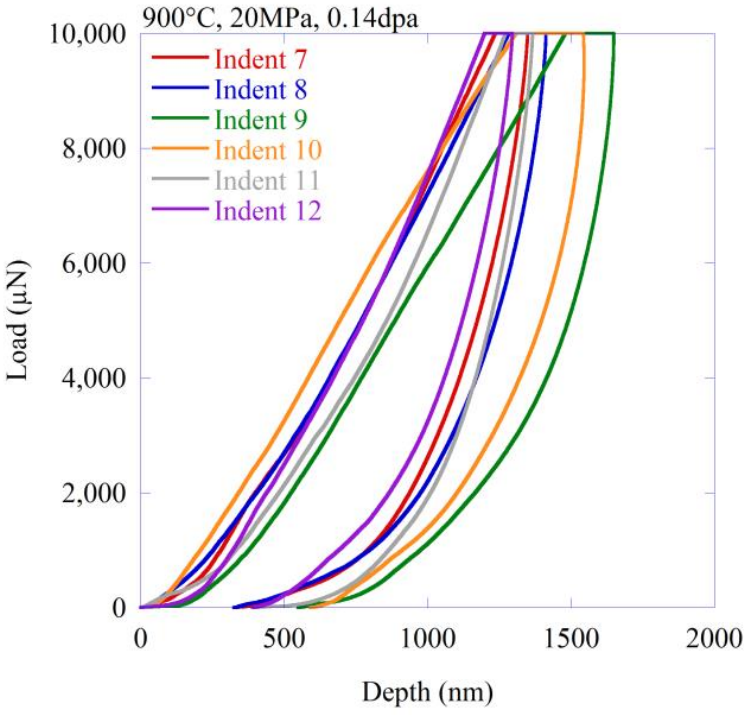

(b)

Figure D.25. Plots of load versus depth for nanoindentation #1-6 (a) and #7-12 (b) for the sample irradiated at 900°C, 20MPa, to a final dose of 0.14dpa.

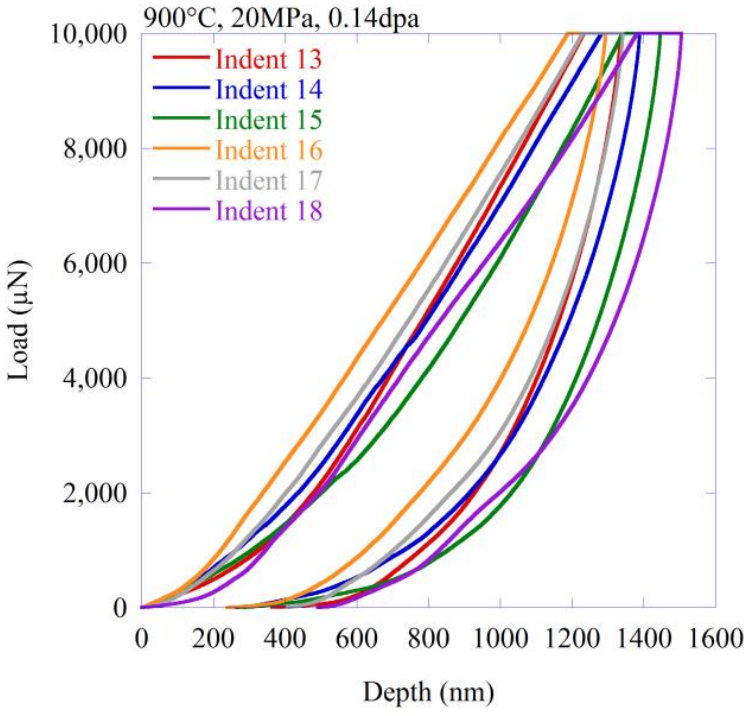

(a)

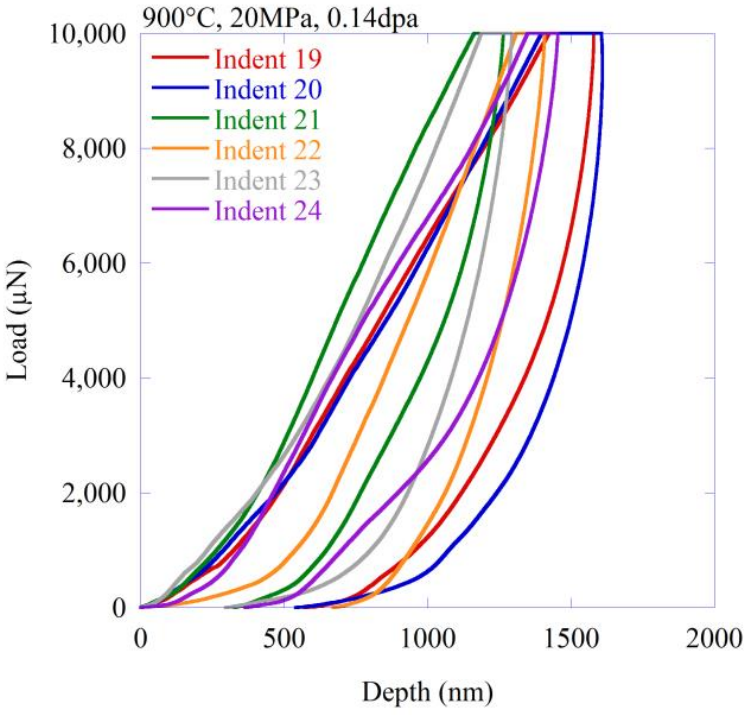

(b)

Figure D.26. Plots of load versus depth for nanoindentation #13-18 (a) and #19-24 (b) for the sample irradiated at 900°C, 20MPa, to a final dose of 0.14dpa.

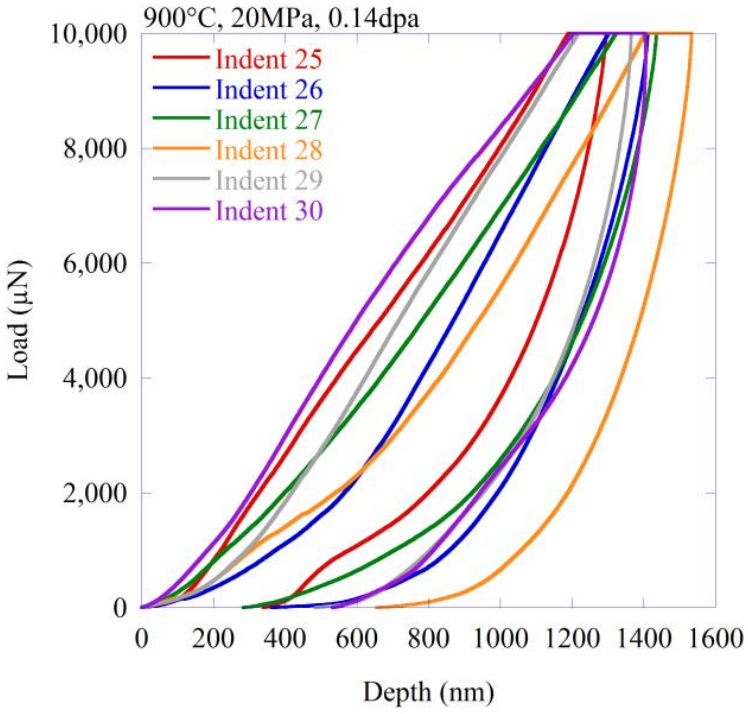

(a)

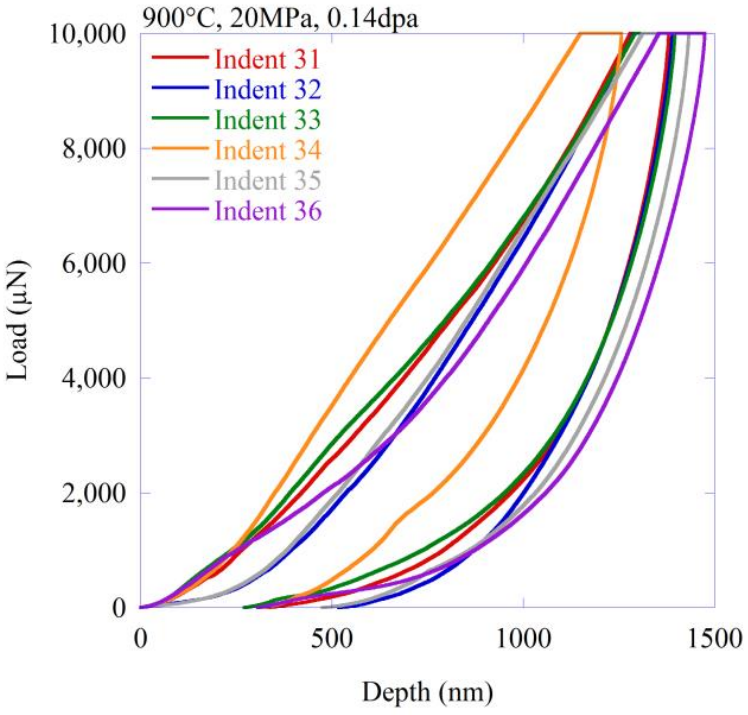

(b)

Figure D.27. Plots of load versus depth for nanoindentation #25-30 (a) and #31-36 (b) for the sample irradiated at 900°C, 20MPa, to a final dose of 0.14dpa.

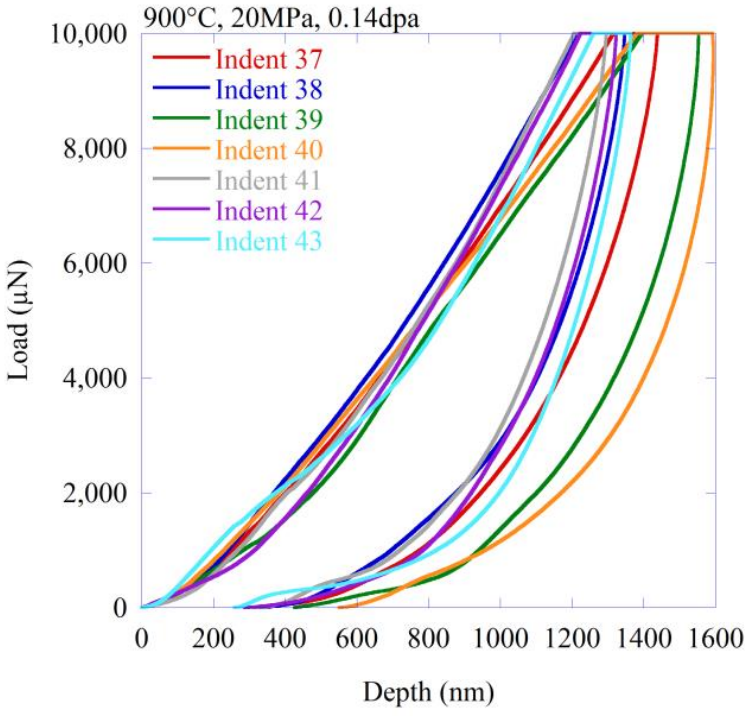

(a)

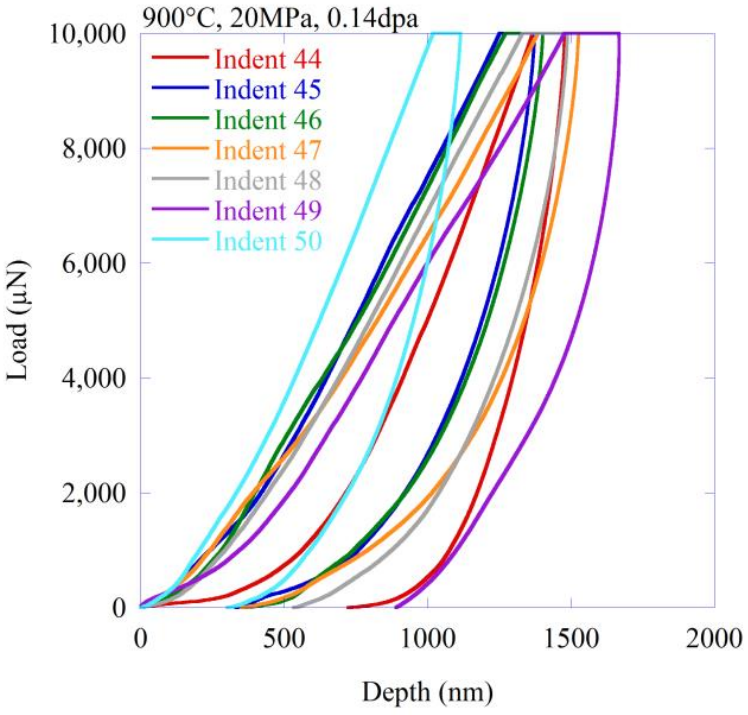

(b)

Figure D.28. Plots of load versus depth for nanoindentation #37-43 (a) and #44-50 (b) for the sample irradiated at 900°C, 20MPa, to a final dose of 0.14dpa.

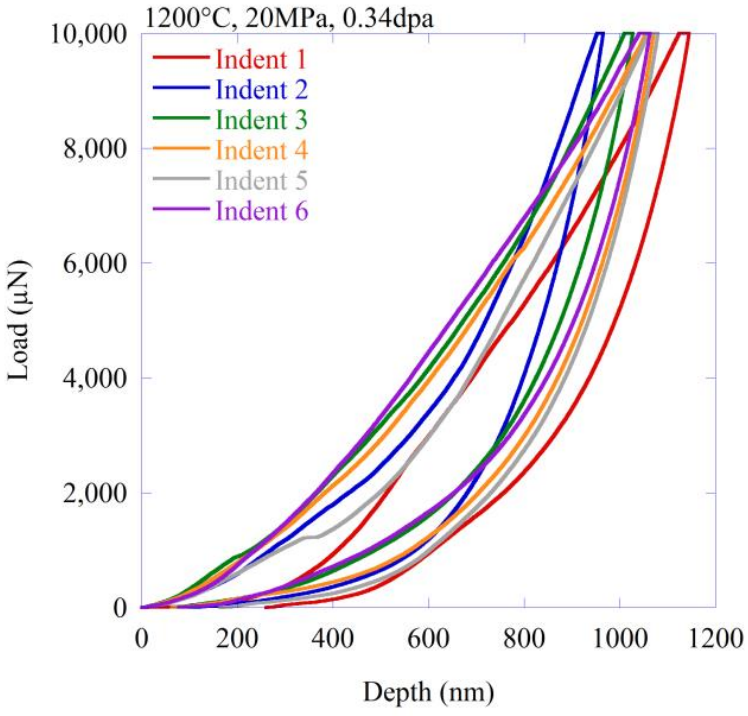

(a)

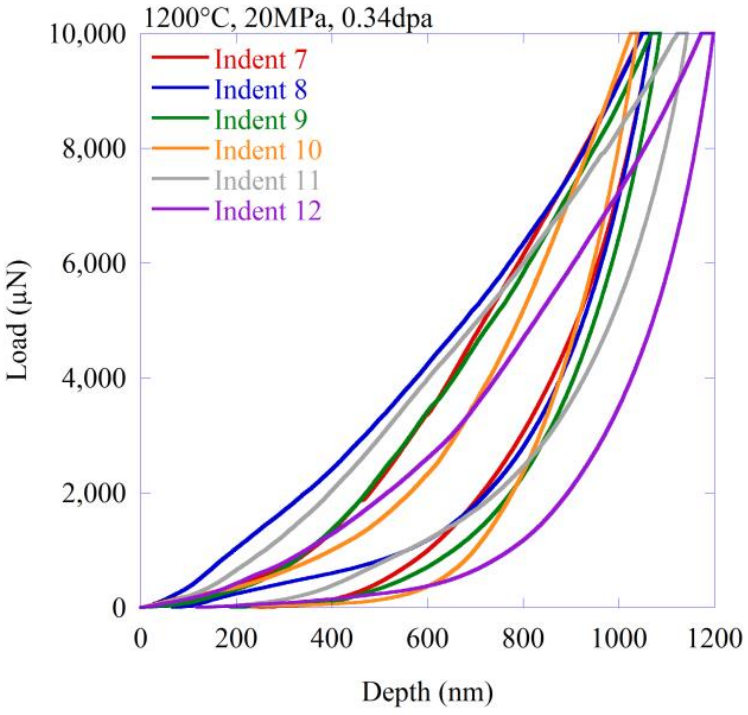

(b)

Figure D.29. Plots of load versus depth for nanoindentation #1-6 (a) and #7-12 (b) for the sample irradiated at 1200°C, 20MPa, to a final dose of 0.34dpa.

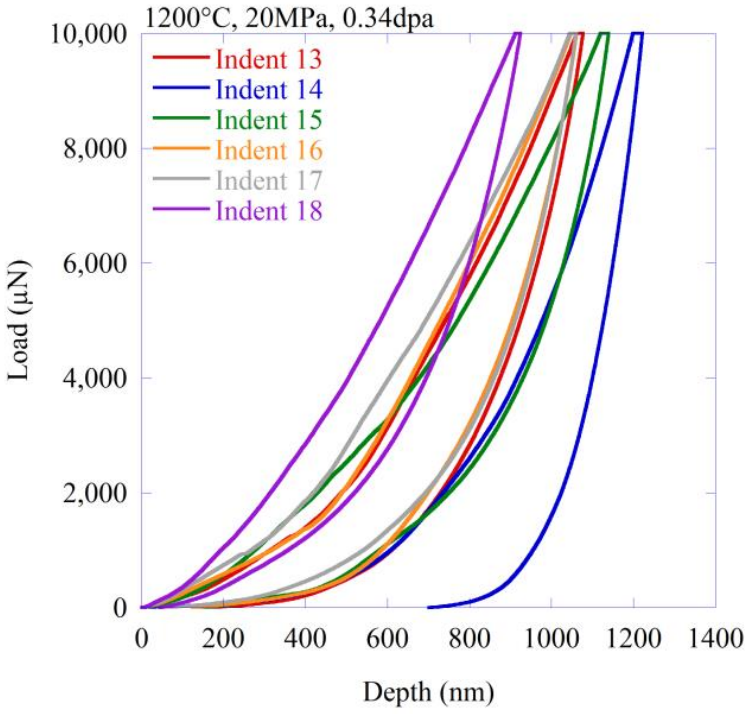

(a)

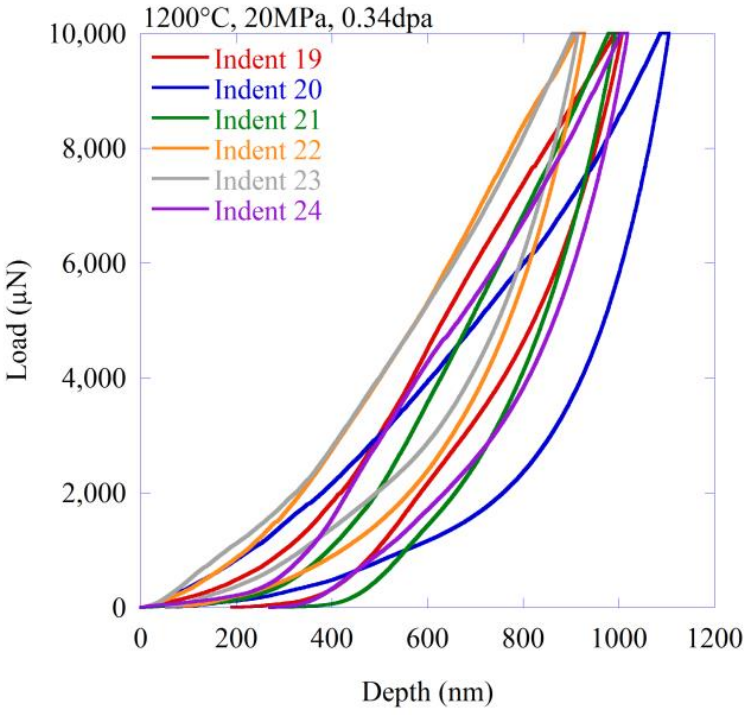

(b)

Figure D.30. Plots of load versus depth for nanoindentation #13-18 (a) and #19-24 (b) for the sample irradiated at 1200°C, 20MPa, to a final dose of 0.34dpa.

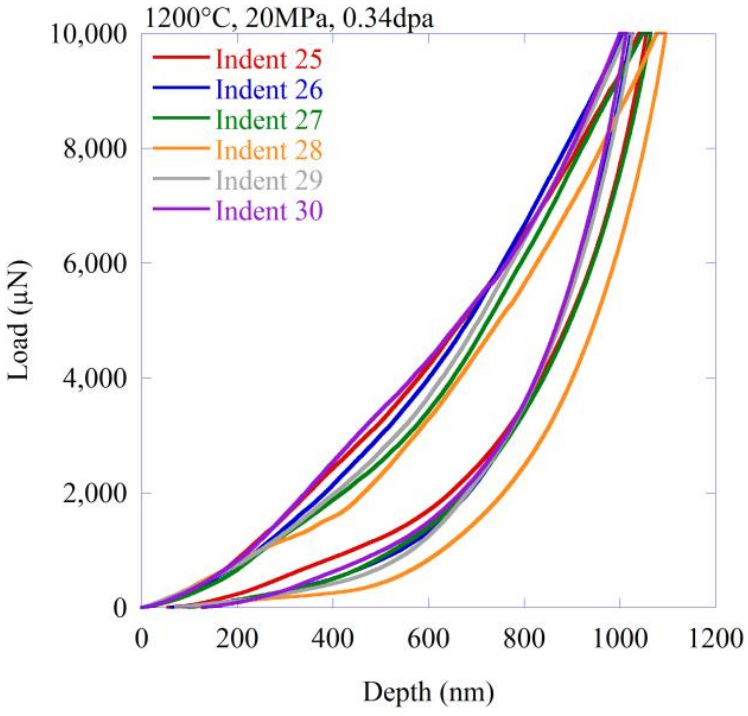

(a)

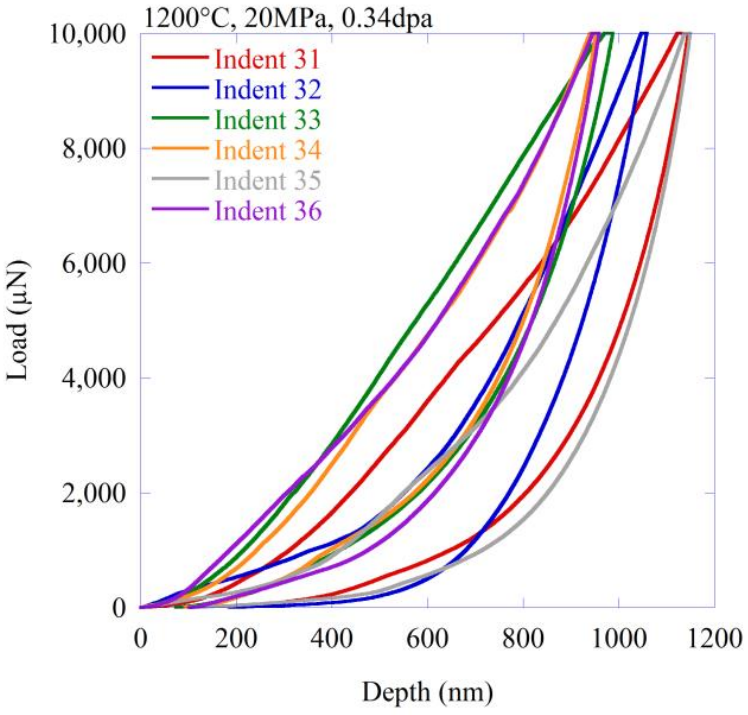

(b)

Figure D.31. Plots of load versus depth for nanoindentation #25-30 (a) and #31-36 (b) for the sample irradiated at 1200°C, 20MPa, to a final dose of 0.34dpa.

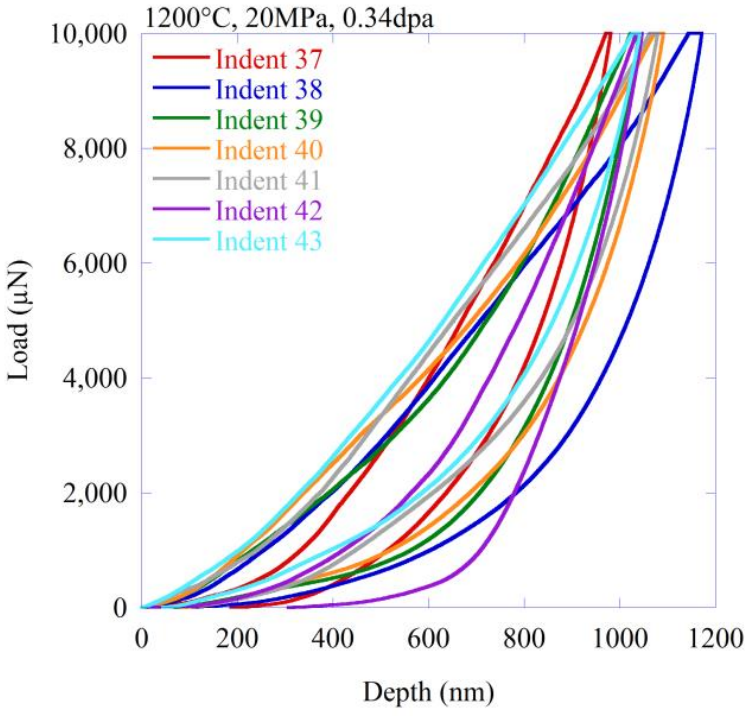

(a)

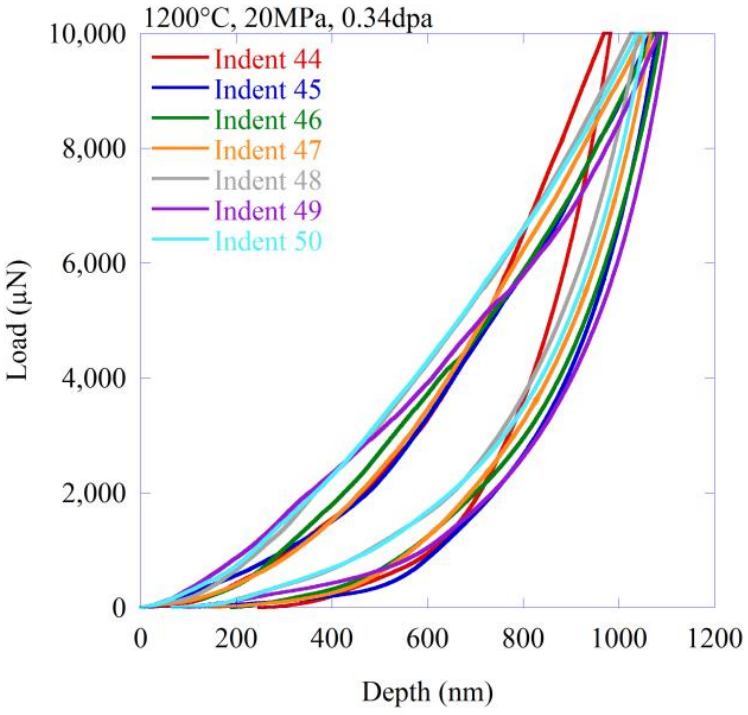

(b)

Figure D.32. Plots of load versus depth for nanoindentation #37-43 (a) and #44-50 (b) for the sample irradiated at 1200°C, 20MPa, to a final dose of 0.34dpa.

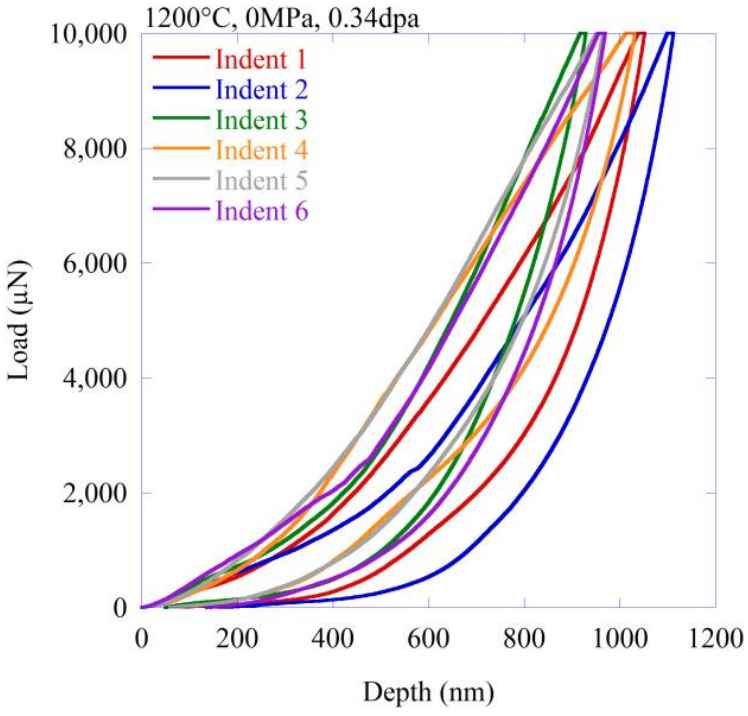

(a)

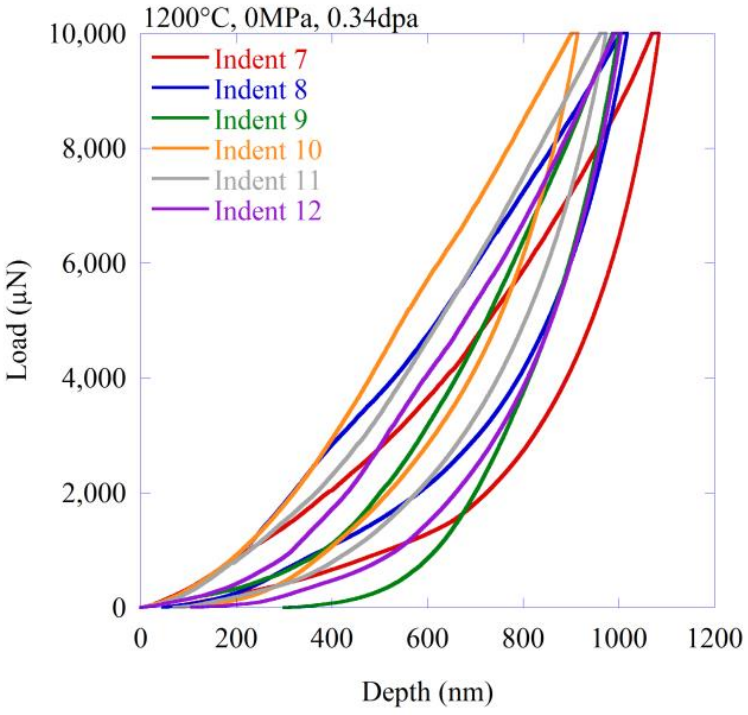

(b)

Figure D.33. Plots of load versus depth for nanoindentation #1-6 (a) and #7-12 (b) for the sample irradiated at 1200°C, 0MPa, to a final dose of 0.34dpa.

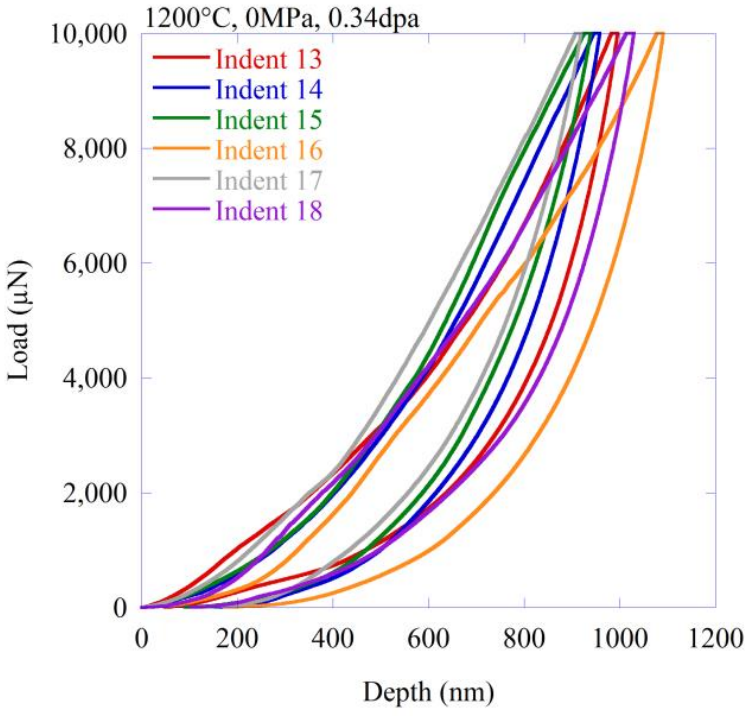

(a)

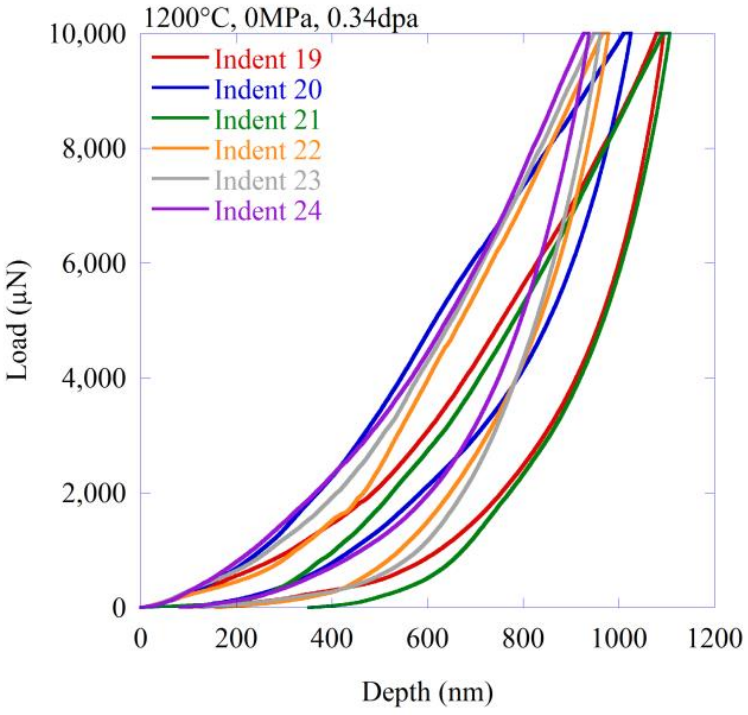

(b)

Figure D.34. Plots of load versus depth for nanoindentation #13-18 (a) and #19-24 (b) for the sample irradiated at 1200°C, 0MPa, to a final dose of 0.34dpa.

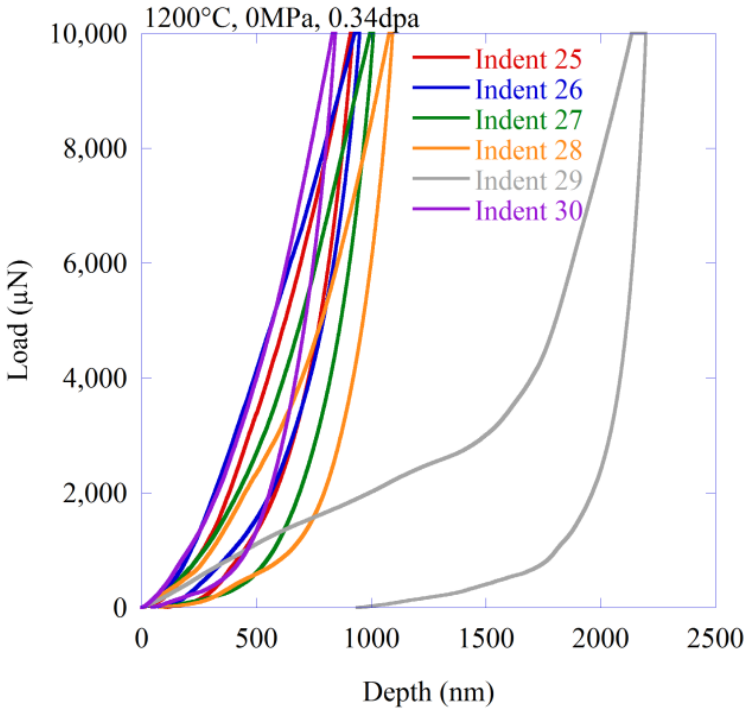

(a)

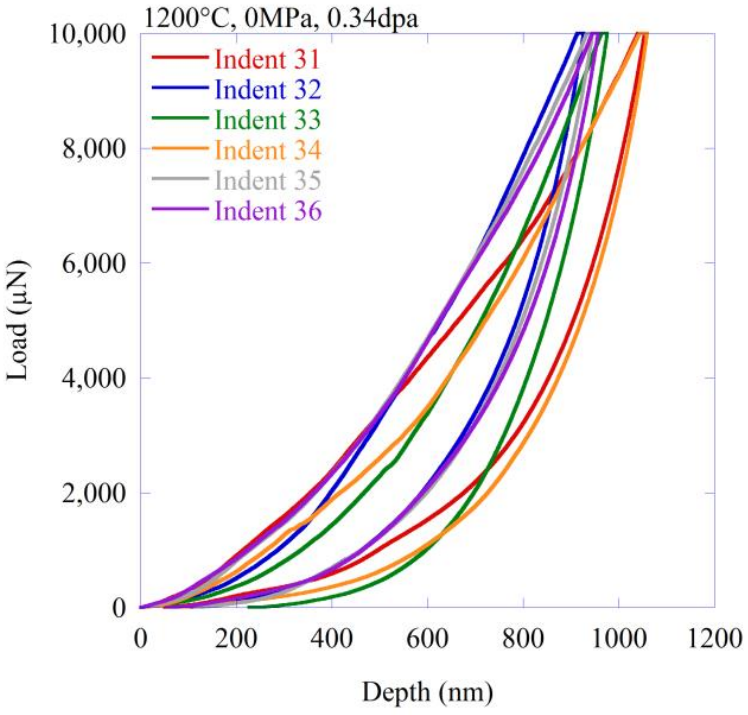

(b)

Figure D.35. Plots of load versus depth for nanoindentation #25-30 (a) and #31-36 (b) for the sample irradiated at 1200°C, 0MPa, to a final dose of 0.34dpa.

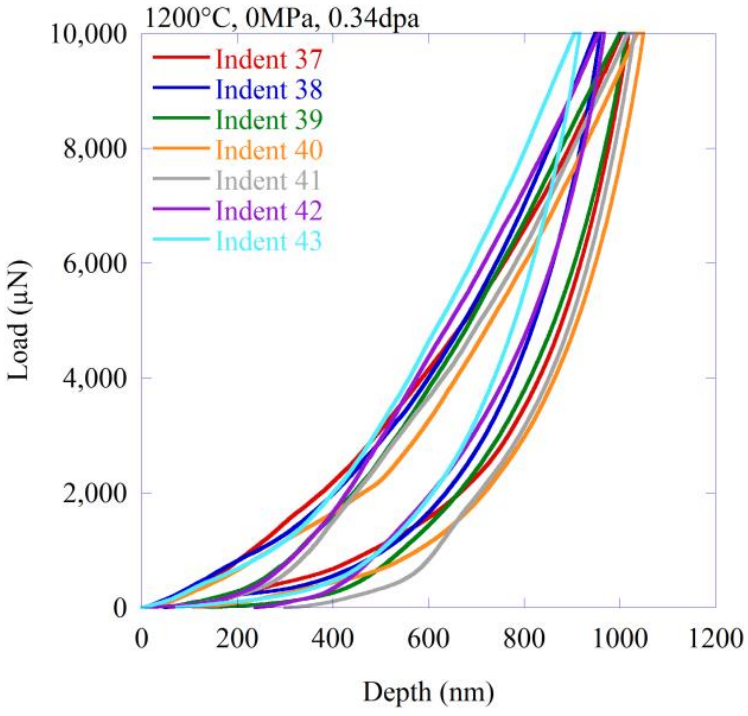

(a)

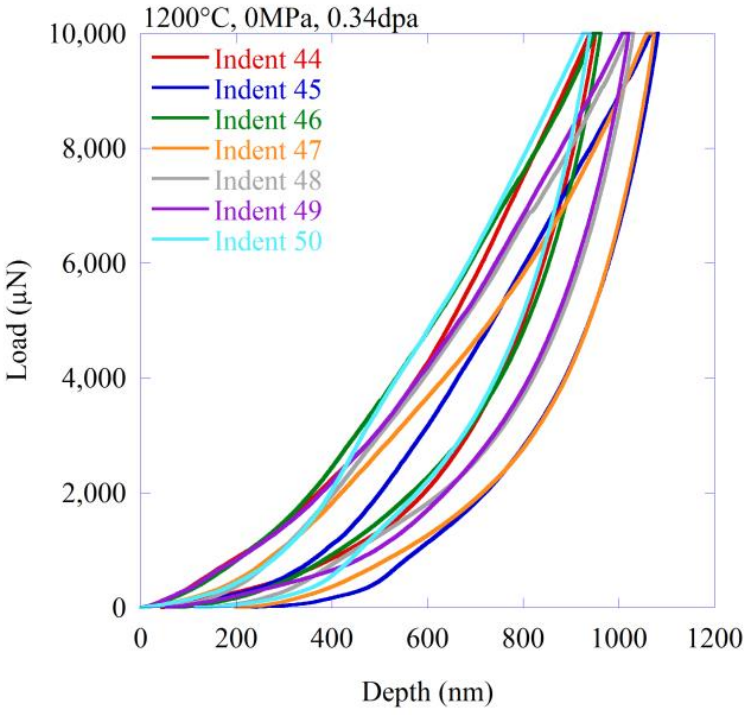

(b)

Figure D.36. Plots of load versus depth for nanoindentation #37-43 (a) and #44-50 (b) for the sample irradiated at 1200°C, 0MPa, to a final dose of 0.34dpa.

REFERENCES

1. Gougar, H.D., "The Very High Temperature Reactor", in *Nuclear Energy Encyclopedia*, 2011, John Wiley & Sons, Inc., p. 289-304.
2. Tsang, D.K.L. and B.J. Marsden, "The development of a stress analysis code for nuclear graphite components in gas-cooled reactors", *Journal of Nuclear Materials*, 350, (2006) 208-220.
3. Karthik, C., J. Kane, D.P. Butt, W.E. Windes, and R. Ubic, "Microstructural Characterization of Next Generation Nuclear Graphites", *Microscopy and Microanalysis*, FirstView, 1-7.
4. Baum, E.M., M.C. Ernesti, H.D. Knox, T.R. Miller, and A.M. Watson, "Nuclides and Isotopes Chart of the Nuclides", 17th ed, 2009, Bechtel Marine Propulsion Corporation.
5. Kelly, B.T., "Nuclear Reactor Moderator Materials", in *Materials Science and Technology, A Comprehensive Treatment*, Vol.10A, Part I, Brian R.T. Frost, Editor, 1994, VHC Publishers, New York, p. 366-417.
6. Nightingale, R.E., "Nuclear Graphite", 1962, New York, Academic Press.
7. Thrower, P.A. and R.M. Mayer, "Point defects and self-diffusion in graphite", *physica status solidi (a)*, 47, (1978) 11-37.
8. Montet, G.L., "Threshold energy for the displacement of atoms in graphite", *Carbon*, 5, (1967) 19-20, IN7-IN9, 21-23.
9. Kelly, B.T., "Physics of Graphite", 1981, London, Applied Science Publishers.
10. Telling, R.H. and M.I. Heggie, "Radiation defects in graphite", *Philosophical Magazine*, 87, (2007) 4797-4846.
11. Ewels, C.P., R.H. Telling, A.A. El-Barbary, M.I. Heggie, and P.R. Briddon, "Metastable Frenkel Pair Defect in Graphite: Source of Wigner Energy?", *Physical Review Letters*, 91, (2003) 025505.
12. Urita, K., K. Suenaga, T. Sugai, H. Shinohara, and S. Iijima, "In Situ Observation of Thermal Relaxation of Interstitial-Vacancy Pair Defects in a Graphite Gap", *Physical Review Letters*, 94, (2005) 155502.
13. Dienes, G.J., "Mechanism for Self-Diffusion in Graphite", *Journal of Applied Physics*, 23, (1952) 1194-1200.
14. Stone, A.J. and D.J. Wales, "Theoretical studies of icosahedral C60 and some related species", *Chemical Physics Letters*, 128, (1986) 501-503.
15. Amelinckx, A., "Dislocations in Particular Structures", in *Dislocations in Solids v.2 Dislocations in Crystals*, F.R.N. Nabarro, Editor, 1979, North-Holland Publishing Company, Amsterdam.
16. Wagner, P. and A.R. Driesner, "High-Temperature Mechanical Properties of Graphite. I. Creep in Compression", *Journal of Applied Physics*, 30, (1959) 148-151.
17. Wagner, P., A.R. Driesner, and L.A. Haskin, "High-Temperature Properties of Graphite. II. Creep in Tension", *Journal of Applied Physics*, 30, (1959) 152-154.
18. Zukas, E.G. and W.V. Green, "The high-temperature creep behavior of a highly-oriented polycrystalline graphite", *Carbon*, 6, (1968) 101-110.
19. Green, W.V., J. Weertman, and E.G. Zukas, "High-temperature creep of polycrystalline graphite", *Materials Science and Engineering*, 6, (1970) 199-211.
20. Jenkins, G.M., "Basal plane distortion in pyrolytic carbon", *Carbon*, 7, (1969) 9-14.

21. Burchell, T.D. and W.P. Eatherly, "The effects of radiation damage on the properties of GraphNOL N3M", *Journal of Nuclear Materials*, 179-181, Part 1, (1991) 205-208.
22. Kelly, B.T., W.H. Martin, A.M. Price, and J.T. Bland, "The mechanism of dimensional changes in the crystals of graphites and carbons under fast neutron irradiation", *Philosophical Magazine*, 14, (1966) 343-356.
23. Bridge, H., B.T. Kelly, and P.T. Nettley, "Effect of high-flux fast-neutron irradiation on the physical properties of graphite", *Carbon*, 2, (1964) 83-93.
24. Henson, R.W., A.J. Perks, and J.H.W. Simmons, "Lattice parameter and dimensional changes in graphite irradiated between 300 and 1350°C", *Carbon*, 6, (1968) 789-806.
25. Kelly, B.T. and T.D. Burchell, "Structure-related property changes in polycrystalline graphite under neutron irradiation", *Carbon*, 32, (1994) 499-505.
26. Ishiyama, S., T.D. Burchell, J.P. Strizak, and M. Eto, "The effect of high fluence neutron irradiation on the properties of a fine-grained isotropic nuclear graphite", *Journal of Nuclear Materials*, 230, (1996) 1-7.
27. Brocklehurst, J.E. and B.T. Kelly, "Analysis of the dimensional changes and structural changes in polycrystalline graphite under fast neutron irradiation", *Carbon*, 31, (1993) 155-178.
28. Bacon, G.E. and B.E. Warren, "X-ray diffraction studies of neutron-irradiated graphite", *Acta Crystallographica*, 9, (1956) 1029-1035.
29. Heggie, M.I., I. Suarez-Martinez, C. Davidson, and G. Haffenden, "Buckle, ruck and tuck: A proposed new model for the response of graphite to neutron irradiation", *Journal of Nuclear Materials*, 413, (2011) 150-155.
30. Karthik, C., J. Kane, D.P. Butt, W.E. Windes, and R. Ubic, "In situ transmission electron microscopy of electron-beam induced damage process in nuclear grade graphite", *Journal of Nuclear Materials*, 412, (2011) 321-326.
31. Perks, A.J. and J.H.W. Simmons, "Radiation-induced creep in graphite", *Carbon*, 1, (1964) 441-449.
32. Jenkins, G.M. and D.R. Stephen, "The temperature dependence of the irradiation induced creep of graphite", *Carbon*, 4, (1966) 67-72.
33. Gray, B.S., J.E. Brocklehurst, and A.A. McFarlane, "The Irradiation Induced Plasticity in Graphite Under Constant Stress", *Carbon*, 5, (1967) 173-180.
34. Brocklehurst, J.E. and R.G. Brown, "Constant stress irradiation creep experiments on graphite in BR-2", *Carbon*, 7, (1969) 487-488, IN9, 489-497.
35. Gray, W.J., "Constant stress irradiation-induced compressive creep of graphite at high fluences", *Carbon*, 11, (1973) 383-386, IN15, 387-392.
36. Oku, T., K. Fujisaki, and M. Eto, "Irradiation creep properties of a near-isotropic graphite", *Journal of Nuclear Materials*, 152, (1988) 225-234.
37. Oku, T., M. Eto, and S. Ishiyama, "Irradiation creep properties and strength of a fine-grained isotropic graphite", *Journal of Nuclear Materials*, 172, (1990) 77-84.
38. Kelly, B.T., "Irradiation creep in graphite--some new considerations and observations", *Carbon*, 30, (1992) 379-383.
39. Kelly, B.T. and T.D. Burchell, "The analysis of irradiation creep experiments on nuclear reactor graphite", *Carbon*, 32, (1994) 119-125.

40. Davies, M.A. and M. Bradford, "A revised description of graphite irradiation induced creep", *Journal of Nuclear Materials*, 381, (2008) 39-45.
41. Burchell, T.D., "Irradiation induced creep behavior of H-451 graphite", *Journal of Nuclear Materials*, 381, (2008) 46-54.
42. Kelly, B.T. and J.E. Brocklehurst, "Analysis of Irradiation Creep in Reactor Graphite", *Proceeding of the Proceedings of the Third Conference on Industrial Carbons and Graphite*, London, Society of Chemical Industry, April 14-17, 1970, (1971),
43. Roberts, A.C. and A.H. Cottrell, "Creep of Alpha Uranium During Irradiation with Neutrons", *Philosophical Magazine*, 1, (1956) 711-717.
44. Cottrell, A.H., "Effect of nuclear radiation on engineering materials", *Journal of the British Nuclear Energy Conference*, 5, (1960) 64-77.
45. Albers, T.L., "High-Temperature Properties of Nuclear Graphite", *Journal of Engineering for Gas Turbines and Power*, 131, (2009) 064501.
46. Malmstrom, C., R. Keen, and J.L. Green, "Some Mechanical Properties of Graphite at Elevated Temperatures", *Journal of Applied Physics*, 22, (1951) 593-600.
47. Gillin, L.M., "Deformation characteristics of nuclear grade graphites", *Journal of Nuclear Materials*, 23, (1967) 280-288.
48. POCO Graphite, Inc., "Properties and Characteristics of Graphite For Industrial Applications", Decature, TX, 2001.
49. Kelly, B.T. and J.E. Brocklehurst, "UKAEA Reactor Group studies of irradiation-induced creep in graphite", *Journal of Nuclear Materials*, 65, (1977) 79-85.
50. Kelly, B.T. and A.J.E. Foreman, "The theory of irradiation creep in reactor graphite--The dislocation pinning-unpinning model", *Carbon*, 12, (1974) 151-158.
51. Veringa, H.J. and R. Blackstone, "The irradiation creep in reactor graphites for HTR applications", *Carbon*, 14, (1976) 279-285.
52. Was, G.S., "Fundamentals of radiation materials science: metals and alloys", 2007, Berlin, Springer, 827.
53. The Stopping and Range of Ions in Matter (SRIM), Ziegler, J.F., M.D. Ziegler, and J.P. Biersack, 2008.04, 2008.
54. Busby, J.T., "Isolation of the Role of Radiation-Induced Segregation in Irradiation- Assisted Stress Corrosion Cracking in Proton-Irradiated Austenitic Stainless Steels", (University of Michigan, 2001)
55. Lam, N.Q., G. Leaf, and R.A. Johnson, "Defect buildup and solute segregation in alloys under pulsed irradiation", *Journal of Nuclear Materials*, 74, (1978) 277-289.
56. Null, M.R. and W. W. Lozier, "134. Spectral reflectance and emissivity of carbon and graphite", *Carbon*, 1, (1964) 393.
57. Autio, G.W. and E. Scala, "The normal spectral emissivity of isotropic and anisotropic materials", *Carbon*, 4, (1966) 13-28.
58. IRCON, *Stinger Thermal Imaging System*, 2006.
59. Bevington, P.R., "Data Reduction and Error Analysis for the Physical Sciences", 1969, McGraw-Hill, Inc.

60. Bacon, G.E., "Unit-Cell Dimensions of Graphite", *Acta Crystallographica*, 3, (1950) 137-139.
61. Hysitron Inc., *TI-950 TriboIndenter User Manual*, 2009.
62. Bacon, G.E., "A Method for Determining the Degree of Orientation of Graphite", *Journal of Applied Chemistry*, 6, (1956) 477-481.
63. Price, R.J. and J.C. Bokros, "Relationship between Preferred Orientation, Thermal Expansion, and Radiation-Induced Length Changes in Graphite", *Journal of Applied Physics*, 36, (1965) 1897-1906.
64. Campbell, A.A., K.B. Campbell, and G.S. Was, "Anisotropy analysis of ultra-fine grain graphite and pyrolytic carbon", *Carbon*, 60, (2013) 410-420.
65. POCO Graphite Inc., "ZXF-5Q Data Sheet", Accessed on: September 27, 2011, Available from: http://www.poco.com/MaterialsandServices/Graphite/IndustrialGrades/ZXF5Q/tabid/87/Default.aspx.
66. *GraphPad Prism 5.0 Learning Guide*, 2007, GraphPad Software Inc.
67. Tian, H.H. and M. Atzmon, "Comparison of X-ray analysis methods used to determine the grain size and strain in nanocrystalline materials", *Philosophical Magazine A*, 79, (1999) 1769-1786.
68. Williamson, G.K. and W.H. Hall, "X-ray line broadening from filed aluminium and wolfram", *Acta Metallurgica*, 1, (1953) 22-31.
69. Konishi, S. and G. Kitagawa, "Information Criteria and Statistical Modeling", 2008, New York, Springer Science.
70. Kelly, B.T., "Dimensional Changes and Lattice Parameter Changes in Graphite Crystals Due to Interstitial Atoms and Vacancies", *Proceeding of the Second Conference on Industrial Carbon and Graphite: Papers Read at the Conference Held in London, 7th-9th April, 1965, with the Discussions that Followed*, Society of Chemical Industry, (1966), 483-492.
71. Reynolds, W.N. and P.A. Thrower, "The nucleation of radiation damage in graphite", *Philosophical Magazine*, 12, (1965) 573-593.
72. Kelly, B.T., "Basal Plane Contraction in Graphite Due to Mono-Vacancies", *Nature*, 207, (1965) 257-259.
73. Kelly, B.T., W.H. Martin, A.M. Price, P. Dolby, and K. Smith, "The annealing of irradiation damage in graphite", *Journal of Nuclear Materials*, 20, (1966) 195-209.
74. Richards, B.P. and E.A. Kellett, "Changes in the structure of graphite on irradiation under restraint", *Journal of Nuclear Materials*, 25, (1968) 45-57.
75. "Carbon Materials for Advanced Technologies", ed. Timothy D. Burchell, 1999.
76. Papadakis, E., "Ultrasonic Wave Measurements of Elastic Moduli E, G, and μ for Product Development and Design Calculations", *ASTM - Journal of Testing and Evaluation*, 26, (1998) 240-246.
77. Marsden, B.J. and G.N. Hall, "4.11 - Graphite in Gas-Cooled Reactors", in *Comprehensive Nuclear Materials*, J. M. Konings Rudy, Editor, 2012, Elsevier, Oxford, p. 325-390.
78. Simmons, J.H.W., "Radiation damage in graphite", International Series of Monographs in Nuclear Energy, Vol. 102, 1965, Oxford, New York, Pergamon Press.

79. IAEA, "Irradiation Damage in Graphite due to Fast Neutrons in Fission and Fusion Systems", IAEA-TECDOC-1154, 2000.
80. Kinchin, G.H. and R.S. Pease, "The Displacement of Atoms in Solids by Radiation", *Reports on Progress in Physics*, 18, (1955) 1-51.
81. Reynolds, W.N. and J.H.W. Simmons, "The Effect of High Flux Neutron Irradiation on the Physical Properties of Graphite", *Proceeding of the Fifth Conference on Carbon*, University Park, Pennsylvania, Vol.1, Pergamon Press, June 19 - 23, (1961), 255-265.
82. Kelly, B.T., D. Jones, and A. James, "Irradiation damage to pile grade graphite at 450° C", *Journal of Nuclear Materials*, 7, (1962) 279-291.
83. Reynolds, W.N., "Radiation Damage in Graphite", in *Chemistry and Physics of Carbon*, Vol.2, P.L. Walker Jr., Editor, 1966, Marcel Dekker, New York, p. 121-196.
84. Nikolaenko, V.A. and V.I. Karpukhin, "Change in the properties of graphite and diamond when irradiated in a reactor for thermal and radiational γ-annealing", *Atomic Energy*, 82, (1997) 81-85.
85. Nikolaenko, V.A., V.I. Karpukhin, V.N. Kuznetsov, P.A. Platonov, V.M. Alekseev, O.K. Chugunov, Y.I. Shtrombakh, V.D. Baldin, B.S. Rodchenkov, Y.I. Smirnov, A.V. Subbotin, Y.É. Khandomirov, and I.G. Lebedev, "Effect of the composition of radiation on the radiation damage to graphite", *Atomic Energy*, 87, (1999) 480-484.
86. Burchell, T.D., "Neutron Irradiation Damage in Graphite and Its Effects on Properties", *Proceeding of the International Carbon Conference CARBON 2002*, Beijing, China, September 15-20, 2002, (2002), Paper # H095.
87. Xu, Z., L. Liu, Y. Huang, Y. Sun, X. Wu, and J. Li, "Graphitization of polyacrylonitrile carbon fibers and graphite irradiated by γ rays", *Materials Letters*, 63, (2009) 1814-1816.
88. Li, B., Y. Feng, K. Ding, G. Qian, X. Zhang, and J. Zhang, "The effect of gamma ray irradiation on the structure of graphite and multi-walled carbon nanotubes", *Carbon*, 60, (2013) 186-192.
89. Goggin, P.R., R.W. Henson, A.J. Perks, and W.N. Reynolds, "Dimensional changes in the irradiated graphite lattice", *Carbon*, 1, (1964) 189-200.
90. Matthews, J.R. and M.W. Finnis, "Irradiation creep models — an overview", *Journal of Nuclear Materials*, 159, (1988) 257-285.
91. Mitchell, B.C., B.J. Marsden, J. Smart, and S.L. Fok, "An irradiation creep law evaluated for nuclear graphite a high dose and temperature", *Nuclear Energy*, 41, (2002) 63-68.
92. Perks, A.J. and J.H.W. Simmons, "Dimensional changes and radiation creep of graphite at very high neutron doses", *Carbon*, 4, (1966) 85-98.